R Nityananda
Raman Research Institute [illegible]

Associate Editor

H R Krishnamurthy
Indian Institute of Science [illegible]

Editorial Board

G S Agarwal, [illegible]
V Balakrishnan, [illegible]
J K Bhattacharjee, [illegible]
D N Bose, [illegible]
B M Deb, [illegible]
Rohini M Godbole, [illegible]
S Kailas, [illegible]
R K Kaul, [illegible]
A V Khare, [illegible]
T Padmanabhan, [illegible]
R Ramaswamy, [illegible]
A K Raychaudhuri, [illegible]
K C Rustagi, [illegible]
E V Sampathkumaran, [illegible]
Abhijit Sen, [illegible]
S K Sikka, [illegible]
Y Singh, [illegible]

Editor of Publications of the Academy

V K Gaur
[illegible]

Annual Subscription Rates

All countries except India [illegible]
(Price includes AIR MAIL charges)

India [illegible]

Annual subscriptions for **individuals** [illegible]

All correspondence regarding subscription [illegible] **Circulation Department** of the Academy

Editorial Office

Indian Academy of Sciences, C V Raman Avenue [illegible]
P.B. No. 8005, Bangalore 560 080, India

[illegible]
[illegible]
[illegible]

Pramana – journal of physics

Volume 48
1996

Published by

Editor

R Nityananda
Raman Research Institute, Bangalore

Associate Editor

H R Krishnamurthy
Indian Institute of Science, Bangalore

Editorial Board

G S Agarwal, *Physical Research Laboratory, Ahmedabad*
V Balakrishnan, *Indian Institute of Technology, Madras*
J K Bhattacharjee, *Indian Assoc. for the Cultivation of Science, Calcutta*
D N Bose, *Indian Institute of Technology, Kharagpur*
B M Deb, *Panjab University, Chandigarh*
Rohini M Godbole, *Indian Institute of Science, Bangalore*
S Kailas, *Bhabha Atomic Research Centre, Bombay*
R K Kaul, *The Institute of Mathematical Sciences, Madras*
A V Khare, *Institute of Physics, Bhubaneswar*
T Padmanabhan, *Inter-Univ. Centre for Astronomy and Astrophysics, Pune*
R Ramaswamy, *Jawaharlal Nehru University, New Delhi*
A K Raychaudhuri, *Indian Institute of Science, Bangalore*
K C Rustagi, *Centre for Advanced Technology, Indore*
E V Sampathkumaran, *Tata Institute of Fundamental Research, Bombay*
Abhijit Sen, *Institute for Plasma Research, Gandhinagar*
S K Sikka, *Bhabha Atomic Research Centre, Bombay*
Y Singh, *Banaras Hindu University, Varanasi*

Editor of Publications of the Academy

V K Gaur
C-MMACS, NAL, Bangalore

Annual Subscription Rates

All countries except India (Price includes AIR MAIL charges)	US$ 200
India	Rs. 200

Annual subscriptions for **individuals** for India and abroad are Rs. 100/- and $50 respectively.

All correspondence regarding subscription should be addressed to the **Circulation Department** of the Academy

---

Editorial Office

Indian Academy of Sciences, C V Raman Avenue,
P.B. No. 8005, Bangalore 560080, India

Telephone: 334 2546
Telex: 845-2178 ACAD IN
Telefax: 91-80-334 6094

Pramana – journal of physics

CONTENTS – VOLUME 48

(January – June 1997)

Numbers 1 and 2

Special Issue on Nonlinearity and Chaos in the Physical Sciences – Parts I and II

Editors' note 1

Preface 3

Mathematical aspects of dynamical systems

Random matrices and matrix models: The JNU lectures .. *Madan Lal Mehta* 7

Hölder exponents of irregular signals and local fractional derivatives .... *Kiran M Kolwankar and Anil D Gangal* 49

Signature of chaos in power spectrum .... *M C Valsakumar, S V M Satyanarayana and V Sridhar* 69

Dynamics of simple one-dimensional maps under perturbation .... *Somdatta Sinha and Parichay K Das* 87

Chaos in modulated logistic systems .... *V M Nandakumaran* 99

Effect of boundary conditions on the invariant density of noisy maps at fully-developed chaos .... *V Balakrishnan, G Nicolis and C Nicolis* 109

Symplectic integration of nonlinear Hamiltonian systems .... *Govindan Rangarajan* 129

Integrable systems and solitons

Painlevé analysis and integrability aspects of some nonlinear partial differential equations .... *K Porsezian* 143

Localized coherent structures of $(2 + 1)$ dimensional generalizations of soliton systems .... *M Lakshmanan and R Radha* 163

Geometry and nonlinear evolution equations .... *Radha Balakrishnan* 189

Nonlinear chiral models: Soliton solutions and spatio-temporal chaos .... *M S Sriram and J Segar* 205

Spatio-temporal chaos, synchronization and control

Characterization and control of chaotic dynamics in a nerve conduction model equation........*S Rajasekar*

Control of chaos........*Sangeeta D Gadre and V S Varma*

Effect of noise on coupled chaotic systems........*Manojit Roy and R E Amritkar*

Lattice dynamical models of adaptive spatio-temporal phenomena........*Sudeshna Sinha*

Control of spatio-temporal chaos: A study with an autocatalytic reaction-diffusion system........*Nita Parekh, V Ravi Kumar and B D Kulkarni*

Turbulence

Some recent advances in the theory of homogeneous isotropic turbulence........*Sujan K Dhar, Anirban Sain, Ashwin Pande and Rahul Pandit*

The randomly stirred fluid–Turbulence as a problem in statistical mechanics........*J K Bhattacharjee*

Quantum aspects of chaos

Chaos in the hydrogen atom interacting with external fields........*K Ganesan and R Gębarowski*

Resonances and chaos in the collinear collision system (He, H_2^+) and its isotopic variants........*Susanta Mahapatra, N Sathyamurthy and Ramakrishna Ramaswamy*

Chaos in intrinsic motion of nuclei and its role in dissipative collective dynamics........*Santanu Pal*

Chaos and localization in coupled quartic oscillators........*M S Santhanam, V B Sheorey and A Lakshminarayan*

Experiments on quantum chaos using microwave cavities: Results for the pseudo-integrable L-billiard........*A Kudrolli and S Sridhar*

Quantum chaology: The photoeffect and beyond........*Bala Sundaram*

Periodic orbits in polygonal billiards........*Debabrata Biswas*

Semiclassical theory for many-body fermionic systems........*Pierre Gaspard and Sudhir R Jain*

Accuracy of trace formulas........*Arul Lakshminarayan*

The phase of the Riemann zeta function........*Avinash Khare*

Exotic spectra, wavefunctions and transport in incommensurate lattices........*A Lahiri, TK Roy and A Bhowal*

Fractal characteristics of critical and localized states in incommensurate quantum systems........*Indubala I Satija and Jukka A Ketoja*

pplications

ynamical signatures of 'phase transitions': Chaos in finite clusters.......... ....*Vishal Mehra, Saroj K Nayak and Ramakrishna Ramaswamy* 603

assical gauge theories as dynamical systems—Regularity and chaos....... ....*S Lakshmibala, Bindu A Bambah, M S Sriram and C Mukku* 617

haos in Josephson junctions..*G Ambika* 637

ollective thermalization in quark gluon plasma................................ ....*S Sengupta, J R Bhatt, P K Kaw and J C Parikh* 655

onlinear propagation of relativistically intense electromagnetic waves in collisionless plasma....................................*P K Kaw and A Sen* 675

he onset of chaos in the wake of an oscillating cylinder: Experiment and the ynamics of the circle map.. ....*D J Olinger, A B Chhabra and K R Sreenivasan* 693

haos in jerky flow—Experimental verification of a theoretical prediction ....*S J Noronha, G Ananthakrishna, L Quaouire and C Fressengeas* 705

haos and predictability of the Indian summer monsoon......*B N Goswami* 719

ome recent applications of cell dynamical modelling to phase ordering ynamics...*Sanjay Puri* 737

oisy nonlinear coupled equations—Some new insights...................... ....*J K Bhattacharjee, Anita Mehta and J M Luck* 749

onlinear fluctuating hydrodynamics and sequence of time scales of relaxion in supercooled liquids......................................*Shankar P Das* 759

Number 3

he Larmor nutation.................*K N Srinivasa Rao and A V Gopala Rao* 775

oherent and squeezed states on physical basis.......................*R R Puri* 787

lassical limit of scattering in quantum mechanics – A general approach..... ....*D Sen, A N Basu and S Sengupta* 799

reation or destruction of sourceless abelian gauge strings in a Robertson–/alker universe.................................*D Bhattacharyya and S Banerji* 811

igher dimensional Vaidya metric in Einstein and de Sitter background..... ....*L K Patel and Lakshmi S Desai* 819

Rapid Communication

Helium atom in intense and superintense laser fields: A new theoretical approach.......................................*Bijoy Kr Dey and B M Deb* 849

Number 4

Surface harmonics for pentagonal point groups.................................
.......................*K Rama Mohana Rao, P Hemagiri Rao and V Satyavathi* 859

Characterization of chaos in a serrated plastic flow model....................
.................................*S V M Satyanarayana, V Sridhar and S Koka* 871

Structural phase transition in substituted La_2CuO_4 and Pr_2CuO_{4-y}.........
................*Meena Chaudhri, Kunal B Modi, K M Jadhav and G K Bichile* 883

A stochastic model for solidification II. Application to binary metallic melts
...............................*Shobha Dass, Gautam Johri and Lakshman Pandey* 891

Superconducting state parameters of metallic glass $Mg_{70}Zn_{30}$ using linearized screened pseudopotential..............*Manish Gupta, K S Sharma and L Dass* 923

Electron paramagnetic resonance studies of photorefractive crystals II: Fe^{3+} doped $Bi_{12}SiO_{20}$ with copper vapour laser illumination in 10–100 K range
....*N K Porwal, R M Kadam, Y Babu, M D Sastry, M D Aggarwal and Putcha Venkateswarlu* 929

Resonance de-enhancement in the $2^1\ A_g$ state of *trans*-azobenzene...........
....*Nandita Biswas and Siva Umapathy* 937

Brief Report

Kramers–Kronig analysis of the reflectance spectra of Pb-doped Bi-4334 type glass and the corresponding glass-ceramic super-conductor....................
...............................*Souri Banerjee, S Chatterjee and B K Chaudhuri* 951

Number 5

The geometric phase and ray space isometries..................*Joseph Samuel* 959

Thomas rotation and polarized light: A non-abelian geometric phase in optics
....*Joseph Samuel and Supurna Sinha* 969

On periodically kicked quantum systems........................*N D Sen Gupta* 977

Weak decay constants of light and heavy pseudoscalar mesons...............
....*N Barik, S Kar and P C Dash* 985

Meson spectroscopy with confined one gluon exchange potential.............
.............................*K B Vijaya Kumar, A K Rath and S B Khadkikar* 997

Two body non-leptonic decays $B \to D\pi$ with heavy quark and chiral symmetry
A K Giri, L Maharana and R Mohanta 1005

Solution of approximate gluon evolution equation for small-x at fixed β .... *A Saikia* 1015

Heavy-ion scattering at low energies: First-order correction to the eikonal phase shift........ *S K Charagi* 1021

Semi-empirical formulae for Λ-binding energy in hypernuclei using mass distribution........ *M Z Rahman Khan, Nasra Neelofer and M A Suhail* 1027

Group theoretical aspects of $U^{B}(6)\otimes U^{F}(20)$ symmetry limits of IBFM related to the $U^{B}(5)$ and $O^{B}(6)$ limits of IBM........ *V K B Kota* 1035

Photon interaction cross-sections and anomalous scattering factors of Cu and Ag........ *Sandiago, T K Umesh and Ramakrishna Gowda* 1077

Number 6

Probability distribution of normalized structure factor magnitudes for a centrosymmetric crystal with planar molecules in the unit cell........ *Sabita Das and G B Mitra* 1091

Activation energy of hydrogen in Lu........ *N Singh and B Kumar* 1095

Electron momentum density distribution in iridium by Compton scattering technique........ *K B Joshi, R K Pandya, B L Ahuja and B K Sharma* 1105

Magnetic behaviour of TbMnFe........ *Keka Chakraborty, S K Paranjpe, V Siruguri, O D Jayakumar and S K Kulshreshtha* 1115

Spin state and exchange in the quasi-one-dimensional anti-ferromagnet $KFeS_2$........ *Satish Kumar Tiwary and Sukumaran Vasudevan* 1123

Field emission theory of dislocation-sensitized photo-stimulated exo-electron emission from coloured alkali halide crystals........ *B P Chandra, R S Chandok and P K Khare* 1135

Thermal quenching of luminescence in erbium doped semiconductors........ *B Chanda and D N Bose* 1145

Spectroscopic properties of Er^{3+} ions in cadmium and alkali cadmium borosulphate glasses........ *C K Jayasankar and V V Ravi Kanth Kumar* 1151

Collisional excitation among the seven lowest states of TiXII........ *M Mohan and A Hibbert* 1161

Brief Report

Compton profiles of electron momentum distribution in β-Ga........ *B K Acharya and N C Mohapatra* 1169

PRAMANA
journal of
physics

© Printed in India

Vol. 48, No. 3,
March 1997
pp. 775–786

The Larmor nutation

K N SRINIVASA RAO and A V GOPALA RAO
Department of Studies in Physics, University of Mysore, Manasagangotri, Mysore 570006,
ndia

MS received 10 June 1996; revised 22 November 1996

Abstract. The classical non-relativistic problem of the motion of a charged particle in an xternal central force field and a weak uniform magnetic field is revisited to show that the motion f the kinetic angular momentum $\mathbf{L} = \mathbf{r} \times \mathbf{p}$ of the particle, in the so-called Larmor approximation, is not a simple precession but is actually a composite motion involving precession as well s a high frequency nutation. The precession-nutation motion of $\mathbf{L}$ is discussed in the Larmor approximation when the Larmor-frame-orbit of the charged particle is an ellipse (or a circle) for ne case of the two central forces namely the Coulomb and the Hooke-law-force, which are the nly two central forces known to permit closed orbits.

Keywords. Larmor precession and nutation; charged-particle orbits in electromagnetic fields; tom in a magnetic field.

PACS Nos **03·20; 32·30; 31·90; 32·60; 41·90; 46·90**

. Introduction

t appears that only one exact solution is available for the classical non-relativistic roblem of a charged particle moving under the combined influence of an attractive entral electric field and a uniform magnetic field. This special solution describes the ircular orbit of a charged particle in a plane perpendicular to the applied uniform nagnetic field. More general exact solutions for this problem do not exist although variety of approximate solutions may be obtained through Larmor's theorem. Larmor's theorem as applied to this problem [1–5] implies that every bounded-orbit [6] of the charged particle moving in an inertial frame under the action of the central orce field and a sufficiently weak magnetic field is approximately a bounded orbit in he same central field, but without the magnetic field, when viewed from an appropriate otating frame called the Larmor frame. If we assume that the motion of the charged particle in such a precessing orbit generates a 'pointlike magnetic dipole-moment whose magnitude is not affected by the motion it undergoes' [4], then it follows that the magnetic dipole precesses uniformly with the Larmor frequency [7]. The assumption hat the orbit is a pointlike magnetic moment is appropriate to permanent magnets or

Since the Larmor theorem is valid for macroscopic orbits also, we may expe
under the conditions of validity of the Larmor theorem, the motion of the vector
be more complex than a simple precession unlike in the case of microscopic
Secondly, since a precessing charged particle orbit is essentially a 'magnetic-to
may expect the Larmor motion of **L** to involve nutation also in complete analog
the problem of a massive top in a gravitational field. In fact, Landau and Lifsh
show that in the case of a point charge executing bounded periodic motion un
influence of a central electrostatic field and a weak magnetic field, a suitabl
averaged motion of **L** is the familiar Larmor precession. In this paper, by rest
ourselves to a study of the motion of **L** in the Larmor approximation, we show t
detailed motion of **L** consists of a precession as well as a high frequency nutati

2. Equation of motion for L and its solution in the Larmor approximation

The equation of motion of a negatively-charged particle [9] of charge $-q < 0$ an
m, moving in an inertial frame under the combined influence of an external centr
field $f(r)\hat{\mathbf{r}}$ and a uniform magnetic field **B** is given by

$$\mathrm{d}(m\mathbf{v})/\mathrm{d}t = f(r)\hat{\mathbf{r}} - q\mathbf{v} \times \mathbf{B}/c,$$

where **r** is the position vector of the particle, $\hat{\mathbf{r}}$ is a unit vector along **r**, $\mathbf{v} = \mathrm{d}\mathbf{r}/\mathrm{d}$
velocity of the particle and c is the speed of light in vacuum. (Note: We w
Gaussian CGS units.) On cross-multiplying this equation by **r**, we get

$$\mathrm{d}\mathbf{L}/\mathrm{d}t = -2m\mathbf{r} \times (\mathbf{v} \times \boldsymbol{\omega}),$$

where $\mathbf{L} = \mathbf{r} \times \mathbf{mv}$ is the kinetic angular momentum of the particle,

$$\boldsymbol{\omega} \equiv q\mathbf{B}/2mc,$$

and $|\boldsymbol{\omega}|$ is the 'Larmor frequency'. Now, if we write the term $-2m\mathbf{r} \times (\mathbf{v} \times \boldsymbol{\omega})$ as t
of two equal halves, express one of them using the Jacobi identity as

$$-m\mathbf{r} \times (\mathbf{v} \times \boldsymbol{\omega}) = m\mathbf{v} \times (\boldsymbol{\omega} \times \mathbf{r}) + m\boldsymbol{\omega} \times (\mathbf{r} \times \mathbf{v}),$$

and add it to the other in equation (2.2), we obtain

$$\mathrm{d}\mathbf{L}/\mathrm{d}t = \boldsymbol{\omega} \times \mathbf{L} + \mathrm{d}\boldsymbol{\Lambda}/\mathrm{d}t,$$

where we have defined

$$\boldsymbol{\Lambda} \equiv m\mathbf{r} \times (\boldsymbol{\omega} \times \mathbf{r}).$$

Although (2.2) and (2.4) are the same, the latter is more convenient in discuss
motion of **L**. In fact (2.4) shows at once [10] that the motion of **L** would be
precession around **B** only when the second term $\mathrm{d}\boldsymbol{\Lambda}/\mathrm{d}t$ on the right hand side of
either zero or is negligible in comparison with the first term $\boldsymbol{\omega} \times \mathbf{L}$. Since bot
terms are of the same order in **B**, it is clear that the motion of **L** can never be a
precession however weak the magnetic field **B** may be.

The vector $\boldsymbol{\Lambda}$ above has a simple interpretation from the standpoint of the sc
Larmor frame, i.e., a reference frame which rotates with the angular velocity $\boldsymbol{\omega}$

eferred to the Larmor frame by an asterisk (*) and the time-rates-of-change with respect to the inertial and Larmor frames by d/dt and d*/dt respectively, then we have [5]

$$\mathrm{d}\mathbf{A}/\mathrm{d}t = \mathrm{d}^*\mathbf{A}/\mathrm{d}t + \boldsymbol{\omega} \times \mathbf{A},$$

which is a general relation valid for all vector functions $\mathbf{A}(t)$. Also, we assume that the origins of the two frames coincide, so that we have $\mathbf{r}(t) = r^*(t)$ and this relation together with the fact that $\boldsymbol{\omega}$ is a constant, leads to the following well-exploited relations for velocity and acceleration:

$$\mathbf{v} = \mathbf{v}^* + \boldsymbol{\omega} \times \mathbf{r}; \quad \mathbf{v} \equiv \mathrm{d}\mathbf{r}/\mathrm{d}t; \quad \mathbf{v}^* \equiv \mathrm{d}^*\mathbf{r}/\mathrm{d}t; \tag{2.6}$$

$$\mathbf{a} = \mathbf{a}^* + 2\boldsymbol{\omega} \times \mathbf{v}^* + \boldsymbol{\omega} \times (\boldsymbol{\omega} \times \mathbf{r}); \quad \mathbf{a} \equiv \mathrm{d}\mathbf{v}/\mathrm{d}t; \quad \mathbf{a}^* \equiv \mathrm{d}^*\mathbf{v}^*/\mathrm{d}t. \tag{2.7}$$

In the same manner, we obtain the following relation connecting kinetic angular momenta in the two frames of reference

$$\mathbf{L} = \mathbf{L}^* + \boldsymbol{\Lambda}; \quad \mathbf{L} \equiv \mathbf{r} \times m\mathbf{v}; \quad \mathbf{L}^* \equiv \mathbf{r} \times m\mathbf{v}^*. \tag{2.8}$$

This relation, somehow, seems to have received little attention in the literature. The vector $\mathbf{L}^*$ in the above equation may be interpreted as the angular momentum relative to the rotating frame and the vector $\boldsymbol{\Lambda}$ as the angular momentum of transport. To appreciate the significance of $\boldsymbol{\Lambda}$ we may note that, for example, in the case of a rigid body, the vector $\mathbf{L}^* = \sum \mathbf{r} \times m\,\mathbf{v}^*$ (where the summation extends over all the constituent particles) vanishes in the body rest frame and therefore the entire angular momentum appears as the transport angular momentum $\boldsymbol{\Lambda}$ in this frame.

On using (2.6)–(2.8), (2.1) and (2.4), we obtain

$$m\mathbf{a}^* = m\mathrm{d}^{*2}\mathbf{r}/\mathrm{d}t^2 = f(r)\,\hat{\mathbf{r}} + m\boldsymbol{\omega} \times (\boldsymbol{\omega} \times \mathbf{r}) \tag{2.9}$$

and

$$\mathrm{d}^*\mathbf{L}^*/\mathrm{d}t = \boldsymbol{\omega} \times \boldsymbol{\Lambda}, \tag{2.10}$$

which are exact equations corresponding to (2.1) and (2.2), but written in the rotating Larmor frame. In the so-called Larmor approximation which corresponds to situations in which the magnetic field $\mathbf{B}$ is sufficiently weak and orbit of the particle is bounded in the sense described earlier, we neglect the second term on the right hand side of (2.9) in comparison with the first and obtain

$$m\,\mathrm{d}^{*2}\mathbf{r}/\mathrm{d}t^2 \approx f(r)\,\hat{\mathbf{r}}. \tag{2.11}$$

Taking the vector product of this equation with $\mathbf{r}$ then yields

$$\mathrm{d}^*\mathbf{L}^*/\mathrm{d}t \approx 0, \tag{2.12}$$

which is the equation of motion of $\mathbf{L}^*$ in the Larmor approximation. Thus, in the Larmor approximation, $\mathbf{L}^*$ is a constant as viewed from the rotating frame, or, equivalently, it is a precessing vector satisfying

$$\mathrm{d}\mathbf{L}^*/\mathrm{d}t \approx \boldsymbol{\omega} \times \mathbf{L}^*, \tag{2.13}$$

as viewed from the inertial frame. It is gratifying to note that there is at least one angular in the Larmor approximation. However, it is **L**, and not $\mathbf{L}^*$, which is the a momentum of the particle in the inertial frame and in view of (2.8), the motion o the inertial frame) is more complex than a simple precession because **L** is the a precessing vector $\mathbf{L}^*$ and the (moving) vector $\mathbf{\Lambda}$.

In passing, we make an interesting observation on the canonical angular mom $\mathbf{L}_c \equiv \mathbf{r} \times (\mathbf{p} - q\mathbf{A}/c)$ of the charged particle in this problem. In a suitable gau vector potential for a uniform magnetic field **B** may be written as $\mathbf{A} = -\mathbf{r} \times \mathbf{B}/2$ this **A**, we obtain $\mathbf{L}_c = \mathbf{L} - \mathbf{\Lambda}$. Comparing this with (2.8) then shows that $\mathbf{L}_c =$ view of this relation, (2.13) may also be interpreted as describing the Larmor pre of $\mathbf{L}_c$. Larmor's theorem in this form, for $\mathbf{L}_c$, may also be obtained directly withou the rotating frame [11].

We now proceed to determine the motion of **L** in the inertial frame. First, we m very briefly about the only exact solution available for equation (2.1). This so describes the uniform circular motion of a particle of charge $-q$ and mass m Coulomb force field of a positive charge q' at rest at the origin of coordinates inertial frame. With a denoting the radius of the circle and $|\omega|$ denoting the co angular frequency, the solution mentioned is given by $\mathbf{r} = (a\cos\omega' t, a\sin\omega' t, 0)$, $\omega' \equiv \omega \pm \sqrt{\omega_0^2 + \omega^2}$; $\omega = q|\mathbf{B}|/2mc$; $\omega_0 = \sqrt{qq'/ma^3} > 0$ and the z-axis of the i frame has been chosen such that $\mathbf{B} = (0, 0, B)$. A simple calculation then $\mathbf{L} = (0, 0, ma^2\omega') =$ constant. (For a further discussion of this solution see the fol references: Purcell [12], Reitz *et al* [13] or Matveev [14].) Leaving aside thi solution which anyway has a constant **L** and is therefore not of interest to consider approximate solutions of equation (2.1) obtained through the Larm orem. (In fact, our interest in these solutions is restricted to a study of the motio angular momenta rather than the orbits themselves.) We have a simple prescript obtaining the orbital angular momentum vector associated with any such solu (2.1) obtained through the Larmor theorem: First, we pick up an arbitrary bo orbit solution $\mathbf{r} = \mathbf{r}_0(t)$ of the problem (2.11). (It is important to note that $\mathbf{r}_0(t)$ so is in fact an exact central force orbit and not an approximate one as required by Then, using this vector $\mathbf{r}_0(t)$, we calculate vector field $\mathbf{\Lambda}(t)$ defined in (2.5). N calculate the conserved orbital angular momentum vector $\mathbf{L}^* = \mathbf{r}_0 \times (m\,\mathrm{d}\mathbf{r}_0/\mathrm{d}t)$ orbit and use it to obtain the vector field $\mathbf{L} = \mathbf{L}^* + \mathbf{\Lambda}$, which is the required angular momentum in the inertial frame (in the Larmor approximation).

We now use this prescription and calculate the **L** associated with an arbitrar solution $\mathbf{r}_0(t)$ of (2.11). Let $\mathbf{r}_0(t)$ expressed in the basis $(\mathbf{i}, \mathbf{j}, \mathbf{k})$ of the inertial frame be g

$$\mathbf{r}_0(t) = x(t)\mathbf{i} + y(t)\mathbf{j} + z(t)\mathbf{k}.$$

Further, let the z-axis of the inertial frame be chosen such that **B** is para antiparallel to **k**. Then

$$\boldsymbol{\omega} = \omega\mathbf{k},$$

hence satisfies (2.13) (now exactly, as $\mathbf{r}_0(t)$ is an exact solution of (2.11)), we may take it to be the general solution of (2.13) given below:

$$\mathbf{L}^* = L_0(\sin\theta\sin\varphi\mathbf{i} - \sin\theta\cos\varphi\mathbf{j} + \cos\theta\mathbf{k}). \tag{2.17}$$

Here L_0 and θ are two constants of integration and [15]

$$\varphi = \omega t. \tag{2.18}$$

The angles $\theta =$ constant and $\varphi - \pi/2 = \omega t - \pi/2$ are evidently the polar and azimuthal angles of $\mathbf{L}^*$ with respect to the inertial frame $(\mathbf{i}, \mathbf{j}, \mathbf{k})$ and these angles clearly show that the vector $\mathbf{L}^*$ precesses around the z-axis with angular frequency $|\omega|$. Now using (2.8), (2.14) and (2.17), we get $\mathbf{L}$ to the desired Larmor approximation as

$$\mathbf{L} = L_x\mathbf{i} + L_y\mathbf{j} + L_z\mathbf{k}, \tag{2.19}$$

where

$$L_x = L_0\sin\theta\sin\varphi - m\omega xz;\ L_y = -L_0\sin\theta\cos\varphi - m\omega yz;$$

$$L_z = L_0\cos\theta + m\omega(x^2 + y^2). \tag{2.20}$$

These equations yield $\mathbf{L}$ once the central force orbit $\mathbf{r}_0(t)$ is specified as in (2.14). This solves the problem in principle. However, in actual calculations it is more convenient to specify the planar orbit $\mathbf{r}_0(t)$ in terms of two variables rather than in terms of the three variables x, y, z as done above. We do this by introducing the rotating Larmor frame $(\mathbf{I}, \mathbf{J}, \mathbf{K})$ with corresponding coordinates, X, Y, Z, as follows [16]. The plane of $\mathbf{r}_0(t)$ is taken to be the $X - Y$ plane so that $\mathbf{L}^*$ is always along the Z-axis. Further, we choose the X-axis to lie along the line of nodes formed by the $X - Y$ plane with the plane of the orbit $\mathbf{r}_0(t)$ as shown in figure 1. Then, constructing the rotation matrix connecting the

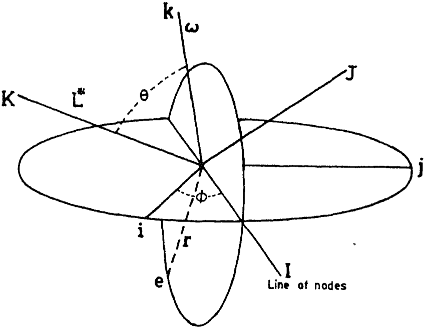

Figure 1. Euler angles specifying the orientation of the Larmor frame relative to the laboratory (inertial) frame.

relating the two frames:

$$x = X\cos\varphi - Y\cos\theta\sin\varphi,\ \ y = X\sin\varphi + Y\cos\theta\cos\varphi,\ \ z = Y\sin\theta.\ ($$

Substituting these in equation (2.20), we finally obtain the required formulae

$$L_x = L_0\sin\theta\sin\varphi - m\omega XY\sin\theta\cos\varphi + m\omega Y^2\sin\theta\cos\theta\sin\varphi,$$

$$L_y = -L_0\sin\theta\cos\varphi - m\omega XY\sin\theta\sin\varphi - m\omega Y^2\sin\theta\cos\theta\cos\varphi,$$

$$L_z = L_0\cos\theta + m\omega X^2 + m\omega Y^2\cos^2\theta. \qquad ($$

The components of **L** relative to the rotating frame (**I**, **J**, **K**) are similarly found t given by

$$\mathbf{L} = m\omega\sin\theta(-XY\,\mathbf{I} + X^2\mathbf{J}) + (L_0 + m\omega r_0^2\cos\theta)\,\mathbf{K}, \qquad ($$

where $r_0^2 \equiv (X^2 + Y^2)$.

Before concluding this section, we restate the Larmor approximation in tern a small dimensionless parameter. We may recall that for a bounded orbit $\mathbf{r} = \mathbf{r}(t)$, r lies in the interval $0 < r_{\min} \leqslant r \leqslant r_{\max} < \infty$. Now, let the magnitude of the central $f(r)\,\hat{\mathbf{r}}$ have its smallest value on the orbit, say, when $r = r_1$. Then, evide $|f(r)\,\hat{\mathbf{r}}| \geqslant |f(r_1)|$. We also note that $|m\boldsymbol{\omega}\times(\boldsymbol{\omega}\times\mathbf{r})| \leqslant m\omega^2 r_{\max}$. Thus, the Larmor proximation condition $|f(r)| \gg |m\boldsymbol{\omega}\times(\boldsymbol{\omega}\times\mathbf{r})|$ may be expressed as

$$|f(r_1)| \gg m r_{\max}\omega^2. \qquad ($$

If we now define a characteristic angular frequency $\Omega > 0$ associated with the bou orbit of the charged particle by

$$m\Omega^2 r_{\max} = |f(r_1)|, \qquad ($$

the condition (2.24) reads

$$\Omega \gg |\omega|. \qquad ($$

Thus, the Larmor approximation describes a situation in which the dimensio parameter $|\omega|/\Omega$ is 'small'. Incidentally, the modulus of ω appears in (2.26) a because ω, we may recall, could be positive as well as negative depending on wh **B** is parallel or antiparallel to **k**.

3. Tracing the motion of L in the case of elliptic Larmor frame orbits

In this section, we study the motion of the unit vector [17] $\hat{\mathbf{L}}$ along **L** in the case of inertial frame orbits $\mathbf{r}(t)$ for which the corresponding Larmor frame orbit (LFO) $\mathbf{r}$ an ellipse. We know that (Bertrand's theorem: see Goldstein [4], p. 93, or Landau Lifshitz [1], p. 32) the attractive inverse square law force and the Hooke law force called the space oscillator force) are the only two central forces which permit cl and hence elliptic orbits. Hence our discussion would cover the cases of both forces.

To study the motion of $\hat{\mathbf{L}}$, we determine the azimuth φ_L and the polar ang of the vector **L** as functions of time. The angle φ_L is given by tan $\varphi_L = L\,/L$

sing (2.22) and performing some elementary trigonometric rearrangement, we ay invert this relation as

$$\varphi_L = \varphi - \frac{\pi}{2} + \eta = \omega t - \frac{\pi}{2} + \eta, \tag{3.1}$$

here we have defined $\eta = \eta(t)$ by

$$\tan\eta = -(m\omega/L_0)XY(1 + \alpha Y^2\cos\theta)^{-1}. \tag{3.2}$$

n the other hand, the polar angle θ_L of **L** may be calculated from the relation

$$\cos\theta_L = L_z/|\mathbf{L}|. \tag{3.3}$$

ow, if the LFO $\{X(t), Y(t)\}$ is specified, we may calculate the angles θ_L and φ_L as nctions of time by using equations (3.1)–(3.3). Then, the motion of $\hat{\mathbf{L}}$ may be studied y considering the vector

$$\mathbf{L}_\perp \equiv \sin\theta_L\cos\varphi_L\mathbf{i} + \sin\theta_L\sin\varphi_L\mathbf{j}, \tag{3.4}$$

hich is the projection of $\hat{\mathbf{L}}$ onto the x–y plane of the inertial frame. The tip of this ector would trace a circle if the motion of $\hat{\mathbf{L}}$ is a pure precession. Any non-circular acing clearly indicates the presence of nutation. This is as far as we can go with general central force field. Thus, we consider the two specific cases of interest.

1 *Coulomb law elliptic orbits*

/e begin by recalling some essential properties of an elliptic orbit ([1], pp. 32–39) of negatively-charged particle of charge $-q < 0$ and mass m moving in the Coulomb eld of another positively-charged particle of charge $q' > 0$ at rest at the coordinate rgin (which also happens to be one of the two foci of the elliptic orbit). The parametric quations describing such an elliptic orbit are

$$X = a\rho;\ Y = b\sigma;\ \rho \equiv (\cos\xi - e);\ \sigma \equiv \sin\xi;\ t = (T_0/2\pi)(\xi - e\sin\xi), \tag{3.5}$$

here $X = a\rho(t)$ and $Y = b\sigma(t)$ are the Cartesian coordinates of the particle tracing the lipse. The constants a, b and e are respectively the semi-major axis, semi-minor axis nd the eccentricity of the ellipse. The eccentric angle $\xi = \xi(t)$ increases by 2π for one omplete passage of the charged particle round the ellipse. The origin of time has been hosen such that $\xi = 0$ at $t = 0$ and $\xi = 2\pi$ at $t = T_0$, where T_0 is the period of the elliptic otion. The angular frequency ω_0 associated with T_0, is given by $\omega_0 = 2\pi/T_0 =$ $_0/mab = \sqrt{-qq'/ma^3}$, where the positive constant L_0 is the magnitude of the onserved angular momentum associated with the elliptic orbit. Lastly, we note that e variables ρ and σ in (3.5) are dimensionless and have the ranges $-(1+e) \leqslant \rho \leqslant (1-e)$ nd $-1 \leqslant \sigma \leqslant 1$.

Now, using (3.5), (3.3) and (2.22), we obtain meter $\varepsilon \equiv \omega/\omega_0$. If we now observe that ε and θ are constants and the varia and σ are periodic under $\xi \to \xi + 2\pi$ which corresponds to $t \to t + T_0$ (see re following (3.5)), it follows that $\cos\theta_L$ given by (3.6) is a periodic function of time the period T_0. This means that, in the Larmor approximation, L nutate a time-period which is precisely the orbital period T_0 of the charged particl elliptic LFO.

Next, since the function $\eta(t)$ defined through (3.2) is also periodic under $t \to t +$ note that whenever $T \equiv 2\pi/|\omega| = NT_0$ where N is an integer, the azimuth L changes by 2π in a time T during which θ_L, which has a time period $T_0 = T/N$, go through exactly N cycles. In other words, when $T = NT_0$, the tip of the unit $\hat{\mathbf{L}}$ would trace a closed curve. When ω and ω_0 are not commensurate, the tip of not trace a closed curve. In any case, the motion of $\hat{\mathbf{L}}$ in the Larmor approxima a composite motion involving both precession and nutation.

Regarding the nutation frequency, we may note that it is given by ω_0 for ellipti of non-zero eccentricities. Interestingly, when e becomes zero, i.e., when the a circle, the nutation frequency changes to $2\omega_0$. This happens because, when $\cos\theta_L$ given by (3.6) becomes increasingly periodic; its period changes from 2π t ξ (or equivalently, T_0 to $T_0/2$ for t), as only even powers of ρ and σ appear in it. note that since the maximum separation $r_{\max}$ between q' and $-q$ on the ellipse $a(1+e)$, the characteristic frequency Ω of (2.25) becomes $\Omega = \omega_0(1+e)^{3/2}$. Th Larmor approximation condition (2.26) now requires $\omega_0 \gg (1+e)^{3/2}|\omega|$. As a quence, the nutation frequencies (ω_0 or $2\omega_0$) are very large compared to the frequency $|\omega|$.

An estimate of the magnitude of $\cos\theta_L$, may be obtained as follows. We note we retain only terms of the order $O(\varepsilon)$ in (3.6), and substitute back for ε as $\omega/$ obtain $\cos\theta_L = \cos\theta + (\omega a/\omega_0 b)\sin^2\theta\rho^2 + O(\varepsilon^2)$. Incidentally, this formula sho

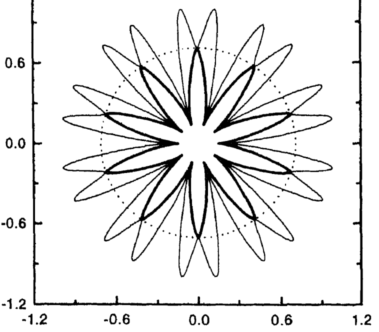

Figure 2a

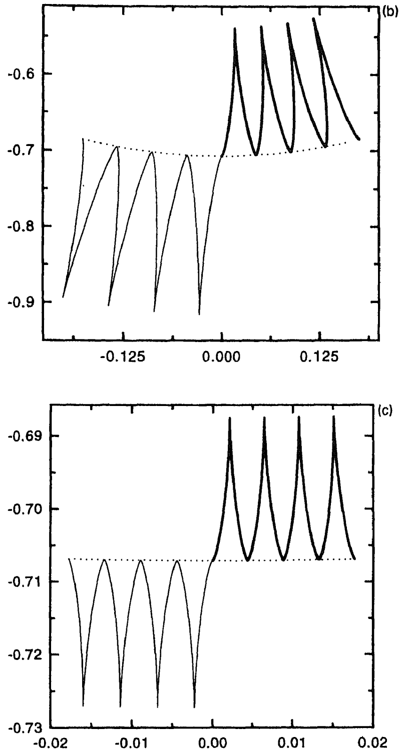

Figures 2b, c.

$\cos\theta_L > \cos\theta$ when $\omega > 0$ and $\cos\,\theta_L < \cos\theta$ when $\omega < 0$. Also, observing that $(\rho^2)_{\max} = (1+e)^2$ and $(\rho^2)_{\min} = 0$, we obtain

$$(\cos\theta_L)_{\max} - (\cos\theta)_{\min} = \pm(\omega a/\omega_0 b)(1+e)^2\sin^2\theta + O(\omega^2), \tag{3.7}$$

where the $+$ sign corresponds to $\omega > 0$ and the $-$ sign to $\omega < 0$. It is important to note

In figure 2, we have shown some model precession-nutation curves for the Coulomb case. These curves have been drawn by setting $L_0 = 1$, $\omega = \pm 1$ and $\theta = \pi/4$. When $\theta = \pi/4$, θ_L also lies in $(0, \pi/2)$ so that $\sin\theta_L$ is positive. Therefore it may be calculated as $\sqrt{1-\cos^2\theta_L}$ through equation (3.6). The angle φ_L has been calculated from (3.1) and (3.2). Further, we have chosen three convenient values for ω_0 namely 10, 100 and 1000 which yield closed nutation curves. In each of the figures 2(a), 2(b) and 2(c), we have shown three different curves. The heavy-solid curve corresponds to $\omega = 1$, the light-solid curve corresponds to $\omega = -1$ whereas the (dashed) circle of radius $\sin\theta = 1/\sqrt{2}$ does not represent any real motion of **L**, but has been drawn only for the sake of reference. (Of course, it corresponds to the circle of $(\cos\theta_L)_{\text{min}} = \cos\theta = 1/\sqrt{2}$ when $\omega > 0$ and to the circle of $(\cos\theta_L)_{\text{max}} = \cos\theta = 1/\sqrt{2}$ when $\omega < 0$). The computed values of the nutation amplitude are as follows. For $\omega = 1$, it is 36·4, 12·4 and 1·6 degrees when $\omega_0 = 10, 100$, and 1000 respectively. Similarly, for $\omega = -1$, it is given by 122·8, 21·4 and 1·6 degrees when $\omega_0 = 10, 100$ and 1000 respectively. These values clearly show that the nutation amplitude decreases as $|\varepsilon|$ decreases. In fact, the precession slows down and the nutation dies out as $|\varepsilon|$ decreases and eventually when $|\varepsilon|$ touches zero, i.e., when $\mathbf{B} = 0$, **L** gets arrested at $\theta_L = \theta$, and $\varphi_L = -\pi/2$ (see (3.1), (3.6) and the remarks following (2.18)).

3.2 *Hooke law elliptic orbits*

Writing the Hooke law central force as $f(r)\hat{\mathbf{r}} = -m\omega_0^2\mathbf{r}$, we obtain the following parametric equations to the elliptic orbit (with the centre of attraction $\mathbf{r} = 0$ at the centre of the ellipse) ([1], p. 70)

$$X = a\cos\xi;\quad Y = b\cos(\xi + \delta);\quad \xi = \omega_0 t, \tag{3.8}$$

where we have set $\xi = 0$ at $t = 0$. The other constant of integration δ, when chosen appropriately, gives the various familiar Lissajous figures. We have specifically

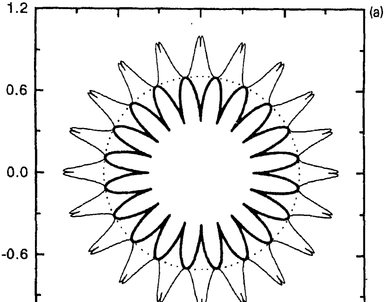

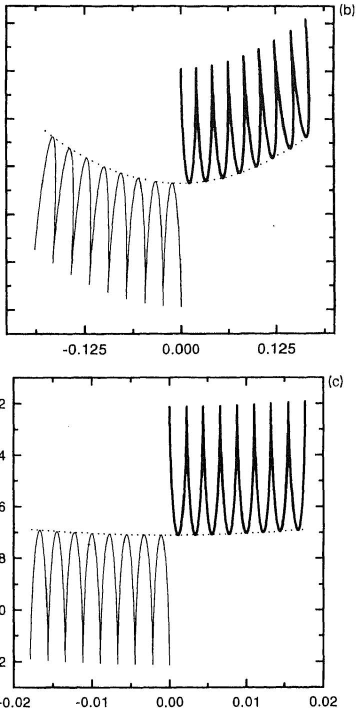

Figures 3b, c.

Figures 2 and 3. Precession-nutation curves in the Coulomb (figure 2) and Hooke cases (figure 3): These are curves traced by the tip of the angular momentum vector projected on to the plane perpendicular **B** (i.e., the x–y plane) of the inertial frame. **L** has been scaled such that its magnitude when $\mathbf{B} = 0$, i.e. L_0, is unity. The curves show nutation of considerable amplitude besides precession.

nsidered the case $\delta = -\pi/2$ which yields $X = a\cos\omega t$ and $Y = b\sin\omega t$ representing central ellipse. Figures 3(a), to 3(b) show some model precession nutation curves awn with $a = 10$ units and $b = 1$ unit. Further $\omega_0 = 10, 100$ and 1000 radians/second spectively in the figures 3(a), 3(b) and 3(c). As before in each figure the heavy solid

0·4 degrees when $\omega_0 = 10, 100$ and 1000 respectively. Similarly, for $\omega = -1$, it is given by 67·5, 4·4 and 0·4 degrees when $\omega_0 = 10, 100$ and 1000 respectively.

Acknowledgements

The authors wish to thank the referee for his comments which have helped in improving the presentation of the paper considerably. They also thank Dr M A Sridhar for generating the nutation curves on a computer.

References

[1] L D Landau and E M Lifshitz, *Mechanics* (Pergamon Press, Oxford, 1976) pp. 32–39, 70

[2] R P Feynman, R B Leighton and M Sands, *The Feynman lectures on physics* (Reading, Massachusetts, Addison-Wesley, 1964) pp. 34-6–34-7

[3] C Kittel, *Introduction to solid state physics*, seventh edition (John Wiley, Singapore, 1995) p. 418

[4] H Goldstein, *Classical Mechanics* (Addison-Wesley, London, 1980) pp. 93, 107–109, 176–177, 233

[5] K R Symon, *Mechanics* (Reading, Massachusetts, Addison-Wesley, 1960) pp. 271–278, 283–285

[6] We call an orbit $\mathbf{r} = \mathbf{r}(t)$ in which $|\mathbf{r}|$ remains finite and non-zero, i.e., $0 < r_{\min} \leqslant |\mathbf{r}| \leqslant r_{\max}$, a bounded-orbit

[7] See equation (2.3) for definition

[8] L D Landau and E M Lifshitz, *The classical theory of fields*, third edition (Pergamon Press, Oxford, 1971) pp. 105–107

[9] Although we specifically consider a particle of charge $-q$, $q > 0$, in our discussion, obviously with the electron in mind, the discussion may be easily modified to cover the case of a positively-charged particle by allowing q to be negative

[10] We may note that, in general, a vector function $\mathbf{A} = \mathbf{A}(t)$ which precesses around another constant vector $\mathbf{C}$ with the angular frequency $|\mathbf{C}|$ satisfies the differential equation $\mathrm{d}\mathbf{A}/\mathrm{d}t = \mathbf{C} \times \mathbf{A}$

[11] A M Portis, *Electromagnetic fields: Sources and media* (John Wiley, New York, 1978) pp. 245–246, 712–713

[12] E M Purcell, *Electricity and magnetism: Berkeley physics course* (Mc Graw Hill, New York, 1965) vol. 2, pp. 370–377

[13] J R Reitz, F J Milford and R W Christy, *Foundations of electromagnetic theory*, third edition (Addison-Wesley, New York, 1979) pp. 222–223

[14] A N Matveev, *Electricity and Magnetism* (Mir Publishers, Moscow, 1986) pp. 277–280

[15] Actually, we get $\varphi = \omega t +$ constant, but we have chosen the constant to be zero in (2.18)

[16] Note the deviation in notation here: As per the convention adopted in arriving at equations (2.6) to (2.8), we must rather have denoted $(\mathbf{I}, \mathbf{J}, \mathbf{K})$ and X, Y, Z respectively by $\mathbf{i}^*, \mathbf{j}^*, \mathbf{k}^*$ and $\mathbf{x}^*, \mathbf{y}^*, \mathbf{z}^*$. But we have deliberately chosen the former set which is simpler. With the exception of these, all other quantities in the Larmor frame are marked by an asterisk as before

[17] We consider the unit vector $\hat{\mathbf{L}}$ as we are interested in studying the change in the orientation of $\mathbf{L}$ with time, rather than in its length

PRAMANA
— journal of
physics

© Printed in India

Vol. 48, No. 3,
March 1997
pp. 787–797

Coherent and squeezed states on physical basis

R R PURI
Theoretical Physics Division, Central Complex, Bhabha Atomic Research Centre, Bombay 400085, India

MS received 6 April 1996; revised 24 December 1996

Abstract. A definition of coherent states is proposed as the minimum uncertainty states with equal variance in two hermitian non-commuting generators of the Lie algebra of the hamiltonian. That approach classifies the coherent states into distinct classes. The coherent states of a harmonic oscillator, according to the proposed approach, are shown to fall in two classes. One is the familiar class of Glauber states whereas the other is a new class. The coherent states of spin constitute only one class. The squeezed states are similarly defined on the physical basis as the states that give better precision than the coherent states in a process of measurement of a force coupled to the given system. The condition of squeezing based on that criterion is derived for a system of spins.

Keywords. Coherent state; squeezed state; Lie algebra; $SU(m,n)$.

PACS Nos 03·65; 02·90

1. Introduction

The hamiltonian of a quantum system is generally a linear combination of a set of operators closed under the operation of commutation i.e. they constitute a Lie algebra. Since their introduction for a hamiltonian linear in harmonic oscillator (HO) operators, the notion of coherent states [1] has been extended to other hamiltonians (see [2–9] and references therein). Physically, the HO coherent states are the minimum uncertainty states of the two quadratures of the bosonic operator with equal variance in the two. Mathematically, they are (i) the eigenstates of the bosonic annihilation operator or, equivalentally, (ii) the states generated from the vacuum by a unitary transformation linear in the bosonic operators. The extension of that notion to non-canonical systems is based on generalizing, not the physics aspect, but the two aforementioned mathematical ways of constructing the HO coherent states. The generalization based on (i) [4, 5] is limited to non-compact Lie algebras whereas that based on (ii) by Perelomov [6] has universal applicability. The coherent states in Perelomov sense are defined as the states obtained by a unitary transformation

tion, see [8].

The Perelomov construction, thus, does not carry the physical spirit of th coherent states. Here we present an approach to coherent states of non-car systems which is based on the generalization of the physics aspect of the HO co states. Following that approach, it turns out that the coherent states of a non-canonical system fall into various classes. Our approach leads, besides the Glauber coherent states, to a new class of coherent states of the harmonic osc That new class consists of the states which are minimum uncertainty states number and position or momentum operator with equal variance. In the case o it turns out that there is only one class of coherent states which consists of well- spin coherent states.

Like the notion of coherent states, the notion of squeezed states of a non-car system is based on the extension of the mathematical aspect of the canonical sq states. For, the notion of a canonical squeezed state was introduced to label those of a HO prepared in which it gives better precision of measurement of a classica coupled linearly to it than what is obtained if it is prepared in a coherent state [1 The canonical squeezed states so defined have smaller variance in a quadratu that in a coherent state. It is the latter property that forms the basis of extensio notion of squeezing to non-canonical systems. That approach, however, le ambiguities because it identifies some of the coherent states of a non-canonical as squeezed whereas the coherent and squeezed states of a canonical system co mutually exclusive classes. The spirit of the notion of canonical squeezed states carried to non-canonical systems if it is based on the criterion of increased sensit compared with that in a coherent state in an appropriate process of measureme derive a measure of the sensitivity of measurement of a force coupled linearly to system. The criterion of squeezing based on those considerations is derived for a of spins.

The paper is organized as follows. In § 2 we introduce the theory of coheren based on the physical considerations. It is applied to a system of harmonic os and of spins in § 3. In § 4 we discuss the criteria of squeezing in a system o A measure of the sensitivity of measurement of a force interacting linearl a dynamical system is derived in § 5. The main conclusions are summarized in

2. Coherent states

In this section we introduce the notion of minimum uncertainty states and the co states of a hamiltonian.

Recall that the variances ΔA^2, ΔB^2 in the measurement of two observables re ted by hermitian operators A and B are related by the uncertainty relation

$$\Delta A^2\,\Delta B^2 \geqslant \tfrac{1}{4}[\langle F\rangle^2 + \langle C\rangle^2],$$

where

$$[A, B] = iC;\ \langle F\rangle = \langle AB + BA\rangle - 2\langle A\rangle\langle B\rangle.$$

Clearly, $\langle F\rangle$ is a measure of the correlation between A and B. If A and B commu (1) is the same as the relation between the variances and the correlation of two andom variables A and B. The equality in (1) is obeyed by the states $|\phi\rangle$, called the inimum uncertainty states (MUS), which solve the eigenvalue equation

$$[A + i\lambda B]|\phi\rangle = [\langle A\rangle + i\lambda\langle B\rangle]|\phi\rangle, \tag{3}$$

here λ is a complex number. It can be shown from (3) that [9]

$$\begin{aligned} \Delta A^2 - \lambda^2 \Delta B^2 &= i\lambda\langle F\rangle, \\ \Delta A^2 + \lambda^2 \Delta B^2 &= \lambda\langle C\rangle. \end{aligned} \tag{4}$$

rom (4) it follows that $\langle F\rangle = 0(\langle C\rangle = 0)$ for λ real (λ imaginary). A coherent state of e given pair of observables is defined as that minimum uncertainty state for which $F\rangle = 0$ and $\Delta A^2 = \Delta B^2 = |\langle C\rangle|/2$. Those states are the solutions of (3) corresponding o $\lambda = \pm 1$.

Consider now a quantum system described by a hamiltonian H given by

$$H = \sum_{i=1}^{r} \alpha_i X_i, \tag{5}$$

here $\alpha_i \equiv (\alpha_1, \alpha_2, \ldots, \alpha_r)$ are real and $\{X_i\} \equiv (X_1, X_2, \ldots, X_r)$ are r independent heritian operators closed under the operation of commutation i.e. they constitute an -dimensional Lie algebra. The elements of the algebra transform amongst each other nder the group of unitary transformations

$$U = \exp\left[i \sum_{i=1}^{r} a_i X_i \right], \tag{6}$$

here $\{a_i\}$ are real constants. If P_1, P_2 are two elements of the given Lie algebra nd $Q_1 = UP_1U^\dagger, Q_2 = UP_2U^\dagger$ then the pairs (P_1, P_2) and (Q_1, Q_2) are said to belong o the same pair-class. Any pair in the pair class is a generator of the other pairs in hat class.

In order to define the minimum uncertainty states of the given hamiltonian we first onstruct the distinct pair-classes generated by non-commuting independent hermitian enerators of the Lie algebra of the hamiltonian. If the minimum uncertainty state for pair in a pair-class is $|\phi\rangle$ then it follows from (3) that the MUS for any other pair in hat class for the same λ is

$$|\psi\rangle_{MU} = U|\phi\rangle. \tag{7}$$

he state $|\phi\rangle$ in (7) can be chosen to be the MUS for the pair of generators of the Lie lgebra in the pair-class under consideration. The set of minimum uncertainty states for ll distinct pair-classes determines completely the minimum uncertainty states of the iven hamiltonian. We will see that the harmonic oscillator or h_4 algebra has two pairlasses whereas the spin or $SU(2)$ algebra has one. The harmonic oscillator hamilonian, therefore, has two classes of minimum uncertainty states whereas spin has one. he generators of the $SU(1,1)$ algebra fall in three pair-classes [12, 13].

The minimum uncertainty states (7) corresponding to $\lambda = \pm 1$ are the coherent states $\psi\rangle_{CS}$ of the hamiltonian.

The operators generating U in (7) may be divisible into two subalgebras; one the other, g, containing the rest of the generators. The group generated by h is calle stability or stationary group of $|\phi\rangle$ [3, 6]. The unitary transformation U, by virtue c group property, can then be written as $U = U_g U_h$, where U_g and U_h are generated b operators belonging to g and h respectively. The transformation U_h on $|\phi\rangle$ evidently rise to only a phase factor. By absorbing the phase factor in the definition of $|\psi\rangle_M$ expression (7) for the minimum uncertainty state can, therefore, be written as

$$|\psi\rangle_{MU} = U_g|\phi\rangle,$$

with the coherent states corresponding to $\lambda = \pm 1$.

The approach developed here has been applied to construct the coherent minimum uncertainty states of $SU(1,1)$ [12, 13]. In that case there are three classes, two of which are discussed extensively in refs [12] and [13]. Recall according to usual approaches, as has been mentioned in § 1, the coherent stat a non-compact group like $SU(1,1)$ can be constructed in two different ways: the eigenstates of a lowering operator [4, 5] and (ii) by following the approac Perelomov [6]. However, by following the approach presented here, those coherent states emerge as special cases of the coherent states of a pair-class wherea coherent states belonging to the other pair class are new [12, 13]. Thus the prop approach is able to present a unified view of the coherent states of $SU(1,1)$. A diff approach to the unification of the $SU(1,1)$ coherent states is presented in ref. [1

In the following we construct all the minimum uncertainty states of a system o and of spins and show that a new class of coherent states emerges even for a syste harmonic oscillator.

3. Minimum uncertainty states of HO and spins

In this section we apply the considerations of the last section to obtain complete minimum uncertainty states for a harmonic oscillator and a system of spins.

3.1 *Minimum uncertainty states of harmonic oscillator*

Consider a hamiltonian linear in the harmonic oscillator operators $\{a^\dagger a,\ q \equiv$ $a^\dagger)/\sqrt{2}, p \equiv i(a^\dagger - a)/\sqrt{2}, \mathrm{I}\}$ where $a, a^\dagger$ are the bosonic operators. That set of oper spans the Lie algebra h_4 [3]. Its subset of canonical operators $q \equiv (a + a^\dagger)/\sqrt{2}$ $(a^\dagger - a)/\sqrt{2}, \mathrm{I}$ spans an invariant subalgebra denoted by h_3 [3]. Clearly there ar pair-classes of h_4. One is constituted by the operators (q, p) and another by $(a^\dagger a,$ equivalently by $(a^\dagger a, q)$. The minimum uncertainty states of the class (q, p) are giv (8) where $|\phi\rangle$ is the solution of the equation

$$\tfrac{1}{2}[(1+\lambda)a + (1-\lambda)a^\dagger]|\psi\rangle = z|\psi\rangle.$$

Here $z = (1/2)\langle(1+\lambda)a + (1-\lambda)a^\dagger]\rangle$ is a complex number. It can be shown tha normalizable solutions of (9) exist only if $\mathrm{Re}(\lambda) > 0$. Hence the coherent states, v correspond to the solution of (9) for $\lambda = \pm 1$ are defined only for $\lambda = 1$. That solut evidently the coherent state $|z\rangle$:

te that a HO group element acting on a coherent state again gives a coherent state.
r $\lambda \neq 1$, (9) can be solved by rewriting it as

$$\exp(-\theta a^\dagger a)\,[a + a^\dagger]\,\exp(\theta a^\dagger a)|\phi\rangle = z|\phi\rangle, \tag{11}$$

ere $\exp(\theta) = \sqrt{(1+\lambda)/(1-\lambda)}$. The solution of (11) may be written as

$$|\phi\rangle = \exp(-\theta a^\dagger a)|x), \tag{12}$$

ere $|x)$ is the eigenstate of q with eigenvalue x. In terms of the zero eigenvalue state $|0)$
q, (12) reads

$$|\phi\rangle = \exp(-\theta a^\dagger a)\exp\{-x(a - a^\dagger)/\sqrt{2}\}|0). \tag{13}$$

e state $|\phi\rangle$ is thus generated by a linear non-unitary transformation on an eigenstate
the position operator. In terms of the eigenstates $|m\rangle$ of $a^\dagger a$ it reads

$$|\phi\rangle = \exp(-x^2/2)\sum_{m=0}^{\infty}\left[\frac{1}{2^m\sqrt{\pi}\,m!}\right]^{1/2} H_m(x)\exp(-\theta m)|m\rangle, \tag{14}$$

ere $H_m(x)$ are the Hermite polynomials.
The expression (12) is not the familiar form [15] of the solution of (9). It is introduced
e in order to compare it with the expression for the minimum uncertainty state for
ns. The familiar form [15] is obtained by writing (9) as

$$\exp[-\tfrac{1}{2}(\xi a^{\dagger 2} - \xi^* a^2)]\,a\,\exp[\tfrac{1}{2}(\xi a^{\dagger 2} - \xi^* a^2)]|\phi\rangle = \alpha|\phi\rangle, \tag{15}$$

ere $\tanh(|\xi|) = (1-\lambda)/(1+\lambda)$. Its solution is given by

$$|\phi\rangle = [\exp(-\tfrac{1}{2}(\xi a^{\dagger 2} - \xi^* a^2)]|\alpha\rangle, \tag{16}$$

ich is the familiar form of the minimum uncertainty states of canonical operators.
e state $|\phi\rangle$ is thus obtained as a result of a non-linear unitary transformation on
oherent state. It is straightforward to verify that (16) leads to (14).
Next we construct the minimum uncertainty states for the second pair class which is
ierated by $(a^\dagger a, p)$ or equivalently by $(a^\dagger a, q)$. By choosing $(a^\dagger a, p)$ as the generating
ir, the desired states are given by (8) where $|\phi\rangle$ is the solution of the equation

$$[a^\dagger a + i\lambda p]|\phi\rangle \equiv \exp(\lambda q)\,[a^\dagger a + \lambda^2]\,\exp(-\lambda q)|\phi\rangle = z|\phi\rangle, \tag{17}$$

ich is evidently solved by $z = m + \lambda^2$ with the corresponding solution given by

$$|\phi_m\rangle = \exp(\lambda q)|m\rangle, \quad m = 0, 1, 2, \ldots. \tag{18}$$

e minimum uncertainty states are given by substituting (18) in (8) where U_g is now
full group element. The MUS in this case is thus obtained by the action of the
itary transformation generated by h_4 on a state generated from a basis state by
on-unitary transformation. For $m = 0$, that non-unitary transformation is evidently
uivalent to a unitary one. In that case $|\phi_0\rangle$ is the coherent state $|-\lambda/\sqrt{2}\rangle$. From (18)
ollows that

$$\langle l|\phi_m\rangle = \sqrt{\frac{m!}{l!}}\exp\left(\frac{\lambda^2}{4}\right)\left(\frac{\lambda}{\sqrt{2}}\right)^{l-m} L_m^{l-m}\left(-\frac{\lambda^2}{2}\right), \quad l \geqslant m, \tag{19}$$

a hamiltonian linear in the harmonic oscillator operators.

3.2 *Minimum uncertainty states of spins*

Consider a system of spins described by the spin operators $\mathbf{S} \equiv (S_x, S_y, S_z)$
components obey the angular momentum commutation relation

$$[\mathbf{a}.\mathbf{S}, \mathbf{b}.\mathbf{S}] = i(\mathbf{a} \times \mathbf{b}).\mathbf{S},$$

where **a** and **b** are arbitrary three dimensional vectors. The state space of the op
is spanned by the eigenstates $|m, S\rangle \equiv |m\rangle$ of the Casimir operator $S_x^2 + S_y^2 + S_z^2$
with eigenvalues $S(S+1)\,(S = 1/2, 1, 3/2, \ldots)$ and $m\,(m = -S, -S+1, \ldots, S)$ resp
ly. The operators $S_\pm = S_x \pm iS_y$ are the raising and lowering operators on
eigenstates such that $S_+|S\rangle = S_-|-S\rangle = 0$. There is clearly only one pair-class
case which is generated by any two, say (S_x, S_y), of the three generators. The mi
uncertainty states of a hamiltonian linear in spin operators is given by (8) wher
the solution of

$$[S_x + i\lambda S_y]|\phi\rangle = z|\phi\rangle,$$

which for $\lambda = \pm 1$ is solved only by $z = 0$ with $|\phi\rangle = |\pm S\rangle$. Since $|\pm S\rangle$ is an eig
of S_z, the transformation U_g in (8) is generated by S_x, S_y leading to the fol
well-known expression for the spin coherent states [15, 16]

$$|\theta, \phi\rangle = \exp\left[\tfrac{\theta}{2}\{\exp(-i\phi)S_+ - \exp(i\phi)S_-\}\right]|\pm S\rangle.$$

Thus the spin coherent states are minimum uncertainty states with equal vari
two orthogonal components $US_xU^\dagger$ and $US_yU^\dagger$ of spin. The variance in each of
given by $|\langle US_zU^\dagger\rangle|/2$ i.e. by half the absolute value of the average of the com
orthogonal to both of them. Note that

$$US_zU^\dagger = \sin(\theta)\cos(\phi)S_x + \sin(\theta)\sin(\phi)S_y + \cos(\theta)S_z \equiv \mathbf{e}(\theta, \phi).\mathbf{S},$$

where $\mathbf{e}(\theta, \phi) \equiv (\sin(\theta\cos(\phi), \sin(\theta)\sin(\phi), \cos(\theta))$ is the unit vector in the di
(θ, ϕ). That is also the direction of the average spin vector $\langle \mathbf{S} \rangle$ as can be s
evaluating

$$\langle S_x \rangle = S\sin(\theta)\cos(\phi), \langle S_y \rangle = S\sin(\theta)\sin(\phi), \langle S_z \rangle = S\cos(\theta).$$

Hence $US_zU^\dagger$ is in the average direction of the spin. A spin coherent state can th
be defined as the state in which the variance in any spin component orthogona
average direction of spin is $S/2$.

The solution of (21) for $\lambda \neq \pm 1$ may be obtained by rewriting it as (ex
$\sqrt{(1+\lambda)/(1-\lambda)}$).

$$[\exp(\beta)S_+ + \exp(-\beta)S_-]|\phi\rangle \equiv \exp(\beta S_z)(S_+ + S_-)\exp(-\beta S_z)|\phi\rangle$$

$$\equiv 2\exp(\beta S_z)\exp\left(-i\frac{\pi}{2}S_y\right)S_z\exp\left(i\frac{\pi}{2}S_y\right)\exp(-\beta S_z)|\phi\rangle$$

$$= z|\phi\rangle,$$

$$|\phi_m\rangle = A_m \exp(\beta S_z)\exp\left(-i\pi\frac{S_y}{2}\right)|m\rangle \equiv A_m \exp(\beta S_z)|m), \qquad (26)$$

where $|m)$ is the eigenstate of S_x. By comparing (26) and (12) the similarity between the minimum uncertainty states of the harmonic oscillator and those of spins is clearly brought out. Recall that in the case of a harmonic oscillator there exists a non-linear unitary transformation (16) equivalent to the linear non-unitary transformation (12). There is, however, no known analogous non-linear transformation equivalent to the linear non-unitary one given by (26) except for $S = 1$. The equivalent non-linear transformation for $S = 1$ is $\exp[\xi S_+^2 - \xi^* S_-^2]$ with ξ appropriately related with the parameters in (26). For higher spins, the equivalent non-linear unitary transformation seems to involve higher powers of spin operators.

We will see that the states (26) are the squeezed spin states.

4. Spin squeezing

The notion of squeezing was introduced in the context of the study of precision of measurement of a force carried by determining the change that it induces in the state of a harmonic oscillator. The precision of measurement depends, amongst other things, on the dynamical variable of the system to which the force is coupled, on the variable on which the measurement is carried and on the initial state of the system. Those states of the oscillator for which the precision of measurement carried by determining the change in the position of the oscillator coupled linearly to the force is more compared with that obtained by preparing it in a coherent state are called the squeezed states. Those states turn out to be the ones for which the variance in a generator; q or p; of the canonical algebra is less than its value 1/2 in a coherent state.

That notion of squeezing has since been extended to non-canonical systems by generalizing the approach based on the uncertainty relation. The standard approach [15] for identifying the squeezed states is to proceed from the definition of coherent state for two observables A and B. In that state the uncertainty relation (1) is satisfied with equality with $\langle F\rangle = 0$; $\Delta A^2 = \Delta B^2 = |\langle C\rangle|/2$. A squeezed state is then defined as the one in which ΔA^2 or ΔB^2 is less than $|\langle C\rangle|/2$. That definition leads to an unambiguous identification of squeezed states in a canonical system because in that case $|\langle C\rangle|$ is the same constant for all the states in the set of the canonical coherent states. In the case of non-canonical operators, $|\langle C\rangle|$ depends on the parameters of the coherent state. There may, therefore, be states in the set of coherent states which satisfy the above mentioned condition of squeezing for some pair of observables. The class of squeezed and the coherent states so constructed are then no longer mutually exclusive. In the case of a system of spins, for example, it can be seen that the coherent states $|\theta, n\pi\rangle$, where n is an integer, satisfy the condition of squeezing with A, B taken as S_x, S_y [15].

The uncertainty relation based approach to squeezing in the case of spins can be made unambiguous by noting, following Kitagawa and Ueda [19], that the variance in any component in a direction orthogonal to the average direction of the spin is $S/2$. One can, therefore, examine the noise in the components orthogonal to the average direction of the spin in the state under investigation. If **a** and **b** are two dire orthogonal to each other such that $\mathbf{a}\times\mathbf{b}=\mathbf{S}/|\mathbf{S}|$ then in a coherent $(\Delta\mathbf{a}.\mathbf{S})^2=(\Delta\mathbf{b}.\mathbf{S})^2\equiv(\Delta S_\mu^\perp)^2=|\langle\mathbf{S}\rangle|/2$ i.e.

$$(\Delta S_\mu^\perp)^2=\frac{S}{2}=\frac{1}{2}|\langle\mathbf{S}\rangle|.$$

A squeezed state is then defined [19] as the state for which

$$(\Delta S_\mu^\perp)^2<|\langle\mathbf{S}\rangle|/2, \qquad SQ(\mathrm{I})$$

It is straightforward to see that the minimum uncertainty states (21) satis condition (28) of spin squeezing.

The criterion $SQ(\mathrm{I})$, based on the uncertainty relation, makes the sets of cohere squeezed states mutually exclusive. A criterion based on the requirement of im ment of sensitivity over what is obtained by using the coherent states in the me ments with spins is derived in the next section. It is shown that the parameter

$$\xi=2S(\Delta S_\mu^\perp)^2/\langle S_\mu\rangle^2,$$

where $S_\mu^\perp$ is a spin component perpendicular to S_μ, is a measure of the sen involving spins. By using (24) and

$$\Delta S_x^2=\frac{S}{2}(1-\sin^2(\theta)\cos^2(\phi)), \quad \Delta S_y^2=\frac{S}{2}(1-\sin^2(\theta)\sin^2(\phi)),$$

$$\Delta S_z^2=\frac{S}{2}\sin^2(\theta),$$

it can be shown that the minimum value of ξ in a spin coherent state is 1 i.e.

$$\xi_{\mathrm{min,coh}}=1.$$

A spin squeezed state is defined as a state for which ξ for some spin componen than unity i.e. a state for which

$$\xi\equiv 2S(\Delta S_\mu^\perp)^2/\langle S_\mu\rangle^2<1 \qquad SQ(\mathrm{II}).$$

It is easy to see that $SQ(\mathrm{II})$ holds only if $SQ(\mathrm{I})$ does. The criterion $SQ(\mathrm{II})$ reduce one derived in [20] in the context of improvement of sensitivity in Ramsey sp copy. The condition $SQ(\mathrm{II})$ in that context has been referred to as spectro squeezing [18].

As shown in [18], the minimum uncertainty states (26) for $\lambda\neq\pm1$ sati condition $SQ(\mathrm{II})$.

A distinguishing feature of the states satisfying (28) and (32) is that the spins i states are correlated [18, 19]. That follows from the fact that, by way of their const the squeezed spin states and the spin coherent states constitute mutually exclusive sensitivity in the process of measurement involving spins.

5. Sensitivity of measurement

A force is measured by determining the changes it induces in an observable of a dynamical system. The observables of a dynamical system described quantum mechanically are, however, inherently statistical in nature thereby limiting the accuracy of measurement. Given the coupling and the observable to be measured, the accuracy depends upon the state in which the measuring system is prepared. In this section we derive the parameter which determines the precision of measurement performed by coupling the force linearly to a system.

Let the hamiltonian of a system coupled to an external force be given by (5) in which one or more α_i are proportional to the external forces to be measured. Let us suppose that α_k is proportional to the strength of the force and that it is to be determined by relating it with the mean value $\langle X_j \rangle$ of the observable X_j after the unitary evolution generated by the hamiltonian. The mean is determined with an accuracy which is proportional to the variance ΔX_j^2. The inaccuracy in the determination of the mean leads to an error $\Delta\alpha_k$ in the inference of α_k. Since $\langle X_j \rangle$ is a function of $\{\alpha_i\}$ it follows that

$$\Delta\alpha_k = \Delta X_j \Big/ \left| \frac{\partial \langle X_j \rangle}{\partial \alpha_k} \right|. \tag{33}$$

Equation (33) determines the error $\Delta\alpha_k$ in the estimation of α_k from the measurements carried on X_j. Smaller the value of $\Delta\alpha_k$ better is the precision of measurement. If $\Delta\alpha_{\text{min., coh.}}$ is the minimum value of $\Delta\alpha_k$ in a coherent state of a pair class containing X_j, then the states for which $\Delta\alpha_k < \Delta\alpha_{\text{min., coh.}}$ may be called squeezed states.

It is straightforward to see that the parameter ξ in the case of a measurement of a force by means of a HO leads to the same expression for the minimum measurable force and hence to the same criteria of squeezing as the ones arrived at by other methods [10, 11]. Here we consider a process of measurement by means of a spin. The hamiltonian in that case is given by $H = \mathbf{a}.\mathbf{S}$. Suppose that one of the components a_k of $\mathbf{a}$ is required to be determined by measuring the spin component $S_l(\mathbf{a})$ orthogonal to a_k after the unitary transformation generated by H. Hence, invoking (32), the error in the estimate of a_k is

$$\Delta a_k = \Delta S_l(\mathbf{a}) \Big/ \left| \frac{\partial \langle S_l \rangle}{\partial a_k} \right|. \tag{34}$$

Since $S_l(\mathbf{a})$ is obtained from S_l by a unitary transformation generated by the hamiltonian, it follows that $\partial S_l(\mathbf{a})/\partial a_k$ is expressible as a commutator of $S_l(\mathbf{a})$ with a spin component, say, $\mathbf{c}.\mathbf{S}$. The commutator, by virtue of (20), is a spin component orthogonal to S_l. Hence, the measure of error in the estimate of a force acting on a spin component is

$$\Delta a_k \sim \Delta S_l(\mathbf{a}) / |\langle S^{\perp}(\mathbf{a}) \rangle|, \tag{35}$$

where $S^{\perp}(\mathbf{a})$ is a component orthogonal to $S(\mathbf{a})$. Hence the squeezing parameter ξ defined by (32) is a measure of the sensitivity of measurement by means of a system of spins. In terms of ξ, (35) reads

$$\Delta\alpha_k \sim \sqrt{\xi/2S}.$$

The expression (36) reduces to the ones derived in [20] and [22] in the context of spectroscopy and $SU(2)$ interferometry respectively. Since the minimum value of ξ i coherent state is 1, it follows that the maximum sensitivity in that case is of th $\sqrt{1/2S}$. On the other hand, there are squeezed spin states for which ξ goes as $1/S$ 22]. In those states the error in the measurement, therefore, is of the order of $1/S$ evidently a marked improvement over the performance of a spin coherent states.

An experimental verification of theoretically predicted quantum noise h carried in the experiments on trapped ions [23].

6. Conclusion

A definition of the coherent states is proposed based on dividing the obse belonging to the Lie algebra of the hamiltonian into classes of pairs of observab that the pairs in a class can be transformed into each other by a unitary transfor generated by the given Lie algebra. A state generated by a unitary transformatio state which is a minimum uncertainty state with equal variance in a pair of obse in a pair class is a coherent state of that class. The set of coherent states of ea class completely determines the coherent states of the given hamiltonian. T proach applied to the hamiltonian of a harmonic oscillator gives, besides th known canonical coherent states, a new set of coherent states. In the case of spi is only one pair-class leading to the known spin coherent state. The notion of sq is similarly sought to be based on a physical requirement by defining a squeezed the one prepared in which the given system gives better precision than obta preparing it in a coherent state in the measurement of a force coupled linearly t condition of squeezing based on that criterion is derived for a system of spins

References

[1] R J Glauber, *Phys. Rev.* **131**, 2766 (1963)

[2] J R Klauder and Bo-Sture Skagerstam (eds), *Coherent states* (World Scientific, Si 1985)

[3] Wei-Min Zhang, D H Feng and R Gilmore, *Rev. Mod. Phys.* **62**, 867 (1990)

[4] A O Barut and C Girardello, *Commun. Math. Phys.* **21**, 41 (1971)

[5] G S Agarwal, *J. Opt. Soc. Am.* **B5**, 1940 (1988)

[6] A M Perelomov, *Commun. Math. Phys.* **26**, 222 (1975); *Generalized coherent states applications* (Springer, Berlin, 1986)

[7] M M Nieto and D R Truax, *Phys. Rev. Lett.* **71**, 2843 (1993)

[8] R R Puri, *Phys. Rev.* **A50**, 5309 (1994)

[9] R R Puri, *Phys. Rev.* **A49**, 2178 (1994)

[10] H N Hollenhorst, *Phys. Rev.* **D19**, 1669 (1979)

[11] R S Bondurant and J H Shapiro, *Phys. Rev.* **D30**, 2548 (1984)

[12] R R Puri and G S Agarwal, *Phys. Rev.* **A53**, 1786 (1996)

[13] R R Puri and G S Agarwal, *Int. J. Mod. Phys.* **B10**, 1563 (1996)

[14] P Shanta, S Chaturvedi, V Srinivasan, G S Agarwal and C L Mehta, *Phys. Rev.* 1447 (1994)

] K Wodkiewicz and J H Eberly, *J. Opt. Soc. Am.* **B2**, 458 (1985)

] J M Radcliffe, *J. Phys.* **A4**, 313 (1971)
F T Arecchi, E Courtens, R Gilmore and H Thomas, *Phys. Rev.* **A6**, 2211 (1972)

] M A Rashid, *J. Math. Phys.* **19**, 1391 (1978)

] G S Agarwal and R R Puri, *Phys. Rev.* **A49**, 4968 (1994)
R R Puri and G S Agarwal, in *Coherent states: Past, present and future* edited by J R Klauder and D H Feng (World Scientific, 1994) p. 447

] M Kitagawa and M Ueda, *Phys. Rev.* **A47**, 5138 (1993)

] D J Wineland, J J Bollinger, W M Itano and F L Moore, *Phys. Rev.* **A46**, 6797 (1992)

] R R Puri, *J. Phys.* **A29**, 5719 (1996)

] B Yurke, S L McCall and J R Klauder, *Phys. Rev.* **A33**, 4033 (1986)
B Yurke, *Phys. Rev. Lett.* **56**, 1515 (1986); *Physica* **B151**, 286 (1988)

] W M Itano, J C Bergquist, J J Bollinger, J M Gilligan, D J Heinzen, F L Moore, M G Raizen and D J Wineland, *Phys. Rev.* **A47**, 3554 (1993)

Classical limit of scattering in quantum mechanics–A general approach

D SEN*, A N BASU and S SENGUPTA
Condensed Matter Physics Research Centre, Department of Physics, Jadavpur University, Jadavpur, Calcutta 700 032, India
*Present address: Barasat Govt. College, Barasat, West Bengal, India

MS received 9 February 1996; revised 19 August 1996

Abstract. The classical and quantum physics seem to divide nature into two domains macroscopic and microscopic. It is also certain that they accurately predict experimental results in their respective regions. However, the reduction theory, namely, the general derivation of classical results from the quantum mechanics is still a far cry. The outcome of some recent investigations suggests that there possibly does not exist any universal method for obtaining classical results from quantum mechanics. In the present work we intend to investigate the problem phenomenonwise and address specifically the phenomenon of scattering. We suggest a general approach to obtain the classical limit formula from the phase shift δ_l, in the limiting value of a suitable parameter on which δ_l depends. The classical result has been derived for three different potential fields in which the phase shifts are exactly known. Unlike the current wisdom that the classical limit can be reached only in the high energy regime it is found that the classical limit parameter in addition to other factors depends on the details of the potential fields. In the last section we have discussed the implications of the results obtained.

Keywords. Scattering theory; quantum mechanics; classical limit.

PACS No. 03·65

1. Introduction

When the conceptual structures of two theories in physics differ significantly it becomes a difficult proposition to derive the approximate theory from the more general one which replaces it. The best approach is to investigate the situations in which the observable result from the two theories would agree. This is well illustrated by the problem of getting the Newton's law of gravitation from the relativistic theory.

The problem of classical limit of quantum mechanics is, however, much more difficult because of a radical difference in the conceptual structures of classical and quantum physics. Even the basic concept, the dynamical state of a system is defined differently in the two theories. The limit $h \to 0$ is often regarded as a convenient way to obtain the classical approximation. It has become increasingly clear that an indiscriminate use of the procedure leads to absurd results. For example if we put $h \to 0$ in the Schrödinger equation nothing meaningful is obtained.

Another difficulty is that the problem of classical limit is not well defined. How muc
of classical physics we expect to recover from quantum mechanics is not precise
known. The domain of validity of classical physics is quite large and one has to recov
not only the laws but also the description of the objective reality which forms the ba
of these laws. It seems that the nature of objective reality undergoes a qualitati
change with the scale of observation. The picture which is so clear at the classical lev
turns hazy and then completely disappears as we approach the atomic domain.
nature this change must occur smoothly. But such a smooth change seems to be rul
out by the formalism of quantum mechanics.

It is well known that even at very large energy regions, there are quantum states [
which violate classical laws. An Arnold cat when treated classically leads to a chao
behaviour. But a quantum mechanical Arnold cat remains perfectly reversible [2
There is a belief that if classical particles are described by narrow wave packets, t
spreading effect will be negligible (as the mass is large compared to those of atoms), a
the motion of the packet will satisfy classical laws. But we can prepare a classic
particle in a state so that its position lies definitely within, say, $x_0 \pm \Delta x$ and momentu
within $p_0 \pm \Delta p$ (Δx, Δp of course satisfy uncertainty relation). But a wave pack
description of such a state require that both $\psi(x,t)$ and its Fourier transform $\phi(k$
must give compact density functions, i.e., $|\psi|^2$ (or $|\phi|^2$) must be zero for $x(/p)$ outsi
the region $x_0 \pm \Delta x(/p_0 \pm \Delta p)$. Quantum mechanics, however, overrules such a pack
It can be shown that if $\rho(x,t)$ is compact, $\rho(k,t)$ cannot be so. Facts like the abo
indicate complexities in the nature of relation between classical and quantu
mechanics.

However, most investigations in the classical limit problem avoid the bigg
question of retrieving from quantum mechanics, a whole domain of classical physi
Instead they confine themselves with calculations in specific areas. The aim is
find in what limiting conditions quantum mechanical results will agree with tho
obtained from classical mechanics. A few examples may be cited. Rowe [3] showed th
in attractive Coulomb scattering ($V(r) = -\gamma/r$), the outgoing density functio
at arbitrary distances from the scatterer, are quite different in classical and quantu
mechanics, though scattering cross-sections agree. In the limit, the dimensionle
parameter $\gamma/\hbar v_0$ (v_0 is the incoming velocity) goes to infinity, the quantum mechanic
density function agrees with the classical value. Bhaumik *et al* [4] showed th
with coherent packets and large average energy one can get the classical Kep
orbit for the hydrogen atom. Born and Ludwig [5] showed that at large energi
a wave packet for a particle confined in a box with rigid walls can be construct
whose motion resembles the classical motion of a particle repeatedly reflected fro
the rigid walls.

In the present paper we shall work out a general approach to recover the classic
limit for the differential scattering cross-section ($\mathrm{d}\sigma/\mathrm{d}\Omega$), starting from the quantu
mechanical expression for the phase shift δ_l. As have been pointed out by Sen *et al* [
the classical definition for $\mathrm{d}\sigma/\mathrm{d}\Omega$ for particles is not exactly the same as the definiti
used in quantum mechanics. But in the classical limit, the difference in the definiti
affects the expression for differential cross-section around a small angle near ze
degree. At all other angles, the differential cross-sections in the two definitions a

Usually the exact expression for δ_l depends on a dimensionless parameter $\alpha = a_0/\hbar$ (a_0 does not involve $\hbar$). The scattering amplitude is given by

$$f(\theta) = \frac{1}{2ik}\sum_0^\infty (2l+1)P_l(\cos\theta)(e^{i2\delta_l} - 1)$$

$$= \frac{1}{2ik}\sum_0^\infty (2l+1)P_l(\cos\theta)e^{i2\delta_l}, \quad \text{if } \theta \neq 0, \tag{1}$$

where k is the incoming particle wave vector and the phase shift δ_l depends, apart from the scattering angle, on the parameter α defined above. We show that in general, if we calculate $f(\theta)$ in the limit $\alpha \to \infty$ then $|f(\theta)|^2$ gives the classical scattering cross-section. In evaluating the sum(1) we use the method of stationary phase [7], when such a stationary phase point exists. In other cases one may use numerical methods.

In the following section we have applied the above method to obtain the classical limit results for scattering by two potential fields, namely the $1/r^2$ and $1/r$ and scattering by the rigid sphere. The last section contains a discussion of the implications of the results obtained and also a comparison between the Landau–Lifshitz method [7] and the present approach.

2. Classical limit calculation for different potentials

a) *Scattering by $V(r) = \gamma/r^2$ potential*

The expression for the phase shift δ_l, has been evaluated and is given by [8]:

$$\delta_l = \frac{\pi}{2}(l + \tfrac{1}{2}) - \frac{\pi}{2}(l + \tfrac{1}{2})\left[1 + \frac{\alpha^2}{(l + (1/2))^2}\right]^{1/2}, \tag{2}$$

where

$$\alpha = (2\gamma m)^{1/2}/\hbar. \tag{2.1}$$

We shall determine $f(\theta)$ in the limit $\alpha \to \infty$. We take α to be so large that $\sqrt{\alpha} \gg 1$. We divide the entire domain of l from 0 to ∞ into three regions: region I from $l = 0$ to $l = l_1$, region II from $l = l_1$ to $l = l_2$, and region III from $l = l_2$ to infinity such that $l_1 < \alpha \leqslant l_2$ and $l_2 - l_1$ is small and of the order $\sqrt{\alpha}$. In region I, we can write δ_l in (2) as

$$\delta_l \approx \frac{\pi}{2}(l - \alpha) + \frac{\pi}{4}, \quad l < \alpha \tag{2.2}$$

and

$$\cos 2\delta_l = (-1)^l \sin \pi\alpha, \qquad \sin 2\delta_l = (-1)^l \cos \pi\alpha. \tag{2.3}$$

In region III, we get

$$\delta_l \approx -\frac{\pi\alpha^2}{2(2l+1)}, \quad l > \alpha. \tag{2.4}$$

Using the above values of δ_l it can be shown that

$$\sum^{l_1} (2l+1)P_l(\cos\theta)e^{i2\delta_l} \simeq 0$$

$$\sum_{l_2}^{\infty}(2l+1)P_l(\cos\theta)\mathrm{e}^{i2\delta_l}\simeq 0. \qquad (2.$$

The details of the arguments leading to the above results are given in Appendix The results are true for $\theta\neq 0$.

For evaluating $f(\theta)$ given by (1) we are now left with the following sum for region I

$$f(\theta)=\frac{1}{2ik}\sum_{l_1}^{l_2}(2l+1)P_l(\cos\theta)\mathrm{e}^{i2\delta_l}. \qquad ($$

Since in this region $l>\alpha$ and $\alpha\gg 1$, we can use the method of stationary phase due Landau and Lifshitz. Assuming that for a given θ the phase δ_l has a stationary value some $l=l(\theta)$, we get from (2)

$$2\frac{\mathrm{d}}{\mathrm{d}l}\delta_l=\pi-\pi\Bigg/\left[1+\frac{\alpha^2}{(l+(1/2))^2}\right]^{1/2} \qquad (3.$$

which on substitution in the following equation (see eq. (111.3) of ref. [7]):

$$2\frac{\mathrm{d}}{\mathrm{d}l}\delta_l\pm\theta=0 \qquad (3.$$

gives the desired l as a function of θ. The value corresponding to the stationary phase thus given by

$$l_\theta^2\simeq\frac{\alpha^2(\pi-\theta)^2}{(2\pi-\theta)\theta}. \qquad (3.$$

Then for the differential cross-section we get using equations (1), (2), (3) and (3.3) t following relation (see appendix B4)

$$|f(\theta)|^2\simeq\frac{\hbar^2}{2m^2v^2\sin\theta}\frac{\mathrm{d}}{\mathrm{d}\theta}l_\theta^2, \qquad (3.$$

$$\frac{\mathrm{d}\sigma}{\mathrm{d}\Omega}=|f(\theta)|^2=\frac{\gamma\pi^2(\pi-\theta)}{E(2\pi-\theta)^2\theta^2\sin\theta} \qquad (3.$$

which agrees with the classical result given by equation (4) in ref. [8]. It shoul however, be emphasized that in this derivation we have not retrieved the classic phenomenon of scattering. In particular we have not recovered the tracks of t individual particles, which play an important role in the classical theory. We sh further discuss this point in the last section.

b) *Scattering by the Coulomb potential* $V(r)=\gamma_0/r$

It may appear trivial to discuss the Coulomb potential as it is well known that t classical and quantum mechanical expressions agree in this case. But it is instructive follow the general approach outlined above and to examine whether $f(\theta)$ evaluated the classical limit as defined here, leads to the correct expression for the different cross-section.

The phase shift for the Coulomb potential is given by [9]

$$\exp(2i\delta_l) = \frac{\Gamma(l+1+i\gamma_0/\hbar v_0)}{\Gamma(l+1-i\gamma_0/\hbar v_0)} = \frac{Ae^{iB}}{Ae^{-iB}} = \exp(2iB), \tag{4}$$

ere B is the argument of $\Gamma(l+1+i\gamma_0/\hbar v_0)$ and

$$2\delta_l = 2B. \tag{4.1}$$

the present case the appropriate parameter is $\alpha_0 = \gamma_0/\hbar v_0$, where v_0 is the velocity of e incident particle. Using Stirling's approximation we get

$$2\delta_l = \alpha_0 \ln\{\alpha_0^2 + (l+1)^2\} + (2l+1)\tan^{-1}\{\alpha_0/(l+1)\}. \tag{4.2}$$

Now let us examine the limiting situation $\alpha_0 \to \infty$. As in the previous case we divide e sum in $f(\theta)$ into three regions $l = 0$ to $l = l_1$, $l = l_1$ to $l = l_2$, and $l = l_2$ to infinity, with $< \alpha_0 < l_2$. In region I, we can approximate δ_l by

$$2\delta_l \simeq 2\alpha_0 \ln \alpha_0$$

ich is a constant independent of l. It then follows that the contribution to $f(\theta)$ from gion I will be zero as seen from the results of the previous example. Similarly for gion III, we can write

$$2\delta_l \simeq 2\alpha_0 \ln l$$

d the contributions to $f(\theta)$ from all these terms vanish due to rapid oscillation of $(\cos\theta)$. Thus the significant range is from l_1 to l_2. Using the method of stationary ase we get from (4.2)

$$2\frac{\mathrm{d}}{\mathrm{d}l}\delta_l = 2\tan^{-1}\{\alpha_0/(l+1)\} = \mp\theta, \quad \text{or}$$

$$l_\theta \simeq \alpha_0 \cot\theta/2 \tag{4.3}$$

d from (3.4) the differential cross-section is given by

$$\frac{\mathrm{d}\sigma}{\mathrm{d}\Omega} = |f(\theta)|^2 = \frac{\hbar^2\alpha_0^2}{4v_0^2\sin^4\theta/2} \tag{4.4}$$

ich is the classical result. It is found that all the assumptions (see appendix B) made in riving (3.4) are valid in the limit $\alpha_0 \gg 1$.

Again we have recovered the classical formula and not the entire classical phenom-on. This leads to the important question that in a specific problem how much of the assical phenomenon is recovered and why the remaining part is not obtained. In the se of Coulomb scattering for example, Rowe [3] has demonstrated that in the tractive Coulomb potential ($V = -\gamma_0/r$), where the classical limit parameter is $(\gamma_0/v\hbar)$ the limit $\hbar \to 0$ or $\gamma_0/v\hbar \to \infty$, the quantum mechanical incoming and outgoing nsity functions go over to the corresponding classical quantities (defined from the assical trajectories) at all values of $\underset{\sim}{r}$. This, however, neither lead to trajectories from

c) *Scattering by a rigid sphere of radius a*

The expression for the phase shift in this case is given by [9]

$$\delta_l = \tan^{-1}\{j_l(\rho)/n_l(\rho)\}, \quad \text{where} \quad \rho = ka = \frac{mv_0 a}{\hbar}$$

and

$$f(\theta) = \frac{1}{2ik}\left\{\sum_0^\infty (2l+1)P_l(\cos\theta)\left(\frac{-2j_l^2}{j_l^2+n_l^2}\right) + i\sum_0^\infty (2l+1)P_l(\cos\theta)\left(\frac{2j_l n_l}{j_l^2+n_l^2}\right)\right\}.$$

In the present case the relevant parameter is ρ which goes to infinity as $\hbar \to 0$. W $l_1 = \rho$ and in region I for $\rho \geqslant l$ to a good approximation we use the asym expansion of $j_l(\rho)$ and $n_l(\rho)$, given by

$$j_l(\rho) = \frac{1}{\rho}\sin\left(\rho - l\frac{\pi}{2}\right)$$

and

$$n_l(\rho) = -\frac{1}{\rho}\cos\left(\rho - l\frac{\pi}{2}\right)$$

and get the value of δ_l for l in region I as

$$\delta_l = l\frac{\pi}{2} - \rho.$$

As in the previous two examples, we can show using the above values of δ_l th contribution from region I to $f(\theta)$ vanishes. Also, we take $l_2 \gg \rho$ and for region I can use the following asymptotic expansion (ρ fixed and $l \gg \rho$)

$$j_l(\rho) \sim (e\rho/2l)^l$$

and

$$n_l(\rho) \sim -(e\rho/2l)^{-l}$$

which gives

$$\frac{j_l(\rho)}{n_l(\rho)} \simeq -(e\rho/2l)^{2l}$$

and from (5) we get

$$|\delta_l| \simeq 0.$$

So the sum in $f(\theta)$ from region III vanishes according to eq. (1). Thus the signi contribution comes from region II, i.e. from the terms between $l_1 \sim \rho$ to $l_2 \sim \rho^{3/2}$.

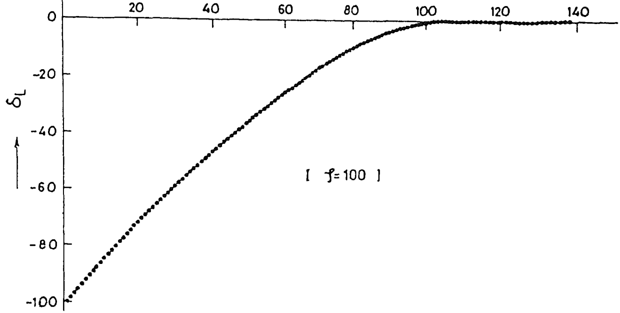

Figure 1. Scattering phase shift δ_l vs. angular momentum quantum number l for $\rho = 100$.

The differential cross-section computed numerically for several values of the scattering angle $\theta > 0$ and $\rho \gg 1$ is shown in table 1. We give results for different values of θ and ρ and notice that as ρ increases the classical values are obtained as a limit.

There is, however, a subtle difference in the definition [6, 10] in classical and quantum mechanics which has caused much confusion in the literature. According to the quantum mechanical calculation, scattering along the forward direction is non-vanishing and the total cross-section in the classical limit situation becomes $2\pi a^2$. This difference is essentially due to difference in the definition of scattering cross-section in quantum and classical mechanics. In ref. [6] we have obtained in the classical limit a general relation between the quantum mechanical and the classical values of total cross-section, σ_{qm} and σ_{cl} for different cases of scattering including that by rigid sphere and have shown that the total cross-section have to satisfy the relation, $\sigma_{\text{qm}} = 2\sigma_{\text{cl}}$. This difference is not only a difference in the facts produced by two theories, but also a difference in the definitions of scattering cross-section in two theories. Both, however, correctly reproduce experimental observation (in approximate limits) with different interpretations.

This analysis brings out an important aspect of the classical limit problem so far overlooked. In addition to demonstrating that the differential cross-section agree at large angles it is essential to prove the above relation for the total cross-section for obtaining correct classical limit. In conclusion we have remarked in ref. [6] that it is ironical that the well known result $\sigma_{\text{qm}} = 2\sigma_{\text{cl}}$, for rigid sphere scattering in the classical limit has been regarded as anomalous in most of the literature on scattering. From the present analyses we conclude that this is the correct classical limit relation. A real anomaly would be produced if the relation came out $\sigma_{\text{qm}} = \sigma_{\text{cl}}$.

Table 1. Some typical computed values for the differential scattering cross-section at selected angles of scattering by a rigid sphere.

	$(4\|f(\theta)\|^2/a^2)$*		
$\rho = ka$	$\theta = 45°$	$\theta = 60°$	$\theta = 90°$
20	1·25	1·10	—
50	1·12	1·04	—
100	1·04	1·01	1·001

*$(4|f(\theta)|^2/a^2)_{\text{classical}} = 1$.

3. Discussion

The examples given in the previous section demonstrate how the general ap suggested may be applied to different scattering cases to calculate the classical l this connection it may be mentioned that the approach suggested by Land Lifshitz [7] and later discussed by Newton [11] has certain limitations from wl present method is free. Landau and Lifshitz have enumerated the followin conditions:

(a) for every scattering angle θ in the classical limit the dominant contributio scattering amplitude must come from large l values centred around $l_0(\theta)$ determ the condition of stationary phase, (b) the total phase factor ($\simeq 2\delta_l \pm \theta_l$) for ea must be large enough so that $f_l(\theta)$ is a rapidly varying function of l near l_0; for necessary that both δ_{l_0} and δ''_{l_0} should be much greater than 1, and (c) there is c value of θ for every classical impact parameter. The above conditions are suffic the main weakness of the method lies in the fact that it cannot state for which value of a dimensionless parameter all these conditions are satisfied. Secon method of stationary phase may not be applicable in all cases. For example, in of rigid sphere scattering the method does not work. Thirdly even if a stationar exists the parabolic formula for the differential cross-section (see appendix become inadequate if the stationary phase point is a broad maxima or minima other hand in the present procedure we have to know the phase shift δ_l as a fur l and the quantum parameter α and then evaluate $f(\theta)$ in the limit $\alpha \to \infty$. N assumptions are required. It would indeed be surprising if the classical lim recovered in this limit.

A counter intuitive and interesting feature that emerges from the present ar that the parameter α which determines the classical limit depends on the sc potential. If we write α in the form $a_0/\hbar$, then a_0 is the action parameter for the and the classical limit is reached when $a_0 \gg \hbar$. For $V = \gamma/r^2$, $a_0 = (2\gamma m)^{1/2}$; for $a_0 = \gamma_1/v_0$; and for a rigid sphere $a_0 = mv_0 a$. These expressions clearly indicat to classical result.

In conclusion we would like to draw attention to the remarks made after equations (3.5) and (4.4). In all works connected with the classical limit of quantum mechanics, attempt is made to derive a particular classical formula from quantum mechanics using a suitable limiting procedure. It is overlooked that by this procedure we do not retrieve the entire classical phenomenon. For example in the present work we derive the classical expression for the differential cross-section but we do not recover from quantum mechanics an ensemble of particle tracks which are the fundamental elements in the classical theory of scattering. This problem raises an important question. Why can we retrieve only some classical formulae without actually recovering the entire classical phenomenon? It seems the answer to this puzzle is not known at present.

Appendix A

Using the value of δ_l in eq. (2.4) it can be shown that

$$\sum_0^{l_1}(2l+1)P_l(\cos\theta)e^{i2\delta_l}=0 \tag{A1}$$

and, using the asymptotic expression for $P(\cos\theta)$ for large l

$$\sum_{l_2}^{\infty}(2l+1)P_l(\cos\theta)e^{i2\delta_l}=\sum_{l_2}^{\infty}(2l+1)\frac{2}{\sqrt{2\pi l\sin\theta}}\sin\left\{(l+\tfrac{1}{2})\theta+\frac{\pi}{4}\right\}e^{i2\delta_l}=0. \tag{A2}$$

because in (A2) the sine-term in the numerator is rapidly oscillating with l and the other l-dependent terms are slowly varying. The vanishing of the first sum (A1) can be shown from the following results. The generating function for $P_l(\cos\theta)$ gives the relations

$$\frac{1-S^2}{(1-2S\cos\theta+S^2)^{1/2}}=\sum_0^{\infty}(2l+1)P_l(\cos\theta)S^l \tag{A3}$$

and

$$\left.\begin{aligned}\sum_0^{\infty}(2l+1)P_l(\cos\theta)=0\\ \sum_0^{\infty}(-1)^l(2l+1)P_l(\cos\theta)=0\end{aligned}\right\}\quad\text{for } \theta\neq 0. \tag{A4}$$

It follows from above that $\Sigma_0^{l_1}(-1)^l(2l+1)P_l(\cos\theta)=0$ because the sum over high l-values vanishes due to rapid oscillation of $P_l(\cos\theta)$ (its asymptotic expression). It may be noted that $\theta=0$ angle is excluded.

Appendix B

In order to project clearly the assumptions under which the expression (3.4) is valid, we briefly outline the derivation of the same and check whether the assumptions have been satisfied in deriving equation (3.5).

As has been shown in Appendix A, in the expression for $f(\theta)$ given by (1), th
over region I and region III vanish. We have to evaluate the sum for region II o
this region all the l's are much greater than 1 and we can use the asymptotic expr
for $P_l(\cos\theta)$ for large l. We use the method of stationary phase to evaluate this su
break up the $\sin\{(l+(1/2))\theta+(\pi/4)\}$ term in (A2) in exponential functions an
sum over l leads to two separate sums with different phase terms. One of the phas
be stationary for $l = l_\theta$ which is given by eq. (3.3). We now expand δ_l about l_θ. S
$x = l - l_\theta$ we get

$$\delta_l = \delta_\theta + x\delta'_\theta + \frac{x^2}{2}\delta''_\theta + \frac{x^3}{6}\delta''_\theta,$$

where $\delta_\theta = \delta_{l=l_\theta}$ and

$$\frac{2l+1}{\sqrt{l}} \simeq 2\sqrt{l} = 2(l_\theta + x)^{1/2} = 2l_\theta^{1/2}\left(1 + \frac{x}{2l_\theta} + \ldots\right).$$

Using the above result in the expression (3.4), we get

$$f(\theta) \simeq -k^{-1}(l_\theta/2\pi\sin\theta)^{1/2}\int_{l_1}^{l_2}\exp i\left[x^2\delta''_\theta + \frac{x^3}{3}\delta'''_\theta + \ldots\right] \times \left(1 + \frac{x}{2l_\theta} + \ldots\right)\mathrm{d}x.$$

From (3.3) we find that $l_\theta \sim \alpha$ and hence $\delta''_\theta \sim 1/\alpha$ and $\delta'''_\theta \sim 1/\alpha^2$. The ra
l between l_1 and l_2 is assumed to be small and of the order of $\sqrt{\alpha}$. Hence x will
than $\sqrt{\alpha}$. Under these condition $x^3\delta'''_\theta$ term will be much less than the $x^2\delta''_\theta$ term
as $\sqrt{\alpha} \gg 1$. Similarly $x/2l_\theta \ll 1$. Neglecting these terms and changing the limits l_1 -
and $l_2 \to +\infty$ (as most of the contribution to the integral comes from a small
around l_θ), we get

$$f(\theta) \simeq -k^{-1}(l_\theta/2ki\delta''_\theta\sin\theta)^{1/2}.$$

From (3.2) we can write

$$\delta''_\theta = \mp\frac{1}{2(\mathrm{d}l_\theta/\mathrm{d}\theta)}.$$

Using these results we get (3.4) for $|f(\theta)|^2$.

References

[1] D Home and S Sengupta, *Il. Nuovo Cimento* **B82**, 214 (1984)
[2] J Ford and G Mantica, *Am. J. Phys.* **60**, 1086 (1992)
[3] E G P Rowe, *J. Phys.* **A20**, 1419 (1987)
[4] D Bhaumik, B Dutta Roy and G Ghosh, *J. Phys.* **A19**, 1355 (1986)
[5] M Born and W Ludwig, *Z. Phys.* **150**, 106 (1958)
[6] D Sen, A N Basu and S Sengupta, *Phys. Lett.* **A184**, 159 (1994)
[7] L D Landau and E M Lifshitz, *Quantum Mechanics: Non-relativistic Theory* (Pe

[8] A N Basu and S Sengupta, *Il. Nuovo Cimento* **B106**, 511 (1991). In eq. (4) herein the factor of 4 should be dropped.
[9] L Schiff, *Quantum mechanics* (Mc-Graw Hill, New York, 1955) pp. 125–142
[10] J B Keller, *Am. J. Phys.* **40**, 1035 (1972)
[11] R G Newton, *Scattering Theory of Waves and Particles*, 2nd edition (Springer-Verlag, New York, 1982)

Creation or destruction of sourceless abelian gauge strings in a Robertson–Walker universe

D BHATTACHARYYA and S BANERJI
Department of Physics, The University of Burdwan, Burdwan 713 104, India

MS received 13 May 1996; revised 24 December 1996

Abstract. Following Morris's [5] consideration of a sourceless abelian gauge string in a Robertson–Walker universe with flat space sections we have generalized the treatment to the case of arbitrary spatial curvature. We find that creation or destruction of the gauge string is not possible if the spatial curvature is nonzero.

Keywords. Cosmology; early universe; cosmic strings.

PACS Nos 04·20; 98·80

1. Introduction

Spontaneous symmetry breaking in gauge theories in the early universe may have given rise to trapped one dimensional regions of a false vacuum called cosmic strings. These strings may have been responsible for the structure formation in the universe. A simple gauge string arising from the breaking of $U(1)$ gauge symmetry will figure in our discussion. Various aspects of such strings have attracted attention [1, 2, 3]. The cosmic gauge string is regarded as an infinitely long very thin mass distribution centred on the symmetry axis of a cylinder. The system of equations describing a single string are so complicated that analytical solutions have not been obtained in the general case. However, Laguna-Castillo and Matzner [4] claimed to have found a regular solution by numerical methods.

Since our universe is expanding, attempts were made to find a solution corresponding to a cosmic string embedded in a Robertson–Walker universe. Morris [5] presented the model of a sourceless abelian gauge string with the complex valued Higgs field completely removed for mathematical simplicity. In this way he showed that such a string in a Robertson–Walker universe with flat space sections could be created or destroyed by a radial inflow of gauge field energy. It is interesting to see what happens if the space sections of Robertson–Walker universe are not flat.

In §2 we present the relevant equations for general curvature k. In §3 we give the solutions corresponding to $k = \pm 1$. Finally, in §4 we present the summary and conclusions. Like Morris, we have assumed that the cosmic scale factor has a power law behaviour. We find that in the case of nonzero spatial curvature no nonstatic exact solution of a cosmic string satisfies the required boundary conditions. This implies that creation or destruction of a straight cosmic string is possible only for a cosmological model with flat space sections. However, we assume that the gauge field structure function can be separated into the product of a space- and time-dependent functions.

2. The equations

We take a Robertson–Walker (RW) metric with general spatial curvature k in cylindrical polar coordinates (ρ, z, ϕ).

$$ds^2 = dt^2 - a^2(t)\left(\frac{d\rho^2}{1-k\rho^2} + (1-k\rho^2)\,dz^2 + \rho^2\,d\phi^2\right). \tag{2.1}$$

Here spatial curvature $k = \pm 1, 0$ and $a(t) \sim t^{\alpha}$ $(2/3 \leqslant \alpha < 1/3)$. If we take $\rho = r\sin\theta$ and

$$z = \tan^{-1}\left(\frac{r\cos\theta}{\sqrt{1-r^2}}\right) \quad \text{for } k = +1, \tag{2.2a}$$

$$= (r\cos\theta) \quad \text{for } k = 0, \tag{2.2b}$$

$$= \tanh^{-1}\left(\frac{r\cos\theta}{\sqrt{1+r^2}}\right) \quad \text{for } k = -1, \tag{2.2c}$$

the metric reduces to the form of RW universe in terms of spherical polar coordinates

$$ds^2 = dt^2 - a^2(t)\left(\frac{dr^2}{1-kr^2} + r^2(d\theta^2 + \sin^2\theta\,d\phi^2)\right). \tag{2.3}$$

The Lagrangian of the $U(1)$ gauge field is given by

$$L = \sqrt{-g}\left(-\frac{1}{4}F_{\mu\nu}F^{\mu\nu}\right) \tag{2.4}$$

and the gauge field energy tensor $F_{\mu\nu}$ can be expressed as

$$F_{\mu\nu} = A_{\nu,\mu} - A_{\mu,\nu}. \tag{2.5}$$

where

$$A_\mu = \frac{1}{e}[P(\rho,t) - 1]\delta_\mu^\phi \tag{2.6}$$

and $P(\rho, t)$ is called the gauge field structure function. The equation of motion of the gauge field is given by

$$F^{\mu\nu}_{;\nu} = \frac{1}{\sqrt{-g}}\left(\sqrt{-g}\,F^{\mu\nu}\right)_{,\nu} = 0. \tag{2.7}$$

The nonvanishing components of the gauge field tensor are

$$F_{t\phi} = \frac{\dot{P}}{e}, \quad F^{t\phi} = -\frac{\dot{P}}{e\,a^2\rho^2}, \tag{2.8a}$$

$$F_{\rho\phi} = \frac{P'}{e}, \quad F^{\rho\phi} = \frac{P'(1-k\rho^2)}{} \tag{2.8b}$$

Here dot and prime represent derivatives with respect to t and ρ respectively. Using (2.7) we obtain

$$\left(\ddot{P} + \frac{\dot{a}}{a}\dot{P}\right) - \frac{(1-k\rho^2)}{a^2}\left[P'' - \frac{P'(1+k\rho^2)}{\rho(1-k\rho^2)}\right] = 0. \tag{2.9}$$

Following Morris [5] the ordinary magnetic field is

$$B_z = \frac{1}{\sqrt{g_{\rho\rho}\,g_{\phi\phi}}} F_{\phi\rho} = -\frac{P'(1-k\,\rho^2)}{e\,a^2\,\rho}. \tag{2.10}$$

The total magnetic flux can be written as

$$\Phi_{\mathrm{T}}(\rho,t) = -\oint_{A_\phi} \mathrm{d}\phi = \frac{2\pi}{e}[1 - P(\rho,t)]. \tag{2.11}$$

But the flux Φ_F associated with the field $F_{\phi\rho}$ in (2.8b) is

$$\Phi_F(\rho,t) = \int_0^{2\pi}\int_0^{\rho} F_{\phi\rho}\,\mathrm{d}\rho\,\mathrm{d}\phi = \frac{2\pi}{e}[P(0,t) - P(\rho,t)]. \tag{2.12}$$

Here $P(0,t)$ need not be identically equal to unity. It implies

$$\Phi_{\mathrm{T}}(\rho,t) \neq \Phi_F(\rho,t). \tag{2.13}$$

Therefore, aside from a magnetic field, the sourceless $U(1)$ gauge theory possesses an additional singular gauge string restricted to the z-axis with an associated string flux

$$\Phi_{\mathrm{S}}(t) = \Phi_{\mathrm{T}}(\rho,t) - \Phi_F(\rho,t) = \frac{2\pi}{e}[1 - P(0,t)]. \tag{2.14}$$

3. The solutions

We assume that the gauge function remains finite throughout the universe. Hence the structure function $P(\rho,t)$ must satisfy the following asymptotic boundary conditions

$$P(\rho,t) \to \text{const.} \quad \text{as} \quad \rho \to \infty, \tag{3.1a}$$

$$P(\rho,t) \to \text{const.} \quad \text{as} \quad t \to \infty. \tag{3.1b}$$

Let us make the extra assumption that $P(\rho,t)$ can be separated as the product of two functions in the following way:

$$P(\rho,t) = F(\rho)\,G(t). \tag{3.2}$$

With this assumption, (2.9) separates into two ordinary equations

$$F'' - \frac{F'}{\rho}\frac{(1+k\rho^2)}{(1-k\rho^2)} - \frac{m^2\,F}{(1-k\rho^2)} = 0, \tag{3.3a}$$

where m^2 is the separation constant and may be positive, negative or zero.

We now consider three cases.

Case I: $k = 0$.

Equation (3.3a) reduces to the form

$$F'' - \frac{F'}{\rho} - m^2 F = 0,$$

$$\ddot{G} + \frac{\dot{a}}{a}\dot{G} - \frac{m^2}{a^2}G = 0.$$

Morris [5] found the general solution of (3.3c) and (3.3d) satisfying the bo condition (3.1a, b) to be

$$P(0,t) = P_0 + P_1 \exp\left[\frac{\Gamma}{1-\alpha}\left\{1 - \left(\frac{t}{t_0}\right)^{1-\alpha}\right\}\right]$$

$$= P_0 + P_1\, G(t),$$

where P_0, P_1 and Γ are constants and $a(t)$ has been taken to be proportional to $(2/3 \leqslant \alpha < 1/3)$. From (2.14) we obtain

$$\Phi_S(t) = \frac{2\pi}{e}\{1 - [P_0 + P_1\, G(t)]\}.$$

Depending upon the values of P_0 and P_1, Φ_S can be an increasing or a dec function of time, i.e. it may represent the creation or the destruction of strings

Case II: $k = -1$.

Equation (3.3a) reduces to the form

$$F'' - \frac{F'(1-\rho^2)}{\rho\,(1+\rho^2)} - \frac{m^2 F}{(1+\rho^2)} = 0.$$

Putting $x = -\rho^2$ and $u(x) = F(\rho)$ we obtain (see Murphy, p. 369, [6])

$$x(1-x)u'' - x\,u' + \frac{m^2}{4}u = 0,$$

$$x(1-x)\,u'' + [c - (1 + a + b)x]u' - abu = 0.$$

Here a prime represents the derivative with respect to x. This is Gauss's hyperge equation where $x = 0$, 1 and ∞ at the regular singular points [7, 8].

Comparing (3.7a) and (3.7b) we get $c = 0$, $a = \pm m/2$, $b = \mp m/2$. We mu $r \geqslant 0$, $\rho \geqslant 0$ and since $x = -\rho^2$, ρ is imaginary. For $x > 0$, the only singular p physical space is at $\rho = 0$, i.e. $x = 0$.

Case IIa: $m^2 < 0$. In this case a and b are imaginary. So the solution is inadm

Case IIb: $m^2 = 0$. Here

$$F(\rho) = A\ln(1+\rho^2) + B$$

Following Morris [5]

$$G(t)=\frac{Dt}{(1-\alpha)\,a(t)}+G_0. \tag{3.9}$$

On account of the boundary conditions

$$F(\rho)=F_0, \quad G(t)=G_0. \tag{3.10}$$

$P(\rho,t)=P_0$ is a constant.

Case IIc: $m^2>0$. Since $c=0$ the general solution is

$$u(x)=(Ax)\,{}_2F_1(1\pm m/2, 1\mp m/2, 2; x). \tag{3.11}$$

${}_2F_1(1\pm m/2, 1\mp m/2, 2; x)$ is a Gauss's hypergeometric function [7].

Hence

$$F(\rho)=A(-\rho^2)\,{}_2F_1(1\pm m/2, 1\mp m/2, 2; -\rho^2), \tag{3.12a}$$

$$G(t)=\exp\left[\frac{\Gamma}{1-\alpha}\left\{1-\left(\frac{t}{t_0}\right)^{1-\alpha}\right\}\right]. \tag{3.12b}$$

Since $F(0)=0, P(0,t)=F(0)\,G(t)=0$, so there is no contribution to string flux in this case.

Case IId (*General case*): The general solution consistent with the boundary conditions (3.1a,b) is

$$P(\rho,t)=F_0G_0=P_0. \tag{3.13}$$

The string flux

$$\Phi_S(t)=\frac{2\pi}{e}[1-P(0,t)]=\frac{2\pi}{e}[1-P_0]. \tag{3.14}$$

So we have neither creation nor destruction of the string.

Case III: $k=+1$.

In this case $\rho=r\sin\theta$ and $z=\tan^{-1}(r\cos\theta/(\sqrt{1-r^2}))$. The metric (2.1) takes the form

$$\mathrm{d}s^2=\mathrm{d}t^2-a^2(t)\left(\frac{\mathrm{d}r^2}{1-r^2}+r^2\,(\mathrm{d}\theta^2+\sin^2\theta\,\mathrm{d}\phi^2)\right). \tag{3.15}$$

The universe has a finite volume. So we cannot proceed to the limit $r\to\infty$. However, we have to examine the limit of the maximum value of ρ. k is positive, r and hence ρ lies between 0 and 1.

So we have the following boundary conditions

$$P(\rho,t)\to\text{const.} \quad \text{as} \quad \rho\to 1 \tag{3.16a}$$

and

Substituting $x=\rho^2$, $F(\rho)\equiv u(x)$ (see Murphy [6], p. 369) we obtain

$$x(1-x)u''-x\,u'-\frac{m^2}{4}u=0,$$

$$x(1-x)u''+[c-(1+a+b)\,x]\,u'-abu=0,$$

where prime represents a derivative with respect to x.

This is Gauss's hypergeometric equation with $x=0,\,1,\,\infty$ at the singular poi

Comparing (3.18a) and (3.18b) we get

$$c=0,\quad a=\pm\sqrt{(-m^2/4)},\quad b=\mp\sqrt{(-m^2/4)}.$$

Case IIIa: $m^2<0$. In this case, we have the solution satisfying (3.1a,b).

$$u(x)=A\,x\;{}_2F_1(1+a,1+b,2;\,x),$$

where the values of a and b are given above. The two regular singular points are x corresponding to $\rho=0,1$. The series converges at both points.

Case IIIb: $m^2=0$. In this case we have the solution

$$F(\rho)=A\ln(1-\rho^2)+F_0.$$

This blows up at $\rho\to 1$. Hence we set $A=0$

$$G(t)=\frac{D\,t}{(1-\alpha)\,a(t)}+G_0.$$

From the boundary conditions (since $A=0$, $D=0$), we have

$$P(\rho,t)=P_0.$$

Case IIIc: $m^2>0$. In this case a and b are imaginary. Hence the solution is missible.

Case IIId (*General case*):

$$P(\rho,t)=P_0+P_2\,\rho^2\,{}_2F_1(1+a,\,1+b,\,2;\,\rho^2)\,G(t),$$

where

$$P_0=F_0\,G_0.$$

${}_2F_1(1+a,\,1+b,\,2;\rho^2)\to 1$ as $\rho\to 0$. Here ${}_2F_1(1+a,\,1+b,\,2;\,\rho^2)$ is the Gauss geometric function.

The string 'magnetic' flux is

$$\Phi_{\mathrm{S}}(t)=\frac{2\pi}{e}[1-P(0,t)]=\frac{2\pi}{e}[1-P_0].$$

Poynting vector for the flat space sections is

$$S_\rho = (-g_{\rho\rho})^{1/2}\, T^{t\rho} = -\frac{\dot{P} P'}{e^2 a^3 \rho^2}. \tag{3.27}$$

The electromagnetic gauge field energy flows radially inwards of the string which may create a string or destroy an already preexisting string.

4. Conclusion

Following Morris's consideration of a sourceless abelian gauge string in a Robertson–Walker universe with flat space sections, we have generalized the treatment to the case of arbitrary spatial curvature. We have found that creation or destruction of the gauge string is possible only if the spatial curvature is zero. If the spatial curvature is negative or positive, we have neither creation nor destuction of the string. We have, however, assumed like Morris that the gauge field structure function can be separated into a space-dependent and a time-dependent part.

Acknowledgements

The authors are thankful to the Department of Science and Technology and the University Grants Commission for financial assistance. They also thank the Relativity and Cosmology Research Centre, Jadavpur University and Inter-University Centre for Astronomy and Astrophysics, Pune for stimulating seminars.

References

[1] E W Kolb and M S Turner, *The Early Universe* (Addision-Wesley, 1990) and references therein
[2] J R Gott, *Astrophys. J.* **288**, 422 (1985)
[3] A K Raychaudhuri, *Phys. Rev.* **D41**, 3041 (1990)
[4] P Laguna-Castillo and R A Matzner, *Phys. Rev.* **D33**, 1546 (1989)
[5] J R Morris, *Phys. Rev.* **D44**, 1015 (1991)
[6] G M Murphy, *Ordinary differential equations and their solutions* (affiliated East West, 1969) pp. 373, 357
[7] M Abramowitz and I A Stegun (eds), *Handbook of Mathematical Functions* (Dover, 1972) p. 556
[8] I N Sneddon, *Special functions of mathematical physics and chemistry* (Ohvir and Boyal, 1966)

Higher dimensional Vaidya metric in Einstein and de Sitter background

L K PATEL and LAKSHMI S DESAI
Department of Mathematics, Gujarat University, Ahmedabad 380 009, India

MS received 14 October 1996; revised 7 December 1996

Abstract. Spherically symmetric non-static higher dimensional metrics are considered in connection with Einstein's field equations. Two exact solutions are derived. One of them corresponds to a mixture of perfect fluid and pure radiation field and represents higher dimensional Vaidya metric in the cosmological background of Einstein static universe. The other corresponds to a pure radiation field and represents higher dimensional Vaidya metric in the background de Sitter universe. For both of these solutions, the cosmological constant is taken to be non-zero. Many known solutions are derived as particular cases.

Keywords. Higher dimensional Vaidya metric; Einstein universe; de Sitter universe.

PACS Nos 04·20; 98·80; 04·50

1. Introduction

Multi-dimensional spacetime is now an active field of research in its attempts to unify gravitation with other forces of nature [1]. In view of recent developments in superstring theory [2, 3], higher dimensional physics has attained a new measure of importance.

The implications of theories in which the dimension of the spacetime is greater than four have been discussed by several authors. What is required from the viewpoint of physics is direct observational evidence supporting theories of higher dimensions. Many exact solutions of Einstein field equations in 4-dimensional spacetime are available in the literature [4]. But the number of articles dealing with exact solutions of Einstein's equations in higher dimensions is relatively small.

In connection with localized sources, the higher dimensional generalizations of Schwarzschild exterior and Reissner–Nordstrom solutions [5, 6] have been obtained. Higher dimensional generalization of the well-known Kerr solution is also available in the literature [7–9]. Iyer and Vishveshwara [10] have generalized the Vaidya metric [11] representing the gravitational field of a radiating star to space times of dimensions greater than four. Their solution can be expressed in the form

$$ds^2 = 2\mathrm{d}u\mathrm{d}r + \left[1 - \frac{2m(u)}{(n-1)r^{n-1}}\right]\mathrm{d}u^2 - r^2\mathrm{d}\Omega_n^2, \tag{1}$$

where

$$\mathrm{d}\Omega_n^2 = \mathrm{d}\theta_1^2 + \sin^2\theta_1\,\mathrm{d}\theta_2^2 + \cdots + \sin^2\theta_1\sin^2\theta_2\cdots\sin^2\theta_{n-1}\,\mathrm{d}\theta_n^2 \tag{2}$$

is the metric on the n-sphere in polar co-ordinates. Here the function $m(u)$ represents the mass of the radiating star.

equations that represent metrics embedded in a cosmological backgroun generalizations of de Sitter's and Friedmann's cosmological solutions with a mass are well-known in the literature [12, 13]. Patel and Akbari [14] have dis the usual Vaidya metric in the cosmological background of Einstein static un Mallett [15] and Vick [16] have examined the field produced by a radiatin in de Sitter universe. It would be interesting to obtain the metric (1) in the c logical backgrounds of Einstein universe and de Sitter universe rather t the standard Minkowskian background, and the purpose of the present to do just that.

The geometry of $(n + 2)$-dimensional Einstein's universe is described by the

$$ds^2 = dt^2 - \frac{d\bar{r}^2}{1 - \frac{\bar{r}^2}{R^2}} - \bar{r}^2 d\Omega_n^2,$$

where R is a constant.

By the coordinate transformation

$$\bar{r} = R\sin\left(\frac{r}{R}\right), \quad u = t - r,$$

the above metric reduces to

$$ds^2 = 2\,du\,dr + du^2 - R^2\sin^2\left(\frac{r}{R}\right)d\Omega_n^2.$$

We shall take the metric of higher dimensional Einstein universe in the fo Similarly one can easily see that the line element of $(n+2)$-dimensional de universe can be expressed in the form

$$ds^2 = 2\,du\,dr + \left[1 - \frac{2\Lambda r^2}{n(n+1)}\right]du^2 - r^2 d\Omega_n^2,$$

where Λ is the cosmological constant.

2. Higher dimensional Vaidya metric in the de Sitter universe

We begin with the line element

$$ds^2 = 2\,du\,dr + 2L\,du^2 - r^2 d\Omega_n^2,$$

where L is a function of r and u and u is the retarded time. We name coordin $x^0 = u$, $x^1 = r$, $x^{i+1} = \theta_i$ $(i = 1, 2, \ldots, n)$.

The non-vanishing components of the Einstein tensor G_{ik} for the metric (5) ar to have the following expressions:

$$G_{01} = \frac{n}{r}L_r + \frac{n(n-1)(2L-1)}{2r^2},$$

$$G_{22}=(n-1)\left[(2L-1)\left(\frac{2-n}{2}\right)-2rL_r\right]-r^2L_{rr}, \tag{6b}$$

$$G_{00}=-\frac{nL_u}{r}+\frac{2nLL_r}{r}+\frac{n(n-1)L(2L-1)}{r^2}, \tag{6c}$$

$$G_2^2=G_3^3=G_4^4=\cdots=G_{n+1}^{n+1}. \tag{6d}$$

Here and in what follows a suffix denotes partial derivative e.g.

$$L_u=\frac{\partial L}{\partial u},\quad L_{rr}=\frac{\partial^2 L}{\partial r^2}\cdots.$$

We wish to solve the field equations

$$G_{ik}=-8\pi\sigma w_i w_k-\Lambda g_{ik}, \tag{7}$$

where $w^i w_i=0$ and σ is the radiation density. One can easily check that

$$w_i=(1,0,0,\ldots,0) \tag{8}$$

is a null vector for the metric (5). In view of eqs (6a)–(6d) and (8), the field equation (7) led to the relation

$$G_{01}=-\Lambda,\quad G_{22}=\Lambda r^2,\quad G_{00}=-8\pi\sigma-2L\Lambda. \tag{9}$$

The equation $G_{01}=-\Lambda$ can be easily integrated to have

$$2L=1-\frac{2m(u)}{(n-1)r^{n-1}}-\frac{2\Lambda r^2}{n(n+1)}, \tag{10}$$

where $m(u)$ is an arbitrary function of u. Using (10) it is easy to verify that the equation $G_{22}=\Lambda r^2$ is identically satisfied. From the last equation in (9), we can determine the value of σ. It is given by

$$8\pi\sigma=-\frac{nm_u}{(n-1)r^n}. \tag{11}$$

Thus the cosmological constant has no effect on the radiation density.

The line element of our above solution can be expressed in the form

$$ds^2=2\,du\,dr+\left[1-\frac{2m(u)}{(n-1)r^{n-1}}-\frac{2\Lambda r^2}{n(n+1)}\right]du^2-r^2\,d\Omega_n^2. \tag{12}$$

In the absence of the source (i.e. $m=0$), the metric (12) reduces to the metric (4) of higher dimensional de Sitter universe. When $\Lambda=0$, the metric (12) becomes the metric (1). Thus the metric (12) describes the higher dimensional Vaidya solution in the cosmological background of the de Sitter universe. When $m=$ constant, the metric (12) represents higher dimensional Schwarzchild exterior metric in the background of the de Sitter universe. In the case $n=2$, the metric (12) gives the usual Vaidya metric

$$ds^2 = 2\mathrm{d}u\mathrm{d}r + 2L\mathrm{d}u^2 - R^2\sin^2\left(\frac{r}{R}\right)\mathrm{d}\Omega_n^2,$$

where L is a function of r and u and u is the retarded time. Here it should be not
a metric more general than (13) has been considered by Chatterjee and Bhui
connection with mass-energy in higher dimensions.

By a routine calculation one can obtain the expressions for Einstein
$G_{ik} = R_{ik} - (1/2)R\, g_{ik}$ for the metric (13). The surviving G_{ik} are listed below fo
reference.

$$G_{11} = -\frac{n}{R^2},$$

$$G_{01} = \frac{n}{R}L_r\cot\left(\frac{r}{R}\right) - \frac{2nL}{R^2} + \frac{n(n-1)}{2R^2}\left[2\cot^2\left(\frac{r}{R}\right)L - \operatorname{cosec}^2\left(\frac{r}{R}\right)\right],$$

$$G_{00} = \frac{2nL}{R}L_r\cot\left(\frac{r}{R}\right) - \frac{nL_u}{R}\cot\left(\frac{r}{R}\right) - \frac{4L^2n}{R^2} + \frac{2L^2n(n-1)}{R^2}\cot^2\left(\frac{r}{R}\right) - \frac{n(n-1)}{R^2}L\operatorname{cosec}^2\left(\frac{r}{R}\right),$$

$$G_{22} = (n-1)\left[2L - 2L_rR\sin\left(\frac{r}{R}\right)\cos\left(\frac{r}{R}\right) - nL\cos^2\left(\frac{r}{R}\right) + \frac{n}{2} - 1\right] - R^2L_{rr}\sin^2\left(\frac{r}{R}\right),$$

$$G_2^2 = G_3^3 = G_4^4 = \cdots = G_{n+1}^{n+1}.$$

We take the space surrounding the radiating particle to be occupied by a
distribution with n-spherical symmetry of density ρ and pressure p. The
Einstein field equations are

$$G_{ik} + \Lambda g_{ik} = -8\pi[(p+\rho)v_iv_k - p\,g_{ik} + \sigma\omega_i\omega_k]$$

with

$$v^iv_i = 1, \quad \omega_i\omega^i = 0, \quad v^i\omega_i = 1.$$

Here v^i is the flow vector of the fluid, ω^i is the null vector and $\sigma\omega^i\omega^k$ is the
momentum tensor arising out of the flowing null radiation.

We take v_i and ω_i in the forms

$$v_i = \left(Lx + \frac{1}{2x}, x, 0, \ldots, 0\right), \quad \omega_i = \left(\frac{1}{x}, 0, 0, \ldots, 0\right),$$

where x is a function of coordinates to be determined from the field equations.
checked that v_i and ω_i given by (17) satisfy the conditions (16).

$$x^2 = \frac{1}{2L} \tag{18}$$

and

$$L_{rr} + \frac{(n-2)}{R} L_r \cot\left(\frac{r}{R}\right) + \frac{(n-1)(1-2L)}{R^2} \operatorname{cosec}^2\left(\frac{r}{R}\right) = 0. \tag{19}$$

Here we have assumed that $2L$ is positive.

The differential equation (19) can be easily integrated and the solution can be expressed in the form

$$2L = 1 - \frac{2m(u)\cos\left(\frac{r}{R}\right)}{(n-1)R^{n-1}\sin^{n-1}\left(\frac{r}{R}\right)}, \tag{20}$$

where $m(u)$ is an arbitrary function of u.

Using (20) we can find explicit expressions for pressure, density and radiation density. They are given by

$$8\pi\, p = \Lambda + \frac{n(2-n)}{2R^2} - \frac{nL}{R^2}, \tag{21}$$

$$8\pi\, \rho = -\Lambda - \frac{n(2-n)}{2R^2} + \frac{3nL}{R^2}, \tag{22}$$

$$16\pi\sigma L = -\frac{nm_u}{(n-1)R^n}\cot^2\left(\frac{r}{R}\right)\sin^{2-n}\left(\frac{r}{R}\right). \tag{23}$$

From the results (21) and (22) it is clear that

$$8\pi(\rho + 3p) = -2\Lambda + \frac{n(2-n)}{R^2}$$

i.e. $\rho + 3p = \text{constant}$.

The metric of our solution can be expressed in the final form as

$$\begin{aligned} ds^2 = {} & 2\,du\,dr - R^2 \sin\left(\frac{r}{R}\right) d\Omega_n^2 \\ & + \left[1 - \frac{2m(u)}{(n-1)R^{n-1}}\cos\left(\frac{r}{R}\right)\sin^{1-n}\left(\frac{r}{R}\right)\right] du^2. \end{aligned} \tag{24}$$

In the absence of the source (i.e. $m = 0$), the metric (24) reduces to the metric (3) of higher dimensional Einstein's universe. When $R \to \infty$, the metric (24) reduces to the higher dimensional Vaidya metric (1). Thus the metric (24) describes the higher dimensional Vaidya solution in the cosmological background of Einstein's universe. When $m = \text{constant}$, the metric (24) describes the higher dimensional Schwarzschild exterior metric in the background of Einstein universe. When $n = 2$, the metric (24) reduces to the Vaidya metric in Einstein universe.

Here it should be noted that our non-radiating (m = constant) me
related to higher dimensional version of the solution obtained by Whitta
assumed the equation of state $\rho + 3p = \text{constant}$.

Acknowledgement

The authors are grateful to Prof. P C Vaidya for useful comments.

References

[1] J Scherk and J H Schwarz, *Phys. Lett.* **B82**, 60 (1979)
[2] J H Schwarz, *Superstrings* (World Scientific, Singapore, 1985)
[3] S Weinberg, *Strings and superstrings* (World Scientific, Singapore, 1986)
[4] D Kramer, H Stephani, E Herlt and M A H Mac Callum, *Exact solutions o*
equations (Cambridge University Press, Cambridge, 1980)
[5] A Chodos and S Detweiler, *Gen. Relativ. Gravit.* **14**, 879 (1982)
[6] G W Gibbons and D L Wiltshire, *Ann. Phys.* **167**, 201 (1986)
[7] R C Myers and M J Perry, *Ann. Phys. (N.Y.)* **172**, 304 (1986)
[8] P O Mazur, *J. Math. Phys.* **28**, 406 (1987)
[9] V P Frolov, A I Zelnikov and U Bleyer, *Ann. Phys.* (*Leipzing*) **44**, 371 (198
[10] B R Iyer and C V Vishveshwara, *Pramana–J. Phys.* **32**, 749 (1989)
[11] P C Vaidya, *Proc. Indian Acad. Sci.* **A33**, 264 (1951)
[12] G C McVittie, *Mon. Not. R. Astron. Soc.* **93**, 325 (1933)
[13] R C Tolman, *Relativity, thermodynamics and cosmology* (Oxford Un
London, 1934) p.245
[14] L K Patel and R P Akabari, *J. Phys.* **A12**, 223 (1979)
[15] R L Mallett, *Phys. Rev.* **D31**, 416 (1985)
[16] D Vick, *Lett. Nuovo Cimento* **44**, 127 (1985)
[17] S Chatterjee and B Bhui, *Int. J. Theor. Phys.* **32**, 471 (1993)
[18] J M Whittaker, *Proc. R. Soc. London*, **A306**, I (1968)

Algebraic expressions for effective potential characteristic parameters in heavy ion scattering

I JAMIR, E F P LYNGDOH and C S SHASTRY
Department of Physics, North-Eastern Hill University, Shillong 793 022, India

MS received 23 September 1996; revised 9 December 1996

Abstract. In this paper, we obtain reliable expressions to calculate the barrier and pocket positions of the real part of the effective phenomenological optical potential having Woods–Saxon form factor, for different partial waves. The comparison of the results obtained from these formulae, when compared with the numerical results obtained using Newton–Raphson iterative procedure are found to be quite accurate, with error less than 1%. We also obtain algebraic expressions for estimating $l_{\rm poc}$, the angular momentum at which the potential pocket vanishes, the accuracy of which is tested with the exact calculations, using self-consistent iterative procedures. These and other expressions deduced in this paper provide simple and useful methods for calculating critical parameters of heavy ion effective potentials like barrier and pocket positions, curvatures at the barrier and pocket positions, $l_{\rm poc}$ and the grazing angular momentum $l_{\rm g}$ to carry out the analysis of heavy ion scattering.

Keywords. Heavy ion scattering; Coulomb barrier.

PACS No. 24·10

1. Introduction

In the study of elastic scattering, fusion, etc, in heavy ion collisions, one generally uses the phenomenological optical model potential (OMP). This has the general form

$$U(r) = -U_{\rm R}\, g(R, a, r) - i\, U_{\rm I}\, g(R_{\rm I}, a_{\rm I}, r) + U_{\rm C}(r)$$

where the most commonly used expression for $g(R, a, r)$ is the Woods–Saxon form factor given by

$$g(R, a, r) = \left[1 + \exp\left(\frac{r - R}{a}\right)\right]^{-1} \quad \text{with} \quad R = r_0(A_1^{1/3} + A_2^{1/3}). \tag{1.1}$$

The quantities r_0 and a are the radius and diffuseness parameters, $U_{\rm R}$ and $U_{\rm I}$ are the depths of the real and imaginary parts of the optical potential and A_1 and A_2 are the mass numbers of the colliding particles having corresponding proton numbers Z_1 and Z_2. Similarly, one uses the following expression for the Coulomb potential:

$$U_{\rm C}(r) = \frac{Z_1 Z_2 e^2}{2\, R_{\rm C}^3}(3R_{\rm C}^2 - r^2), \quad r < R_{\rm C} \tag{1.2a}$$

$$= \frac{Z_1 Z_2 e^2}{r}, \quad r > R_{\rm C}, \tag{1.2b}$$

where $R_C = r_C\,(A_1^{1/3} + A_2^{1/3})$ and r_C is the Coulomb radius parameter.

When this OMP is used in the radial Schrodinger equation, the effective potential governing the radial motion becomes

$$U_{\text{eff}}(l,r) = -\,U_R\,g(R,a,r) - iU_I\,g(R_I,a_I,r) + U_C(r) + \frac{l(l+1)\hbar^2}{2mr^2}, \tag{1.3}$$

where the last term is the centrifugal energy term and m is the reduced mass of the two colliding nuclei having masses m_1 and m_2.

The effective potential $U_{\text{eff}}(l,r)$ in general is characterized by strong absorption, large Coulomb barrier and a potential pocket interior to the Coulomb barrier for most of the significant partial waves. The positions, heights and curvatures of the potential barrier are important in characterizing different aspects of the collision like nucleus-nucleus fusion around the Coulomb barrier [1], barrier region resonances, back angle oscillations generated by interference of barrier and internal regions [2–4] etc. [5] gives approximate methods to calculate some of these quantities. Similarly, the angular momentum $l = l_{\text{poc}}$ where the potential pocket vanishes and the grazing partial wave l_g such that Real $(U_{\text{eff}}(l_g, r)) = E$ where E is the centre of mass energy, are important in the study of heavy ion collisions.

For a global heavy ion potential having exponential form, Broglia and Winther [6] have given an approximate empirical expression for the position of the s-wave real potential barrier as

$$R_{B0} = 1{\cdot}07\,(A_1^{1/3} + A_2^{1/3}) + 2{\cdot}72 \tag{1.4}$$

and starting from this, the barrier position R_{Bl} and pocket position R_{Ml} can be calculated using the Newton–Raphson iterative procedure. This procedure requires judicious choice of initial values to avoid numerical complications when R_{Ml} and R_{Bl} are close to each other.

Similarly, based on a global potential, [7] gives an empirical expression for l_{poc} as

$$l_{\text{poc}} = \left[m\,(R_1 + R_2)^3 \left(4\pi\gamma R_{12} - \frac{Z_1 Z_2 e^2}{(R_1 + R_2)^2} \right) \right]^{1/2} \tag{1.5}$$

where $R_i = 1{\cdot}233\,A_i^{1/3} - 0{\cdot}978\,A_i^{-1/3}$, $R_{12} = R_1 R_2/(R_1 + R_2)$ and

$$\gamma = 0{\cdot}95 \left[1 - 1{\cdot}8 \left(\frac{N_1 - Z_1}{A_1} \right) \left(\frac{N_2 - Z_2}{A_2} \right) \right],$$

N_1 and N_2 being the neutron numbers of the two nuclei.

However, we find that for the most commonly used OMP having Woods–Saxon form factor, there appears to be no simple formulae to calculate R_{Bl} and l_{poc}. This is important in view of the fact that l_{poc} calculated from (1.5) and R_{BO} from (1.4) can be significantly different for the OMP with Woods–Saxon form factor. In view of these, we

Algebraic expressions for $R_{\mathrm{B}l}$, $R_{\mathrm{M}l}$ and l_{poc}

r heavy ion systems, it is found that as l increases from 0 to l_{poc}, $R_{\mathrm{B}l}$ shifts towards the terior region by about a fermi. Similarly, the pocket position shifts to the exterior gion by about a fermi as l varies from 1 to l_{poc}. When $l = l_{\mathrm{poc}}$, the barrier and pocket sitions practically merge, generating a point of inflexion. We exploit this feature in ducing the algebraic formulae for $R_{\mathrm{B}l}$ and $R_{\mathrm{M}l}$.

1 *Expression for the barrier position $R_{\mathrm{B}l}$*

nce $R_{\mathrm{B}l}$ is in the vicinity of $R_{\mathrm{B}0}$, we can expand (1.1) around $r = R_0 = R_{\mathrm{B}0}$ for the rrier position calculation so that

$$g(R, a, r) = f(x) = \frac{1}{1 + Ce^{x}}, \tag{2.1}$$

here $C = \exp((R_0 - R)/a)$ and $x = ((r - R_0)/a)$.

Expanding $f(x)$ around $x = 0$, we get

$$f(x) = f(0) + xf_1(0) + \frac{x^2}{2\,!}f_2(0) + \frac{x^3}{3!}f_3(0) + \ldots, \tag{2.2}$$

here

$$f(0) = \frac{1}{1 + C}, \qquad f_1(0) = -\frac{C}{(1 + C)^2}$$

$$f_2(0) = \frac{C(C - 1)}{(1 + C)^3}, \qquad f_3(0) = -C\left(\frac{(C - 2)^2 - 3}{(1 + C)^4}\right).$$

ere, $f_i(0)$ denotes the ith order derivative of $f(x)$ at $x = 0$.

The radius of convergence of series (2.2) is

$$|x_0| = \sqrt{\left(\frac{R_0 - R}{a}\right)^2 + \pi^2}$$

hereas the corresponding radius of convergence if one sets $C = 1$ is π (i.e. if the pansion is done at $r = R$). This means that, by expanding the original function ound $r = R_0$, one increases the radius of convergence and hence approximating $f(x)$ neglecting the fourth and higher order terms becomes reasonable.

We note that, in general, $R_{\mathrm{B}l} > R_{\mathrm{C}}$. Hence, we use the following expansions r $1/r$ and $1/r^2$ for handling the Coulomb and centrifugal terms of the effective tential

$$\frac{1}{r} = \frac{1}{R}\left[1 - \left(\frac{a\,x}{R}\right) + \left(\frac{a\,x}{R}\right)^2 - \left(\frac{a\,x}{R}\right)^3 + \cdots\right], \tag{2.3}$$

$$V_{\text{eff}}(l,x)=\frac{2m}{\hbar^2}\left(-U_{\text{R}}\,g(R,a,r)+\frac{Z_1Z_2e^2}{r}+\frac{\lambda^2\hbar^2}{2mr^2}\right), \tag{2.5}$$

where $\lambda^2=l(l+1)\simeq(l+\frac{1}{2})^2$ for large l. Writing

$$\xi=\frac{Z_1Z_2e^2m}{\hbar^2},\quad V_{\text{R}}=\frac{2m}{\hbar^2}U_{\text{R}}$$

and using (2.1)–(2.5), the effective potential, after neglecting terms higher than x^3 becomes

$$V_{\text{eff}}(l,x)=-\left(\frac{4a^3\lambda^2}{R_0^5}+\frac{2\xi a^3}{R_0^4}+\frac{V_{\text{R}}f_3(0)}{6}\right)x^3+\left(\frac{3a^2\lambda^2}{R_0^4}+\frac{2\xi a^2}{R_0^3}-\frac{V_{\text{R}}f_2(0)}{2}\right)x^2$$
$$-\left(\frac{2a\,\lambda^2}{R_0^3}+\frac{2\xi a}{R_0^2}+V_{\text{R}}f_1(0)\right)x+\left(\frac{\lambda^2}{R_0^2}+\frac{2\xi}{R_0}-V_{\text{R}}f(0)\right). \tag{2.6}$$

Thus

$$V'_{\text{eff}}(l,x)=a_{\text{B}}x^2+b_{\text{B}}x+c_{\text{B}},$$

where

$$a_{\text{B}}=-\left(\frac{12a^3\lambda^2}{R_0^5}+\frac{6\xi a^3}{R_0^4}+\frac{V_{\text{R}}f_3(0)}{2}\right),\ b_{\text{B}}=\frac{6a^2\lambda^2}{R_0^4}+\frac{4\xi a^2}{R_0^3}-V_{\text{R}}f_2(0),$$
$$c_{\text{B}}=-\left(\frac{2a\,\lambda^2}{R_0^3}+\frac{2\xi a}{R_0^2}+V_{\text{R}}f_1(0)\right).$$

Next, we evaluate the appropriate zero of $V'_{\text{eff}}(l,x)$ (which is a quadratic function in x) to get $x_{\text{B}l}$:

$$x_{\text{B}l}=\frac{-b_{\text{B}}-(b_{\text{B}}^2-4a_{\text{B}}c_{\text{B}})^{1/2}}{2a_{\text{B}}} \tag{2.7}$$

and

$$R_{\text{B}l}=a\,x_{\text{B}l}+R_0. \tag{2.8}$$

The other root of $x_{\text{B}l}$ gives values of $R_{\text{B}l}$ that increase with l and hence does not correspond to the barrier position. It does not correspond to the pocket position either as the true pocket position lies deeper inside. This root is therefore ignored. Equation (2.8) can be used to calculate $R_{\text{B}l}$ for all l's from $l=0$ to l_{poc}.

2.2 *Expression for the pocket position* $R_{\text{M}l}$

It is found that for different l's, the minimum of the potential occurs mostly in the region interior to $r=R$. We have found that if $f(x)$ is expanded around $R_0=R-3a$, minima calculations are quite accurate. The procedure is similar to that for the maxima except for the Coulomb part which can be written in the following exact orm in x using (1.2a).

$$V_{\mathrm{C}}(x)=\left(\frac{3\xi}{R_{\mathrm{C}}}-\frac{\xi R_0^2}{R_{\mathrm{C}}^3}\right)-\frac{2a\xi R_0}{R_{\mathrm{C}}^3}x-\frac{\xi a^2}{R_{\mathrm{C}}^3}x^2, \qquad r<R_{\mathrm{C}}.$$

In the neighbourhood of $x=0$. i.e. $r=R-3a$, we get the following approximate xpression after ignoring higher terms:

$$\begin{aligned}V_{\mathrm{eff}}(l,x)=&-\left(\frac{4a^3\lambda^2}{R_0^5}+\frac{V_{\mathrm{R}}f_3(0)}{6}\right)x^3+\left(\frac{3a^2\lambda^2}{R_0^4}-\frac{\xi a^2}{R_{\mathrm{C}}^3}-\frac{V_{\mathrm{R}}f_2(0)}{2}\right)x^2\\&-\left(\frac{2a\lambda^2}{R_0^3}+\frac{2\xi a R_0}{R_{\mathrm{C}}^3}+V_{\mathrm{R}}f_1(0)\right)x\\&+\left(\frac{\lambda^2}{R_0^2}-\frac{\xi R_0^3}{R_{\mathrm{C}}^3}+\frac{3\xi}{R_{\mathrm{C}}}-V_{\mathrm{R}}f(0)\right)+\cdots\end{aligned}\tag{2.9}$$

nd

$$V'_{\mathrm{eff}}(l,x)=a_{\mathrm{M}}x^2+b_{\mathrm{M}}x+c_{\mathrm{M}},$$

here

$$a_{\mathrm{M}}=-\left(\frac{12a^3\lambda^2}{R_0^5}+\frac{V_{\mathrm{R}}f_3(0)}{2}\right),\quad b_{\mathrm{M}}=\frac{6a^2\lambda^2}{R_0^4}-\frac{2\xi a^2}{R_{\mathrm{C}}^3}-\mathrm{V}_{\mathrm{R}}f_2(0),$$

$$c_{\mathrm{M}}=-\left(\frac{2a\lambda^2}{R_0^3}+\frac{2a\xi R_0}{R_{\mathrm{C}}^3}+V_{\mathrm{R}}f_1(0)\right).$$

he expression for $x_{\mathrm{M}l}$ becomes

$$x_{\mathrm{M}l}=\frac{-b_{\mathrm{M}}+(b_{\mathrm{M}}^2-4a_{\mathrm{M}}c_{\mathrm{M}})^{1/2}}{2a_{\mathrm{M}}},\tag{2.10}$$

$$R_{\mathrm{M}l}=a\,x_{\mathrm{M}l}+R_0,\tag{2.11}$$

here once again, the other root is neglected as this gives rise to values of $R_{\mathrm{M}l}$ that decrease ith increasing l. One may note here also that the radius of convergence for $f(x)$ in (2.9) is

$$|x_0|=\sqrt{9+\pi^2}=4{\cdot}34.$$

his is significantly greater than π and supports the reliability of our approximation.

3 *Calculation of l_{poc}*

t angular momentum $l=l_{\mathrm{poc}}$, the effective potential does not have a maxima or minima but has a point of inflexion. It is found that this point is in the vicinity of $r=R$. n expansion for $f(x)$ appropriate for r in the vicinity of R is

$$f(x)=\frac{1}{2}\left(1-\tanh\frac{x}{2}\right)$$

e. $$f(x)=\frac{1}{\ }\left[1-\left(\frac{x}{\ }-\frac{x^3}{\ }+\cdots\right)\right],\tag{2.12}$$

Using this, we get the following approximate expressions for $V'_{\text{eff}}(l, x)$ and $V''_{\text{eff}}(l, x)$. For $r < R_{\text{C}}$,

$$V'_{\text{eff}}(l, x) = -\left(\frac{V_0}{16} + \frac{12a^3\lambda^2}{R^5}\right)x^2 + \left(\frac{6a^2\lambda^2}{R^4} - \frac{2\xi a^2}{R_{\text{C}}^3}\right)x + \left(\frac{V_0}{4} - \frac{2\xi a R}{R_{\text{C}}^2} - \frac{2a\lambda^2}{R^3}\right) \tag{2.13a}$$

and

$$V''_{\text{eff}}(l, x) = -\left(\frac{V_0}{8} + \frac{24a^3\lambda^2}{R^5}\right)x + \left(\frac{6a^2\lambda^2}{R^4} - \frac{2\xi a^2}{R_{\text{C}}^3}\right).$$

For $r > R_{\text{C}}$

$$V'_{\text{eff}}(l, x) = -\left(\frac{V_0}{16} + \frac{6\xi a^3}{R^4} + \frac{12a^3\lambda^2}{R^5}\right)x^2 + \left(\frac{4\xi a^2}{R^3} + \frac{6a^2\lambda^2}{R^4}\right)x + \left(\frac{V_0}{4} - \frac{2\xi a}{R^2} - \frac{2a\lambda^2}{R^3}\right) \tag{2.13b}$$

and

$$V''_{\text{eff}}(l, x) = -\left(\frac{V_0}{8} + \frac{12\xi a^3}{R^4} + \frac{24a^3\lambda^2}{R^5}\right)x + \left(\frac{4\xi a^2}{R^3} + \frac{6a^2\lambda^2}{R^4}\right).$$

If, for a given l near l_{poc}, $R_{\text{B}l}$ and $R_{\text{M}l}$ are present, by setting $V'_{\text{eff}}(l, x) = 0$, one can obtain their positions. However, when the roots of this equation in x become complex, we can say that the condition $l = l_{\text{poc}}$ has been reached. The critical condition for this is that the discriminants of the quadratic equations (2.13a) and (2.13b) vanish. The expression for λ_{poc} with this condition corresponding to (2.13a) and (2.13b) are

$$\lambda_{\text{poc}} = \left[\frac{\dfrac{4\xi^2 a^4}{R_{\text{C}}^6} + \dfrac{V_{\text{R}}^2}{16} - \dfrac{V_{\text{R}}\xi a R}{2R_{\text{C}}^3}}{\dfrac{120a^4\xi}{R^4 R_{\text{C}}^3} + \dfrac{V_{\text{R}}a}{2R_{\text{C}}^3} - \dfrac{12V_{\text{R}}a^3}{R^5}}\right]^{1/2} \tag{2.14a}$$

and

$$\lambda_{\text{poc}} = \left[\frac{\dfrac{6\xi V_{\text{R}}a^3}{R^4} - \dfrac{32\xi^2 a^4}{R^6} + \dfrac{V_{\text{R}}^2}{16} - \dfrac{V_{\text{R}}\xi a}{2R^2}}{\dfrac{96a^4\xi}{R^7} + \dfrac{V_{\text{R}}a}{2R^3} - \dfrac{12a^3 V_{\text{R}}}{R^5}}\right]^{1/2}. \tag{2.14b}$$

One can also calculate l_{poc} by a different manner. We can find by a self-consistent calculation that both $V'_{\text{eff}}(l, x)$ and $V''_{\text{eff}}(l, x)$ vanish when $r = R_{\text{poc}}$ and $l = l_{\text{poc}}$. In this connection, we note that $g(R, a, r)$ varies most rapidly at $r = R$ and hence $g'(R, a, r)$ has a maxima at $r = R$. However, in the close vicinity of $r = R$, $g'(R, a, r)$ changes very rapidly, i.e. $r = R$ is a sharp maxima of $g'(R, a, r)$. And due to this, R_{poc} is very close to R.

ence, one may get the following first approximation to l_{poc} corresponding to (2.13a) nd (2.13b) by setting $V'_{\text{eff}}(l_{\text{poc}}, R) = 0$ at $r = R$.

$$\lambda_{\text{poc}} = \sqrt{\frac{R^3}{2a}\left(\frac{V_{\text{R}}}{4} - \frac{2\xi a R}{R_{\text{C}}^3}\right)}, \tag{2.15a}$$

$$\lambda_{\text{poc}} = \sqrt{\frac{R^3}{2a}\left(\frac{V_{\text{R}}}{4} - \frac{2\xi a}{R^2}\right)}. \tag{2.15b}$$

hus, we have three alternative procedures to estimate l_{poc} namely formulae (2.14a) and .14b), formulae (2.15a) and (2.15b), and the self consistent calculations. In table 2, we ive the results of the calculations done using these procedures.

.4 *Some other features*

nother advantage of the availability of algebraic expressions for $R_{\text{B}l}$ and $R_{\text{M}l}$ is that sing them, one can easily get the curvature of the effective potential α and β at the naxima and the minima, in the parabolic approximation [3]. For example, near the naxima and minima, one can write

$$U_{\text{eff}}(l, r) = U_{\text{B}l} - \frac{1}{2}\alpha(r - R_{\text{B}l})^2, \quad \text{for maxima,}$$

$$= U_{\text{M}l} + \frac{1}{2}\beta(r - R_{\text{M}l})^2, \quad \text{for minima,}$$

vhere $U_{\text{B}l}$ and $U_{\text{M}l}$ are the barrier and pocket heights.

It may be noted that the energy levels E of the potential pocket in the parabolic pproximation are related to β by the formula

$$E = \hbar\,\omega_{\text{M}l}, \qquad \omega_{\text{M}l} = \sqrt{\frac{\beta}{m}}.$$

Similarly, the parameter α can be related to the barrier top resonances. Due to this, he α and β factors have considerable significance in several cases of heavy ion ollisions. It is clear that

$$\alpha = U''_{\text{eff}}(l, r)\big|_{r = R_{\text{B}l}}, \qquad \beta = U''_{\text{eff}}(l, r)\big|_{r = R_{\text{M}l}}$$

nd these can be readily calculated using $R_{\text{B}l}$ and $R_{\text{M}l}$.

Hence a knowledge of $R_{\text{B}l}$ and $R_{\text{M}l}$ readily helps us to determine additional features of he quantal states associated with the effective potential. For completeness, we also note hat the grazing angular momentum λ_{g} at any centre of mass energy E above the Coulomb arrier, can be calculated [8] using the approximate formula, valid for Woods–Saxon type orm factors (for the nuclear part of the effective potential), given below.

$$\left(1 + \frac{\lambda_{\text{g}}^2}{\eta^2}\right)^{1/2} = \frac{2}{V_{\text{CB}}}\left[E - \frac{1}{2}(V_{\text{CB}} + 2V_{\text{NB}}) + \frac{(E - E_{\text{B}})\,V_{\text{NB}}}{E_{\text{B}}}\right],$$

vhere V_{CB} and V_{NB} are the Coulomb and nuclear potentials at $R_{\text{B}0}$, $E_{\text{B}} = V_{\text{CB}} + V_{\text{NB}}$ and

The expressions deduced in this section help in readily calculating R_{Bl}, R_{Ml}, l_{poc}, l_g, ω_{Ml} and ω_{Bl} for OMP with Woods–Saxon form factors. However, it is necessary to verify the accuracy of the formulae for R_{Bl}, R_{Ml} and l_{poc} by comparing with the exact calculation of these quantities. This is described in the next section.

3. Results and discussion

In order to verify the accuracy of our formulae for R_{Bl} and l_{poc}, we have used a number of optical potentials corresponding to systems of different heavy ion pairs. The OMP parameters are listed in table 1. In figures 1 and 2, we give a typical set of results for the variation of R_{Bl} and R_{Ml} as a function of l obtained from our expressions (2.7), (2.8) and (2.10), (2.11) respectively and compare the same with the corresponding exact results obtained using Newton–Raphson iterative method. It is seen that our formula (2.7), (2.8), and (2.10), (2.11) give R_{Bl} and R_{Ml} quite accurately and in general, the error is less than 1% and in many cases, the accuracy is still better. Typical results are given in figures 1 and 2. We have verified that results similar to those indicated in figures 1 and 2 are obtained for all the heavy ion systems listed in table 1. The results shown in figures 1 and 2 include both shallow (^{40}Ca + ^{40,44}Ca) and deep potential wells (^{16}O + ^{208}Pb).

In table 2, we list the l_{poc} values obtained from the different procedures. Column A corresponds to the result obtained from the self-consistent calculation of $V'_{\text{eff}}(l, x) = 0$ and $V''_{\text{eff}}(l, x) = 0$ using the cubic polynomial approximation (2.12) to $V_{\text{eff}}(l, x)$. Columns

Table 1. Optical model parameters used in the calculations.

System	a (fm)	r_0(fm)	U_R (MeV)	r_C(fm)	References
$^{16}O_8 + {}^{144}Nd_{60}$	0·57	1·34	20·0	1·25	[9]
$^{16}O_8 + {}^{148}Sm_{62}$	0.57	1·34	20·0	1·25	[10, 11]
$^{16}O_8 + {}^{152}Sm_{62}$	0·57	1·34	20·0	1·25	[10, 11]
$^{16}O_8 + {}^{154}Sm_{62}$	0·57	1·34	20·0	1·25	[10, 11]
$^{16}O_8 + {}^{208}Pb_{82}$	0·50	1·25	100·0	1·25	[12, 11]
$^{32}S_{16} + {}^{58}Ni_{28}$	0·65	1·20	50·0	1·20	[13]
$^{32}S_{16} + {}^{64}Ni_{28}$	0·65	1·20	50·0	1·20	[13]
$^{37}Cl_{17} + {}^{123}Sb_{51}$	0·51	1·25	41·8	1·25	[9]
$^{40}Ar_{18} + {}^{122}Sn_{50}$	0·51	1·25	41·8	1·25	[14, 11]
$^{40}Ca_{20} + {}^{40}Ca_{20}$	0·43	1·35	35·0	1·35	[15, 11]
$^{40}Ca_{20} + {}^{44}Ca_{20}$	0·43	1·35	35·0	1·35	[15, 11]
$^{58}Ni_{28} + {}^{124}Sn_{50}$	0·294	1·26	58·1	1·26	[17, 11]
$^{64}Ni_{28} + {}^{118}Sn_{50}$	0·294	1·26	58·1	1·26	[17, 11]
$^{64}Ni_{28} + {}^{96}Zr_{40}$	0·55	1·25	40·0	1·25	[9]
$^{80}Se_{34} + {}^{80}Se_{34}$	0·55	1·25	40·0	1·25	[9]
$^{81}Br_{35} + {}^{90}Zr_{40}$	0·43	1·35	35·0	1·35	[11]
$^{81}Br_{35} + {}^{94}Zr_{40}$	0·43	1·35	35·0	1·35	[11]
$^{81}Br_{35} + {}^{96}Mo_{42}$	0·43	1·35	35·0	1·35	[11]
$^{81}Br_{35} + {}^{104}Ru_{44}$	0·43	1·35	35·0	1·35	[11]
$^{58}Ni_{28} + {}^{18}O_8$	0·50	1·22	90·0	1·22	[18]
$^{58}Ni_{28} + {}^{58}Ni_{28}$	0·55	1·20	40·0	1·25	[16, 11]

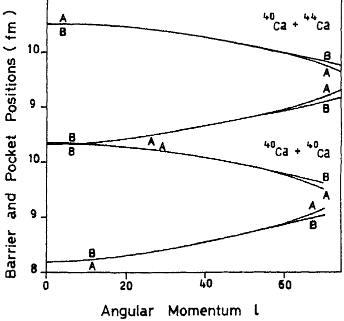

Figure 1. Variation of barrier position (R_{Bl}) and pocket position (R_{Ml}) as a function of l for systems ^{40}Ca + ^{40,44}Ca, obtained from algebraic expressions given in the text and these curves are denoted by symbol B. Symbol A denotes the corresponding results obtained using the Newton-Raphson iterative procedure. Upper pair of curves denote barrier positions and lower pair the pocket positions.

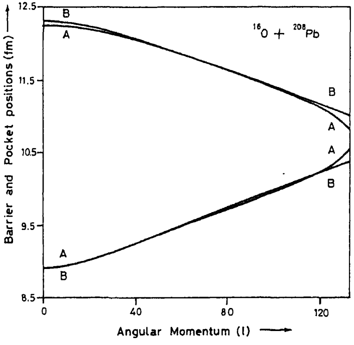

Figure 2. Same as figure 1 for system (^{16}O + ^{208}Pb).

C are the results for l_{poc} obtained from (2.15b) and (2.14b) respectively. The results under column D estimates l_{poc} setting the condition that at $l = l_{\text{poc}}$ the difference een $V_{\text{eff}}(l, x)$ at its maximum and minimum values is less than 0.1 MeV and using on–Raphson procedures to calculate the maximum and minimum. We have d that this procedure can give rise to numerical problems of

The l_{poc} values under columns (A) and (D) are obtained from the self-consistent calculation and Newton–Raphson method respectively. The l_{poc} values under columns (B) and (C) are obtained from (2·15b) and (2·14b) respectively.

System	l_{poc} A	l_{poc} B	l_{poc} C	l_{poc} D
$^{16}O_8 + {}^{144}Nd_{60}$	31	30	31	29
$^{16}O_8 + {}^{148}Sm_{62}$	30	29	30	28
$^{16}O_8 + {}^{152}Sm_{62}$	31	30	31	29
$^{16}O_8 + {}^{154}Sm_{62}$	31	31	32	30
$^{16}O_8 + {}^{208}Pb_{82}$	133	131	135	132
$^{32}S_{16} + {}^{58}Ni_{28}$	57	55	58	56
$^{32}S_{16} + {}^{64}Ni_{28}$	60	58	62	59
$^{37}Cl_{17} + {}^{123}Sb_{51}$	83	82	84	81
$^{40}Ar_{18} + {}^{122}Sn_{50}$	86	84	86	84
$^{40}Ca_{20} + {}^{40}Ca_{20}$	72	71	73	71
$^{40}Ca_{20} + {}^{44}Ca_{20}$	76	75	77	75
$^{58}Ni_{28} + {}^{124}Sn_{50}$	209	208	210	207
$^{64}Ni_{28} + {}^{118}Sn_{50}$	217	216	217	214
$^{64}Ni_{28} + {}^{96}Zr_{40}$	70	68	70	67
$^{80}Se_{34} + {}^{80}Se_{34}$	69	67	70	66
$^{81}Br_{35} + {}^{90}Zr_{40}$	103	102	103	99
$^{81}Br_{35} + {}^{94}Zr_{40}$	107	106	107	103
$^{81}Br_{35} + {}^{96}Mo_{42}$	103	102	103	99
$^{81}Br_{35} + {}^{104}Ru_{44}$	104	103	104	100
$^{58}Ni_{28} + {}^{18}O_8$	82	80	84	79
$^{58}Ni_{28} + {}^{58}Ni_{28}$	54	53	55	51
$^{58}Ni_{28} + {}^{64}Ni_{28}$	59	58	60	55

$l = l_{\text{poc}}$ due to the closeness of the maximum and minimum. For the purpose of comparison, we may treat results in column A obtained from self consistent calculations of R_{poc} and l_{poc} as exact results. We find that the result from algebraic expressions corresponding to columns B and C give very good estimates of l_{poc} and difference of ± 1 in most cases originate due to rounding off to the nearest integer. Further we note that the simple formula (2.15b) is a very good estimate of l_{poc} for OMP with Woods–Saxon form factor. The results from (2.14a) and (2.15a) also give substantially similar results except for the cases of OMP where $R_C < R$. Hence, we give only the numerical results obtained from (2.14b) and (2.15b) and the self-consistent calculation.

It may be noted that the cubic polynomial expression for $V_{\text{eff}}(l, x)$ around the barrier region given by (2.6) is quite accurate (error $< 1\%$) near the barrier region $(R_{B0} - s) < r < (R_{B0} + s)$, $s \leqslant 1$ fm. Similarly, $V_{\text{eff}}(l, x)$ approximation by the cubic polynomial (2.9) around $r = (R - 3a)$ is also a reliable expression in the region $(R - 3a - s) < r < (R - 3a + s)$, where $s \leqslant 1$ fm. Hence, one may use appropriate generalization of this approach for complex OMP to calculate algebraically the turning points of the effective potential in the WKB analysis of the heavy ion collisions. However, to have accurate results, one should use complex optical potentials. Further, ally lengthy. Hence, we have not listed the expressions here.

4. Summary

We have obtained algebraic expressions for calculating the barrier and pocket positions for all partial waves of the real effective OMP's with Woods–Saxon form factor and have verified their accuracy in a number of cases for heavy ion systems. We have also obtained simple algebraic expressions for calculating l_{poc} where the effective potential vanishes. This gives a very good estimate of l_{poc} obtained from the self-consistent calculation. The algebraic expression for R_{Bl}, R_{Ml} and $V_{\text{eff}}(l,x)$ in the barrier and pocket regions are useful in calculating easily the curvature parameters ω_{Bl} and ω_{Ml} near the barrier and pocket positions in the parabolic approximation. The approximate expressions for $V_{\text{eff}}(l,x)$ are also useful in the calculation of the turning points in the WKB analysis of heavy ion collisions.

Acknowledgement

The authors thank Dr B Sahu for his useful comments on the manuscript and the Nuclear Science Centre, New Delhi for extending the facilities provided to (IJ) and (CSS) during their stay.

References

[1] U Mosel, in *Treatise on heavy-ion science* edited by D Allan Bromley (Plenum Press, New York, 1984) vol. 2, pp. 3–46

[2] D M Brink and N Takigawa, *Nucl. Phys.* **A279**, 159 (1977)

[3] D M Brink, in *Semi-classical methods in nucleus-nucleus scattering* (Cambridge University Press, Cambridge, 1985) pp. 105–108

[4] C S Shastry and I Parija, *Phys. Rev.* **C27**, 2042 (1983)

[5] V J Menon, S N Mukherjee, C S Shastry and B Sahu, *Phys. Rev.* **C41**, 1031 (1990)

[6] R A Broglia and A Winther, in *Heavy ion reactions* parts I and II (Addison-Wesley, Massachusetts, 1991) pp. 115–116

[7] P R Christensen and A Winther, *Phys. Lett.* **B65**, 19 (1976)

[8] N Rowley and E Plagnol, *Phys. Lett.* **B56**, 221 (1975)

[9] B T Kim, T Udagawa and T Tamura, *Phys. Rev.* **C33**, 370 (1986)

[10] R G Stokestad and E E Gross, *Phys. Rev.* **C23**, 281 (1981)

[11] T Udagawa, B T Kim and T Tamura, *Phys. Rev.* **C32**, 124 (1985)

[12] F Videback, R B Goldstein, L Grodzins, S G Steadman, T A Belote and J D Garrett, *Phys. Rev.* **C15**, 954 (1977)

[13] A M Stefanini, G Montagnoli, G Fortuna, R Menegazzo, S Beghini, C Signorini, A Derosa, G Inglima, M Sandoli, F Rizzo, G Pappalardo and G Cardella, *Phys. Lett.* **B185**, 15 (1987)

[14] H C Britt, B H Erkkila, R R Stokes, H H Gutbrod, F Plasil, R L Ferguson and M Blann, *Phys. Rev.* **C13**, 1483 (1976)

[15] H Doubre, J C Jacmart, E Plagnol. N Poffe, M Riou and J C Roynette, *Phys. Rev.* **C15**, 693 (1977)

[16] F Plasil, *Nucl. Phys.* **A400**, 417c (1983)

[17] W Henning, in *Proc. Int. Conf. on fusion reactions below the Coulomb barrier, MIT, Cambridge, Mass.* edited by S G Steadman (Springer, Berlin, 1984) p. 150

[18] F Videback, P R Christensen, O Hansen and K Ulbak, *Nucl. Phys.* **A256**, 301 (1976)

on-leptonic weak charmed baryon decays in the $SU(4)$ midynamical scheme

1 SHEIKHOLESLAMI*
ysics Department, Institute for Studies in Theoretical Physics and Mathematics,
). Box 19395–5746, Tehran-Iran
iysics Department, Tehran University, Tehran, Iran

received 8 November 1995; revised 24 June 1996

stract. We study here the Cabibbo enhanced charmed baryon decays in the $SU(4)$ semi-amical model. The weak Hamiltonian $20'' + 15 + 45 + 45^*$ can have the parity violating plitude for charmed baryon decays. Decay width and α for some modes are also calculated.

/words. Flavor symmetry; charmed baryon decays; asymmetry parameter.

CS Nos 11·30; 13·30

Introduction

e decays and spectroscopy of charmed particles have been studied intensively in ent years. The weak nonleptonic decays of charmed baryons have been studied lier using $U(2,2)$ quark model [1], non relativistic $SU(6)$ wave functions [2], and the T bag model [3, 5]. For the nonleptonic hyperon decays one employs the conven-nal soft-meson technique [6], where the equal time commutator and the pole terms ld the *s*- and the *p*-wave amplitudes respectively. It has been known for quite netime that although the current-algebra approach gives the direct relative sign for nd *p* wave amplitudes [7], it fails to reproduce their relative magnitudes. To improve agreement between theory and experiment, additional mechanisms such as the son pole terms [8], factorizable contributions [9–11] and (1/2)-low lying baryon le contribution [12], have been attempted.

in a semidynamical consideration [13], most of the observed features of the nleptonic decays of ordinary hyperons have been obtained. Taking the decay $\rightarrow B' + P$ as weak spurion-baryon scattering process $S + B \rightarrow B' + P$ and assuming dominance of nonexotic intermediate states [14], and *s*-*u* channel symmetry [15] octet dominance has been obtained, allowing $\Delta I = 3/2$ contribution for Ω^- decay nultaneously. The scheme probes further structure of weak baryon decays. Parity lating (PV) decays are shown to occur through *t* channel only, where parity nserving (PC) decays are found to arise through the *s* and *u* channels dominantly. ese results are in accordance with the results of current algebra [6], duality argument 5] and the constituent rearrangement quark model [17].

Encouraged by the success of the semidynamical scheme in the $SU(3)$ flavor

PV decay amplitudes vanish for $20''$ as well as for 84 parts of the GIM Hamiltonian and for the PC mode 84 representation contributes only through the t-channel. Keeping in mind the unsatisfactory aspects of the GIM model the possibility of other $SU(4)$ representations, have been considered, the admixture of 15-representation showed a better agreement [20] with experiment at that time. However, because $20'' + 84 + 15$ Hamiltonian has no contribution to parity violating sector of charmed baryon decays. it does not agree with the latest measured asymmetry parameter values like $\alpha(\Lambda_c^+ \to \Lambda + \pi^+) = -0{\cdot}94$. A possible way out is to look at other representations present in the weak Hamiltonian, that is $45 + 45^*$. These representations may appear in the weak Hamiltonian in several way such as $SU(4)$ breaking [21], gluon-exchange [10, 22], generating penguin diagram, Melosh transformations on the left handed quark [23], etc.

In this paper we discuss $20'' + 15 + 45 + 45^*$ weak Hamiltonian within the semidynamical model framework looking at the Cabibbo enhanced charmed baryon weak decays. We observed that the parity violating part can be produced within this framework. In particular, the obtained value for the asymmetry parameter $\alpha(\Lambda_c^+ \to \Lambda + \pi^+)$ agrees with the experimental value. However, the same parameter disagrees for the case of $\Lambda_c^+ \to \Sigma^+ + \pi^0$). Asymmetry parameter α and decay width for some other modes are also calculated. In § 2 we present the method and in § 3 the weak Hamiltonian. Section 4 describes the decay amplitude and the result.

2. Method

We treat the effective nonleptonic weak Hamiltonian as a symmetry-breaking spurion S and the decay $B \to B' + P$ as the process $S + B \to B' + P$. The transition amplitudes are then expressed in terms of reduced amplitudes in s, t, and u channels of the process corresponding to each intermediate state $|m\rangle$ and are defind as follows:

$$\langle B' \| P \| m \rangle \langle m \| S \| B \rangle$$

for s channel $(S + B \to B' + P)$,

$$\langle P' \| S \| m \rangle \langle m \| B' \| B \rangle$$

for t channel $(B' + B \to \bar{S} + P)$ and

$$\langle B' \| \bar{S} \| \mathrm{m} \rangle \langle m \| \bar{P} \| B \rangle$$

for u channel $(B + \bar{P} \to B' + S)$. The baryonic intermediate states appear in the s and u channels while the mesons are exchanged in the t-channel. We assume that the main contribution to the decays come through the single-particle nonexotic intermediate state. Thus only 4^*, $20'$, 20 baryonic multiplets occur as the intermediate states in the s and u channels, while singlet fifteen-plet mesons are exchanged in the t-channel. Secondly, we assume that the weak Hamiltonian is symmetric in s and u channels. Mathematically speaking, this amounts to

$$\langle B' \| P \| m \rangle \langle m \| S \| B \rangle = \langle B' \| \bar{S} \| \mathrm{m} \rangle \langle m \| \bar{P} \| B \rangle$$

The hadronic part of the weak V-A left handed quark current,

$$J_\mu = \bar{u}\gamma_\mu(1-\gamma_5)(d\cos(\theta)) + s\sin(\theta)) + \bar{c}\gamma_\mu(1-\gamma_5)(s\cos\theta - d\sin\theta)$$

transforms like the 15 representation of $SU(4)$. The general current ⊗ current weak interaction Hamiltonian,

$$H_\mathrm{w} = \frac{G}{\sqrt{2}}(J^\mu J_\mu^+ + J^{\mu^+} H_\mu), \tag{1}$$

may thus belong to the $SU(4)$ representations present in the direct product

$$15 \otimes 15 = 1 \oplus 15 \oplus 15 \oplus 20'' \oplus 45 \oplus 45^* \oplus 84. \tag{2}$$

Because of the symmetric nature of the Hamiltonian, only representations 1, 15_s, 20″ and 84 contribute. The singlet can not contribute to the strangeness or charm changing decays. It is also a specific property of the GIM Hamiltonian [24] that the bilinears in current do not contain adjoint representation in the next $SU(4)$ limit [25]. Therefore, 15 also does not contribute. The GIM Hamiltonian thus transforms as

$$H_\mathrm{w}^\mathrm{GIM} = H^{20''} + H^{84}, \tag{3}$$

The 15 and 45 + 45* representations may reappear in the weak Hamiltonian in several ways such as $SU(4)$ breaking [21], gluon-exchange [10,22], generating penguin diagram, Melosh transformations on the left handed quark [23], etc.

Thus the most general weak Hamiltonian for $B \to B' + P$ decays is then

$$H = H_\mathrm{w}^{20''} + H_\mathrm{w}^{84} + H_\mathrm{w}^{15} + H_\mathrm{w}^{45} + H_\mathrm{w}^{45^*}, \tag{4}$$

where

$$\begin{aligned} H_\mathrm{w}^{20''} = {} & a_1 B^c_{[a,b]} B^{[n,d]}_m P^m_n H^{[a,b]}_{[c,d]} + a_2 B^m_{[a,d]} B^{[n,c]}_m P^d_n H^{[a,b]}_{[c,d]} \\ & + a_3 B^m_{[a,b]} B^{[c,d]}_n P^n_m H^{[a,b]}_{[c,d]} + a_4 B^m_{[n,b]} B^{[c,d]}_a P^n_m H^{[a,b]}_{[c,d]} \\ & + a_5 B^n_{[m,a]} B^{[c,d]}_n P^m_b H^{[a,b]}_{[c,d]} + a_6 B^c_{[m,n]} B^{[m,n]}_a P^d_b H^{[a,b]}_{[c,d]} \\ & + a_7 B^m_{[n,a]} B^{[n,c]}_m P^d_b H^{[a,b]}_{[c,d]}, \end{aligned} \tag{5}$$

$$\begin{aligned} H_\mathrm{w}^{84} = {} & + b_1 B^c_{[e,f]} B^{[e,f]}_a P^d_b H^{(a,b)}_{(c,d)} + b_2 B^c_{[f,a]} B^{[e,d]}_b P^f_e H^{(a,b)}_{(c,d)} \\ & + b_3 B^e_{[a,f]} B^{[c,f]}_e P^d_b H^{(a,b)}_{(c,d)} + b_4 B^e_{[a,f]} B^{[c,f]}_b P^d_e H^{(a,b)}_{(c,d)} \\ & + b_5 B^c_{[a,f]} B^{[d,f]}_e P^e_b H^{(a,b)}_{(c,d)} + b_6 B^c_{[e,f]} B^{[e,d]}_a P^f_b H^{(a,b)}_{(c,d)} \\ & + b_7 B^c_{[e,a]} B^{[e,f]}_b P^d_f H^{(a,b)}_{(c,d)} \end{aligned} \tag{6}$$

$$\begin{aligned} H_\mathrm{w}^{15} = {} & A_1 B^m_{[n,c]} B^{[b,c]}_a P^n_m H^a_b + A_2 B^m_{[c,d]} B^{[c,d]}_a P^b_m H^a_b \\ & + A_3 B^m_{[d,a]} B^{[b,d]}_c P^c_m H^a_b + A_4 B^b_{[m,c]} B^{[c,d]}_a P^m_d H^a_b \\ & + A_5 B^c_{[m,d]} B^{[b,d]}_c P^m_a H^a_b + A_6 B^c_{[m,a]} B^{[b,d]}_c P^m_d H^a_b \\ & + A_7 B^m_{[c,d]} B^{[c,d]}_m P^b_a H^a_b + A_8 B^b_{[c,d]} B^{[c,d]}_m P^m_a H^a_b \\ & + A_9 B^m_{[a,d]} B^{[d,c]}_m P^b_c H^a_b + A_{10} B^b_{[a,d]} B^{[d,n]}_m P^m_n H^a_b, \end{aligned} \tag{7}$$

$$\begin{aligned} H_{\mathrm{w}}^{45} = {} & d_1 B^{c}_{[e,f]} B^{[e,f]}_{a} P^{d}_{b} H^{[a,b]}_{(c,d)} + d_2 B^{c}_{[f,a]} B^{[e,d]}_{b} P^{f}_{e} H^{[a,b]}_{(c,d)} \\ & + d_3 B^{e}_{[a,f]} B^{[c,f]}_{e} P^{d}_{b} H^{[a,b]}_{(c,d)} + d_4 B^{e}_{[a,f]} B^{[c,f]}_{b} P^{d}_{e} H^{[a,b]}_{(c,d)} \\ & + d_5 B^{c}_{[a,f]} B^{[d,f]}_{e} P^{e}_{b} H^{[a,b]}_{(c,d)} + d_6 B^{c}_{[e,f]} B^{[e,d]}_{a} P^{f}_{b} H^{[a,b]}_{(c,d)} \\ & + d_7 B^{c}_{[e,a]} B^{[e,f]}_{b} P^{d}_{f} H^{[a,b]}_{(c,d)} + d_8 B^{d}_{[a,b]} B^{[m,c]}_{n} P^{n}_{m} H^{[a,b]}_{(c,d)} \end{aligned} \tag{8}$$

and

$$\begin{aligned} H_{\mathrm{w}}^{45*} = {} & d'_1 B^{c}_{[e,f]} B^{[e,f]}_{a} P^{d}_{b} H^{[a,b]}_{(c,d)} + d'_2 B^{c}_{[f,a]} B^{[e,d]}_{b} P^{f}_{e} H^{[a,b]}_{(c,d)} \\ & + d'_3 B^{e}_{[a,f]} B^{[c,f]}_{e} P^{d}_{b} H^{[a,b]}_{(c,d)} + d'_4 B^{e}_{[a,f]} B^{[c,f]}_{b} P^{d}_{e} H^{[a,b]}_{(c,d)} \\ & + d'_5 B^{c}_{[a,f]} B^{[d,f]}_{e} P^{e}_{b} H^{[a,b]}_{(c,d)} + d'_6 B^{c}_{[e,f]} B^{[e,d]}_{a} P^{f}_{b} H^{[a,b]}_{(c,d)} \\ & + d'_7 B^{c}_{[e,a]} B^{[e,f]}_{b} P^{d}_{f} H^{[a,b]}_{(c,d)} + d'_8 B^{m}_{[n,a]} B^{[c,d]}_{b} P^{n}_{m} H^{[a,b]}_{(c,d)} \end{aligned} \tag{9}$$

CP-invariance demands

$$a_1 = -a_4, \quad a_2 = -a_5, \quad a_3 = a_6 = a_7 = 0, \tag{10a}$$

$$b_4 = -b_5, \quad b_6 = -b_7, \quad b_1 = b_2 = b_3 = 0, \tag{10b}$$

$$\begin{aligned} & A_1 = A_{10}, \quad A_2 = -A_8, \quad A_5 = A_9, \\ & A_3 = A_4 = A_6 = A_7 = 0, \end{aligned} \tag{10c}$$

$$\begin{aligned} & d_1 = d'_1, \quad d_2 = -d'_2, \quad d_3 = d'_3, \quad d_4 = -d'_5, \\ & d_5 = d'_4, \quad d_6 = d'_7, \\ & d_7 = -d'_6, \quad d_8 = d'_8 \end{aligned} \tag{10d}$$

for the PV mode and

$$a_1 = a_4, \quad a_2 = a_5, \tag{11a}$$

$$b_4 = b_5, \quad b_6 = b_7, \tag{11b}$$

$$A_1 = -A_{10}, \quad A_2 = A_8, \quad A_5 = -A_9, \tag{11c}$$

$$\begin{aligned} & d_1 = -d'_1, \quad d_2 = d'_2, \quad d_3 = -d'_3, \quad d_4 = d'_5, \quad d_5 = -d'_4, \\ & d_6 = -d'_7, \quad d_7 = d'_6, \end{aligned} \tag{11d}$$

$$d_8 = -d'_8, \tag{11e}$$

for the PC mode. The dominance of non exotic intermediate states yields

$$a_4 = a_5 = a_6 = a_7 = 0, \tag{12a}$$

$$b_3 = b_5 = 0, \quad b_2 = b_6, \quad 2b_1 = -b_7, \tag{12b}$$

$$2A_7 = 2A_8 = A_9 = A_{10}, \quad A_5 = A_6, \tag{12c}$$

$$2d_1 = -d_7, \quad -d_2 = d_7, \quad d_3 = d_5 = d_8 = 0, \quad d'_2 = d'_6,$$

$$a_1 = a_2 = a_3 = a_4 = a_5 = 0, \tag{13a}$$

$$b_2 = b_4 = b_5 = b_6 = b_7 = 0, \tag{13b}$$

$$A_1 = A_3 = A_4 = A_6 = A_{10} = 0, \tag{13c}$$

$$d_2 = d_4 = d_5 = d_6 = d_7 = d_8 = 0, \tag{13d}$$

$$d'_2 = d'_4 = d'_5 = d'_6 = d'_7 = d'_8 = 0, \tag{13e}$$

for the t-channel, and

$$a_1 = a_2 = a_6 = a_7 = 0, \tag{14a}$$

$$b_3 = b_4 = 0, \quad 2b_1 = -b_6, \quad b_2 = b_7, \tag{14b}$$

$$A_9 = -A_6, \quad 2A_7 = 2A_2 = -A_5 = -A_1, \tag{14c}$$

$$d_2 = d_7, \quad d_1 = d_3 = d_4 = d_6 = 0, \tag{14d}$$

$$-2d'_1 = d'_6, \quad d'_2 = d'_7, \quad d'_3 = d'_4 = d'_8 = 0, \tag{14c}$$

for the u-channel.

4. Decay amplitude

The matrix elements for baryon decay processes can be written as [6]

$$m = -\langle B'P|H_{\mathrm{w}}|B\rangle = u_{B'}(A + B\gamma_5)u_B\phi_p, \tag{15}$$

where A and B are parity violating and parity conserving amplitudes respectively. For the Cabibbo enhanced $\Delta C = \Delta S = -1$ mode, the charm changing effective weak Hamiltonian is

$$H^{\mathrm{eff}} = \frac{G}{\sqrt{2}}\cos^2\theta[\bar{u}\gamma_\mu(1-\gamma_5)d][\bar{s}\gamma^\mu(1-\gamma_5)c]. \tag{16}$$

The ground state s-wave $(1/2)^+$ baryons belong to $20'$ representation of $SU(4)$ with the following isospin and $SU(3)$ content

$$20' = 8_0\begin{pmatrix} N \\ \Lambda \\ \Sigma \\ \Xi \end{pmatrix} + 3^*_1\begin{pmatrix} \Lambda_c \\ \Xi'_c \end{pmatrix} + 6_1\begin{pmatrix} \Sigma_c \\ \Xi_c \\ \Omega_c \end{pmatrix} + 3_2\begin{pmatrix} \Xi_{cc} \\ \Omega_{cc} \end{pmatrix}, \tag{17}$$

where the subscript c denotes the charm quantum number. According to the observed masses of $(1/2)^+$ baryons [26], and the mass pattern expected in the DGG mode [27], 3^*_1, 3_2 and Ω (css) state of 6_1 are stable against the strong and electromagnetic interactions and so must decay weakly. Before determining the amplitudes we notice that the constraints (10), (12)–(14) and the CP invariance plus the absence of the exotic intermediate states forbid $20''$ and 84 components of the Hamiltonian to contribute to the decays in all the s, t and u channels. Thus the parity violating decays of the charmed baryons are forbidden in the $SU(4)$ symmetry limit. The same result has earlier been obtained in the duality frame work [28] and in the constituent rearrangement quark model [17]. It is also consistent with the observation that the factorizable contribution to s-wave amplitudes vanish in the $SU(4)$ symmetric limit [4, 5]. Thus parity violating decays seem to arise purely from the $SU(4)$ breaking [29]. The symmetry breaking terms $(45 + 45^*)$ have contribution to PV and PC modes through t-channel only. And 15 does not contribute to the charmed baryon decays, but to the hyperon decays through both PV and PC. We express the decay amplitudes for the hyperon and charmed baryon decays in terms of the parameters in tables 1–4.

To determine the parameters, we work in $20'' + 15 + 45 + 45^*$ mode. Fixing the parameters (in unit of $10^4 \times \mathrm{MeV}^{-1/2}$)

$$(8d_1 - 2d_3) = 2{\cdot}5, \tag{18}$$

using hyperon decay Λ^0_-, Ξ^-_-, Σ^-_- as input for parity violating sector, and

$$a_3 = -8{\cdot}3, \quad (8d_1 - 2d_3) = 42{\cdot}6, \quad (4a_6 - a_7) = 5{\cdot}0, \tag{19}$$

from $\Lambda^0_0, \Sigma^+_+ \cdot . \Sigma^0_+, \Xi^-_-, B(\Lambda^+_c \to p + \bar{k}^0)$ for parity conserving sector. We then compute [6] the branching ratio and α of the charmed baryon decays in table 3. We observed that the obtained asymmetry parameter $\alpha(\Lambda^+_c \to \Lambda + \pi^+) = -0{\cdot}61$ has the correct sign and reasonable amplitude in comparison with the experimental value $\alpha^{\mathrm{expt}} = -0{\cdot}94$

Table 1. The s wave decay amplitudes for hyperon decays. All carry a factor of $(1/\sqrt{2})\sin(\theta)\cos(\theta)$.

	45 + 45*		15		Experimental values $\times \mathrm{MeV}^{-1/2}\mathrm{S}^{-1/2}$
	d_1	d_3	A_2	A_5	A
Λ^0_-	$\frac{8}{\sqrt{6}}$	$\frac{-2}{\sqrt{6}}$	$\frac{4}{\sqrt{6}}$	$\frac{1}{\sqrt{6}}$	12600·288
Λ^0_0	0	0	$\frac{-4}{2\sqrt{3}}$	$\frac{-1}{2\sqrt{3}}$	$\begin{cases} -9250{\cdot}921 \\ -3416{\cdot}6612 \end{cases}$
Σ^+_+					[illegible]
Σ^-_-		[illegible]			[illegible]
Σ^+_0				[illegible]	−12702·51
Ξ^+_+	$\frac{4}{\sqrt{6}}$	−4	$\frac{2}{\sqrt{6}}$	$\frac{2}{\sqrt{6}}$	17518·10
Ξ^0_0	0	0	$\frac{1}{2\sqrt{3}}$	$\frac{2}{2\sqrt{3}}$	13376·47

Table 2. The p wave decay amplitudes for hyperon decays. All carry a factor of $(1/\sqrt{2})\sin(\theta)\cos(\theta)$.

	20″			84		45 + 45*		15				Experimental valu × MeV$^{-1/2}$S$^{-1/}$
	a_3	a_6	a_7	b_1	b_3	d_1	d_3	A_2	$A_2^{\prime}$	A_3	A_5	B
Λ^0_-	$\frac{4}{\sqrt{6}}$	$\frac{-4}{\sqrt{6}}$	$\frac{1}{\sqrt{6}}$	$\frac{-4}{\sqrt{6}}$	$\frac{1}{\sqrt{6}}$	0	0	$\frac{-6}{\sqrt{6}}$	$\frac{-4}{\sqrt{6}}$	$\frac{-1}{\sqrt{6}}$	$\frac{1}{\sqrt{6}}$	85671·26
Λ^0_0	$\frac{-4}{2\sqrt{3}}$	$\frac{4}{2\sqrt{3}}$	$\frac{-1}{2\sqrt{3}}$	$\frac{-4}{2\sqrt{3}}$	$\frac{1}{2\sqrt{3}}$	$\frac{8}{2\sqrt{3}}$	$\frac{-2}{2\sqrt{3}}$	$\frac{6}{2\sqrt{3}}$	$\frac{4}{2\sqrt{3}}$	$\frac{1}{2\sqrt{3}}$	$\frac{-1}{2\sqrt{3}}$	− 61935·41 − 167695·8
Σ^+_+	4	0	0	0	0	00	0	− 2	0	− 1	0	164369·8
Σ^-_-	0	0	1	0	1	0	0	− 4	0	0	1	− 5567·90
Σ^+_0	$\frac{4}{\sqrt{2}}$	0	$\frac{-1}{\sqrt{2}}$	0	$\frac{1}{\sqrt{2}}$	0	$\frac{-2}{\sqrt{2}}$	$\frac{2}{\sqrt{2}}$	0	$\frac{-1}{\sqrt{2}}$	$\frac{-1}{\sqrt{2}}$	104118·7
Ξ^-_-	0	$\frac{-2}{\sqrt{6}}$	$\frac{2}{\sqrt{6}}$	$\frac{-2}{\sqrt{6}}$	$\frac{2}{\sqrt{6}}$	0	0	$\frac{-6}{\sqrt{6}}$	$\frac{-2}{\sqrt{6}}$	$\frac{1}{\sqrt{6}}$	$\frac{2}{\sqrt{6}}$	− 68094·1
Ξ^0_0	0	$\frac{-2}{2\sqrt{3}}$	$\frac{2}{2\sqrt{3}}$	$\frac{2}{2\sqrt{3}}$	$\frac{-2}{2\sqrt{3}}$	$\frac{-4}{2\sqrt{3}}$	$\frac{4}{2\sqrt{3}}$	$\frac{-6}{2\sqrt{3}}$	$\frac{-2}{2\sqrt{3}}$	$\frac{1}{2\sqrt{3}}$	$\frac{2}{2\sqrt{3}}$	− 47634·2

Table 3. The s and p wave decay amplitudes, asymmetry parameter and decay width (in unit of $\times 10^{-10}$ MeV) for charmed baryon decays. All carry a factor of $(1/\sqrt{2})\cos^2(\theta)$.

	PV 45 + 45*		45 + 45*		PC 20″			84		A	B		
	d_1	d_3	d_1	d_3	a_3	a_6	a_7	b_1	b_3	$\times 10^5$	$\times 10^5$	α	Γ
$3^* \to 3 + 9$													
$\Lambda_c^+ \to p\bar{K}^0$	0	0	$\frac{8}{\sqrt{6}}$	$\frac{-2}{\sqrt{6}}$	0	$\frac{-4}{\sqrt{6}}$	$\frac{1}{\sqrt{6}}$	$\frac{4}{\sqrt{6}}$	$\frac{-1}{\sqrt{6}}$	0	1·0	0	0·66
$\to \Sigma^+\pi^0$	0	0	0	0	$\frac{4}{2\sqrt{3}}$	0	0	0	0	0	−0·64	0	0·20
$\to \Sigma^+\eta^{0\prime}$	0	0	0	0	$\frac{2}{\sqrt{6}}$	0	0	0	0	0	−0·37	0	0·04
$\to \Lambda + \pi^+$	$\frac{16}{6}$	$\frac{-4}{6}$	0	0	$\frac{4}{6}$	$\frac{-8}{6}$	$\frac{2}{6}$	$\frac{-8}{6}$	$\frac{2}{6}$	0·06	−0·48	−0·61	0·15
$\to \Sigma^0\pi^+$	0	0	0	0	$\frac{-4}{2\sqrt{3}}$	0	0	0	0	0	0·64	0	0·20
$\to \Xi^0 K^+$	0	0	0	0	$\frac{4}{\sqrt{6}}$	0	0	0	0	0	−0·91	0	0·18
$\Xi_c^{\prime +} \to \Sigma^+\bar{K}^0$	0	0	$\frac{8}{\sqrt{6}}$	$\frac{-2}{\sqrt{6}}$	0	$\frac{-4}{\sqrt{6}}$	$\frac{1}{\sqrt{6}}$	$\frac{4}{\sqrt{6}}$	$\frac{-1}{\sqrt{6}}$	0	1·0	0	2·50

Continued

Table 3. (*Continued*)

	PV 45 + 45*		45 + 45*		PC 20″			84		A	B		
	d_1	d_3	d_1	d_3	a_3	a_6	a_7	b_1	b_3	$\times 10^5$	$\times 10^5$	α	Γ
$\rightarrow \Xi^0 \pi^+$	$\frac{-8}{\sqrt{6}}$	$\frac{-2}{\sqrt{6}}$	0	0	0	$\frac{4}{\sqrt{6}}$	$\frac{-1}{\sqrt{6}}$	$\frac{4}{\sqrt{6}}$	$\frac{-1}{\sqrt{6}}$	−0·07	0·14	−0·88	0·03
$\Xi_c'^0 \rightarrow \Sigma^+ K^-$	0	0	0	0	$\frac{4}{\sqrt{6}}$	0	0	0	0	0	−0·91	0	2·07
$\rightarrow \Lambda \bar{K}^0$	0	0	$\frac{-8}{6}$	$\frac{2}{6}$	$\frac{4}{6}$	$\frac{4}{6}$	$\frac{-1}{6}$	$\frac{-4}{6}$	$\frac{1}{6}$	0	−0·78	0	0·36
$\rightarrow \Sigma^0 \bar{K}^0$	0	0	$\frac{-8}{2\sqrt{3}}$	$\frac{2}{2\sqrt{3}}$	$\frac{-4}{2\sqrt{3}}$	$\frac{4}{2\sqrt{3}}$	$\frac{-1}{2\sqrt{3}}$	$\frac{-4}{2\sqrt{3}}$	$\frac{1}{2\sqrt{3}}$	0	0·69	0	0·24
$\rightarrow \Xi^0 \pi^0$	0	0	0	0	0	0	0	0	0	0	0	#	0
$\rightarrow \Xi^0 \eta$	0	0	0	0	$\frac{2}{\sqrt{6}}$	0	0	0	0	0	−0·45	0	0·07
$\rightarrow \Xi^- \pi^+$	$\frac{-8}{\sqrt{6}}$	$\frac{2}{\sqrt{6}}$	0	0	0	$\frac{4}{\sqrt{6}}$	$\frac{-1}{\sqrt{6}}$	$\frac{4}{\sqrt{6}}$	$\frac{-1}{\sqrt{6}}$	0·03	0·14	0·98	0·02
$6 \rightarrow 8 + 9$													
$\Omega_c^0 \rightarrow \Xi^0 \bar{K}^0$	0	0	2	0	0	0	−1	0	1	0	#	#	#

(*Continued*)

Table 3. (*Continued*)

	PV 45 + 45*		45 + 45*		PC 20″			84		A	B		
	d_1	d_3	d_1	d_3	a_3	a_6	a_7	b_1	b_3	$\times 10^5$	$\times 10^5$	α	Γ
$3 \rightarrow 8 + 3^*$													
$\Omega_{cc}^+ \rightarrow \Xi^0 D_s^+$	0	0	0	0	0	0	0	0	0	0	0	#	0
$\Xi_{cc}^+ \rightarrow \Xi^0 D_s^+$	0	0	0	0	4	0	0	0	0	0	$-2{\cdot}23$	0	1·17
$\rightarrow \Sigma^0 D^+$	0	0	0	0	$\frac{-4}{\sqrt{2}}$	0	0	0	0	0	1·58	0	1·08
$\rightarrow \Sigma^+ D^0$	0	0	0	0	4	0	0	0	0	0	$-0{\cdot}91$	0	0·42
$\rightarrow \Lambda D^+$	0	0	0	0	$\frac{4}{\sqrt{6}}$	0	0	0	0	0	$-2{\cdot}23$	0	2·20
$\rightarrow \Sigma^+ D^+$	0	0	0	0	0	0	0	0	0	0	0	#	0

	PV		PC						
	$45+45^*$		$45+45^*$			$20''$		84	
	d_1	d_3	d_1	d_3	a_3	a_6	a_7	b_1	b_3
$3\to 3^*+9$									
$\Omega_{cc}^+\to\Xi'^+\bar{K}^0$	0	0	$\frac{-4}{\sqrt{6}}$	$\frac{-4}{\sqrt{6}}$	0	$\frac{2}{\sqrt{6}}$	$\frac{-2}{\sqrt{6}}$	$\frac{-2}{\sqrt{6}}$	$\frac{2}{\sqrt{6}}$
$\Xi_{cc}^+\to\Xi'^0\pi^+$	$\frac{-4}{\sqrt{6}}$	$\frac{4}{\sqrt{6}}$	0	0	0	$\frac{2}{\sqrt{6}}$	$\frac{-2}{\sqrt{6}}$	$\frac{2}{\sqrt{6}}$	$\frac{-2}{\sqrt{6}}$
$\to\Xi'^+\pi^0$	0	0	0	0	0	0	0	0	0
$\to\Xi'^+\eta$	0	0	0	0	0	0	0	0	0
$\Xi_{cc}^+\to\Lambda_c^+\bar{K}^0$	0	0	0	$\frac{4}{\sqrt{6}}$	0	$\frac{-2}{\sqrt{6}}$	$\frac{2}{\sqrt{6}}$	$\frac{2}{\sqrt{6}}$	$\frac{-2}{\sqrt{6}}$
$\Xi_{cc}^{++}\to\Xi'^+\pi^+$	$\frac{-4}{\sqrt{6}}$	$\frac{-4}{\sqrt{6}}$	0	0	0	$\frac{2}{\sqrt{6}}$	$\frac{-2}{\sqrt{6}}$	$\frac{2}{\sqrt{6}}$	$\frac{-2}{\sqrt{6}}$
$3\to 6+9$									
$\Omega_{cc}^+\to\Omega_c^0\pi^+$	-4	0	0	0	0	2	0	2	0
$\to\Xi_c^+\bar{K}^0$	0	0	$\frac{4}{\sqrt{2}}$	0	0	$\frac{-2}{\sqrt{2}}$	0	$\frac{2}{\sqrt{2}}$	0
$\Xi_{cc}^+\to\Omega_c^0K^+$	0	0	0	0	0	0	0	0	0
$\to\Xi_c^0\pi^+$	$\frac{-4}{\sqrt{2}}$	0	0	0	0	$\frac{2}{\sqrt{2}}$	0	$\frac{2}{\sqrt{2}}$	0
$\to\Xi_c^+\pi^0$	0	0	0	0	0	0	0	0	0
$\to\Xi_c^+\eta^0$	0	0	0	0	0	0	0	0	0
$\to\Sigma^+\bar{K}^0$	0	0	$\frac{4}{\sqrt{2}}$	0	0	$\frac{-2}{\sqrt{2}}$	0	$\frac{2}{\sqrt{2}}$	0
$\to\Sigma^{++}K^-$	0	0	0	0	0	0	0	0	0
$\Xi_{cc}^{++}\to\Xi_c^+\pi^+$	$\frac{-4}{\sqrt{2}}$	0	0	0	0	$\frac{2}{\sqrt{2}}$	0	$\frac{2}{\sqrt{2}}$	0
$\to\Sigma_c^{++}\bar{K}^0$	0	0	0	0	0	2	0	-2	0

$(+0{\cdot}21 - 06)$. But there is a disagreement for the case of $\alpha(\Lambda_c^+ \to \Sigma^+ + \pi^0)$. However the present data on these decays are meagre and we cannot say much about other decays and also the contribution of the 84 representations.

Acknowledgement

The author gratefully acknowledge R C Verma for useful discussions.

References

[1] J G Korner, G Kramer and J Willrodt, *Z. Phys.* **C2**, 117 (1979)
[2] F Hussain and M D Scadron, *Nuovo Cimento* **A79**, 248 (1984)
[3] B Guberina, D Tadic and J Trampetic, *Z. Phys* **C13**, 251 (1982)
[4] D Ebert and W Kallies, *Phys. Lett.* **B131**, 183 (1983)
[5] H Y Cheng, *Z. Phys.* **C29**, 453 (1985)
[6] R E Marshak, Riazzudin and C P Ryan, *Theory of weak interactions in particle physics* (Wiley, New York, 1969)
[7] M D Scadron and L R Thebaud, *Phys. Rev.* **D8**, 2190 (1973)
[8] C Itzykson and M Jacob, *Nuovo Cimento* **A48**, 655 (1967)
[9] J F Donoghue, E Golowich and B R Holstein, *Phy. Rev.* **D12**, 2875 (1975)
J F Donoghue, E Golowich, W A Ponce and B R Holstein, *Phys. Rev.* **D21**, 186 (1980)
[10] H Galic, D Tadic, and J Trampetic, *Nucl. Phys.* **B152**, 306 (1979)
D Tadic and J Trampetic, *Phys. Rev.* **D23**, 144 (1981)
[11] A I Vainshtein, V I Zakharov and M A Shifman, *Zh. Eksp. Theor. Fiz.* **72**, 1275 (1977) [*Sov. Phys. JETP* **45**, 670 (1977)]
[12] M Bonvin, *Nucl. Phys.* **B238**, 241 (1984)
[13] R C Verma and M P Khanna, *J. Phys.* **G5**, 1033 (1979)
R C Verma M P Khanna and M M Gupta, *Phys. Rev.* **D20**, 810 (1979)
[14] J L Rosner, *Phys. Rev. Lett.* **21**, 950 (1968)
D P Roy and M Suzuki, *Phys. Lett.* **B28**, 558 (1969)
H J Lipkin, *Nucl. Phys.* **B9**, 349 (1969)
[15] Y Kohara and K Nishijima, *Prog. Theor. Phys.* **47**, 648 (1972)
[16] S Nussinov and J L Rosner, *Phys. Rev. Lett.* **23**, 126 (1965)
K Kawrabazaski and S Kitakodo, *Phys. Rev. Lett.* **23**, 440 (1965)
[17] Y Igarashi *et al*, *Prog. Theor. Phys. Suppl.* **83**, 177 (1978)
[18] R C Verma and M P Khanna, *Phys. Rev.* **D21**, 812 (1980)
[19] S Kanwar, R C Verma and M P Khanna, *Phys. Rev.* **D24**, 117 (1981)
[20] S M Sheikholeslami, M P Khanna and R C Verma, *Phys. Rev.* **D43**, 170 (1991)
[21] Y Igarashi and M Shin-Mura, *Nucl. Phys.* **B129**, 483 (1977)
M Shin-Mura, *Prog. Theor. Phys.* **59**, 917 (1977)
[22] M A Shifman, A I Vainshtein and V J Zakharov, *Nucl. Phys.* **B120**, 315 (1977)
[23] Y Abe, M Bando, K Fujii and T Okazaki, *Phys. Rev.* **D19**, 3470 (1979)
[24] S Glashow, J Iiopoules and L Maiani, *Phys. Rev.* **D2**, 1285 (1970)
[25] M B Einhorn and C Quigg, *Phys. Rev.* **D12**, 2015 (1975)
[26] Particle Data Group, *Phys. Rev.* **D49** (1994); CLEO collaboration
E R F Hyatt *et al*, *Phys. Lett.* **B350**, 256 (1995)
[27] A DeRujula, H Georgi and S L Glashow, *Phys. Rev.* **D12**, 147 (1975)
[28] J Ellis, M K Gaillard and D V Nanopoulos, *Nucl. Phys.* **B100**, 313 (1975)
[29] J G Korner, G Kramer and J Wilrodt, *Phys. Lett.* **B78**, 492 (1978); *Z. Phys.* **C2**, 117 (1979)

new theoretical approach

IJOY KR DEY and B M DEB*

ieoretical Chemistry Group, Department of Chemistry, Panjab University, Chandigarh
0014, India

Also at the Jawaharlal Nehru Centre for Advanced Scientific Research, Jakkur, Bangalore
0064, India

Author for correspondence

S received 24 December 1996

bstract. A quantum hydrodynamical study is made of the dynamical changes of a lium atom interacting with lasers of two different intensities, but having the same freiency. Under the intense laser field, electron density oozes out of the helium atom by sorbing laser photons and getting promoted to higher excited states including the continuum. nder the superintense field, electron density partly moves away from the helium nucleus but mains in the "quasi-bound" dressed states along with the laser field, thus suppressing nization.

eywords. Helium; laser fields.

aser pulses are known to control a particular atomic or molecular process. For ample, one bond in a polyatomic molecule can be broken selectively [1] by properly signing the laser field. Similarly, an atom can exhibit different types of behaviour hen probed by a laser of controlled intensity, e.g., atoms can undergo ionization ree possible types of ionization are: above-threshold [2, 3], tunneling [4] and quential [5, 6]), excitation leading to emission of radiation [7, 8] (including gh-order harmonic generation) and stabilization with respect to ionization , 10]. Here, we report a new theoretical, quantum hydrodynamical study of e dynamical changes of a helium atom probed by lasers of two different intensities) having the same frequency (0·1382 a.u.). When $I = 5{\cdot}6 \times 10^{13}\,\mathrm{W\,cm^{-2}}$ (intense ld) electron density oozes out (ionization) of the helium atom by absorbing ser photons and getting promoted to higher excited states including the continuum. However, when $I = 5{\cdot}6 \times 10^{18}\,\mathrm{W\,cm^{-2}}$ (superintense field), electron density rtly moves away from the helium nucleus but remains in the "quasi-bound" essed states along with the laser field, thereby suppressing ionization. We provide pport for this conclusion by calculating the extra stabilization energy gained the electrons in the presence of the laser field. The non-perturbative methoology devised in our laboratory is applicable to any time-dependent quantum echanical process.

We consider the electron density in an atom as that of a continuous "classical" fluid which obeys two quantum mechanical equations [11, 12] viz., a continuity equation and a Navier–Stokes-type equation of motion, as follows:

$$\partial_t a^2 + \nabla_q\left(a^2 \frac{\nabla_q S}{m}\right) = 0; \quad \partial_t = \frac{\partial}{\partial t}, \tag{1}$$

$$\partial_t S + \frac{(\nabla_q S)^2}{m} - \frac{\hbar^2}{2m}\frac{\nabla_q a}{a} + V_c^{qu}(a) + V(q,a) = 0, \tag{2}$$

where $V_c^{qu}(a)$ is a non-classical additional term needed for more than two-electron systems, which gives the additional kinetic energy in addition to the Weizsäcker contribution. $V(q,a)$ is a density (a^2)-dependent non-linear potential given by

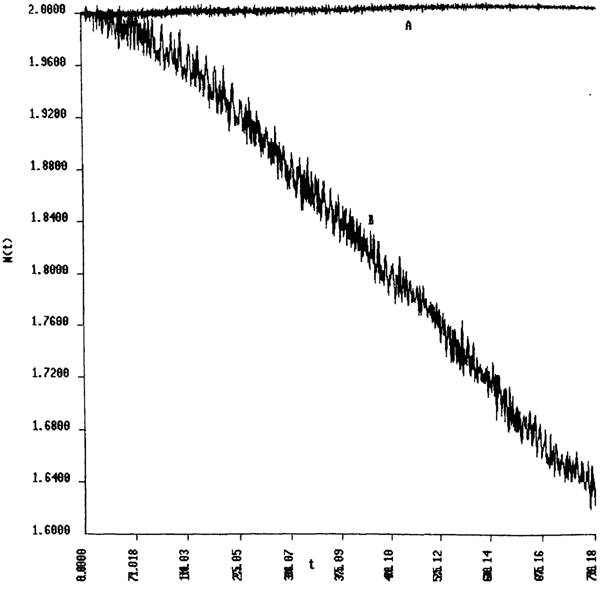

(x, exchange; c, correlation; I, interaction)

$$V(q,a) = \frac{\delta E_x[a]}{\delta a} + \frac{\delta E_c[a]}{\delta a} + \frac{\delta E_{\mathrm{el-el}}[a]}{\delta a} + \frac{\delta E_{\mathrm{nu-el}}[a]}{\delta a} + \frac{\delta E_I[a]}{\delta a}. \tag{3}$$

Under the construction of an effective hamiltonian, H_{eff} is given as

$$H_{\mathrm{eff}} = -\frac{\hbar^2}{2m}\nabla_q^2 + V(q,a) + V_c^{qu}(a), \tag{4}$$

and a hydrodynamical "wave" function,

$$\Psi_{\mathrm{hy}} = a\mathrm{e}^{\mathrm{i}S/\hbar}; \quad a, S \text{ real} \tag{5}$$

which gives a collective description of all the electrons, we obtain a generalized non-linear Schrödinger equation (GNLSE) in three-dimensional space unlike the conventional Schrödinger equation in 3N-dimensional configuration space. The GNLSE may be written as

$$i\hbar\frac{\partial\Psi_{\mathrm{hy}}(q)}{\partial t} = H_{\mathrm{eff}}\Psi_{\mathrm{hy}}^{(q)}. \tag{6}$$

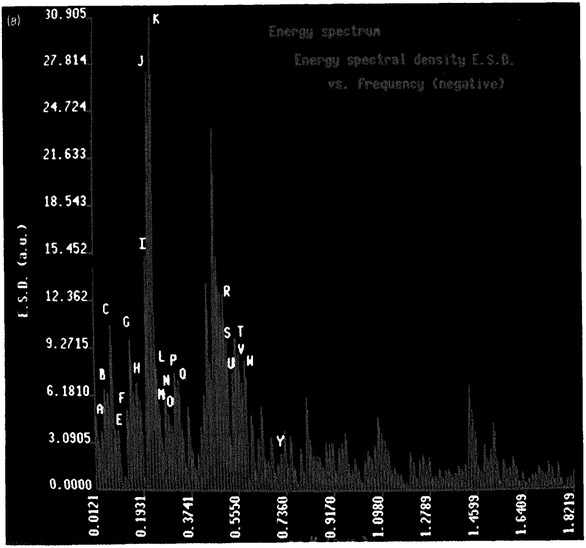

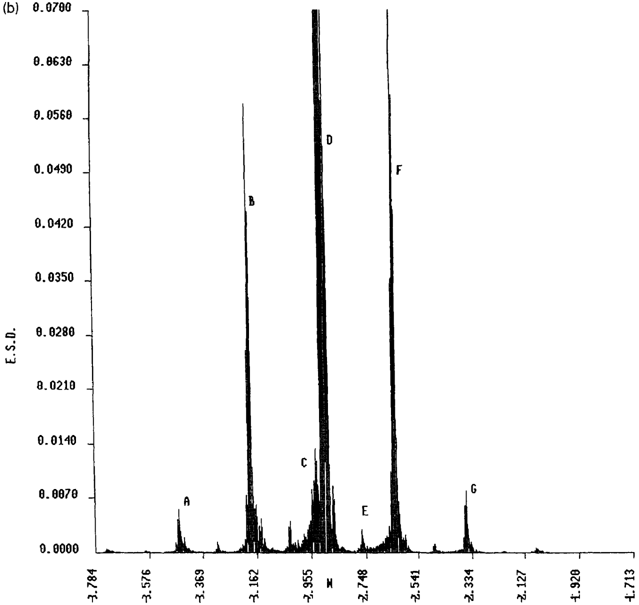

Figure 2. Calculated energy spectrum (a.u.) showing the spectral density (E.S.D.) for different states of energy, *W*. A large number of states with different labels signifying higher excitation and consequent ionization can be seen for $I = 5{\cdot}6 \times 10^{13}\ \mathrm{W\,cm^{-2}}$ (**a**). For $I = 5{\cdot}6 \times 10^{18}\ \mathrm{W\,cm^{-2}}$ (**b**), only a few quasi-bound "dressed" states are noticed. Some of the quasi-bound states have lower energy than the ground state energy of He atom (b).

This formulation is closer to the classical description of quantum systems in the sense that the reduction of 3N degrees of freedom in the Schrödinger wave function to 3 in the hydrodynamical wave function (eq. (5)), results in the loss of interference—a characteristic feature of quantum systems. Thus, Ψ_{hy} is essentially a "reduced" form of Schrödinger wave function.

To understand the behavioural change of atomic systems under varying laser fields, one often resorts to varying techniques ranging from time-dependent Schrödinger equation and time-dependent Hartree–Fock equation to Kramer–Henneberger-frame number of time steps, each of which amounts to propagating Ψ_{hy} forward by an amount Δt, given by

$$\Delta t = \begin{cases} \dfrac{\pi}{2700\,\omega_{\text{L}}}, & \text{up to the 30th time-step} \\ \dfrac{\pi}{90\,\omega_{\text{L}}}, & \text{after the 30th time-step}\cdot \end{cases} \tag{7}$$

The above propagation is done with a coherent oscillating laser pulse of frequency, $\omega_{\text{L}} = 0{\cdot}1382$ a.u. propagating along the axis $(\tilde{z})$ of the cylinder given by

$$E(t) = E_0 f(t) \sin(\omega_{\text{L}} t), \tag{8}$$

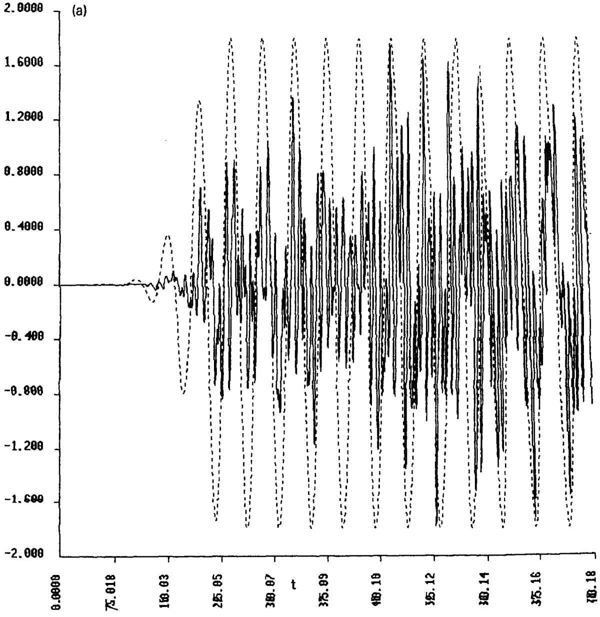

Figure 3a.

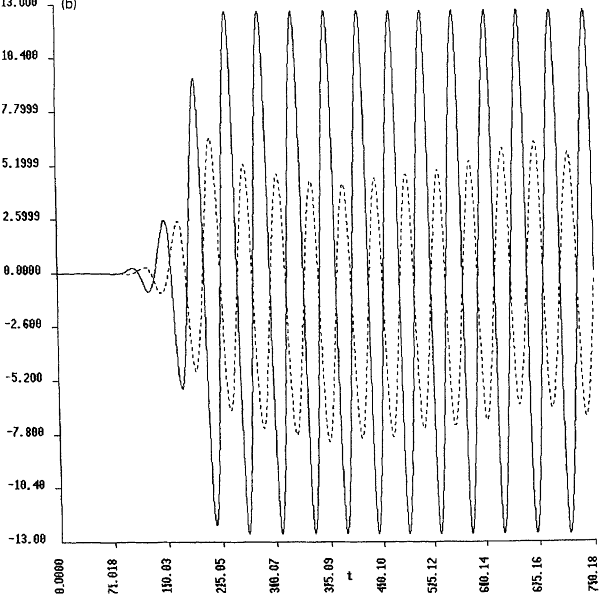

Figure 3. Average $\tilde{z}$-directional expectation value (a.u.) of electronic charge distribution (solid line) along with the laser electric field (dotted line) for both the lasers. The two oscillations are seen to be non-resonant for $I = 5{\cdot}6 \times 10^{13}\,\mathrm{W\,cm^{-2}}$ (**a**) and the amplitude for electronic charge oscillation (solid line) is much higher than that for electric field (dotted line). In figure 3a, the ordinate is to be divided by 45 for the electric field (dotted line). For $I = 5{\cdot}6 \times 10^{18}\,\mathrm{W\,cm^{-2}}$ (**b**), the two oscillations are seen to be resonant with little phase difference. Here the amplitude of electronic charge oscillation (dotted line) is much lower than that of electric field (solid line). In figure 3b, the ordinate is to be divided by 15 for the electronic charge oscillation (dotted line).

where the pulse-shape function, $f(t)$ is given by

$$f(t) = \begin{cases} e^{-\alpha(t-t_0)^2}, & t < t_0 \\ 1, & t \geqslant t_0 . \end{cases} \tag{9}$$

Starting from the ground-state Hartree–Fock density of the He atom, the results of our

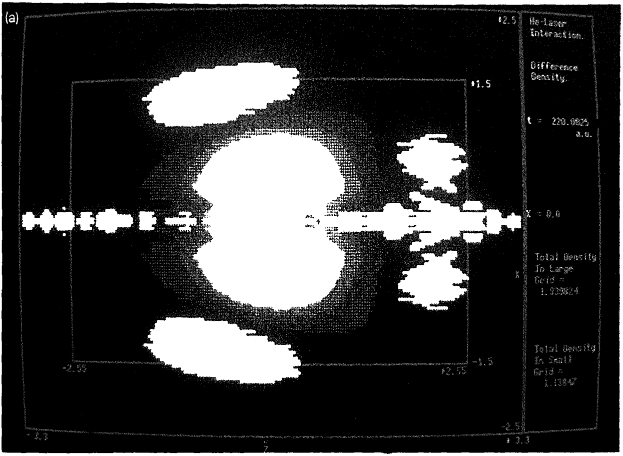
(a)
+2.5
+1.5
-1.5
-2.5
-2.55
+2.55
-3.3
+3.3
y
X
He-Laser Interaction.
Difference Density.
t = 220.0825 a.u.
X = 0.0
Total Density In Large Grid = 1.939824
Total Density In Small Grid = 1.13847

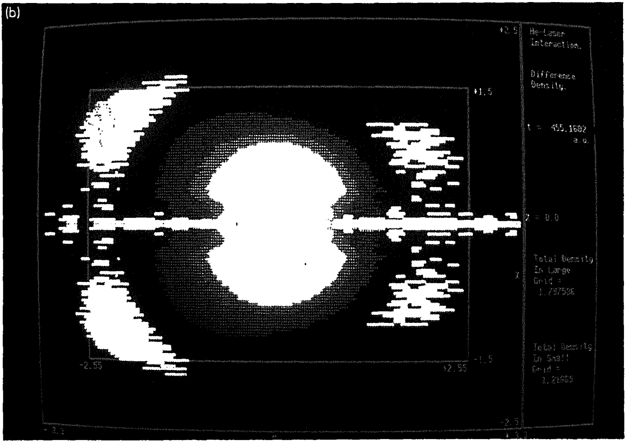
(b)
+2.5
+1.5
-1.5
-2.5
-2.55
+2.55
-3.3
+3.3
z
X
He-Laser Interaction.
Difference Density.
t = 455.1602 a.u.
Z = 0.0
Total Density In Large Grid = 1.797596
Total Density In Small Grid = 1.21553

ionization of He atom (decrease in the electronic charge, N) under $I = 5{\cdot}6 \times 10^{13}$ W cm^{-2} whereas no ionization ($N = 2$ remains practically fixed) is seen for $I = 5{\cdot}6 \times 10^{18}$ W cm^{-2}. The ionization at $I = 5{\cdot}6 \times 10^{13}$ W cm^{-2} is due to the higher absorption of energy out of the laser photons, leading to a dynamical state having contributions from higher singly-excited, doubly-excited (autoionizing) and continuum states of He atom. The presence of a large number of these states can be seen from the energy spectrum displayed in figure 2a. The same plot (figure 2b) for $I = 5{\cdot}6 \times 10^{18}$ W cm^{-2}, however, shows only a few low-lying quasi-bound "dressed" states, some of whose energies lie lower than the ground-state energy of He atom ($-2{\cdot}90312$ a.u.). Thus, very little absorption leading to excitation occurs for $I = 5{\cdot}6 \times 10^{18}$ W cm^{-2}. At first sight this might appear to be counter-intuitive, but the qualitative explanation of this phenomenon is relatively simple.

The high absorption of laser photons for $I = 5{\cdot}6 \times 10^{13}$ W cm^{-2} is attributed to the fact that the oscillations of electronic charge density along the polarization direction of the laser field cannot follow those of the laser field and thus the two types of oscillations show a pronounced phase-difference—a non-resonant phenomenon. However, for $I = 5{\cdot}6 \times 10^{18}$ W cm^{-2}, the atom–laser interaction is nearly resonant with little phase difference (maximum, 1·13 rad.) between the two oscillations. This can be seen from figures 3a and 3b which display the z-directional expectation value of the electron density and electric field for both the lasers. The small phase difference at $I = 5{\cdot}6 \times 10^{18}$ W cm^{-2} is the cause of the small absorption, excitation and practically no ionization. In other words, at the superintense field, electronic behaviour is dictated by the laser field rather than the nuclear field while at the intense field, the nuclear field still dominates over the laser field.

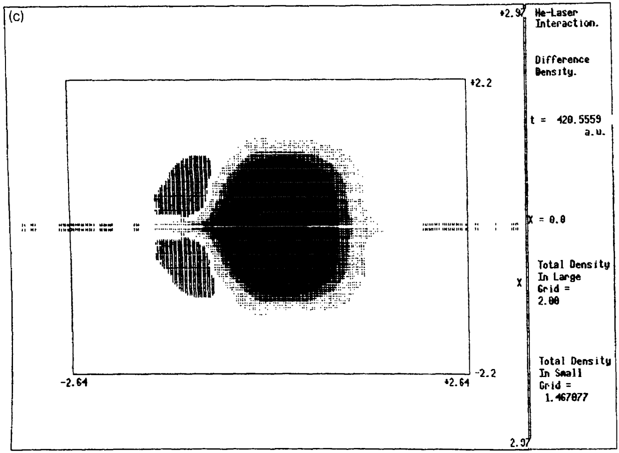

Figure 4.

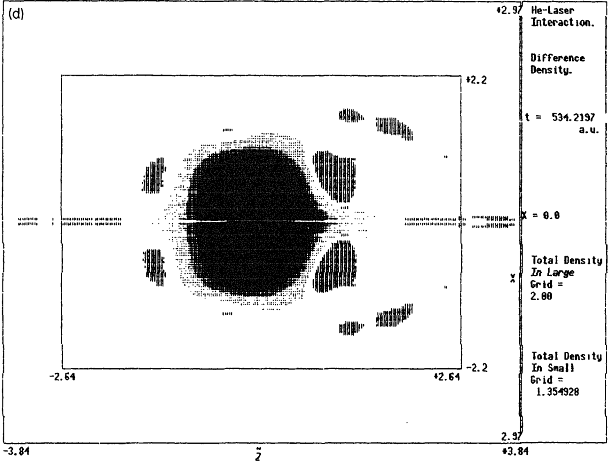

Figure 4. Difference electronic charge density (a.u.) in the $(\tilde{\rho}, \tilde{z})$ plane for $I = 5{\cdot}6 \times 10^{13}\,\mathrm{W\,cm^{-2}}$ at $t = 220{\cdot}0025$ a.u. (**a**), $t = 455{\cdot}1602$ a.u. (**b**) and for $I = 5{\cdot}6 \times 10^{18}\,\mathrm{W\,cm^{-2}}$ at $t = 420{\cdot}5559$ a.u. (**c**), $t = 534{\cdot}2197$ a.u. (**d**). A small window inscribed into the large grid monitors the departure of electronic density from the nuclear site. In figures 4a and 4b, the magenta-coloured region signifies an increase in the density and the blue-coloured onion-layered region signifies a decrease of the same whereas in figures 4c and 4d the increase and decrease in the density are denoted by dots and lines, respectively.

For $I = 5{\cdot}6 \times 10^{18}\,\mathrm{W\,cm^{-2}}$, the large number of photons provides the electrons an extra stabilization energy, $E_{\mathrm{stab}} = -\int \tilde{z} E(t)\, \rho(\mathbf{r}) \mathrm{d}\mathbf{r}$ ($E_{\mathrm{stab}} = -6{\cdot}013$ a.u. at $t = 602{\cdot}165$ a.u.) which is higher than that of the electron–nuclear attraction energy ($E_{\text{nu-el}} = -3{\cdot}659$ a.u. at $t = 602{\cdot}165$ a.u.) whereas for $I = 5{\cdot}6 \times 10^{13}\,\mathrm{W\,cm^{-2}}$ the extra stabilization energy ($E_{\mathrm{stab}} = -0{\cdot}046$ a.u. at $t = 602{\cdot}165$ a.u.) is very small compared to electron–nuclear attraction ($E_{\text{nu-el}} = -2{\cdot}1488$ a.u. at $t = 602{\cdot}165$ a.u.). This difference in the two E_{stab} values is responsible for higher excitation/ionization at $I = 5{\cdot}6 \times 10^{13}\,\mathrm{W\,cm^{-2}}$ and extra stabilization for $I = 5{\cdot}6 \times 10^{18}\,\mathrm{W\,cm^{-2}}$.

The significant difference in the behaviour of electron density for the two lasers in the $(\tilde{\rho}, \tilde{z})$-space can be vividly seen from the plots (figure 4) of difference electronic density, $\Delta\rho = \rho(\mathbf{r}, t) - \rho(\mathbf{r}, 0)$ showing the topography of positive and negative values of difference density. These plots also show that electronic movement follows the electric field more closely for $I = 5{\cdot}6 \times 10^{18}\,\mathrm{W\,cm^{-2}}$ than for $I = 5{\cdot}6 \times 10^{13}$ W figures 4a and 4b whereas figures 4c and 4d show a fall in density in the small grid but fixed in the large grid.

The above suppression of ionization for superintense laser field will sustain till the laser field is present, provided no nonlinear dissipative mechanism leading to the loss of photons is introduced during the interaction.

Our primary goal in this work has been to demonstrate that time-dependent quantum fluid density functional theory can be applied in a unified manner to explain the detailed features in the dynamical evolution of atoms under various time-dependent processes occurring generally in femtoseconds. Manifold aspects of these phenomena will be published elsewhere (see also ref. [6]).

Acknowledgements

The authors would like to thank the Department of Atomic Energy and the Council of Scientific and Industrial Research, India for financial support. They are grateful to Prof. N Satyamurthy for his assistance in computation.

References

[1] W S Warren, H Rabitz and M Dahleh, *Science* **259**, 1581 (1993)

[2] G G Paulus, W Nicklich, H Xu, P Lambropoulos and H Walther, *Phys. Rev. Lett.* **72**, 2851 (1994)

[3] K J Schafer, B Yang, L F DiMauro and K C Kulander, *Phys. Rev. Lett.* **70**, 1599 (1993)

[4] D N Fittinghoff, P R Boltom, B Chang and K C Kulander, *Phys. Rev. Lett.* **69**, 2642 (1992)

[5] J Peatross, B Buerke and D D Meyerhofer, *Phys. Rev.* **A47**, 1517 (1993)

[6] Bijoy Kr Dey and B M Deb, in Thirty years of density functional theory, *Int. J. Quantum Chem.* **56**, 707 (1995)

[7] M Lewenstein, Ph Balcou, M Yu Ivanov, A L'Huillier and P B Corkum, *Phys. Rev.* **A49**, 2117 (1994)

[8] Bijoy Kr Dey and B M Deb, *J. Chem. Phys.* (submitted)

[9] J H Hoogenraad and L D Noordam, in *Super-Intense Laser-Atom Physics of* NATO Advanced Study Institute, Series B edited by B Piraux, A L'Huillier and K Rzazewski (Plenum, NY, 1993), vol. 316, p. 269

[10] R B Vrigen, J H Hoogenraad, H G Muller and L D Noordam, *Phys. Rev. Lett.* **70**, 3016 (1993)

[11] B M Deb and S K Ghosh, in *The single-particle density in physics and chemistry* edited by N H March and B M Deb (Academic Press, London, 1987)

[12] B M Deb, P K Chattaraj and S Mishra, *Phys. Rev.* **A43**, 1248 (1991)

Surface harmonics for pentagonal point groups

K RAMA MOHANA RAO, P HEMAGIRI RAO* and V SATYAVATHI**
Department of Applied Mathematics, Andhra University, Visakhapatnam 530 003, India
*Department of Mathematics, Bapatla Engineering College, Bapatla 522 101, India
**Department of Applied Mathematics, A.U.P.G. Centre, Nuzvid 521 201, India

MS received 14 June 1996; revised 19 November 1996

Abstract. Surface harmonics for the seven pentagonal point groups $5(C_5)$, $\bar{5}(S_{10})$, $\overline{10}(C_{5h})$, $\overline{10}m2(D_{5h})$, $52(D_5)$, $5m(C_{5v})$ and $\bar{5}2m(D_{5d})$ that represent the symmetries of quasicrystals in two and three dimensions are obtained, employing the projection operator method [11] and the simplified (authors) method. The results obtained are tabulated and are briefly discussed.

Keywords. Pentagonal point groups; quasicrystals; spherical and surface harmonics; Euler angles, induced representations.

PACS No. 78·20

1. Introduction

The discovery of Al–Mn quasicrystal for the first time by Schectman *et al* [1], the subsequent discovery of Al_6–Li_3–Cu icosahedral phase by Dubost *et al* [2], followed by Al–Cu–Fe system and Al–Pd–Mn quasicrystal by Tsai *et al* [3, 4] have initiated a tremendous burst of theoretical and experimental activity in condensed matter physics, for determining the symmetry, structure, neutron and X-ray diffraction of quasicrystals. The study of the properties of these materials have already emerged from their infancy and work on some prominent physical properties such as electrical resistivity, magnetism, elasticity, photoelasticity and transport phenomenon have been undertaken, employing both experimental and group theoretical [5–8] methods. In this work the seven point groups with five-fold rotations namely: the $5(C_5)$, $\bar{5}(S_{10})$, $\overline{10}(C_{5h})$, $\overline{10}m2(D_{5h})$, $52(D_5)$, $5m(C_{5v})$ and $\bar{5}2m(D_{5d})$ are considered and the surface harmonics (symmetrized linear combinations of spherical harmonics) for the seven pentagonal point groups that represent the symmetry groups of a class of quasicrystals in 2-d and 3-d, have been obtained and tabulated.

Evaluation of spherical harmonics with the symmetry of the regular polyhedrons, particularly for electrostatic problems involving polyhedral conductors, created some interest in group theoretical physicists since a long time. Owing to the connection that existed with the structure of some proteins, interest in the icosahedral groups has arisen. Whereas the spherical harmonics up to $l = 21$ for the total symmetric representation of the icosahedral point groups were derived by Laporate [9], expansions in spherical harmonics up to and including $l = 14$ for all the irreducible representations (IRs) of the icosahedral point groups were derived by Cohan [10], employing the projection operator method of Altmann [11]. Following this commonly used method, the spherical harmonics for all the IRs of the 32 crystallographic point groups were obtained and tabulated by Bradley and Cracknell [12]. Similar work for space groups was carried out by Altmann and Cracknell [13], Altmann and Bradley [14].

We contend that considerable simplification can be achieved in the process of obtaining the surface harmonics of point groups by combining the little group technique [15], of inducing the IRs of a finite group G_i from those of the IRs of its little group, with the projection operator method of Altmann [11]. In § 2, the projection operator method of Altmann is briefly discussed and applied succinctly, to illustrate the case of degenerate IRs of the point group 52 (D_5). In § 3, the authors' simple and elegant method is applied to derive (i) the surface harmonics of the point group 52 from those of its normal subgroup 5 by considering the composition series $\overline{10}m2 \supset 52 \supset 5 \supset 1$ and in turn obtain (ii) the surface harmonics of the point group $\overline{10}m2$ from those of the point group 52. In § 4, the results obtained in this work are briefly summarized. The results obtained in respect of all the seven considered pentagonal point groups are tabulated.

2. Projection operator method

We now briefly summarize the operational technique of the projection operator method given by Altmann [11]. Suppose G is a point group under consideration and let $R, S, \ldots \in G$. Suppose $D^i(R), D^i(S), \ldots$ denote the matrix representation of G. For the generating functions we take the spherical harmonics $Y_l^m(\theta, \phi)$. Then one has to evaluate

$$W_{ts}^i\, Y_l^m(\theta,\phi) = \left\{ d_i/|G| \sum_{R\in G} P_R\, D^i(R)_{ts}^*\, R \right\} Y_l^m(\theta,\phi), \quad -l \leqslant m \leqslant l. \qquad (2.1)$$

To proceed with (2.1) one needs an expression for $RY_l^m(\theta,\phi)$. In (2.1), $R \in G$ may be a proper or an improper rotation. If R is a proper rotation, we find its Euler angles (α, β, γ) and evaluate $RY_l^m(\theta,\phi)$ using the equation

$$R(\alpha,\beta,\gamma)\, Y_l^m(\theta,\phi) = \sum_{n=-l}^{l} Y_l^n(\theta,\phi)\, D^l\{R(\alpha,\beta,\gamma)\}_{nm}. \qquad (2.2)$$

In equation (2.2)

$$D^l\{R(\alpha,\beta,\gamma)\}_{nm} = C_{nm} \exp(-in\gamma)\, d^l(\beta)_{nm} \exp(-im\alpha) \qquad (2.3)$$

with the usual notation of Bradley and Cracknell [12]. On the other hand if R is improper i.e. $R = IQ$, we use the Euler angles (α, β, γ) for proper rotation Q, evaluate $QY_l^m(\theta,\phi)$ by means of eq. (2.2). To complete the evaluation of $RY_l^m(\theta,\phi)$, we use

$$I\, Y_l^m(\theta,\phi) = (-1)^l\, Y_l^m(\theta,\phi) \qquad (2.4)$$

for the transform of $IY_l^n(\theta,\phi)$. This simply adds an extra factor $(-1)^l$ if R is an improper rotation. Hence (2.1) in conjunction with (2.2), (2.3) and (2.4) becomes

$$W_{ts}^i\, Y_l^m(\theta,\phi) = d_i/|G| \sum_{R\in G} P_R\, D^i(R)_{ts}^*$$

$$\times \left[\exp(-im\alpha) \sum C \quad \exp(-in\gamma)\, d^l(\beta) \quad Y^n(\theta,\phi)\right] \qquad (2.5)$$

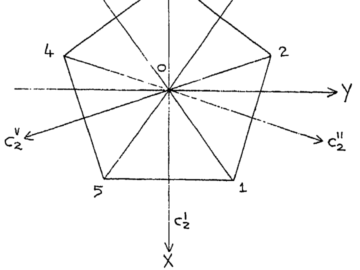

Figure 1. The pentagon depicting the five-fold symmetry. (In figure 1, OZ is taken as the 5-fold axis, which is perpendicular to the plane of the paper.)

Table 1. Euler angles for the elements of the point group 52(D_5)*.

Symmetry element	α	β	γ
E	0	0	0
C_5	$2\pi/5$	0	0
C_5^2	$4\pi/5$	0	0
C_5^3	$6\pi/5$	0	0
C_5^4	$8\pi/5$	0	0
C_2^{I}	π	π	0
C_2^{II}	$\pi/5$	π	0
C_2^{III}	$7\pi/5$	π	0
C_2^{IV}	$3\pi/5$	π	0
C_2^{V}	$9\pi/5$	π	0

*The symmetry operations listed in table 1 are taken in active convention.

wherein, if R is an improper rotation, we take in the RHS the quantities corres-ponding to the associated proper rotation Q. In eq. (2.5), P_R is taken as unity when R is proper and $(-1)^l$ when R is improper.

We shall now apply this method towards obtaining the surface harmonics for the IRs of the point group 52. For this we consider the following pentagon as a reference figure (figure 1), relative to which the nomenclature of the group elements and their Euler angles (table 1) are specified.

From the character table of the point group 52, it can be seen that (x, Y) transform as the 2-d IR E_1 and $(x^2 - Y^2, xy)$ transform as the IR E_2 of 52. With this information, we matrices obtained for the point group 52 (D_5) are listed in table 2.

In table 2, the symbols a, b, c and d stands for the constants (numbers) $a = \cos\omega$, $b = \sin\omega$, $c = \cos 2\omega$, $d = \sin 2\omega$ with $\omega = 2\pi/5$. Now using (2.1) through (2.5), one can straightaway obtain the surface harmonics having the symmetry of the IRs A_1, A_2, E_1 and E_2 of 52.

Table 2. Matrices for the degenerate representations of the point group 52.

Irreducible representation of 52	Symmetry element g of the group 52	Matrix representative for the element g in the chosen degenerate representation of 52
E_1	E	$\begin{bmatrix} 1 & 0 \\ 0 & 1 \end{bmatrix}$
	C_5	$\begin{bmatrix} a & -b \\ b & a \end{bmatrix}$
	C_5^2	$\begin{bmatrix} c & -d \\ d & c \end{bmatrix}$
	C_5^3	$\begin{bmatrix} c & d \\ -d & c \end{bmatrix}$
	C_5^4	$\begin{bmatrix} a & b \\ -b & a \end{bmatrix}$
	C_2^{I}	$\begin{bmatrix} 1 & 0 \\ 0 & -1 \end{bmatrix}$
	C_2^{II}	$\begin{bmatrix} c & d \\ d & -c \end{bmatrix}$
	C_2^{III}	$\begin{bmatrix} a & -b \\ -b & a \end{bmatrix}$
	C_2^{IV}	$\begin{bmatrix} a & b \\ b & -a \end{bmatrix}$
	C_2^{V}	$\begin{bmatrix} c & d \\ -d & -c \end{bmatrix}$
E_2	E	$\begin{bmatrix} 1 & 0 \\ 0 & 1 \end{bmatrix}$
	C_5	$\begin{bmatrix} c & -2d \\ d/2 & a \end{bmatrix}$

(*continued*)

Table 2. (*Continued*)

Irreducible representation of 52	Symmetry element g of the group 52	Matrix representative for the element g in the chosen degenerate representation of 52
	C_5^2	$\begin{bmatrix} a & 2b \\ -b/2 & a \end{bmatrix}$
	C_5^3	$\begin{bmatrix} a & -2b \\ b/2 & a \end{bmatrix}$
	C_5^4	$\begin{bmatrix} c & 2d \\ -d/2 & c \end{bmatrix}$
	C_2^{I}	$\begin{bmatrix} 1 & 0 \\ 0 & -1 \end{bmatrix}$
	C_2^{II}	$\begin{bmatrix} a & -2d \\ -b/2 & -a \end{bmatrix}$
	C_2^{III}	$\begin{bmatrix} c & -2d \\ -d/2 & -c \end{bmatrix}$
	C_2^{IV}	$\begin{bmatrix} c & 2d \\ d/2 & -c \end{bmatrix}$
	C_2^{V}	$\begin{bmatrix} a & 2b \\ b/2 & -a \end{bmatrix}$

To exemplify, the procedure for the non-degenerate IRs, we consider the IR A_1 of $52\,(D_5)$.

$$W^{A_1}\, Y_l^m = 1/10\,[(1 + e^{-im\omega} + e^{-2im\omega} + e^{-3im\omega} + e^{-4im\omega})\, Y_l^m$$

$$+ (-1)^l (e^{-im\pi} + e^{-im\pi/5} + e^{-im7\pi/5} + e^{-im3\pi/5} + e^{-im9\pi/5})\, Y_l^{-m}],$$

$$\omega = 2\pi/5$$

$$= 1/10\,[1 + 2\cos m\omega + 2\cos 2m\omega]\,[\,Y_l^m + (-1)^{l+m}\, Y_l^{-m}]. \quad (2.6)$$

It can be seen that the coefficients in the R.H.S of (2.6) is zero for all non-negative values of m excepting $m = 0, 5, 10, 15, \ldots$. Also we find that, when $m = 0$ and l is odd, the function in the curly bracket is zero. Thus for the IR A_1 of 52, the surface harmonics can be taken as

Y_l^0, l even

Table 3. Surface harmonics for the irreducible representations of the point group 52.

52	$l \bmod (+2)$	$m \bmod (+5)$
A_1	0	0
	5	5
A_2	1	0
	6	5
E_1	1	1
	2	1
	4	4
	5	4
E_2	2	2
	3	2
	3	3
	4	3

The surface harmonics that transform as the other IRs A_2, E_1 and E_2 of the point group 52 are obtained in a similar way and a resumé of the results obtained are provided in table 3. An apparent disadvantage and difficulty in applying (2.1) or (2.6) to the considered degenerate IR Γ_i of a chosen point group G lies in that, one has to construct the matrices $D^i(R)$ for all elements $R \in G$ under consideration. This difficulty is overcome in the authors simplified method, discussed in § 3.

3. The simplified (authors) method

From what has been discussed in § 2, one can see that, in the case of non-degenerate IRs of the point groups, the character of an element $R \in G$ in the considered IR Γ_i is sufficient to obtain the corresponding surface harmonics for Γ_i. One has to construct the matrices for the IR in respect of all the elements of the point group G under consideration, in the case of the degenerate IRs. This is the formidable difficulty that one encounters in the projection operator method discussed in § 2. The authors contend here that this tediousness involved in the calculation of matrices, can be avoided if one combines the projection operator method with (i) the theory of allowable IRs of little groups, (ii) the theory of induced representations and (iii) the idea of composition series that may exist for the generating point groups G, in terms of its maximal normal subgroups G_{i+1}.

It can easily be seen that if G is the symmetry (point) group and H is a properly chosen normal subgroup of G, all the 1-d IRs of G can be obtained from those of the IRs of the factor group G/H, through the process of engendering. Also, the 2-d IRs of G can be seen to be induced from those of the pairs of 1-d complex representations of H since H coincides with the little group L. In short, the proper choice of the normal subgroup H facilitates the process of engendering and inducing the required IRs of G. For example, in the case of the pentagonal point group $G = 52(D_5)$, if $H = 5(C_5)$ is chosen

52/5 engender respectively the total symmetric IR A_1 and the alternating IR A_2 of the point group 52. The character table of the factor group 52/5 is given hereunder.

$52/5 \cong 2$	E5	$C_2 5$
Γ_1	1	1
Γ_2	1	-1

It can be readily seen that the pair of 1-d complex representations $^1E'$ and $^1E''$ of the point group 5 induce the 2-d IR E_1 of 52 and the remaining pair of 1-d complex IRs; $^2E'$ and $^2E''$ of 5 together induce the other 2-d IR E_2 of 52. Thus by a proper choice of the maximal normal subgroup G_{i+1} of G_i in the composition series for G, a degenerate IR Γ_i of G_i can be seen to be induced by a 1-d real or complex IR of G_{i+1}.

We now formulate the composition series such that the maximal normal subgroups $G_{i+1} = H$ is a subgroup of index two to the generating point group G_i so that, the surface harmonics transforming according to an IR Γ of G_i can be obtained from those of the surface harmonics transforming as the appropriate IR γ_i of $H = G_{i+1}$ where γ_i induce the IR Γ of G_i.

3.2 Formulation of composition series

It is well known that if $G = G_0$ is a finite group and G_1 is a maximal normal subgroup of G_0 and G_2 is a maximal normal subgroup of G_1, etc., then these groups can be expressed in terms of composition series of the form $G = G_0 \supset G_1 \supset \cdots \supset G_i \supset G_{i+1} \supset \ldots \supset G_s = E$. Since G_0 is of finite order, this process shall ultimately terminate with group G_s consisting of the identity element $\{E\}$ only. Because a maximal normal subgroup G_{i+1} of a group G_i may not be unique, we may write several such composition series for a group G_0 under consideration. However, the factor groups G_i/G_{i+1} are unique but for isomorphism, they need not occur in the same order.

The six composition series expressed in table 4 are just sufficient for the purpose of obtaining the required surface harmonics of the pentagonal point groups. International (Hermann–Maugüin) notation is adopted for denoting the point groups in the various series. From table 4, it can be noted that the seven pentagonal point groups are subgroups of either $\overline{10}\,m2$ or $\bar{5}\,2m$.

Table 4. Pentagonal point groups in terms of the chosen composition series.

Chosen composition series
$\overline{10}\,m2 \quad \supset 52 \quad \supset 5 \quad \supset 1$

To obtain the surface harmonics for the IR Γ of a point group G_i in a consid series using the authors simplified method, consider an IR γ of G_{i+1} such that th μ of the little group $L(G_i, G_{i+1}, \gamma)$ induces the IR Γ of G_i. To obtain a basis of the IR G_i, we first employ the projection operator method [11] and obtain the basis of th μ of the little group $L(G, H, \gamma)$. This does not pose much difficulty since this grou usually a group of smallest order in the composition series. On this obtained basis o IR μ, we apply the generator g that generates G_i from G_{i+1}. The resulting set becc a basis for the IR Γ of G_i.

3.3 Evaluation of surface harmonics employing the simplified (authors) method

We shall now exemplify the authors method, also with the composition s $\overline{10}\,m2 \supset 52 \supset 5 \supset 1$. Evaluation of the surface harmonics for the point group 1 is tri Since the point group 5 contains all 1-d IRs, the surface harmonics for the point gr 5 can be obtained using either the projection operator method discussed in § 2 o simplified method discussed in § 3. The results obtained for the point group 5 provided in table 5. We shall now proceed to evaluate the surface harmonics fo point group 52 from those of the point group 5.

From the character table of the point gorup 5, it can be easily seen that either o 1-d complex representations $^1\mathrm{E}'$ and $^1\mathrm{E}''$ of 5 induces the 2-d IR E_1 of 52. Also symmetry element $\mathrm{C}_2 \in 52$ can generate the point group 52 from the point group 5. S the IRs A_1 and A_2 of 52 are 1-d, one can obtain the surface harmonics for these using either the projection operator method or the simplified method. The su harmonics transforming as the 1-d complex IR $^1\mathrm{E}'$ of 5 is Y_l^m; $m = 1, 6, 11, \ldots$. To ge basis for the 2-d IR E_1 of D_5 we apply the generator C_2 on this Y_l^m. From table 1 Euler angles for C_2 is $R(\pi, \pi, 0)$. Hence $\mathrm{C}_2\, Y_l^m = (-1)^{l+m}\, Y_l^{-m}$; $m = 1, 6, \ldots$.

Thus $Y_l^m = (-1)^{l+m}\, Y_l^{-m}$; $m = 1, 6, 11 \ldots$, forms a basis of the 2-d IR E_1 of D_5. Simi the surface harmonics transforming as the 1-d complex IR $^1\mathrm{E}''$ is Y_l^m; $m = 4, 9, 1$ Applying the generator C_2 on this Y_l^m one gets $\mathrm{C}_2\, Y_l^m = (-1)^{l+m}\, Y_l^{-m}$; $m = 4, 9, 14,$. a basis of 2-d IR E_1 of 52. Combining these two results, we find

$$1/\sqrt{2}\,[\,Y_l^m + (-1)^{l+m}\, Y_l^{-m}];\quad 1/\sqrt{2}\,[\,Y_l^m - (-1)^{l+m}\, Y_l^{-m}]$$

are the surface harmonics that transform as the IR E_1 of the point group 52. In a si manner one can evaluate the surface harmonics for the IR E_2 of 52. The results obtaine the point group 52 are listed in table 3.

Table 5. Surface harmonics for the irreducible representation of the point gorup $\mathrm{C}_5(5)$.

C_5	m mod (5)
A	0
$^1\mathrm{E}'$	1
$^1\mathrm{E}''$	4
$^2\mathrm{E}'$	2
$^2\mathrm{E}''$	3

Table 6. Surface harmonics for the irreducible representations of the point group $\overline{10}\,m2$.

$\overline{10}\,m2$	l mod $(+2)$	m mod $(+10)$
A_1'	0	0
	5	5
A_2'	5	5
	10	10
A_1''	6	5
	11	10
A_2''	1	0
	6	5
E_1'	1	1
	4	4
	6	6
	9	9
E_2'	2	2
	3	3
	7	7
	8	8
E_1''	2	1
	5	4
	7	6
	10	9
E_2''	3	2
	4	3
	8	7
	9	8

To obtain the surface harmonics that transform as the IRs of the point group $\overline{10}\,m2$ in the considered composition series, we proceed as follows: We know that σ_h is the generator from 52 to $\overline{10}\,m2$ and the Euler angles for symmetry operator σ_h can be taken as $R(0, \pi, 0)$. We now obtain the surface harmonics that transform according to the IRs of $\overline{10}\,m2$ as: $\sigma_h\, Y_l^m = R(0, \pi, 0)\; Y_l^m = (-1)^{l+m}\; Y_l^m$.

The results obtained in respect of all the IRs of $\overline{10}m2$, are provided in table 6. By proceeding in much the same manner as has been done in the case of the point groups $\overline{10}m2$, 52 and 5 from the considered series, the surface harmonics transforming as those of the IRs of the point groups contained in the rest of the composition series can be evaluated. The results are listed in tables 3, 5–10.

4. Discussion

The elegance of the simplified method, adopted by the authors in this paper lies in the fact that the surface harmonics pertaining to the irreducible representations of various other

Table 7. Surface harmonics for the irreducible representations of the point group $\bar{5}$.

$\bar{5}$	$l \bmod (2)$	$m \bmod (5)$
A_g	0	0
A_u	1	0
$^1E'_g$	2	1
$^1E'_u$	1	1
$^1E''_g$	2	1
$^1E''_u$	1	-1
$^2E'_g$	2	2
$^2E'_u$	3	2
$^2E''_g$	2	-2
$^2E''_u$	3	3

Table 8. Surface harmonics for the irreducible representations of the point group $\overline{10}$.

$\overline{10}$	$l \bmod (+2)$	$m \bmod (10)$
A'	0 5	0 5
A''	1 6	0 5
$^1E'_1$	1 4	1 4
$^2E'_1$	1 4	-1 4
$^1E'_2$	2 3	2 -3
$^2E'_2$	2 3	-2 3
$^1E''_1$	2 5	1 -4
$^2E''_1$	2 5	-1 4
$^1E''_2$	3 4	2 -3
$^2E''_2$	3 4	-2 3

can be obtained simultaneously from those of the surface harmonics of the group G_i This method of combining the little group technique with the projection operat method avoids the tedious calculations involved in finding the matrices for t elements $g \in G$ (in the case of degenerate IRs E) for all the IRs of the group G

Table 9. Surface harmonics for the irreducible representations of the point group 5 *m*.

5*m*	*l* mod (2)	*m* mod (+ 5)
A_1	0	0
	5	5
A_2	1	0
	5	5
E_1	1	1
	2	1
	4	4
	5	4
E_2	2	2
	3	2
	3	3
	4	3

Table 10. Surface harmonics for the irreducible representations of the point group $\bar{5}$ 2*m*.

$\bar{5}$ 2*m*	*l* mod (+ 2)	*m* mod (+ 5)
A_{1g}	0	0
A_{1u}	5	5
A_{2g}	6	5
A_{2u}	1	0
E_{1g}	2	1
	4	4
E_{1u}	1	1
	5	4
E_{2g}	2	2
	4	3
E_{2u}	2	2
	3	3

Notation: In tables 3–10, *l* mod (5) stands for the succession of values $m = 1, -4, 6, -9, \ldots$ and *l* mod (+ 5) stands for the succession of values $m = 1, 6, 11, 16, 21, 26, \ldots$.

Surface harmonics are found to be of immense utility in many physical situations, for example, when the variational cellular method [16], is applied to investigate the band structure of a metal, one requires expansions that reproduce the symmetry of the group of the *k*-vectors. Also in augmented plane wave method [17] and tight binding method, one requires expansions in spherical harmonics that belong to a given IR of a symmetry

The seven point groups for which the surface harmonics are calculated, have interesting geometrical and physical applications. As such the results obtained and reported here, we believe, have physical significance.

Acknowledgements

The authors wish to thank Prof. L S R K Prasad for his constant encouragement.

References

[1] D Schectman, I Blech, D Gratias and J W Cohn, *Phys. Rev. Lett.* **53**, 1951 (1984)
[2] B Dubost, J M Lang, M Tanaka, P Sainfort and M Audia, *Nature (London)* **324**, 48 (1986)
[3] A P Tsai, A Inoue and T Masumoto, *Jpn. J. Appl. Phys.* **29**, L1161 (1990)
[4] A P Tsai, A Inoue, T Masumoto and Y Yokoyama, *Meter. Trans. JIM* **31**, 98 (1990)
[5] K Rama Mohana Rao and P Hemagiri Rao, *J. Phys.* **C4**, 5997–6008 (1992)
[6] K Rama Mohana Rao and P Hemagiri Rao, *J. Phys.* **C5**, 5513–5524 (1993)
[7] K Rama Mohana Rao and P Hemagiri Rao, *Pramana–J. Phys.* **42**, 167–173 (1994)
[8] K Rama Mohana Rao and P Hemagiri Rao, *Pramana–J. Phys.* **43**, 373–377 (1994)
[9] O Laporate, *Z. Naturforsch.* **3a**, 447 (1948)
[10] N V Cohan, *Proc. Camb. Philos. Soc. Math. Phys. Sci.* **54**, 28–38 (1958)
[11] S L Altmann, *Proc. Camb. Philos. Soc. Math. Phys. Sci.* **53**, 343–367 (1957)
[12] C J Bradley and A P Cracknell, *The mathematical theory of symmetry in solids* (Clarendon Press, Oxford, 1974)
[13] S L Altmann and A P Cracknell, *Rev. Mod. Phys.* **37**, 19–32 (1965)
[14] S L Altmann and C J Bradley, *Rev. Mod. Phys.* **37**, 33–45 (1965)
[15] S Bhagavantham and T Venkatarayudu, *Theory of groups and its applications to physical problems* (Academic Press, London, 1969)
[16] J R Liete, *Int. J. Quantum Chem.* **13**, 395–402 (1979)
[17] Jr Reitz, *Solid state physics* (Academic Press, New York, 1955) vol. 1, pp. 1–95

Characterization of chaos in a serrated plastic flow model

S V M SATYANARAYANA, V SRIDHAR and S KOKA
Materials Science Division, Indira Gandhi Centre for Atomic Research, Kalpakkam 603 102, India

MS received 23 May 1996; revised 30 December 1996

Abstract. We report new results on a dynamical model of serrated yielding. These essentially pertain to the full spectrum of Lyapunov exponents of the non-linear (chaotic) model and fractal characterization of the associated strange attractor. The power spectrum of scalar time series extracted from the phase space trajectories decays exponentially with increase of frequency and the decay constant is found proportional to the Kolmogorov–Sinai entropy.

Keywords. Chaos; Lyapunov exponents; fractal measures; time series; Kolmogorov–Sinai entropy; plastic flow.

PACS Nos 05·45; 62·20; 83·50

1. Introduction

The phenomenon of repeated and discontinuous yielding of materials under stress is of considerable interest, mainly because it is related to the basic issue of stability of materials. This phenomenon manifests itself as serrations in the stress-strain curve when a specimen of the material is subjected to constant strain rate. There exists a rich literature on the subject of serrated yielding, also known by various names like, jerky flow, Portevin–Le Chatelier (PLC) effect etc., addressing both theoretical [1–5] and experimental aspects [6–9]. Several models have been proposed to understand serrated yielding that include the solute-atom hypothesis of Cottrell [1], an improvement proposed by McCormic [2] and Van den Beukel [3, 4], the Coulomb friction model of Bodner and Rosen [5], to name only a few. In this paper we shall be concerned with a nonlinear dynamical model proposed by Ananthakrishna [10] in the early eighties. This model, which we shall refer to as Anantha oscillator, seeks to explain the phenomenon of serrated yielding as occurring due to nonlinear interactions amongst three types of dislocations namely the mobile, the immobile and the ones surrounded by a cloud of solute atoms. Anantha oscillator has explained several experimental observations [10–12], principal amongst which is jumps in the creep curves. An important prediction of the model is that the dynamics underlying the plastic flow is chaotic for certain strain rates. Recently Anantha oscillator has attracted renewed attention owing mainly to the fact that two independent studies of two different experimental data on serrated yield [13–15] have shown that there is *prima facie* evidence for a low dimensional chaotic dynamical mechanism responsible for and underlying the experimental scalar time series. This has motivated us to revive interest in this model and carry out some of the unfinished tasks like, estimating the full spectrum of Lyapunov expone and characterizing the invariant measure of the strange attractor in terms of sca exponents of the partition function, generalized Renyi entropy dimensions and spectrum of singularities. We also verify the validity of the Kaplan–Yorke conject [16] that relates the (dynamical) Lyapunov exponents to the (static) fractal measur the strange attractor. Also a scalar time series extracted from this continuous t chaotic dynamical system, has a power spectrum that decays exponentially at la frequencies. A recent study [17] of different chaotic systems showed that the expor tial decay constant is nearly proportional to the Kolmogorov–Sinai (KS) entro given by the sum of the positive Lyapunov exponents. We demonstrate that s a relation between the exponential decay constant, which is a characteristic of stationary time series and the Lyapunov exponents, which characterize the unsta dynamics, holds good for Anantha oscillator also.

This paper is organized as follows. In §2, we present a set of four coupled nonlin equations that form the central descriptor of the Anantha oscillator, and desc briefly the variables of the equations of motion and the control parameters. We s the nature of the chaotic mechanism predicted by the model and the values of control parameter that lead to chaotic solutions. Section 3 contains a brief descrip of the computational procedure adopted for estimating the Lyapunov exponents. In we characterize the fractal measures of the strange attractor. In §5, we report result Lyapunov dimension and verify the Kaplan–Yorke conjecture. We construct sev scalar time series from the four dimensional phase space trajectory, and for e calculate the constant characterizing the exponential decay of the power spectrur large frequencies. We show that the exponential decay constant is same for all the t series and is proportional to the Kolmogorov–Sinai entropy. These are described in A summary of the principal conclusions of the study is given in §7.

2. Model for serrated yielding: Anantha oscillator

The Anantha model considers three types of dislocations; the mobile, the immobile the ones with cloud of solute atoms. The corresponding scaled densities are denote x_1, x_2 and x_3 respectively. Using well-known dislocation reaction mechanisms, the equations for the densities of dislocations were set up and then coupled to mac equation for the rate of change of applied stress, x_4 [10]. The set of four cou nonlinear equations that describe the dynamics are

$$\frac{\mathrm{d}x_1}{\mathrm{d}t} = x_4^m x_1 - bx_1^2 - ax_1 + x_2 - x_1 x_2,$$

$$\frac{\mathrm{d}x_2}{\mathrm{d}t} = b(bx_1^2 - x_2 - x_1 x_2 + ax_3),$$

$$\frac{\mathrm{d}x_3}{\mathrm{d}t} = c(x_1 - x_3),$$

$$\mathrm{d}x_4$$

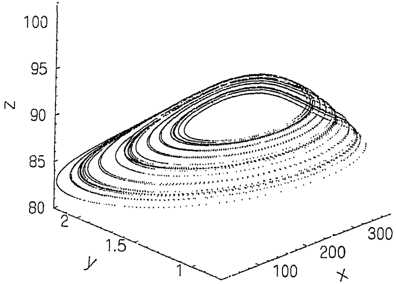

Figure 1. Strange attractor of Anantha oscillator.

where a refers to the concentration of the solute atoms; b, the strength of reactivation of immobile dislocations; c^{-1}, the time scales over which the slowing down occurs; d, the effective modulus; e, the applied strain rate and m, the velocity exponent which describes the dependence of velocity of dislocations on the stress. For a certain range of values of the parameters, the steady state is unstable. Analysis is carried out for these parameter values and the applied strain rate e is taken as the drive parameter.

There have been several studies on Anantha model [10–12, 18–20]. The system exhibits periodic solutions called limit cycles [18]. In a certain range of the applied strain rate e, the model exhibits chaotic oscillations through period doubling route. Feigenbaum number corresponding to the period doubling bifurcation is 4·669. The strange attractor associated with the chaotic dynamics was also constructed and figure 1 depicts a three dimensional section of the strange attractor. In this paper we compute the full Lyapunov spectrum and the fractal measures of the associated strange attractor, for the following values of the parameters: $a = 0{\cdot}7$, $b = 0{\cdot}002$, $c = 0{\cdot}008$, $d = 0{\cdot}0001$, $m = 2{\cdot}0$ and $e = 184{\cdot}9$. For this purpose the four nonlinear equations were solved numerically employing fourth order Runge-Kutta technique with time step of 0.1. First 40,000 time steps of evolution were treated as transients and rejected.

3. Lyapunov exponents

Lyapunov exponents quantify the exponential divergence/convergence of the neighbouring trajectories. We estimate the Lyapunov exponents employing the method described by Wolf [21].

Consider the four dimensional continuous time dynamical system described by equations (1–4). These can be expressed as this sphere would get distorted by the equations of motion, to a four dimensional ellipsoid with principal axes, $l_1 \geqslant l_2 \geqslant l_3 \geqslant l_4$. The size of $\{l_i;\ i=1,4\}$ represents the convergence ($l_i < 1$) or the divergence ($l_i > 1$) of the trajectories emanating from the neighbourhood of $\mathbf{x}_0$. Formally we write $l_i = \exp(\lambda_i t)$, where $\{\lambda_i;\ i=1,4\}$ are the Lyapunov exponents. Thus we have,

$$\lambda_i = \lim_{t\to\infty} \frac{1}{t} \ln(l_i) \tag{6}$$

and $\lambda_1 \geqslant \lambda_2 \geqslant \lambda_3 \geqslant \lambda_4$

We start with four orthonormal vectors $\{\xi^\beta(0);\ \beta=1,4\}$, located at $\mathbf{x}(0)$. These vectors, which define a sphere of initial conditions, is evolved up to T via the linearized version of the equation of motion

$$\frac{\mathrm{d}\xi_i^\beta(t)}{\mathrm{d}t} = \sum_j F_{ij}\xi_j^\beta(t), \tag{7}$$

where $F_{ij} = \partial f_i/\partial x_j$. $|\xi_i^\beta(T) - \xi_i^\beta(0)|$ gives $(l_i)_1$ in time T, for $i=1,4$. At T we re-orthonormalize $\xi^\beta(T)$ using Gram–Schmidt orthogonalization procedure. Using this as a unit sphere of initial conditions at T, the linearized evolution is continued up to $2T$ and $(l_i)_2$ is computed. This procedure is continued N times and the average Lyapunov exponents are then computed as

$$\lambda_i = \frac{1}{N}\sum_{j=1}^{N} \frac{\ln(l_i)_j}{T}. \tag{8}$$

These are given in table 1. The error bars on the Lyapunov exponents have been obtained by monitoring the sample fluctuations.

We observe that the exponent λ_1 is positive, indicative of chaos. λ_2 is positive, but very small. We conclude that λ_2 characterizes the tangential flow [23]. The other two exponents λ_3 and λ_4 are negative. Also the sum of the Lyapunov exponents is negative indicating that the system is dissipative (the phase space volume is contracting on the average).

4. Fractal measures of the strange attractor

To calculate the fractal measures of the strange attractor we evolve a dynamical trajectory for N time steps; N is taken adequately large to span the strange attractor

Table 1. Numerical results.

Model	Parameters	λ_i	d_{KY}	$\Sigma_i \lambda_i^+$	μ	$\mu/\Sigma_i \lambda_i^+$
Anantha	$a=0{\cdot}7$					
oscillator	$b=0{\cdot}002$	$\lambda_1 = 0{\cdot}00887 \pm 0{\cdot}0003$				
	$c=0{\cdot}008$	$\lambda_2 = 0{\cdot}00088 \pm 0{\cdot}0002$				
	$d=0{\cdot}0001$	$\lambda_3 = -0{\cdot}03688 \pm 0{\cdot}0002$	$2{\cdot}27 \pm 0{\cdot}15$	$0{\cdot}00975$	$0{\cdot}0097$	$0{\cdot}9949$
	$e=184{\cdot}9$	$\lambda_4 = -0{\cdot}60051 \pm 0{\cdot}0001$				
	$m=2{\cdot}0$					

reasonably well. We determine the smallest four dimensional paralellopiped that can hold all the N discrete phase space points of the dynamical trajectory. The coordinates of these points are scaled in such a way that they are contained in a hyper-cube of unit side. This unit hyper-cube is further divided into non-overlapping hyper-cubes each of side, ε, where $\varepsilon = N^{-1/4}$. Let $p_i(\varepsilon) = n_i/N$ denote the fractional number of phase space points that are contained within the ith hyper-cube. The partition function is defined as

$$Z(q,\varepsilon) = \sum_i p_i^q(\varepsilon), \tag{9}$$

where the sum over i runs only over the non-empty boxes, and $-\infty < q < +\infty$. For calculating partition function, we have employed the fast box counting algorithm, see [24]. The scaling ansatz reads as

$$Z(q,\varepsilon) \overset{\varepsilon \to 0}{\sim} \varepsilon^{\tau(q)}. \tag{10}$$

Figure 2(a) depicts ln $Z(q,\varepsilon)$ versus $\ln(\varepsilon)$ for representative values of q. For a given q, all the points fall on a straight line, verifying the scaling ansatz. The slope of the straight line yields the scaling exponent $\tau(q)$. Due to limitations on the computer resources, we could verify the scaling ansatz over a small range of ε only. Employing an alternate technique [25] we could establish the scaling behaviour over a range of resolution exceeding one order of magnitude, see figure 2(b). However, there are numerical problems associated with this technique which are discussed in the appendix. Figure 3 depicts the variation of $\tau(q)$ with q. Scaling exponent, $\tau(q)$ is not linear and exhibits well defined change of slope, showing that the invariant dynamical measure on the strange attractor is a multifractal. The generalized Renyi dimensions $D(q)$ are given by

$$D(q) = \frac{\tau(q)}{q-1} \tag{11}$$

for $q \neq 1$. For $q = 1$ we calculate $D(q)$ by taking the limit $q \to 1$. The variation of $D(q)$ with q is as depicted in figure 4. We find $D(q)$ is a monotonically non-increasing function of q. For $q = 0, 1$ and $2, D(q)$ are known as capacity, information and correlation dimensions, respectively, and these are 2·100, 1·882 and 1·799.

The singularity spectrum is obtained by taking the Legendre transform of $\tau(q)$, as below

$$f(\alpha) = -\tau(q) + q\alpha, \tag{12}$$

$$\alpha = \frac{\mathrm{d}\tau(q)}{\mathrm{d}q}. \tag{13}$$

Figure 5 shows the singularity spectrum of $f(\alpha)$ versus α. It is convex, with a single maximum at $q = 0$ with $f(\alpha(q = 0)) = D(0)$. We find that $\alpha_{\max} = D(q \to -\infty) = 3{\cdot}98$, indicating that the rarest region is very nearly (phase) space filling with fractal

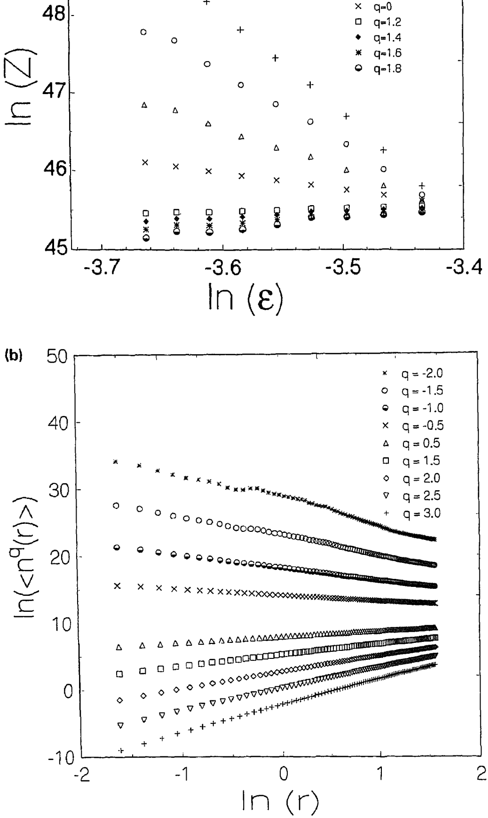

Figure 2. (a) Scaling behaviour of the partition function. **(b)** Scaling behaviour of the moments (see appendix).

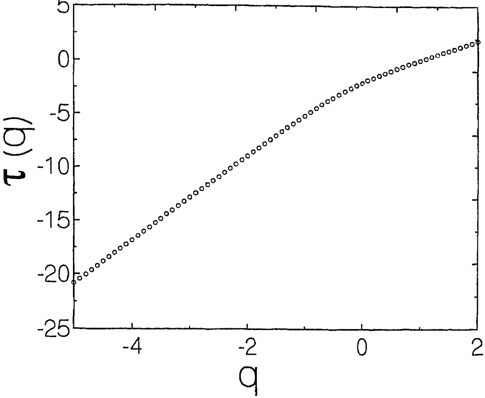

Figure 3. The scaling exponent.

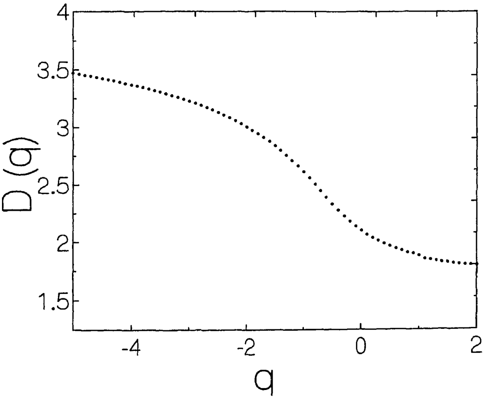

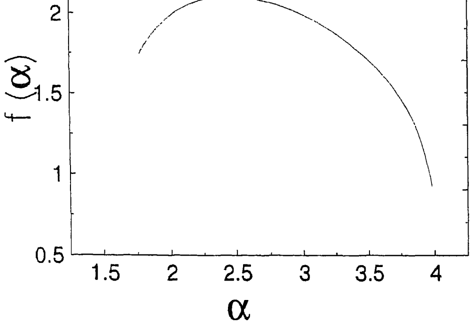

Figure 5. Singularity spectrum.

5. Lyapunov dimension

The Lyapunov spectrum is closely related to the fractal dimension of the associa strange attractor. It has been conjectured by Kaplan and Yorke [16] that Lyapu dimension d_{KY} is related to the Lyapunov spectrum as given by

$$d_{\mathrm{KY}} = j + \sum_{i=1}^{j} \frac{\lambda_i}{|\lambda_{j+1}|},$$

where j is determined by the condition

$$\sum_{i=1}^{j} \lambda_i > 0 \quad \text{and} \quad \sum_{i=1}^{j+1} \lambda_i < 0.$$

The Lyapunov dimension calculated for this model is in the range 2·122 to 2·423. spread in the calculated value of d_{KY} is due to the error bars on λ_i (see table 1). Wi numerical accuracy, the Lyapunov dimension matches with the capacity dimens $D(0)$, verifying the conjecture of Kaplan and Yorke.

6. Decay of the power spectrum

It is generally believed that the power spectrum of a time series taken from a continu time dynamical system decays exponentially at high frequencies [22]. We can repre the decay as

$$P(f) \sim \mathrm{e}^{-f/\mu},$$

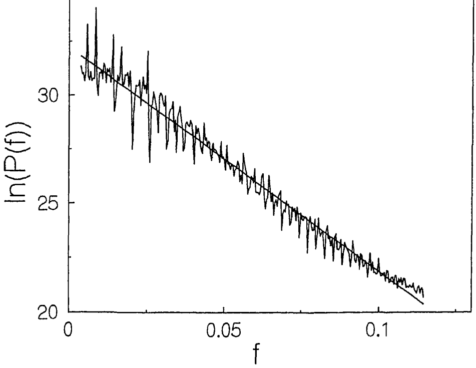

Figure 6. Exponential decay of the averaged power spectrum corresponding to time series $x_1(t)$.

where μ is the decay constant. It has been shown recently [17] that μ is proportional to the Kolmogorov–Sinai entropy given by the sum of the positive Lyapunov exponents. The ratio of μ to Kolmogorov–Sinai entropy is found to fall within a narrow range of 0·64 to 2·46 for a variety of systems exhibiting chaos with attractor dimensions varying from 2 to 20.

We have studied the exponential decay of the time series taken from Anantha model, whose attractor dimension is 2·1. Superimposed on the exponential decay are oscillations. These oscillations get largely smoothened out when we average the power spectrum over several time series. Figure 6 depicts the power spectrum for $x_1(t)$, averaged over several time series. The exponential decay is clearly seen in the picture. The decay constant μ has been calculated and the ratio of μ to K-S entropy is found to be 0·9949.

Discretely sampled data results in aliasing of the power spectrum as given by

$$P_a(f) = \sum_{j=-\infty}^{+\infty} P_N(f \pm 2jf_c), \tag{17}$$

where f is the frequency and $f_c = (2\delta t)^{-1}$ is Nyquist frequency. δt is the sampling interval. $P_N(f)$ is the power spectrum of the time series of size N and $P_a(f)$ is the aliased power spectrum. Invariably, we find that the exponential decay is followed by a power law flattening. This feature seems to be generic in character in the sense that finite size discrete time series extracted from a variety of chaotic oscillators exhibit this property. Such power law flattening can also be seen clearly in the figures of the power spectrum

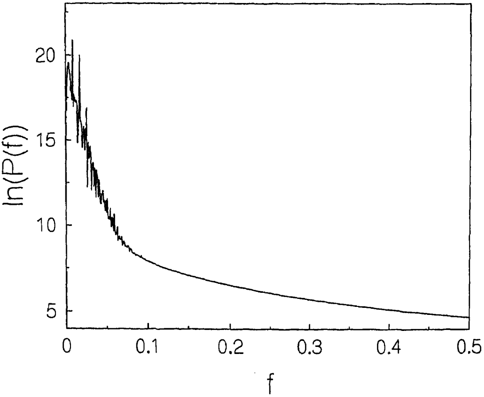

Figure 7. Full power spectrum of $x_4(t)$ exhibiting an exponential decay followed by a power law flattening.

depicted in [17]. For the Anantha oscillator, figure 7 shows a power spectrum that decays exponentially followed by a power law flattening. An interesting question in this context relates to the origin of the power law flattening. A recent study [26] has shown that the decay is $1/f^2$ after correcting analytically for aliasing arising due to finite sampling interval. Also this study suggests that this portion of the tail goes to zero in the limit of the length of the time series going to infinity, demonstrating that the observed power law flattening is an artifact of the finite size, and the true power spectrum is indeed band width limited with exponential decay at the far end.

7. Summary and conclusions

We have (i) studied the Anantha oscillator which has been proposed to model the chaotic behaviour of serrated yielding phenomenon, (ii) calculated the full spectrum of Lyapunov exponents for this model and (iii) characterized the fractal measures of strange attractor. We find that power spectrum of the time series extracted from the Anantha oscillator decays exponentially at large frequencies and the calculated exponential decay constant is proportional to Kolmogorov–Sinai entropy.

Acknowledgements

The authors are grateful to K P N Murthy and M C Valsakumar for suggesting this problem and for many useful discussions. One of the authors (SK) acknowledges CSIR

Appendix

The fractal measures of the Anantha attractor were calculated in §4, employing the traditional box counting algorithm incorporating recent improvements suggested in [24]. These improvements helped us overcome largely, the problem of (computer) memory requirements and rendered possible fractal characterization of the Anantha attractor. Despite these improvements we could establish the scaling ansatz over a small range of r only, due to the fact that we set $r = N^{-1/4}$ for numerical stability, where N is the length of the dynamical trajectory. There are alternate numerical techniques introduced for fractal characterization of chaotic strange attractor and we consider below one of them proposed by Paladin and Vulpiani [25].

We define the number of points in a four dimensional ball of radius r centered at $\mathbf{x}_i$ as

$$n_i(r) = \operatorname*{Lt}_{N\to\infty} \frac{1}{N-1} \sum_{j=1(j\neq i)}^{N} \Theta(r - |\mathbf{x}_i - \mathbf{x}_j|), \tag{A1}$$

where Θ is the usual Heaviside step function. We then introduce a set of exponents, $\phi(q)$ under the scaling ansatz

$$\langle n^q(r) \rangle = \operatorname*{Lt}_{M\to\infty} \frac{1}{M} \sum_{i=1}^{M} n_i^q(r) \underset{r\to 0}{\sim} r^{\phi(q)}. \tag{A2}$$

In figure 2(b), we establish numerically the scaling ansatz for values of r varying more than an order of magnitude. We evolve the trajectory for $N = 2^{20}$ time steps and take the resolution r_0 to be the minimum of the distances between any two phase space points. We let r vary from $\approx 10r_0$ to $\approx 1000r_0$. We find that averaging over $M (\ll N)$ randomly chosen centers is adequate to determine $\phi(q)$. Anantha oscillator has a hole in the interior; hence most of the centers selected randomly, fall on the inner or outer surface of the attractor and as a result most of the four dimensional balls are sparse: fractal dimensions are hence underpredicted. In fact we found that if we take the number of centers as low as 1000, the fractal dimension, $D(0)$ is 1·3. However $D(0)$ increases with increasing M and saturates at 1·9 for $M \geqslant 25000$, which is still 10% less than the box counting dimension. We would remark that this technique has a tendency to underpredict the fractal dimension especially when the strange attractor encloses a hole, as in the case of Anantha oscillator. Nevertheless, we find that $\phi(q)$ is nonlinear in q, $D(q)$ is monotonic and $f(\alpha)$ upward convex.

We are presenting the results on $\tau(q)$, $D(q)$ and $f(\alpha)$ obtained from the improved box counting algorithm. The estimates of fractal characteristics from box counting algorithm are known to be robust if we link the linear dimension of the box to the length of the dynamical trajectory (see [27]). This appendix is intended to serve a limited purpose of establishing the scaling ansatz over a longer range (see figure 2(b)).

References

[1] A H Cottrell, *Philos. Mag.* **44**, 829 (1953)
[2] P G McCormic, *Acta Metall.* **219**, 351 (1972)
[3] A Van den Beukel, *Phys. Status Solidi* **A30**, 197 (1975)

[5] S R Bodner and A Rosen, *J. Mech. Phys. Solids* **13**, 65 (1967)

[6] E Pink and A Grinberg, *Mater. Sci. Engg.* **51**, 1 (1981)

[7] G G Saha, P G McCormic and P Rama Rao, *Mater. Sci. Engg.* **62**, 187 (1984)

[8] S Venkadesan, C Phaniraj, P V Sivaprasad and P Rodriguez, *Acta Metall. Mater.* **40** (1992)

[9] S Venkadesan, S Venugopal, P V Sivaprasad and P Rodriguez, *Mater. Trans. Jpn. Met.* **33**, 1040 (1992)

[10] G Ananthakrishna and M C Valsakumar, *J. Phys.* **D15**, L171 (1982)

[11] G Ananthakrishna and D Sahoo, *J. Phys.* **D14**, 2081 (1981)

[12] G Ananthakrishna and D Sahoo, *J. Phys.* **D14**, 2091 (1981)

[13] G Ananthakrishna, *Scr. Metall. Mater.* **29**, 1183 (1993)
G Ananthakrishna, C Fressengeas, M Grosbars, J Vergnol, C Engelke, J Ples
H Neuhäuser, E Bouchaud, J Planés and L P Kubin, *Scr. Metall. Mater.* **32**, 1731 (1

[14] S Venkadesan, K P N Murthy and M C Valsakumar, in Non Linear Phenome
Materials Science III – Instabilities and Patterning, *Solid State Phenomena* edite
G Ananthakrishna, L P Kubin and G Martin (SCITEC Publications, 1995) vol. 4
p. 287
S Venkadesan, M C Valsakumar, K P N Murthy and S Rajasekar, *Phys. Rev.* **E54**
(1996)

[15] G Ananthakrishna and S J Noronha, in Nonlinear phenomena in Materials Sc
III – Instabilities and Patterning, *Solid State Phenomena* edited by G Ananthakri
L P Kubin and G Martin (SCITEC Publlications, 1995) vols 42–43, p. 277

[16] David A Russel, James D Hanson and Edward Ott, *Phys. Rev. Lett.* **45**, 1175 (1980)

[17] David E Sigeti, *Physica*, **D82**, 136 (1995)

[18] M C Valsakumar and G Ananthakrishna, *J. Phys.* **D16**, 1055 (1983)

[19] G Ananthakrishna and M C Valsakumar, *Phys. Lett.* **A95**, 69 (1983)

[20] G Ananthakrishna and T M John, *Directions in chaos* edited by Hao Bai-lin (V
Scientific, 1990) p. 133

[21] Alan Wolf, Jack B Swift, Harry L Swinney and John A Vastano, *Physica*, **D16**, 285 (

[22] D Sigeti and W Horsthemke, *Phys. Rev.* **A35**, 2276 (1987)

[23] G Ananthakrishna (1995) (personal communication)

[24] Larry S Liebovitch and Tibor Toth, *Phys. Lett.* **A141**, 386 (1989)

[25] G Paladin and A Vulpiani, *Phys. Rep.* **156**, 147 (1987)

[26] M C Valsakumar, S V M Satyanarayana and V Sridhar (1996) (unpublished)

[27] K P N Murthy, L K Galos, P Argyrakis and K W Kehr, *Phys. Rev.* **E54**, 1 (
K P N Murthy, S Rajasekar and K W Kehr, *J. Phys.* **A27**, L107 (1994)

Structural phase transition in substituted La_2CuO_4 and Pr_2CuO_{4-y}

MEENA CHAUDHRI, KUNAL B MODI*, K M JADHAV and G K BICHILE
Department of Physics, Dr. B.A.M. University, Aurangabad 431 004, India
*Department of Physics, Saurashtra University, Rajkot 360 005, India

MS received 30 April 1996; revised 23 October 1996

Abstract. The structural phase transition from orthorhombic (T) phase to tetragonal (T′) phase in substituted $La_{2-x}R_xCuO_4$ (R = Pr, Nd, Sm, Eu and Gd) and T′ to T-phase in $Pr_{2-x}M_xCuO_{4-y}$ (M = Sr, Ca) has been studied by X-ray diffraction technique. The T-phase of La_2CuO_4 is transferred to T′ phase abruptly at $x = 0{\cdot}8$, 0·4, 0·4, 0·3 and 0·4 respectively for substitution of Pr, Nd, Sm, Eu and Gd for La in La_2CuO_4 without evidence of the T* phase. The T′ structure of Pr_2CuO_4 ($x = 0{\cdot}0$) gets transformed to the T* structure at 30% Ca doping ($x = 0{\cdot}6$) and then to the T structure at 50% Ca doping ($x = 1{\cdot}0$), while for Sr-content $x = 0{\cdot}0$, 0·4 and 1·0 it shows T′, T* and T structure respectively.

Keywords. Superconductor; phase transition; X-ray diffraction.

PACS Nos 74·00; 61·10; 64·70

1. Introduction

Since the discovery of high T_c superconductivity [1] in the $La_{2-x}Ba_xCuO_4$ system which has a distorted K_2NiF_4 structure (or the so-called T phase), superconductivity has also been found in two other K_2NiF_4-related structures, T′ and T* phases [2, 3]. The T′ phase R_2CuO_4 (R = rare earth) is exhibited by most rare earths whereas the cuprate T phase is found only when R = La. One major difference between the T and T′ phases (figure 1) is the coordination of copper. Copper in the T phases has a 6-fold coordination with four of the oxygen atoms in the CuO_2 plane, and the remaining two oxygen atoms (called apical oxygen) above and below the Cu atoms. In contrast, copper in the T′ phase is in 4-fold coordination (i.e. no apical oxygen). Intermediate between the T and T′ phases is the T* phase. The T* phase has one apical oxygen atom associated with the CuO_5-square pyramids (figure 1).

The superconductors with T* or T structure are *p*-type (i.e. the carriers are holes) whereas the superconductors with the T′ structure are *n*-type (i.e. the carriers are electrons). Finally the T* phase, whole unit cell can be viewed as containing half of the unit cell of the *p*-type T phase and half of the unit cell of *n*-type T′ phase, appears as an attractive system in which one could expect, depending on the nature of the chemical doping, to achieve either *p* or *n*-type superconductivity.

To our knowledge, there have been very few studies on such type of systems [2–5]. We considered it interesting to investigate the nature of transition from T-phase to

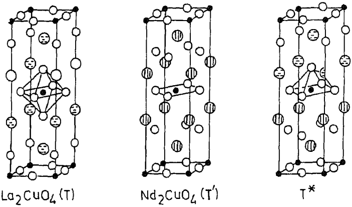

Figure 1. The T–La_2CuO_4, T′–R_2CuO_4 and T*–phases (LaR′)CuO_4, (closed circle (●): Cu; open circle (○): oxygen; large circle with hatches (⊖): rare earth ions).

T′-phase by examining their crystal structures. For the present investigations, solid solutions of $La_{2-x}R_xCuO_4$ (R = Pr, Nd, Sm, Eu and Gd) are prepared.

In view of the appearance of the three possible structural phases T, T′ and T* in the divalent substituted 2-1-4 type systems, we have initiated a study on the structural behaviour of pure and Sr and Ca doped $Pr_{2-x}M_xCuO_{4-y}$ system with different concentration (x).

2. Experimental details

All the samples were prepared using standard ceramic method [6]. The samples were characterized by X-ray diffraction using CuKα radiations at room temperature within the 2θ range of 20° to 50°. The observed X-ray peaks were indexed and analyzed using REFEDT least squares programme, to obtain the values of lattice parameters.

The parent compounds La_2CuO_4, Nd_2CuO_4, Sm_2CuO_4, Pr_2CuO_4, Eu_2CuO_4 and Gd_2CuO_4 and a series of compounds $La_{2-x}R_xCuO_4$ (R = Pr, Nd, Sm, Eu and Gd) were prepared under identical conditions using the stoichiometric quantities of fine powders of La_2O_3, Pr_6O_{11}, Nd_2O_3, Sm_2O_3, Eu_2O_3, Gd_2O_3 and CuO (all 99·99% pure, Aldrich make). The accurately weighed powders were thoroughly mixed in an agate mortar and pestle and heated at 900°C for 24 h in platinum crucibles. The reacted product was reground and re-heated at 950°C for 24 h to obtain homogeneous, single phase samples. The black product, thus obtained, was pulverized and cold pressed into pellets of uniform thickness by applying suitable pressure. The pellets were then sintered in air at 1000°C for 24 h. The samples were cooled to room temperature at the rate of 2°C/min, during all the heating stages.

Polycrystalline materials of $Pr_{2-x}M_xCuO_{4-y}$ (M = Sr, Ca) with x = 0·0, 0·2, 0·4, 0·6, 0·8 and 1·0 were synthesized by solid state reaction technique [6]. High purity (99·99% pure, Aldrich) dried powders of Pr_6O_{11}, $SrCO_3$, $CaCO_3$ and CuO were thoroughly

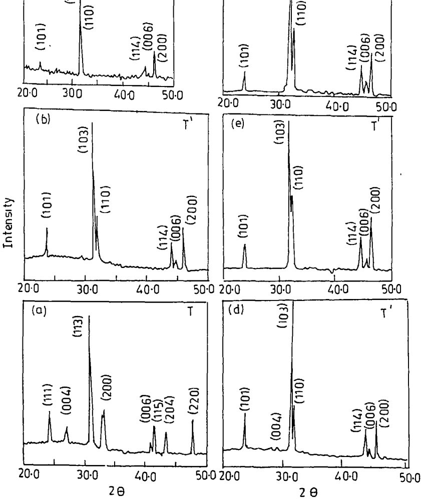

Figure 2. X-ray diffraction patterns of (**a**) La_2CuO_4 (**b**) Nd_2CuO_4 (**c**) Sm_2CuO_4 (**d**) Pr_2CuO_4 (**e**) Eu_2CuO_4 and (**f**) Gd_2CuO_4 systems.

3. Results and discussion

3.1 *The R_2CuO_4 compounds (R = La, Pr, Nd, Sm, Eu and Gd)*

The X-ray diffraction patterns of the parent compounds La_2CuO_4, Nd_2CuO_4, Sm_2CuO_4, Pr_2CuO_4, Eu_2CuO_4 and Gd_2CuO_4 are shown in figure 2. The absence of extra peaks confirms the phase purity of the samples prepared. The observed X-ray peaks were indexed and values of lattice parameters were calculated using REFEDT least squares programme. The lattice parameters and structure of the above compound are tabulated in table 1. The unit cell parameters agree very well with the reported values [8].

The T′-phase R_2CuO_4 (R = Pr, Nd, Sm, Eu and Gd) is exhibited by most rare earths were the cuprate T-phase is found only when R = La. The CuO_4 square in the T′-phase is considerably expanded and c axis shrunk, relative to the T-phase structure. This can also be seen from table 1 that there is relative shrunk in *c*-axis of T′-phase structure with respect to T-phase structure.

Sm, Eu and Gd) systems.

System	Lattice parameters		Structure
	a(Å)	c(Å)	
La_2CuO_4	3·797	13·174	T
Pr_2CuO_4	3·969	12·224	T′
Nd_2CuO_4	3·946	12·168	T′
Sm_2CuO_4	3·949	12·061	T′
Eu_2CuO_4	3·924	11·992	T′
Gd_2CuO_4	3·899	11·895	T′

3.2 *The* $La_{2-x}R_xCuO_4$ *(R = Pr, Nd, Sm, Eu and Gd)*

Any attempt to induce metallic behaviour in La_2CuO_4 through doping can be achieved only without degrading the critical structural stability. In other words, one cannot reduce the (La–O) bond-length and/or increase the (La–O) bond length upon doping. The substitution of La by any other trivalent rare earths which have smaller ionic radius than La will invariably lead to a reduction in the (R–O) bond-length and thus to an eventual collapse of the T-phase. In pure R_2CuO_4 if R is smaller than La (1·15 Å) then T-phase cannot be stabilized as in the case of other smaller rare earth based 2-1-4 systems with R = Pr(0·92 Å), Nd(1·08 Å), Sm(1·04 Å), Eu(1·12 Å) and Gd(1·02 Å). Since La_2CuO_4 is already at the critical point of structural instability due to the large tension experienced by the (La–O) bond, one may rotate these bonds by 45° with respect to the (Cu–O) bond to improve the match of (La–O) with (Cu–O) and achieve the atomic arrangement of the T′ phase. As a result of this rotation, the (R–O) bond in the T′-phase is under compression in contrast to the T-phase for La_2CuO_4. Smaller R's are then more favorable for the T′-R_2CuO_4, consistent with the experimental observations of T′-phase with R = Pr, Nd, Sm, Eu and Gd. For these smaller R's, the oxygen atoms tend to move toward the space between the R-layers due to the stronger attraction associated with R and due to the conservation of charge. Xue *et al* [5] suggested that within the experimental resolution, the (R–O) bond is either under compression and the (Cu–O) bond is either under tension (R = Nd and Pr) or slight compression (R = Eu and Gd) in these compounds.

Thus the substitution of other rare earths smaller than La, for La in La_2CuO_4 system having T-phase structure may lead to T′-phase structure. Thus attempt has been made to gain insight into structural phase transition in T-phase La_2CuO_4 by substituting Pr, Nd, Sm, Eu and Gd for La as a function of concentration (x) in system $La_{2-x}R_xCuO_4$ (R = Pr, Nd, Sm, Eu and Gd).

The X-ray diffraction patterns of $La_{2-x}Pr_xCuO_4$, $La_{2-x}Nd_xCuO_4$, $La_{2-x}Sm_xCuO_4$, $La_{2-x}Eu_xCuO_4$ and $La_{2-x}Gd_xCuO_4$ for different concentration (x) are shown in figures 3 and 4. The values of unit cell parameters, cell volume, c/a ratio and structure obtained from the XRD data for the systems $La_{2-x}Pr_xCuO_4$, $La_{2-x}Nd_xCuO_4$ and $La_{2-x}Sm_xCuO_4$ are presented in table 2 and those for systems $La_{2-x}Eu_xCuO_4$ and $La_{2-x}Gd_xCuO_4$ are tabulated in table 3.

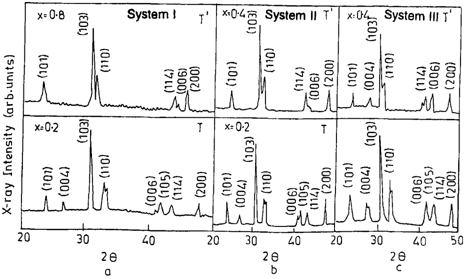

Figure 3. Typical X-ray diffraction patterns of $La_{2-x}Pr_xCuO_4$, $La_{2-x}Nd_xCuO_4$ and $La_{2-x}Sm_xCuO_4$ systems.

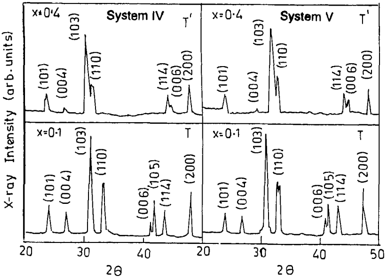

Figure 4. Typical X-ray diffraction patterns of $La_{2-x}Eu_xCuO_4$ and $La_{2-x}Gd_xCuO_4$ systems.

For the system $La_{2-x}Pr_xCuO_4$ the structure remains in the earlier orthorhombic T-phase until $x = 0{\cdot}6$. For $x > 0{\cdot}6$, the phase transition from T to T′-phase occurs..For the systems $La_{2-x}Nd_xCuO_4$ and $La_{2-x}Sm_xCuO_4$ the structural phase transition occurs at $x = 0{\cdot}4$, while for the systems $La_{2-x}Eu_xCuO_4$ and $La_{2-x}Gd_xCuO_4$ at $x = 0{\cdot}3$ and $x = 0{\cdot}4$ it shows structural phase transition from orthorhombic T to tetragonal T′-phase.

For all the five systems $La_{2-x}Pr_xCuO_4$, $La_{2-x}Nd_xCuO_4$, $La_{2-x}Sm_xCuO_4$, $La_{2-x}Eu_xCuO_4$ and $La_{2-x}Gd_xCuO_4$ the structural phase transition is accompanied by notable change in cell volume and *c*/*a* ratio (tables 2 and 3). This volume change is opposite to the expected view based on the basis of the smaller size of the substituent

CuO$_4$, La$_{2-x}$Nd$_x$CuO$_4$ and La$_{2-x}$Sm$_x$CuO$_4$ systems.

Sample x	Lattice parameters a(Å) = b(Å)	c(Å)	Volume V(Å)^3	c/a	Struct
La$_{2-x}$Pr$_x$CuO$_4$					
0·0	3·797	13·174	189·93	3·469	T
0·2	3·785	13·131	188·32	3·469	T
0·4	3·778	13·137	187·51	3·477	T
0·6	3·735	13·167	183·68	3·525	T
0·8	3·991	12·257	195·23	3·071	T′
1·0	3·969	12·268	193·25	3·090	T′
La$_{2-x}$Nd$_x$CuO$_4$					
0·2	3·788	13·162	188·91	3·474	T
0·4	3·998	12·311	196·78	3·079	T′
0·6	3·991	12·332	196·42	3·090	T′
0·8	3·980	12·330	195·31	3·097	T′
1·0	3·976	12·348	195·20	3·105	T′
La$_{2-x}$Sm$_x$CuO$_4$					
0·2	3·792	13·119	188·65	3·459	T
0·4	3·983	12·397	196·07	3·112	T′
0·6	3·966	12·336	194·03	3·110	T′
0·8	3·965	12·333	193·89	3·110	T′
1·0	3·961	12·296	192·92	3·104	T′

Table 3. Lattice parameters, cell volume, c/a ratio and structure of La$_{2-x}$Eu$_x$C
and La$_{2-x}$Gd$_x$CuO$_4$ systems.

Sample x	Lattice parameters a(Å) = b(Å)	c(Å)	Volume V(Å)^3	c/a	Struct
La$_{2-x}$Eu$_x$CuO$_4$					
0·1	3·801	13·165	190·30	3·463	T
0·2	3·797	13·147	189·55	3·462	T
0·3	3·797	13·113	188·63	3·457	T′
0·4	3·905	12·415	189·32	3·179	T′
0·5	3·895	12·419	188·41	3·188	T′
La$_{2-x}$Gd$_x$CuO$_4$					
0·1	3·799	13·174	190·13	3·467	T
0·2	3·799	13·159	189·91	3·464	T
0·3	3·799	13·142	189·68	3·459	T
0·4	3·912	12·183	186·44	3·114	T′
0·5	3·904	12·345	188·15	3·162	T′

in the T′ structure than in the T structure, packing would be less efficient in the for
thereby causing increase in cell volume at composition when the structural p
transition occurs.

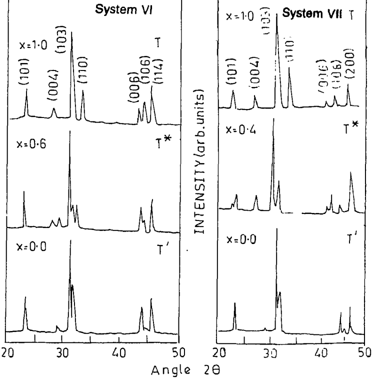

Figure 5. Typical X-ray diffraction patterns of $Pr_{2-x}Sr_xCuO_{4-y}$ and $Pr_{2-x}Ca_xCuO_{4-y}$ systems.

Table 4. Lattice parameters, $c/3a$ ratio and structure of $Pr_{2-x}Sr_xCuO_{4-y}$ and $Pr_{2-x}Ca_xCuO_{4-y}$ systems

Sample x	Lattice parameters a(Å)	 c(Å)	$c/3a$	Structure
$Pr_{2-x}Sr_xCuO_{4-y}$				
0·0	3·959	12·224	1·029	T′
0·2	3·956	12·336	1·042	T′
0·4	3·867	12·535	1·080	T*
0·6	3·877	12·506	1·077	T*
0·8	3·866	12·562	1·083	T*
1·0	3·796	12·974	1·139	T
$Pr_{2-x}Ca_xCuO_{4-y}$				
0·0	3·958	12·224	1·029	T′
0·2	3·961	12·227	1·028	T′
0·4	3·969	12·229	1·027	T′
0·6	3·868	12·367	1·065	T*
0·8	3·835	12·217	1·061	T*
1·0	3·752	12·859	1·142	T

Typical XRD patterns of $Pr_{2-x}Sr_xCuO_{4-y}$, with $x = 0·0$, 0·4 and 1·0 are shown in figure 5. The observed X-ray diffraction peaks were modelled by modified Gaussian functions and refined unit cell parameters were calculated using standard least squares programme. The measured values of lattice parameters including the $c/3a$ ratios are listed in table 4. The $c/3a$ ratios were useful to distinguish related T, T′ and T* phases [8]. Typical values of $c/3a$ ratio are 1·028, 1·085 1·151 for T′ (Nd_2CuO_4), [7] T* ($La_{0.84}Sm_{0.96}Sr_{0.2}CuO_{4-y}$) and T($La_2CuO_4$) ph respectively (since La_2CuO_4 forms in an orthorhombically distorted T struc at room temperature, a quasi tetragonal a(Å) parameter is used to calculate ratio) [9]. The presence of a structural phase was also confirmed by compa the observed X-ray patterns with standard patterns reported in the literature [The observed $c/3a$ ratios for $x = 0{\cdot}0$, 0·4 and 1·0 are consistent with the T′, T* T structures respectively. Also, one can clearly notice these structures from observed X-ray peaks.

Typical X-ray diffractograms of $Pr_{2-x}Ca_xCuO_{4-y}$ with $x = 0{\cdot}6$ and 1·0 shown in figure 5. Table 4 gives the details of the lattice parameters, $c/3a$ and structures. As evident from table 4, the T′ structure of Pr_2CuO_4 gets tr formed to the T * structure at 30% Ca doping ($x = 0{\cdot}6$) and then to the T struc at 50% Ca doping ($x = 1{\cdot}0$).

From table 4 it can be seen that the substitution of Sr for Pr increases the parameters and decreases a(Å) parameters by 0·75 Å and 0·163 Å. Similarly fo substitution also increases the c(Å) parameters by 0·635 Å and decrease a(Å) ameters by 0·206 Å for the range studied. Increase in c(Å) parameters for both Sr an suggest that substituted Sr or Ca for Pr are located along the c-axis.

Thus the X-ray diffraction study on present systems suggest that

(i) the T-phase La_2CuO_4 is transferred to T′-phase by substitution of L R(R = rare earth) having smaller ionic radius than La and is accompanie change in lattice parameters.

(ii) for the systems $Pr_{2-x}Sr_xCuO_{4-y}$ and $Pr_{2-x}Ca_xCuO_{4-y}$ the divalent (Sr an substitution for Pr lead to an evolutionary structural phase transformatio T′ → T* → T.

References

[1] J G Bendnorz and K A Muller, *Z. Phys.* **B64**, 189 (1986)

[2] Y Tokura, H Takagi and S Uchida, *Nature* (*London*), **337**, 345–347 (1989)

[3] E Takayama Muromachi, Y Matsui, Y Uchida, F Izumi, M Oneda and K Kato, *J Appl. Phys.* **27**, L2283 (1988)

[4] K K Singh, P Ganguly and C N R Rao, *Mater. Res. Bull.* **17**, 493 (1982)

[5] Y Y Xue, P H Hor, R L Meng, Y K Tao, Y Y Sun, Z J Hunang, L Gao and C W *Physica* **C165**, 357 (1990)

[6] G K Bichile, Smita Deshmukh, D G Kuberkar and R G Kulkarni, *Physica* 154 (1991)

[7] N Nguyen, J Choisnet and B Raveau, *Mater. Res. Bull.* **17**, 567 (1982)

[8] R Saez Puche, N Norton and W S Glaunsinger, *Mater. Res. Bull.* **17**, 1523 (1982)

[9] K Takahashi, B Okai, M Kosuga and M Ohta, *Jpn. J. Appl. Phys.* **27**, LI374 (1988)

[10] H Y Hwang, S W Cheong, A S Cooper, L W Rupp, G H Kwei, Z Tan and B Ba *Physica* **C192**, 362 (1992)

A stochastic model for solidification II. Application to binary metallic melts

SHOBHA DASS, GAUTAM JOHRI* and LAKSHMAN PANDEY*
Govt. M. H. College of Science and Home Science, Jabalpur 482 002, India
*Department of Post Graduate Studies and Research in Physics, Rani Durgavati University, Jabalpur 482 001, India

MS received 8 November 1995

Abstract. A stochastic model to study the solidification process developed in part I is applied to various binary alloys having different values of interaction energies. The results obtained for the time evolution of temperature and concentration, rate of growth and shape of the solid–liquid interface are presented.

Keywords. Stochastic; solidification; binary melt.

PACS No. 81·10

1. Introduction

The properties of materials are governed to a large extent by their microstructure which in turn is greatly influenced by the solidification process and the kinetics at the solid–liquid interface. A correlation between solidification parameters and the resulting microstructure must be known to produce materials having desired and reproducible properties.

So far the theoretical approach to solidification phenomenon has been confined mostly to the construction of equilibrium phase diagrams [1–3]. Whereas during solidification the system is far from thermodynamic equilibrium. Nonequilibrium thermodynamics was used by Caroli *et al* [4] to study solidification. The concept of kinetic phase diagrams using a stochastic approach was developed by Chvoj [5–8] to describe processes where equilibrium phase diagrams cannot be used. However Chvoj's model does not include interdependence of temperature and concentration. Also it has not been solved for a binary system in three-dimensions (2-space, 1-time). A three-dimensional (2-space, 1-time) model describing the solidification of binary melts is given in the preceding paper alongwith the analysis and numerical scheme to solve the resulting coupled equations. In this paper the results obtained for six representative systems having different values of interaction energies are given.

2. The model

A solid can be grown from the melt if the melt is below its equilibrium melting temperature. Departure from the equilibrium is always required for the solidification

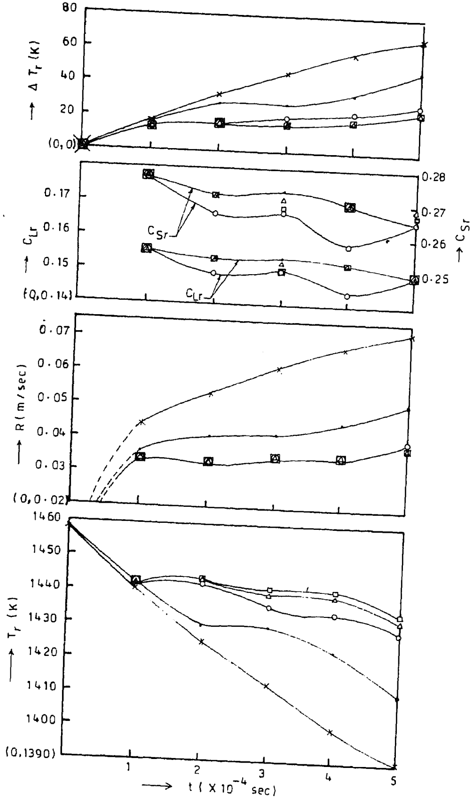

Figure 1. Variation of T_r, R, $C_{\mathrm{L}r}$, $C_{\mathrm{S}r}$ and ΔT_r with time at (1) $y = 0$ (∗–∗–∗), (2) $y = g$ (●–●–●), (3) $y = 4g$ (○–○–○), (4) $y = 7g$ (△-△-△), (5) $y = 10g$ (□-□-□) for a system with $C_{\mathrm{L}0} = 0{\cdot}2$, $T_1 = 1458\,\mathrm{K}$, $\Omega_{\mathrm{L}} = 2{\cdot}8 \times 10^{-20}\,\mathrm{J/atom}$, $\Omega_{\mathrm{S}} = 2{\cdot}33 \times 10^{-20}\,\mathrm{J/atom}$.

process to proceed. The equations describing th

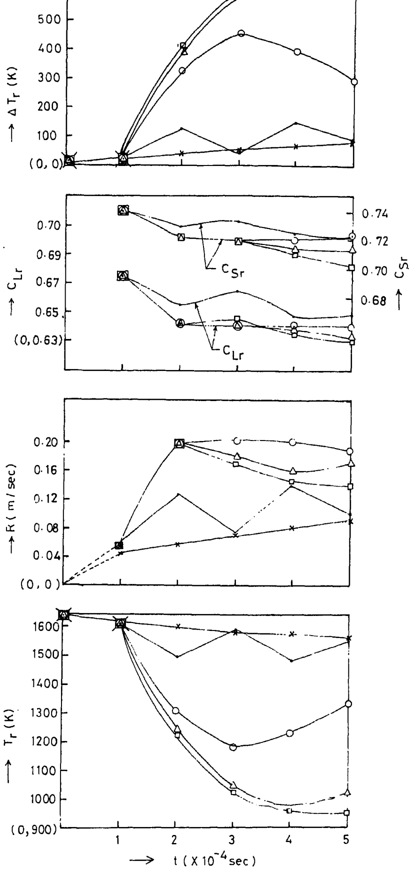

Figure 2. Variation of T_r R, C_{Lr}, C_{Sr} and ΔT_r with time at (1) $y = 0$ (∗–∗–∗), (2) $y = g$ (●–●–●), (3) $y = 4g$ (○–○–○), (4) $y = 7g$ (△-△-△), (5) $y = 10g$ (□-□-□) for a system with $C_{L0} = 0{\cdot}7$, $T_1 = 1643\,\text{K}$, $\Omega_L = 2{\cdot}8 \times 10^{-20}$ J/atom, $\Omega_S = 2{\cdot}33 \times 10^{-20}$ J/atom.

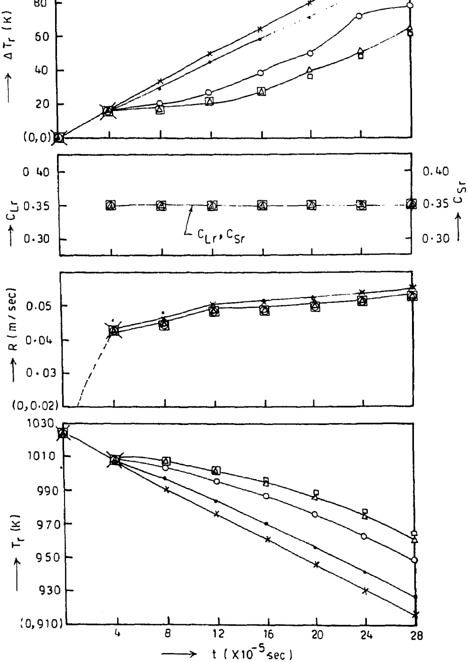

Figure 3. Variation of T_r, R, C_{Lr}, C_{Sr} and ΔT_r with time at (1) $y = 0$ (∗–∗–∗), (2) $y = g$ (•–•–•), (3) $y = 4g$ (o–o–o), (4) $y = 7g$ (△-△-△), (5) $y = 10g$ (□-□-□) for a system with $C_{L0} = 0{\cdot}35$, $T_1 = 1025\,\mathrm{K}$, $\Omega_L = 2{\cdot}8 \times 10^{-21}$ J/atom, $\Omega_S = 2{\cdot}8\times 10^{-20}$ J/atom.

effect of external fields can be written as [9, 10]

$$\frac{\partial T}{\partial t}(x, y, t) = D_{TC}\nabla^2 C_L(x, y, t) + D_T\nabla^2 T(x, y, t) + \mathbf{R}\cdot\nabla T(x, y, t) + \mathrm{div}F_T + \mathrm{div}E_T + \frac{\wedge\mathbf{R}}{C_v\rho}\delta(\mathbf{x} - \mathbf{X}_r(y; t)) \tag{1}$$

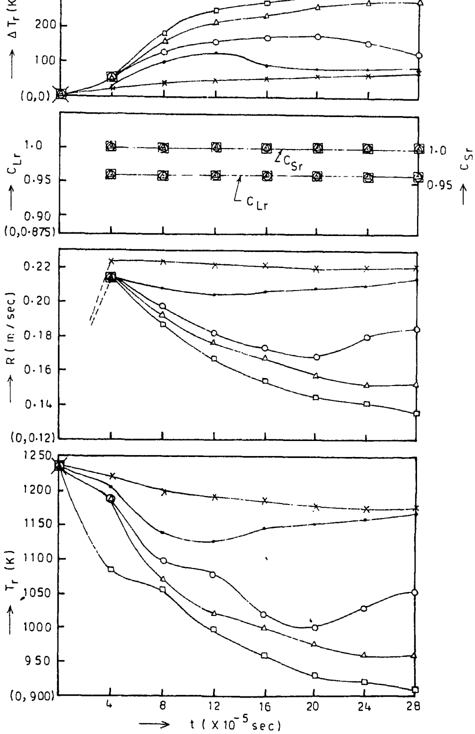

Figure 4. Variation of T_r, R, C_{Lr}, C_{Sr} and ΔT_r with time at (1) $y = 0$ (∗–∗–∗), (2) $y = g$ (●–●–●), (3) $y = 4g$ (○–○–○), (4) $y = 7g$ (△-△-△), (5) $y = 10g$ (□-□-□) for a system with $C_{L0} = 0{\cdot}98$, $T_1 = 1240\,\mathrm{K}$, $\Omega_L = 2{\cdot}8 \times 10^{-21}$ J/atom, $\Omega_s = 2{\cdot}8\times 10^{-20}$ J/atom.

and

$$\begin{aligned}\frac{\partial C_L}{\partial t}(x,y,t) =& D_C\nabla^2 C_L(x,y,t) + D_{CT}\nabla^2 T(x,y,t) + \mathbf{R}\cdot\nabla C_L(x,y,t)\\ &+ \mathrm{div}F_C + \mathrm{div}E_C + (C_{Sr} - C_{Lr})\mathbf{R}\delta(\mathbf{x} - \mathbf{X}_r(y,t)),\end{aligned} \tag{2}$$

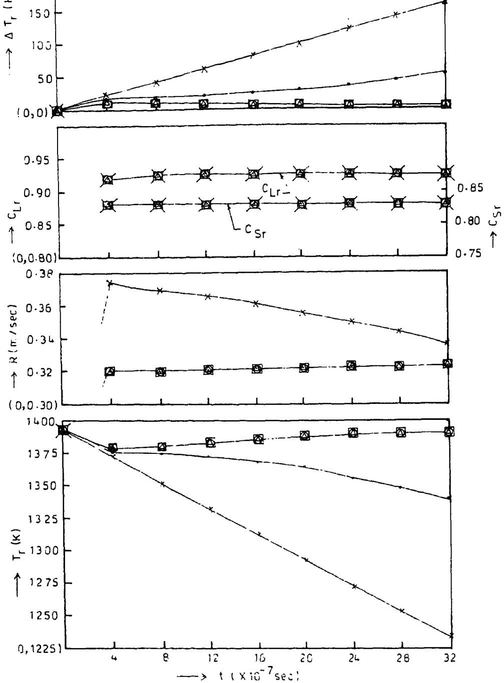

Figure 5. Variation of T_r. R, C_{Lr}, C_{Sr} and ΔT_r with time at (1) $y = 0$ (∗–∗–∗), (2) $y = g$ (•–•–•), (3) $y = 4g$ (o–o–o), (4) $y = 7g$ (△-△-△), (5) $y = 10g$ (□-□-□) for a system with $C_{L0} = 0{\cdot}9$, $T_1 = 1393\,\mathrm{K}$, $\Omega_L = 2{\cdot}8 \times 10^{-19}\,\mathrm{J/atom}$, $\Omega_S = 2{\cdot}8 \times 10^{-20}\,\mathrm{J/atom}$.

where C_L is the relative concentration of B atoms in A–B system, T is the temperature of the melt, D_T is the diffusivity, C_v is the volume specific heat and ρ is the density of the solid volume. D_C is the diffusion coefficient, D_{CT} and D_{TC} are related to the Onsager's coefficients due to interdependence of mass and heat flow, **R** is the rate of growth of the solid phase, x is the direction of growth and y is the coordinate perpendicular to it, t is the time coordinate, E_T and E_C are the heat and mass flux controlled by external fields,

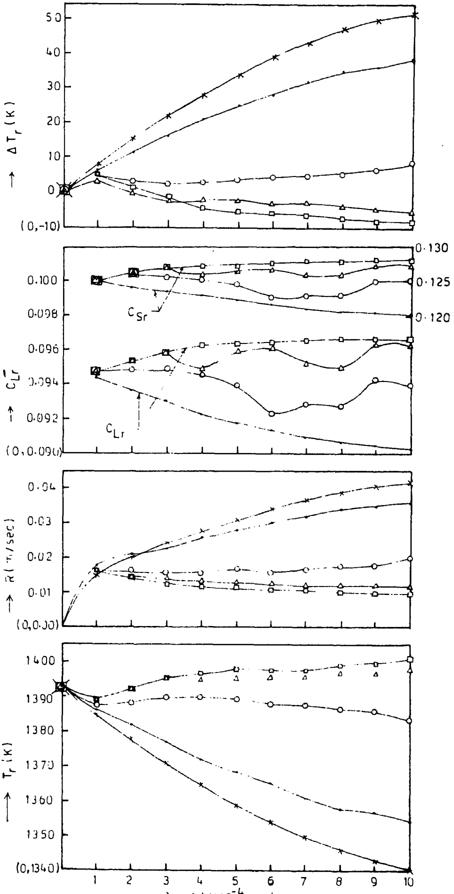
→ ΔT_r (K)
50
40
30
20
10
0
(0,-10)
0·130
0·125
0·120
→ C_Sr
C_Sr
→ C_Lr
0.100
0.098
0.096
0.094
0.092
(0,0.090)
C_Lr
→ R (m/sec)
0·04
0·03
0·02
0·01
(0,0.00)
→ T_r (K)
1400
1390
1380
1370
1360
1350
(0,1340)
1
2
3
4
5
6
7
8
9
10

respectively, F_T and F_C are the stochastic terms that represent the flux of heat and m due to fluctuations, $C_{\mathrm{S}r}$ and $C_{\mathrm{L}r}$ are the solid and liquid concentrations at the interf $\mathbf{X}_r(t)$, respectively, $\wedge$ is the latent heat per unit volume.

For evaluation of the fluctuation terms F_T and F_C, the Langevin method of stocha differential equations has been used [7, 9, 11]. According to this method the averag the random fluctuations can be written as

$$\langle \operatorname{div} F_T \rangle = \langle \operatorname{div} F_C \rangle = 0$$

which is the characteristic of a Markov process. The position of the solid–liquid interf

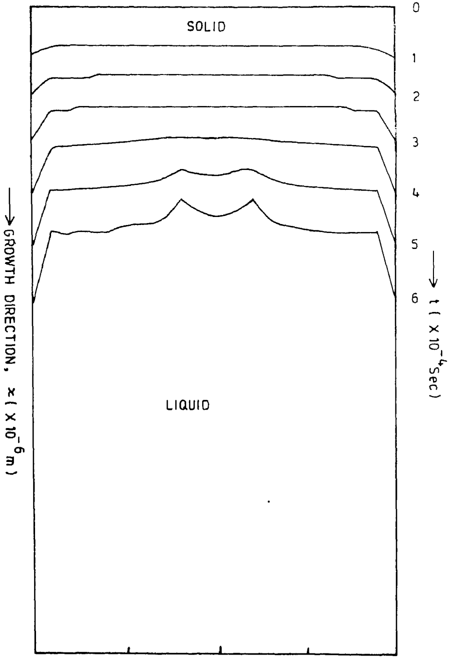

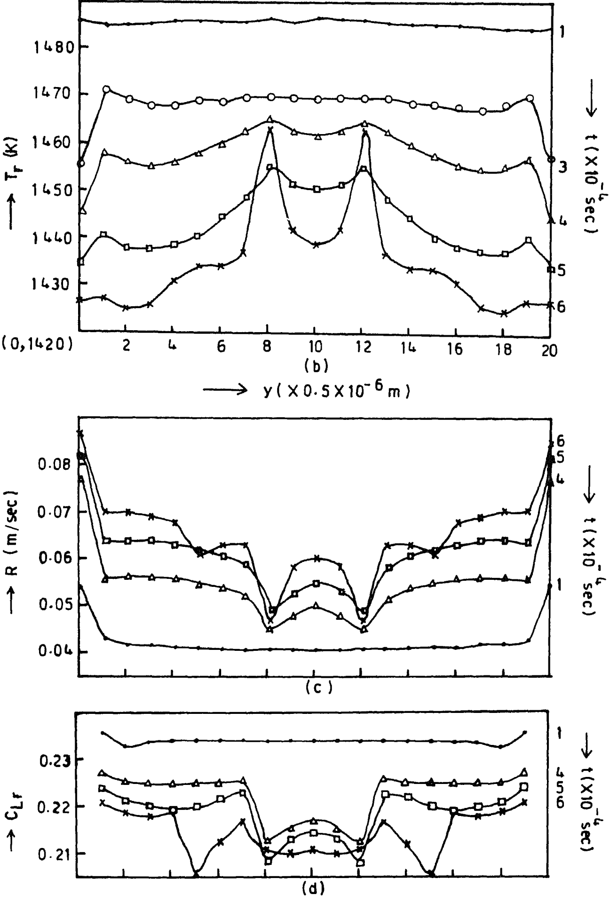

1480
1470
1460
1450
1440
1430
→ T_r (K)
1
3
4
5
6
↓ t (×10⁻⁴ sec)
(0,1420)
2
4
6
8
10
12
14
16
18
20
(b)
→ y (× 0.5 × 10⁻⁶ m)
0.08
0.07
0.06
0.05
0.04
→ R (m/sec)
6
5
4
1
↓ t (×10⁻⁴ sec)
(c)
0.23
0.22
0.21
→ C_{Lr}
1
4
5
6
↓ t (×10⁻⁴ sec)
(d)

Figures 7(b–d).

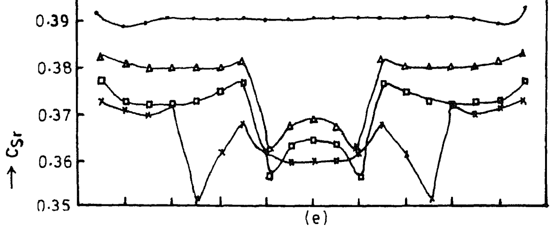

Figures 7(b–e). Time evolution of the interface: (**b**) temperature, (**c**)
growth, (**d**) concentration of the liquid phase, (**e**) concentration of the solid pha
system with $C_{\mathrm{L0}} = 0{\cdot}3$, $T_1 = 1503\,\mathrm{K}$, $\Omega_{\mathrm{L}} = 2{\cdot}8 \times 10^{-20}\,\mathrm{J/atom}$, $\Omega_{\mathrm{S}} =$
$10^{-20}\,\mathrm{J/atom}$.

is given by

$$\mathbf{X}_r(t) = \mathbf{n}_r \int_{t_0}^{t} R(t')\mathrm{d}t' + \mathbf{X}_r(t_0),$$

where $\mathbf{n}_r$ is normal to the interface and $\mathbf{X}_r(t_0)$ is its initial position.

The kinetic processes at the solid–liquid interface have been modeled u
microscopic description of the process of solidification i.e., by assigning probabil
individual atoms as they make transition from a liquid-like configuration to a so
configuration and then averaging over the corresponding phases to determine t
bability of formation of the new phase. The probability of creation of new mon
layer of the solid phase with concentration $C'_{\mathrm{S}r}$ per unit time can be written as [

$$P_0(C_{\mathrm{S}r}, C'_{\mathrm{S}r}, t) = P^{\mathrm{B}}_{\rho\Delta\times C_{\mathrm{S}r}} P^{\mathrm{A}}_{\rho\Delta\times(1-C_{\mathrm{S}r})},$$

where

$$\begin{aligned}
P^{\mathrm{A,B}}_{m_{\mathrm{A,B}}} &= \begin{pmatrix} N^{\mathrm{S}}_{\mathrm{A,B}} \\ m_{\mathrm{A,B}} \end{pmatrix} \left(P^{\mathrm{A,B}}_{\mathrm{B}}\right)^{(m_{\mathrm{A,B}})} \left(1 - P^{\mathrm{A,B}}_{\mathrm{B}}\right)^{(N^{\mathrm{S}}_{\mathrm{A,B}} - m_{\mathrm{A,B}})}, \\
N^{\mathrm{S}}_{\mathrm{A}} &= \nu^{\mathrm{L}}_{\mathrm{A}}(1 - C_{\mathrm{L}r})\rho^{\mathrm{L}}, \\
N^{\mathrm{S}}_{\mathrm{B}} &= \nu^{\mathrm{L}}_{\mathrm{B}} C_{\mathrm{L}r}\rho^{\mathrm{L}}, \\
m_{\mathrm{A}} &= \overline{(1 - C_{\mathrm{S}r})\rho^{\mathrm{S}}(y)\Delta x} = N^{\mathrm{S}}_{\mathrm{A}} P^{\mathrm{A}}_3, \\
m_{\mathrm{B}} &= \overline{C_{\mathrm{S}r}\rho^{\mathrm{S}}(y)\Delta x} = N^{\mathrm{S}}_{\mathrm{B}} P^{\mathrm{B}}_3, \\
P^{\mathrm{A}}_3 &= P^{\mathrm{A}}_1 F_{\mathrm{A}}(T_r(x,y,t), C_{\mathrm{L}r}(x,y,t), C_{\mathrm{S}r}(x,y,t)), \\
P^{\mathrm{B}}_3 &= P^{\mathrm{B}}_1 F_{\mathrm{B}}(T_r(x,y,t), C_{\mathrm{L}r}(x,y,t), C_{\mathrm{S}r}(x,y,t)), \\
P^{\mathrm{A}}_1 &= \exp(-U_{\mathrm{A}}/K_{\mathrm{B}}T_r),
\end{aligned}$$

$$F_{\mathrm{A}} = \left[1 - \exp\left(-\frac{\Delta\mu_{\mathrm{A}}}{K_{\mathrm{B}}T_r}\right)\right],$$

$$F_{\mathrm{B}} = \left[1 - \exp\left(-\frac{\Delta\mu_{\mathrm{B}}}{K_{\mathrm{B}}T_r}\right)\right].$$

$\Delta\mu_{\mathrm{A,B}}$ is the change in chemical potential per A,B atom transfer from the solid to the liquid phase, K_{B} is the Boltzmann constant, T_r is the interface temperature, $P_3^{\mathrm{A,B}}$ is the probability of one A,B atom joining the solid phase per unit time, $P_1^{\mathrm{A,B}}$ is the probability of one A,B atom transition from liquid to solid phase, $U_{\mathrm{A,B}}$ is the activation

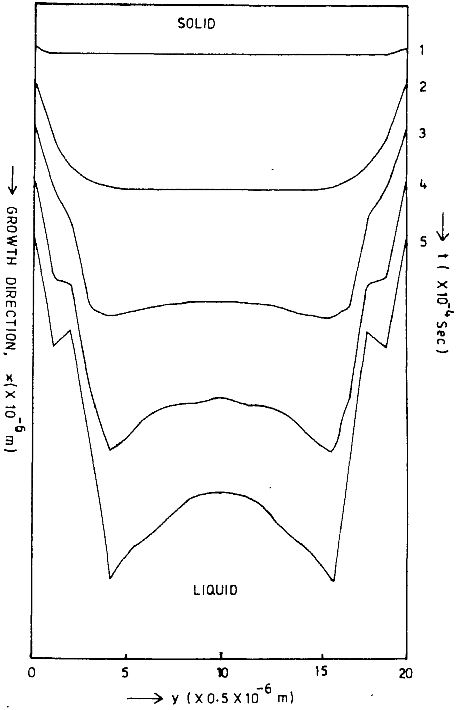

Figure 8(a). Time evolution of the solid–liquid interface for a system with energy of transition of one A,B atom from liquid to solid phase across the inter $\rho^{L,S}$ is the total number of atoms per unit volume in a monoatomic layer at interface in the liquid, solid phase, Δx is the thickness of the solid grown, m_A anc are respectively the number of A and B component that cross the interface from li to solid phase per unit area in the time interval Δt, $N^S_{A,B}$ is the number of pos transitions of one A,B atom from the liquid to the solid phase across the interface unit time and $\nu^L_{A,B}$ is the frequency of thermal vibrations of the atoms of A,B compo in the liquid phase.

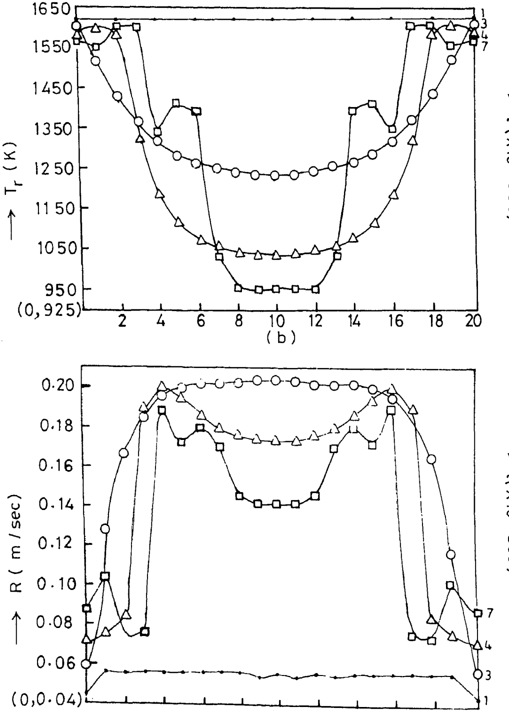

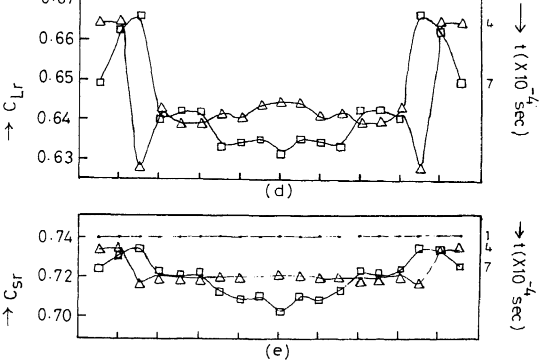

Figures 8(b–e). Time evolution of the interface: (**b**) temperature, (**c**) rate of growth, (**d**) concentration of the liquid phase, (**e**) concentration of the solid phase for a system with $C_{\mathrm{L}0} = 0{\cdot}7$, $T_1 = 1643\,\mathrm{K}$, $\Omega_{\mathrm{L}} = 2{\cdot}8 \times 10^{-20}\,\mathrm{J/atom}$, $\Omega_{\mathrm{S}} = 2{\cdot}33 \times 10^{-20}\,\mathrm{J/atom}$.

The average concentration and rate of growth of the solid phase have been evaluated by using the probability of formation of a new monoatomic layer and are given by [9]

$$\overline{C}_{\mathrm{S}r}(x,y,t) = \frac{C_{\mathrm{L}r}F_{\mathrm{B}}(T_r, C_{\mathrm{L}r}, C_{\mathrm{S}r})}{C_{\mathrm{L}r}F_{\mathrm{B}}(T_r, C_{\mathrm{L}r}, C_{\mathrm{S}r}) + (1 - C_{\mathrm{L}r})F_{\mathrm{A}}(T_r, C_{\mathrm{L}r}, C_{\mathrm{S}r})} \tag{5}$$

and

$$\overline{R}(x,y,t) = a_0 \nu P_1^{\mathrm{B}}[C_{\mathrm{L}r}F_{\mathrm{B}}(T_r, C_{\mathrm{L}r}, C_{\mathrm{S}r}) + (1 - C_{\mathrm{L}r})F_{\mathrm{A}}(T_r, C_{\mathrm{L}r}, C_{\mathrm{S}r})], \tag{6}$$

where a_0 is the lattice constant of the solid. The change in chemical potential per A,B atom transfer from solid to liquid phase, $\Delta\mu_{\mathrm{A,B}}$, for the non ideal solutions taking into account the interaction effects of the constituents of the binary alloy are given by [9]

$$\Delta\mu_{\mathrm{A}} = \frac{\Delta H_{\mathrm{A}}(T_{\mathrm{A}} - T_r)}{T_{\mathrm{A}}} + K_{\mathrm{B}}T_r \ln\frac{(1 - C_{\mathrm{L}r})}{(1 - C_{\mathrm{S}r})} + \Omega_{\mathrm{L}}(C_{\mathrm{L}r})^2 - \Omega_{\mathrm{S}}(C_{\mathrm{S}r})^2 \tag{7}$$

and

$$\Delta\mu_{\mathrm{B}} = \frac{\Delta H_{\mathrm{B}}(T_{\mathrm{B}} - T_r)}{T_{\mathrm{B}}} + K_{\mathrm{B}}T_r \ln\frac{C_{\mathrm{L}r}}{C_{\mathrm{S}r}} + \Omega_{\mathrm{L}}(1 - C_{\mathrm{L}r})^2 - \Omega_{\mathrm{S}}(1 - C_{\mathrm{S}r})^2, \tag{8}$$

where $\Delta H_{\mathrm{A,B}}$ is the enthalpy of fusion of A,B component at its melting temperature $T_{\mathrm{A,B}}$ [2].

evolution of temperature, concentration of the liquid phase, interface shape, concentration of the solid phase and rate of growth respectively.

Finite difference method alongwith successive over-relaxation method has been used to solve these equations. The boundary conditions chosen correspond to crystal pulling technique of crystal growth. The details of the numerical scheme alongwith the boundary conditions are given in ref. [9, 10]. Calculations were performed to obtain time evolution of temperature, concentrations of the liquid and solid phase, rate of growth of the solid phase and evolution of the solid–liquid interface shape. The representative systems

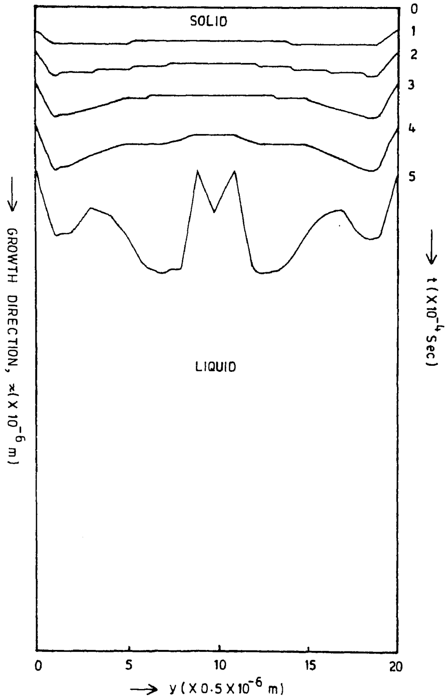

Figure 9a. Time evolution of the solid–liquid interface for a system with $C_{L0} = 0{\cdot}9$, $T_1 = 1703\,\mathrm{K}$, $\Omega_L = 2{\cdot}8 \times 10^{-20}$ J/atom, $\Omega_S = 2{\cdot}33 \times 10^{-20}$ J/atom

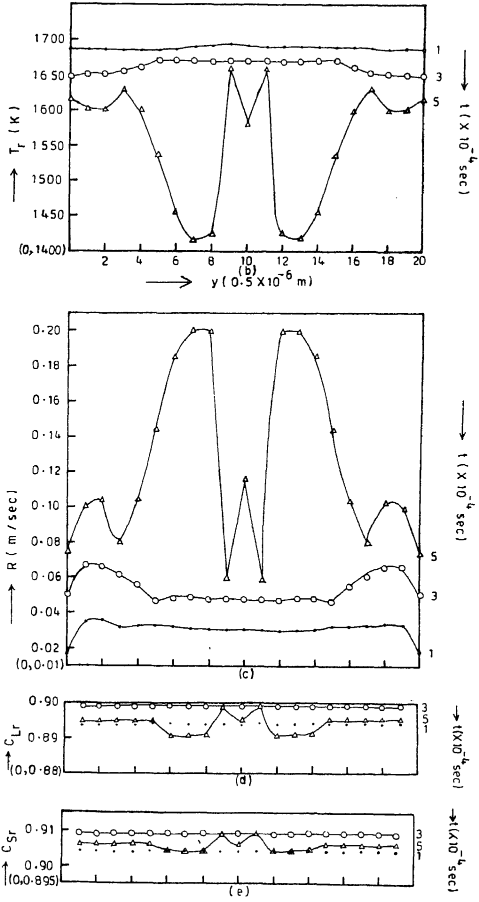
1700
16 50
1600
1 550
1500
1 450
(0,1400)
→ T_r (K)
2
4
6
8
10
12
14
16
18
20
(b)
→ y (0·5 X 10^{-6} m)
1
3
5
← t (X 10^{-4} sec)
0·20
0·18
0·16
0·14
0·12
0·10
0·08
0·06
0·04
0·02
(0,0·01)
→ R (m / sec)
5
3
1
← t (X 10^{-4} sec)
(c)
0·90
0·89
(0,0·88)
→ C_{Lr}
3
5
1
← t(X 10^{-4} sec)
(d)
0·91
0·90
(0,0·895)
→ C_{Sr}
3
5
1
← t(X 10^{-4} sec)
(e)

System I	$\Omega_L = 2{\cdot}8 \times 10^{-20}$ J/atom	$\Omega_S = 2{\cdot}33 \times 10^{-20}$ J/atom
System II	$\Omega_L = 2{\cdot}8 \times 10^{-21}$ J/atom	$\Omega_S = 2{\cdot}8 \times 10^{-20}$ J/atom
System III	$\Omega_L = 2{\cdot}8 \times 10^{-19}$ J/atom	$\Omega_S = 2{\cdot}8 \times 10^{-20}$ J/atom
System IV	$\Omega_L = -2{\cdot}33 \times 10^{-20}$ J/atom	$\Omega_S = -2{\cdot}47 \times 10^{-20}$ J/atom
System V	$\Omega_L = -2{\cdot}8 \times 10^{-20}$ J/atom	$\Omega_S = -2{\cdot}8 \times 10^{-19}$ J/atom
System VI	$\Omega_L = -2{\cdot}8 \times 10^{-20}$ J/atom	$\Omega_S = -2{\cdot}8 \times 10^{-21}$ J/atom

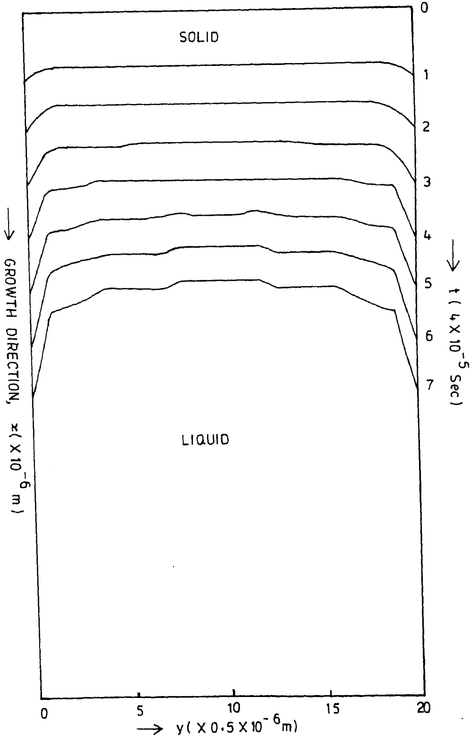

Figure 10a. Time evolution of the solid–liquid interface for a system with $C_{L0} = 0{\cdot}9$, $T_1 = 1200$ K, $\Omega_L = 2{\cdot}8 \times 10^{-21}$ J/atom, $\Omega_S = 2{\cdot}8 \times 10^{-20}$ J/atom.

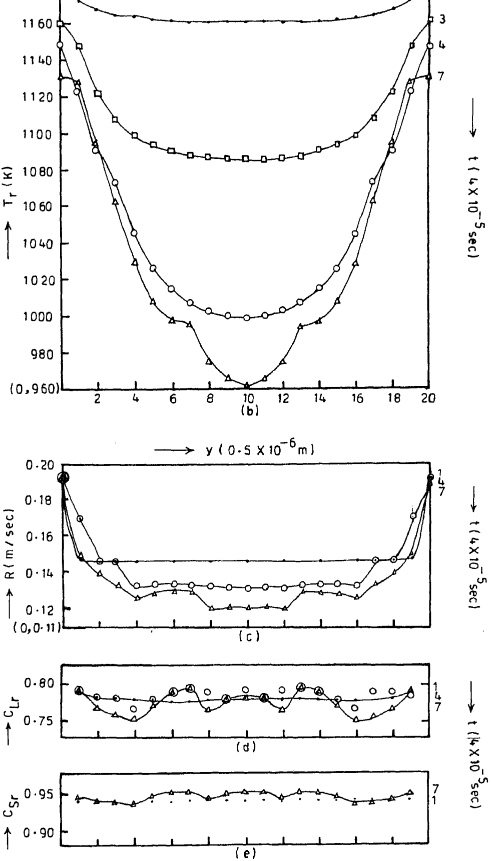

Figures 10(b–e). Time evolution of the interface: (**b**) temperature, (**c**) rate of growth, (**d**) concentration of the liquid phase, (**e**) concentration of the solid phase for a system with $C_{L0} = 0{\cdot}9$, $T_1 = 1200\,\mathrm{K}$, $\Omega_L = 2{\cdot}8 \times 10^{-21}$ J/atom, $\Omega_S = 2{\cdot}8 \times 10^{-20}$ J/atom.

3.1 *Time evolution of interface temperature T_r, concentrations C_{Lr} and C_{Sr}, r* *growth R and undercooling ΔT_r at various points along the interface*

The time evolution of interface temperature T_r, concentrations C_{Lr} and C_{Sr}, ra growth R and undercooling $\Delta T_r(T_l - T_r)$ for all the six systems mentioned abo shown in figures 1–6. These figures show the time dependence at edge (point '0 point next to the wall of the container), the centre of the specimen ($10g$) and at three points ($g, 4g, 7g$) between edge and the centre, along the interface (viz. the y direc

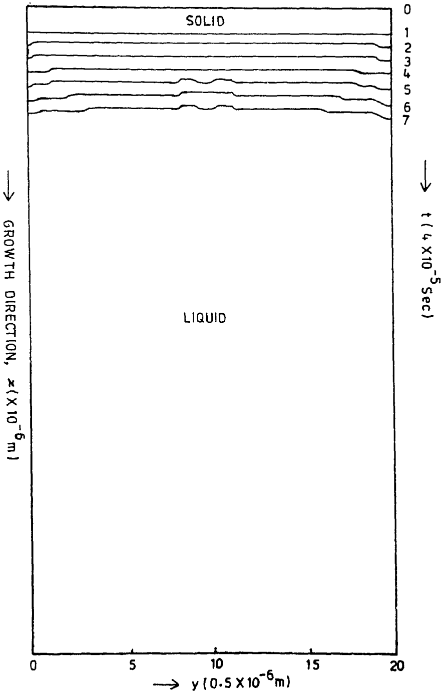

Figure 11(a). Time evolution of the solid–liquid interface for a syste $C_{L0} = 0{\cdot}25$, T_l=1050 K, $\Omega_L = 2{\cdot}8 \times 10^{-21}$ J/atom, $\Omega_S = 2{\cdot}8 \times 10^{-20}$ J/ator

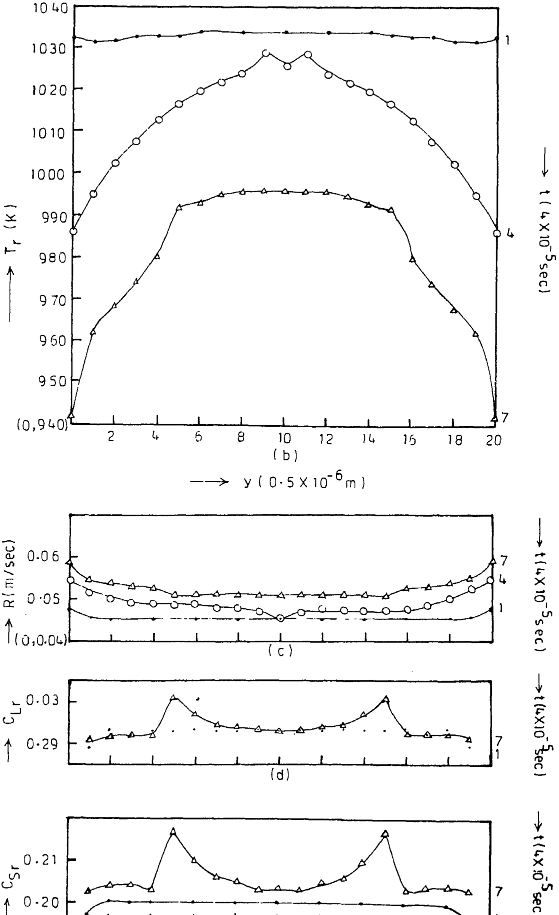
1040
1030
1020
1010
1000
990
980
970
960
950
(0,940)
→ T_r (K)
1
4
7
2
4
6
8
10
12
14
16
18
20
(b)
→ y (0.5 X 10^{-6}m)
→ t (4 X 10^{-5}sec)
0.06
0.05
(0,0.04)
→ R(m/sec)
7
4
1
(c)
→ t(4X10^{-5}sec)
→ C_{Lr}
0.03
0.29
7
1
(d)
→ t(4X10^{-5}sec)
→ C_{Sr}
0.21
0.20
7
→ t(4X10^{-5}sec

through the middle of the specimen parallel to the direction of growth (i.e. x-axis), observations only up to the centre point ($10g$) are given. Some typical results are discussed below.

System I. From figure 1 it is observed that the temperature of the interface at the edge decreases nonlinearly with time, rate of growth increases nonlinearly and shows a tendency to become constant. Both solid and liquid concentrations decrease below the equilibrium value and attain a constant difference ($C_{Sr} - C_{Lr}$) in time and the undercooling increases with time nonlinearly.

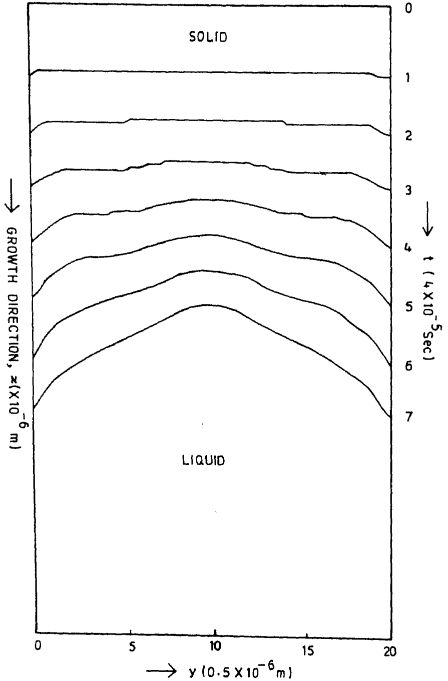

Figure 12(a). Time evolution of the solid–liquid interface for a system with $C_{L0} = 0{\cdot}98$, $T_1 = 1240\,\mathrm{K}$, $\Omega_L = 2{\cdot}8 \times 10^{-21}$ J/atom, $\Omega_S = 2{\cdot}8 \times 10^{-20}$ J/atom.

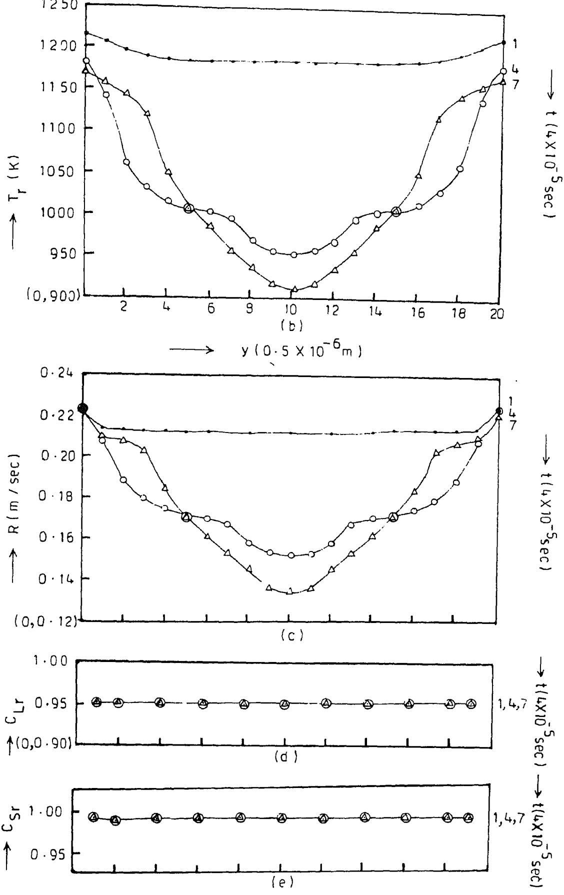

Figures 12(b–e). Time evolution of the interface: (**b**) temperature, (**c**) rate of growth, (**d**) concentration of the liquid phase, (**e**) concentration of the solid phase for a system with $C = 0.98$, $T = 1240$ K, $\Omega = 2.8 \times 10^{-21}$ J/atom, $\Omega = 2.8\times$

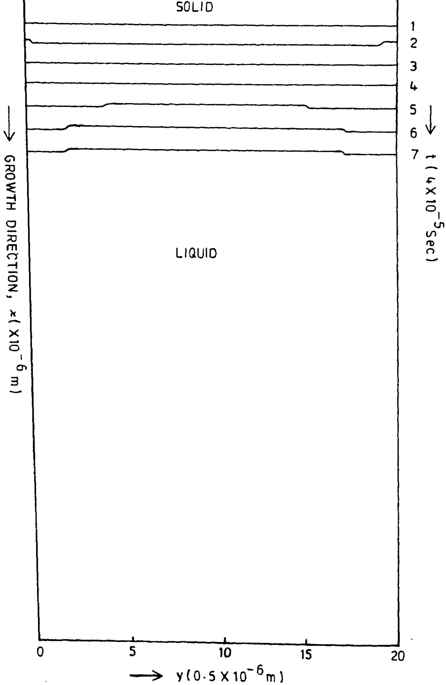

Figure 13(a). Time evolution of the solid–liquid interface for a syste
$C_{L0} = 0{\cdot}02$, $T_1 = 1190\,\mathrm{K}$, $\Omega_L = 2{\cdot}8 \times 10^{-21}$ J/atom, $\Omega_S = 2{\cdot}8 \times 10^{-20}$ J/at

Moving inside from the edge along the interface, the interface temperature g increasing and the interface is less undercooled at the inside points with minir undercooling occurring at the centre. The rate of growth as well as the concentra the liquid and solid phase decreases along the interface towards the centre.

These plots show the effect of cooling the sample equally from the boundaries v exponential external temperature gradient is maintained in the growth directic effect of cooling reaches the centre of the sample some time later.

The plots shown in figure 2 show different characteristics than that shown in f Here the temperature at the edge of the interface decreases linearly, at a dis it fluctuates about a decreasing trend, at distance 4g and 7g it decreases expon

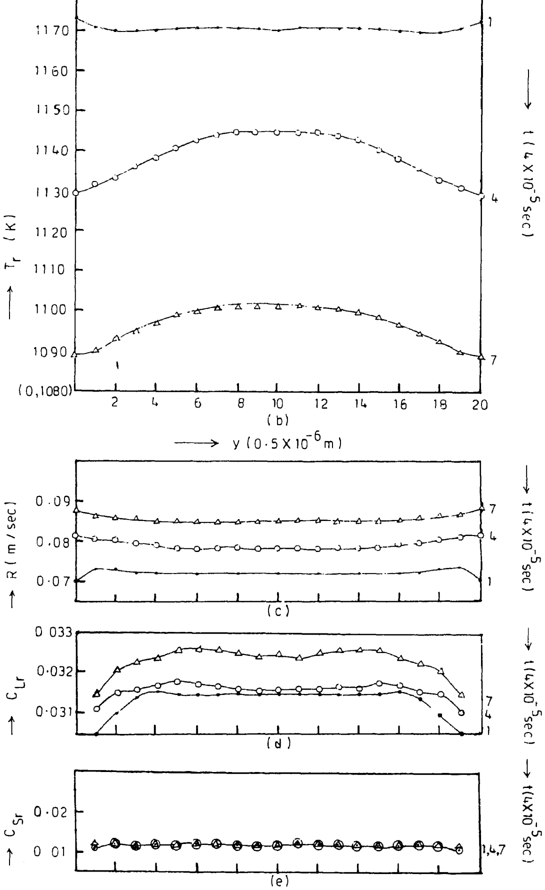

Figures 13(b–e). Time evolution of the interface: **(b)** temperature, **(c)** rate of growth, **(d)** concentration of the liquid phase, **(e)** concentration of the solid phase for a system with $C_{L0} = 0{\cdot}02$, $T_1 = 1190\,\mathrm{K}$, $\Omega_L = 2{\cdot}8 \times 10^{-21}\,\mathrm{J/atom}$, $\Omega_S = 2{\cdot}8\times$

values.

A relative analysis of the plots for this system shows that the fluctuations mentioned above are observed only when the average liquid concentration C_{L0} is equal to or greater than 0·5. Also the rate of growth is maximum when $C_{L0} = 0{\cdot}9$, and minimum at $C_{L0} = 0{\cdot}2$, which shows dependence of rate of growth on concentration C_{L0}.

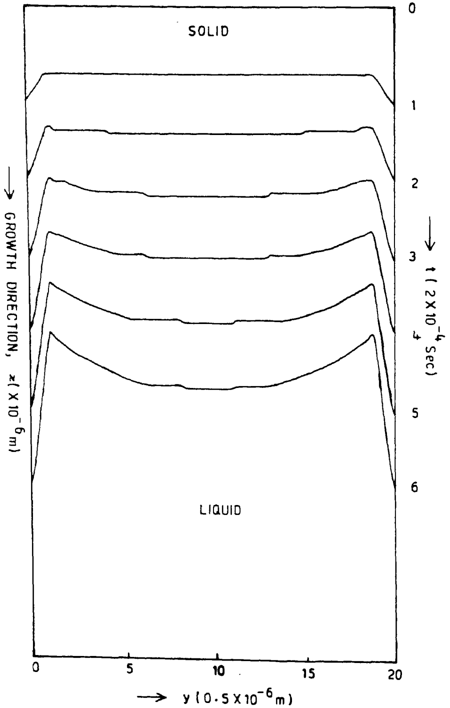

Figure 14(a). Time evolution of the solid–liquid interface for a system with $C_{L0} = 0{\cdot}5$, $T_1 = 1065$ K, $\Omega_L = 2{\cdot}8 \times 10^{-21}$ J/atom, $\Omega_S = 2{\cdot}8 \times 10^{-20}$ J/atom.

System II. A linear decrease in temperature of the various points of interface with time can be seen in figure 3. Temperature increases gradually along the interface towards the centre of the sample. The rate of growth varies nonlinerly with time and shows a tendency to achieve steady state growth conditions. Also, it is maximum at the edge and minimum at the centre of the sample. The solid and the liquid concentrations are practically

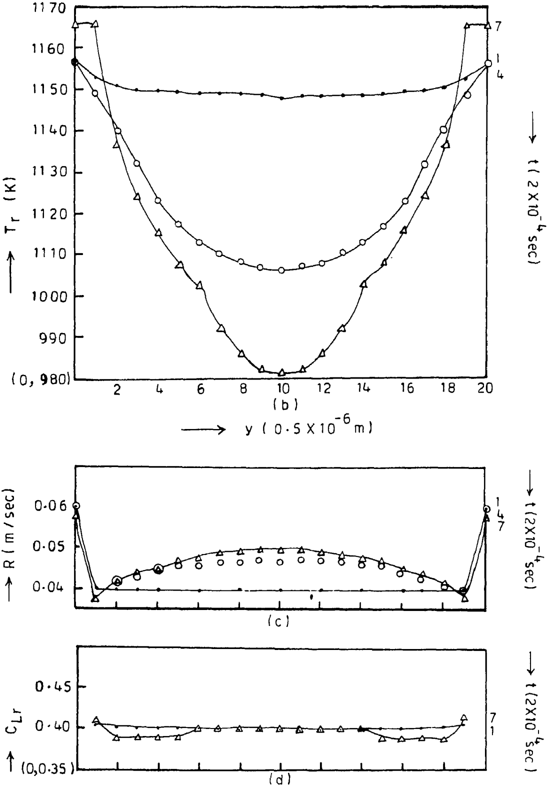

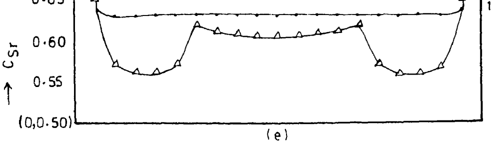

Figures 14(b–e). Time evolution of the interface: (**b**) temperature, (**c**) growth, (**d**) concentration of the liquid phase, (**e**) concentration of the solid ph system with $C_{L0} = 0{\cdot}5$, $T_1 = 1065\,\mathrm{K}$, $\Omega_L = 2{\cdot}8 \times 10^{-21}$ J/atom, $\Omega_S = 2{\cdot}8$ J/atom.

constant with time, which means the ratio C_{Sr}/C_{Lr} (the so called segregation coe is fixed.

For this system at $C_{L0} = 0{\cdot}35$ the congruent melting takes place (both C $C_{Sr} = 0{\cdot}35$). For $C_{L0} \geq 0{\cdot}5$, fluctuations in C_{Lr} and C_{Sr} can be seen. The extreme shown in figure 4 for $C_{L0} = 0{\cdot}98$. The temperature as well as the rate of growt centre of the sample is the lowest in this case, i.e. a decrease in rate of growth is o with a decreasing temperature. Both C_{Lr} and C_{Sr} are constant in time. The decrea rate of growth with decreasing temperature shows that it is in the region of the co growth where the rate of growth decreases by further increase in undercooling

System III. A linear decrease in interface temperature with time at the edge of the can be seen in figure 5. With time the temperature at the centre of the sampl interface stays approximately close to the equilibrium melting temperature. The growth is very high (0·9 m/s) at $C_{L0} = 0{\cdot}5$ and decreases for $C_{L0} > 0{\cdot}5$ or C_L With time the rate of growth of the various points at the interface approximately the same value. Both C_{Lr} and C_{Sr} are practically constant. Congruent melting tak at $C_{L0} = 0{\cdot}5$, where both C_{Lr} and C_{Sr} are equal (i.e. 0·5).

System IV. The behaviour of the plots shown in figure 6 is the same as those of for system I except that in the time–temperature plots an increase in temperatu $T_{eq}(= T_1)$ at the centre of the sample is observed.

The plots for system V are similar to plots of system III and the plots for syste similar to those of system II.

In all the system only some typical results are given. The trends shown by these all the six systems therefore agree with the experimentally observed results. Th are also similar to Chvoj's [12] results for single component system and also dimensional binary system [6]. From this study the effect of concentration o growth can be observed.

3.2 *Evolution of the solid–liquid interface shape $X_r(y)$*

In this section the plots of solid–liquid interface shape with time are given along plots of its temperature, solid and liquid concentrations and rate of growth. In th model the solid–liquid interface is chosen to be a flat surface initially. As the solidification proceeds the heat of fusion is evolved at this surface and the solute atoms diffuse away according to the boundary conditions given in § 3.1 of part I. Many interesting shapes of the interface observed are discussed below.

System I. It is seen in figure 7(a) that the interface remains smooth up to two time steps and becomes progressively curved with kinks at points 8*g* and 12*g*. The temperature–time plots, given in figure 7(b) show large heating of these points. The rate of growth is the

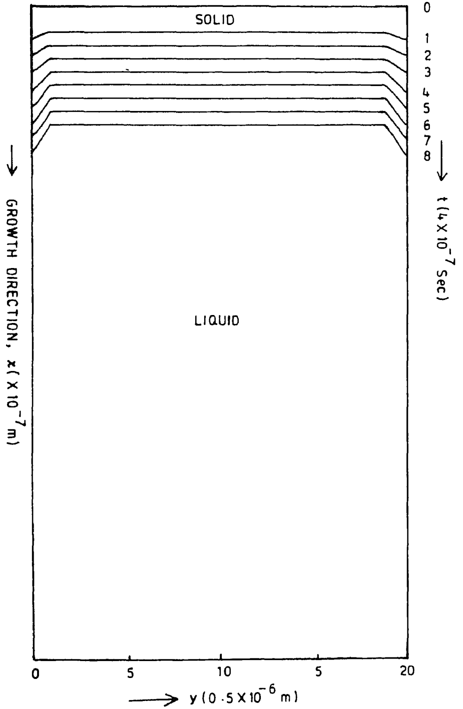

Figure 15(a). Time evolution of the solid–liquid interface for a system with figures 7(c, d, e) respectively.

The corresponding plots for $X_r(y)$ with $C_{L0} = 0{\cdot}7$ are shown in figure 8(a). Kinks can be seen at points $2g$ and $4g$ and symmetrically at $16g$ and $18g$ indicating a possible formation of a dendrite tip. The temperature profile shows a sharp decrease and the rate

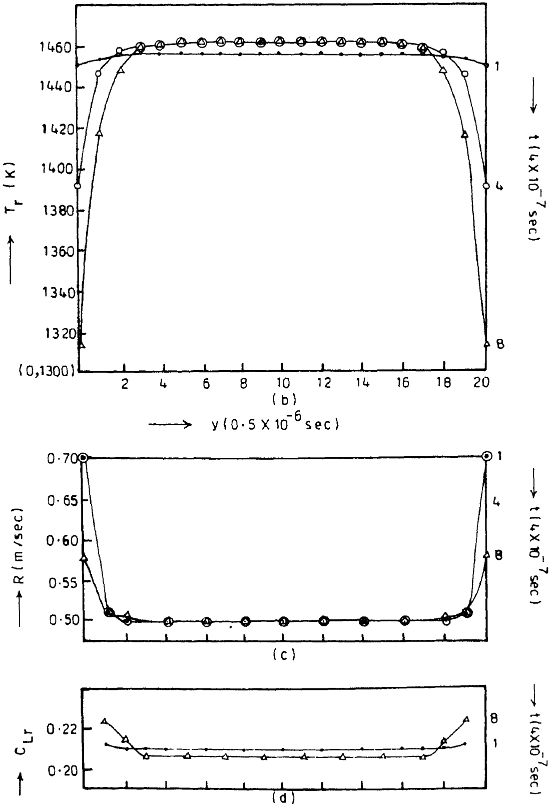

Figures 15(b–d).

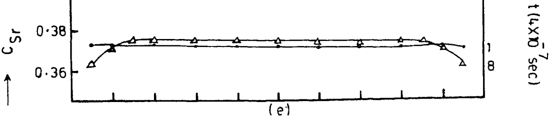

Figures 15(b–e). Time evolution of the interface: (**b**) temperature, (**c**) rate of growth, (**d**) concentration of the liquid phase, (**e**) concentration of the solid phase for a system with $C_{L0} = 0{\cdot}3$, $T_1 = 1473$ K, $\Omega_L = 2{\cdot}8 \times 10^{-19}$ J/atom, $\Omega_S = 2{\cdot}8 \times 10^{-20}$ J/atom.

profile shows a sharp increase at these points as shown in figures 8(b, c) respectively. C_{Lr} and C_{Sr} profiles show very small fluctuations about an average parabolic behaviour (figures 8(d, e)).

Figure 9(a) shows an even more complex structure of the interface. Temperature and rate of growth of this interface follow a similar trend as in case above and the concentrations on the interface surface are constant as shown in figures 9(b, c, d, e).

System II. The interface surface shown in figure 10(a) is nearly parabolic with curvature towards the solid phase and it exhibits a tendency to develop kinks near the middle of the sample. The temperature plots in figure 10(b) show considerable undercooling of the interface. The rate of growth decreases with time (figure 10(c)), which is characteristics of diffusion controlled growth. The concentration plots (figures 10(d, e)) show only small variations. The other shapes are shown in figures 11(a–e) to figures 14(a–e) for average liquid concentration $C_{L0} = 0{\cdot}25$, $0{\cdot}98, 0{\cdot}02$ and $0{\cdot}5$ respectively. An analysis of these curves depicts that the $X_r(y)$ shapes have the same characteristics for all C_{L0}, but the trends of T_r, C_{Lr}, C_{Sr} and R plots are reversed about $C_{L0} = 0{\cdot}5$.

System III. In this case the initially flat interface (figure 15(a)) retains its shape moving nearly equal distance in each time step except at the boundaries (edges) which are moving faster than the remaining points. The temperature plots show a cooling of the boundaries and the rate of growth plots show that the boundaries move slower than the other points. The liquid and the solid concentration curves are practically constant.

System IV. In figure 16(a) $X_r(y)$ is a parabolic surface with curvature towards the solid phase and boundaries move faster in the liquid phase. Temperature T_r, concentrations C_{Lr} and C_{Sr} surfaces evolve into parabolic shapes. The rate of growth profiles are also parabolic with curvature in a direction opposite to that of T_r, C_{Lr} and C_{Sr} plots. The evolution of surface for all time steps cannot be shown as their values lie close.

The $X_r(y)$, T_r, C_{Lr}, C_{Sr} and R plots for system V are similar to those obtained for system III and for system VI same patterns are obtained as for system II.

Thus it is seen from these plots that the radius of curvature of the solid–liquid interface changes during the solidification process and it also depends on the kinetic parameters planar interface growth occurs. It is believed that if the flux boundary condition i into account more rigorously while solving the four coupled equations, it mi possible to obtain dendrite, eutectic and cellular growth also.

The concentration of the solid phase varies and is different at different poi times. This shows that if the crystal is quenched at a particular time, a cross secti will show the solid concentration variation as predicted by these calculations.

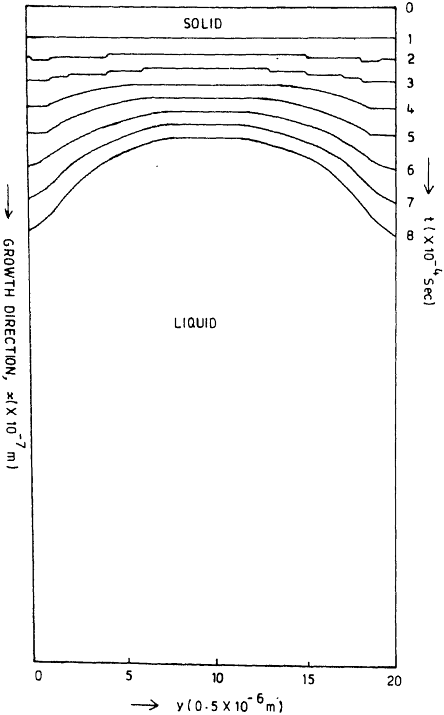

Figure 16(a). Time evolution of the solid–liquid interface for a syste $C_{L0} = 0{\cdot}5$, $T_1 = 1557\,\mathrm{K}$, $\Omega_L = -2{\cdot}33 \times 10^{-20}$ J/atom, $\Omega_S = -2{\cdot}47 \times 10^{-20}$

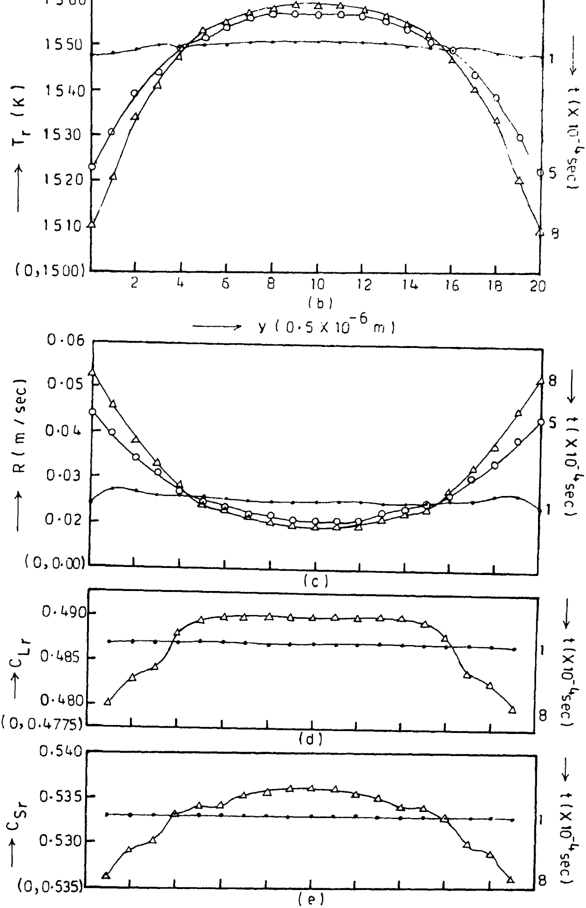

Figures 16(b–e). Time evolution of the interface: (**b**) temperature, (**c**) rate of growth, (**d**) concentration of the liquid phase, (**e**) concentration of the solid phase for a

From the various results presented in §3 it is evident that phenomenon of solidificatio binary melts can be studied comprehensively by using a stochastic model given in pa These results qualitatively reproduce many of the phenomena observed experimenta e.g., the phase diagrams obtained for various systems with different interac parameters, effect of concentration and temperature on growth process, change of pla interface to various shapes.

Theories which neglect the kinetic processes at the solid–liquid interface [13] ca be used for the systems in which the kinetic processes control the phase transit Nonequilibrium solidification theories are more suitable to study crystal growth as du solidification the system is far from thermodynamic equilibrium.

The model presented here has been developed under an approximation that the sys is not far from equilibrium. Nonequilibrium conditions are ascertained by high coo rates of the order of 10^6–10^8 K/s. The rate of growth of the solid–liquid interface is t dependent, therefore the growth of the new phase is essentially under non-steady s conditions. During nonequilibrium solidification the concentrations of solid and li phases, rate of growth, undercooling and boundary conditions vary with time. T variations are included in this model enabling the determination of the composition microstructure of the new phase. The various approximations can easily be relaxed in model. However, a better explanation of the various interface shapes obtained ca given after considering the flux boundary condition more rigorously.

The model can be further extended to 4-dimensions (3-space, 1-time) an multicomponent systems. Also, solution is obtained only for one type of boun conditions which corresponds to crystal pulling technique of crystal growth. T boundary conditions can easily be modified to suit other experimental techniques.

References

[1] F C Flemings, in *Solidification processing* (Mc-Graw Hill Inc., New York, 1974)

[2] P Gordon, in *Principles of phase diagrams in materials* (Mc-Graw Hill, 1968; Jersey,

[3] A K Jena and M C Chaturvedi, in *Phase transformation in materials* (The Metals Soc Englewood Cliffs, New Jersey, 1992)

[4] B Caroli, C Caroli and B J Roulet, *J. Cryst. Growth* **66**, 575 (1984)

[5] Z Chvoj, *Cryst. Res. Technol.* **21**, 8, 1003 (1986)

[6] Z Chvoj, *Czech. J. Phys.* **B37**, 607 (1987)

[7] Z Chvoj, *Czech. J. Phys.* **B40**, 473 (1990)

[8] Z Chvoj, *Czech. J. Phys.* **B40**, 483 (1990)

[9] S Dass, *A stochastic approach to the study of solidification*, Ph.D. Thesis (Rani Durg University, 1994)

[10] S Dass, G Johri and L Pandey, *Pramana – J. Phys.* **47**, 447 (1996)

[11] C W Gardiner, in *Handbook of stochastic methods* (Springer-Verlag, Berlin, 1985)

[12] Z Chvoj, *Czech. J. Phys.* **B36**, 863 (1986)

[13] J S Langer and L A Turski, *Phys. Rev.* **A22**, 2189 (1980)

Superconducting state parameters of metallic glass $Mg_{70}Zn_{30}$ using linearized screened pseudopotential

MANISH GUPTA, K S SHARMA* and L DASS[†]
Department of Physics, SMM Government Girls PG College, Bhilwara 311 001, India
*Department of Physics, Govt. MSJ College, Bharatpur 321 001, India
[†]Department of Physics, University of Rajasthan, Jaipur 302 004, India

MS recieved 30 March 1996; revised 3 December 1996

Abstract. A linearized form for the screened form factors of electron-phonon interaction in the metallic glass $Mg_{70}Zn_{30}$ is applied for the first time to predict the superconducting state parameters viz. electron-phonon coupling strength (λ), Coulomb pseudopotential (μ^*), transition temperature (T_c), isotope effect exponent (α) and the interaction strength ($N_0 V$). Computed results agree with the experimental data available in the literature.

Keywords. Superconductivity; metallic glass; superconducting state parameters; pseudopotential.

PACS Nos 74·30; 62·20; 61·40

1. Introduction

The basic problem of determining the superconducting transition temperature T_c of a superconductor has two separate aspects; firstly, understanding the material properties (electron-phonon coupling strength, λ), the Coulomb pseudopotential (μ^*), and the phonon spectrum, which is usually over simplified by some frequency (ω), and secondly calculating $T_c\,\{\lambda, \mu^*, \omega\}$. This paper deals with both the aspects of glassy materials. These materials have interested scientists, engineers and technologists because of their widespread applications in material science and engineering. Extensive work has been done on vibrational dynamics [1, 2], elastic [3] and transport properties of metallic glasses. However, the superconductivity in these materials has, to our knowledge, not been much explored [4–6] and this prompted us to study the superconductivity in the metallic glasses.

With this aim, we apply BCS–Eliashberg McMillan model [7–9] to these materials for computation of superconducting properties of metallic glass $Mg_{70}Zn_{30}$. For achieving this goal, we have constructed the form factors for this metallic glass by using a quadratic form of screened potential, called linearized screened pseudopotential by Sharma *et al* [10], as it provides almost linear form for $V_s(q) - q$ curve in the limit $0 < q < 2k_F$. Parameters of this pseudopotential are determined by graph fitting method to realistic pseudopotential form factors of the relevant constituent metal as obtained from HA potential [11] and modify these parameters as suggested by Saxena *et al* [12]. The form factors of glass obtained by this potential are then used to calculate superconducting state properties, namely electron-phonon coupling strength (λ), Coulomb pseudopotential (μ^*), transition temperature (T_c), isotope effect coefficient (α) and the interaction strength (N_0V).

2. Theory

The linearized screened pseudopotential by Sharma *et al* [10] has the following quadratic form,

$$V_s(q) = \frac{\langle k+q|w|k\rangle}{\varepsilon_q} = A_1 + B_1 q + C_1 q^2 \tag{1}$$

where A_1, B_1 and C_1 are the potential parameters and q is the momentum transfer. If we define $x = q/2k_F$, where k_F is the Fermi momentum, then potential form reduces to

$$V_s(x) = A + Bx + Cx^2 \tag{2}$$

where A, B and C are the new potential parameters.

We modify this potential (2) by incorporating the concept of mean effective density dependent interatomic potential in glass forming alloy of the type $\alpha_{Ç_\alpha}\beta_{Ç_\beta}$ [12]

$$V_{\rm eff}(x) = Ç^2{}_\alpha V_{\alpha\alpha}(x) + 2Ç_\alpha Ç_\beta V_{\alpha\beta}(x) + Ç^2{}_\beta V_{\beta\beta}(x). \tag{3}$$

Here, $V_{\alpha\alpha}(x)$ is the pair potential for the α-α component, $V_{\alpha\beta}(x)$ for α-β component and $V_{\beta\beta}(x)$ for the β-β component in the $\alpha_{Ç_\alpha}\beta_{Ç_\beta}$ metallic glass alloy, having concentrations $Ç_\alpha$ of α-type and $Ç_\beta$ of β-type. Now pair potentials using (2) are

$$V_{\alpha\alpha} = A_\alpha + B_\alpha x + C_\alpha x^2 \tag{4}$$

$$V_{\beta\beta} = A_\beta + B_\beta x + C_\beta x^2 \tag{5}$$

$$V_{\alpha\beta} = A_{\alpha\beta} + B_{\alpha\beta} x + C_{\alpha\beta} x^2. \tag{6}$$

Substituting (4), (5) and (6) into (3), new form of linearized screened potential obtained is

$$\begin{aligned} V_s(x) = {} & (Ç^2{}_\alpha A_\alpha + 2Ç_\alpha C_\beta A_{\alpha\beta} + Ç^2{}_\beta A_\beta) \\ & + (Ç^2{}_\alpha B_\alpha + 2Ç_\alpha C_\beta B_{\alpha\beta} + Ç^2{}_\beta B_\beta)x \\ & + (Ç^2{}_\alpha C_\alpha + 2Ç_\alpha C_\beta C_{\alpha\beta} + Ç^2{}_\beta C_\beta)x^2. \end{aligned} \tag{7}$$

The parameters of $V_{\alpha\alpha}$ i.e. A_α, B_α, C_α and the parameters of $V_{\beta\beta}$ i.e. A_β, B_β, C_β are determined by the graph fitting method to the form factors of the HA potential [11] for the constituents of the metallic glass $Mg_{70}Zn_{30}$. Defining again new potential parameters A', B' and C', (7) finally takes the form

$$V_s(x) = A' + B'x + C'x^2, \tag{8}$$

where

$$A' = Ç^2{}_\alpha A_\alpha + 2Ç_\alpha C_\beta A_{\alpha\beta} + Ç^2{}_\beta A_\beta,$$

$$B' = C^2 B + 2C C B + C^2 B$$

parameters of metallic glass $Mg_{70}Zn_{30}$. The electron-phonon coupling strength for the alloy $\alpha_{\text{Ç}_\alpha}\beta_{\text{Ç}_\beta}$ may be written as follows by extending the relevant formula for metals [13]

$$\lambda = \frac{12m^* z^*}{M\langle\omega^2\rangle}\int_0^1 \mathrm{d}x\,|V_s(x)|^2 x^3, \tag{9}$$

where $M = \text{Ç}_\alpha M_\alpha + \text{Ç}_\beta M_\beta$ is the ionic mass, $m^* = \text{Ç}_\alpha m_\alpha^* + \text{Ç}_\beta m_\beta^*$ is the effective mass. In the effective mass relation, m_α^* and m_β^* are the effective masses of Mg and Zn respectively, which are taken as $m_\alpha^* = 1{\cdot}33$ and $m_\beta^* = 0{\cdot}86$ from [14].

$V_s(x)$ is the pseudopotential used, defined by (8), and $\langle\omega^2\rangle$ is the average square phonon frequency of the glassy system under consideration defined as given by Butler [15]

$$\langle\omega^2\rangle^{1/2} = 0{\cdot}69\,\Theta_D \tag{10}$$

where Θ_D is the Debye temperature for the glass, which is obtained using the GrimVall formula [16]

$$\frac{1}{(\Theta_D)^2} = \frac{\text{Ç}_\alpha}{(\Theta_{D\alpha})^2} + \frac{\text{Ç}_\beta}{(\Theta_{D\beta})^2}. \tag{11}$$

Here $\Theta_{D\alpha}$ and $\Theta_{D\beta}$ are the Debye temperatures for Mg and Zn respectively, which are taken as $\Theta_{D\alpha} = 342$ K and $\Theta_{D\beta} = 235$ K from [17]. The effective balance Z^* used in (9) for glass is computed by [18]

$$z^* = (2 - m_E)z. \tag{12}$$

Here z is the mean balance of the glassy system and m_E is the component of effective mass. The values for m_E are 0·92 and 0·89 for Mg and Zn respectively [14].

Electron-phonon coupling strength formula (9), after substituting potential (8) and simplified takes the form

$$\lambda = \frac{12m^* z^*}{M\langle\omega^2\rangle}\left[\frac{A'^2}{4} + \frac{B'^2}{6} + \frac{C'^2}{8} + \frac{2}{5}A'B' + \frac{1}{3}A'C' + \frac{2}{7}B'C'\right]. \tag{13}$$

Other parameter Coulomb pseudopotential (μ^*) is given by Rajput and Gupta [19]

$$\mu^* = \frac{m^*}{\pi k_F}\int_0^1 \frac{\mathrm{d}x}{x\varepsilon(x)} \Bigg/ \left[1 + \frac{m^*}{\pi k_F}\ln\left(\frac{k_F^2}{20\Theta_D}\right)\int_0^1 \frac{\mathrm{d}x}{x\varepsilon(x)}\right]. \tag{14}$$

Here $\varepsilon(x)$ is the dielectric screening function, which is taken in the Hartree form [20] for simplicity. The relevant expression for the transition temperature (T_c) and isotope effect exponent α are respectively given [20] by

$$T_c = \frac{\Theta_D}{1{\cdot}45}\exp\left[\frac{-1{\cdot}04(1+\lambda)}{\lambda - \mu^*(1 + 0{\cdot}62\lambda)}\right] \tag{15}$$

and

$$\alpha = \frac{1}{2}\left[\ln - \left(\mu^* \ln\frac{\Theta_D}{1{\cdot}45\,T_c}\right)^2 \frac{1 + 0{\cdot}62\lambda}{1{\cdot}04(1+\lambda)}\right]. \tag{16}$$

3. Results and discussion

The form factors of $V_{\alpha\alpha}$ and $V_{\beta\beta}$ i.e. pair-potential for Mg-component and Zn-cor nent, have been compared with that of the HA potential in figures 1 and 2. The form factors show an excellent agreement with that of the HA potential. The valu parameters A', B' and C' as computed through (8) are given in table 1.

In the calculation of superconducting state parameters, the input parameters use listed in table 2. The superconducting state parameters for the present work as w others [5, 6, 21] are shown in table 3. The evaluated value of the electron-phonon cou strength (λ) is 0·48, which shows that there should be a weak coupling between elec and phonons. The Coulomb pseudopotential (μ^*) is found to be of the same ord suggested by Allen and Dynes [13], which strengthens the present theory for this new of material. The T_c value 1·21 K shows the best agreement with the experimental $T_c = 0{\cdot}7$ K due to Calka *et al* and with $T_c = 1{\cdot}4$ K as reported in [6]. The present res also in good agreement with the other theoretical result $T_c = 0{\cdot}369$ K [21] for this me glass. In [21], the superconducting state parameters of this metallic glass have calculated by applying Ashcroft's empty core model potential which is different fron pseudopotential used in the present work. The positive value N_0V, in table 3 reveal superconducting character of the metallic glass $Mg_{70}Zn_{30}$.

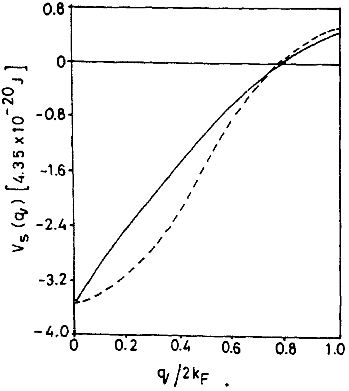

Figure 1. Comparison of present work form factors with HA for Mg: —— mo linearized potential, -.- HA.

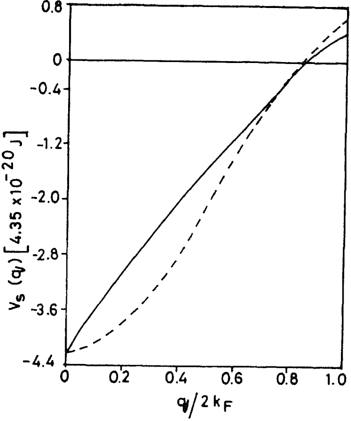

Figure 2. Comparison of present work form factors with HA for Zn: —— modified linearized potential, -.- HA.

Table 1. Values of parameters A', B', C' computed through (8).

A'	B'	C'
−0·2748	0·4542	−0·1424

Table 2. Input parameters used in the calculation.

Parameters	m^*	z^*	M 10^{-28} kg	Θ_D (K)	k_F ($10^{10}\,m^{-1}$)
Values	1·189	2·178	844·400	295·950	1·390

Table 3. Superconducting state parameters of the metallic glass $Mg_{70}Zn_{30}$.

	λ	μ^*	T_c(K)	α	N_0V
Present work	0·48	0·14	1·21	+0·232	+0·238
[5]	–	–	0·70	–	–
[6]	–	–	1·40	–	–
[21]	0·30	0·12	0·260	+0·185	+0·130

Finally, we may conclude that overall satisfactory reproduction of all the
conducting state parameters confirms the validity of the proposed very
pseudopotential i.e. the quadratic form of potential called linearized sc
pseudopotential by its proposers [10]. Because of its simple form and since scree
the bare ion potential is not required in this method, this potential is being app
the other metallic glasses also in our group and the results will be reported short
fitting of the pseudopotential to the form factors of standard HA potential will b
realistic if we add more terms i.e. beyond quadratic in (1). But addition of mor
makes handling of the potential more complex in the calculation of supercon
state parameters. But since the potential parameters are fitted to the realist
factors given by HA potential [11], the variation in the results is expected to be
However, the investigation of changes on this account may certainly be of the
interest. We therefore propose to carry out this investigation in future.

Acknowledgement

The author (MG) expresses his gratitude to Prof. S L Kakani for many
suggestions and also thankful to the Head, Department of Physics, MSJ C
Bharatpur for providing the necessary departmental facilities.

References

[1] P C Agarwal and C M Kachava, *Physica* **B179** 43–47 (1992)
[2] R N Singh and A B Bhatia, *Phys. Rev.* **B21**, 4751 (1985)
[3] J R Campanha and M M Shukla, *Phys. Status Solidi* (1996) to be published
[4] Manish Gupta, P C Agarwal, K S Sharma and Lachhman Dass, *Phys. Status Soli*
(in press)
[5] A Calka, M Madhaua, D E Polk, B C Giessen, H Matyja and J van der Sande, *Scr*
11, 65 (1977)
[6] A V Narlikar and S N Ekbote, *Superconductivity and superconducting material*
Asian Publishers, New Delhi, Madras, 1983) p. 185
[7] J Bardeen, L N Cooper and J R Schrieffer, *Phys, Rev.* **108**, 1175 (1957)
[8] G M Eliashberg, *Zh. Eksp. Teor. Fiz.* **38**, 966 (1960); **39**, 1437 (1960); *Sov. Phys, J*
696 (1960); **12**, 1000 (1961)
[9] W L McMillan, *Phys. Rev.* **167**, 331 (1968)
[10] R Sharma, K S Sharma and L Dass, *Phys. Status Solidi* **B133**, 701 (1986)
[11] W A Harrision, *Pseudopotential in the theory of metals* (Benzamin Inc., New Yor
[12] N S Saxena, Meeta Rani, Arun Pratap, Prabhu Ram and M P Saksena, *Phys. F*
8093 (1988)
[13] P B Allen and R C Dynes, *Phys. Rev.* **B12**, 905 (1975)
[14] H Ehrenreich, F Seitz and D Turnbull, *Solid State Physics* (Academic Press, Ne
1970) vol. 24
[15] W H Butler, *Phys. Rev.* **B15**, 5267 (1977)
[16] G Grimvall, *Thermodynamical properties of metals* (North Holland, Amsterdam,
[17] P Morel and P W Anderson, *Phys. Rev.* **125**, 1263 (1962)
[18] H Khan, V Singh and K S Sharma, *Indian J. Pure Appl. Phys.* **31**, 628 (1993)
[19] J S Rajput and A K Gupta, *Phys. Rev.* **181**, 743 (1969)
[20] R Sharma and K S Sharma, *Czech. J. Phys.* **B34**, 325 (1984)
[21] Manish Gupta, K S Sharma and Lachhman Dass, *Materials Science Forum* (Tra
Publications, Switzerland, 1996) vols 223–224 pp. 387–390

Electron paramagnetic resonance studies of photorefractive crystals II: Fe^{3+} doped $Bi_{12}SiO_{20}$ with copper vapour laser illumination in 10–100 K range

N K PORWAL, R M KADAM, Y BABU, M D SASTRY, M D AGGARWAL* and
PUTCHA VENKATESWARLU*
Radiochemistry Division, Bhabha Atomic Research Centre, Trombay, Mumbai 400 085, India
*Department of Physics, Alabama A&M University, Normal, Alabama 35762, USA

MS received 14 June 1996

Abstract. Photo-induced charge transfer and its kinetics were investigated in $Bi_{12}SiO_{20}$ in 10–300 K temperature range, using EPR of Fe^{3+} centre, under *in situ* illumination with copper vapour laser (CVL). The decay kinetics was found to follow double exponential behaviour. Relaxation of the photo-induced electron transfer to the preillumination condition occurred even at 10 K. Shallow traps were, therefore, associated with the electron trapping, leading to a better understanding of the fast photorefractive response of BSO.

Keywords. Electron paramagnetic resonance; bismuth silicon oxide; photorefraction; laser.

PACS No. 76·30

1. Introduction

Over the last decade the photorefractive behaviour, a change in the refractive index of crystals due to the spatial variation in the intensity of the incident light, has been a subject of intense research. Prominent crystals exhibiting this phenomenon are $LiNbO_3$, $BaTiO_3$, $Bi_{12}GeO_{20}$, $Bi_{12}SiO_{20}$, $Bi_{12}TiO_{20}$, etc. Among these, $LiNbO_3$ and $BaTiO_3$ are the most thoroughly investigated photorefractive materials primarily because of very large values of the electro-optic tensor component, yielding correspondingly large values of grating efficiency, beam coupling strength, and four-wave mixing reflectivity when interference pattern is produced in the body of the crystal [1]. The grating formation is primarily due to net charge transfer from the bright regions of the interference pattern to the dark regions. In spite of the many advantages in beam coupling and phase conjugation characteristics, $BaTiO_3$ and more significantly $LiNbO_3$ suffer from sluggish growth and decay of the gratings in the body of the crystals. A crystal which exhibits much faster and contrasting photorefractive response is bismuth silicon oxide ($Bi_{12}SiO_{20}$). Photo-induced charge transfer processes in photorefractive materials are of immense current interest because of their potential applications in optical data processing [2].

Bismuth silicon oxide (BSO), having the formula $Bi_{12}SiO_{20}$ and belonging to the sillenite family of crystals, has interesting photorefractive properties [1]. It has some

crystals, $BaTiO_3$ and $LiNbO_3$. Whereas $BaTiO_3$ and $LiNbO_3$ are ferroelectric, I
paraelectric cubic crystal at room temperature. Unlike the other two crystals, I
fast response times and lower beam coupling strengths. In BSO, the photo
electron transport is known to be longer than Debye screening length, so
electron/hole trapping is not in the immediate vicinity of the donor sites. In the
$BaTiO_3$ and $LiNbO_3$, the Fe^{3+} impurity is believed to play an important ro
photorefractive mechanism. We have investigated $LiNbO_3$ with a less
impurity ion U^{5+}, for photoinduced electron transfer and its kinetics [3]. The
paper is the second in the series of our papers on photorefractive materials; and d
$Bi_{12}SiO_{20}$.

Jani and Halliburton [4] have investigated the effect of photoillumination on
of Fe^{3+} in BSO. They found that excitation with 350 nm light indeed changed the
of Fe^{3+} at 77 K and it recovered to its original state only on warming the crystal
temperature. They did not, however, find any photoinduced valence change of
room temperature. BSO crystal has a band gap of 3·25 eV ($\approx$ 380 nm). Exci
energies more than the band gap would result in interband electron tran
subsequent trapping of electron at defect sites. Therefore, it is not surprising
system relaxes back only on thermal stimulation which releases the trapped elec
view of the role of Fe^{3+} as a trapping site for electrons in the sub-room tem
region, they suggested that Fe^{3+} ions may play an important role in the photor
effect at room temperature. Baquedano *et al* [5] have also investigated the EPR
by illuminating with He/Cd (442 nm) laser, and xenon arc lamp. They iden
intrinsic trapped hole center which was bleached by photoexcitation. In the pres
we have investigated the effect of *in situ* laser illumination with 10 W copper va
on the EPR of Fe^{3+} in BSO in 300–10 K range.

2. Experimental

The BSO crystal used in the present study was grown using Czochralski tech
CVL, having 10 W average power and emission wavelengths at 510 nm and 57
used for *in situ* illumination of BSO crystal inside the optical transmission cavit
spectrometer. The EPR spectra were recorded using a Bruker ESP-300 spec
equipped with an optical transmission cavity and operating in the x band.
cryogenics closed cycle helium refrigerator together with a lakeshore m
autotuning temperature controller was used for temperature variation in t
of 10–300 K.

3. Results

The EPR spectrum of Fe^{3+} in BSO single crystal at room temperature, consi
broad line around $g \approx 2{\cdot}00$. The line position was found to be isotropic. The li
however, was found to be anisotropic with maximum width for $H^{\|}\langle 1$
suggests that this line contains unresolved structure whose anisotropy is such
best resolved for $H^{\|}\langle 100\rangle$. The intensity of the line increased with low

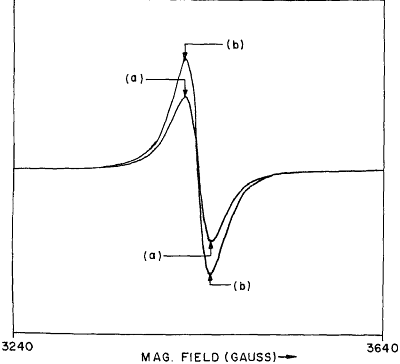

Figure 1. EPR spectrum of Fe^{3+} in BSO at 10 K: (**a**) with and (**b**) without laser illumination. A clear reduction in intensity with laser illumination can be seen.

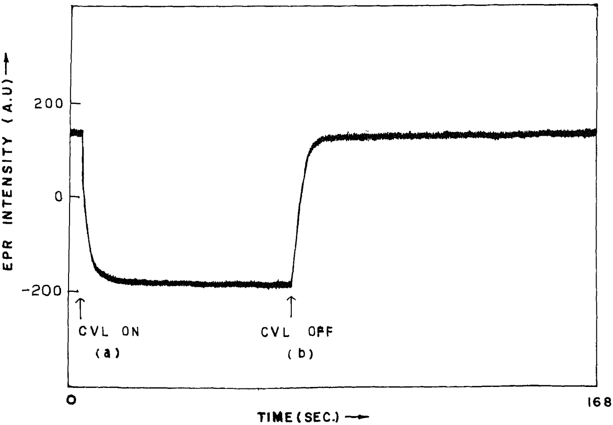

Figure 2. Decay (**a**) and recovery (**b**) of Fe^{3+} signal with laser illumination on and

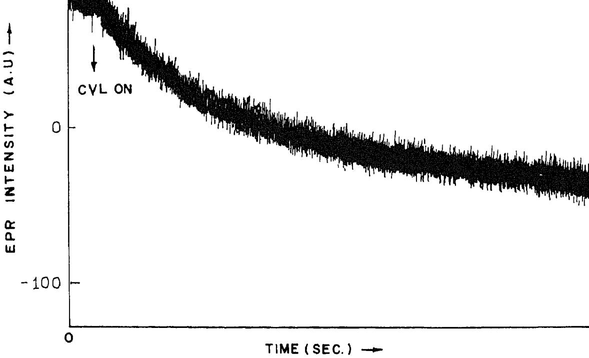

Figure 3a. Decay of Fe^{3+} signal at 70 K with expanded time axis.

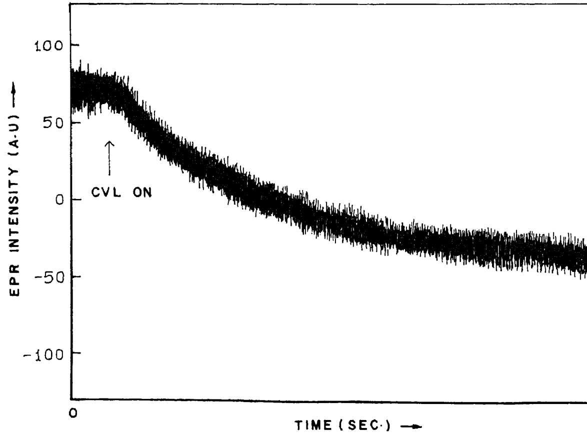

Figure 3b. Decay of Fe^{3+} signal at 100 K with expanded time axis.

Table 1. Time constants for the double exponential decay of Fe^{3+} EPR signal intensity on CVL illumination.

Temperature (K)	τ_1 (s)	τ_2 (s)
10	7	210
40	7	40
70	7	33
100	7	30

temperature from 300 K to 10 K and the line became sharper. In order to investigate the photoinduced charge transfer, the intensity of the line was monitored with and without illumination by copper vapour laser (10 W average power). The intensity reduced significantly on laser illumination at 10 K (figure 1). The kinetics of the changes were monitored by locking the magnetic field to the peak position of the line in the derivative presentation (not the resonance field) and following the change in intensity as a function of time with and without CVL illumination. Typical growth and decay patterns obtained at different temperatures are shown in figures 2, 3(a) and (b). Intensity of the spectrum went down on laser illumination and its intensity recovered completely when the laser illumation was stopped. The decay curves were fitted to a double exponential expression. The time constants obtained at different temperatures are given in table 1. These results are in contrast with those of Jani and Halliburton [4] and also Baquedano *et al* [5]. BSO crystal was illuminated at 77 K with CVL and its TL was monitored by warming the sample to room temperature. The sample did not show any TL between 100 and 300 K region.

4. Discussion

EPR spectrum of Fe^{3+} at cubic sites would consist of five ($\Delta M_S = \pm 1$) fine structure transitions, which are often unresolved or partially resolved due to small value of fourth order cubic crystal field constant.

The crystal structure of BSO has been studied by Abrahams *et al* [6]. The possible sites for Fe^{+} occupancy in BSO lattice are:

(a) *Si^{4+} site*: $Bi_{12}SiO_{20}$ has a body centred cubic cell with SiO_4 tetrahedra occupying the corners and centre of the cube. The four oxygen atoms around each Si atom form a geometrically perfect terrahedron. The $\langle 111 \rangle$ axes of the cube pass through the respective three-fold axes of all the SiO_4 tetrahedra.
(b) *Bi^{3+} site*: Bi^{3+} is coordinated to seven oxygen atoms with a coordination which is somewhat a mixture of an octahedron and a tetrahedron. Five of the seven oxygens take the places of nearly regular octahedral positions, and the sixth position of the ligand is taken by two oxygens, with O–Bi–O angle of 107·3°, which is nearly equal to the tetrahedral angle.

The larger line width for $H^{\parallel}\langle 100 \rangle$ is consistent with the unresolved cubic fine structure in that direction. The fine structure would be most resolved only along this direction.

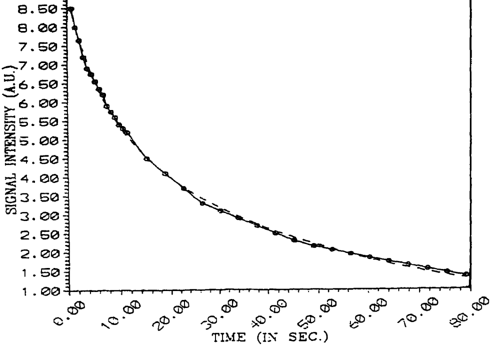

Figure 4. The fitting of the decay of EPR signal of Fe^{3+} to a double expon
40 K). The dashed curve is the theoretical fit.

Therefore on photoillumination any hole generated in the lattice could be trappec
it Fe^{4+}. Due to the half filled nature, Fe^{3+} is more stable compared to Fe^{4+} and h
system relaxes back to its original state after the laser illumination was put off

The decay (with light on) of Fe^{3+} signal was monitored at different temperat
satisfactory fit was obtained with a double exponential. The theoretical
exponential points at 40 K is shown in figure 4. In the computing process
constant ($\tau_1 = 7$ s) was found to be nearly temperature independent whereas the
(τ_2) has shown strong temperature dependence (see table 1).

Absence of TL between 100 and 300 K together with the observation of the rec
the signal after putting off the illumination even at 10 K, shows that the elect
centres we are dealing with are not those reported by Jani and Halliburton
Baquedano *et al* [5]. The double exponential form of the decay suggests that ther
modes of charge transfer from/to Fe^{3+} impurity. The temperature indepen
probably involves a charge transfer between two Fe^{3+} and another close by de

The temperature dependent τ_2 has shown an activation energy of $0{\cdot}36 \times 10^{-3}$
is expected to be associated with the mobility of the charge carriers, as such a lo
cannot be associated with any e/h trap. Therefore the photoinduced electron tr
510 nm appears to be associated with

$$Fe^{3+} \underset{\text{light off}}{\overset{\text{light on}}{\rightleftharpoons}} Fe^{4+} \text{ process.}$$

The life time of decay constants extrapolated to room temperature was fou
≈ 20 s. It may be pointed out that Attard and Brown [7] using a two wav
experiment have postulated the existence of trapping centres with 100 ms, 120 s

faster in Attard and Brown [7]. The apparent differences of 100 ms and 20 s arise due to the infinite fringe width approximation valid for uniform illumination in EPR, in contrast to the much smaller fringe width in two-wave mixing experiments.

In summary, by EPR experiments we have shown that $Fe^{3+} \leftrightarrow Fe^{4+}$ processes are involved, without any associated deep trap, in photoinduced charge transfer.

References

[1] P Günter and J P Huignard (eds), *Topics in applied physics: photorefractive materials and their applications I* (Springer-Verlag, 1988)
[2] A M Glass, *Opt. Eng.* **17**, 47 (1978)
[3] N K Porwal, Mithlesh Kumar and M D Sastry, *Pramana – J. Phys.* **47**, 481 (1996)
[4] M G Jani and L E Halliburton, *J. Appl. Phys.* **64**, 2022 (1988)
[5] J A Baquedano, F J Lopez and J M Cabrera, *Solid State Commun.* **72**, 233 (1989)
[6] S C Abrahams, P B Jamieson and J L Bernstein, *J. Chem. Phys.* **47**, 4034 (1967)
[7] A E Attard and T X Brown, *Optics* **25**, 3253 (1986)

Resonance de-enhancement in the $2^1 A_g$ state of *trans*-azobenzene

NANDITA BISWAS and SIVA UMAPATHY*
Department of Inorganic and Physical Chemistry, Indian Institute of Science, Bangalore 560012, India
*Author to whom correspondence should be addressed
Email: umapathy @ ipc.iisc.ernet.in

MS received 20 August 1996; revised 2 December 1996

Abstract. We analyze the origin of de-enhancement for a number of vibrational modes in the 2^1A_g excited state of *trans*-azobenzene. We have used the time-dependent wave packet analysis of the RR intensities by including the multimode damping effects in the calculation. This avoids the use of unrealistically large values for the damping parameter. It is concluded that the de-enhancement is caused by the interference between the two uncoupled electronic states, and that the intensities observed under the so-called symmetry forbidden $2^1A_g \leftarrow 1^1A_g$ transition are purely due to resonance excitation. It is also observed that the use of the time-dependent approach to study the de-enhancement effects caused by multiple electronic states on the RR intensities is not necessarily useful if one is interested in the structural dynamics.

Keywords. Resonance Raman intensities; de-enhancement; time-dependent wave-packet analysis; *trans*-azobenzene.

PACS No. 33·20

1. Introduction

Resonance Raman (RR) intensities observed at different excitation wavelengths, termed the Raman excitation profiles (REPs), can be used to infer structure and dynamics in the resonant excited state [1–3]. In general, REPs provide information on the vibrational mode-dependent dynamics, in contrast to an absorption spectrum, which contains information on all the vibrational modes associated with that particular transition. Thus, RR intensities have been utilized constructively, through modeling and simulation, to relate to the distortions in the excited state of a given vibrational mode [1–4]. However, the intensities observed experimentally are occasionally far less than expected under resonance excitation, which has been ascribed to de-enhancement effects [4–18].

Raman intensity is proportional to the modulus square of transition polarizability ($\alpha_{f \leftarrow i}$), which is given by Kramers–Heisenberg–Dirac (KHD) expression [19, 20] and depends on the electronic transition moment (M), the vibrational overlap factors and the energy difference between the incident laser light and the energy gap between ground and excited electronic levels. Assuming very small dependence of M on the nuclear coordinate Q, it can be expanded in Taylor's series about the ground state equilibrium geometry (Q_0). Thus

$$M(Q) = M_0 + \sum_j (\partial M/\partial q_j)_0 q_j + 1/2 \sum_{j,k} (\partial^2 M/\partial q_j \partial q_k)_0 q_j q_k + \cdots . \tag{1}$$

The first term M_0 which is independent of the nuclear coordinate Q has maximum contribution to the Franck–Condon (A') term of the transition polarizability under resonance excitation. Thus, the vibrations that are totally symmetric can be strongly A'-term enhanced, only when there is significant distortion upon electronic excitation which leads to considerable values for the vibrational overlap integrals. A'-term gains importance only when resonance is approached and thus implicitly depends on nuclear coordinate displacement.

Due to the explicit dependence of M on Q (i.e. the first order term in (1)), vibronic coupling may occur within the same electronic state s (viz. $\langle s|h_a|s\rangle$, where $h_a \equiv (\delta H/\delta Q_a)Q_0$ is the coupling operator and the subscript a refers to the normal mode. This gives rise to the A term contribution to the transition polarizability or, between two different electronic states e and s (viz. $\langle s|h_a|e\rangle$ i.e. B term contribution to the transition polarizability). A and B terms are important when incident energy is off-resonant from a particular electronic state.

The origin of de-enhancement in the REPs is well documented [9, 14, 16, 21] as due to the interference from an electronic state other than the resonant excited state. However, the modelling of these effects depends very much on such factors as the energy difference between the resonant and interfering state, the transition moments of the two electronic states, nature (spin state, symmetry and polarization) of the two states involved and the vibronic coupling between them. The A and B terms arising due to vibronic coupling may interfere with the strongly resonant (Franck–Condon) A'-term of the polarizability tensor to give an anti-resonance effect in the REP of a totally symmetric vibration. This approach has been utilized successfully for a number of systems [4–7, 9]. Another plausible explanation of the observed de-enhancement is the interference between the resonant scattering A'-terms of $\alpha_{f\leftarrow i}$ from two different electronic states e (the resonant state) and s (the interfering state). When the scattering tensor $\alpha_{f\leftarrow i}$ contains contributions from A'_e (i.e. the resonant electronic state 'e') and A'_s (viz. the pre-resonant state 's'), the RR intensity (I_R) is proportional to the product of the scattering tensors $\alpha_{f\leftarrow i}$ and its complex conjugate, i.e.

$$I_R \propto \alpha_{f\leftarrow i} \alpha^*_{f\leftarrow i} \tag{2a}$$

or

$$I_R \propto (A'_{res} + A'_{pre})(A'^*_{res} + A'^*_{pre}) \tag{2b}$$

or

$$I_R \propto |A'_e|^2 + |A'_s|^2 + A'_e A'^*_s + A'_s A'^*_e . \tag{2c}$$

Thus, destructive or constructive interference may occur depending on the sign and relative magnitude of the respective polarizability terms [9(a), 16].

Recently, a time-dependent wave packet dynamical approach has been presented by Shin and Zink [16], taking into consideration the correlation functions of two excited approach deals with individual modes and therefore involves large damping constants [16]. In this paper we have utilized a similar approach to study the REPs of *trans*-azobenzene (TAB) but included a multi-mode damping parameter, such that the damping factor used is more realistic than the earlier values. We find that the time-dependent approach is very effective in predicting the origin of de-enhancement.

TAB absorption spectrum exhibits a lowest energy symmetry forbidden ($2^1A_g \leftarrow 1^1A_g$) transition with unusually large absorption coefficient, in addition to the strongly allowed ($1^1A_u \leftarrow 1^1A_g$) transition [21]. As a result, TAB undergoes isomerization via two different mechanisms, depending on the excitation wavelength [23–25]. In an earlier paper [25] we have modelled the REPs of ten totally symmetric (polarized) fundamentals recorded under the $2^1A_g \leftarrow 1^1A_g$ transition, using Heller's wavepacket formalism. A comparison of the simulated REPs with experimental results shows that only five out of ten vibrational modes fit very well with the experimental results. The other five modes have structure in the REPs, thus deviating considerably from the theoretically predicted profiles [25]. Further, the experimental REPs are expected to follow the shape of the absorption spectrum if the intensities observed are purely due to resonant excitation [1, 26, 27]. But in TAB, the experimetal REPs for a few vibrational modes at 1439, 1312, 1181, 1142 and 1000 cm^{-1} show a decrease in Raman intensity near the maximum of $2^1A_g \leftarrow 1^1A_g$ absorption band.

In this paper, we have analyzed the REPs of TAB using Zink's approach [16] and find that the experimental profile can be successfully simulated if the influence of an additional electronic state is taken into account. In particular, we have addressed the question of using Zink's approach to studying the resonance de-enhancement for polyatomic systems, where mode-dependent dynamics is different in the two interfering states. This is an important question considering that the earlier studies [16] based on this approach have assumed the ratio of vibrational displacements to be the same in the two electronic states. Maintaining the ratio of displacements will only be valid, if the Raman intensities retain the same ratio among all the modes of interest in the two electronic states (which is rarely the case in most systems).

Further, a comparative study of the results obtained from two-mode as well as multi-mode calculations is presented. These results show that the de-enhancement is caused by interference between two uncoupled excited electronic surfaces and the simulated values of displacements obtained from multi-mode calculations lead to valuable clues regarding the extent of contribution of a given vibration to the dynamics involved, on excitation.

2. Theory and computational methods

Resonance Raman intensities can be calculated using either the sum over states [28, 29] or the time-dependent method [22]. In the time-dependent picture, the Raman amplitude for the transition from the initial state $|i\rangle$ to the final state $|f\rangle$ (where both the vibrational eigenstates $|i\rangle$ and $|f\rangle$ correspond to the electronic ground state) is expressed as a half Fourier transform of the Raman correlation function $\langle f|i(t)\rangle$,

$$\alpha_{f\leftarrow i}(E_L)=\frac{i}{\hbar}\int_0^\infty M^2\langle f|i(t)\rangle \exp\left[i\frac{(E_L+E_i)t}{\hbar}-\frac{\Gamma t}{\hbar}\right]\mathrm{d}t, \tag{3}$$

where, E_i the zero point energy of the ground electronic state, E_L the energy of incident photon, M the electronic transition dipole moment, and Γ the pheno enological line width parameter, $\hbar = h/2\pi$ (h being Planck's constant), and $|i(t)\rangle$ is evolving wavepacket at various intervals of time, i.e,

$$|i(t)\rangle = \exp\left(-\frac{iH_{\text{ex}}t}{\hbar}\right)|i\rangle,$$

where, H_{ex} is the excited state Hamiltonian. The Raman intensity can thus be relate the polarizability as folllows

$$I_{\text{R}} \propto E_L E_{\text{S}}^3 |\alpha_{f\leftarrow i}|^2$$

where, E_{S} is the energy of the scattered photon.

The autocorrelation $\langle i|i(t)\rangle$ and the Raman correlation function $\langle f|i(t)\rangle$ are comput using the extended Simpson's rule [30, 33] from the time-evolving wavepacket $|i(t)\rangle$. full Fourier transform of the former gives the absorption spectrum, and the half Fou transform of the latter gives the REP. Thus, when there is only one excited electronic st the expression for polarizability ($\alpha_{f\leftarrow i}$) in the time-domain (eq. (3)) holds good. But whe consider two excited electronic states, interfering and resonant states, the Raman corr tion functions are computed separately, multiplied by the square of the respective transit dipole moments and then summed up to give the total correlation function. The Fourier transform of the total Raman correlation function gives the final expression for polarizability ($\alpha_{f\leftarrow i}$) in a two state model.

$$\alpha_{f\leftarrow i}(E_L) = \frac{i}{\hbar}\int_0^\infty (M_{\text{R}}^2 O_{\text{R}} + M_{\text{I}}^2 O_{\text{I}})\exp\left[i\frac{(E_L+E_i)t}{\hbar} - \frac{\Gamma t}{\hbar}\right]\mathrm{d}t,$$

where M_{R} and M_{I} are the transition dipole moments and O_{R} and O_{I} are the Ra correlation functions of the resonant and interfering excited electronic states resp ively. From this expression, it is seen that the factors which influence the polarizab are (i) the relative transition dipole moments of the resonant and interfering exc electronic states (since $\alpha_{f\leftarrow i}$ is related to the square of the transition dipole moment, state having the largest transition dipole moment may dominate the REPs), (ii) displacement (Δ) of the excited potential surfaces from the minimum of the ground s along the normal modes, and (iii) the damping factor Γ.

The de-enhancement phenomenon observed in TAB has been systematically stu using the above approach. In particular, all those factors which significantly influe the RR intensities have been critically considered. Both two mode and multi-m calculations have been carried out and a comparative picture is presented in §3. In absence of Duschinsky mixing, the multi-mode Raman correlation function is give the product of correlation function $\langle f_k|i_k(t)\rangle$ for the Raman active mode (k) and autocorrelation function $\langle i_j|i_j(t)\rangle$ for the rest of the vibrational modes (j).

$$\langle f|i(t)\rangle_M = \langle f_k|i_k(t)\rangle \prod_{j=1,\, j\neq k}^{N-1} \langle i_j|i_j(t)\rangle,$$

where N is the total number of vibrational modes present. The polarizability $\alpha_{f\leftarrow i}$ for

Using (3) where the evolution of the wavepacket is carried out with the grid technique [30–32], a model calculation was done for a two-mode system in order to test the validity of our computational method. The fitting parameters used here are exactly the same as those used in Zink's model [16]. The frequencies of two modes are 500 and 700 cm^{-1} respectively. The zero-zero energies for the resonant (E^{R}_{00}) and the interfering (E^{I}_{00}) excited electronic states are 20 000 cm^{-1} and 30 000 cm^{-1}. The dimensionless displacement (Δ) is 1·0 for the two modes in both the excited electronic states. The value of the homogeneous broadening (Γ) is 700 cm^{-1}, and the ratio of the squares of the transition dipole moments in the two electronic states ($M_{\mathrm{R}}^2/M_{\mathrm{I}}^2$) is 1/60. The simulated real and imaginary parts of $\alpha_{f\leftarrow i}$ for the two electronic states are shown in figure 1 (a), and the REPs for three cases when (*i*) $M_{\mathrm{I}} = 0$, (ii) $M_{\mathrm{R}}^2/M_{\mathrm{I}}^2 = 1/30$ and (iii) $M_{\mathrm{R}}^2/M_{\mathrm{I}}^2 = 1/60$ are shown in figure 1(b). These results are consistent with the literature data [16] confirming our computational algorithm.

3. Results and discussion

The absorption spectrum and the REPs of all the ten Raman active vibrational modes of TAB under the symmetry forbidden ($2^1A_g \leftarrow 1^1A_g$) transition (assuming a point

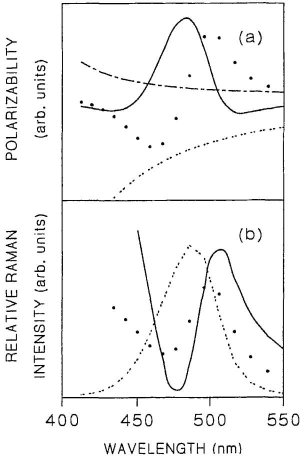

Figure 1. **(a)** Real and imaginary parts of the polarizability (α) for two electronic states. Real (........ resonant state, and –·–·– interfering state) and imaginary (—— resonant state and ------- interfering electronic state) parts for the 700 cm^{-1} mode when $M_{\mathrm{R}}^2/M_{\mathrm{I}}^2 = 1/60$. **(b)** Resonance Raman excitation profiles for the 700 cm^{-1} mode when (i) $M_{\mathrm{I}} = 0$ (------), (ii) $M_{\mathrm{R}}^2/M_{\mathrm{I}}^2 = 1/30$ (.........) and, (iii) $M_{\mathrm{R}}^2/M_{\mathrm{I}}^2 = 1/60$ (——). The displacements are 1.0 for the modes and $\Gamma = 700$ cm^{-1} in both excited

group of C_i symmetry [34]) was simulated on a single excited potential energy surface [25]. Since the low temperature absorption spectrum of TAB does not show any vibrational structure in the visible region, we have considered the short time dynamics to analyze the RR intensities. For systems undergoing short-time dynamics it is assumed that the resonance Raman intensities (I_R) of the normal modes are

$$I_R \propto \Delta^2 \omega^2, \tag{8}$$

where Δ and ω are the dimensionless displacement of the excited electronic state with respect to the ground state and the frequency for the normal coordinate in cm^{-1} respectively. Also, the TAB absorption spectrum as well as Raman spectrum is insensitive to solvent effects. As a result, the effect of solvent induced broadening function has not been taken into consideration.

REPs of various vibrational modes of TAB in resonance with the absorption band of $2^1A_g \leftarrow 1^1A_g$ transition have been calculated [25] using this time-dependent approach assuming (a) all the potential energy surfaces are harmonic except the torsional mode which is considered to be linear and dissociative in the excited electronic state, (b) the normal coordinates are not mixed in the excited state (no Duschinsky effect), (c) the transition dipole moments are constant, and (d) the frequencies for all the vibrational modes are the same in both ground and excited electronic states. The propagation of the wavepacket on the excited electronic surface has been carried out using the time-dependent quantum-mechanical (TDQM) method involving a grid technique [30–32]. The REPs, as shown in figure 4 of [25] did not fit the experimental data accurately for five of the vibrational modes. In all these cases the experimental REPs show structure with an inflexion near the absorption spectral maximum and a peak towards the higher wavelength.

In order to account for the possibilities of the structure in REPs of five totally symmetric modes of TAB, we have measured (i) the positions of the peak maximum and that of the dip, (ii) the full width at half maximum (FWHM) of the peak as well as the full width at half depth (FWHD) of the dip and these are given in table 1 for the respective modes.

First concentrating on the occurrence of the peak, it is found that the position of the peak maximum is about 478–516 nm (see table 1). As observed earlier by Rimai *et al* [15(a)] for naphthalene, the peak positions in REPs could correspond to a dipole forbidden transition. In their study, Rimai *et al* concluded that the peak observed was

Table 1. Trans-azobenzene Raman frequencies (ω in cm^{-1}), position of the dip and the peak in the REPs of the modes undergoing de-enhancement and their FWHM.

Frequency (ω cm^{-1})	Position of dip (nm)	FWHD of dip (cm^{-1})	Point of peak (nm)	FWHM of peak (cm^{-1})
1439	458	–	478	–
1312	441	2098	516	4775
1181	441	2304	496	2449
1142	441	2070	497	2850
1000	465	2446	512	2486

due to a triplet state since the phosphorescence peak maximum matched with that of the REP peak. Similarly, in TAB, excited states inaccessible by an electric dipole transition may be considered responsible for the peak maximum in the REPs. In fact, Monti *et al* [35] have predicted, from *ab initio* calculations that the presence of a dipole forbidden state with an E_{00} value of 591·3 nm. but, as shown in table 1, the peak maxima for these vibrations are at $\sim 478-516$ nm and the FWHM of the peak is $\sim 60-70$ nm for most of the modes, with the exception of 1312 cm^{-1} (FWHM $\sim$ 130 nm). Therefore, it is unlikely that a dipole forbidden state is responsible for the structure observed in the REPs. Moreover, no experimental evidence for the presence of a triplet state in TAB has been reported so far, which provides further justification for discarding the presence of a dipole forbidden state as a probable reason for the peak observed in REPs.

Next we consider the inflexion observed in the REPs, which can be attributed to resonance de-enhancement. The loss of RR intensity can be ascribed either to (a) destructive interference between the real or imaginary parts of the polarizability of two nearby electronic states or, (b) population interference [17] (curve crossing) between the resonant and the nearby electronic states.

In the case of (a), the relative magnitude of interference on the observed polarizability mainly depends on (i) the energy difference, (ii) individual vibrational mode displacements and (iii) transition dipole moments of the interfering and resonant electronic states. In the case of (b), specific signatures in the experimentally observed REPs provide clues to the existence of curve crossing. In particular, it has been suggested [17] that the width at half depth (FWHD) of the de-enhanced REP is expected to be of the order of one vibrational quantum and the de-enhancement minimum of the resonant REP occurs near the energy at which the two potential energy curves cross. The FWHD and the wavelength at which the lowest RR intensity is observed for all the Raman active vibrations of TAB are given in table 1 First, the width at half depth of the de-enhanced REPs, in our case, is obviously not of the order of one vibrational quantum. Secondly, the lowest intensity is observed at or near the peak maximum ($\sim$ 441 nm) of the electronic absorption spectrum, which is more an indication of destructive interference of polarizability tensors of the two electronic states [16, 17] (*vide infra*). Thus, occurrence of population interference due to curve crossing is unlikely and it seems reasonable to conclude that the de-enhancement must originate from a destructive interference induced by a state close to the resonant electronic state.

The origin of de-enhancement in the case of (a) occurs when either (i) both the interfering and resonant electronic excited states are well separated in energy ($\sim$ 10 000 cm^{-1}) and the transition dipole moment (M_{I}) for the interfering state is much higher than the transition dipole moment (M_{R}) for the resonant electronic state, or, (ii) both the interfering and resonant electronic excited states are close in energy ($\sim$ 1000 cm^{-1}) and the values of M_1 and M_{R} are comparable. Both (i) and (ii) can be explained in terms of destructive interference of the imaginary parts of the polarizability ($\alpha_{f\leftarrow i}$). In the previously studied examples [16] it is found that this kind of interference due to the imaginary parts leads to a minimum in the REPs at wavelengths near the maximum of the resonant absorption band, as observed in this study on TAB.

In addition, in the case of TAB there are no electronic states close to the

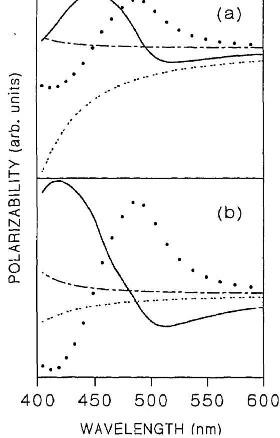

Figure 2. Real and imaginary parts of the polarizability (α) for two electronic s Real (......... resonant state, — - — interfering state) and imaginary (—— reso state and ------ interfering electronic state) parts for **(a)** 1181 cm^{-1} mode **(b)** 1491 cm^{-1} mode when $M_R = 0{\cdot}8$ Å and $M_I = 2{\cdot}52$ Å. Δ_1 and Δ_2 for 1181 cm^{-1} and 1491 cm^{-1} modes are given in table 3. E^R_{00} and E^I_{00} are 20470 c and 27710 cm^{-1} respectively and $\Gamma = 1200$ cm^{-1} for both excited states.

corresponding to the ($1^1A_u \leftarrow 1^1A_g$) transition is present, that is well separated in en from the resonant electronic transition and that has a much higher value of transition dipole moment. Also, unsuccessful attempts were made to fit the experi tal REPs by considering the presence of a dipole forbidden state (*vide supra*) lying to the resonant electronic state with similar transition probabilities. Thus, in present study, we find that the possibility of interference between ($2^1A_g \leftarrow 1^1A_g$) ($1^1A_u \leftarrow 1^1A_g$) transitions are most probable.

The REPs for the ring H rock ($\omega = 1181$ cm^{-1}) and ring stretch ($\omega = 1491$ cm TAB in resonance with the ($2^1A_g \leftarrow 1^1A_g$) transition and interference ($1^1A_u \leftarrow 1^1A_g$) transition have been simulated, first, by taking only these two modes consideration. These two modes (1181 exhibiting de-enhancement and 1491 wit de-enhancement in the experimental REPs) were specifically chosen to test the val of the use of two mode calculations as has been successfully carried out earlier [16 other systems. The zero-zero energies (E^R_{00} and E^I_{00}) for the first and the se electronic states and the transition dipole moments (M_R and M_I) which were obta from the absorption spectrum are 20470 cm^{-1} and 27710 cm^{-1} and 0·8 Å and 2· respectively. Results obtained from the two mode calculations are shown in figu

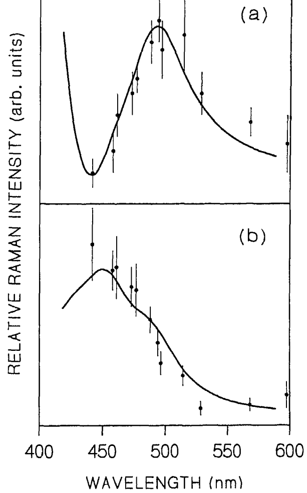

Figure 3. REPs for **(a)** 1181 cm^{-1} mode and **(b)** 1491 cm^{-1} mode obtained from two-mode calculations. Solid lines are the simulated curves and dotted line with error bar shows the experimental curve.

l 3. In figures 2(a) and 2(b), the real and imaginary parts of the polarizability tensor the two vibrational modes are shown. These simulations required large damping ameters ($\Gamma \sim 1200$ cm^{-1}). Initially, the values of dimensionless displacements of the modes are estimated from the experimental RR intensities under the resonant ctronic state, which after successive iterations give the best possible displacements that can reproduce the experimental REPs for the respective modes. The best fit nensionless displacements Δ_1 and Δ_2 are 1·5 and 1·45 for 1181 cm^{-1} (Δ_1 and Δ_2 for 1491 cm^{-1} mode being 0·67 and 0·15) for figure 3(a) and 2·0 and 0·15 for 1491 cm^{-1} and Δ_2 for the 1181 cm^{-1} mode being 0·67 and 1·45) for figure 3(b). Large Δ_2 ues result in strong de-enhancement, whereas small Δ_2 values give no de-enhance- nt in the REPs. Also, small Δ_1 values give low FWHM for the peak and the position reduced intensity is observed at higher wavelengths. The reverse is true for large Δ_1 ues. A strong anti-resonance effect is observed near the absorption maximum of the nmetry forbidden transition in 1181 cm^{-1} (figure 3(a)). This is because of destructive erference between the imaginary parts of the polarizability tensor ($\alpha_{f\leftarrow i}$) for the two ited electronic states. The imaginary parts of both resonant and interfering states ve comparable magnitudes and are opposite in sign near the maxima of the first giving rise to reduced intensity at that position. Since the magnitude of the imagin part of ($\alpha_{f\leftarrow i}$) for the interfering electronic state, 1491 cm^{-1}, is negligible in compari to that of the resonant electronic state (figure 2(b)), the REP for the 1491 cm^{-1} m (figure 3(b)) is dominated by the polarizability of the latter electronic state, and he no interference effect is seen in this case. These figures clearly demonstrate the effec Δ_1 and Δ_2 on the REPs of TAB, as was shown previously by Zink *et al* [16] for a mo system. An important point to note is that it has been possible to maintain the ratio the displacements (i.e. not consistent with experimental RR intensities) of the t modes in order to match the simulated REPs to the experimental ones. However, if take into consideration all the ten modes, then the simulated REPs fit well with thos the experiment, as shown below.

Clark *et al* [36] suggested that the excited state lifetime Γ in most cases is small, a rarely exceeds 0.5ω (ω being frequency in wave numbers of the vibrational mode), for the two mode calculations a fairly large Γ value has been used. Hence, we carried

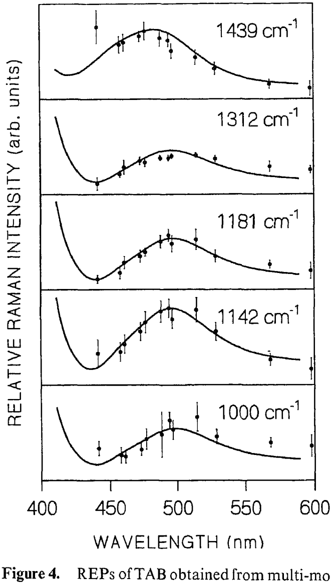

Figure 4. REPs of TAB obtained from multi-mode calculations. Solid lines are simulated curves and dotted line with error bar shows the experimental cu $E^{\mathrm{R}}_{00} = 20470$ cm^{-1} and $E^{\mathrm{I}}_{00} = 27710$ cm^{-1}. Γ is 50 cm^{-1}, $M_{\mathrm{R}} = 0.8$Å $M_{\mathrm{I}} = 2.52$Å.

a multi-mode calculation involving all the ten Raman active totally symmetric modes of TAB in order to simulate the REPs for the five vibrational modes undergoing de-enhancement. Multi-mode simulations not only require small values of Γ but are also much more realistic. The REPs for the modes 1439, 1312, 1181, 1142 and 1000 cm^{-1} are shown in figure 4. The $E^{\rm R}_{00}$ and $E^{\rm I}_{00}$ values for the two electronic states and $M_{\rm R}$, $M_{\rm I}$ are same as that of the two mode calculation. The damping parameter Γ is 50 cm^{-1}. Thus, from figure 4 it can be seen that multi-mode calculations, which include an interfering state, reproduce the experimental REPs well for the five modes undergoing de-enhancement. In figure 4, only the modes that display de-enhancement effects are shown, but simulations have also been carried out for all the ten modes. These compare well with the REPs observed experimentally in terms of the relative intensities, band widths and band positions. For the sake of simplicity, the dimensionless displacements (Δ) for the excited electronic potential energy surfaces of all the totally symmetric vibrations have been taken to be positive, but in reality displacements can be either positive or negative. Further, using the values of Δs, $M_{\rm R}$, $M_{\rm I}$, $E^{\rm R}_{00}$, $E^{\rm I}_{00}$ and Γ used in the REP simulation, the absorption spectrum for the $(2^1A_g \leftarrow 1^1A_g)$ transition is computed. A comparison of the simulated and the experimental absorption spectrum of TAB in CCl_4 is shown in figure 5. A very good fit of this simulation with the experimental spectrum confirms that the assumptions and parameters used for the REP simulations are valid. In table 2 the vibrational frequencies, their assignments and the simulated displacement values are given. As suggested by Shin and Zink [16], it is seen from table 2 that the five vibrational modes exhibiting de-enhancement do have the expected large Δ_2 values compared to all the other vibrational modes.

This confirms that the de-enhancement effect is caused by the interference due to an electronic state with a transition moment larger than the resonant state. Further, it may be concluded that there is no evidence of a curve crossing between the two electronic states. Since the simulations have been carried out with the symmetry forbidden state as

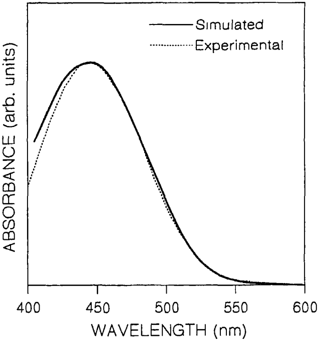

Figure 5. Simulated (————) and experimental (.....) absorption spectrum of

Table 2. Description of vibrations of *trans*-azobenzene, their Raman frequencies (ω in cm^{-1}) and respective dimensionless displacements (Δ_1 and Δ_2) in the resonant and interfering electronic states.

Description of vibrations	Frequency (ω in cm^{-1})	Δ_1	Δ_2
C–C–H ben	939	0·47	0·05
ring def	1000	0·60	1·10
C–N str	1142	1·03	1·70
ring H rock, C–C–H ben	1181	0·67	1·45
ring str, N=N str, C–C–H ben	1312	0·28	0·65
N=N str	1439	0·95	0·70
ring str	1470	0·76	0·15
ring str	1491	0·67	0·15
ring str	1592	0·49	0·08

def: deformation, ben: bending, str: stretching. Linear dissociative mode: $\omega = 912\ \mathrm{cm}^{-1}$ and slope $\beta = 980\ \mathrm{cm}^{-1}$.

Table 3. *Trans*-azobenzene excited state displacements for $1181\ \mathrm{cm}^{-1}$ and $1491\ \mathrm{cm}^{-1}$ vibrations.

Frequency	Two mode		Ten mode	
(ω in cm^{-1})	Δ_1	Δ_2	Δ_1	Δ_2
1181	1·5	1·45	0·67	1·45
1491	2·0	0·15	0·67	0·15

the resonant electronic state, we infer that the intensities observed are due to pure resonance for all the vibrational modes observed, albeit some of the modes show de-enhancement. However, we note that in order to unequivocally confirm that the intensities are due to resonance, further experiments are being carried out to observe the overtone intensities and also to measure the depolarization ratios.

4. Displacements under de-enhancement

A comparative account of displacements obtained from two mode and ten mode calculations are presented in table 3 for 1181 and $1491\ \mathrm{cm}^{-1}$, respectively. From the table it is evident that simulations taking only two modes into consideration overestimate the dimensionless displacement in the resonant electronic state, and hence the displacement ratios are not maintained in relation to the experimental intensities. We hasten to add that attempts to retain the ratios of the displacements at values same as the ratio of experimental resonant intensities, could not reproduce the experimental REPs very well.

It is recognized, however, that maintaining the ratio of displacements of two modes and Zink [16]. But, in cases like TAB it is not applicable since it is already known that two different types of dynamics (therefore, different ratios of relative Raman intensities for the various vibrational modes) is expected on excitation under the two electronic states in consideration [23–25]. Thus, the displacements for the vibrational modes in the two different electronic states are unlikely to retain the same ratio. Further, even if we assume the same ratio of displacements in both the electronic states, it is not possible to directly relate the two sets of displacements (Δ_1 and Δ_2) to the structural distortions under the single resonant excitation, Individual displacement values, corresponding to a given vibrational mode, in dimensionless units when converted to actual bond length or bond angle changes can give us an idea regarding the distortions experienced by the molecule upon photo-excitation [1–3, 16], The two sets of displacements obtained here for each mode, however, can be used for a qualitative understanding of the extent of displacements of the various vibrational modes in the two electronic states. For example, the modes having large Δ_2 values undergo de-enhancement, suggesting that these modes are dynamically active (structurally distorted) both in $(1^1A_u \leftarrow 1^1A_g)$ and $(2^1A_g \leftarrow 1^1A_g)$ transitions, but the vibrations with small Δ_2 values undergo no de-enhancement and hence, are expected to be inactive in the $(1^1A_u \leftarrow 1^1A_g)$ transition.

In order to quantitatively relate the displacements to dynamics it is neccessary to determine a unique/single value for the displacement for each mode after the influence of an interfering state. Further work is in progress along this direction by treating the interference of the Franck Condon A'-term with the A-term from the $(1^1A_u \leftarrow 1^1A_g)$ transition leading to reduced intensity of totally symmetric modes in the region of symmetry forbidden $(2^1A_g \leftarrow 1^1A_g)$ transition.

From this theoretical study it is concluded that utilizing time-dependent wave packet calculations, de-enhancement observed in the REPs in resonance with a symmetry forbidden transition can be accounted for as due to interference from a higher energy transition. In spite of its simplicity and accurate description of the de-enhancement effect, the time-dependent approach cannot effectively be used to derive excited state distortions of vibrational modes in which de-enhancement is severe. This is caused by the use of correlation functions in which displacements in both the electronic states are taken into consideration. To study the dynamics in the excited state for vibrational modes involving de-enhancement, it would be realistic to treat vibronic coupling within the same electronic state as the major source of interference.

Acknowledgements

The authors would like to acknowledge the financial assistance from the National Laser Program, Department of Science and Technology, the Council of Scientific and Industrial Research, Government of India and the Jawaharlal Nehru Centre for Advanced Scientific and Industrial Research.

References

[1] A B Myers and R A Mathies, in *Biological Applications of Raman Spectroscopy* edited by T G Spiro (John Wiley and Sons Inc., New York, 1987) vol. 2, p. 1

[2] J I Zink and K-S K Shin, in *Advances in Photochemistry* (John Wiley and Sons Inc., New

[3] A B Myers, in *Laser Techniques in Chemistry* edited by A B Myers and T R Rizzo (John Wiley and Sons Inc., New York, 1995) vol. 23, p. 325
[4] D L Phillips and A B Myers, *J. Chem. Phys.* **95,** 226 (1991)
[5] F Markel and A B Myers, *J. Chem. Phys.* **98,** 21 (1993)
[6] G A Schick and D F Bocian, *J. Raman Spectrosc.* **11,** 27 (1981)
[7] L A Nafie, R W Pastor, J C Dabrowiak and W H Woodruff, *J. Am. Chem. Soc.* **98,** 8007 (1976)
[8] (a) S P A Fodor, R A Copeland, C A Grygon and T G Spiro, *J. Am. Chem. Soc.* **111,** 5509 (1989)
(b) Y M Bosworth and R J H Clark, *J. Chem. Soc. Dalton Trans.* p. 1749 (1974)
(c) Y M Bosworth, R J H Clark and P C Turtle, *J. Chem. Soc. Dalton Trans.* p. 2027 (1975)
[9] (a) P Stein, V Miskowski, W H Woodruff, J P Griffin, K G Werner, B P Gaber and T G Spiro, *J. Chem. Phys.* **64,** 2159 (1976)
(b) B B Johnson and W L Peticolas, *Ann. Rev. Phys. Chem.* **27,** 465 (1976)
(c) T G Spiro and P Stein, *Ann. Rev. Phys. Chem.* **28,** 501 (1977)
[10] (a) M Z Zgierski, *J. Raman Spectrosc.* **6,** 53 (1977)
(b) M Z Zgierski, *J. Raman Spectrosc.* **5,** 181 (1976)
[11] G M Korenowski, L D Ziegler and A C Albrecht, *J. Chem. Phys.* **68,** 1248 (1978)
[12] S A Asher and C R Johnson, *J. Phys. Chem.* **89,** 1375 (1985)
[13] P Hildebrandt, M Tsuboi and T G Spiro, *J. Phys. Chem.* **94,** 2274 (1990)
[14] W Siebrand and M Z Zgierski, *J. Chem. Phys.* **71,** 3561 (1979)
[15] (a) L Rimai, M E Heyde, H C Heller and D Gill, *Chem. Phys. Lett.* **10,** 207 (1971)
(b) J Friedman and R M Hochstrasser, *Chem. Phys. Lett.* **32,** 414 (1975)
[16] K-S K Shin and J I Zink, *J. Am. Chem. Soc.* **112,** 7148 (1990)
[17] C Reber and J I Zink, *J. Phys. Chem.* **96,** 571 (1992)
[18] I W Sztainbuch and G E Leroi, *J. Chem. Phys.* **93,** 4642 (1990)
[19] H A Kramers and W Heisenberg, *Z. Phys.* **31,** 681 (1925)
[20] P A M Dirac, *Proc. R. Soc. London* **114,** 710 (1927)
[21] A C Albrecht and M C Hutley, *J. Chem. Phys.* **55,** 4438 (1971)
[22] (a) E J Heller, *J. Chem. Phys.* **62,** 1544 (1975)
(b) E J Heller, *J. Chem. Phys.* **68,** 2066 (1978)
(c) K C Kulander and E J Heller, *J. Chem. Phys.* **69,** 2439 (1978)
(d) S-Y Lee and E J Heller, *J. Chem. Phys.* **71,** 4777 (1979)
(e) E J Heller, *Acc. Chem. Res.* **14,** 368 (1981)
(f) A B Myers, R A Mathies, D J Tannor and E J Heller, *J. Chem. Phys.* **77,** 3857 (1982)
(g) D J Tannor and E J Heller, *J. Chem. Phys.* **77,** 202 (1982)
(h) E J Heller, R L Sundberg and D J Tannor, *J. Phys. Chem.* **86,** 1822 (1982)
[23] H Rau, in *Photochromism: Molecules and systems* edited by H Durr and H Bouas-Lauran, (Amsterdam, Elsevier, 1990) p.165
[24] H Rau and S Yu-Quan, *J. Photochem. Photobiol. A: Chemistry* **42,** 321 (1988)
[25] N Biswas and S Umapathy, *Chem. Phys. Lett.* **236,** 24 (1995)
[26] H Okamoto, H Hamaguchi and M Tasumi, *Chem. Phys. Lett.* **130,** 185 (1986)
[27] A B Myers and R A Mathies, *J. Chem. Phys.* **81,** 1552 (1984)
[28] J Tang and A C Albrecht, in *Raman Spectroscopy* edited by H A Szymanski (Plenum, New York, 1970) vol. 2, p. 33
[29] A C Albrecht, *J. Chem. Phys.* **34,** 1476 (1961)
[30] N Biswas, S Umapathy, C Kalyanaraman and N Sathyamurthy, *Proc. Indian Acad. Sci.* **107,** 233 (1995)
[31] R Kosloff, *J. Phys. Chem.* **92,** 2087 (1988)
[32] S O Williams and D G Imre, *J. Phys. Chem.* **92,** 3363 (1988)
[33] M Abramowitz and I A Stegun, *Handbook of Mathematical Function* (Dover, New York, 1968) p. 886
[34] B Tellerer, H H Hacker and J Brandmuller, *Indian. J. Pure Appl. Phys.* **9,** 903 (1971)
[35] S Monti, G Orlandi and P Palmieri, *Chem. Phys.* **71,** 87 (1982)
[36] R J H Clark and T J Dines, *Angew Chem. Int. Ed. Engl.* **25,** 131 (1986)

Pb-doped Bi-4334 type glass and the corresponding glass-ceramic superconductor

SOURI BANERJEE, S CHATTERJEE and B K CHAUDHURI
Department of Solid State Physics, Indian Association for the Cultivation of Science, Calcutta 700 032, India

MS received 5 August 1996; revised 26 November 1996

Abstract. The room temperature reflectance spectra in UV–VIS–NIR region (energy range of 0·6 to 6·2 eV) for glassy, partially crystalline and its fully crystalline superconducting ceramic phases of $Bi_{3\cdot9}Pb_{0\cdot1}Sr_3Ca_3Cu_4O_x$ have been studied by Kramers–Kronig (KK) analysis. A comparative study of the energy loss function $[-\mathrm{Im}(1/\varepsilon)]$ and the absorption coefficient $[\alpha(E)]$ has been done. Excitons in the superconducting phase hitherto evidenced by the authors are located in the polarizable layers of the superconducting cuprate and their implications for superconductivity have been pointed out. An estimate of the optical band gap energy (E_g) has also been made from the linear fit of α^2 vs. E curve for the superconducting phase. Jezierski's method of R-extrapolations in the higher energy has been used to show that both methods yield results that agree quantitatively and can be relied upon.

Keywords. Optical reflectivity; superconductivity; exciton.

PACS Nos 63·61; 74·25

The glassy precursors for high T_c superconductors like $Bi_{4-n}Pb_nSr_3Ca_3Cu_4O_x$ ($n=$ 0·1–1·0) are important for its possible applications in making superconducting wires/tapes, thick films etc. [1–5a]. These precursor glasses also show some interesting electric and dielectric properties [2], not exhibited in other transition metal oxide glasses which do not become superconducting in their respective crystalline (ceramic) phases. Thus the study of optical properties of these glasses and the corresponding superconducting glass-ceramics appears to be interesting. To the best of our knowledge, no such comparative analysis of the reflectance spectra of the glassy precursors and the corresponding superconducting glass-ceramic has been done so far.

In the present paper we report, for the first time, results of Kramers–Kronig (KK) analysis of the room temperature reflectivity spectra (in the photon energy range 0·6–6·2 eV) of the as-quenched glassy phase and the corresponding partially and fully crystalline phases of $Bi_{3\cdot9}Pb_{0\cdot1}Sr_3Ca_3Cu_4O_x$. Optical parameters like the energy loss function $[-\mathrm{Im}\{1/\varepsilon(E)\}]$ and the absorption coefficient $\alpha(E)$ have been calculated for all the three phases. In our previous communication [6] we have discussed the results of KK analysis of the superconducting phase only where we have shown evidences of the existence of Wannier excitons in Bi-based superconducting cuprates. In this brief report, apart from a comparative analysis of the three subsequent phases of $Bi_{3\cdot9}Pb_{0\cdot1}Sr_3Ca_3Cu_4O_x$, we have discussed the mode of excitonic absorption and the corresponding energy band gap. We have also tried to locate possible positions of the exciton peaks and discuss their role in bringing about superconductivity in these layered cuprates. At the end, we have briefly discussed the different aspects regarding the choice of high energy ($E \geqslant 6{\cdot}2$ eV) extrapolating functions used by other researchers, needed to carry out the KK analysis. This is important because the artificial R-extrapolation never gives the exact value of the phase (θ) which agree with the experimental reflectance curve and so there is always an experimental error in the values of optical constants in the experimental range calculated by the KK analysis.

The preparation technique of the Pb doped Bi–Sr–Ca–Cu–O glasses and the corresponding glass-ceramic have been discussed in detail elsewhere [7]. The glassy and the partially-crystalline phases of $Bi_{3{\cdot}9}Pb_{0{\cdot}1}Sr_3Ca_3Cu_4O_x$ are semiconducting whereas the glass-ceramic phase (having mostly 2212 phase) is superconducting with $T_{co} \sim 72$ K [7]. The reflectivity measurements have been performed on the Pb doped Bi–Sr–Ca–Cu–O systems for all its three subsequent phases discussed above, separately, with a UV–VIS–NIR spectrophotometer (Hitachi U3410) in the spectral range of 200–2200 nm at 297 K and at normal incidence.

The basic principles involved to carry out KK analysis and its fruitful application to extract different optical parameters of a physical system have been discussed in detail in our previous communication [6]. It is seen that the low energy ($E \leqslant 0{\cdot}6$ eV) extrapolation function used by us has been consistent with reproducible data for different high T_c superconducting oxides. But in the higher energy range ($E \geqslant 6{\cdot}2$ eV) several approaches like Philipp–Taft formula [8] or Jezierski formula [9] or Roessler formula [10] have been used. We feel that as there are more than one method for high energy extrapolation it needs an examination as to how well they can be relied upon to yield comparable data. We approach the problem in the following way:

According to Philipp–Taft formula one has, $R(E) = R(E_b)(E_b/E)^A$ where, E_b is the upper limit of the energy range used and A is a constant where the continuity condition for $R(E)$ at $E = E_b$ is included explicitly. Jezierski used the following formula for $R(E)$ viz.

$$R(E) = R(E_b)(E_b/E)^{\gamma} \quad \text{for} \quad E \geqslant E_b, \tag{1}$$

where, $\gamma = [A_1(E_b/E)^{B_1} + A_2(E_b/E)^{B_2} + 4]$. The values of B_1 and B_2 are chosen arbitrarily from the consistency conditions and A_1, A_2 are determined from a set of equations. We have applied this formula to evaluate $\alpha(E)$ for the superconducting phase with typical values of $B_1 = 0{\cdot}5$ and $B_2 = 10$ following the arguments of Jezierski. The values A_1 and A_2 are then obtained by fitting (1) to the data points in the range of 5–6·2 eV by the least squares method and then refining these values of A_1 and A_2 by the parameter search programme.

Figures 1a–c describes the behaviour of the measured reflectance $R(E)$ for the respective three phases of the Pb doped Bi–Sr–Ca–Cu–O system. The reflectance spectra for the superconducting $Bi_{3{\cdot}9}Pb_{0{\cdot}1}Sr_3Ca_3Cu_4O_x$ having predominant Bi-2212 character resembles that obtained by Terasaki *et al* [11] for single crystal of Bi–Sr–

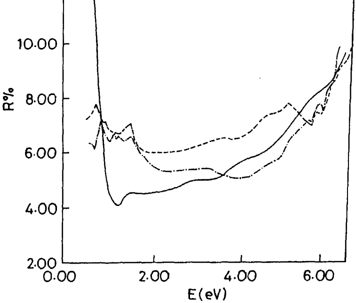

Figure 1. Optical reflectance ($R\%$) vs. photon energy (E) in the range of 0·6–6·2 eV for (**a**) glassy, (**b**) partially crystalline and (**c**) the ceramic superconducting phase of $Bi_{3\cdot 9}Pb_{0\cdot 1}Sr_3Ca_3Cu_4O_x$, (c) is from ref. [6].

$E \geqslant 4$ eV, all the three phases of $Bi_{3\cdot 9}Pb_{0\cdot 1}Sr_3Ca_3Cu_4O_x$ have comparable reflectances, in contrast to their behaviour at lower energies where the superconducting sample only shows a strong decrease in reflectivity between 0·6 and 1·0 eV, followed by a minimum. This indicates that some sort of absorption process is taking place in the NIR range ($E \sim 1$ eV) only in the superconducting phase of $Bi_{3\cdot 9}Pb_{0\cdot 1}Sr_3Ca_3Cu_4O_x$.

Figure 2 (inset) shows the plot of $-\mathrm{Im}\{1/\varepsilon(E)\}$ vs. E for the superconducting glass-ceramic phase of the present Pb doped Bi-system showing a sharp "plasmon" peak in the lower energy region ($\sim$ 1·0 eV) which could be assigned to the excitations from O–2p to Cu–3d (upper Hubbard) state [6]. Furthermore, it is interesting to note that the plasmon-minimum (which is believed to be characteristic for a-b response of high T_c superconductors) is clearly present in the reflectivity spectrum (figure 1) of the superconducting phase only, as expected [i.e. around 1 eV]. Figure 2 (inset) also apparently suggests that among the various layers (Cu–O, Bi–O, Sr–O, etc.) gradually formed in the fully crystalline superconducting phase of $Bi_{3\cdot 9}Pb_{0\cdot 1}Sr_3Ca_3Cu_4O_x$, not all of them have any direct contribution to superconductivity. Otherwise absorption would not have been that weak below 5 eV, indicating that only the carriers of the conducting CuO_2 layers participate in such low energy excitations. Rao [12] had studied in detail the structure of Bi-based superconducting cuprates which has established that Bi–O and Sr–O layers possibly have no direct correspondence to superconductivity in Bi-based compounds. Then those layers just behave like dielectric (polarizable) layers having the properties of an insulator.

Strikingly, the energy loss functions ($-\mathrm{Im}\{1/\varepsilon(E)\}$) for the semiconducting glassy and partially annealed Pb doped Bi–Sr–Ca–Cu–O systems have exhibited a negligible

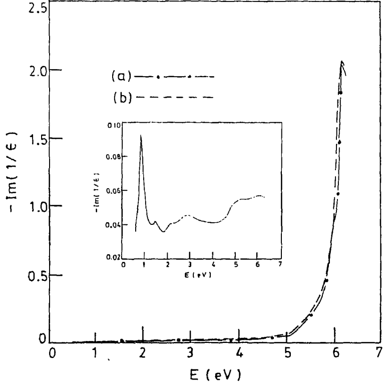

Figure 2. Plot of loss function $[-\text{Im}\{1/\varepsilon(E)\}]$ vs. E for (**a**) semiconducting gla phase and (**b**) partially crystalline phase of $Bi_{3\cdot9}Pb_{0\cdot1}Sr_3Ca_3Cu_4O_x$. Inset: Plo loss-function $[-\text{Im}\{1/\varepsilon(E)\}]$ vs. E for the superconducting ceramic phase $Bi_{3\cdot9}Pb_{0\cdot1}Sr_3Ca_3Cu_4O_x$ (from ref. [6]). The sharp peak around 1.0 eV is likely to excitations of O–$2p$ to Cu–$3d$ states.

loss for a wide range of energy ($\sim 0\cdot6$–$4\cdot5$ eV) and no plasmon peak has been observ in the low energy range (figure 2). This may be attributed to the fact that in semiconducting glassy or partially crystalline phases of $Bi_{3\cdot9}Pb_{0\cdot1}Sr_3Ca_3Cu_4O_x$ charge carriers are in localized states [7] and hence enough free carriers are available to give rise to plasma oscillation. Here one must note that the normal st behavior of the superconducting phase of $Bi_{3\cdot9}Pb_{0\cdot1}Sr_3Ca_3Cu_4O_x$ is metal-l with a larger number of free carriers.

Figure 3a–c shows the variation of the absorption coefficient (α) with photon ene for the three phases of $Bi_{3\cdot9}Pb_{0\cdot1}Sr_3Ca_3Cu_4O_x$. It is important to note that both glassy and partially crystalline phases have an absorption tail common to ot amorphous or quasi-crystalline semiconductors, whereas the ceramic superconduct phase has pronounced peaks around 1·5 eV and it was proposed that the pe correspond to an excitonic absorption [6]. In this context it will be relevant to ment that if one looks at the plot of α vs. E for CuO, one of the basis ingredients in all h T_c cuprates, one observes presence of absorption peaks at 1·0, 1·3 and 1·5 eV wh could be associated with Wannier excitons formed between the holes at O site the electrons at Cu site. Now recalling the fact that our system being a layered cupr superconductor in the glass-ceramic phase, one might expect excitons, if they formed, will be of Cu–O type.

Now the question is, if at all excitons are there, where they can be? The ansv lies in the fact that the present system in its glass-ceramic phase is predominar

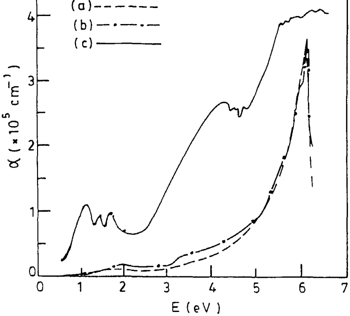

Figure 3. Variation of absorption coefficient $\alpha(E)$ with E for (**a**) glassy phase, (**b**) partially crystalline phase and (**c**) superconducting ceramic phase of $Bi_{3.9}Pb_{0.1}Sr_3Ca_3Cu_4O_x$.

of Bi-2212 has revealed high anisotropy of resistivity between the directions parallel and perpendicular to the c-axis indicating presence of both dielectric and metallic layers [13]. Thus it is plausible that those dielectric layers may sustain excitons and free carriers in the metallic layers are responsible for conductivity. In this context it is worthwhile to mention that Ghosh *et al* [14] have shown the existence of excitons at room temperature in the dielectric (polarizable) layers of a polycrystalline $YBa_2Cu_3O_x$ superconductor from a similar point of view. It is also quite obvious that the main difference in the spectra of the superconducting $Bi_{3.9}Pb_{0.1}Sr_3Ca_3Cu_4O_x$ and its non-superconducting glassy and partially crystalline phases is the presence of exciton bands around 1·5 eV in the former compound and is almost absent in the latter two. The cause may be speculated by considering that for amorphous/quasi-crystalline materials, the presence of a large number of carriers in the localized states would screen the formation of a sufficient number of hole-electron pairs or excitons so that the probability of excitonic interaction will be largely reduced. However, it may be argued that CuO displays the same exciton band structure but is not superconducting. CuO is an insulator and there are not enough carriers to be paired. Recent reflectance and transmittance studies [15] have also not revealed any excitonic absorption. There should not only be enough carriers to be paired but the system should sustain excitons if the latter should play any part in bringing about superconductivity or an enhancement of transition temperature. Gradual annealing of the as-quenched glassy precursors to a fully crystalline superconducting system, increases the conductivity [7] so that the glass-ceramic phase of $Bi_{3.9}Pb_{0.1}Sr_3Ca_3Cu_4O_x$ is metal-like. However, elaborate investigations by other methods are necessary before coming to a definite conclusion about the presence of an exciton and its consequences in Bi-based superconductors.

An estimate of the value of optical band gap (E_g) for the superconducting phase of $Bi_{3.9}Pb_{0.1}Sr_3Ca_3Cu_4O_x$ can also be made from the spectral analysis. It is well known

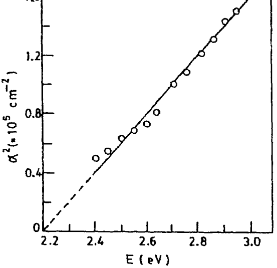

Figure 4. Plot of α^2 vs. E for the ceramic phase of $\mathrm{Bi_{3\cdot9}Pb_{0\cdot1}Sr_3Ca_3Cu_4}$
A good linear fit indicates that the allowed transition is direct.

that if valence band and conduction band extrema are located at $k = 0$ and the bar are parabolic in the region, then for direct allowed transition, $\alpha(E) \propto (E - E_g)^{1/2}$ and indirect allowed transition, $\alpha(E) \propto (E - E_g)^2$ where $E = \hbar w$. For the superconducti phase one finds that the plot of $[\alpha(E)]^2$ vs. E (figure 4) is a better linear fit than that $[\alpha(E)]^{1/2}$ vs. E. This indicates that the allowed transition is direct and E_g is found to 2·20 eV. Both of these findings agree well with the results of similar observation ma by other researchers [13, 16] for different high T_c cuprates.

As further check on our results we have calculated the effective number of carrie $N_{\mathrm{eff}}(E)$ for the superconducting phase using the relation

$$N_{\mathrm{eff}}(E) = (m/2\pi^2 e^2) \int_0^E E' \mathrm{Im}[\varepsilon(E')]\, \mathrm{d}E',$$

which is found to be nearly 7 up to 6 eV. This agrees well with that obtained by Nuc *et al* [17] for Bi-2212 superconducting system.

Finally we discuss the use of R-extrapolation at higher energy as mentioned earl Figures 5a and 5b respectively show the plots of absorption spectra with incid photon energy in the range 0·6–6·2 eV for the superconducting sample only (as a typi example) using the method as discussed earlier and the method of Jezierski [9] for h energy extrapolation. These two plots indicate that even in the absence of additio information such realistic extrapolation formulae yield results which agree with ea other and can be relied upon.

In conclusion, we note that the reflectance spectra for the as-quenched semicondu ing glassy and the partially crystalline phases of $\mathrm{Bi_{3\cdot9}Pb_{0\cdot1}Sr_3Ca_3Cu_4O_x}$ are disti from its corresponding completely crystalline superconducting phase in the range cl to 0·6 eV. Superconducting phase exhibits a plasmon peak at around 1·0 eV whicl caused by the excitation of charge carriers of O–2p and Cu–3d states. Interestingly such plasmon peak is observed for the glassy and partially annealed phases

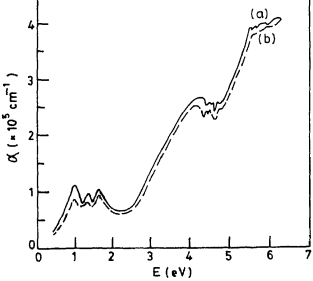

Figure 5. Plot of α vs. E for the superconducting $Bi_{3\cdot 9}Pb_{0\cdot 1}Sr_3Ca_3Cu_4O_x$ by (**a**) our method discussed above and (**b**) by the method of Jezierski.

$Bi_{3\cdot 9}Pb_{0\cdot 1}Sr_3Ca_3Cu_4O_x$. The cause of the appearance of absorption peaks at around $E \sim 1\cdot 5$ eV in superconducting $Bi_{3\cdot 9}Pb_{0\cdot 1}Sr_3Ca_3Cu_4O_x$ has been discussed in the light of a possible excitonic absorption with excitons being sustained by the insulating layers of the present Bi-based superconducting glass-ceramic. However, thorough investigation of the structure of the DOS near Fermi surface would be necessary to ascertain our speculation as to why the formation of excitons is apparently not favoured in the glassy and partially crystalline phases of $Bi_{3\cdot 9}Pb_{0\cdot 1}Sr_3Ca_3Cu_4O_x$ as seen from our experimental results. Nevertheless, the present investigation reasonably suggests that superconductivity in layered cuprates might be brought about when excitons in the polarizable layers and carriers in the conducting layers are both present in sufficient numbers. We have also discussed the applicability of the Jezierski method of R-extrapolation formulae in the higher energy range which can be successfully adopted to perform KK analysis.

Acknowledgement

The authors are grateful to Prof A Nag for his kind help and DST for financial assistance to carry out the research work.

References

[1] Y Abe, H Hosono, M Hosoe and Y Kubo, *Appl. Phys. Lett.* **531**, 1341 (1988)
[2] S Mollah, S Chatterjee, S Chakraborty and B K Chaudhuri, *Philos. Mag.* **B71**, 151 (1995)
[3] K B R Varma, K J Rao and C N R Rao, *Appl. Phys. Lett.* **54**, 69 (1989)
[4] T Komatsu, R Sato, K Matusita and T Yamashita, *Jpn. J. Appl. Phys.* **30**, 1169 (1989)
[5] N P Bansal, preprint
[5a] T Komatsu, *Math. Sci. Forum,* **130–132**, 97 (1993)
[6] Souri Banerjee, S Chatterjee and B K Chaudhuri, *Solid State Commun.* **98**, 665 (1996)

[8] H R Philipp and E A Taft, *Phys. Rev.* **113**, 1002 (1959)

[9] K Jezierski, *J. Phys.* **C17**, 475 (1984)

[10] D M Roessler, *Brit. J. Appl. Phys.* **16**, 1119 (1965)

[11] I Terasaki, S Tajima, H Eisaki, H Takaji, K Uchinokura and S Uchida, *Phys. Rev.* **B41** (1990)

[12] C N R Rao, *Chemical and structural aspects of high T_c superconductivity* (1988) p.159

[13] S Martin, A T Fiory, R M Fleming, L F Schneemeyer and J V Waszczaak, *Phys. Rev.* **60**, 2194 (1988)

[14] B Ghosh, C Neogy, S K Dev and A Nag, *Phys. Status Solidi* **B184**, 267 (1994)

[15] F Marabelli, G B Parravicini and F S Drioll, *Phys. Rev.* **B52**, 1433 (1995)

[16] W Y Ching, Y Xu, G L Ghao, K W Wong and F Zandiehnadem, *Phys. Rev. Lett.* **59**, (1987)

[17] N Nucker, H Romberg, S Nakai, B Scheerer, J Fink, Y F Yan and Z X Zhao, *Phys.* **B39**, 12379 (1989)

The geometric phase and ray space isometries

JOSEPH SAMUEL
Raman Research Institute, Bangalore 560 080, India

MS received 18 January 1997; revised 24 March 1997

Abstract. We study the behaviour of the geometric phase under isometries of the ray space. This leads to a better understanding of a theorem first proved by Wigner: isometries of the ray space can always be realised as projections of unitary or anti-unitary transformations on the Hilbert space. We suggest that the construction involved in Wigner's proof is best viewed as an use of the Pancharatnam connection to 'lift' a ray space isometry to the Hilbert space.

Keywords. Symmetry in quantum mechanics; geometric phase.

PACS No. 03·65

1. Introduction

The states of a quantum system are in one-to-one correspondence with rays in Hilbert space. The 'overlap' between rays is a measure of the distance between them and can be directly measured in the laboratory as a transition probability. A symmetry [1] of a quantum system maps the ray space onto itself preserving distances – i.e, it is a ray space isometry. Since it is inconvenient to work directly on the ray space (defined as an equivalence class of states in Hilbert space), most quantum mechanical calculations are carried out in Hilbert space. Wigner [2] proved that any ray space isometry can be realised on the Hilbert space of quantum mechanics by either a unitary or antiunitary transformation. This theorem underlies much of the study of symmetry in quantum mechanics. A complete and elementary account of Wigner's proof of his theorem is given by Bargmann [3]. More abstract and axiomatic accounts exist [4]. Our purpose here, is to use geometric phase ideas [5], which have recently been of interest, to shed light on Bargmann's exposition of Wigner's theorem. This work follows on an observation by Mukunda and Simon [6] regarding the relation between Bargmann's paper and the geometric phase. This paper is structured as follows. We first review some well-known facts about the geometric phase to set this paper in context and then fix our notation in § 2. In § 3, we study the behaviour of the Pancharatnam excess phase under ray space isometries. In § 4 we state Wigner's theorem and discuss its significance. In § 5 we use the result of § 3 to prove Wigner's theorem by an explicit construction. Section 6 is a concluding discussion. A fine point from § 3 is relegated to an appendix.

Berry [7] noticed many years ago that standard treatments of the adiabatic theorem in quantum mechanics had overlooked an important phenomenon: when a quantum system in a slowly changing environment returns to its original ray, the state of the system picks expects on dynamical grounds. Berry's phase attracted wide attention because of its essentially geometric character. The phase depends only on the path traversed by the system in ray space and not on its rate of traversal. It is a measureable and gauge invariant quantity, independent of phase conventions. An important paper by Barry Simon [8] shows that Berry's phase is a consequence of the curvature of the natural connection on a line bundle over the ray space. Berry's original observation was made in the context of the adiabatic theorem of quantum mechanics. Aharonov and Anandan [9] showed how one could see Berry's phase even in nonadiabatic situations. The key input here was to identify the dynamical phase as the time integral of the expectation value of the Hamiltonian. When this dynamical phase is removed, the geometrical picture described by Simon [8] applies. Although one starts with the Schrödinger equation, after one identifies and removes the dynamical phase, the resulting parallel transport law is *purely* kinematic and depends only on the geometry of the Hilbert space. For this reason, Berry's phase is also known as the 'geometric phase'.

It was pointed out by Ramaseshan and Nityananda [10] that Berry's phase had been anticipated by Pancharatnam [11] in his studies of the interference of polarized light in the fifties. They showed that Berry's phase for a two state system was a special case of Pancharatnam's general study of interference of polarized light. Pancharatnam had given a physically motivated criterion for comparing the phases of two beams of polarized light. He went on to notice that this criterion was not integrable. Two beams $\mathbf{A}$ and $\mathbf{B}$ in phase with a third beam $\mathbf{C}$ are not in phase with each other. The phase difference between $\mathbf{A}$ and $\mathbf{B}$ is equal to half the solid angle subtended by the triangle $(\mathbf{ABC})$ on the Poincaré sphere [12, 13]. In the limit that the discrete points approach a continuous curve, the Pancharatnam phase reduces to Berry's phase for a two state system.

In ref. [14], Pancharatnam's ideas were carried over to the Hilbert space of quantum mechanics. The Pancharatnam criterion was used to compare the phases of states on any two non-orthogonal rays. One defines two states to be 'in phase' if their inner product is real and positive. This permits us to define the Pancharatnam lift: Given a discrete sequence of rays (successive rays not orthogonal), one can use the Pancharatnam connection to 'lift' the discrete set of rays to Hilbert space. This connection contains the natural connection as a special case and tends to it in the limit that the sequence of points becomes a continuous curve.

The importance of geodesics on the ray space of quantum mechanics was emphasized in ref. [14], which states and proves the geodesic rule: Pancharatnam's criterion is equivalent to parallel transport of the phase along the shortest geodesic in the ray space. Given three non-orthogonal rays, one finds that Pancharatnam's excess phase is the integral of a two form over a *geodesic* triangle in the ray space. This is the direct analogue of Pancharatnam's 'half the solid angle' result. This general framework permits an extension of Berry's work to nonunitary and noncyclic situations. Needless to say, this work also subsumes the unitary and cyclic situations as a special case. It is also observed in ref. [14] that Berry's phase appears in systems subject to quantum measurements. Analogue optical experiments demonstrating this effect are reported in refs [15, 16]. A review of the field and a collection of papers upto 1989 is contained in the book by Shapere and Wilczek [5]. A more recent and detailed treatment is given by Mukunda and Simon [6], who note the connection between Pancharatnam's excess phase and invariants considered by Bargmann [3]. Here, we follow on this observation made in [6]. We show how Pancharatnam's connection can be used to better understand a construction due to Wigner. We show below how one can use the Pancharatnam connection to 'lift' a given ray space isometry to the Hilbert space.

2. Preliminaries

Let $\mathcal{H}$ be the Hilbert space of a quantum system and $\mathcal{N} := \mathcal{H} - \{0\}$ the space of normalizable states. We define [17] rays to be equivalence classes of normalizable states differing only by multiplication by a nonzero complex number. We define two elements $|\Psi_1\rangle$ and $|\Psi_2\rangle$ of $\mathcal{N}$ to be equivalent ($|\Psi_1\rangle \sim |\Psi_2\rangle$) if $|\Psi_1\rangle = \alpha|\Psi_2\rangle$, where $\alpha \in \mathbb{C}$, $\alpha \neq 0$. The ray space is defined as the quotient of $\mathcal{N}$ by the equivalence relation

$$\mathcal{R} = \mathcal{N}/\sim .$$

Elements of both $\mathcal{H}$ and $\mathcal{N}$ will be written as kets $|\,\rangle$. The natural projection

$$\Pi : \mathcal{N} \to \mathcal{R}$$

maps each normalizable state $|\Psi\rangle$ to the ray $\boldsymbol{\Psi}$ on which it lies. We define the *overlap* between two rays $\boldsymbol{\Psi}_1$ and $\boldsymbol{\Psi}_2$ as follows:

$$|\boldsymbol{\Psi}_1 \cdot \boldsymbol{\Psi}_2|^2 := \frac{\langle\Psi_1|\Psi_2\rangle\langle\Psi_2|\Psi_1\rangle}{\langle\Psi_1|\Psi_1\rangle\langle\Psi_2|\Psi_2\rangle}.$$

By Schwartz inequality, $|\boldsymbol{\Psi}_1 \cdot \boldsymbol{\Psi}_2| \leqslant 1$ and $|\boldsymbol{\Psi}_1 \cdot \boldsymbol{\Psi}_2| = 1$ if and only if $\boldsymbol{\Psi}_1 = \boldsymbol{\Psi}_2$. We define the distance $\delta(\boldsymbol{\Psi}_1, \boldsymbol{\Psi}_2)$ between the rays $\boldsymbol{\Psi}_1$ and $\boldsymbol{\Psi}_2$ by

$$|\boldsymbol{\Psi}_1 \cdot \boldsymbol{\Psi}_2| = \cos(\delta/2),$$

where δ lies between zero and π. Note that $\delta(\boldsymbol{\Psi}_1, \boldsymbol{\Psi}_2) = 0$ if and only if $\boldsymbol{\Psi}_1 = \boldsymbol{\Psi}_2$.

Let $\{\gamma(\lambda), 0 \leqslant \lambda \leqslant 1\}$ be a curve in $\mathcal{R}$ and $|\gamma(0)\rangle$ a vector on the ray $\gamma(0)$. We define the 'horizontal lift' of $\gamma(\lambda)$ as the unique curve $|\gamma(\lambda)\rangle$ starting from $|\gamma(0)\rangle$ which satisfies $\Pi(|\gamma(\lambda)\rangle) = \gamma(\lambda)$ and

$$\left\langle \gamma(\lambda) \middle| \frac{\mathrm{d}\gamma}{\mathrm{d}\lambda} \right\rangle = 0. \tag{1}$$

Equation (1) gives us a rule (mathematically a connection) for comparing vectors on neighbouring rays.

The Pancharatnam connection which we now describe is a more general notion that permits a comparison of vectors on *any* two non-orthogonal rays. Let $|A\rangle$ and $|B\rangle$ be two non-orthogonal vectors. We define them as being 'in phase' if the inner product $\langle A|B\rangle$ is real and positive. Given $|A\rangle$ and a ray $\mathbf{B}$, there is an unique $|B\rangle$ which is *in phase* with $|A\rangle$ and has the same size ($\langle B|B\rangle = \langle A|A\rangle$). We refer to $|B\rangle$ as the Pancharatnam lift of $\mathbf{B}$

where, $|A\rangle, |B\rangle$ and $|C\rangle$ are representative elements from the corresponding rays. $\Delta_{\mathbf{A}}$
depends only on the rays $\mathbf{A}, \mathbf{B}, \mathbf{C}$ and not on the representatives. We will sometin
abbreviate $\Delta_{\mathbf{ABC}}$ to Δ. The phase β of the complex number $\Delta = \rho \exp(i\beta)$ is
Pancharatnam excess phase, which is well defined (modulo 2π) if $\rho \neq 0$.

An *isometry* of the ray space is a map

$$\mathbf{T} : \mathcal{R} \rightarrow \mathcal{R}$$

which preserves distances. Writing

$$\Psi' = \mathbf{T}\,\Psi,$$

$\mathbf{T}$ is an isometry if

$$|\mathbf{A}' \cdot \mathbf{B}'| = |\mathbf{A} \cdot \mathbf{B}|.$$

Under isometries the rays $\mathbf{A}, \mathbf{B}, \mathbf{C}$ go to $\mathbf{A}', \mathbf{B}', \mathbf{C}'$ and $\Delta_{\mathbf{ABC}}$ goes to $\Delta_{\mathbf{A'B'C'}}$, which
will abbreviate to Δ'.

3. Isometries and the Pancharatnam phase

We now study the transformation of Δ under ray space isometries. Let $\mathbf{A}, \mathbf{B}, \mathbf{C}$ be th
distinct pairwise non-orthogonal rays. Let us choose unit representatives $|A\rangle, |B\rangle,$
from these rays. Further, let us choose the phases of these representatives so that $|B\rangle$ is
phase with $|A\rangle$ (their inner product $\langle A|B\rangle$ is real and positive)

$$\langle A|B\rangle = \cos c/2$$

and $|C\rangle$ is in phase with $|A\rangle$

$$\langle C|A\rangle = \cos b/2.$$

This of course means that $|C\rangle$ is not (in general) in phase with $|B\rangle$. In fact,

$$\langle B|C\rangle = \cos a/2 \exp(i\beta).$$

a, b and c above are the distances (lengths of the shortest geodesics in $\mathcal{R}$) between
rays $(\mathbf{A}, \mathbf{B}, \mathbf{C})$. (a, b, c) are the sides of the geodesic triangle with vertices $(\mathbf{A}, \mathbf{B}, \mathbf{C})$ a
take values strictly between 0 and π.

Let

$$|\mu_B\rangle = |B\rangle - \cos(c/2)|A\rangle$$

be the component of $|B\rangle$ orthogonal to $|A\rangle$. Since $\langle \mu_B|\mu_B\rangle = \sin^2(c/2)$, we define the u
vector

$$|\hat{\mu}_B\rangle = |\mu_B\rangle / \sin(c/2). \qquad ($$

projects down to the shortest geodesic $\gamma_B(\lambda)$ connecting **A** and **B** ($\gamma_B(0) = \mathbf{A}$, $\gamma_B(1) = \mathbf{B}$).

The tangent vector to the curve $|\gamma_B(\lambda)\rangle$ at $\lambda = 0$ is

$$|\dot{\gamma}_B(0)\rangle = (c/2)|\hat{\mu}_B\rangle. \tag{12}$$

Similarly $\{|\gamma_C(\lambda)\rangle, 0 \leqslant \lambda \leqslant 1\}$ defined as

$$|\gamma_C(\lambda)\rangle = \cos(\lambda b/2)|A\rangle + \sin(\lambda b/2)|\hat{\mu}_C\rangle \tag{13}$$

is the horizontal lift of the shortest geodesic connecting **A** with **C**. In (13) $|\hat{\mu}_C\rangle$ is the normalized vector $|\hat{\mu}_C\rangle = |\mu_C\rangle / \sin(b/2)$ where $|\mu_C\rangle = |C\rangle - \cos(b/2)|A\rangle$. The tangent vector to the curve $|\gamma_C(\lambda)\rangle$ at $\lambda = 0$ is

$$|\dot{\gamma}_C(0)\rangle = b/2|\hat{\mu}_C\rangle. \tag{14}$$

The angle A between the geodesics $\gamma_B(\lambda)$ and $\gamma_C(\lambda)$ at **A** is given by

$$\cos(A) = \frac{\Re(\langle\dot{\gamma}_B|\dot{\gamma}_C\rangle)}{(\langle\dot{\gamma}_B|\dot{\gamma}_B\rangle\langle\dot{\gamma}_C|\dot{\gamma}_C\rangle)^{1/2}}, \tag{15}$$

where $\Re(\alpha)$ means the real part of its α. This is easily worked out as

$$\cos(A) = \frac{\cos(a/2)\cos(\beta) - \cos(b/2)\cos(c/2)}{\sin(c/2)\sin(b/2)}. \tag{16}$$

This gives us the formula

$$\cos(\beta) = \frac{\cos(A)\sin(c/2)\sin(b/2) + \cos(b/2)\cos(c/2)}{\cos(a/2)} \tag{17}$$

for the cosine of the Pancharatnam phase. The right hand side of this equation contains only the sides a, b, c and (one of) the angles of the geodesic triangle connecting the rays **A**, **B**, **C**. All these quantities are manifestly invariant under isometries of the ray space. It follows that $\cos(\beta)$ is also an isometry invariant. Since $\rho = |\Delta|$ is clearly isometry invariant, it follows that $\Re(\Delta)$ is isometry invariant and hence

$$\Delta' = \chi(\Delta) \tag{18}$$

where $\chi(\alpha) = \alpha$ or $\chi(\alpha) = \overline{\alpha}$. Equation (18) is valid for *all* triplets of rays (including orthogonal ones, for which it becomes trivial). Since the map **T** is continuous, the function χ must be the *same* all over the ray space (see appendix) and can be determined [3] from **T** [18].

4. Statement of the theorem

We address the following problem. Given a ray space isometry **T**, construct a map $T : \mathcal{N} \to \mathcal{N}$ so that the following diagram commutes

$$\begin{tikzcd}
\mathcal{N} \arrow[r, "T"] \arrow[d, "\Pi"'] & \mathcal{N} \arrow[d, "\Pi"] \\
\mathcal{R} \arrow[r, "\mathbf{T}"] & \mathcal{R}
\end{tikzcd}$$

$$\Pi(T(\Psi\rangle)) = \mathbf{T}(\Pi(|\Psi\rangle)). \qquad \text{(1}$$

T is called the 'lift' of $\mathbf{T}$. Clearly, there are many such lifts T since, given $|\Psi\rangle$, v could pick as its image $|\Psi'\rangle$ an arbitrary point from the fibre above $\mathbf{T}(\Pi(|\Psi\rangle))$. V could, in fact turn this nonuniqueness to advantage and demand that the lift has some nice properties. For instance, we could demand that T be continuous. V *will* assume below that T is continuous but even this restriction allows mu residual freedom. For example, if $\mathbf{T}$ is the identity map, for each continuou nonzero complex function f on $\mathcal{N}$, T_f defined by $T_f(|\Psi\rangle) = f|\Psi\rangle$ is a continuo lift. Clearly, we can do much better and demand that T has some *more* ni properties. The conditions we impose should be as strong as we can demand (that the lift has desirable properties and is reasonably unique) and yet weak enou that a lift exists. Continuity of T is clearly too weak. We are free to impose mo conditions on the lift T. Wigner's theorem does just that. Wigner showed that one c find a continuous lift which preserves intensities (**W1** below) as well as superpositio (**W2** below).

Wigner's theorem. There exists a lift T of $\mathbf{T}$ which

W1 satisfies $\langle\Psi'|\Psi'\rangle = \langle\Psi|\Psi\rangle$
W2 when extended to $\mathcal{H}$ by $T|0\rangle = |0\rangle$ satisfies

$$T(|A\rangle + |B\rangle) = T(|A\rangle + |B\rangle).$$

The lift is unique up to an overall phase [18].

The content of Wigner's theorem is that *all* ray space isometries (i.e all maps $\mathbf{T}$ whi satisfy (5)) can be realised by maps on $\mathcal{H}$ satisfying (**W1,W2**). No other isometries ex and nothing is lost by restricting attention to maps T which satisfy (**W1,W2**). We pro Wigner's theorem below by explicitly constructing the map T.

5. Wigner's construction

Let $|e\rangle$ be any fixed vector in $\mathcal{N}$, $\mathbf{e}$ its ray and $\mathbf{e}'$ the image of $\mathbf{e}$ under $\mathbf{T}$. Let us arbitrari pick $|e'\rangle$ from $\mathbf{e}'$ satisfying $\langle e'|e'\rangle = \langle e|e\rangle$ and define $T|e\rangle$ to be $|e'\rangle$. $|e'\rangle$ is arbitrary up a phase. This is the only arbitrariness in the entire construction which follows. L $\mathcal{P} = \{|\Psi\rangle \in \mathcal{H} | \langle e|\Psi\rangle = 0\}$ be the set of elements in $\mathcal{H}$ orthogonal to $|e\rangle$. And let $\mathcal{P}^c$ be complement – the set of elements in $\mathcal{H}$ which are *not* orthogonal to $|e\rangle$. We now defi the action of T on all elements of $\mathcal{P}^c$ using the Pancharatnam lift. Let $|\Psi\rangle \in \mathcal{P}^c$ be su an element. From (5), it follows that $|(\mathbf{\Psi}', \mathbf{e}')|$ is not zero. We map $|\Psi\rangle$ to the uniq element $|\Psi'\rangle \in \mathbf{\Psi}'$ which satisfies (20, 21) below.

$$\langle\Psi'|\Psi'\rangle = \langle\Psi|\Psi\rangle \qquad \text{(2}$$

determines the amplitude of $|\Psi'\rangle$. Since $|\langle e'|\Psi'\rangle| = |\langle e|\Psi\rangle|$, we can choose the phase $|\Psi'\rangle$ to satisfy

$$\langle e'|\Psi'\rangle = \chi(\langle e|\Psi\rangle). \qquad \text{(2}$$

$$\frac{\langle e'|A'\rangle\langle A'|B'\rangle\langle B'|e'\rangle}{\langle e'|e'\rangle\langle A'|A'\rangle\langle B'|B'\rangle} = \chi\left(\frac{\langle e|A\rangle\langle A|B\rangle\langle B|e\rangle}{\langle e|e\rangle\langle A|A\rangle\langle B|B\rangle}\right) \tag{22}$$

that if $|A\rangle$ and $|B\rangle$ are any two vectors in $\mathcal{P}^c$, $|A'\rangle$ and $|B'\rangle$ defined as in (20,21) above satisfy

$$\langle A'|B'\rangle = \chi(\langle A|B\rangle). \tag{23}$$

Note that this lift preserves superpositions. For if $|\Psi\rangle = |A\rangle + |B\rangle$, (all $|\,\rangle$s in $\mathcal{P}^c$), a simple calculation shows that the norm of

$$|\phi'\rangle = |\Psi'\rangle - (|A'\rangle + |B'\rangle)$$

vanishes. It follows that

$$|\Psi'\rangle = |A'\rangle + |B'\rangle. \tag{24}$$

Actually, more is true. If $|A\rangle + |B\rangle = |C\rangle + |D\rangle$ (all $|\,\rangle$s in $\mathcal{P}^c$), we find that $|A'\rangle + |B'\rangle = |C'\rangle + |D'\rangle$. The proof as before, is to just compute the norm of the difference of both sides and use (23). Note that the sum $|A\rangle + |B\rangle$ need not be in $\mathcal{P}^c$. We can therefore define the action of T on elements of $\mathcal{P}$ by superposition. Any element $|\Phi\rangle \in \mathcal{P}$ can be written as sums of elements in $\mathcal{P}^c$. For example

$$|\Phi\rangle = (|\Phi\rangle - |e\rangle) + |e\rangle. \tag{25}$$

In fact there are many ways to express $|\Phi\rangle$ as sums of elements of $\mathcal{P}^c$. It does not matter which of these ways one chooses and that the extension of T to $\mathcal{P}$ is well defined. We have thus defined T on all of $\mathcal{H}$ satisfying **(W1,W2)**.

6. Conclusion

The key new observation of [6] which led to the present work is that the quantity Δ which has recently been of interest in the context of the Pancharatnam phase is exactly what was used by Bargmann to discriminate between unitary and anti-unitary transformations. Bargmann remarks [3] that one can determine the function $\chi(\alpha)$ merely from a knowledge of the map $\mathbf{T}$ (for $\dim(\mathcal{H}) > 1$ [18]). One starts with Δ, which is defined on the ray space. Using $\mathbf{T}$, one determines Δ' and from $\Delta' = \chi(\Delta)$, one can determine χ.

The main difference between our exposition and ref. [3] is that Bargmann deduces (18) as a *corollary*, after constructing a lift of $\mathbf{T}$. We reverse the order and, using geometric phase ideas, first prove (18) as a geometric identity on the ray space. This result is then used as an *input* for constructing the lift and showing that it does have the desired properties **(W1,W2)**. This leads to a considerably simplified and elementary exposition of Wigner's theorem based on ideas from the geometric phase.

We have derived a formula (17) expressing the cosine of the Pancharatnam excess phase in terms of isometry invariants. This leads to two distinct possibilities for the transformation of the Pancharatnam phase under isometries: it is either preserved or reversed. The lift T is accordingly unitary or anti-unitary. Note that the Pancharatnam phase β itself is *not* an isometry invariant, but only its cosine. The non-invariance of β is *precisely* what Bargmann uses to distinguish between unitary and anti-unitary transformations.

It is interesting to note that trigonometry in ray space is qualitatively different from plane or spherical trigonometry. In ray space, the sides of a triangle (a,b,c) do not determine its angles (A,B,C). To see this, it is enough to consider a 3 (complex) dimensional Hilbert space $\mathcal{H}$ (since three rays are involved). A triangle in $\mathcal{R}$ is determined by 3 distinct rays in $\mathcal{R}$. Since $\mathcal{R} = C\mathbb{P}^2$ is 4 (real) dimensional, the set of triangles is 12 (real) dimensional. The isometry group of $C\mathbb{P}^2$ is 8 (real) dimensional and acts freely on triangles. It follows that a triangle in the ray space has 4 independent isometry invariants. We chose to express (17) $\cos(\beta)$ in terms of the four independent variables (a,b,c,A). One could equally choose any four of these six variables.

For simplicity, we assumed that a symmetry maps the ray space $\mathcal{R}$ to itself. More generally, one can have maps between different ray spaces. Such a situation arises if there is more than one superselection sector in the theory. An example of such a mapping is charge conjugation, which maps different charge superselection sectors to each other. Our analysis is easily adapted to mappings between different superposition sectors.

To mathematicians, the ray space is a Kähler manifold [19, 20], with three interlinked structures: a metric, a symplectic structure and a complex structure. Any two of these determine the third. Physically, the metric represents transition probabilities and the symplectic 2-form is the curvature of the natural connection that emerges from Berry's phase [21]. Isometries of $\mathcal{R}$ preserve the metric, but may reverse the symplectic structure. Then the complex structure is also reversed.

We feel that this paper provides an interesting application of the Pancharatnam connection. Note that the Pancharatnam connection has been used in an essential way. The natural connection only permits a comparison of neighbouring rays and therefore could be used only in the tangent space around $|e\rangle$. The global nature of the Pancharatnam connection allows us to define a lift of $\mathbf{T}$ for (almost) all rays at once. The gaps are then filled in by superposition.

Acknowledgement

The author thanks Rajaram Nityananda for several discussions and a critical reading of the manuscript.

Appendix

In this appendix we show that continuity implies that χ is the same all over ray space. There is a subtlety here stemming from the fact that there are regions in ray space where $\Im(\Delta)$, the imaginary part of Δ vanishes and the two possibilities for χ coincide. Let us fix rays $\mathbf{A}, \mathbf{B}$ and consider Δ as a function of ray $\mathbf{C}$. Let us define $\mathcal{R}^+$ as the set of points of $\mathcal{R}$ where $\Im(\Delta) > 0$ and similarly $\mathcal{R}^-$ is the set where $\Im(\Delta) < 0$. We first show that $\mathcal{R}^+$ is path connected. Let $\mathbf{C}$ and $\tilde{\mathbf{C}}$ be two rays in $\mathcal{R}^+$. Let us choose a representative vector $|C\rangle$ and decompose it into components $|C^{\parallel}\rangle$ in the $|A\rangle - |B\rangle$ plane and $|C^{\perp}\rangle$ orthogonal to it. By continuously decreasing the orthogonal component of $|C\rangle$ to zero, one can deform $|C\rangle$ to $|C^{\parallel}\rangle$ in the $|A\rangle - |B\rangle$ plane. In the expression (2) for Δ, $|C^{\perp}\rangle$ does not contribute to the numerator and the denominator is real and positive. It follows that the sign of $\Im(\Delta)$ does not change in the process of decreasing the orthogonal component of $|C\rangle$ and so the deformation is entirely within $\mathcal{R}^+$. Likewise $|\tilde{C}\rangle$ can also be deformed within $\mathcal{R}^+$ to $|\tilde{C}^{\|}\rangle$ in the $|A\rangle - |B\rangle$ plane. The resulting kets are now in the two dimensional subspace spanned by $|A\rangle$ and $|B\rangle$ and we can now visualize the situation on the Poincaré sphere. Let C be the great circle through the points $\mathbf{A}$ and $\mathbf{B}$ on the Poincaré sphere. C divides the sphere into two hemispheres. $\Im(\Delta)$ vanishes only for points belonging to C, and $\Im(\Delta)$ is strictly positive on one hemisphere and strictly negative on the other. Since $\mathbf{C}$ and $\tilde{\mathbf{C}}$ belong to $\mathcal{R}^+$, the rays $\mathbf{C}^{\|}$ and $\tilde{\mathbf{C}}^{\|}$ corresponding to the vectors $|C^{\|}\rangle$, $|\tilde{C}^{\|}\rangle$ lie in the same hemisphere. They can therefore be deformed into each other without passing through the equator. Throughout this deformation, $\Im(\Delta)$ is positive and it follows that $\mathcal{R}^+$ is connected. (An identical argument shows that $\mathcal{R}^-$ is connected.)

Since $\mathcal{R}^+$ is connected, continuity of $\mathbf{T}$ implies that χ must be the same all over $\mathcal{R}^+$. Likewise, χ must be the same all over $\mathcal{R}^-$. If χ were to differ between $\mathcal{R}^+$ and $\mathcal{R}^-$, both $\mathcal{R}^+$ and $\mathcal{R}^-$ would be mapped to the same component ($\mathcal{R}^+$ or $\mathcal{R}^-$). This contradicts the fact that the map $\mathbf{T}$ is onto. Therefore χ must be the same all over $\mathcal{R}$.

References

[1] A symmetry of a quantum system is also required to leave the Hamiltonian invariant. This is not relevant here as we will not be concerned with Hamiltonians in this paper

[2] E P Wigner, *Group theory* (Academic Press Inc., NY, 1959)

[3] V Bargmann, *J. Math. Phys.* **5**, 862 (1964)

[4] G Emch and C Piron, *J. Math. Phys.* **4**, 469 (1963)

[5] A Shapere and F Wilczek, *Geometric phases in physics* (World Scientific, Singapore, 1989)

[6] N Mukunda and R Simon, *Ann. Phys. (NY)* **228**, 205 (1993)

[7] M V Berry, *Proc. R. Soc.* **A392**, 45 (1984)

[8] B Simon, *Phys. Rev. Lett.* **51**, 2167 (1983)

[9] Y Aharonov and J Anandan, *Phys. Rev. Lett.* **58**, 1593 (1987)

[10] S Ramaseshan and R Nityananda, *Curr. Sci. (India)* **55**, 1225 (1986)

[11] S Pancharatnam, *Proc. Indian Acad. Sci.* **A44**, 247 (1956)

[12] H Poincaré, *Theorie Mathematique de la Lumiere* edited by George Carre (Paris, 1892) p. 275

[13] G N Ramachandran and S Ramaseshan, *Crystal optics in Handbuch der Physik* (Springer, Berlin, 1961) vol. 25, part I

[14] J Samuel and R Bhandari, *Phys. Rev. Lett.* **60**, 2339 (1988)

[15] R Bhandari, *Phys. Lett.* **A180**, 21 (1993)

[16] P Hariharan, Hema Ramachandran, K S Suresh and J Samuel, *The Pancharatnam phase as a strictly geometric phase: a demonstration using pure projections* RRI-96-18, to appear in the *J. Mod. Opt.*

[17] The definition of a ray here differs from [14, 3, 6], where only a phase and not the amplitude is ‘modded out’. The present definition is the usual one in the mathematical literature

[18] The case dim $\mathcal{H} = 1$ is exceptional. In this case Δ is real and $\mathbf{T}$ does not determine χ. Either choice of χ is allowed. As a result there is an additional, discrete, two-fold ambiguity in the lift

[19] V I Arnold, *Mathematical methods of classical mechanics* (Springer-Verlag, NY, 1978) Appendix 3

[20] M C Abbati, R Cirelli, P Lanzavecchia and A Mania, *Il Nuovo Cimento* **B83**, 43 (1984)

[21] V Cantoni and L Mistrangioli, *Int. J. Theor. Phys.* **31**, 937 (1992)

Thomas rotation and polarized light: A non-abelian geometric phase in optics

JOSEPH SAMUEL and SUPURNA SINHA
Raman Research Institute, Bangalore 560 080, India

MS received 18 January 1997; revised 21 February 1997

Abstract. We describe a *non-abelian* Berry phase in polarization optics, suggested by an analogy due to Nityananda between boosts in special relativity and the effect of elliptic dichroism on polarized light. The analogy permits a simple optical realization of the non-abelian gauge field describing Thomas rotation. We also show how Thomas rotation can be understood geometrically on the Poincaré sphere in terms of the Pancharatnam phase.

Keywords. Geometric phase; polarized light; Thomas rotation; non-abelian phase.

PACS No. 03·65

1. Introduction

Shortly after Berry's discovery of the geometric phase [1], the idea was generalized in various directions [2–5]. Here we follow on the work of Wilczek and Zee [2], who noted that in quantum systems with N-fold degeneracy, the 'phase' is no longer abelian, but an element of $U(N)$, the unitary group in N dimensions. These non-abelian phases have been studied in nuclear quadrupole resonance (NQR) [5].

There have been several demonstrations of the geometric phase [6–11] in polarization optics. However, *all* of these experiments deal with the *abelian* phase that Berry's work drew wide attention to. The purpose of this paper is to point out that the *non-abelian* phase of Wilczek and Zee [2] can also be realized in polarization optics. Since optical systems are much easier to set up than NQR experiments, we feel that our observation will aid experimental studies of the non-abelian phase.

There has been some interest in the gauge theoretic aspects of Thomas rotation [12, 13], which can be abstractly [13] viewed as an $SO(3)$ gauge field living on the space of inertial observers. More concretely, Mathur [12] pointed out that the Thomas precession gauge field (TPGF) appears as a non-abelian Berry phase due to Kramer's degeneracy of the Dirac electron. Our purpose in this article is to present another concrete realization of the TPGF in polarization optics. We believe our work may be of general interest, as it permits a simple optical demonstration of Thomas rotation (TR). While our study is both theoretical and experimental, this paper is devoted to theoretical aspects. Experimental details will be reported elsewhere.

In § 2 we review the gauge theoretic aspects of Thomas rotation as a prelude to concluding discussion.

2. Thomas rotation

As is well-known in the special theory of relativity, *pure* boosts (changes of frame without rotation of the spatial axes) along different spatial directions do not commute with each other. In fact, the commutator of two infinitesimal boosts is a rotation and this leads to Thomas precession [14, 15]. We deal here with the *finite* version of this effect, the Thomas rotation [16, 13]. Let u_1^μ, $(\mu = 0, 1, 2, 3)$ be the four-velocity of an observer and $\Lambda_{21}, \Lambda_{32}$ and Λ_{13} a sequence of pure boosts (Λ is given explicitly in [13]) applied to u_1. The sequence of pure boosts takes u_1 to u_2 $(= \Lambda_{21}u_1)$, u_3 $(= \Lambda_{32}u_2)$ and finally back to u_1 $(= \Lambda_{13}u_3)$. Since the final four-velocity $\Lambda_{13}\Lambda_{32}\Lambda_{21}u_1$ is equal to the initial four-velocity u_1, we say that the sequence of boosts *closes* (returns the observer to the original frame). In general, the product $\Lambda = \Lambda_{13}\Lambda_{32}\Lambda_{21}$ of boosts is not the identity, but $\Lambda = R$, where R is a rotation matrix representing the Thomas rotation. The rotation matrix R can be expressed as a path ordered product or Wilson loop

$$R = P\exp\left[\oint A(u)\mathrm{d}u\right], \tag{1}$$

where the integral is over the geodesic triangle $u_1 - u_2 - u_3 - u_1$ on the unit hyperboloid $\mathcal{H}^+$ of four velocities $\mathcal{H}^+ = \{u^\mu | u\cdot u = 1,\ u^0 > 0\}$. The gauge field A describing Thomas rotation is a 3×3 antisymmetric matrix, whose components (in a convenient [13] global gauge choice over $\mathcal{H}^+$) are $A^i_j = (1 + u^0)^{-1}(\mathrm{d}u^i u_j - \mathrm{d}u_j u^i)$, where $i, j = 1, 2, 3$. A closed sequence of three boosts must lie in a plane [13]. This is no longer true for a closed sequence of M (four or more) boosts, which involves M inertial observers with M four-velocities $u_1, u_2, \ldots, u_M$. However, one can consider these M observers in triplets by triangulating the broken geodesic curve $C = u_1 - u_2 - \cdots - u_M - u_1$ and applying the previous argument. The Thomas rotation is then expressed as a Wilson loop over C. In general C is a (closed, piecewise geodesic) *space* curve in $\mathcal{H}^+$ and path ordering in (1) becomes necessary, revealing the essentially *non-abelian* nature of the gauge field. One can also consider the limit $M \to \infty$ of an infinite number of infinitesimal boosts. The integral in (1) is then over a continuous closed curve in $\mathcal{H}^+$, which is in general nonplanar. Each boost distorts (alters the distances between points on) the celestial sphere of an observer due to the well-known phenomenon of aberration of light [15, 17] from the sky. When the sequence of boosts closes, the distortions cancel and the net result is an undistorted but rotated celestial sphere, the rotation matrix being given by (1).

3. Analogue of Thomas rotation in optics

In order to realize the TPGF A^i_j in optics, we draw on an observation by Nityananda [18] regarding the effect of an anisotropic absorber on the polarization of light. Let $\hat{n}$ be a unit vector representing a general point on the Poincaré sphere. Suppose that light is passed through an absorber $A_{\hat{n}}$ that preferentially absorbs the polarization state $\hat{s}$ orthogonal to $\hat{n}$. If the incident light is in the state $\hat{n}$ or $\hat{s}$, its polarization state will not be affected by the material (although its intensity may diminish). Any other polarization state $\hat{p}$ on the Poincaré sphere can be resolved in terms of $\hat{n}$ and $\hat{s}$ and, since the $\hat{s}$ component of $\hat{p}$ is preferentially absorbed, will move towards $\hat{n}$ along the great circle [19] joining $\hat{p}$ to $\hat{n}$. The key observation due to Nityananda [18] is that the effect of an absorber $A_{\hat{n}}$ on the Poincaré sphere is identical to the effect of a pure Lorentz boost in the direction $\hat{n}$ on the celestial sphere of an observer in special relativity.

The optical element $A_{\hat{n}}$ discussed above is purely absorbing (dichroic) in the sense that it introduces only a relative attenuation between two orthogonal states and not a relative phase. Dichroic elements $A_{\hat{n}}$ distort the Poincaré sphere. There are also birefringent elements $R_{\hat{n}}$ (retarders, such as wave plates), which introduce a *pure* phase difference between two orthogonal states, and rigidly rotate the Poincaré sphere about an axis $\hat{n}$. The effect of absorbers and retarders on the Poincaré sphere is qualitatively different. Yet, by exploiting the analogy with special relativity, we see that a sequence of absorptions along different directions can give rise to a net rigid rotation of the Poincaré sphere. A sequence of elliptic dichroids can result in a net elliptic birefringence. This is the optical analogue of Thomas rotation.

Before developing this analogy in quantitative terms, we briefly clarify our terminology, which some readers may find unfamiliar. Traditionally, optical elements which cause a rotation of the Poincaré sphere about the x or y axis are called birefringent, whereas those which generate a rotation about the z axis are called optically active. There is no standard terminology for an element which causes a rotation of the Poincaré sphere about an arbitrary axis. Since these are merely rotations about different axes, there is no fundamental difference between them. We adopt a generalized terminology and refer to all of these as elliptically birefringent elements. Special cases of elliptic birefringence are linear (ordinary birefringence), and circular (optical activity). We also use the word dichroism in the same general sense to refer to elliptic dichroism and not just linear or circular dichroism.

Consider an absorbing optical device $A_{\hat{n}}$ whose effect on a state $|n\rangle$ is to reduce its amplitude to $e^{-\alpha_1}|n\rangle$ and whose effect on the state $|s\rangle$ orthogonal to $|n\rangle$ is to reduce its amplitude to $e^{-\alpha_2}|s\rangle$ (we assume $\alpha_2 > \alpha_1$, so state $|s\rangle$ is preferentially absorbed). It is convenient to introduce the relative and overall absorption coefficients $\alpha = \alpha_2 - \alpha_1$ and $\alpha_0 = (\alpha_1 + \alpha_2)/2$ respectively. Since we are not interested in the overall intensity and phase of the light beam (these are not represented on the Poincaré sphere), we do not need to normalize our state vectors. A general (unnormalized) state $|p\rangle$ can be expanded in the orthonormal basis $\{|n\rangle, |s\rangle\} : |p\rangle = |n\rangle + z|s\rangle$, where $z = \tan(\theta/2)e^{i\phi}$ with θ the angle between $\hat{p}$ and $\hat{n}$ on the Poincaré sphere (the 'colatitude') and ϕ the 'longitude'. The effect of $A_{\hat{n}}$ on $|p\rangle$ is to transform it to $|p'\rangle = |n\rangle + e^{-\alpha}z|s\rangle$ (where we have discarded an overall factor which does not affect the polarization state). On the Poincaré sphere $\hat{p}'$ has the same 'longitude' as $\hat{p}$ and makes an angle θ' with $\hat{n}$ where $\tan(\theta'/2) = e^{-\alpha}\tan(\theta/2)$. A little algebra shows that $\cos\theta' = (\cos\theta + \tanh\alpha)/(1 + \cos\theta\tanh\alpha)$. Letting $\beta = \tanh\alpha$, we notice that this is identical to the aberration formula [15]. The relative absorption α plays the role of rapidity in the analogue relativistic system and β is the velocity in units of the speed of light [20]. An absorber with rapidity α. By applying successive boosts $K_{\hat{n}}(\alpha)$ to the initial four-velocity u_1 (say $(1,0,0,0)$), one can trace the path of the equivalent relativistic system [21] on $\mathcal{H}^+$.

4. Optical view of Thomas rotation

We now show how Thomas rotation can be understood in purely optical terms, using the Pancharatnam phase [22–24]. Let a light beam pass through a sequence of three absorbers $A_{\hat{n}_1}, A_{\hat{n}_2}$ and $A_{\hat{n}_3}$ which closes (the combination $A = A_{\hat{n}_3}A_{\hat{n}_2}A_{\hat{n}_1}$ preserves distances between points on the Poincaré sphere). Consider the set of points $\mathcal{C}$ on the great circle through $\hat{n}_1$ and $\hat{n}_2$. Since these points are 'dragged' *along* $\mathcal{C}$ by both $A_{\hat{n}_1}$ and $A_{\hat{n}_2}$, the set $\mathcal{C}$ is left invariant by both these absorbers.

Lemma 1. *If the sequence* $A_{\hat{n}_1}, A_{\hat{n}_2}, A_{\hat{n}_3}$ *closes,* $\hat{n}_3$ *must lie on the great circle* $\mathcal{C}$.

Proof. If $\hat{n}_3$ is not on $\mathcal{C}$, it must lie on one of the hemispheres into which $\mathcal{C}$ divides the Poincaré sphere. $A_{\hat{n}_1}$ and $A_{\hat{n}_2}$ leave $\mathcal{C}$ invariant, but the effect of $A_{\hat{n}_3}$ is to drag all points of $\mathcal{C}$ into the hemisphere containing $\hat{n}_3$. Antipodal points of $\mathcal{C}$ (which are separated by a distance π) will no longer be antipodal since they are in the same hemisphere. This contradicts the assumption that the sequence of three absorbers closes. It follows that the points $\hat{n}_1, \hat{n}_2, \hat{n}_3$ lie on a great circle.

$\mathcal{C}$ is left invariant by all the three absorptions and therefore by their composition $A = A_{\hat{n}_3}A_{\hat{n}_2}A_{\hat{n}_1}$. Let $\hat{n}$ and $\hat{s}$ be the two points on the Poincaré sphere which satisfy $\hat{n}\cdot\hat{n}_i = \hat{s}\cdot\hat{n}_i = 0$ for $i = 1,2,3$.

Lemma 2. $\hat{n}$ *and* $\hat{s}$ *are returned to their original positions by the sequence* $A = A_{\hat{n}_3}A_{\hat{n}_2}A_{\hat{n}_1}$.

Proof. Since $\mathcal{C}$ is invariant under the action of $A_{\hat{n}_3}, A_{\hat{n}_2}$ and $A_{\hat{n}_1}$, points on the Poincaré sphere do not cross $\mathcal{C}$. Since $\hat{n}$ is the only point on its hemisphere which is $\pi/2$ away from $\mathcal{C}$, $\hat{n}$ must be mapped to itself by A. Similarly, $\hat{s}$, which is antipodal to $\hat{n}$, is also mapped to itself.

Lemma 3. *The action of* A *on the Poincaré sphere is a rotation about the* $\hat{n} - \hat{s}$ *axis.*

Proof. Under the action of $A_{\hat{n}_3}A_{\hat{n}_2}A_{\hat{n}_1}$, $\hat{n}$ and $\hat{s}$ are dragged along great circles towards $\hat{n}_1, \hat{n}_2$ and $\hat{n}_3$ as shown in figure 1. (The closure of this sequence of geodesic arcs is guaranteed by Lemma 2). From Pancharatnam's theorem [22, 23], we see that the state $\hat{n}$ picks up a geometric phase $\Omega/2$, where Ω is the solid angle subtended by the geodesic triangle traced by the state $\hat{n}$ as it traverses the geodesic arcs. From figure 1, note that states $\hat{n}$ and $\hat{s}$ pick up equal and opposite geometric phases $\pm\Omega/2$. It follows from the invariance of $\mathcal{C}$ that A introduces no relative attenuation between states $\hat{n}$ and $\hat{s}$. This is the signature of elliptic birefringence in the $\hat{n} - \hat{s}$ direction. The effect of A on the Poincaré sphere is a rotation through an angle Ω about the $\hat{n} - \hat{s}$ axis. It is elementary to verify that Ω is equal to the Thomas rotation angle [16].

It now follows that the rotation of the Poincaré sphere due to a closed sequence of M

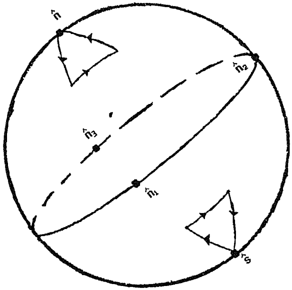

Figure 1. The Poincaré sphere representation of the trajectories of the two orthogonal elliptic polarizations $\hat{n}$ and $\hat{s}$. These trajectories are mirror images of each other in the plane containing $\hat{n}_1, \hat{n}_2$ and $\hat{n}_3$. Note that by Pancharatnam's theorem, these two polarizations pick up equal and opposite geometric phases $\pm\Omega/2$. This corresponds to a rotation of the Poincaré sphere by an angle Ω about the axis passing through the orthogonal elliptic states $\hat{n}$ and $\hat{s}$.

can be represented as a piecewise geodesic closed space curve C in $\mathcal{H}^+$. By triangulation, one can reduce the traversal of C into a sequence of traversals of triangles. Each triangle causes a rotation about some axis as discussed above in Lemma 3. Since C is not in general planar, the rotations caused by different triangles are about *different* axes. As a result, one has to *compose* the sequence of rotations (and not just add the rotation angles, as one does in the abelian case). The final answer is a path ordered product of individual rotations (1).

5. Conclusion

A particular case of the optical effect discussed here has been noticed earlier: linear dichroism can lead [25, 26] to optical activity (circular birefringence). Kitano *et al* [26] studied Lorentz group Berry phases, but since they use only *linear absorbers*, they only explore an *abelian* phase. As Zee [27] pointed out in the context of the NQR experiment of Tycko [28], this amounts to exploring a one parameter *abelian subgroup* of the full *non-abelian gauge group*. There is also a difference between our approach and ref. [26], which views the linear absorbers as 'squeezing' the polarization ellipse similar to Berry's discussion of the time dependent oscillator [29]. The relevant group is then $SO(2,1)$ and the abelian phase, a $U(1)$ phase. Our approach is based on *distortions of the Poincaré sphere*. The relevant group here is language used in the Berry phase literature, the birefringence is the dynamic 'ph and has to be 'subtracted out' before one sees the geometric 'phase'. In our exposi we chose optical elements which are purely absorbing so that the dynamic 'phase zero. This is similar in spirit to recent demonstration of the Pancharatnam ph from pure projections [10, 11] where the dynamic phase is manifestly zero. Indeed the limit of infinite relative absorption ($\alpha \rightarrow \infty$) absorbers become projectors. It sho be borne in mind that this limit is highly singular, corresponding in the relativi language, to boosting a frame to the speed of light.

There is a mathematical similarity between the effect described here and Pancharatnam effect. Both demonstrate the mathematical phenomenon of anholonomy which there are numerous instances in physics [5]. In both cases, the mathemat structure explored is a connection on a fiber bundle $(\mathcal{P}, \mathcal{B}, \Pi)$, where $\mathcal{P}$ is the total sp $\mathcal{B}$, the base space and Π a projection from $\mathcal{P}$ to $\mathcal{B}$. $\Pi^{-1}(b)$ is called the fiber over connection on a fiber bundle gives a rule for comparing points on neighboring fibers general, the connection is not integrable. When one parallel transports a point $p \in \Pi^{-}$ along a closed curve in $\mathcal{B}$, one returns to the same fiber, but not in general to the sa point on that fiber. This is a reflection of the curvature of the connection or nonintegrability of the rule for comparison of points. In the context of the Pancharatn phase, the base space $\mathcal{B}$ is the Poincaré sphere S^2, the fiber is the phase $U(1)$ and the t space $\mathcal{P}$ is S^3. In the case of present interest, the base space is the unit hyperboloid $\mathcal{H}$ four-velocities and the fiber is the rotation group $SO(3)$ and the total space is the Lor group.

The optical realization of TPGF is a simple analogue experiment which can easily performed. In the Dirac electron realization of TPGF [12], relativistic eff like TR are small under normal laboratory conditions. In the analogue opt system, attaining 'relativistic' speeds is quite easy. One just uses an absorber wi high relative absorption. One is limited only by one's ability to detect the resi intensity of preferentially absorbed polarization. In preliminary studies, we h measured Thomas rotation angles of up to 50° in the optics laboratory. A poss application of the ideas described in this paper is the design of achromatic (wavelen independent) birefringent elements. Because of the geometric character of the eff birefringent devices (optical rotators or wave plates) constructed from dichroic elem as described above will introduce the same phase difference independent of wavelen provided of course, the dichroism is not wavelength dependent in the freque bandwidth of interest.

Historically, polarized light has played a significant role in elucidating the fiel geometric phases. We believe our paper goes further in this direction by showing *non-abelian* phases can also be seen in optics.

Acknowledgements

It is a pleasure to thank Rajaram Nityananda, V A Raghunathan and T N Ruckmonga for discussions and N Narayanaswamy, V Venu, Manohar Modgekar and C Ateequllah for technical support in the laboratory. We thank Rajendra Bhandari drawing our attention to ref. [26]

References

[1] M V Berry, *Proc. R. Soc.* **A392**, 45 (1984)
[2] F Wilczek and A Zee, *Phys. Rev. Lett.* **52**, 2111 (1984)
[3] Y Aharonov and J Anandan, *Phys. Rev. Lett.* **58**, 1593 (1987)
[4] J Samuel and R Bhandari, *Phys. Rev. Lett.* **60**, 2339 (1988)
[5] A Shapere and F Wilczek, *Geometric phases in physics* (World Scientific, Singapore, 1989)
[6] R Bhandari and J Samuel, *Phys. Rev. Lett.* **60**, 211 (1988)
[7] R Simon, H J Kimble and E C G Sudarshan, *Phys. Rev. Lett.* **61**, 19 (1988)
[8] T H Chyba, L J Wang, L Mandel and R Simon, *Opt. Lett.* **13**, 562 (1988)
[9] P Hariharan and M Roy, *J. Mod. Opt.* **39**, 1811 (1992)
[10] M V Berry and S Klein, *J. Mod. Opt.* **43**, 165 (1996)
[11] P Hariharan, Hema Ramachandran, K A Suresh and J Samuel, *The Pancharatnam phase as a strictly geometric phase: a demonstration using pure projections* RRI-96-18, *J. Mod. Opt.* (to appear)
[12] H Mathur, *Phys. Rev. Lett.* **67**, 3325 (1991)
R Shankar and H Mathur, *Phys. Rev. Lett.* **73**, 1565 (1994)
[13] J Samuel, *Phys. Rev. Lett.* **76**, 717 (1996)
[14] L H Thomas, *Philos. Mag.* **3**, 1 (1927)
[15] J D Jackson, *Classical electrodynamics* (Wiley Eastern Limited, New Delhi, 1978)
[16] H Urbantke, *Am. J. Phys.* **58**, 747 (1990)
[17] R Penrose and W Rindler, *Spinors and Spacetime* (Cambridge University Press, Cambridge, 1984) vol. I
[18] See the remark attributed to R Nityananda on page 245 in the article by S Ramaseshan in *Essays on Particles and Fields* edited by R R Daniel and B V Sreekantan (Indian Academy of Sciences, Bangalore, 1989)
[19] G N Ramachandran and S Ramaseshan, Crystal Optics in *Handbuch der Physik* (Springer, Berlin, 1961) vol. 25, part I
[20] In passing, we note that the aberration formula is considerably simplified by using an angular variable σ defined by $\cos\theta = \tanh\sigma$. The aberration formula then reads $\sigma' = \sigma + \alpha$
[21] If one forms the (impure) density matrix $\rho = u^0 + \mathbf{u}\cdot\sigma$, the components $(u^0, \mathbf{u})$ have an optical interpretation in terms of the Stokes [19] parameters (I, Q, U, V) of a partially polarized light beam described by that density matrix
[22] S Pancharatnam, *Proc. Indian Acad. Sci.* **A44**, 247 (1956); reprinted in *Collected works of S Pancharatnam* (Oxford University Press, London, 1975)
[23] S Ramaseshan and R Nityananda, *Curr. Sci. (India)* **55**, 1225 (1986)
[24] M V Berry, *J. Mod. Opt.* **34**, 1401 (1987)
[25] G S Ranganath, K A Suresh, S R Rajagopalan and U D Kini, *Pramana Special Supplement* **1**, 353 (1975)
[26] M Kitano and T Yabuzaki, *Phys. Lett.* **A142**, 321 (1989)
[27] A Zee, *Phys. Rev.* **A38**, 1 (1988)
[28] R Tycko, *Phys. Rev. Lett.* **58**, 2281 (1987)
[29] M V Berry, *J. Phys.* **A18**, 15 (1985)

On periodically kicked quantum systems

N D SEN GUPTA
Tata Institute of Fundamental Research, Mumbai 400 005, India

MS received 26 September 1996

Abstract. The time evolution of a multi-dimensional system which is kicked periodically with a potential is obtained. The most interesting aspects of the investigation are (i) if the operator corresponding to the potential has invariant subspaces (a characteristic property of multi-dimensional systems), the states belonging to these subspace in its evolution are confined to these invariant subspaces respectively and there cannot be any mixing of states between these subspaces. Further, (ii) it leads to the existence of quasi-stationary states (determined again by the potential) which evolves independent of other similar quasi-stationary states. The method followed in the paper is the direct integration of the Schrödinger equation and then to construct the wave function from the initial wave function.

Keywords. Schrödinger equation; kicked systems; Floquet's theorem; quasi-stationary states.

PACS No. 03·65

1. Introduction

In recent years, attempts have been made to understand the quantum features of systems with time in the form of delta-function kicks, depending on a potential. In most of the papers, [1–17] the discussion is confined to one-dimensional system. Recently, in a paper [19iv] the problem of kicked multi-dimensional system with potential has been investigated, where it has been shown that the system in its evolution is confined to suitable subspaces related to the invariant subspaces of the operator corresponding to the potential. The investigation was for random (δ-function) kicks. Though periodic kicks are special case of random kicks, yet periodic systems have their own characteristics. This is due to Floquet's theorem on linear differential equation with periodic coefficients. This theorem prescribes the general nature of the solution, which considerably simplifies the process to obtain the solution. Further periodic systems are of interest from the point of view of applications.

Since all information pertaining to a system can be obtained from the wave function, it is sufficient to obtain the wave function with its evolution in time. Analytically this is also simpler than treating the problem with evolution operator. The latter seems to be begging the question. In general, the evolution operator is constructed from the wave function. The general nature of the wave function in these problems has also been discussed qualitatively.

The main object of the paper is to investigate the qualitative nature of a finite dimensional periodically kicked quantum system.

The problem is formulated in the following section. Section 3 is devoted to process of solving the Schrödinger equation. The nature of the time evolution of wave function is examined, in detail, in § 4. As a simple example, the case of cons potential is considered in § 5. The paper ends with a short discussion.

2. Formulation of the problem

2.1 *Periodic kicking*

The periodic kicking is represented by

$$D(t) = \sum_{-\infty}^{\infty} \delta(t - n\tau)$$

where τ is the period. It can be easily shown that [19i]

$$D(t) = \frac{1}{\tau} \sum_{-\infty}^{\infty} \exp . i2\pi m t/\tau,$$

(n, m are integers).

2.2 *Quantum system*

The Hamiltonian of the general quantum system consists of two terms as

$$H(q,p;t) = H_0(p,q) + \varepsilon f(q) D(t).$$

q stands for a (finite) set of generalized co-ordinates $\{q_i\}$ and $p \equiv \{p_i\}$ the correspon momenta.

(a) *Discrete systems*. Let the discrete eigenvalues of $H_0(p,q)$ be $\{E_\alpha\}$ and ϕ_α corresponding eigenfunctions, concomitant to the prescribed (steady) boundary co tion. $\{\phi_\alpha\}$ belongs to a Hilbert space (L^2). They are assumed to form a complete s orthonormal functions. The degeneracy (the order of which is finite) is taken care indexing. Thus

$$H_0(q,p)\phi_\beta = E_\beta \phi_\beta, (\phi_\alpha \cdot \phi_\beta) = \delta_{\alpha\beta}.$$

The time dependent perturbation (kicks) is given by the second term in (3).

(b) *Potential*. $f(q)$ is the steady potential and ε represents the strength of the poten The operator $f(q)$ is real and symmetric (this is implicitly assumed in literature)

$$f(q)\phi_\beta(q) = \sum_{0}^{\infty} F_{\gamma\beta}\phi_\gamma(q),$$

$$F_{\gamma\beta} = \int \phi_\gamma(q) f(q) \phi_\beta(q) \mathrm{d}q.$$

Since the coefficient of (6) is periodic, the solutions are of the form (Floquet's Theorem)

$$\Psi_\alpha(q,t) = \sum_{-\infty}^{\infty} \exp . i(\lambda_\alpha + 2\pi n/\tau)t \cdot \Phi_\alpha^n(q). \tag{7}$$

Since ϕ_β's form a complete set, $\Phi_\alpha^n(q)$ may be expressed as linear combination ϕ_β. Thus

$$\Phi_\alpha^n(q) = \sum_0^\infty A_{\alpha,\beta}^n \phi_\beta(q) \tag{8}$$

[subscripts in Roman represent Fourier components $(-\infty < n < \infty)$ and those in Greek, represent components in Hilbert space $(0 \leqslant \beta < \infty)$]. The general solution is the sum of expressions (7) with $\alpha = 1, 2, \ldots$;

$$\Psi(q,t) = \sum_0^\infty \Psi_\alpha(q,t). \tag{9}$$

λ_α are the constant characteristic exponents to be determined in the sequel and $A_{\alpha,\beta}^n$ are to be determined from the wave equation and the initial wave function.

3. Process of solving

3.1 *Preliminary*

It is clear from eqs (7)–(9) that one has to determine λ_α and $A_{\alpha,\beta}^n$ to construct the solution. As a prelude, one notes from (2)

$$D(t) \sum_{-\infty}^{\infty} g_n \exp . i2\pi nt/\tau = \frac{1}{\tau} \sum_{-\infty}^{\infty} \left(\sum_{-\infty}^{\infty} g_m \right) \exp . i2\pi nt/\tau \tag{10}$$

for any Fourier series with coefficients g_n, [19i].

3.2 *Determination of the characteristic exponent λ*

Substituting the expression for $\Psi_\alpha(x,t)$ from (7), in (6) and equating the Fourier coefficients and those of $\phi_\beta(q)$, one obtains, (note $\varepsilon \neq 0$)

$$\left\{ \hbar\left(\lambda_\alpha + 2\pi \frac{n}{\tau} \right) + E_\beta \right\} A_{\alpha,\beta}^n + \frac{\varepsilon}{\tau} \sum_0^\infty F_{\beta\gamma} \sum_{-\infty}^{\infty} A_{\alpha,\gamma}^m = 0 \tag{11}$$

$$A_{\alpha,\beta}^n + \frac{\varepsilon}{2\hbar} \left\{ (\lambda_\alpha + E_\beta/\hbar)\frac{\tau}{2} + \pi n \right\}^{-1} \sum_{-\infty}^{\infty} F_{\beta\gamma} a_{\alpha,\gamma} = 0 \tag{12}$$

with

$$a_{\alpha,\beta} = \sum_{-\infty}^{\infty} A_{\alpha,\beta}^m . \tag{13}$$

(Note $-\pi/\tau \leqslant \lambda \leqslant \pi/\tau$, as if λ is a solution, then $\lambda + 2\pi n/\tau$ is also a solution $- n$ integer.) Summing over n on both sides, we get

$$a_{\alpha,\beta} + \frac{\varepsilon}{2\hbar} \cot \Lambda_{\alpha,\beta} \cdot \sum_0^\infty F_{\beta\gamma} a_{\alpha,\gamma} = 0 \tag{14}$$

$$\Lambda_{\alpha,\beta} = \frac{\tau}{2}\left(\frac{E_\beta}{\hbar} + \lambda_\alpha \right). \tag{14'}$$

$$a'_{\alpha,\beta} + \frac{\varepsilon}{2\hbar}\sum F'_{\beta,\gamma}a'_{\alpha,\gamma} = 0, \tag{15}$$

where

$$F'_{\beta\gamma} = \sqrt{\cot\Lambda_{\alpha,\beta}}\,F_{\beta\gamma}\,\sqrt{\cot\Lambda_{\alpha,\gamma}} \tag{15'}$$

and

$$a'_{\alpha,\beta} = a_{\alpha,\beta}\sqrt{\tan\Lambda_{\alpha,\beta}}. \tag{15''}$$

The matrix $F'_{\beta\gamma}$ is real and symmetric. It can be written in terms of its normalized eigenvectors $\mathbf{v}^0$ and eigenvalues η^0, as

$$F'_{\beta\gamma} = \sum_0^\infty \eta^0 v^0_\beta v^0_\gamma. \tag{16}$$

From eq. (15)

$$\left(1 + \frac{\varepsilon}{2\hbar}\eta^\alpha\right)\sum_0^\infty v^\alpha_\beta a'_{\alpha,\beta} = 0. \tag{17}$$

For non-trivial solution, noting $\varepsilon \neq 0$

$$1 + \frac{\varepsilon}{2\hbar}\eta^\alpha = 0. \tag{18}$$

This relation determines λ_α as the eigenvalues η^α depends on λ_α from eqs (14') and (15').

3.3 *Determination of* $a_{\alpha,\beta}$ and $A^n_{\alpha,\beta}$

Next, $A^n_{\alpha,\beta}$ is obtained directly from (12), in terms $a_{\alpha,\gamma}$ of eq. (13). On the other hand from eq. (15), it is clear that $a'_{\alpha,\gamma}$ is the eigenvector corresponding to some eigenvalue μ^α. Hence, one can write

$$a_{\alpha,\beta} = p^\alpha v^\alpha_\beta \tag{19}$$

(no sum over α), where p^α are constant to be determined from initial condition, ($\mathbf{v}^\alpha$ are normalized).

Thus the computations related to the Hill's determinant in this case is reduced simply to obtain the eigenvalues and eigenvectors of $F_{\gamma\beta}$ (eq. (5)). It needs to be mentioned that the eigenvalues and eigenvector of $F'_{\gamma\beta}$ (eq. (15')) are easily obtained from those of $F_{\gamma\beta}$. Since they are symmetric, the eigenvectors are mutually orthogonal, i.e.,

$$\mathbf{v}^\alpha \cdot \mathbf{v}^\gamma = \delta_{\alpha\gamma}. \tag{20}$$

3.4 *Initial state and determination of* p^α

The most general wave function is thus a superposition of $\Psi_\alpha(q,t)$ (eqs (7) and (9))

$$\Psi(q,t) = \sum_{-\infty}^{\infty}\sum_0^\infty\sum_0^\infty \varepsilon\exp.i\left(\lambda_\alpha + 2\pi\frac{n}{\tau}\right)t\cdot p^\alpha v^\alpha_\beta \phi_\beta/2(\pi n + \Lambda_\alpha). \tag{21}$$

Hence

$$p^\alpha = \sum_0^\infty v^\alpha_\beta \int \Psi(q,0)\phi_\beta(q)\mathrm{d}q. \tag{22}$$

Given the initial wave function (at $t = 0$), $\Psi(q, 0)$ the right hand side of eq. (22) is known, which determines p^{α}. It can be easily checked that if the wave function is initially normalized it remains so for all time (averaged over a period).

4. Time evolution of the wave-function

Though apparently (21) shows that the wave function at any instant is, in general, spread over all the eigenstates of the unperturbed (unkicked) Hamiltonian, a little critical examination reveals that there are some collections of states which evolves among themselves independent of other states. Amid these states there are two important classes.

4.1 *Evolution in sub-spaces*

Let us consider the class of potentials $f(q)$, which has invariant subspaces, i.e., there exists a subset $\phi_{\beta}^{0} \equiv (\phi_{\beta_j}; j = 1, 2, \ldots, k)$ such that for any $\phi_{\beta_i} \in \phi_{\beta}^{0}$ and $f(q)\phi_{\beta_i} \in \Phi_{\beta}^{0}$: The corresponding matrix $F_{\alpha\beta}$ in this case (eq. (5′)) have block diagonal structure. Hence the eigenvectors of $F_{\alpha\beta}$ are confined in these respective blocks. According to eq. (21) any state belonging to this subspace during its evolution will be confined in this subspace. In fact, the initial states belonging to these subspaces will always remain in the respective subspaces. Further, since the evolution equation, i.e., the Schrödinger equation, is linear, the states belonging initially to the subspaces evolve in the respective subspaces and there is no mixing of states among different subspaces. Thus there is no possibility of dispersion of states throughout the entire space by the kicking, as it is usually supposed to be.

This property (having invariant subspaces) of the operator corresponding to the potential function manifest itself most frequently in multidimensional problems. Even in the case of two-dimensional problems in a plane, if the unperturbed (unkicked) Hamiltonian commutes with angular momentum operator and the potential ($f(q)$) depends only on the radial variable, then the kickings do not mix up the angular momentum states and the states with same angular momentum evolve among themselves.

4.2 *Quasi-stationary states and their evolution*

(a) *Quasi-stationary states.* Let us examine the state $\Psi_{\alpha}(x, t)$ in eq. (21), with a fixed 'α'

$$\Psi_{\alpha}(q, t) = \sum_{0}^{\infty} T_{\alpha}(t) \cdot p^{\alpha} \cdot v_{\beta}^{\alpha} \cdot \phi_{\beta}(q) \tag{23}$$

(no sum over α), where

$$T(t) = \frac{\varepsilon}{2\hbar} e^{i\lambda_{\alpha}t} \sum_{-\infty}^{\infty} \frac{\exp. i2\pi nt/\tau}{\pi n + \Lambda_{\alpha\beta}}. \tag{23′}$$

Hence

$$|\Psi_{\alpha}|^{2} \propto \{|p^{\alpha}|^{2} + O_{\mathrm{sc}}(t, \tau)\}. \tag{24}$$

This class of states can be looked upon as quasi-stationary states. These states superposition of stationary states $\phi_\beta(q)$ of the unperturbed system. They evolve a common oscillatory time dependent part, which has two factors – one factor exp and the other an oscillatory factor which is periodic with period τ.

Another important property of these states are that they are mutually orthog From

$$\Phi^\alpha(q) = \sum_0^\infty v_\beta^\alpha \cdot \phi_\beta(q)$$

$$\int \Phi^\alpha(q) \cdot \Phi^{\alpha'}(q) \mathrm{d}q = \sum_0^\infty v_\beta^\alpha v_\gamma^{\alpha'} \int \phi_\beta(q) \phi_\gamma(q) \mathrm{d}q$$

$$= \sum_0^\infty v_\beta^\alpha v_\beta^{\alpha'} = \delta_{\alpha\alpha'}.$$

Since $\mathbf{v}^\alpha$ forms a complete set of vector, $\Phi^\alpha(q)$ are also a complete set of orthono functions.

(b) *Time-evolution of quasi-stationary states.* (1) If all the p's excluding p^α ($\neq 0$ zero, (from eq. (23) the initial state is $\Phi^\alpha(q)$), then

$$\Psi(q,t) = \Psi_\alpha(q,t) = T_\alpha(t)\Psi_\alpha(q,0) = T_\alpha \Phi^\alpha(q).$$

Thus the evolution manifest itself by the oscillatory time-dependent factor and th no dispersion among these states.

(2) Next, since the evolution equation (eq. (6)) is linear, for any initial states whic some linear superposition of $\Psi_\alpha(q,0)$

$$\Psi(q,0) = \sum_\alpha p^\alpha \Psi_\alpha(q,0),$$

the time evolved state is simply a superposition of the individual time evolved states

$$\Psi(q,t) = \sum_\alpha T_\alpha(t) p^\alpha \Psi_\alpha(q,0).$$

Thus, these quasi-stationary states evolve independent of each other and there mixing among them due to the kicking. Next, since any arbitrary initial state,

$$\Psi(q,0) = \sum_0^\infty B_\gamma \phi_\gamma(q)$$

$$= \sum_0^\infty (B_\gamma v_\gamma^\alpha)(v_\beta^\alpha \phi_\beta) = \sum_0^\infty (B_\gamma v_\gamma^\alpha) \Psi_\alpha(q,0)$$

5. A special case

In order to show explicitly the effect of kicking on the system, one can consider the simple case of constant potential, $f(q)=1$, i.e., $F_{\alpha\beta}\equiv\delta_{\alpha\beta}$ (say) eq. (14), now reduces to

$$\left\{1+\frac{\varepsilon}{2\hbar}\cot\left(\lambda_\beta+\frac{E_\beta}{\hbar}\right)\frac{\tau}{2}\right\}a_\beta=0. \tag{31}$$

Consequently, for nontrivial solution

$$\frac{\tau}{2}\left(\lambda_\beta+\frac{E_\beta}{\hbar}\right)=-\cot^{-1}\frac{2\hbar}{\varepsilon}\equiv K\,(\text{say}) \tag{31'}$$

and

$$\lambda_\beta=-\frac{E_\beta}{\hbar}+\frac{2K}{\tau}, \tag{31''}$$

where K is a number. Since, in this special case, E_β and ϕ_β corresponds to a distinct λ, one can omit double indices. Finally, from eq. (23)

$$\Psi_\beta(q,t)=\frac{\varepsilon}{2\hbar}\exp.-i\left(\frac{E_\beta}{\hbar}-\frac{2K}{\tau}\right)t.\sum_{-\infty}^{\infty}\frac{\exp.i2\pi nt/\tau}{\pi n+K}\phi_\beta. \tag{32}$$

It is clear that each individual term with ϕ_β is a solution of eq. (6). Thus, if initially the system is at any one of the unperturbed state ϕ_β, it remains in that state even with the kicks. They only introduce the oscillatory factor of period τ. In general

$$\Psi(q,t)=\sum_0^\infty B_\beta\Psi_\beta(q,t) \tag{33}$$

when the initial state is

$$\Psi(q,0)=\sum_0^\infty B_\beta\phi_\beta(q). \tag{33'}$$

This is also expected as q-independent potential do not produce any force. The only change is the phase factor at each kick. Consequently, each unperturbed initial stationary state evolves independently to the corresponding quasi-stationary state and the time average over a period τ remains the same.

6. Discussion

The essential point, which needs to be emphasized is that there are states which evolve independently without mixing with other states, by the kicking. These quasi-stationary states are specified by the potential. Hence any initial state, is not necessarily dispersed over all the states by kicking. Thus, there is no loss of its memory as it is often mentioned.

envisaged in [18] for a system with periodic coefficient.) But, this is apparent as each of them contains a series as a factor of the form

$$\sum_{-\infty}^{\infty} \exp . i\pi(p+k)\frac{t}{\tau}\Big/(p+k).$$

This diverges at $t = n\tau$, as it should be due to δ-function in the coefficient of eq. (6). In fact the derivative of the above series is a δ-function, which leads to discontinuous change at $t = n\tau$.

References

[1] G Casati, R V Chirkov, F M Izralev and J Ford, in *Stochastic behaviour in classical and quantum Hamiltonian systems* edited by G Casati and J Ford, Lecture Notes in Physics (Springer Verlag, Berlin, 1979) **93**, 334

[2] M V Berry, N L Balazs, M Tabor and A Voros, *Ann. Phys. (New York)* **122**, 26 (1979)

[3] F M Izrailev and D L Shepelyanskii, *Theor. Math. Phys.* **43**, 553 (1980)

[4] G M Zaslavsky, *Phys. Rep.* **80**, 157 (1981)

[5] H J Korsch and M V Berry, *Physica* **D3**, 627 (1981)

[6] S Fishman, D R Grempel and R E Prange (i) *Phys. Rev. Lett.* **49**, 509 (1982) and (ii) *Phys. Rev.* **A29**, 1639 (1984)

[7] T Hogg and B A Huberman (i) *Phys. Rev. Lett.* **48**, 711 (1982) and (ii) *Phys. Rev.* **A28**, 22 (1983)

[8] M V Berry, *Proc. Les-Houches Summer School* edited by G Ioosse, R G Hellman and R Stora (North Holland, Amsterdam, 1983) 107

[9] G P Berman and A R Kolovsky, *Physica* **D8**, 117 (1983)

[10] R Blumel, R Meir and V Smilasky, *Phys. Lett.* **A103**, 353 (1984)

[11] J Bellissard, in (*i*) *Trends and developments in the eighties* edited by S Albeverio and Ph. Blanchard (World Scientific, Singapore, 1985) 1 and (ii) *Stochastic process in quantum and classical systems* (Springer Verlag, 1986) 24

[12] G Casati, J Ford, I Guarneri and F Vivaldi, *Phys. Rev.* **A34**, 1413 (1986)

[13] J V Jose, *Phys. Rev. Lett.* **56**, 290 (1986)

[14] A Cohen and S Fishman, *Int. J. Mod. Phys.* **2**, 103 (1988)

[15] M Combescure, *J. Stat. Phys.* **59**, 679 (1990)

[16] B Milek and P Seba, *Phys. Rev.* **A42**, 3213 (1990)

[17] A K Sikri and M L Narchal, *Pramana – J. Phys.* **41**, 509 (1993)

[18] F Gesztesy and H Mitter, *J. Phys.* **A14**, L79 (1981)

[19] N D Sengupta (i) *Phys. Stat. Solidi* **B65**, 351 (1974), (ii) *Phys. Lett.* **A134**, 170 (1988), (iii) *Indian J. Phys.* **49**, 49 (1975), (iv) *Letters in Mathematical Physics* **38**, 275 (196)

Weak decay constants of light and heavy pseudoscalar mesons

N BARIK, S KAR* and P C DASH*
Physics Department, Utkal University, Bhubaneswar 751 004, India
* Physics Department, Prananath College, Khurda 752 057, India

MS received 27 August 1996

Abstract. We investigate the weak leptonic decays of light and heavy pseudoscalar mesons in a relativistic quark model of independent quarks. We perform a static calculation of the decay constant f_M purely on grounds of simplicity. In order to minimize the possible uncertainty in the static calculation, we estimate the ratios of the decay constants which are found to be in good agreement, in the heavy flavor sector, with the predictions of other models available in the literature and existing experimental data. However, there is a noticeable discrepancy in the current prediction for pion decay constant which demonstrates the inherent limitations of the static approximation in the study of non-strange light mesons.

Keywords. Pseudoscalar mesons; quark model; decay constants; static approximation.

PACS Nos 13·20; 12·40

1. Introduction

Knowledge of the pseudoscalar decay constants f_M has been realized to be quite useful in extracting information on the fundamental quantities of the standard model such as the CKM-matrix elements and the top quark mass as well as on the rare B-meson decays. In addition, the decay constants govern the strength of several leptonic, semileptonic and non-leptonic processes. Because of their theoretical and phenomenological importance, there has been several attempts to have reliable estimations of these decay constants within the framework of various suitable schemes.

A theoretical estimation of the decay constants for the decays of pseudoscalar mesons of the type $(M \rightarrow l\bar{\nu}_l)$ requires a rigorous field theoretic formulation of the quark–antiquark annihilation inside the meson-bound-state; which like many other low-energy phenomena, cannot be studied in a straight-forward manner by the first-principle-application of QCD–the underlying theory of strong interaction between quarks and gluons at the structural level of hadrons. Therefore, various phenomenological models [1–16] have been proposed to study the weak leptonic decays of light as well as heavy pseudoscalar mesons giving widely different predictions on the decay constants. While predictions of various models in this sector are not consistent, the experiments have so far made limited progress. In view of this, Barik and Dash [17] investigated the weak leptonic decays of light as well as heavy pseudoscalar harmonic potential [17–21]. The model predictions [17] are not only found to agree remarkably well with the experimental data [22] for f_π and f_K in the light flavor sector, but also consistent with the findings of many other model calculations giving

$$f_{B_c} > f_{B_s} > f_B;\ f_{D_s} > f_D;\ f_D > f_B;\ f_\pi > f_B.$$

In this work [17], the quark–antiquark annihilation inside the meson-bound-state is treated field theoretically with the construction of the decaying meson state as appropriate momentum-wave-packets reflecting the respective constituent quark–antiquark momentum distribution amplitudes obtained from the bound quark eigen-mode of the model.

In the present work we would like to tackle the same problem in a straight-forward manner in the same model [17–21] through a different approach without incorporating rigorously the mesonic core-state as a momentum wave-packet. Instead one can use the possible expansion of the quark–antiquark field operators appearing in the effective interaction Hamiltonian density that describes the S-matrix operator for the decay process, by a linear combination of the complete set of quark eigen-modes available in the model. The quark annihilation and the antiquark creation operator in the corresponding flavor and eigen-modes provide the appropriate co-efficients of the expansion. The decaying pseudoscalar meson can be considered in the ground state by the usual spin flavor SU (6)-expression with the quark–antiquark creation operators corresponding to the lowest eigen-modes. The transition amplitudes for the decay would then involve essentially the lowest eigen-modes of the quark–antiquark. Such an approach effectively taken in a static limit, which makes the calculation quite straight-forward and tractable, has been applied successfully in the study of the weak radiative decays of the charmed pseudoscalar mesons [19] and the radiative decays of light and heavy mesons [20, 21]. The results so obtained are found to be reasonably satisfactory except in the decays involving the light mesons especially the pion. Going beyond the static limit and adding some momentum dependence due to recoil effect in a more realistic calculation [20], the predictions in the light meson (especially the pion)-decays can get significantly improved. However, the predictions in heavier meson decays remain almost the same as obtained from the static calculation [19]. Therefore, a calculation of the individual decay constants in weak decays like ($M \rightarrow l\bar{\nu}_l$), in a 'static'-approximation may not be adequate enough. Nevertheless we do believe that a reliable estimation can still be made for the ratio of the weak decay constants corresponding to the different mesons particularly in heavy sector. With this contention in mind we would prefer to revisit the weak leptonic decays of light and heavy pseudoscalar mesons in the present model employing a 'static'-approximation purely on grounds of simplicity.

This paper is organized in the following manner. In §2 we provide some relevant conventions and consequences of the present model. We describe the transition matrix elements and derive the partial decay width with correct kinematic factors from which we extract the expression for the pseudoscalar decay constants in §3. Section 4 embodies our results and discussion.

2. Model framework

According to this model, a meson is pictured as a color singlet assembly of a quark and an antiquark independently confined by an average flavor independent potential of the form [17–21] non-perturbative multigluon mechanism. The possible quark–gluon interaction at short distance originating from one gluon exchange and the quark–pion interaction required in the non-strange light-flavor sector to preserve chiral symmetry are presumed to be residual interactions compared to the dominant confining part. Although this residual interactions treated perturbatively in the model are crucial in generating meson-mass-splittings [23, 24], their role in the decays of mesons are considered less significant. Therefore, to a first approximation, it is believed that the zeroth order quark dynamics inside the meson-core generated by the confining part of interaction, can provide an adequate description of the meson decay process. In such a picture, the independent quark Lagrangian density in zeroth order is

$$\mathscr{L}^{0}_{q}(x) = \bar{\psi}_{q}(x)\left[\frac{i}{2}\gamma^{\mu}\overleftrightarrow{\partial}_{\mu} - m_{q} - U(r)\right]\psi_{q}(x). \tag{2}$$

The ensuing Dirac equation with $E'_q = (E_q - V_0/2)$, $m'_q = (m_q + V_0/2)$, $\lambda_q = (E'_q + m'_q)$ and $r_{0q} = (a\lambda_q)^{-1/4}$ admits static solution of positive and negative energy in zeroth order. Corresponding to the ground state mesons, these solutions can be obtained in the form

$$\phi^{(+)}_{q\lambda}(\mathbf{r}) = \frac{1}{\sqrt{4\pi}}\begin{pmatrix} i g_q(r)/r \\ \boldsymbol{\sigma}\cdot\hat{r} f_q(r)/r \end{pmatrix}\chi_{\lambda},$$

$$\phi^{(-)}_{q\lambda}(\mathbf{r}) = \frac{1}{\sqrt{4\pi}}\begin{pmatrix} i(\boldsymbol{\sigma}\cdot\hat{r}) f_q(r)/r \\ g_q(r)/r \end{pmatrix}\tilde{\chi}_{\lambda}. \tag{3}$$

Here the two component spinors χ_λ and $\tilde{\chi}_\lambda$ stand for

$$\chi_{\uparrow} = \begin{pmatrix} 1 \\ 0 \end{pmatrix}, \chi_{\downarrow} = \begin{pmatrix} 0 \\ 1 \end{pmatrix} \quad \text{and} \quad \tilde{\chi}_{\uparrow} = \begin{pmatrix} 0 \\ -i \end{pmatrix}, \tilde{\chi}_{\downarrow} = \begin{pmatrix} i \\ 0 \end{pmatrix}$$

respectively. The reduced radial parts in the upper and lower component solutions corresponding to the quark-flavor 'q' are

$$g_q(r) = \mathcal{N}_q\left(\frac{r}{r_{0q}}\right)\exp\left(-r^2/2r_{0q}^2\right),$$

$$f_q(r) = -\frac{\mathcal{N}_q}{\lambda_q r_{0q}}\left(\frac{r}{r_{0q}}\right)^2 \exp\left(-r^2/2r_{0q}^2\right), \tag{4}$$

where the normalization factor $\mathcal{N}_q$ is given by

$$\mathcal{N}_q^2 = \frac{8\lambda_q}{\sqrt{\pi}\, r_{0q}}\frac{1}{(3E'_q + m'_q)}. \tag{5}$$

The quark binding energy of zeroth order in the meson ground-state is derivable from the bound-state condition

$$\sqrt{\frac{\lambda_q}{a}}(E'_q - m'_q) = 3. \tag{6}$$

This provides a brief outline of the model and its conventions which can now be adopted to re-investigate the weak leptonic decays of pseudo-scalar mesons [12–17] using a simplified approach based on static-approximation.

3. Weak decay constant

In this section we consider the weak leptonic decays of charged pseudoscalar mesons such as $\pi^\pm, K^\pm, D^\pm, D_s^\pm, B^\pm$ and $B_c^\pm$ using the model convention described in the previous section in the static approximation. Assuming that the main contribution to the weak leptonic decay comes from annihilation of the bound quark–antiquark inside the meson into a single virtual W-boson which ultimately disintegrates into a leptonic pair $(l\bar{\nu}_l)$, we can illustrate it by the corresponding Feynman diagram in figure 1 from which S-matrix element is effectively written as

$$S_{fi} = -i\frac{G_F}{\sqrt{2}}\mathscr{V}_0\int \mathrm{d}^4x\, T[\langle l(\mathbf{k}_l,\lambda_l)\nu(\mathbf{k}_\nu,\lambda_\nu)\,|\,\bar{\psi}_\nu(x)\gamma^\mu(1-\gamma_5)\psi_l(x)$$

$$\times\sum_{\mathrm{q}}\bar{\psi}_{\mathrm{q}_1}(x)\gamma_\mu(1-\gamma_5)\psi_{\mathrm{q}_2}(x)\,|\,M\rangle]. \tag{7}$$

Here $\mathscr{V}_0 = \cos\theta_c(\sin\theta_c)$ with θ_c being Cabibbo angle. The usual lepton field operator and quark field operator are taken respectively in the form

$$\psi_l(x) = \sum_{\lambda_l}\frac{1}{(2\pi)^{3/2}}\int\frac{\mathrm{d}\mathbf{k}_l}{\sqrt{2E_l}}\,[\hat{d}_l(\mathbf{k}_l,\lambda_l)u(\mathbf{k}_l,\lambda_l)\exp(-ik_lx)$$

$$+\hat{\tilde{d}}{}_l^{\dagger}(\mathbf{k}_l,\lambda_l)v(\mathbf{k}_l,\lambda_l)\exp(ik_lx)] \tag{8}$$

and

$$\psi_{\mathrm{q}}(x) = \sum_{\xi}[\hat{b}_{\mathrm{q}\xi}\,\phi_{\mathrm{q}\xi}^{(+)}(r)\exp(-iE_{\mathrm{q}\xi}t) + \hat{\tilde{b}}{}_{\mathrm{q}\xi}^{\dagger}\phi_{\mathrm{q}\xi}^{(-)}(r)\exp(iE_{\mathrm{q}\xi}t)], \tag{9}$$

where 'q' stands for quark flavor, ξ for the set of Dirac quantum numbers specifying all possible eigenmodes; $\hat{b}_{\mathrm{q}\xi}$ and $\hat{\tilde{b}}{}_{\mathrm{q}\xi}^{\dagger}$ are quark annihilation and antiquark creation operators; $\phi_{\mathrm{q}\xi}^{(+)}(\mathbf{r})$ and $\phi_{\mathrm{q}\xi}^{(-)}(\mathbf{r})$ are the quark and antiquark wave functions with quark binding energy $E_{\mathrm{q}\xi}$ corresponding to the eigen-modes 'ξ'.

The quark field operators $\psi_{\mathrm{q}}(x)$ appearing in the effective interaction Hamiltonian density that describes the S-matrix element in (7) finds its expansion as a linear combination of all possible quark eigen-modes $\phi_{\mathrm{q}\xi}^{(+)}(\mathbf{r})$ and $\phi_{\mathrm{q}\xi}^{(-)}(\mathbf{r})$ available in the

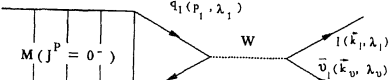

$q_1(\vec{p}_1, \lambda_1)$
W
$l(\vec{k}_l, \lambda_l)$
$M(J^P = 0^-)$
$\bar{\nu}_l(\vec{k}_\nu, \lambda_\nu)$

model with quark annihilation and antiquark creation operators ($\hat{b}_{q\xi}$ and $\hat{\tilde{b}}^{\dagger}_{q\xi}$) as appropriate co-efficient of expansion. Since the decaying meson is considered in its ground state in the present calculation based on a 'static' approximation, the relevent S-matrix element here, in the long run, would essentially acquire contribution of only the lowest eigen-modes present in the field expansion of (9). Therefore to avoid unnecessary complication, we treat the quark field expansion effectively in terms of the lowest eigen-modes as given in (3) corresponding to the ground-state meson without affecting the final result in any way. With this contribution, the leptonic and hadronic parts can be simplified separately in the vacuum insertion technique to find the effective S-matrix element in the form

$$S_{fi} = \frac{-i}{(2\pi)^2} \frac{G_F}{\sqrt{2}} \mathscr{V}_0 \, \delta(E_l + E_\nu - M) \times l^\mu(\mathbf{k}_l, \mathbf{k}_\nu; \lambda_l, \lambda_\nu) \, h_\mu \tag{10}$$

where the leptonic and hadronic amplitude parts are

$$l^\mu(\mathbf{k}_l, \mathbf{k}_\nu; \lambda_l, \lambda_\nu) = \frac{\bar{u}_l(\mathbf{k}_l, \lambda_l)\gamma^\mu(1-\gamma_5)v_\nu(\mathbf{k}_\nu, \lambda_\nu)}{\sqrt{4E_l E_\nu}} \tag{11}$$

and

$$\begin{aligned} h_\mu = \int \mathrm{d}r \exp[i(\mathbf{k}_l + \mathbf{k}_\nu)\cdot\mathbf{r}] \Big\langle 0 \Big| \sum_{q,m} \hat{\tilde{b}}_{q_1,m_1} \hat{b}_{q_2,m_2} \bar{\phi}^{(-)}_{q_1,m_1}(\mathbf{r}) \gamma_\mu \\ \times (1-\gamma_5) \phi^{(+)}_{q_2,m_2}(\mathbf{r}) \Big| M \Big\rangle. \end{aligned} \tag{12}$$

It must be noted that there is an obvious difficulty encountered here in realizing the required energy conservation at the quark-boson vertex; since the sum total of the kinetic energy of the constituent quark and antiquark in the process in not equal to the mass–energy of the decaying pseudoscalar meson considered in its rest frame. This is a common feature with all the phenomenological models based on leading order calculation. In the absence of any rigorous field theoretic formulation of the bound quark–antiquark annihilation inside the meson, we assume that the differential amount of energy is somehow made available to the W-boson when the quark–antiquark pair annihilation takes place with the disappearance of meson-bound-state. In doing so the sum total of quark–antiquark energy ($E_q + E_{\bar{q}}$) is replaced by the meson rest-mass M in the argument of the energy delta function.

In calculating the S-matrix element from (10), the decaying pseudoscalar meson M in its ground state is described here by the usual spin-flavor $SU(6)$-expressions with the quark and antiquark creation operators corresponding to the lowest eigen-mode. Then in the flavor $SU(2)$-symmetry ($m_u = m_d \neq m_s$), the hadronic part h_μ is obtained in the form

$$h_\mu = \sqrt{\frac{3}{2}} \int \mathrm{d}\mathbf{r} \exp[i(\mathbf{k}_l + \mathbf{k}_\nu)\cdot\mathbf{r}][\bar{\phi}^{(-)}_{q\downarrow}(r)\gamma_\mu(1-\gamma^5)\phi^{(+)}_{q\uparrow}$$

$$\Gamma(M\to l\nu)=\sum_{\lambda_l,\lambda_\nu}\int\frac{|S_{fi}|^2}{T}\frac{V\mathrm{d}\mathbf{k}_l}{(2\pi)^3}\frac{V\mathrm{d}\mathbf{k}_\nu}{(2\pi)^3}\tag{14}$$

in the form

$$\Gamma(M\to l\nu)=\frac{3G_F^2\mathscr{V}_0^2}{2(2\pi)^5}\int\mathrm{d}\mathbf{k}_l\mathrm{d}\mathbf{k}_\nu\delta(E_l+E_\nu-M)\,L^{\mu\nu}H_{\mu\nu}.\tag{15}$$

The contribution of the space-like part of the hadronic amplitude, in fact, vanishes in the angular integration and the only non-vanishing contribution to S_{fi} is effectively derived from its time-like component h_0 which, in terms of reduced radial parts of the upper and lower component solutions $g_{\mathrm{q}}(r)$ and $f_{\mathrm{q}}(r)$, is obtained as

$$h_0=\frac{\sqrt{2}}{4\pi}\int\mathrm{d}\mathbf{r}\exp\left[i(\mathbf{k}_l+\mathbf{k}_\nu)\cdot\mathbf{r}\right]\left[\frac{f_{\mathrm{q}_1}(r)f_{\mathrm{q}_2}(r)-g_{\mathrm{q}_1}(r)g_{\mathrm{q}_2}(r)}{r}\right]^2.\tag{16}$$

It is then straight forward to find the effective hadronic as well as leptonic tensor in the respective forms as

$$H_{00}=\left|\frac{\sqrt{2}}{4\pi}\int\mathrm{d}\mathbf{r}\exp\left[i(\mathbf{k}_l+\mathbf{k}_\nu)\cdot\mathbf{r}\right]\left[\frac{f_{\mathrm{q}_1}(r)f_{\mathrm{q}_2}(r)-g_{\mathrm{q}_1}(r)g_{\mathrm{q}_2}(r)}{r}\right]^2\right|^2\tag{17}$$

and

$$L^{00}=\frac{1}{4E_lE_\nu}\mathrm{Tr}\left[(\not{k}_l+m_l)\gamma^0(1-\gamma_5)(\not{k}_\nu+m_\nu)\gamma^0(1-\gamma_5)\right].\tag{18}$$

It is convenient to integrate the quantity in (15) by a transformation of co-ordinates with the substitution of relative momentum **p** and centre of mass momentum **P** as

$$\mathbf{p}=\tfrac{1}{2}(\mathbf{k}_l-\mathbf{k}_\nu);\quad\mathbf{P}=(\mathbf{k}_l+\mathbf{k}_\nu).\tag{19}$$

Of course, **P** is constrained by energy conservation; but because momentum conservation is not automatically guaranteed while describing the meson state in terms of its basic constituents (quark–antiquark) bound inside the meson, the final state leptons need not have $|\mathbf{P}|=|\mathbf{k}_l+\mathbf{k}_\nu|=0$. We must, however, hope that most of $\Gamma(M\to l\nu)$ comes from $|\mathbf{P}|$ small compared to M if this model calculation is to have any resemblance to the physical decays. We, therefore, proceed by setting $|\mathbf{P}|=0$ in l^μ as well as in the energy delta function $\delta(E_f-E_i)$ only; but not in h_μ, thus preserving the typical bound-state-characteristics of the constituent quark and antiquark. Calculating the leptonic part and hadronic part in (15) appropriately in the above expression after integration; one obtains

$$\Gamma(M\to l\nu)=\frac{3G_F^2\mathscr{V}_0^2}{2(2\pi)^5}\mathscr{L}^{00}\mathscr{H}_{00}\tag{20}$$

with

$$\mathscr{L}^{00}=2\pi m_l^2\left(1-\frac{m_l^2}{M^2}\right)^2\tag{21}$$

$$\mathscr{H}_{00} = 4\pi^2 \int_0^{\infty} \mathrm{d}r \left[\frac{f_{q_1}(r) f_{q_2}(r) - g_{q_1}(r) g_{q_2}(r)}{r} \right]^2 . \tag{22}$$

Then using the explicit forms of $f_q(r)$ and $g_q(r)$ given in (4), the hadronic part $\mathscr{H}_{00}$ can be integrated out in a closed form so as to finally obtain the decay width in the usual form as

$$\Gamma(M \to l\nu) = \frac{G_F^2 \mathscr{V}_0^2}{8\pi} M m_l^2 \left(1 - \frac{m_l^2}{M^2}\right)^2 f_M^2 . \tag{23}$$

Here the weak leptonic decay constant f_M has been extracted out, after realizing the correct kinematic factors in (23). Thus in terms of the model quantities the weak decay constant f_M is realized here in the form

$$f_M^2 = \frac{3}{4\sqrt{\pi} M} \left(\frac{\mathscr{N}_{q_1} \mathscr{N}_{q_2}}{r_{0q_1} r_{0q_2}} \right)^2 \left(\frac{r_{0q_1}^2 r_{0q_2}^2}{r_{0q_1}^2 + r_{0q_2}^2} \right)^{3/2}$$
$$\times \left[\frac{15}{4\lambda_{q_1}^2 \lambda_{q_2}^2 (r_{0q_1}^2 + r_{0q_2}^2)^2} - \frac{3}{\lambda_{q_1} \lambda_{q_2} (r_{0q_1}^2 + r_{0q_2}^2)} + 1 \right] . \tag{24}$$

Hence f_M for the specific pseudoscalar meson decay can be calculated from (24) with the relevant input-parameters available from the constituent level description of the meson. Although we extract here the expression for the weak decay constant f_M through the calculation of the corresponding decay width, it is always possible to obtain it directly from the hadronic part of the transition matrix element. Therefore, we can use (24) as a general expression for the decay constant even for the neutral pseudoscalar meson such as B_s^0.

4. Results and discussion

In this section we evaluate the decay constants for the weak leptonic decays of pseudoscalar mesons such as $\pi^{\pm}$, $K^{\pm}$, $D^{\pm}$, $D_s^{\pm}$, $B^{\pm}$, B_s^0 and $B_c^{\pm}$ from the expression in (24). The input parameters that are primarily required are the potential parameters (a, V_0) of the model and the quark masses ($m_u = m_d$, m_s, m_c, m_b). The potential parameters (a, V_0) are given according to ref. [17–21] as

$$(a, V_0) \equiv (0{\cdot}0171626\,\mathrm{GeV}^3,\ -0{\cdot}1375\,\mathrm{GeV}) \tag{25}$$

and the quark masses [17–21] are taken from the model in its earlier applications demonstrating its success in wide-ranging hadronic phenomena. The meson masses appearing in the expression for f_M in (24) are taken to be the experimental meson masses [22]. However in the decay of the heavy meson $B_c^{\pm}$, the corresponding experimental data for the mass M_{Bc} is not yet available and therefore we take our model mass as $M_{Bc} = 6{\cdot}2642$ GeV [17]. The model dynamics provides other relevant quantities such as E_q, λ_q, r_{0q} and $\mathscr{N}_q$ etc. which are given in table 1.

Table 2 provides our result for the decay constants in comparison with those of some previous calculations [6–8, 10, 11, 14, 17]; along with the experimental data. The predictions of almost all the model calculations available in the literature except a few

E_q along with other relevant model solutions for the potential param
$(a, V_0) \equiv (0{\cdot}017166\,\mathrm{GeV}^3, -0{\cdot}1375\,\mathrm{GeV})$.

Quark 'q'	m_q (GeV)	E_q (GeV)	λ_q (GeV)	r_{0q} $(\mathrm{GeV})^{-1}$	$\mathcal{N}_q$ (GeV)
u	0·07875	0·47125	0·55	3·20806	0·689
d	0·07875	0·47125	0·55	3·20806	0·689
s	0·31575	0·59100	0·90675	2·83114	0·805
c	1·49276	1·57951	3·07227	2·08674	1·021
b	4·77659	4·76633	9·54292	1·57185	1·194

such as ref. [2, 16] indicate that f_B is smaller than both f_π and f_D. The present calc tion not only confirms this but also predicts $f_K = 148$ MeV in reasonable agreer with the experimental value. The prediction on f_D and f_{D_s} are also found to be withi experimental error limit [22]. This model calculation in the static limit, like n others [8, 10, 13, 14] also concludes that

$$f_{B_c} > f_{B_s} > f_B;\ f_{D_s} > f_D;\ f_D > f_B;\ f_\pi > f_B.$$

It is, in fact, more reliable to evaluate the ratio R of the decay constants w minimizes the possible model constraints in such calculation. In ref. [17] these rati calculated from this model beyond static approximation have been compared those of several other model calculations providing an overall agreement. In table provide a comparison between these ratios obtained in the static limit here and tho ref. [3, 4, 6, 8, 10, 11, 13–15, 17], to find that the ratios obtained from both approa agree each other very well in the decays of heavy-flavored mesons. This vindicate earlier contention that in the study of heavier meson decays whether one adop approach in the static limit or beyond, the final results are almost the same.

However a noticeable discrepancy is observed here in the pionic sector; predi $f_\pi \simeq 215$ MeV. Though such a prediction on f_π is comparable to that of Hay and U $[f_\pi = 195\,\mathrm{MeV}]$ and even better than that of Gunduc, Hay and Wa $[f_\pi = 408{\cdot}18\,\mathrm{MeV}]$ in their bag model calculations [12] based on static cavity app mation, it is certainly an over-estimation compared to the previous prediction [1 this model as well as the experimental value [22]. The failure of the present approa describing the weak decay of light meson especially the most illusive pion is ther ascribed to the inherent limitation of the static calculation in this sector. Moreove quark model description of the pion is that of $q\bar{q}$ bound-state which is different fro pion of PCAC. Admittedly though there exists an apparent dichotomy betwee $q\bar{q}$-structure and the Goldstone-boson facet of the pion, a somewhat blended pi [23, 25] can not be totally ruled out. Thus no conclusive remark has been given regard to real dynamics of the pion constituents consisting of the lightest flavor (up down) quark–antiquark. Until a clear understanding of such intriguing nature of is available through some more complete theoretical formulation, such a simp approach as the present one is perhaps quite inadequate to describe the real dyna involved in this sector and hence the discrepancy in the predicted value for f_π. This vindicates our contention that the static calculation is not entirely trustwort

Table 2. Decay constants of pseudoscalar meson in MeV in comparison with the predictions of other models and the experiment.

Model	f_π	f_K	f_D	f_{D_s}	f_B	f_{B_s}	f_{B_c}
Expt [22]	$131·73 \pm 0·15$	$160·6 \pm 1·3$	< 310	—	—	—	—
Present work	215·2	148·1	108·9	134·6	75·8	96·1	134·9
Relativized quark [8] set 2	60	101	109	129	71	91	133
Relativized quark [8] set 3	79	138	131	175	83	119	204
Potential [8] set 2^b	100	153	149	160	96	111	141
Potential [17]	138	157	161	205	122	154	221
Potential [14]	139	176	150	210	125	175	425
Bag [10]	178	182	148	166	98	—	—
Bag [11]	—	—	172	196	149	170	255
Lattice [6]	—	—	174 ± 53	234 ± 72	105 ± 34	155 ± 75	—
Lattice [7]	141 ± 21	155 ± 21	282 ± 18	—	183 ± 28	—	—

Table 3. Ratios of the decay constants in comparison with the prediction of other models.

Model	f_B/f_D	f_{B_s}/f_{D_s}	f_{B_s}/f_B	f_{D_s}/f_D
Present work	0·70	0·71	1·27	1·24
Relativized quark [8] set 2	0·65	0·71	1·28	1·18
Relativized quark [8] set 3	0·63	0·68	1·43	1·34
Potential [8] set 2^b	0·64	0·69	1·16	1·07
Potential [17]	0·75	0·76	1·27	1·27
Potential [13]	0·63	0·67	1·26	1·19
Potential [14]	0·83	0·83	1·40	1·40
Factorization [15]	0·68	0·68	1·25	1·25
Bag [10]	0·66	—	—	1·12
Bag [11]	0·87	0·87	1·13	1·14
Sum Rule [3]	1·10	0·92	1·07	1·25
Lattice [4]	0·62	0·70	1·07	1·11
Lattice [6]	0·60	0·66	1·48	1·34

describing the decays of light flavored meson especially the pion. Obviously the ratio f_K/f_π is found to be under-estimated compared to that in ref. [17] and the experiment [22].

On the whole, the predictions of the present model calculations in the static limit in the decays of heavy mesons are in reasonable agreement with those of our previous calculation [17] beyond static limit justifying the applicability of the static calculation in the heavy flavor sector. On the other hand, the quantitative discrepancy observed in the decay of light meson such as the pion is due to the inherent limitation of static approximation in the light (especially the non-strange light)-flavor sector. This has been overcome quite satisfactorily in extending the model application to this sector beyond the static limit [17]. Thus within the working approximation, the present model [17-21], adopting a static calculation on the grounds of simplicity alone, provides a suitable and straight-forward frame-work to study the weak leptonic decays of heavy pseudoscalar mesons.

References

[1] S N Sinha, *Phys. Lett.* **B178**, 110 (1986)
S Godfrey, *Phys. Rev.* **D33**, 1391 (1986)
[2] L J Reinders, *Phys. Rev.* **D38**, 947 (1988)
C A Dominguez and N Paver, *Phys. Lett.* **B197**, 423 (1987)
[3] S Narison, *Phys. Lett.* **B198**, 104 (1987); **285**, 141 (1992)
[4] M B Gavela *et al*, *Phys. Lett.* **B206**, 113 (1988)
[5] T A De Grand and R D Loft, *Phys. Rev.* **D38**, 954 (1988)
R M Woloshyn *et al*, *Phys. Rev.* **D39**, 978 (1989)
[6] C Bernard, T Draper, G Hockney and A Soni, *Phys. Rev.* **D38**, 3540 (1988)
[7] H W Hamber, *Phys. Rev.* **D39**, 896 (1989)
[8] S Capstick and S Godfrey, *Phys. Rev.* **D41**, 2856 (1990)
[9] S Godfrey and N Isgur, *Phys. Rev.* **D32**, 189 (1985)
[10] E Golowich, *Phys. Lett.* **B91**, 271 (1980)

Iays and M V K Ulehla, *Phys. Rev.* **D13**, 1339 (1976)
Gunduc, A J G Hay and P J Walters, *Phys. Rev.* **D21**, 271 (1980)
O'Donnell, *Phys. Lett.* **B261**, 136 (1991)
Krasemann, *Phys. Lett.* **B96**, 397 (1980)
osner, *Phys. Rev.* **D42**, 3732 (1990)
Cea, P Colangelo, L Cosmai and G Nardulli, *Phys Lett.* **B206**, 691 (1988)
S Mathur and T Yamawaki, *Phys. Lett.* **B107**, 127 (1981); *Phys. Rev.* **D29**, 2057 (1984)
Barik and P C Dash, *Phys. Rev.* **D47**, 2788 (1993)
Barik, B K Dash and M Das, *Phys. Rev.* **D31**, 1652 (1985); **D32**, 1725 (1985)
Barik and B K Dash, *Phys. Rev.* **D33**, 1925 (1986); **D34**, 2092 (1986); 2803 (1986)
Barik, P C Dash and A R Panda, *Phys. Rev.* **D46**, 3856 (1992); **47**, 1001 (1993)
Barik and P C Dash, *Phys. Rev.* **D47**, 2788 (1993); **D53**, 1366 (1996)
Barik and P C Dash, *Mod. Phys. Lett.* **A10**, 103 (1995)
Barik and P C Dash, *Phys. Rev.* **D49**, 299 (1994)
Barik P C Dash and A R Panda, *Phys. Rev.* **D46**, 3856 (1992)
view of particle properties, *Particle Data Group*
Montanet *et al*, *Phys. Rev.* **D50**, part I (1994)
E Palladino and P Leal Ferreira, IFT-Sao Paulo Report No. IFT/P-35/88 (unpublished)
Barik, B K Dash and P C Dash, *Pramana--J. Phys.* **29**, 543 (1987)
E De Tar, *Phys. Rev.* **D24**, 752 (1981)

Meson spectroscopy with confined one gluon exchange potential

K B VIJAYA KUMAR, A K RATH* and S B KHADKIKAR†
Department of Physics, Mangalore University, Mangalagangotri, Mangalore 574 199, India
*P.G. Department of Physics, Sambalpur University, Sambalpur 768 019, India
†Physical Research Laboratory, Navrangpura, Ahmedabad 380 009, India

MS received 7 October 1996; revised 20 January 1997

Abstract. Confined gluons-exchange among relativistically confined quarks is used to calculat the ground state masses and the radially excited states of pseudo scalar and vector meson A good agreement is obtained with the experimental masses. The limitation of the perturbativ treatment of estimating the $N-\Delta$ and $\pi-\rho$ splitting using one-gluon-exchange potential i pointed out.

Keywords. Quark model; harmonic model; confined gluon; current confinement.

PACS No. 13·76

1. Introduction

There is a wealth of experimental data [1] in hadron spectroscopy that woul constitute a good testing ground for nonperturbative quantum chromodynamic (QCD). Since the exact form of confinement from QCD is not known, one has to go fo phenomenological models. The phenomenological models are either non-relativisti quark models (NRQM) [2–10] with a suitable chosen potential, or relativistic model [11–15, 18] where the interaction is treated perturbatively.

The earliest QCD based models employed to study hadron spectroscopy was b De Rujula *et al* [2]. Here, it was argued that the effective short-range force arise from one gluon exchange potential (OGEP). The model had a reasonable succes and could explain the origin and sign of the Σ-Λ splitting and also predicted th masses of charmed mesons and baryons. Further, Bhaduri *et al* [4] examine several phenomenological non-relativistic quark–antiquark ($q\bar{q}$) potential with different radial dependences, for the confinement along with the inclusion the conventional OGEP. The relativistic effects were completely ignored. Though the model was successful in explaining the spectra of mesons and the masses ground state baryons, the π-ρ splitting remained unexplained [4]. A comprehensiv list of references on potential models may be found in a review paper by Lichtenber [5]. In recent years there are varieties of NRQM essentially making use of OGEP wit various forms of confinement potentials essentially to study heavy quark spectroscop [7–10]. Meson spectroscopy also has been studied by integration of Schrödinge equation numerically [6].

Among the relativistic models, Ferreira *et al* [11, 12] investigated several properties of low-lying hadrons under the assumption that quarks are confined by a Lorentz scalar and vector potential. Both, linear and quadratic forms of confinement schemes were used. The results were fairly satisfactory as they could account for the decreasing spacing between radially excited states of a given orbital angular momentum in both meson and baryon spectra. Bander *et al* [13] used a relativistic bound state formalism, in order to make a simultaneous study of all meson system from those composed of only heavy quarks to those made up of only light quarks. In a relativized quark model, Isgur and his collaborators [14, 15] used a parametrized potential and incorporated relativisitic kinematics to describe all mesons in the same framework. In the model [14], attempts were made to identify all types of relativistic effects, including smearing, nonlocality and momentum dependent effective potentials. The results of the model were supported by an extensive analysis of strong, electromagnetic and weak meson couplings. In spite of the profound success, in the model, to cope up with relativistic effects, new set of parameters was added which, in principle, should have been calculated from the basic theory. In recent years, mock-meson method has been widely used for calculation of hadronic matrix elements to examine the decay constants of heavy–light mesons [7-9, 14–17].

In this paper we have investigated the effect of exchange of confined gluons on the masses of mesons and their radially excited states in the framework of relativisitic harmonic model (RHM) [18]. The earlier phenomenological quark models [2–17] put forth to explain the baryon and meson spectroscopy have incorporated the confinement of quarks, but the effect of confinement of gluons on the mesonic/baryonic states has not been taken into account. The essential new ingredient is the investigation of the mesonic states, taking into account the confinement of gluons in addition to the conventional confinement of quarks. In the quark potential model, Fermi–Breit interaction which give rise to the $N - \Delta$ and $\pi - \rho$ splitting are treated as perturbation. The OGEP being attractive for π, and for a nucleon a naive perturbative treatment of one gluon hyperfine interaction is incorrect and hence one obtains a high value for the pion mass. This leads to further renormalization of strength of interaction for a better fit. Also, the most prominent flaw of non-relativisitic potential models is the neglect of relativistic effects and gluon dynamics [2–6].

In our present work, for the quarks we have made use of the relativistic harmonic oscillator Lorentz scalar and vector (RHM) confinement model [18]. The RHM for the light hadrons with constant effective one gluon exchange hyperfine interaction gave quite an impressive account of hadronic masses and baryonic magnetic moments. The current confinement model (CCM) developed in the spirit of RHM has been successful in describing the glue-ball spectra [19–21]. The confined gluon propagators (CGP) are derived in CCM. We have used CGP to obtain the confined one gluon exchange potential (COGEP) [21–23]. The hamiltonian which we are using in our investigation has only kinetic energy and the confinement potential, in addition to two-body COGEP. In our earlier work it was shown that the terms in the COGEP arising out of confinement of gluons give the required intermediate range attraction in the nucleon–nucleon interaction [22, 23]. Also, we obtained good n–p and p–p differential cross

The paper is divided into five sections. In § 2, a brief review of the RHM model is given. In § 3, COGEP is obtained using CGP. In § 4, we discuss the formulation of the problem and in § 5, we summarize and state the important conclusions.

2. Relativistic harmonic model (RHM)

In the RHM [18], quarks in a hadron are confined through the action of a Lorentz scalar plus a vector harmonic oscillator potential

$$\tfrac{1}{2}(1+\gamma_0)\alpha^2 r^2 + M, \tag{1}$$

where $\gamma_0 = \begin{bmatrix} 1 & 0 \\ 0 & -1 \end{bmatrix}$, and M is a constant mass and α^2 is the confinement strength. In the RHM the quark wave function (ψ) is given by

$$\psi = N \begin{bmatrix} \phi \\ \dfrac{\sigma\cdot\mathbf{P}}{E+M} \quad \phi \end{bmatrix}, \tag{2}$$

where

$$N = \sqrt{\frac{2(E+M)}{3E+M}}. \tag{3}$$

Here it is to be noted that E is an eigenvalue of the single particle Dirac equation with the interaction given in (1). We perform a similarity transformation to eliminate the lower component such that

$$U\psi = \phi, \tag{4}$$

where U is given by

$$\frac{1}{N\left[1+\dfrac{\mathbf{P}^2}{(E+M)^2}\right]} \begin{bmatrix} 1 & \dfrac{\sigma\cdot\mathbf{P}}{E+M} \\ -\dfrac{\sigma\cdot\mathbf{P}}{E+M} & 1 \end{bmatrix}. \tag{5}$$

Here U is a momentum and state (E) dependent transformation operator. With this transformation, ϕ satisfies the 'harmonic oscillator' wave equation

$$\left(\frac{p^2}{E+M} + \alpha^2 r^2\right)\phi = (E-M)\phi. \tag{6}$$

Any operator (O) acting on ψ is then transformed to $\tilde{O}$ acting on ϕ.

$$\tilde{O} = (U^+)^{-1} O U^{-1}. \tag{7}$$

The eigenvalue of (6) is given by

where Ω_N is the energy dependent oscillator size parameter given by

$$\Omega_N = \alpha(E_N + M)^{1/2}.$$

The total energy or the mass of the hadron is obtained by adding the indivi contributions of the quarks. The spurious centre of mass (CM) is corrected [24 using intrinsic operators for the $\Sigma_i r_i^2$ and $\Sigma_i \nabla_i^2$ terms appearing in the Hamilto This amounts to just subtracting the CM motion zero contribution from th expression. It should be noted that this method is exact for the 0S state quarks a CM motion is also in the 0S state.

The parameters in our model [18] α^2, E, M, b $(1/\sqrt{\Omega})$, where b is the oscillato parameter, are chosen in the RHM to give reasonable values for the root mean sq charge radii and the magnetic moments of the nucleon. The constant M is determ by the ratio of the axial coupling to the vector coupling. The confinement strength fixed by the stability condition for the nucleon mass against the variation of the parameter b.

$$\frac{\partial}{\partial b}\langle N|H|N\rangle = 0.$$

The parameters used in our calculation are specified in table 1.

3. Derivation of the COGEP

The COGEP [21–23] is obtained from the relativistic expression for the 'scatt amplitude' for the quarks,

$$M_{fi} = \frac{g^2}{4\pi}\bar{\psi}_i\gamma^\mu\frac{\lambda_i^a}{2}\psi_i D_{\mu\nu}^{ab}(q)\bar{\psi}_j\gamma^\nu\frac{\lambda_j^b}{2}\psi_j,$$

where, $\bar{\psi} = \psi^+\gamma_0$, $\psi_{i/j}$ (eq. (2)) are the wave functions of the quarks in the R $D_{\mu\nu}^{ab} = \delta_{ab}D_{\mu\nu}$ are the zero energy CCM gluon propagators in momentum repres tion and q is the four-momentum transfer. The $g_s^2/4\pi$ $(=\alpha_s)$ is the quark–g coupling constant and λ_i is the color $SU(3)_c$ generator of the ith quark. For pleteness, we give a short description of the gluon propagators. In CCM the coupled non-linear terms in the equation of motion of a gluon are simu by a self induced color current $j_\mu = \theta_\mu^\nu A_\nu$ $(=m^2 A_\mu)$ or equivalently an effe mass term for all the gluons with $m^2 = cr^2 - 2c^2\delta_{\mu 0}$. The equations of mo $A_\mu + m^2 A_\mu = 0$ are easily solved by using harmonic oscillator modes in gauge $\partial^\mu A_\mu = 0$. The consistency of $\partial^\mu A_\mu = 0$ and $\partial^\mu j_\mu = \partial^\mu(m^2 A_\mu) = 0$ im a secondary gauge condition $(\nabla\cdot A + c^2 r\cdot A) = a\cdot A = 0$ termed 'oscillator ga [19–21] where a is the usual harmonic oscillator annihilation operator.

$$D_1(r,r',E=0) \equiv \left\langle r \left| \frac{c}{2a\cdot a^\dagger + 3} \right| r' \right\rangle = c \sum_{\{N\}} \frac{\psi_M^*(r)\psi_M(r')}{2N+3}. \qquad (1$$

Transferring the source point (r') to origin we obtain ($r - r' \to r$)

$$D_1(r,0,E=0) \equiv D_1 =$$

$$c \sum_{\{N\}} \frac{\psi_N(r)\psi_N(0)}{2N+3} = \frac{\Gamma_{3/4}}{(4\pi)^{3/2}} c(cr)^{-3/2} W_{0;-1/4}(c^2r^2). \qquad (1$$

Similarly,

$$D_0(r,0,E=0) \equiv D_0 =$$

$$c \sum_{\{N\}} \frac{\psi_N(r)\psi_N(0)}{2N+1} = \frac{\Gamma_{1/4}}{(4\pi)^{3/2}} c(cr)^{-3/2} W_{1/2;-1/4}(c^2r^2), \qquad (1$$

where W's are the Whittaker functions. The complete propagators are given by

$$D_{00}(r) = 4\pi D_0(r), \qquad (1$$

where $D_0(r)$ is given by (14). The $D_{ik}(r)$ is given by

$$D_{ik}(r) = -4\pi \left\{ \delta_{ik} - \frac{a_i^+ a_k}{a\cdot a^+} \right\} D_1(r), \qquad (1$$

where $D_1(r)$ is given by eq. (13). The scattering amplitude can be written as

$$M_{fi} = 4\pi\alpha_s N^4 \lambda_i \lambda_j \phi_i'^+ \phi_j'^+ [U[p_i,p_j,q]]\phi_i\phi_j. \qquad (1$$

The function $U(p_i,p_j,q)$ is the particle interaction operator in the momentum represen tation and by taking the Fourier transformation of each term in the scatterin amplitude, we get the potential operator $U(\hat{p}_i,\hat{p}_j,r)$ in the co-ordinate space. Th central part of the COGEP in the static limit is

$$\widetilde{V}_{ij}^{\text{cen}}(r) = \frac{\alpha_s N^4}{4} \lambda_i \cdot \lambda_j \left[D_0(r) + \frac{1}{(E+M)^2} [4\pi\delta^3(r) - c^4r^2 D_1(r)][1 - 2/3\,\sigma_1\cdot\sigma_j] \right. \qquad (1$$

Here, we have ignored higher order terms in a and a^+ in the spirit of Fermi–Bre interaction. It should be noted that the COGEP obtained above is energy dependen In addition to the above interaction, full COGEP has the usual tensor, Darwin an orbit–orbit terms [21–23].

The single parameter c in CCM [19–21] was obtained by fitting the io (1440 MeV)0^{-+} (the oldest glue ball candidate) as a digluon glue ball. The othe low-lying digluon and trigluon states were predicted which were found to be in goo agreement with the other existing candidates [20].

of n_{max}.

n_{max}	π	K	η	η_c	D
0	449·40	768·12	927·57	3412·78	2413·41
1	259·45	581·09	656·42	3162·10	2016·22
2	170·16	516·91	571·13	3039·27	1924·30
3	143·32	498·32	556·20	2996·23	1882·64
4	137·42	494·56	552·34	2987·12	1874·78
5	137·36	493·02	551·03	2986·49	1873·03
Expt.	139·57	493·68	548·8	2981·0	1869

Table 3. The vector meson masses (in MeV) for various values of n_{max}.

n_{max}	ρ	K^*	ϕ	ω	J/ψ	D^*
0	770·37	895·12	1022·78	782·23	3097·43	2011·89
1	769·63	893·33	1021·20	781·57	3096·57	2010·23
2	769·62	893·19	1021·12	781·43	3096·13	2010·12
3	769·58	893·10	1021·07	781·19	3096·09	2010·08
4	769·51	893·07	1021·02	781·05	3096·04	2010·03
5	769·49	893·02	1021·0	781·02	3096·04	2010·02
Expt.	768	892	1020	783	3097	2010

4. Results and discussion

In our present study of meson spectroscopy the product of the quark–antiquark oscillator wave functions are expressed in terms of oscillator wave functions corresponding to the relative and CM coordinates using the Moshinsky transformations [25]. We have restricted the CM wave functions to the 0S state. The total energy or the mass of the meson is obtained by calculating the energy eigenvalue of the hamiltonian in the harmonic oscillator basis spanned over a space extending up to the radial quantum number $n_{\mathrm{max}} = 5$.

The masses of the pseudo scalar and vector mesons after diagonalization for various values of n_{max} are listed in table 2 and table 3 respectively. For example, with $n = 0$, the naive mass of the π meson turned out to be 449 MeV. Since the COGEP is attractive inside π, the diagonalization in the space of radially excited pion states bring down the value of π close to the physical mass. The parameters used in the calculation are listed in table 1. These are the same set of parameters used in our earlier investigation of $n-n$ interaction [23]. With $n = 5$, the physical masses of π and ρ mesons are found to be 137·36 MeV and 769·49 MeV respectively. Further increase of the oscillator basis does not lead to any significant change in the masses. For ρ there is no change in the mass (table 3) as COGEP is repulsive for vector mesons and hence perturbative techniques are fully adequate and are justified. Tables 4 and 5 give the predicted radially excited states of pseudo scalar and vector mesons after diagonalization in comparison with the experimental masses [1]. The results predict decreasing spacing between radially

Table 4. The dominant spectral composition and predicted masses of states of pseudo scalar particles in MeV. The experimental masses are taken from the particle data group [1]. The spectroscopic notation is $N^{(2S+1)}L_J$, where the symbols have their usual meaning ('*'symbol in the table implies the state is yet to be confirmed).

Meson	Mass (MeV)	State ($N^{(2S+1)}L_J$)				
		$1\,^1S_0$	$2\,^1S_0$	$3\,^1S_0$	$4\,^1S_0$	$5\,^1S_0$
π	Theory	137·36	1312·45	1731·34	2167·23	2289·45
	Experiment	139·56	1300·0	1770·0		
K	Theory	493·02	1456·34	1902·56	2256·45	2413·47
	Experiment	493·68	1460·0	1830·0		
η	Theory	551·03	1234·12	1679·67	1832·23	2003·34
	Experiment	548·8	1295·0	1760·0	2100·0*	
η_c	Theory	2986·49	3632·89	4023·48	4321·37	4523·50
	Experiment	2981·0	3590·0	4060·0*		

Table 5. The dominant spectral composition and predicted masses of states of vector particles in MeV. The experimental masses are taken from the particle data group [1]. The spectroscopic notation is $N^{(2S+1)}L_J$, where the symbols have their usual meaning ('*'symbol in the table implies the state is yet to be confirmed).

Meson	Mass	State ($N^{(2S+1)}L_J$)				
		$1\,^3S_1$	$2\,^3S_1$	$3\,^3S_1$	$4\,^3S_1$	$5\,^3S_1$
ρ	Theory	769·49	1457·23	1923·25	2331·35	2435·96
	Experiment	768·0	1450·0	2110·0*		
K^*	Theory	893·02	1632·24	2256·0	2546·78	2734·21
	Experiment	892·0	1680·0			
ϕ	Theory	1021·0	1717·26	2238·39	2567·78	2772·35
	Experiment	1020·0	1680·0			
ω	Theory	781·02	1412·71	1867·72	2208·28	2456·02
	Experiment	783·0	1390·0			
J/ψ	Theory	3096·04	3702·94	4187·72	4321·28	4556·02
	Experiment	3097·0	3680·0	4100·0		

excited states in the meson spectra which are in agreement with the experiment and with the predictions of the other models [11, 14]. The color electric terms of COGEP contribute significantly to the masses.

5. Conclusion

In this paper we have obtained the ground state masses and the radially excited states of pseudo scalar and vector mesons in the framework of RHM. It is shown that the computation of mesonic masses/mass splittings using the Fermi–Breit interaction is exactly. For attractive COGEP within pseudo scalar mesons, the contribution from the off-diagonal elements is found to be significant. It is shown that diagonalization of the interaction matrix in RHM states leads to the lowering of the masses for the pseudo scalar particles, so as to agree with the observed masses. The explicit formulas derived here may be applied to baryon spectroscopy. The method and formulas employed here may prove to be a starting point for further investigation. Work in this direction is in progress.

References

[1] Particle Data Group, Review of Particle Properties, *Phys. Rev.* **D50**, part 1 (1994)
[2] A De Rujula, H Georgi and S L Glasow, *Phys. Rev.* **D12**, 147 (1975)
[3] O W Greenberg, *Ann. Rev. Nucl. Part. Phys.* **28**, 327 (1978)
[4] R K Bhaduri, L E Cohler and Y Nogami, *Nuovo Cimento* **A65**, 376 (1981)
[5] D B Lichtenberg, *Int. J. Mod. Phys.* **A2**, 1669 (1987)
[6] M Narodetskii, R Ceuleneer and C Semay, *J. Phys.* **G18**, 1901 (1992)
[7] N Isgur, D Scora, B Grinstein and M B Wise, *Phys. Rev.* **D39**, 799 (1989)
[8] D Scora and N Isgur, *Phys. Rev.* **D52**, 2783 (1995)
[9] M G Olsson, S Veseli and K Williams, *Phys. Rev.* **D51**, 5079 (1995); *Phys. Rev.* **D52**, 5041 (1995)
[10] R F Labed, *Phys. Rev.* **D47**, 1134 (1993)
[11] P L Ferreira and N Zagury, *Nuovo Cimento* **A20**, 511 (1977)
[12] P L Ferreira, J A Helayel and N Zagury, *Nuovo Cimento* **A55**, 215 (1980)
[13] M Bander, D Silverman, B Klima and U Maor, *Phys. Rev.* **D29**, 2038 (1984)
[14] S Godfrey and N Isgur, *Phys. Rev.* **D32**, 189 (1985)
[15] S Capstick and N Isgur, *Phys. Rev.* **D34**, 2809 (1986)
[16] A Le Yaouanc, L Oliver, O Pene and J C Raynal, *Phys. Rev.* **D9**, 2636 (1974)
[17] C Hayne and N Isgur, *Phys. Rev.* **D25**, 1944 (1982)
[18] S B Khadkikar and S K Gupta, *Phys. Lett.* **B124**, 523 (1983)
[19] S B Khadkikar, *Pramana–J. Phys.* **24**, 63 (1985)
[20] S B Khadkikar and P C Vinod Kumar, *Pramana–J. Phys.* **29**, 39 (1987)
[21] P C Vinod Kumar, K B Vijaya Kumar and S B Khadkikar, *Pramana–J. Phys.* **39**, 47 (1992)
[22] S B Khadkikar and K B Vijaya Kumar, *Phys. Lett.* **B254**, 320 (1991)
[23] K B Vijaya Kumar and S B Khadkikar, *Nucl. Phys.* **A556**, 396 (1993)
[24] G Gartenhaus and C Schwartz, *Phys. Rev.* **108**, 482 (1957)
[25] M Moshinsky, *Nucl. Phys.* **13**, 104 (1959)

Two body non-leptonic decays $B \to D\pi$ with heavy quark and chiral symmetry

A K GIRI, L MAHARANA and R MOHANTA
Physics Department, Utkal University, Bhubaneswar 751 004, India

MS received 11 September 1996; revised 30 December 1996

Abstract. We have analysed the two body non-leptonic charmed–meson decays of heavy B meson based on the factorization assumption. The transition matrix elements and the corresponding decay widths are calculated in the heavy quark and chiral symmetry limit and the Isgur–Wise function present in the expression is determined by the wave function model of Ali *et al.* The results obtained are quite interesting and agree reasonably well with the experimental data.

Keywords. Heavy quark symmetry; chiral symmetry; factorization approximation; Isgur–Wise function.

PACS Nos 11·30; 13·30

1. Introduction

Non-leptonic weak decays of hadrons contain a lot of valuable information on electroweak interaction of quarks. However these decays are notoriously difficult to handle and never been understood in a satisfactory way. In fact, some approximations and/or assumptions have been used in these analyses. One of the techniques is the factorization hypothesis, which has been successfully used in studying some of the non-leptonic decays of mesons, when one of the decay products is light. The work of ref. [1] has gone in some way in establishing the usefulness of this approximation from a purely phenomenological standpoint. Hioki *et al* [2] performed the test of the hypothesis in a straight forward way. Dugan and Grinstein [3] have formulated a QCD basis for factorization in the decays of heavy mesons. So far there have been many theoretical approaches [4–7] to explain the test of factorization in the non-leptonic decays of the heavy mesons.

In this present investigation we intend to study the two body non-leptonic decays of B and B_s mesons considering the factorization hypothesis alongwith heavy quark symmetry formalism. Heavy quark symmetry (HQS) was formulated a few years back in several publications [8–13]. It arises in the limit of QCD where the mass of the heavy quark is taken formally to infinity. In this limit, two new symmetries, above and beyond those usually associated with QCD arise. These symmetries are a spin symmetry and a flavor symmetry. The implication of these symmetries are that, the spin and mass of the heavy quark are decoupled from the hadronic dynamics. These symmetries which are not manifest in the original QCD Lagrangian, become explicit in an effective theory, the so called heavy quark effective theory (HQET) [8--13]. The discovery of HQS and subsequent formulation of HQET have substantially improved the theoretical understanding of hadronic systems involving heavy quarks. In fact, HQET provides a convenient framework to analyse the weak decays of heavy hadrons as shown in refs [12–18]. The semileptonic decays of two heavy mesons are of particular importance. In the limit of infinite quark masses, all the hadronic form factors can be expressed in terms of a single universal function $\xi(v \cdot v')$, the Isgur – Wise function [9, 10, 13]. The function depends only on the transfer of the four velocities of the heavy particles and is normalized at zero-recoil.

We, therefore, consider it worthwhile to analyse the two body non-leptonic decays of the heavy B meson using HQET in conjuction with factorization approximation. The use of the HQET implies that, the expressions for the decay widths should contain the universal Isgur–Wise (IW) function. Since HQET does not predict the shape of the IW function, it makes sense to calculate it using a model. However, heavy quark symmetry predicts the normalization of the Isgur–Wise function at the zero-recoil point, so a good model must give the same result in the appropriate limit. Here we have employed the wave function model of Ali *et al* [19] to calculate this universal function. There are several reasons to choose this model. First, the model is well established, second, it is very simple and the model parameters are fixed in its earlier applications.

There are several theoretical calculations of the non-leptonic B decays, based on different approaches, available in the literature. Reader and Isgur [7] have performed the model independent test of factorization for hadronic B-decays, by using the model dependent resonance dominance mechanism, where $\bar{B} \to D + n\pi$ amplitudes are dominated by $B \to D^{(i)}$; $D^{(i)}$ represent intermediate charmed meson states i.e., D, D^*, D_2^* etc., which further decay strongly to $D + (n - m)\pi$. Using the factorization approximation Deandrea *et al* [20] analysed the two body non-leptonic decays of heavy B and B_s mesons. They have used the semileptonic decay amplitudes, calculated earlier and considering the exclusive D-decay data as input, predicted the decay rates for B meson systems. Mannel *et al* [21] applied the formalism of heavy quark effective theory in addition to the factorization assumption for the non-leptonic decays of B mesons. They have suggested that factorization assumption is valid when one of the decay products is light. Here we also apply the factorization hypothesis alongwith heavy quark and chiral symmetry to study the non-leptonic decays of B mesons. Our approach is quite simple and different from the work of Reader and Isgur [7], in which they have considered the transitions $B \to D + n\pi$ are dominated by the intermediate charmed meson states, and the IW function is parametrized to an exponential form. Where as in this paper we have considered the transition $B \to D\pi$ without any intermediate state and the Isgur – Wise function is evaluated in the well established wave function model of Ali *et al* [19], using the ground state harmonic oscillator wave function. Our results concerning the branching ratios of several possible non-leptonic B decays are in good agreement with the currently available data.

We organize the paper as follows. Assuming factorization approximation, we give an explicit evaluation of the non-leptonic B meson decay widths in the heavy quark and chiral symmetry limit in § 2. The use of HQET imply that the expressions for the

$$\mathscr{H}_{\text{eff}} = \frac{G_F}{\sqrt{2}} V_{cb} V^*_{q_1 q_2} [C_1(\bar{c}b)_\mu(\bar{q}_1 q_2)^\mu + C_2(\bar{c}q_1)_\mu(\bar{q}_2 b)^\mu]. \tag{1}$$

In the above expression we have used the notation $(\bar{q}_1 q_2)_\mu = \bar{q}_1 \gamma_\mu (1-\gamma_5) q_2$, where q_1 and q_2 stand for the u and d light quarks. The Wilson coefficients C_1 and C_2, evaluated at the b-quark mass scale m_b are given in refs. [1, 23] as

$$C_1(m_b) = 1{\cdot}1, \quad C_2(m_b) = -0{\cdot}24. \tag{2}$$

The usual way to evaluate the matrix element of the operator in eq. (1) for the non-leptonic B-decays is to assume the factorization hypothesis. In this hypothesis, one assumes that the matrix element of a product of operators may be expressed as the product of matrix elements of the same operator i.e., one uses $\langle M_1 M_2 | J_\mu J^\mu | B\rangle = \langle M_1 | J_\mu | B\rangle \langle M_2 | J^\mu | 0\rangle$ to describe the process $B \to M_1 M_2$. All the two body modes are then expressed in terms of two parameters a_1 and a_2, with a_1 controlling the 'class-I' $B^0 \to M_1^+ M_2^-$, a_2 the 'class-II' $B^0 \to M_1^0 M_2^0$ transitions and both quantities contribute coherently to the 'class-III' transitions $B^- \to M_1^0 M_2^-$ [1]. The coefficients a_1 and a_2 are

$$a_1 = C_1 + \eta C_2 \quad \text{and} \quad a_2 = C_2 + \eta C_1, \tag{3}$$

where C_1 and C_2 are given in (1) and (2). η is called the color suppression factor and naively expected to be 1/3. Literally speaking factorization implies $\eta = 1/N_C = 1/3$; the deviation of η from 1/3 parametrize, in a certain way, the non-factorizable contributions. The non-factorizable contributions show up even in perturbation theory, but these seem to be numerically very small. Isospin analysis of two body non-leptomic decays of B meson [24] with factorization approximation allows us to write the transition amplitude for different $B \to D\pi$ decays as

$$\mathscr{M}(\bar{B}^0 \to D^+\pi^-) = \frac{G_F}{\sqrt{2}} V_{cb} V^*_{ud} a_1 \langle \pi^- | (\bar{d}u)_\mu | 0\rangle \langle D^+ | (\bar{c}b)^\mu | \bar{B}^0\rangle, \tag{4}$$

$$\mathscr{M}(\bar{B}^0 \to D^0\pi^0) = \frac{G_F}{\sqrt{2}} V_{cb} V^*_{ud} a_2 \langle D^0 | (\bar{c}u)_\mu | 0\rangle \langle \pi^0 | (\bar{d}b)^\mu | \bar{B}^0\rangle, \tag{5}$$

and

$$\begin{aligned}\mathscr{M}(B^- \to D^0\pi^-) = \frac{G_F}{\sqrt{2}} V_{cb} V^*_{ud} [&a_1 \langle \pi^- | (\bar{d}u)_\mu | 0\rangle \langle D^0 | (\bar{c}b)^\mu | B^-\rangle \\ &+ a_2 \langle D^0 | (\bar{c}u)_\mu | 0\rangle \langle \pi^- | (\bar{d}b)^\mu | B^-\rangle].\end{aligned} \tag{6}$$

Similar relations hold for $B \to D^*\pi$ decays with D meson state replaced by D^* state. The transition amplitude for $B_s^0 \to D_s^+\pi^-$ decay is given as

$$\mathscr{M}(\bar{B}_s^0 \to D_s^+\pi^-) = \frac{G_F}{\sqrt{2}} V_{cb} V^*_{ud} a_1 \langle \pi^- | (\bar{d}u)_\mu | 0\rangle \langle D_s^+ | (\bar{c}b)^\mu | \bar{B}_s^0\rangle. \tag{7}$$

To obtain the decay amplitudes for these processes we have to calculate the factorized amplitudes, and in doing so, we use the following matrix elements. The current matrix elements between a pseudoscalar/vector meson (P/V) and vacuum is related to the corresponding decay constants as

$$\langle P(p)|(\bar{q}q')^{\mu}|0\rangle = -if_P p^{\mu}, \tag{8}$$

$$\langle V(p,\varepsilon)|(\bar{q}q')^{\mu}|0\rangle = f_V \varepsilon^{*\mu} M_V. \tag{9}$$

The matrix element representing the decay $B\rightarrow\pi$ can be taken from the corresponding semi-leptonic decays which are parametrized in terms of two invariant form factors [25] as

$$\langle\pi(p)|(\bar{u}b)_{\mu}|\bar{B}(P)\rangle = \left\{(P+p)_{\mu} - \frac{M_B^2 - m_{\pi}^2}{q^2}q_{\mu}\right\}F_1(q^2) + \frac{M_B^2 - m_{\pi}^2}{q^2}q_{\mu}F_0(q^2), \tag{10}$$

where $q_{\mu} = (P-p)_{\mu}$ and $F_{(0,1)}(q^2)$ are Lorentz invariant form factors, functions of the square of the momentum transfer $q^2 = (P-p)^2$. The following constraint relation is needed to cancel the poles at $q^2 = 0$,

$$F_0(0) = F_1(0). \tag{11}$$

For the q^2 dependence of the form factors we have assumed a simple pole formula

$$F(q^2) = \frac{F(0)}{(1 - q^2/M_P^2)}, \tag{12}$$

with the pole mass M_P given by the lowest lying meson with the appropriate quantum number i.e. $J^P = 0^+$ for F_0 and 1^- for F_1. For numerical estimation we have taken the pole masses as $M_P(0^+) = 5{\cdot}78$ GeV and $M_P(1^-) = 5{\cdot}32$ GeV from ref. [20]. The values of the form factors at zero momentum transfer are also taken from [20] as $F_0(0) = F_1(0) = 0{\cdot}53$, which are calculated earlier using the heavy quark and chiral symmetry by Casalbuoni *et al* [26].

In addition to this the matrix element $\langle D|(\bar{c}b)^{\mu}|B\rangle$ may be calculated using the HQET. The current in the full theory of QCD can be related to the current in the effective theory as [10]

$$\bar{c}\gamma^{\mu}(1-\gamma_5)b = C_{cb}\bar{h}_{v'}^{(c)}\gamma^{\mu}(1-\gamma_5)h_v^{(b)}. \tag{13}$$

In the leading logarithmic approximation, C_{cb} is given as

$$C_{cb} = \left(\frac{\alpha_s(m_b)}{\alpha_s(m_c)}\right)^{6/(33-2N_f)}. \tag{14}$$

The extra symmetries of HQET allows us to write the matrix element of the current operator as [13]

$$\langle D(v')|(\bar{c}b)_{\mu}|B(v)\rangle = C_{cb}\sqrt{m_b m_c}\,\xi(v\cdot v')(v_{\mu} + v'_{\mu}) \tag{15}$$

and

$$\langle D^*(v',\varepsilon)|(\bar{c}b)_{\mu}|B(v)\rangle = C_{cb}\sqrt{m_b m_c}\,\xi(v\cdot v') \times (i\varepsilon_{\mu\nu\alpha\beta}\varepsilon^{*\nu}v'^{\alpha}v^{\beta} + (v\cdot v'+1)\varepsilon_{\mu}^{*} - (\varepsilon^{*}\cdot v)v'_{\mu}), \tag{16}$$

where $\xi(v\cdot v')$ is the universal Isgur–Wise function.

The corresponding decay widths are calculated from the amplitudes $\mathcal{M}(\bar{B}\to D\pi)$ according to the standard formula

$$\Gamma(\bar{B}\to D\pi)=\frac{|\mathbf{p}|}{8\pi M_B^2}|\mathcal{M}(\bar{B}\to D\pi)|^2, \tag{17}$$

where $|\mathbf{p}|$ is the magnitude of the three-momentum of the emitted pion in the rest frame of initial B meson. Thus with eqs (4–17) we obtain the partial decay widths for different B decays in the chiral symmetry limit i.e. ($m_\pi \simeq 0$) and in the rest frame of initial B meson as

$$\Gamma(\bar{B}^0\to D^+\pi^-)=\frac{\tilde{G}_F^2}{8\pi M_{B^0}^2}a_1^2 C_{cb}^2 m_c m_b f_\pi^2 \xi^2(v\cdot v')(1+Y)^2|\mathbf{p}|^3, \tag{18}$$

$$\Gamma(\bar{B}^0\to D^0\pi^0)=\frac{\tilde{G}_F^2|\mathbf{p}|}{8\pi}a_2^2 f_D^2 F_0^2(M_{D^0}^2)M_{B^0}^2. \tag{19}$$

$$\Gamma(B^-\to D^0\pi^-)=\frac{\tilde{G}_F^2|\mathbf{p}|}{8\pi M_B^2}[a_1 f_\pi|\mathbf{p}|C_{cb}\sqrt{m_c m_b}(1+Y)\,\xi(v\cdot v')$$
$$+\,a_2 f_D F_0(M_{D^0}^2)M_B^2\,]^2, \tag{20}$$

$$\Gamma(\bar{B}^0\to D^{*+}\pi^-)=\frac{\tilde{G}_F^2}{8\pi M_{B^0}^2}a_1^2 C_{cb}^2 m_c m_b f_\pi^2 \xi^2(v\cdot v')(1+Y^*)^2|\mathbf{p}|^3, \tag{21}$$

$$\Gamma(\bar{B}^0\to D^{*0}\pi^0)=\frac{\tilde{G}_F^2|\mathbf{p}|}{8\pi M_{B^0}^2}a_2^2 f_{D^*}^2 M_{D^{*0}}^2 F_1^2(M_{D^*}^2)(M_{B^0}^2(Y^{*2}-2)+M_{D^*}^2), \tag{22}$$

$$\Gamma(B^-\to D^{*0}\pi^-)=\frac{\tilde{G}_F^2|\mathbf{p}|}{8\pi M_B^2}[a_1^2 f_\pi^2|\mathbf{p}|^2 C_{cb}^2 m_c m_b\,\xi^2(v\cdot v')(1+Y^*)^2$$
$$+\,a_2^2 f_{D^*}^2 M_{D^{*0}}^2 F_1^2(M_{D^{*0}}^2)(M_B^2(Y^{*2}-2)+M_{D^{*0}}^2)] \tag{23}$$

and

$$\Gamma(\bar{B}_s\to D_s^+\pi^-)=\frac{\tilde{G}_F^2}{8\pi M_{Bs}^2}C_{cb}^2 m_c m_b\, a_1^2 f_\pi^2 \xi^2(v\cdot v')\left(1+\frac{M_{B_s}}{M_{D_s}}\right)^2|\mathbf{p}|^3, \tag{24}$$

where we have defined $\tilde{G}_F=(G_F/\sqrt{2})V_{cb}V_{ud}^*$, $Y=M_B/M_D$ and $Y^*=M_B/M_{D^*}$. The expressions for decay widths (18–24) contain besides the known quantities, the unknown Isgur–Wise function $\xi(v\cdot v')$. Our next objective is to find out the Isgur–Wise function present in the decay widths considering the kinematics of the system.

3. Wave function model and Isgur–Wise function

Here we have presented the evaluation of the Isgur–Wise function proceeding in the same manner as suggested by ref. [19]. The Isgur–Wise function calculated in the model predicts the decay widths for rare $B\to K^*\gamma$ decays [19] and radiative decay

$$I(v') = \int \frac{d^3p}{(2\pi)^3} \tilde{\Phi}_F^*(\mathbf{p} + \Lambda \mathbf{v}')\tilde{\Phi}_I(\mathbf{p})$$

$$= \int d^3x \Phi_F^*(\mathbf{x})\Phi_I(\mathbf{x}) \exp(-i\Lambda \mathbf{v}' \cdot \mathbf{x})$$

where the labels I and F denote wave function of the initial and final meson pectively. The inertia parameter Λ corresponds to the mass of light degrees of free taken as

$$\Lambda = \frac{M_P \cdot m_q}{m_Q + m_q}.$$

The quark masses are taken to be $m_u = m_d = 330$ MeV and $m_s = 550$ The wave functions are chosen to be the eigenfunctions of orbital angular mome L. Since both the initial and final mesons will have $L = 0$, the wave function given by

$$\Phi_{I/F}(\mathbf{x}) = Y_0^0\left(\frac{\mathbf{x}}{|\mathbf{x}|}\right)\phi_{I/F}(|\mathbf{x}|),$$

with normalization

$$\int d^3x \Phi_{I/F}^*(\mathbf{x})\Phi_{I/F}(\mathbf{x}) = \int r^2 \, dr \, \phi_{I/F}^*(r)\phi_{I/F}(r) = 1.$$

Inserting the wave functions as given in eq. (27) into the overlap integral (25 choosing the quantization axis of orbital angular momentum in the directi velocity, the overlap integral becomes

$$I(v') = \int r^2 \, dr \, \phi_F^*(r)\, \phi_I(r) j_0(\Lambda r |\mathbf{v}'|),$$

where j_0 is the spherical Bessel function of zeroth order. This expression holds i rest frame of the heavy meson. In a general frame, eq. (29) becomes

$$I(v \cdot v') = \int r^2 \, dr \, \phi_F^*(r)\, \phi_I(r) j_0(\Lambda r \sqrt{(v \cdot v')^2 - 1}).$$

This overlap integral is identified as the usual Isgur–Wise function, which is cor normalized at zero recoil i.e. $v \cdot v' = 1$, since $j_0(0) = 1$. To evaluate the overlap in (30), we insert the radial wave functions of the harmonic oscillator in the form

$$\phi(r) = \left(\frac{4\beta^3}{\sqrt{\pi}}\right)^{1/2} \exp(-\beta^2 r^2/2),$$

with oscillator strength β. However, the values of β_B and β_D fitted in ref. [2 $\beta_D = 0{\cdot}39$ GeV and $\beta_B = 0{\cdot}41$ GeV are not equal. Thus, breaking of the heavy symmetry causes the violation of the normalization condition $\xi(1) = 1$. So to est average of β_D and β_B for both wave functions. Thus we obtain $\xi(v \cdot v')$ to be

$$\xi(v \cdot v') = \exp(-a^2/4\beta_{\text{ave}}^2), \tag{32}$$

where $a = \Lambda(\sqrt{(v \cdot v')^2 - 1})$ and $\beta_{\text{ave}} = (\beta_{\text{B}} + \beta_{\text{D}})/2$.

The product $(v \cdot v')$ is determined by considering the kinematics of the system. Since we are dealing with the two body decays $\bar{B}(v) \to D(v')\pi(p)$, momentum conservation implies

$$M_B v^\mu = M_D v'^\mu + p^\mu \tag{33}$$

or

$$p^2 = m_\pi^2 = M_B^2 + M_D^2 - 2(v \cdot v') M_B M_D. \tag{34}$$

In the chiral symmetry limit i.e. $m_\pi = 0$ [29], we have

$$v \cdot v' = \frac{M_B^2 + M_D^2}{2M_B M_D}. \tag{35}$$

Thus, with the help of eq. (35) we have calculated explicitly the values of the Isgur–Wise function from eq. (32), as presented in table 1.

4. Results and discussion

Having derived the expressions for the decay widths (18–24) for the two body nonleptonic B mesons to charmed mesons, using factorization approximation, we now present the numerical results. For the calculation of the theoretical branching ratios, we take the heavy quark masses as $m_c = 1500$ MeV and $m_b = 4500$ MeV. The QCD scale Λ_{QCD} is taken to be 200 MeV. The masses of B- and D-mesons and the life times of B mesons are taken from ref. [30]. The decay constants used are $f_\pi = 130{\cdot}7$ MeV [30], $f_D = 170$ MeV and $f_{D^*} = 240$ MeV [31]. The CKM matrix elements are taken from ref. [30] as $V_{cb} = 0{\cdot}041$ and $V_{ud} = 0{\cdot}9736$. With these values, we obtain the branching ratios for various decay processes as tabulated in table 1. The overall agreement between the predicted and experimental results are quite remarkable.

In this paper, we have applied the factorization approximation and HQET to study some of the non-leptonic decays of B-mesons like $\bar{B}^0 \to D^+\pi^-$,

Table 1. The branching ratios for the two body non-leptonic $B \to D\pi$ and $B \to D^*\pi$ in the heavy quark and chiral symmetry limit.

Decay process	$\xi(v \cdot v')$	$\lvert\mathbf{p}\rvert$ in MeV	Theory	Experiment
$\bar{B}^0 \to D^+\pi^-$	0·7628	2308·65	$3{\cdot}738 \times 10^{-3}$	$3{\cdot}0 \pm 0{\cdot}4 \times 10^{-3}$
$B^- \to D^0\pi^-$	0·7625	2310·18	$5{\cdot}328 \times 10^{-3}$	$5{\cdot}3 \pm 0{\cdot}5 \times 10^{-3}$
$\bar{B}^0 \to D^0\pi^0$	—	2310·35	$0{\cdot}534 \times 10^{-4}$	$< 4{\cdot}8 \times 10^{-4}$
$\bar{B}_s \to D_s^+\pi^-$	0·5448	2323·8	$1{\cdot}843 \times 10^{-3}$	$< 0{\cdot}12$
$\bar{B}^0 \to D^{*+}\pi^-$	0·772	2256·957	$3{\cdot}217 \times 10^{-3}$	$2{\cdot}6 \pm 0{\cdot}4 \times 10^{-3}$
$B^- \to D^{*0}\pi^-$	0·7718	2258·04	$3{\cdot}524 \times 10^{-3}$	$5{\cdot}2 \pm 0{\cdot}8 \times 10^{-3}$
$\bar{B}^0 \to D^{*0}\pi^0$	—	2258·21	$0{\cdot}831 \times 10^{-4}$	$< 9{\cdot}7 \times 10^{-4}$

Assuming the factorization approximation, we have calculated the transition matrix elements in the heavy quark effective theory. These matrix elements contain the single universal form factor $\xi(v \cdot v')$, the Isgur–Wise function which is evaluated using the wave function model of Ali *et al* [19]. The hadronic matrix elements for class-II and class-III operators, which involve the $B \rightarrow \pi$ transition are conventionally expressed in terms of appropriate Lorentz invariant form factors $F_{0,1}(q^2)$. As suggested by Hioki *et al* [2] they may be extracted from a study of the corresponding semileptonic decay $B \rightarrow \pi l v$. We therefore assumed a simple pole formula for $F_{0,1}(q^2)$ as given by Wirbel *et al* [25] in the study of exclusive semileptonic decays of heavy mesons. After knowing all the required form factors $F_{0,1}(q^2)$ and $\xi(v \cdot v')$, we have calculated the corresponding decay widths in the chiral symmetry limit. The results obtained are presented in table 1 and are in good agreement with the currently available experimental data [30].

In conclusion, we have performed in the factorization approximations an analysis of two body non-leptonic decays of B and B_s mesons. Our study has been based on the use of the factorization approximation along with chiral symmetry and heavy quark symmetries. The results so obtained are in agreement with the experimental results. Thus within the working approximation adopted here, the present calculation provides a simple framework to explain reasonably the two-body non-leptonic decays of B measons to $D(D^*)$ mesons.

Acknowledgements

We are thankful to Prof. B B Deo and Prof. N Barik for useful discussions. RM would like to thank CSIR, Government of India, for a fellowship.

References

[1] M Bauer, B Stech and M Wirbel, *Z. Phys.* **C34**, 103 (1987)
[2] Z Hioki, T Hasuike, T Hattoro, T Hayashi and S Wakaizumi, *Phys. Lett.* **B299**, 115 (1993)
[3] M J Dugan and B Grinstein, *Phys. Lett.* **B255**, 583 (1991)
[4] D Bortoletto and S Stone, *Phys. Rev. Lett* **65**, 2951 (1990)
[5] J L Rosner, *Phys. Rev.* **D42**, 3732 (1990)
M Tanimoto, K Goda and K Senba, *Phys. Rev.* **D42**, 3741 (1990)
A Acker, S Pakvasa, S F Tuan and S P Rosen, *Phys. Rev.* **D43**, 3083 (1991)
T Mannel *et al*, *Phys. Lett.* **B259**, 359 (1991)
[6] V Rieckert, *Phys. Rev.* **D47**, 3053 (1993)
[7] C Reader and N Isgur, *Phys. Rev.* **D47**, 1007 (1993)
[8] M Neubert, *Phys. Rep.* **245**, 259 (1994)
[9] N Isgur and M B Wise, *Phys. Lett.* **B232**, 113 (1989)
[10] N Isgur and M B Wise, *Phys. Lett.* **B237**, 527 (1990)
[11] A F Falk and B Grinstein, *Phys. Lett.* **B247**, 406 (1990); *Phys. Lett.* **249**, 314 (1990)
[12] H Georgi, *Phys. Lett.* **B240**, 447 (1990); *Nucl. Phys.* **B348**, 293 (1991)
[13] A F Falk, H Georgi, B Grinstein and M B Wise, *Nucl. Phys.* **B343**, 1 (1990)
[14] E Eichen and B Hill, *Phys. Lett.* **B234**, 511 (1990); **243**, 427 (1990)
[15] B Grinstein, *Nucl. Phys.* **B339**, 253 (1990)
[16] T Mannel, W Roberts and Z Ryzak, *Nucl. Phys.* **B368**, 204 (1992)
[17] M E Luke, *Phys. Lett.* **B252**, 447 (1990)
[18] A F Falk, B Grinstein and M E Luke, *Nucl. Phys.* **B357**, 185 (1991)

[19] A Ali, T Ohl and T Mannel, *Phys. Lett.* **B298**, 195 (1993)
[20] A Deandrea, N Di Bartolomeo, R Gatto and G Nardulli, *Phys. Lett.* **B318**, 549 (1993)
[21] T Mannel, W Roberts and Z Ryzak, *Phys. Lett.* **B259**, 359 (1991)
[22] P Blasi, P Colangelo, G Nardulli and N Paver, *Phys. Rev.* **D49**, 238 (1994)
[23] G Alterelli, G Curci, G Martinelli and S Petrarca, *Nucl. Phys.* **B187**, 461 (1981)
[24] H Yamamoto, Harvard University preprint, HUTP-94/A006 (1994)
[25] M Wirbel, B Stech and M Bauer, *Z. Phys.* **C29**, 637 (1985)
[26] R Casalbuoni, A Deandrea, N D Bartolomeo, R Gatto, F Feruglio and G Nardulli, *Phys. Lett.* **B299**, 139 (1993)
[27] A K Giri, L Maharana and R Mohanta, *Pramana –J. Phys.* **47**, 225 (1996)
[28] N Isgur, D Scora, B Grinstein and M B Wise, *Phys. Rev.* **D39**, 799 (1989)
[29] A A Bolokhov, A N Manashov, V V Vereshagin and M V Polyakov, *Phys. Rev.* **D50**, 4713 (1994)
[30] Particle Data Group, Review of Particle Properties, *Phys. Rev.* **D54** Part I (1996)
[31] V M Belyaev, V M Braun, A Khodjamirian and R Ruckl, *Phys. Rev.* **D51**, 6177 (1995)

Solution of approximate gluon evolution equation for small-x at fixed 'ρ'

A SAIKIA
Department of Physics, Arya Vidyapeeth College, Guwahati 781 016, India

MS received 6 November 1996

Abstract. A simple method has been applied to solve the approximate gluon evolution equation for small-x at fixed $\rho(\equiv\sqrt{\ln(x_0/x)/\ln[\ln(Q^2/\Lambda^2)/\ln(Q_0^2/\Lambda^2)]}$. Numerical comparison is made with the predictions from 'double asymptotic scaling' and fit. Better agreement is found between our solution and fit near $\rho = 1$. The solution gives approximate double scaling in this region having 'hard' pomeron with small contamination.

Keywords. Gluon evolution equation; double scaling variables; small-x; soft and hard pomeron.

PACS No. 12·35

In the small-x region, the DGLAP gluon evolution equation (for lowest order) [6, 7] can be written in the form of a wave equation in terms of the variables $\xi(\equiv\ln(x_0/x))$ and $\zeta(\equiv\ln[\ln(Q^2/\Lambda^2)/\ln(Q_0^2/\Lambda^2)]$ (x_0 and Q_0^2 being the starting scales of perturbative evolution) [1]. In the asymptotic limit this equation is solved by Ball and Forte [1]. The solution predicts 'double asymptotic scaling' (DAS) in terms of the scaling variables $\sigma(\equiv\sqrt{\xi\zeta})$ and $\rho(\equiv\sqrt{\xi/\zeta})$. Here, we present a simple analytical solution of the wave equation at fixed ρ. In this solution, there is no need of any input x or Q^2 distributions of gluon. The boundary conditions automatically predict the x and Q^2 distributions at the boundaries. Next, we compare our results with that of [1] and the fit obtained by Glück, Reya and Vogt (GRV) [2]. It was found that DAS result does not agree well with the fit below $\rho\simeq 1{\cdot}13$ [3]. Our solution agrees well with the fit below this value of ρ only. The contribution of the damping term in our solution is different from that of the DAS result which indicates – this term ($e^{-\delta\zeta}$) is not only a factor of the final solution, which is found to be true in the asymptotic limit only. In the intermediate range of σ and ρ, there may be a mixing of the damping coefficient (δ) and DLA [8] growth. Next, we attempt to find heuristically, whether the process below $\rho\simeq 1{\cdot}13$ is a 'hard' or 'soft' one, though there is a similarity between our result at large ρ and ζ and the result of Ball and Forte [1] with 'soft' pomeron input.

In [1] it has been shown that the DGLAP equation for gluon evolution at small-x can be written as

$$\left(\frac{\partial^2}{\partial\xi\,\partial\zeta}+\delta\frac{\partial}{\partial\xi}-\gamma^2\right)G(\xi,\zeta)=0, \tag{1}$$

where $G(\xi, \zeta) = xg(x, Q^2)$ is the gluon momentum distribution function,

$$\delta = \frac{11 + 2n_f/27}{11 - 2n_f/3}, \quad \gamma = \sqrt{\frac{12}{11 - 2n_f/3}}$$

and n_f is the number of active flavours participating in the process.

Under fixed ρ condition, the second order partial differential equation (1) can be converted to ordinary second order differential equation.

Since,

$$\rho = \sqrt{\xi/\zeta}$$

hence, (1) can be written as

$$\left(\frac{d^2}{d\zeta^2} + \delta\frac{d}{d\zeta} - \rho^2\gamma^2\right)G(\zeta\rho^2, \zeta) = 0. \tag{2}$$

The general solution of this differential equation is

$$G(\zeta\rho^2, \zeta) = A\,e^{(-\delta + \sqrt{\delta^2 + 4\gamma^2\rho^2})\zeta/2} + B\,e^{(-\delta - \sqrt{\delta^2 + 4\gamma^2\rho^2})\zeta/2}, \tag{3}$$

where A and B are constants, which are to be evaluated from the boundary conditions.

When $\rho \to 0$, we obtain

$$G(0, \zeta) = A + B\,e^{-\delta\zeta} \tag{4}$$

(which is the required boundary condition introduced in [1]).

When ζ is large,

$$G(0, \zeta_{\text{large}}) \simeq A. \tag{5}$$

Since we cannot find $G(\xi = 0, \zeta = 0)$, because ρ becomes indeterminate, hence, either from data or from fit, for different values of ζ, the constant B is to be evaluated.

When ρ as well as ζ is large (that is, σ is large), eq. (3) can be approximated as

$$G(\zeta\rho^2, \zeta) = A\,e^{\gamma\rho\zeta - \delta\zeta/2}$$

$$\text{or, } G(\sigma, \rho) = A\,e^{\gamma\sigma - \delta(\sigma/2\rho)}. \tag{6}$$

This solution has similarity with DAS result with 'soft' pomeron input except that the slope is half in logarithmic scale of $G(\sigma, \rho)$, predicting 'double scaling'.

For quantitative analysis, we use [3]

$$G(\sigma, \rho) = \frac{3{\cdot}3586}{\sqrt{4\pi\gamma\sigma}}\exp\left[2\gamma\sigma - \delta\left(\frac{\sigma}{\rho}\right)\right] \tag{7}$$

for DAS prediction.

For 4 flavour case, γ is 1·2 and δ is 1·3556, σ and ρ are evaluated using $x_0 = 0{\cdot}1$

(3) and (7) with the fit in the low σ and ρ region, because for high σ and ρ values predictions from (9) is in agreement with the fit. The fit predicted by GRV is (for lowest order)

$$G(x,Q^2)=\left[x^a(A+Bx+Cx^2)\left(\ln\frac{1}{x}\right)^b+S^\alpha\exp\left(-E+\sqrt{E's^\beta\cdot\ln\frac{1}{x}}\right)\right](1-x)^D, \tag{8}$$

where $\mu_{\mathrm{LO}}^2=0{\cdot}25\,\mathrm{GeV}^2$, $\Lambda=0{\cdot}232\,\mathrm{GeV}$, $\alpha=0{\cdot}558$, $\beta=1{\cdot}218$, $b=0$, $E'=4{\cdot}066$,

$$\begin{aligned}
S&=\ln\left[\frac{\ln(Q^2/\Lambda^2)}{\ln(\mu_{\mathrm{LO}}^2/\Lambda^2)}\right],\\
a&=1{\cdot}00-0{\cdot}17\,s,\\
A&=4{\cdot}879\,s-1{\cdot}383\,s^2,\\
B&=25{\cdot}92-28{\cdot}97\,s+5{\cdot}596\,s^2,\\
C&=-25{\cdot}69+23{\cdot}68\,s-1{\cdot}975\,s^2,\\
D&=2{\cdot}537+1{\cdot}718\,s+0{\cdot}353\,s^2,\\
E&=0{\cdot}595+2{\cdot}138\,s.
\end{aligned}$$

Predictions from (3), (7) and (8) are represented in figure 1 for $\rho=0{\cdot}5$ and $1{\cdot}0$. From the analysis, we found that our solution is in better agreement with the fit than the DAS solution for low σ and ρ values. Predictions from (3), (8) are plotted in figure 2 for $\sigma\in[0{\cdot}4,1{\cdot}1]$ and $\rho=0{\cdot}7, 0{\cdot}8, 0{\cdot}9$ and $1{\cdot}1$. The differences in results are below 10% of the fit within these ranges. Hence, we conclude that for low values of σ and ρ, the

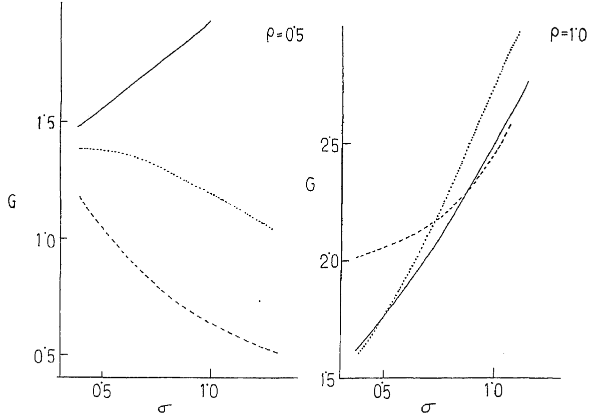

Figure 1. Plots of $G(\sigma,\rho)$ vs. σ from our result (in solid lines), from DAS (in dashed lines) and from GRV fit (dotted lines) for $\rho=0{\cdot}5$ and $1{\cdot}0$.

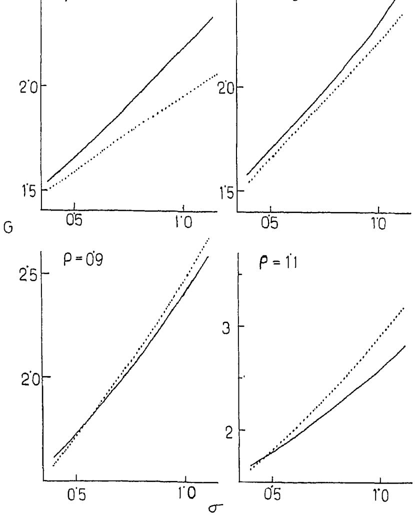

Figure 2. Plots of $G(\sigma, \rho)$ vs. σ from our result (in solid lines) and from GRV fit (dotted lines) for $\rho = 0\cdot 7, 0\cdot 8, 0\cdot 9$ and $1\cdot 1$ and $\sigma \in [0\cdot 4, 1\cdot 1]$.

predictions from our solution are in good agreement with the fit. For $\rho > 1\cdot 13$, the DAS result with 'soft' pomeron input is better than our result. For $\sigma < 0\cdot 4$ and $\rho < 0\cdot 7$, we conjecture that not only the gluon part but also the singlet structure function part of the gluon evolution equation is to be considered (since, for $\sigma = 0\cdot 4$ and $\rho = 0\cdot 7$, $x = 0\cdot 076$ and $Q^2 = 9\cdot 64\,\mathrm{GeV}^2$). So, the wave equation is not valid in this region.

Since, in the region $\rho \sim 1$, our result is in better agreement with the fit, so we try to find heuristically the gluon momentum distribution function in this region. Keeping ζ fixed (say ζ_0), we can vary ξ infinitesimally such that $\rho \simeq 1$ and $\xi\zeta_0 = \sigma^2 \sim 1$.

From (3), we have

$$G(\xi, \zeta_0) = A\,\mathrm{e}^{\gamma\sqrt{\xi\zeta_0} - \delta\zeta_0/2}.$$

(The second term has been neglected, because, the contribution from this term is nearly 1.2% of the first term at $\sigma = 1$ and $\rho = 1$.) Hence

$$G(\xi, \zeta_0) \propto A\,\mathrm{e}^{\gamma(\xi + \zeta_0)/2}$$

or

$$G(\xi) \propto \mathrm{e}^{\gamma\xi/2},$$

$$G(x) \propto x^{-\gamma/2}$$

Since $\gamma = 1{\cdot}2$, hence $G(x) \alpha x$, which implies that, in this region Lipatov 'hard' pomeron ($\lambda \sim 0{\cdot}5$) [5] is participating in the process. We have the damping 'factor' (δ) with the DLA growth [8] indicating that there are other small contaminations in the 'hard' gluon process. So, in the intermediate range of Q^2, 'hard' pomeron process is predominant [1]. If that is true, then not only the 'soft' pomeron but also 'hard' pomeron may show approximate double scaling behaviour near $\rho = 1$. (It is approximate because contribution of the damping term is present in this region.)

Thus, we have shown that the wave equation for gluon evolution can be solved easily (keeping ρ fixed), which predicts gluon evolution in low ranges of σ and ρ. We found (heuristically) that validity of DAS result near $\rho = 1$ does not mean that 'soft' pomeron is participating in the process. 'Hard' pomeron may show approximate double scaling in intermediate x and Q^2.

References

[1] R D Ball and S Forte, *Phys. Lett.* **B335**, 77 (1994); **B336**, 77 (1994)
[2] M Glück, E Reya and A Vogt, *Z. Phys.* **C53**, 127 (1992)
[3] A Saikia, *Pramana–J. Phys.* **47**, 393 (1996)
[4] J R Forshaw and R G Roberts, *Phys. Lett.* **B351**, 308 (1995)
[5] L N Lipatov, *Sov. J. Nucl. Phys.* **23**, 338 (1976)
V S Fadin, E A Kuraev and L N Lipatov, *Phys. Lett.* **B60**, 50 (1975); *Sov. Phys. JETP* **44**, 443 (1976); **45**, 199 (1977)
Y Y Balitski and L N Lipatov, *Sov. J. Nucl. Phys.* **28**, 822 (1978)
[6] V N Gribov and L N Lipatov, *Sov. J. Nucl. Phys.* **15**, 438 (1972)
L N Lipatov, *Sov. J. Nucl. Phys.* **20**, 94 (1974)
G Altarelli and G Parisi, *Nucl. Phys.* **B126**, 298 (1977)
[7] Y L Dokshitzer, *Sov. Phys. JETP* **46**, 641 (1977)
[8] L V Gribov, E M Levin and M G Ryskin, *Phys. Rep.* **C100**, 1 (1983)

Heavy-ion scattering at low energies: First-order correction to the eikonal phase shift

S K CHARAGI
Nuclear Physics Division, Bhabha Atomic Research Centre, Mumbai 400085, India

MS received 14 November 1996.

Abstract. The first-order non-eikonal correction has been applied to calculate heavy-ion reaction cross sections at low energies. The numerical investigations show that, for many heavy-ion systems, reaction cross sections and elastic scattering angular distributions thus calculated, are in good agreement with the optical model calculations.

Keywords. Heavy-ion scattering; eikonal approximation; Glauber model; heavy-ion reaction cross section.

PACS Nos 25·70; 24·10

1. Introduction

The heavy-ion elastic scattering and reaction cross sections, have been studied in the framework of a microscopic Glauber theory, based on the individual nucleon–nucleon collision in the overlap volume of the colliding nuclei, in the high energy domain [1–6]. In these studies nucleus–nucleus reaction cross section is given as $\sigma_R = 2\pi\int b\mathrm{d}b[1-\Omega(b)]$, where $\Omega(b) = \exp(-\sigma_{\mathrm{nn}}\int \rho_{\mathrm{p}}(b,z)\rho_{\mathrm{t}}(b,z)\mathrm{d}z)$, is the overlap integral of the nuclear densities, σ_{nn} is the nucleon–nucleon cross section, ρ_{p} and ρ_{t} are the projectile and target nucleus densities and b is the impact parameter.

This model has been extended to low energies by taking into account the deviation due to the effect of the Coulomb field, in the straight line trajectory of the colliding nuclei [7–11]. This is achieved by calculating $\Omega(b)$ at the distance of closest approach, b' as $\Omega(b')$. This approach is called the Coulomb-modified Glauber model(CMGM). A simple, closed-form analytic expression for the heavy-ion reaction cross section, involving nuclear densities of the colliding nuclei and the nucleon–nucleon cross section, has been obtained within the framework of this model [10, 11]. The reaction cross section and the elastic scattering angular distribution of a large number of heavy-ion systems, over a wide energy range, has been obtained [9–11]. Thus, CMGM provides a unified and easy-to-apply microscopic theoretical framework for analyzing heavy-ion reaction cross section and elastic scattering data.

Earlier Waxman *et al* [12] have shown that the inclusion of the first-order non-eikonal correction in the Glauber model approach considerably improves the agreement with data for elastic scattering of 800 MeV protons by nuclei. Recently, Faldt *et al* [13] carried out the numerical investigation of higher order non-eikonal corrections to the Glauber model at intermediate energies. They applied these corrections to elastic

$V(b,z)$ as $\chi(b) = -\mu/\kappa\int_{-\infty}^{\infty} V(b,z)\mathrm{d}z$. Further, quite recently Cha and Kim [14] applied these corrections for the analysis of the scattering data of $^{16}\mathrm{O} + {}^{40}\mathrm{Ca}$ and $^{16}\mathrm{O} + {}^{90}\mathrm{Zr}$ at 1503 MeV. In this paper we extend the scope of these corrections to a larger number of heavy-ion systems at low energies by calculating the phase shift function at b' as $\chi(b')$. This is the Coulomb-modified phase shift function [14]. This accounts for the deviation in the straight line trajectory due to the Coulomb field.

The plan of the paper is as follows. In § 2 we describe the formalism used in the calculation of the heavy-ion reaction cross section. In § 3 we summarize the results and also draw a few conclusions.

2. Formalism

The nucleus–nucleus reaction cross section σ_{R}, is given by

$$\sigma_{\mathrm{R}} = \frac{\pi}{k^2}\sum(2l+1)(1-|S_l|^2), \tag{1}$$

where k is the wave number and S_l the scattering matrix element given by

$$S_l = \mathrm{e}^{2i\delta_l}. \tag{2}$$

Also

$$|S_l|^2 = \mathrm{e}^{-4\mathrm{Im}(\delta_l)}, \tag{3}$$

where $\mathrm{Im}(\delta_l)$ is the imaginary part of the nuclear phase shift. Wallace [15, 16] has given the following expression for the nuclear phase shift

$$\delta_l^n = -\frac{k[\mu/(\hbar k)^2]^{n+1}}{(n+1)!\,b^{2n}}\left[b^2\left(1+b\frac{\mathrm{d}}{\mathrm{d}b}\right)\right]^n\int_0^{\infty} V^{n+1}[(b^2+z^2)^{1/2}]\mathrm{d}z. \tag{4}$$

We have considered only first two terms of the nuclear phase shift function i.e. δ_l^0 and δ_l^1, the first order correction to the eikonal phase shifts and evaluated them at b', the distance of the closest approach to account for the deflection effect of the Coulomb field. We write

$$\delta_l^0 = -\frac{\mu}{\hbar^2 k}\int_0^{\infty} V_{\mathrm{N}}(b',z)\,\mathrm{d}z \tag{5}$$

and

$$\delta_l^1 = -\frac{\mu^2}{2\hbar^4 k^3}\left(1+b'\frac{\mathrm{d}}{\mathrm{d}b'}\right)\int_0^{\infty} V_{\mathrm{N}}^2(b',z)\,\mathrm{d}z, \tag{6}$$

where

$$V_{\mathrm{N}}(b',z) = V_{\mathrm{N}}[(b'^2+z^2)^{1/2}]. \tag{7}$$

The distance of closest approach b' is obtained from

$$kb' = \eta + [\eta^2 + k^2 b^2]^{1/2}, \tag{8}$$

where η, is the Sommerfeld parameter. The real part of the nuclear potential is written as

$$\mathrm{Re}[V_{\mathrm{N}}(r)] = -V_0/[1 + \mathrm{e}^{[r - r_V(A_1^{1/3} + A_2^{1/3})]/a_V}], \tag{9}$$

and the imaginary part of the nuclear potential is

$$\mathrm{Im}[V_{\mathrm{N}}(r)] = -W_0/[1 + \mathrm{e}^{[r - r_W(A_1^{1/3} + A_2^{1/3})]/a_W}]. \tag{10}$$

The nucleus–nucleus differential cross section $\mathrm{d}\sigma/\mathrm{d}\Omega$ is deduced from the complex phase shift through

$$\frac{\mathrm{d}\sigma}{\mathrm{d}\Omega} = |f(\theta)|^2, \tag{11}$$

for nonidentical spinless nuclei, and the scattering amplitude for charged particles is given by

$$f(\theta) = f_c(\theta) + \frac{1}{2ik}\sum_l (2l+1)\mathrm{e}^{2i\sigma_l}(\mathrm{e}^{2i\delta_l} - 1)P_l(\cos\theta), \tag{12}$$

where the Coulomb phase shift σ_l and the Coulomb amplitude $f_c(\theta)$ are calculated in standard form.

3. Results and conclusions

In the present study, reaction cross sections of heavy-ion systems have been calculated in the framework of the formalism given above. Column 1 of table 1 lists all the heavy-ion systems considered in the present study. The optical potential parameters and the optical model reaction cross section of these systems are well established. Therefore, these systems are excellent candidates of this study. The optical model parameters are listed in columns 3–6 of table 1. Column 2 gives the energies of these systems and column 7 gives the reference. Here, we have used $a_V = a_W$ and $r_V = r_W$.

We have not considered the heavy-ion reaction below 8 MeV. It has been shown [17], that at very low energies, i.e. below 9 MeV/nucleon, even the small values of

Table 1. Optical potential parameters of the heavy-ion systems listed in the table.

Heavy-ion system	Energy MeV	V_0 MeV	W_0 MeV	a_V fm	r_V fm	Ref.
$^{12}C + ^{28}Si$	131·5	18·78	52·4	0·9	1·073	[18]
$^{16}O + ^{28}Si$	215·2	24·53	79·0	0·9	1·03	[18]
$^{16}O + ^{40}Ca$	214·1	21·23	13·8	1·3	0·54	[18]
$^{16}O + ^{208}Pb$	192·0	40·00	35·0	1·226	0·634	[19]
	312·6	19·32	11·4	1·3	0·6	[18]
$^{16}O + ^{209}Bi$	164	17·68	46·38	0·58	1·22	[20]
	170	53·73	42·48	0·58	1·22	[20]
$^{12}C + ^{208}Pb$	96	40·0	25·0	0·56	1·256	[19]
	116·4	41·1	26·71	0·7	1·2	[19]
$^{16}O + ^{208}Pb$	129·5	40·0	25·0	0·615	1·240	[19]

sections. Cal I is the eikonal model result with only $\delta^0(b')$ part of the phase shift. Cal II is the result obtained using first two terms $\delta^0(b')$ and $\delta^1(b')$ of the phase shift. Cal III includes two terms $\delta^0(b)$ and $\delta^1(b)$ in the phase shift.

Heavy-ion system	Energy MeV	σ_R mb Cal I	σ_R mb Cal II	σ_R mb Optical	σ_R mb Cal III
$^{12}C + ^{28}Si$	131·5	2236	2267	2273	2645
$^{16}O + ^{28}Si$	215·2	2463	2487	2484	2839
$^{16}O + ^{40}Ca$	214·1	2026	2116	2105	2545
$^{16}O + ^{208}Pb$	192·0	2810	2894	2930	5013
	312·6	3327	3429	3452	4697
$^{16}O + ^{209}Bi$	164	2405	2442	2486	3065
	170	2454	2543	2591	3025
$^{12}C + ^{208}Pb$	96	1609	1727	1806	4761
	116·4	2159	2276	—	4787
$^{16}O + ^{208}Pb$	129·5	1944	2030	2095	5230

l contribute to the scattering matrix in a non-trivial manner and $|S_l|^2$ shows oscillations. In such a situation there is a risk of underpredicting the reaction cross sections.

The earlier studies of the non-eikonal corrections [13, 14] have shown that the effect of the second order correction is negligible. Therefore, we have not considered the second order term in our calculations. Cha and Kim have considered the effect of the higher order correction in the case of two heavy-ion systems ($^{16}O + ^{40}Ca$ and $^{16}O + ^{90}Zr$) at higher energies (1503 MeV). We extended the scope of the first-order non-eikonal corrections to other heavy-ion systems at low energies.

Table 2 gives the comparison of our calculation of σ_R, the heavy-ion reaction cross section with the optical model results. These optical model results have been taken from the corresponding references given in the previous table. The calculation labeled as Cal I given in column 3 is the σ_R calculated by us including only δ^0 part of the phase shift, evaluated at b'. Cal II on the other hand is the σ_R calculation including both the terms of the phase shift (δ^0 and δ^1), evaluated at b'. There is a few per cent enhancement in the prediction of σ_R by including the first-order term in the phase shift. The agreement between the optical model calculation and the eikonal model with the first-order non-eikonal corrections (Cal II) is good. Also for comparision, we have given in the last column of the table, the prediction of σ_R, using δ^0 and δ^1, evaluated at impact parameter b (Cal III). Cal III fails to reproduce the cross sections.

The fit to elastic scattering angular distribution is given in figure 1 for the heavy-ion system $^{16}O + ^{208}Pb$ at three different energies. In this figure the solid line is the optical model fit [18] and the dotted line is the fit using Cal II results. Except for a few forward angles, the two fits are identical. Also shown in figure 1 as dot-dash line is the plot using Cal III results. Clearly the ineffectiveness of eikonal approximation without Coulomb correction is demonstrated.

Figure 2 gives similar fits for the heavy-ion system $^{12}C + ^{208}Pb$. In this figure, the dotted line is a plot of Cal I result and the solid line is the plot of Cal II results. There is a consistent improvement in the fits by including first order term of the phase shift.

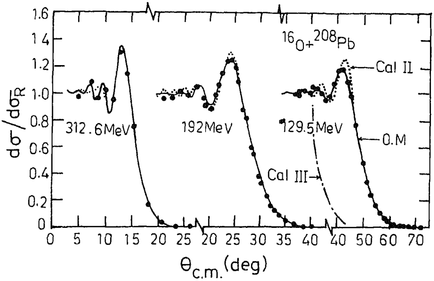

Figure 1. Elastic angular distribution for the scattering of ^{16}O on ^{208}Pb at different energies. The solid line is the optical model fit [18]. The dotted line is the plot of Cal II results· Also shown as dot-dash line is Cal III.

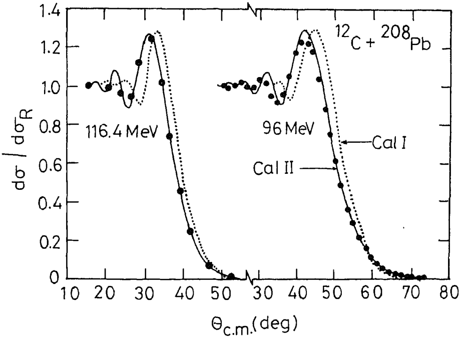

Figure 2. Elastic angular distribution for the scattering of ^{12}C on ^{208}Pb at two different energies. The dotted line in Cal I plot. The solid line is Cal II plot.

We conclude that a good description of the heavy-ion elastic scattering and reaction cross section at low energies, can be given by calculating the first two terms of the phase shift at the distance of closest approach. This is a simple and economical procedure as it requires little numerical effort. The predictions of the σ_R and the elastic scattering angular distribution in the present formalism are as good as the optical model predictions. This good agreement is also an independent verification of the goodness of the optical potential parameters. Since the eikonal calculation with first-order non-

Coulomb potentials, we can obtain a new set of effective potentials for these h systems at low energies in the framework of the eikonal approximation.

References

[1] R J Glauber, *Lectures on Theoretical Physics* (Inter-Science, New York, 1959),
[2] P J Karol, *Phys. Rev.* **C11**, 1203 (1975)
[3] R M Devries and J C Peng, *Phys. Rev.* **C22**, 1055 (1980)
[4] J C Peng, R M Devries and N DiGiacomo, *Phys. Lett.* **B98**, 244 (1981)
[5] A Vitturi and F Zardi, *Phys. Rev.* **C36**, 1404 (1987)
[6] S M Lenzi, A Vitturi and F Zardi, *Phys. Rev.* **C38**, 1086 (1988)
[7] S M Lenzi, A Vitturi and F Zardi, *Phys. Rev.* **C40**, 2114 (1989)
[8] J Chauvin, D Lebrun, F Durand and M Buenerd, *J. Phys.* **G11**, 261 (1985)
[9] S K Charagi and S K Gupta, *Phys. Rev.* **C46**, 1982 (1992)
[10] S K Charagi and S K Gupta, *Phys. Rev.* **C41**, 1610 (1990)
[11] S K Charagi, *Phys. Rev.* **C48**, 452 (1993)
[12] D Waxman, C Wilkin, J F Germond and R J Lombard, *Phys. Rev.* **C24**, 578 (1
[13] G Faldt, A Ingemarsson and J Mahalanabis, *Phys. Rev.* **C46**, 1974 (1992)
[14] M H Cha and Y J Kim, *Phys. Rev.* **C51**, 212 (1995)
[15] S J Wallace, *Ann Phys. (N.Y.)* **78**, 190 (1973)
[16] S J Wallace, *Phys. Rev.* **D8**, 1846 (1973)
[17] S K Charagi, *Phys. Rev.* **C51**, 3521 (1995)
[18] G R Satchler and W G Love, *Phys. Rep.* **55**, 183 (1979)
[19] J B Ball, C B Fulmer, E E Gross, M L Halbert, D C Hensley, C A Ludemann, M J and G R Satchler, *Nucl. Phys.* **A252**, 208 (1975)
[20] P Singh, S Kailas, A Chatterjee, S S Kerekatte, A Navin, A Nijasure and B John, **A555**, 606 (1993)

Semi-empirical formulae for Λ-binding energy in hypernuclei using mass distribution

M Z RAHMAN KHAN, NASRA NEELOFER and M A SUHAIL*
Department of Physics, Aligarh Muslim University, Aligarh 202 002, India
*Department of Applied Physics, Z. H. College of Engineering and Technology, Aligarh Muslim University, Aligarh 202 002, India

MS recieved 24 June 1996

Abstract. Semi-empirical formulae for ground state Λ-binding energy of heavy hypernuclei, in inverse powers of the mass number, using the mass distribution in the folding model, under fairly reasonable assumptions about the range of the Λ-nucleon force are obtained in more than one plausible way. However, they are found to give nearly identical results. A reasonable estimate of the Λ well-depth is obtained from a chi-square fit of the available ground state Λ-binding energy data of medium and heavy nuclei.

Keywords. Semi-empirical; binding emergy.

PACS No. 21·80

1. Introduction

In our earlier analysis [1], we presented a semi-empirical formula for ground state Λ-binding energy (B_Λ) in hypernuclei, in inverse powers of core mass number (A_c) obtained from the Λ-nucleus folded potential. The proton charge distribution was assumed to be same as the neutron density distribution of the core nuclei, implying that the range of the ΛN potential equals the proton size. This approach may not be appropriate, particularly for nuclei having different number of neutrons (N) and protons (Z).

In the present work, we take the point proton and neutron density distribution available in the scientific literature [2]. First one has to broadly discuss what the Λ 'sees' of the core nucleus. There are mainly three apparently different possibilities: namely, whether the Λ 'sees' a single-particle potential obtained by averaging over the separate proton and the neutron potentials of the Λ or it 'sees' the two separate single-particle potentials distinctly or it 'sees' an average density giving rise to an average potential. For light nuclei having $N = Z$, these different possibilities do not arise as the neutron and the proton distribution may be taken to be the same. However, as we are dealing with medium and heavy hypernuclei where, in most cases N is considered larger than Z, we have to consider these different approaches.

In the folding model approach of Deloff [3] and following the method given by Flügge [4], with the single-particle Woods–Saxon (W–S) Λ-nucleus potential, a semi-empirical formula for B_Λ is obtained in inverse powers of A_c. The B_Λ for the second and third approaches can be written down analytically in this way, but this cannot be done if the Λ 'sees' an option seems to be to perform numerical calculations. The formulae for the last two situations mentioned above are given in the next section. Calculations are performed using these two analytical formulae. However, calculations of Λ-binding energy by numerically solving the Schrödinger equation are carried out for all the three approaches.

Here, in our analysis, we have considered the B_Λ data of five hypernuclei, ${}^{28}_{\Lambda}\mathrm{Si}$, ${}^{32}_{\Lambda}\mathrm{S}$, ${}^{40}_{\Lambda}\mathrm{Ca}$, ${}^{51}_{\Lambda}\mathrm{V}$, and ${}^{89}_{\Lambda}\mathrm{Y}$, these being the only presently available data on medium and heavy hypernuclei [5, 6]. As the analytical formulae have been obtained from the s-state solution of the Schrödinger equation, we consider only the ground state B_Λ data of these hypernuclei i.e. there are only five data-points when the analytical formula is used for the second and the third approaches. However, for the numerical analyses, we consider the ground as well as the available bound excited state B_Λ data of these hypernuclei, making altogether 11 data-points, after excluding two excited states of a doubtful nature as discussed later.

The value of the chi-square (χ^2) as well as the value of the single parameter D_Λ, for the two analytical formulae, obtained in the second and third approach, are more or less same.

The numerical calculations performed for all the three approaches, for the 11 data-points, are also found to give almost similar results in terms of the value of their χ^2, implying that the three approaches are nearly indistinguishable, at least with regard to the B_Λ data of the ground as well as the excited states of the hypernuclei considered. However, it may be pointed out that although the χ^2 are nearly same in all cases, in one case D_Λ is somewhat different.

Predictions are made regarding the B_Λ values [5, 7] of ${}^{16}_{\Lambda}\mathrm{O}$ and the heavy and spallation hypernuclei. ${}^{16}_{\Lambda}\mathrm{O}$ is being excluded from the fit because it is a light hypernucleus and the other heavy and spallation hypernuclei [7] are excluded due to large uncertainties in their B_Λ data and in the core mass number assignment.

2. Formulae

2.1 *Derivation of the B_Λ formulae*

In the first approach, the Λ is supposed to 'see' an average of the potentials constituted by the protons alone and that constituted by the neutrons alone. These seperate potentials are given as

$$V_{\Lambda Z}(r) = -Z\rho_p(r)V_{0p} \quad \text{and} \quad V_{\Lambda N}(r) = -N\rho_n(r)V_{0n}, \tag{2.1.1}$$

which are obtained by folding point proton density, $\rho_p(r)$, with a zero-range Λp potential and point neutron density, $\rho_n(r)$, with a zero-range Λn potential, respectively. We may emphasize that these are point mass and not charge densities. Both point proton and point neutron densities, normalized to unity are taken to be of the W–S form

$$\rho_q(r) = \rho_q^{(0)}\{1 + \exp[(r - R_q)/a_q]\}^{-1},$$

(index q denotes p or n), $\rho_q^{(0)}$ is obtained from the normalization conditions. The forms of R_q and a_q, taken from ref. [2] are

$$R_q = C_{0q} + C_{1q}A_c^{1/3} + C_{2q}(N - Z)A_c^{-1},$$

$$a_q = A_{0q} + A_{1q}(N - Z)A_c^{-1}. \tag{2.1.2}$$

here. For neutron and proton, the parameters in (2.1.2) are taken from ref. [2], while for the average nuclear density, it is indicated at the appropriate place, depending on how these may be obtained. The single-particle Λ-nucleus potential, in the first approach, is then obtained by taking an average of $V_{\Lambda Z}(r)$ and $V_{\Lambda N}(r)$. Thus

$$V_{\Lambda}(r) = \frac{Z}{A_c} V_{\Lambda Z}(r) + \frac{N}{A_c} V_{\Lambda N}(r). \tag{2.1.3}$$

With this average Λ-nucleus potential, only numerical calculations of B_{Λ} are possible.

In the second approach, with $V_{\Lambda Z}(r)$ and $V_{\Lambda N}(r)$, as given by (2.1.1), the relevant eigenvalue equation for $B_{\Lambda Z}$ and $B_{\Lambda N}$, in the approximation $e^{-(R_q/a_q)} \ll 1$, is solved. The details are already given in ref. [1]. The expression for $B_{\Lambda Z}$ and $B_{\Lambda N}$, which are a series in powers of A_c^{-1}, are given by

$$B_{\Lambda Z} = D_{\Lambda Z} - \frac{\hbar^2 \pi^2}{2\mu_{\Lambda Z}} [C'_{0p} A_c^{-2/3} - C'_{1p} A_c^{-1} + C'_{2p} A_c^{-4/3} - \cdots] \tag{2.1.4a}$$

and

$$B_{\Lambda N} = D_{\Lambda N} - \frac{\hbar^2 \pi^2}{2\mu_{\Lambda N}} [C'_{0n} A_c^{-2/3} - C'_{1n} A_c^{-1} + C'_{2n} A_c^{-4/3} - \cdots]\text{'} \tag{2.1.4b}$$

where

$$\mu_{\Lambda Z} = \frac{m_{\Lambda} m_p Z}{m_{\Lambda} + m_p Z}$$

and

$$\mu_{\Lambda N} = \frac{m_{\Lambda} m_n N}{m_{\Lambda} + m_n N}$$

are the $\Lambda - Z$ and $\Lambda - N$ reduced mass. The coefficients $C'_{iq} (i = 0, 1, 2 \cdots)$ are defined as

$$\begin{aligned} &C'_{0q} = C_{1q}^{-2},\ C'_{1q} = B_{1q} - B_{2q} W_{qQ},\ C'_{2q} = B_{3q} - B_{4q} W_{qQ} + B_{5q} W_{qQ}^2, \\ &C'_{3q} = B_{6q} - B_{7q} W_{qQ} + B_{8q} W_{qQ}^2 - B_{9q} W_{qQ}^3, \ldots, \end{aligned} \tag{2.1.5}$$

where

$$W_{qQ} = \sum_{n=1}^{\infty} \left[\frac{a_q K_{0Q}}{n(n + a_q K_{0Q})} \right]^{1/2},\ K_{0Q} = \left[\frac{2\mu_{\Lambda Q} D_{\Lambda Q}}{\hbar^2} \right]^{1/2}$$

(Q denotes Z or N) and

$$\begin{aligned} &B_{1q} = 2C_{0q} C_{1q}^{-3} + 2C_{1q}^{-3} K_{0Q}^{-1}, \quad B_{2q} = 4A_{0q} C_{1q}^{-3}, \\ &B_{3q} = 3C_{0q}^2 C_{1q}^{-4} + 6C_{0q} C_{1q}^{-4} K_{0Q}^{-1} + 3C_{1q}^{-4} K_{0Q}^{-2}, \\ &B_{4q} = 12C_{0q} C_{1q}^{-4} A_{0q} + 12A_{0q} C_{1q}^{-4} K_{0Q}^{-1}, \quad B_{5q} = 12A_{0q}^2 C_{1q}^{-4}, \\ &B_{6q} = 12C_{0q}^2 C_{1q}^{-5} K_{0Q}^{-1} + 12C_{0q} C_{1q}^{-5} K_{0Q}^{-2} + 4C_{1q}^{-5} K_{0Q}^{-3}, \\ &B_{7q} = 24C_{0q}^2 C_{1q}^{-5} A_{0q} + 48A_{0q} C_{0q} C_{1q}^{-5} K_{0Q}^{-1} + 24A_{0q} C_{1q}^{-5} K_{0Q}^{-2}, \\ &B_{8q} = 48A_{0q}^2 C_{0q} C_{1q}^{-5} + 48A_{0q}^2 C_{1q}^{-5} K_{0Q}^{-1}, \quad B_{9q} = 32A_{0q}^3 C_{1q}^{-5}, \ldots. \end{aligned}$$

In writing down the above, (2.1.2) have been used. The B_{Λ} is then obtained by averaging the $B_{\Lambda Z}$ and $B_{\Lambda N}$ as

$$B_\Lambda = \frac{Z}{A_c} B_{\Lambda Z} + \frac{N}{A_c} B_{\Lambda N}. \tag{2.1.6}$$

In the third approach, the point nucleon density, $\rho_N(r)$, is expressed as an average of $\rho_p(r)$ and $\rho_n(r)$,

$$\rho_N(r) = \frac{Z}{A_c} \rho_p(r) + \frac{N}{A_c} \rho_n(r). \tag{2.1.7}$$

The single particle Λ-nucleus potential, obtained by folding zero-range ΛN potential with the point nucleon density of the core nucleus, follows the density distribution of the core and is written as

$$V_\Lambda(r) = -D_\Lambda \rho(r), \tag{2.1.8}$$

where $\rho(r)$ is the average nuclear density of the core nucleus given as $A_c \rho_N(r)$ and D_Λ is the average potential depth. With this Λ-nucleus potential, the solution of the eigenvalue equation for B_Λ, in the approximation $e^{\langle -R/a \rangle} \ll 1$, leads to the familiar expression for B_Λ:

$$B_\Lambda = D_\Lambda - \frac{\hbar^2 \pi^2}{2\mu_{\Lambda A}} [C'_0 A_c^{-2/3} - C'_1 A_c^{-1} + C'_2 A_c^{-4/3} - C'_3 A_c^{-5/3} + \cdots], \tag{2.1.9}$$

where $\mu_{\Lambda A} = m_\Lambda m_N A_c / (m_\Lambda + m_N A_c)$ is the Λ-core reduced mass. The above coefficients C'_i are same as defined in ref. [1]. Then the parameters of $\rho_N(r)$ are substituted. How we obtain the parameters of $\rho_N(r)$ is briefly described in the next section.

3. Results and discussion

For all the three approaches, the expression of the radius R and diffuseness a as well as their parameters for the proton and neutron distribution are taken from the standard literature [2] as already mentioned. For stable and β unstable nuclei, the values of the parameters of R and a are listed in table 1 for ready reference. The radius and diffuseness parameters of the average nucleon density distribution $\rho_N(r)$ are obtained from the least square fit to (2.1.7), for nuclei over a large mass number range. However, a number of parameter sets become available in this way depending upon the initial choice of these parameters, but in most cases their least squares do not differ significantly. Fitting of the experimental B_Λ data was carried out with different parameter sets. The radius and diffuseness parameter set, which gives a good fit to the B_Λ data, is being quoted in table 1.

With these parameters, the χ^2 fit to the ground state B_Λ values of ${}^{28}_{\Lambda}\mathrm{Si}$, ${}^{32}_{\Lambda}\mathrm{S}$, ${}^{40}_{\Lambda}\mathrm{Ca}$, ${}^{51}_{\Lambda}\mathrm{V}$ and ${}^{89}_{\Lambda}\mathrm{Y}$ is carried out, where χ^2 is defined as

Table 1. Radius and diffuseness parameters for proton and neutron taken from ref. [2] and the corresponding calculated radius and diffuseness parameters of nucleon distribution.

Radius and diffuseness parameters	For proton (fm)	For neutron (fm)	Calculated nucleon distribution parameters (fm)
C_0	−0·5401	−0·4415	−0·4092
C_1	1·2490	1·2131	1·2265
C_2	−0·9532	0·8931	0·0643
A_0	0·4899	0·4686	0·3709
A_1	−0·1236	0·0741	−0·0635

Table 2. The results of a χ^2 fit to the experimental ground state B_Λ values, using analytical formula (2.1.9). Here $D_\Lambda = 29{\cdot}47$ MeV with total $\chi^2 = 2{\cdot}46$.

Hypernuclei	B_Λ^{exp}(MeV)	B_Λ^{cal}(MeV)
${}^{28}_{\Lambda}$Si	16·0	16·2
${}^{32}_{\Lambda}$S	17·5	17·1
${}^{40}_{\Lambda}$Ca	18·6	18·6
${}^{51}_{\Lambda}$V	19·8	20·1
${}^{89}_{\Lambda}$Y	22·5	22·4

the symbols having their usual meaning. The experimentally quoted value is
$i) \pm \Delta B_\Lambda^{\text{exp}}(i)$. Since the experimental errors are not available, the error bar in the
rimental data, $\Delta B_\Lambda^{\text{exp}}(i)$, is assumed to be a certain fixed percentage error (5%) for
e nuclei considered, which seems quite realistic and is only a criterion for adjusting
arameters and judging the quality of the fits.

ght hypernuclei are excluded from the fit as the analytical formulae, being based on
distribution are not valid for these. The analytical formula for B_Λ, obtained in the
nd approach, involves two parameters, the well depth felt by Λ in the proton
bution $D_{\Lambda Z}$ and that in the neutron distribution $D_{\Lambda N}$. Whereas the analytical
ula, in the third approach, obtained using the average density involves a single-
meter i.e. the Λ-well depth, D_Λ, in some average sense. However, we shall treat the
er also as a single-parameter formula assuming $D_{\Lambda Z} = D_{\Lambda N}$.

$_\Lambda$ obtained using formula (2.1.6) is 29·57 MeV, with χ^2 for 5 data-points equal to
Total χ^2, using formula (2.1.9), for the 5 data-points, with best fit value of $D_\Lambda =$
7 MeV, is 2·46. The D_Λ and χ^2 obtained by both the analytical formulae is almost
ame. Here, we report the results obtained using the formula (2.1.9) in table 2.

r the sake of comparison of the results obtained here and that in ref. [1], we
rm χ^2-fitting for the same 5 data-points using the B_Λ formula given in ref. [1].
l χ^2, with the best fit value of $D_\Lambda = 34{\cdot}37$ MeV, is found to be 21·81 as compared to

density. D_Λ was found to be 28·40 MeV. Total χ^2 for 11 data-points is 22·76. The calculated B_Λ values marked by an asterisk are the predicted values with the obtained value of D_Λ.

	B_Λ^{exp}(MeV)				B_Λ^{cal}(MeV)			
Hypernuclei	s	p	d	f	s	p	d	f
$^{28}_{\Lambda}$Si	16·0	7·2	−2·2	—	16·4	6·1	unbound	—
$^{32}_{\Lambda}$S	17·5	—	—	—	17·3	—	—	—
$^{40}_{\Lambda}$Ca	18·6	9·2	1·7	—	18·8	10·0	0·6*	—
$^{51}_{\Lambda}$V	19·8	13·1	3·9	−2·2	20·2	12·5	3·7	unbound
$^{89}_{\Lambda}$Y	22·5	16·0	9·2	2·0	22·7	17·1	10·3	2·8*

semi-empirical formulae are certainly an improvement over our earlier formula [1]. The applicability of both these formulae is, however, again restricted to the stable nuclei as well as to the nuclei close to stability and also to the ground states of medium and heavy hypernuclei.

Numerical calculations are also carried out in all the three cases mentioned above, for ground as well as the available excited Λ-single-particle bound states of the nuclei considered. The excited state B_Λ data of $^{40}_{\Lambda}$Ca, corresponding to angular momentum $l = 2$ and that of $^{89}_{\Lambda}$Y corresponding to $l = 3$ were found to contribute very heavily to the total χ^2 in all three cases. When these excited states are taken out of the fitting, the situation is considerably improved. These excited states have been taken out in all the three approaches. The results given in table 3, corresponding to the case of average nucleon density, are those obtained after exclusion of these two excited states from the fitting. However, predicted values for these two excited states are quoted in the table and are marked by an asterisk.

The D_Λ values, obtained from exact calculations in the first and the second approach, are found to be 31·83 and 31·81 MeV, for the 11 data-points, with their respective χ^2 as 22·60 and 22·44. The D_Λ value, obtained in the third approach, using the average nucleon density is, however, 28·40 MeV, with $\chi^2 = 22{\cdot}76$. We have about the same χ^2 in all the three cases, thereby showing that the calculations cannot distinguish between the different approaches considered here. At the same time, this poses the problem of the ambiguity of determining the empirical value of D_Λ with which theoretical value of the Λ-binding to infinite nuclear matter is to be compared. In this context, a very reliable semi-empirical formula has to be developed.

The calculated D_Λ parameter, obtained from χ^2 fitting, by analytical formulae and that obtained from exact calculations in all the three approaches, are used to predict the B_Λ values [5, 7] of $^{16}_{\Lambda}$O and the heavy and spallation hypernuclei. The former being a light hypernucleus was not included in the fit while the latter had not been included as precise B_Λ values and their assignment to the core nuclei are not available. The upper bound [7] of B_Λ data, on heavy and spallation hypernuclei, is assigned, to only the stable nuclei or nuclei close to stability, corresponding to two mass number ranges of by analytical formula and exact calculations using average density. Wherever, hypernuclei having same A_c appear in the first column, their average theoretical B_Λ value is given. Apart from $^{16}_{\Lambda}$O, experimental B_Λ for all the other hypernuclei are only the upper limits.

			B_Λ^{pred} (MeV)	
Hypernuclei	A_c	B_Λ^{exp} (MeV)*	Using formula (2·1·9)	From exact calculations
$^{16}_{\Lambda}$O	15	12·2	7·4	11·7
$^{36}_{\Lambda}$Cl	35	21·9	17·9	18·2
$^{45}_{\Lambda}$Ca, $^{45}_{\Lambda}$Ti	44	23·0	19·7	19·5
$^{53}_{\Lambda}$Cr	52	22·5	20·8	20·4
$^{66}_{\Lambda}$Cu	65	22·8	22·0	21·5
$^{76}_{\Lambda}$As	75	23·7	22·7	22·1

*Except for $^{16}_{\Lambda}$O, B_Λ^{exp} are only the upper limits.

Table 5. Predicted values of B_Λ for higher mean values of A_c, by analytical formula and exact calculations using average density. Wherever, two hypernuclei having same A_c appear in the first column, their average theoretical B_Λ value is given.

			B_Λ^{pred} (MeV)	
Hypernuclei	A_c	B_Λ^{exp} (MeV) (upper limits)	Using formula (2·1·9)	From exact calculations
$^{64}_{\Lambda}$Cu	63	21·9	21·9	21·3
$^{73}_{\Lambda}$Ge	72	23·0	22·7	21·9
$^{81}_{\Lambda}$Se, $^{81}_{\Lambda}$Kr	80	22·5	23·0	22·3
$^{94}_{\Lambda}$Zr, $^{94}_{\Lambda}$Nb	93	22·8	23·7	22·9
$^{104}_{\Lambda}$Rh	103	23·7	24·1	23·3

If there are two stable nuclei [8] having same A_c, the predicted B_Λ is taken to be the average value of the two. However, as the results obtained are almost same by both analytical formulae and also from numerical calculations in all the three cases, we quote only the results obtained in the third approach. The experimental and the predicted B_Λ for $^{16}_{\Lambda}$O and other hypernuclei with lower mean values of the A_c are presented in table 4, whereas for the higher mean values of A_c, the results are presented in table 5. The predicted B_Λ, in some cases, for higher mean values of A_c, using analytical formula (2.1.9) and for one case from the exact calculations, are higher than the experimental upper limits of the B_Λ values. Thus, the experimental upper limits of should be assigned to the lower mean values of the core mass number range.

4. Conclusion

All the three approaches considered here seem equally good and it is not possibl prefer any one of these on the basis of the χ^2. The present analytical formulae for B_Λ better than our earlier formula [1], obtained by folding with the charge density.

References

[1] N Neelofer, Mohammad Shoeb and M Z Rahman Khan, *Pramana–J. Phys.* **37**, 419 (1

[2] I Angeli, M Beiner, R J Lombard and D Mas, *J. Phys.* **G6**, 303 (1989)

[3] A Deloff, *Nucl. Phys.* **B27**, 149 (1971)

[4] S Flügge, *Practical quantum mechanics* (Springer-Verlag, Berlin, Heidelberg, New Y 1971) vol. I, p. 162

[5] P H Pile, *Nuovo Cimento* **102**, 413 (1989)
P H Pile *et al*, *Phys. Rev. Lett.* **66**, 2585 (1991)

[6] R Bertini *et al*, *Phys. Lett.* **B83**, 306 (1979)

[7] D P Goyal, *Nucl. Phys.* **83**, 639 (1966)

[8] L R B Elton, *Int. Nucl. Theory* (ELBS and Sir Isaac Pitman and Sons Ltd., London, 1 p. 259

Group theoretical aspects of $U^{\mathrm{B}}(6) \otimes U^{\mathrm{F}}(20)$ symmetry limits of IBFM related to the $U^{\mathrm{B}}(5)$ and $O^{\mathrm{B}}(6)$ limits of IBM

V K B KOTA
Physical Research Laboratory, Navrangpura, Ahmedabad 380 009, India

MS received 6 February 1997

Abstract. The $U^{\mathrm{B}}(6) \otimes U^{\mathrm{F}}(20)$ Bose–Fermi dynamical symmetry of interacting boson–fermion model arises when the odd nucleon occupies single particle orbits with $j = 1/2, 3/2, 5/2$, and $7/2$. The subgroup structures of $U^{\mathrm{B}}(6) \otimes U^{\mathrm{F}}(20)$ related to the $U^{\mathrm{B}}(5)$ and $O^{\mathrm{B}}(6)$ limits of sdIBM ($U^{\mathrm{B}}(6)$) are analysed. Broadly speaking, $U^{\mathrm{B}}(6) \otimes U^{\mathrm{F}}(20)$ admits $U^{\mathrm{BF}}(5) \otimes U^{\mathrm{F}}_{s}(4)$, $\mathrm{Spin}^{\mathrm{BF}}(5) \otimes U^{\mathrm{F}}_{k}(5)$ and $U^{\mathrm{BF}}(5) \otimes U^{\mathrm{F}}_{s}(2)$ limits with $U^{\mathrm{B}}(5)$ core and $\mathrm{Spin}^{\mathrm{BF}}(6)$, $O^{\mathrm{BF}}(5) \otimes U^{\mathrm{F}}_{s}(4)$, $\mathrm{Spin}^{\mathrm{BF}}(6) \otimes U^{\mathrm{F}}_{k}(5)$ and $O^{\mathrm{BF}}(6) \otimes U^{\mathrm{F}}_{s}(2)$ limits with $O^{\mathrm{B}}(6)$ core respectively. For each of these seven symmetry limits, group chains, quantum numbers labelling the basis states, generators and Casimir operators for the various subgroups and energy formulas are given. Recoupling coefficients (reduced Wigner coefficients) for constructing wavefunctions of low-lying states are tabulated and these will allow (together with sdIBM $U^{\mathrm{B}}(5)$ and $O^{\mathrm{B}}(6)$ limit results) one to calculate $B(E2)$'s, $B(M1)$'s, one and two nucleon transfer strengths etc. in the seven symmetry limits. Experimental examples for the $U^{\mathrm{B}}(6) \otimes U^{\mathrm{F}}(20)$ symmetry limits are briefly discussed.

Keywords. Interacting boson model; interacting boson–fermion model; odd-mass nuclei; dynamical symmetries; $U(5)$ limit; $O(6)$ limit; $U^{\mathrm{B}}(6) \otimes U^{\mathrm{F}}(20)$.

PACS Nos 21·10; 21·60; 23·20

1. Introduction

The *sd* interacting boson model (*sd*IBM) with its three dynamical $U^{\mathrm{B}}_{d}(5)$, $SU^{\mathrm{B}}_{sd}(3)$ and $O^{\mathrm{B}}_{sd}(6)$ symmetries is established to be a standard model for describing low-lying quadrupole collective states in heavy ($A > 100$) even–even nuclei [1,2]; in practice usually the proton–neutron IBM (pn-*sd*IBM) is used for numerical analysis of experimental data (see [2,3] and references therein). Similarly the *sd* interacting boson-fermion model (*sd*IBFM), where a quasi-particle (q.p.) is coupled to the even-even core *sd*IBM (or pn-*sd*IBM) nucleus possesses a wide variety of Bose–Fermi (BF) dynamical symmetries and it is now used as a standard model for describing low-lying quadrupole collective states in heavy odd-mass nuclei [4]; see [2,5] and references therein for recent numerical calculations in *sd*IBFM and pn-*sd*IBFM. Our concern in this article is with dynamical symmetries of *sd*IBFM. From here onwards the prefix '*sd*', '*d*' etc. are dropped when there is no confusion. It should be stressed that dynamical symmetries of IBFM generate band structures in odd-mass nuclei and hence their importance in the spectroscopy of odd-*A* nuclei. The IBFM symmetries depend not only on the IBM symmetries but also on the *j* values of the single particle orbits occupied by the odd fermion (nucleon). The BF dynamical symmetries related to odd several experimental examples showing the band structures generated by these dynamical symmetries are found. These results are well documented in several books and review articles [4, 6, 7]. A case that received some attention but for which a complete account is not available in literature, is the case of coupling of a particle in $j = 1/2, 3/2, 5/2$ and $7/2$ orbits. In this case the model space of IBFM is defined by $\{N\} \otimes \{1\}$ of $U^{\mathrm{B}}(6) \otimes U^{\mathrm{F}}(20)$; to ensure symmetry among bosons, the symmetric irreducible representation (irrep) $\{N\}$ of $U^{\mathrm{B}}(6)$ is taken in direct product with the irrep $\{1\}$, for the single odd fermion, of $U^{\mathrm{F}}(20)$, where $20 = \sum_j (2j + 1)$. Preliminary work on various symmetry limits of $U^{\mathrm{B}}(6) \otimes U^{\mathrm{F}}(20)$ was done by Ling *et al* [8], Kota [9, 10], Jolie *et al* [11], Bijker and Kota [12] and Kota and Van Isacker [13]. The purpose of the present article is to give a complete description of the group theoretical aspects of $U^{\mathrm{B}}(6) \otimes U^{\mathrm{F}}(20)$ dynamical symmetry limits and also to briefly discuss the present status of the search for empirical examples for these symmetry limits. The $U^{\mathrm{B}}(6) \otimes U^{\mathrm{F}}(20)$ is rich in its content as all the symmetry schemes with $(j = 1/2)$, $(j = 3/2)$, $(j = 1/2, 3/2)$, $(j = 3/2, 5/2)$ and $(j = 1/2, 3/2, 5/2)$ orbits occur at some level within this scheme. Another important aspect is that some of the symmetry limits of this scheme are realizable in purely fermionic models (see § 5 ahead). Now we will give a preview.

In § 2 classification of symmetry limits of $U^{\mathrm{B}}(6) \otimes U^{\mathrm{F}}(20)$ is presented. The symmetry limits with $SU^{\mathrm{B}}(3)$ core are discussed in detail by Bijker and Kota [12] in a more general context (with odd fermion in $j = 1/2, 3/2, \ldots, (\eta + 1/2)$ orbits with η any positive integer; in the present case $\eta = 3$) and therefore, the $SU^{\mathrm{B}}(3)$ based symmetry limits of $U^{\mathrm{B}}(6) \otimes U^{\mathrm{F}}(20)$ are not discussed in this article. The symmetry limits related to the $U^{\mathrm{B}}(5)$ and $O^{\mathrm{B}}(6)$ limits of IBM are described in detail in §§ 3 and 4 respectively. Section 5 gives a brief presentation of the present status of experimental examples for these symmetry limits, current interest in $U^{\mathrm{B}}(6) \otimes U^{\mathrm{F}}(20)$ and some concluding remarks.

2. Classification of symmetry limits of $U^{\mathrm{B}}(6) \otimes U^{\mathrm{F}}(20)$

The BF symmetries of $U^{\mathrm{B}}(6) \otimes U^{\mathrm{F}}(20)$ are defined via the group chain

$$U^{\mathrm{B}}(6) \otimes U^{\mathrm{F}}(20) \supset G^{\mathrm{B}} \otimes G^{\mathrm{F}} \supset \cdots \supset \mathrm{Spin}\,(3) \supset \mathrm{Spin}\,(2), \tag{1}$$

where Spin (3) generates angular momentum J and Spin (2) its projection M (from now on the Spin (2) and/or M label are often dropped). In general, three classes of BF symmetries can be distinguished, which will be denoted by BF-1, BF-2 and BF-12 symmetries. In the BF-1 or spinor symmetries [14, 15], the subgroups G^{B} and G^{F} are isomorphic, $G^{\mathrm{B}} \sim G^{\mathrm{F}}$. The BF-2 or pseudo-spin symmetries arise [16] by decoupling the j-values (in the present case $j = 1/2, 3/2, 5/2, 7/2$) into pseudo-spin (s) and pseudo-orbital (k_i) parts so that $G^{\mathrm{F}} \supset G^{\mathrm{F}}_k(\Omega_k) \otimes G^{\mathrm{F}}_s(\Omega_s)$, where $\Omega_k = \Sigma_i (2k_i + 1)$, $\Omega_s = (2s + 1)$ and $\Sigma_j (2j + 1) = \Omega_k \Omega_s$; the pseudo orbital group $G^{\mathrm{F}}_k(\Omega_k)$ or one of its subgroups coincides with G^{B} and hence can be combined with it. The BF-12 symmetries are a combination of BF-1 and BF-2 symmetries; at some stage in the group reduction a spinor symmetry occurs and at another stage use is made of a pseudo-spin symmetry. The $U^{\mathrm{B}}(6) \otimes U^{\mathrm{F}}(20)$ admits all the three different types of symmetry limits as pointed out first in [9, 10], and in the following they are classified accordingly.

2.1 *BF-1 symmetry limits*

The $U^{\mathrm{F}}(20)$ group admits $SU^{\mathrm{F}}(4)$ as a subgroup as the $\{21\}$ irrep of $SU^{\mathrm{F}}(4)$ or equivalently the $[3/1, 1/2, 1/2]$ irrep of $\mathrm{Spin}^{\mathrm{F}}(6)$ group contains [17] angular momenta $j = 1/2, 3/2, 5/2, 7/2$. Note that $\{abc\}_{SU(4)} \rightarrow [(a+b-c)/2, (a-b+c)/2, (a-b-c)/2]_{O(6)}$ and $[abc]_{O(6)} \rightarrow \{a+b, a-c, b-c\}_{SU(4)}$. $SU(4)$ group admits three irreps with dimension 20 and they are $\{21\}$, $\{3\}$ and $\{22\}$. They correspond to $O(6)$ irreps $[3/2, 1/2, 1/2]$, $[3/2, 3/2, 3/2]$ and $[2]$ respectively. Upon reduction to $O(5) \supset O(3), [3/2, 1/2, 1/2] \rightarrow \{[1/2, 1/2] \oplus [3/2, 1/2]\}_{O(5)} \rightarrow \{(3/2) \oplus (1/2, 5/2, 7/2)\}_{O(3)}, [3/2, 3/2, 3/2] \rightarrow \{[3/2, 3/2]\}_{O(5)} \rightarrow \{(3/2, 5/2, 9/2)\}_{O(3)}$ and $[2] \rightarrow \{[2] \oplus [1] \oplus [0]\}_{O(5)} \rightarrow \{(2,4) \oplus (2) \oplus (0)\}_{O(3)}$. Using the isomorphism $O^{\mathrm{B}}(6) \sim SU^{\mathrm{F}}(4)$, the $\mathrm{Spin}^{\mathrm{BF}}(6)$ group can be formed by adding the generators of the boson and fermion groups. Thus $U^{\mathrm{B}}(6) \otimes U^{\mathrm{F}}(20)$ has $\mathrm{Spin}^{\mathrm{BF}}(6)$ BF-1 symmetry limit [8]. Boson and fermion generators can be combined at a level lower than $O^{\mathrm{B}}(6) \sim U^{\mathrm{F}}(4)$, leading to the three symmetry limits contained in the group lattice shown in figure 1.

2.2 *BF-2 symmetry limits*

The single particle angular momenta $j = 1/2, 3/2, 5/2, 7/2$ can be decomposed into pseudo-spin $s = 1/2$ and pseudo-orbital angular momenta $l = 1, 3$, giving rise to the $U_k^{\mathrm{F}}(10) \otimes U_s^{\mathrm{F}}(2)$ subgroup of $U^{\mathrm{F}}(20)$. (a) The $U_k^{\mathrm{F}}(10)$ admits $U_k^{\mathrm{F}}(5)$ as a subgroup as (spatial) antisymmetric coupling of two particles carrying angular momentum $l = 2$

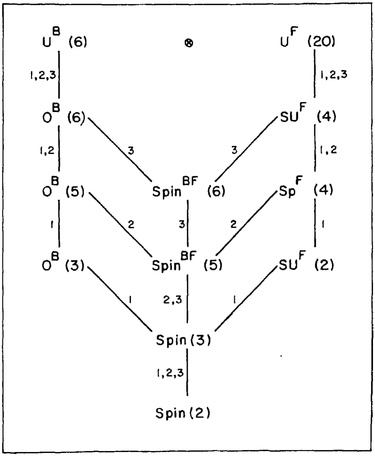

gives $L=1,3$. Thus the irrep $\{1\}$ of $U_k^{\rm F}(10)$ correspond to the irrep $\{11\}$ or $\{111\}$ (hole irrep) of $U_k^{\rm F}(5)$. By combining boson and fermion generators at the level of $U(5)$, the $U^{\rm BF}(5)\otimes U_s^{\rm F}(2)$ and $\bar{U}^{\rm BF}(5)\otimes U_s^{\rm F}(2)$ limits of $U^{\rm B}(6)\otimes U^{\rm F}(20)$ are obtained, the first one if the irrep $\{11\}$ is taken and the second one if $\{111\}$ is used. In general it is possible to combine the boson and fermion groups at a level lower than $U(5)$, leading to various other symmetry limits in the group lattice shown in figure 2a. For the sake of brevity the $\bar{U}^{\rm BF}(5)\otimes U_s^{\rm F}(2)$ limits are not shown explicitly; they can be obtained by replacing $U^{\rm BF}(5)$ with $\bar{U}^{\rm BF}(5)$ in figure 2a. (b) The $U_k^{\rm F}(10)$ also admits $O_k^{\rm F}(6)$ as a subgroup as (spatial) symmetric coupling of two particles carrying angular momentum $j=3/2$ gives $J=1,3$. Thus the irrep $\{1\}$ of $U_k^{\rm F}(10)$ correspond to the irrep $[111]$ of $O_k^{\rm F}(6)$. By combining boson and fermion generators at the level of $O(6)$, the $O^{\rm BF}(6)\otimes U_s^{\rm F}(2)$ limit of $U^{\rm B}(6)\otimes U^{\rm F}(20)$ is obtained. Once again it is possible to combine the boson and fermion groups at a level lower than $O(6)$, leading to various other symmetry limits in the group lattice shown in figure 2b.

For completeness it should be mentioned that $U_k^{\rm F}(10)$ contains $SU_k^{\rm F}(3)$ as a subgroup and as mentioned in the introduction, this case was dealt with in detail in [12]. In addition there is also the seniority (pairing) subgroup $O_k^{\rm F}(10)$ of $U_k^{\rm F}(10)$ which in turn contains $O_k^{\rm F}(5)$ as a subgroup. As we restrict ourselves to one fermion ($M_{\rm F}=1$) case, however, the $O_k^{\rm F}(10)$ subgroup is not really relevant.

2.3 *BF-12 symmetry limits*

The single particle angular momenta $j=1/2,3/2,5/2,7/2$ can be decomposed into pseudo-spin $s=3/2$ and pseudo-orbital angular momentum $l=2$, giving rise to the $U_k^{\rm F}(5)\otimes U_s^{\rm F}(4)$ subgroup of $U^{\rm F}(20)$. The BF-12 class symmetries occur because of the presence of $U_k^{\rm F}(5)$ and $SU_s^{\rm F}(4)\sim O_s^{\rm F}(6)$ and by combining them with the corresponding boson groups. Four possible cases occur. (a) In the $U^{\rm B}(5)$ limit for the bosons, $U^{\rm B}(5)$ is combined with $U_k^{\rm F}(5)$ to form $U^{\rm BF}(5)$. By virtue of the isomorphism $O^{\rm B}(5)\sim Sp^{\rm F}(4)$, the generators of the $O^{\rm BF}(5)$ subgroup of $U^{\rm BF}(5)$ can be added to the generators of $Sp_s^{\rm F}(4)$ subgroup of $U_s^{\rm F}(4)$, to form ${\rm Spin}^{\rm BFF}(5)$. This is the $U^{\rm BF}(5)\otimes U_s^{\rm F}(4)$ limit of $U^{\rm B}(6)\otimes U^{\rm F}(20)$. Note that similarly the $\bar{U}^{\rm BF}(5)\otimes U_s^{\rm F}(4)$ can be constructed by considering the irrep $\{1111\}$ of $U_k^{\rm F}(5)$. (b) In this case the $O^{\rm B}(6)$ limit is taken for the bosons enabling the formation of $O^{\rm BF}(5)$ (out of $O^{\rm B}(5)$ and $O_k^{\rm F}(5)$) which can be combined with $Sp_s^{\rm F}(4)$ to form ${\rm Spin}^{\rm BFF}(5)$. This is the $O^{\rm BF}(5)\otimes U_s^{\rm F}(4)$ limit of $U^{\rm B}(6)\otimes U^{\rm F}(20)$. (c) In the $O^{\rm B}(6)$ limit for bosons, $O^{\rm B}(6)$ is combined with $SU_s^{\rm F}(4)$ to form ${\rm Spin}^{\rm BF}(6)$. The generators of ${\rm Spin}^{\rm BF}(5)$ subgroup of ${\rm Spin}^{\rm BF}(6)$ can be added to the generators of $O_k^{\rm F}(5)$ subgroup of $U_k^{\rm F}(5)$, to form ${\rm Spin}^{\rm BFF}(5)$. This is the ${\rm Spin}^{\rm BF}(6)\otimes U_k^{\rm F}(5)$ limit of $U^{\rm B}(6)\otimes U^{\rm F}(20)$. (d) In this case the $U^{\rm B}(5)$ limit is taken for the bosons enabling the formation of ${\rm Spin}^{\rm BF}(5)$ (out of $O^{\rm B}(5)$ and $Sp_s^{\rm F}(4)$) which can be combined with $O_k^{\rm F}(5)$ to form ${\rm Spin}^{\rm BFF}(5)$. This is the ${\rm Spin}^{\rm BF}(5)\otimes U_k^{\rm F}(5)$ limit of $U^{\rm B}(6)\otimes U^{\rm F}(20)$. In all the four cases (a – d), it is possible to combine the boson and fermion generators at a level lower than $U^{\rm B}(5)$ or $O^{\rm B}(6)$. The different symmetry limits resulting from the various couplings contained in the four group lattices are shown in figure 3. For the sake of brevity, the $\bar{U}^{\rm BF}(5)\otimes U_s^{\rm F}(4)$ limits are not shown explicitly; they can be obtained by replacing $U^{\rm BF}(5)$ with $\bar{U}^{\rm BF}(5)$ in figure 3a.

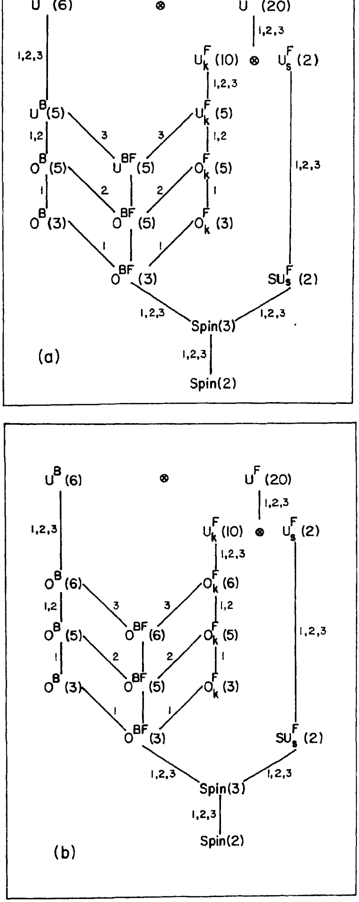

Figure 2. The BF-2 symmetry limits of $U^{\mathrm{B}}(6)\otimes U^{\mathrm{F}}(20)$: (a) the $U^{\mathrm{BF}}(5)\otimes U_s^{\mathrm{F}}(2)$ limit; (*b*) the $O^{\mathrm{BF}}(6)\otimes U_s^{\mathrm{F}}(2)$ limit.

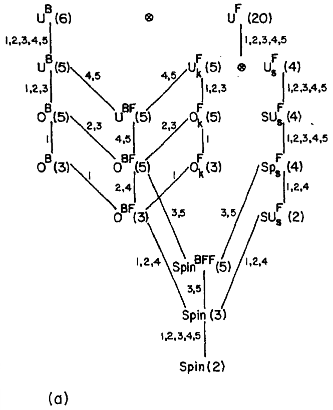

$U^B(6)$ ⊗ $U^F(20)$
1,2,3,4,5
1,2,3,4,5
$U^B(5)$
4,5
4,5
$U_k^F(5)$ ⊗ $U_s^F(4)$
1,2,3
1,2,3
1,2,3,4,5
$O^B(5)$
$U^{BF}(5)$
2,3
2,3
$O_k^F(5)$
$SU_s^F(4)$
1
4,5
1
1,2,3,4,5
$O^B(3)$
1
$O^{BF}(5)$
1
$O_k^F(3)$
$Sp_s^F(4)$
2,4
1,2,4
$O^{BF}(3)$
3,5
3,5
$SU_s^F(2)$
1,2,4
$Spin^{BFF}(5)$
1,2,4
3,5
$Spin(3)$
1,2,3,4,5
$Spin(2)$
(a)

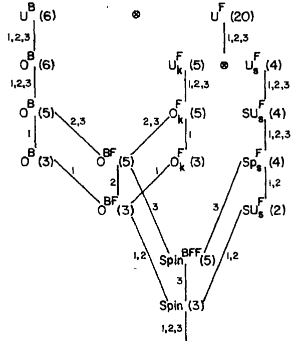

$U^B(6)$ ⊗ $U^F(20)$
1,2,3
1,2,3
$O^B(6)$
$U_k^F(5)$ ⊗ $U_s^F(4)$
1,2,3
1,2,3
1,2,3
$O^B(5)$
2,3
2,3
$O_k^F(5)$
$SU_s^F(4)$
1
1
1,2,3
$O^B(3)$
1
$O^{BF}(5)$
1
$O_k^F(3)$
$Sp_s^F(4)$
2
1,2
$O^{BF}(3)$
3
3
$SU_s^F(2)$
1,2
$Spin^{BFF}(5)$
1,2
3
$Spin(3)$
1,2,3

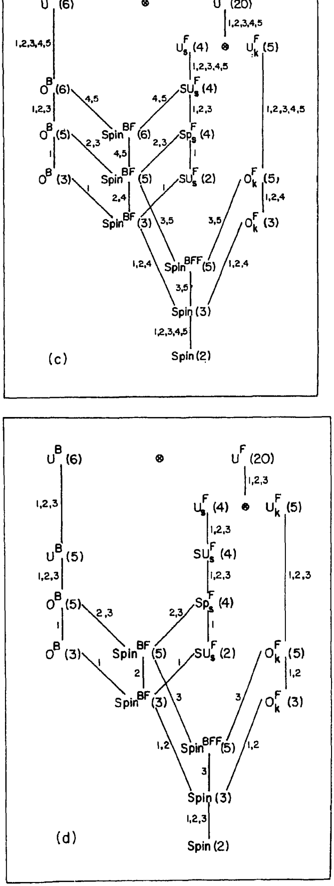

Figure 3. The BF-12 symmetry limits of $U^{\mathrm{B}}(6)\otimes U^{\mathrm{F}}(20)$: (**a**) the $U^{\mathrm{BF}}(5)\otimes U_s^{\mathrm{F}}$ limit; (**b**) the $O^{\mathrm{BF}}(5)\otimes U_s^{\mathrm{F}}(4)$ limit; (**c**) the Spin$^{\mathrm{BF}}(6)\otimes U_k^{\mathrm{F}}(5)$ limit; (**d**) Spin$^{\mathrm{BF}}(5)\otimes U_k^{\mathrm{F}}(5)$ limit.

enumerated in the figures. Of most importance are the coupling schemes in which boson and fermion groups are combined at the level of $U^{\mathrm{B}}(5)$ or $O^{\mathrm{B}}(6)$, since they correspond to a moderate to strong core-particle interaction in the IBFM hamiltonian, while a coupling scheme involving the combination of $O^{\mathrm{B}}(3)$ and $SU^{\mathrm{F}}(2)$ to Spin(3) only correspond to a weak-coupling basis. Thus in §§ 3 and 4 we limit ourselves to study those symmetries in which the boson–fermion couplings are maximal (highest-numbered in figures 1–3). These are seven in number as given in § 2.1, § 2.2 a, b and § 2.3 a, b, c, d. The properties of other symmetry limits can be derived easily from the latter, as will be indicated in §§ 3 and 4.

3. Symmetry limits related to $U^{\mathrm{B}}(5)$

In this section, the $U^{\mathrm{BF}}(5) \otimes U_s^{\mathrm{F}}(4)$, $\mathrm{Spin}^{\mathrm{BF}}(5) \otimes U_k^{\mathrm{F}}(5)$ and $U^{\mathrm{BF}}(5) \otimes U_s^{\mathrm{F}}(2)$ limits of $U^{\mathrm{B}}(6) \otimes U^{\mathrm{F}}(20)$ which are all related to $U^{\mathrm{B}}(5)$ limit of IBM are analysed. In each case given are the generators of the various groups involved and the spectrum generating hamiltonian as well as the quantum numbers labelling the states in the case $M_{\mathrm{F}} = 1$ (one fermion) relevant for odd-mass nuclei. In the symmetry limits, the knowledge of some $U(5) \supset O(5)$ and $O(5) \supset O(3)$ reduced Wigner coefficients (sometimes called isoscalar factors [18]), together with the results of Arima and Iachello [19] for the $U^{\mathrm{B}}(5)$ limit of IBM will enable one to calculate matrix elements of any observable such as electromagnetic moments and transition strengths, one and two nucleon transfer intensities etc. (see Appendix A). As a result, instead of giving analytic results for all the observables, which would make this paper unnecessarily long, tabulations of the appropriate reduced Wigner coefficients are given. Part of these tables will also be of use for the symmetry limits involving $O^{\mathrm{B}}(6)$ discussed in § 4.

3.1 $U^{\mathrm{BF}}(5) \otimes U_s^{\mathrm{F}}(4)$ *limit*

The group chain (see figure 3a, group chain 5) and basis states in this limit are

$$\left| \begin{array}{llllll} U^{\mathrm{B}}(6) \otimes U^{\mathrm{F}}(20) \supset & U^{\mathrm{B}}(5) \otimes & U_k^{\mathrm{F}}(5) \otimes & U_s^{\mathrm{F}}(4) \supset & U^{\mathrm{BF}}(5) \otimes SU_s^{\mathrm{F}}(4) & \\ \{N\} \quad M_{\mathrm{F}} = 1 & \{n_d\} & \{1\} & \{1\} & \{n_1\, n_2\} & \\ \multicolumn{6}{l}{O^{\mathrm{BF}}(5) \otimes [Sp_s^{\mathrm{F}}(4) \sim \mathrm{Spin}_s^{\mathrm{F}}(5)] \supset \mathrm{Spin}^{\mathrm{BFF}}(5) \supset \mathrm{Spin}(3) \supset \mathrm{Spin}(2)} \\ \multicolumn{6}{l}{[v_1\, v_2] \qquad\qquad [1/2, 1/2] \qquad\qquad [\bar{\tau}_1\, \bar{\tau}_2] \qquad \alpha J \qquad\quad M} \end{array} \right\rangle . \tag{2}$$

First the generators of the various groups in (2) (leaving out the trivial ones) are given and then the enumeration of the allowed values of the state labels is described (it is clear from (2) that in many cases a given irrep contains more than one label and in these cases, often the labels are seperated by a space, sometimes no space is inserted when there is no confusion and sometimes a comma is inserted to seperate them). The generators of $U^{\mathrm{B}}(5)$, $U_k^{\mathrm{F}}(5)$ and $SU_s^{\mathrm{F}}(4)$ are

$$\begin{aligned} U^{\mathrm{B}}(5)&: D_\mu^\kappa(\mathrm{B});\ \kappa = 0, 1, 2, 3, 4 \\ U_k^{\mathrm{F}}(5)&: K_\mu^\kappa(\mathrm{F});\ \kappa = 0, 1, 2, 3, 4 \\ U_s^{\mathrm{F}}(4)&: S_\mu^\kappa(\mathrm{F});\ \kappa = 0, 1, 2, 3 \\ SU_s^{\mathrm{F}}(4)&: S_\mu^\kappa(\mathrm{F});\ \kappa = 1, 2, 3 \end{aligned} \tag{3}$$

$$K^{\kappa}_{\mu}(\mathrm{F}) = -\sum_{j,j'} [(2j'+1)/5]^{1/2}\, U(j'\kappa 3/2\, 2; j\, 2)\, (a^{\dagger}_{j}\, \tilde{a}_{j'})^{\kappa}_{\mu},$$

$$S^{\kappa}_{\mu}(\mathrm{F}) = \sum_{j,j'} [(2j+1)/4]^{1/2}\, U(j\kappa 2\, 3/2; j'\, 3/2)\, (a^{\dagger}_{j}\, \tilde{a}_{j'})^{\kappa}_{\mu}.$$

Note that $\tilde{a}_{jm} = (-1)^{j-m} a_{j-m}$. Introducing the linear combinations

$$A^{\kappa}_{\mu}(\mathrm{BF}) = D^{\kappa}_{\mu}(\mathrm{B}) + K^{\kappa}_{\mu}(\mathrm{F})$$

$$C^{\kappa=1}_{\mu}(\mathrm{BFF}) = D^{1}_{\mu}(\mathrm{B}) + K^{1}_{\mu}(\mathrm{F}) - \frac{1}{\sqrt{2}} S^{1}_{\mu}(\mathrm{F})$$

$$C^{\kappa=3}_{\mu}(\mathrm{BFF}) = D^{3}_{\mu}(\mathrm{B}) + K^{3}_{\mu}(\mathrm{F}) + \frac{1}{\sqrt{2}} S^{3}_{\mu}(\mathrm{F})$$

$$\begin{aligned} J^{1}_{\mu} &= \sqrt{10}(d^{\dagger}\tilde{d})^{1}_{\mu} - \sum_{j} [j(j+1)(2j+1)/3]^{1/2} (a^{\dagger}_{j}\tilde{a}_{j})^{1}_{\mu} \\ &= \sqrt{10}\, C^{1}_{\mu}(\mathrm{BFF}), \end{aligned} \tag{4}$$

the generators of the coupled groups in (2) are

$$\begin{aligned} &U^{\mathrm{BF}}(5)\colon \{A^{\kappa}_{\mu}(\mathrm{BF}),\ \kappa = 0,1,2,3,4\} \\ &O^{\mathrm{BF}}(5)\colon \{A^{\kappa}_{\mu}(\mathrm{BF}),\ \kappa = 1,3\} \\ &\mathrm{Spin}^{\mathrm{BFF}}(5)\colon \{C^{\kappa}_{\mu}(\mathrm{BFF}),\ \kappa = 1,3\} \\ &\mathrm{Spin}(3)\colon \{J^{1}_{\mu}\}. \end{aligned} \tag{5}$$

The generators in (3–5) follow directly from the earlier work on the Spin (5) [20] and $U(5)\otimes U(2)$ (of $U(6)\otimes U(10)$) [21, 22] limits of IBFM. Ignoring the labels that are obvious ($M_{\mathrm{F}} = 1$ etc.) in (2), the basis states in the $U^{\mathrm{BF}}(5)\otimes U^{\mathrm{F}}_{s}(4)$ limit are labelled by

$$|N\, n_d\, \{n_1\, n_2\}\, [v_1\, v_2]\, [\bar{\tau}_1\, \bar{\tau}_2]\, \alpha\, J\rangle. \tag{6}$$

Making use of the multiplication rules of the $U(N)$, $O(N)$ and $Sp(N)$ groups given in [23] (especially using eqs (86a–c) of [23]) the irrep labels in (6) are obtained. The following rules are derived:

$$\begin{aligned} &U^{\mathrm{B}}(5)\colon N \to n_d = 0, 1, \ldots, N \\ &U^{\mathrm{BF}}(5)\colon \{n_d\}\otimes\{1\} \to \{n_1, n_2\} = \{n_d+1, 0\} \oplus \{n_d, 1\} \\ &O^{\mathrm{BF}}(5)\colon \{n_d+1, 0\} \to [v_1, v_2] = [n_d+1, 0] \oplus [n_d-1, 0] \oplus \cdots \oplus [0,0] \text{ or } [1,0] \\ &\qquad \{n_d, 1\} \to [v_1, v_2] = [n_d-1, 0] \oplus [n_d-3, 0] \oplus \cdots \oplus [2,0] \text{ or } [1,0] \\ &\qquad\qquad \oplus [n_d, 1] \oplus [n_d-2, 1] \oplus [2,1] \text{ or } [1,1], \end{aligned} \tag{7}$$

$$\mathrm{Spin}^{\mathrm{BFF}}(5)\colon [\bar{\tau}_1, \bar{\tau}_2] = [v, 0]\otimes[1/2, 1/2] = [v+1/2, 1/2] \oplus [v-1/2, 1/2]$$

or

$$[\bar{\tau}_1, \bar{\tau}_2] = [v, 1] \otimes [1/2, 1/2] = [v + 1/2, 1/2] \oplus [v - 1/2, 1/2] \\ \oplus [v + 1/2, 3/2] \oplus [v - 1/2, 3/2].$$

The angular momentum content of the $\mathrm{Spin}^{\mathrm{BFF}}(5)$ irrep $[v + 1/2, 1/2]$ is given by [15, 20]

$$\begin{aligned} \mathrm{Spin}(3){:}[v + 1/2, 1/2] \to J = \sum_r \{&[(2r + 3/2) \oplus (2r + 1/2) \oplus \cdots \oplus (r + 3/2)] \\ &\oplus [(2r - 3/2) \oplus (2r - 5/2) \oplus \cdots \oplus (r - 1/2)]\}; \\ \text{where} \quad r = v, v - 3, &v - 6, \ldots, 2 \text{ or } 1 \text{ or } 0. \end{aligned} \tag{8}$$

From (8) it is seen that a given J in $[v + 1/2, 1/2] \to J$ can occur more than once and therefore the need for the multiplicity label α in (6). The $[v + 3/2, 3/2] \to J$ reductions follows from the known result for $[v, 1] \to L$ (see (29) ahead) and the results in (7, 8). For example $[3/2, 3/2] \to J = 3/2, 5/2, 9/2$ and $[5/2, 3/2] \to J = 1/2, 3/2, 5/2, (7/2)^2, 9/2, 11/2, 13/2$.

The most general one plus two-body hamiltonian in the $U^{\mathrm{BF}}(5) \otimes U_s^{\mathrm{F}}(4)$ limit, in terms of the (linear and quadratic) Casimir operators of the groups in (2), is

$$\begin{aligned} H_{\{U^{\mathrm{BF}}(5) \otimes U_s^{\mathrm{F}}(4)\}} = a_0 &+ a_1 C_1(U^{\mathrm{B}}(5)) + a_2 C_2(U^{\mathrm{B}}(5)) + a_3 C_2(U^{\mathrm{BF}}(5)) \\ &+ a_4 C_2(O^{\mathrm{BF}}(5)) + a_5 C_2(\mathrm{Spin}^{\mathrm{BFF}}(5)) + a_6 C_2(\mathrm{Spin}\,(3)), \end{aligned} \tag{9}$$

where $C_n(G)$ denotes nth order Casimir operator of the group G. In (9), $(a_0, a_1, a_2, a_3, a_4, a_5, a_6)$ are free parameters. In terms of the generators in (3–5), the Casimir operators in (9) are

$$\begin{aligned} C_1(U^{\mathrm{B}}(5)) &= \sqrt{5} D_0^0(\mathrm{B}) = \hat{n}_d, \\ C_2(U^{\mathrm{B}}(5)) &= \hat{n}_d(\hat{n}_d + 4), \\ C_2(U^{\mathrm{BF}}(5)) &= \sum_{\kappa=0}^{4} A^{\kappa}(\mathrm{BF}) \cdot A^{\kappa}(\mathrm{BF}), \\ C_2(O^{\mathrm{BF}}(5)) &= 2 \sum_{\kappa=1,3} A^{\kappa}(\mathrm{BF}) \cdot A^{\kappa}(\mathrm{BF}), \\ C_2(\mathrm{Spin}^{\mathrm{BFF}}(5)) &= 2 \sum_{\kappa=1,3} C^{\kappa}(\mathrm{BFF}) \cdot C^{\kappa}(\mathrm{BFF}), \\ C_2(\mathrm{Spin}\,(3)) &= J \cdot J. \end{aligned} \tag{10}$$

The eigenvalues of the hamiltonian (9) in terms of the labels in (6) are given by

$$\begin{aligned} &E_{\{U^{\mathrm{BF}}(5) \otimes U_s^{\mathrm{F}}(4)\}}(N n_d \{n_1\, n_2\}\, [v_1\, v_2]\, [\bar{\tau}_1\, \bar{\tau}_2]\, \alpha\, J) \\ &= a_0 + a_1 n_d + a_2 n_d(n_d + 4) + a_3 [n_1(n_1 + 4) + n_2(n_2 + 2)] \\ &\quad + a_4 [v_1(v_1 + 3) + v_2(v_2 + 1)] + a_5 [\bar{\tau}_1(\bar{\tau}_1 + 3) + \bar{\tau}_2(\bar{\tau}_2 + 1)] + a_6 J(J + 1). \end{aligned}$$

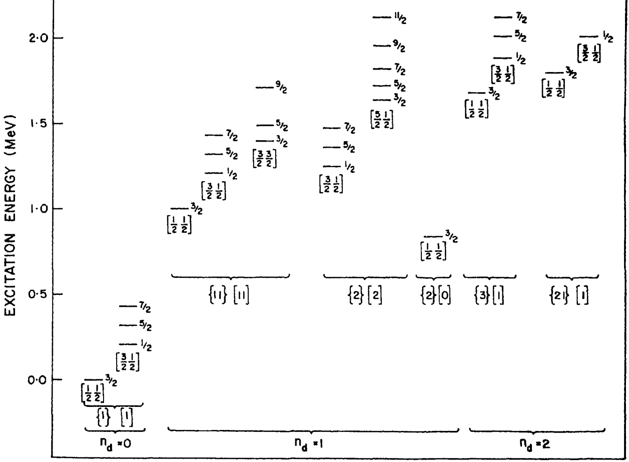

Figure 4 Typical spectrum in the $U^{\mathrm{BF}}(5) \otimes U_s^{\mathrm{F}}(4)$ limit. States are characterized with the labels defined in (2, 6). The parameters in the energy formula (11) are (in keV): $a_1 = 1000$, $a_2 = 0$, $a_3 = -20$, $a_4 = 30$, $a_5 = 50$ and $a_6 = 15$.

Using (6–8, 11) typical spectrum in the $U^{\mathrm{BF}}(5) \otimes U_s^{\mathrm{F}}(4)$ limit is constructed as shown in figure 4. To calculate the matrix elements, corresponding to various observables, in the symmetry limit, the basis states (6) are expanded in terms of particle-vibrator coupled states $|N n_d v_d L_d; j; J\rangle$ as,

$$
\begin{aligned}
&|N n_d \{n_1\, n_2\} [v_1\, v_2] [\bar{\tau}_1\, \bar{\tau}_2] \alpha J\rangle \\
&= \sum_{v_d,\, L_d,\, L,\, j} U(L_d 2 J 3/2; Lj) \langle \{n_d\} [v_d] \{1\} [1] \parallel \{n_1\, n_2\} [v_1\, v_2] \rangle_{U(5) \supset O(5)} \\
&\quad \langle [v_d] L_d [1] 2 \parallel [v_1\, v_2] L \rangle_{O(5) \supset O(3)} \langle [v_1\, v_2] L [1/2, 1/2] 3/2 \parallel [\bar{\tau}_1\, \bar{\tau}_2] \alpha J \rangle_{O(5) \supset O(3)} \\
&\quad |N n_d\, v_d\, L_d; j; J\rangle. \qquad (12)
\end{aligned}
$$

The $U(5) \supset O(5)$ reduced Wigner coefficient in (12) follows from the quasispin formalism of pairing hamiltonian together with their orthonormality properties [24]; table 1 gives the relevant results. The $O(5) \supset O(3)$ reduced Wigner coefficients in (12) for $[v] \otimes [1] \rightarrow [v \pm 1]$ follow from the work in [19], the ones of the type $[v] \otimes [1] \rightarrow [v, 1]$ are obtained in the studies on $U^{\mathrm{BF}}(5) \otimes U^{\mathrm{F}}(2)$ limits of IBFM [21, 22, 25], and the ones of the type $[v] \otimes [1/2, 1/2] \rightarrow [v \pm 1/2, 1/2]$ follow from the work in the Spin (5) limit of IBFM [20]. All these Wigner coefficients together with (7, 8) and the diagonalization of the operator $a C_2(U^{\mathrm{BF}}(5)) + b C_2(O^{\mathrm{BF}}(5)) + c C_2(\mathrm{Spin}^{\mathrm{BFF}}(5))$ with a, b and c being free

Table 1. $U(2l+1) \supset O(2l+1)$ reduced Wigner coefficients $\langle \{n\}[v]\{1\}[1] \| \{n_1 n_2\}[v_1 v_2] \rangle$.

$[v_1 v_2]$	$\{n_1 n_2\} = \{n+1, 0\}$	$\{n_1 n_2\} = \{n, 1\}$
$[v-1]$	$\left[\dfrac{(n-v+2)(2\Omega+v-3)}{(n+1)(2\Omega+2v-4)}\right]^{1/2}$	$-\left[\dfrac{(v-1)(2\Omega+n+v-2)}{(n+1)(2\Omega+2v-4)}\right]^{1/2}$
$[v+1]$	$\left[\dfrac{(v+1)(2\Omega+n+v)}{(n+1)(2\Omega+2v)}\right]^{1/2}$	$\left[\dfrac{(n-v)(2\Omega+v-1)}{(n+1)(2\Omega+2v)}\right]^{1/2}$
$[v, 1]$	…	1

Note: $\Omega = (2l+1)/2$.

Table 2. $O(5) \supset O(3)$ reduced Wigner coefficients $\langle [v]\, L[1]2 \| [v+1]L' \rangle$.

L	L'	$\langle [v]\, L[1]2 \| [v+1]L' \rangle$
$2v$	$2v+2$	1
$2v$	$2v$	$\left[\dfrac{2(2v+1)}{(v+1)(4v-1)}\right]^{1/2}$
$2v-2$	$2v$	$\left[\dfrac{(v-1)(4v+3)}{(v+1)(4v-1)}\right]^{1/2}$
$2v$	$2v-1$	$-\left[\dfrac{2(v-1)(4v+1)}{(v+1)(2v-1)(4v-1)}\right]^{1/2}$
$2v-2$	$2v-1$	$\left[\dfrac{3(2v+1)}{(v-1)(v+1)(4v-1)}\right]^{1/2}$
$2v-3$	$2v-1$	$\left[\dfrac{v(v-2)(2v+1)}{(v-1)(v+1)(2v-1)}\right]^{1/2}$
$2v$	$2v-2$	$\left[\dfrac{32v(v-1)(v-2)}{(v+1)(2v-1)(2v+3)(4v-3)(4v-1)}\right]^{1/2}$

parameters, yield the reduced Wigner coefficients for $[v, 1] \otimes [1/2, 1/2] \rightarrow [\bar{\tau}_1, \bar{\tau}_2]$. The various $O(5) \supset O(3)$ reduced Wigner coefficients calculated in [19, 20, 21, 22, 25] and also in [26], are derived with different phase conventions and therefore can not be used simultaneously. The Wigner coefficients listed in tables 1–5 are obtained in a consistent phase convention and enable us to construct states in (12) with $n_d \leqslant 2$. Using (12), the results in tables 1–5, $U^{\mathrm{B}}(5)$ limit results in [19] and standard angular momentum algebra [27], it is easy to calculate matrix elements corresponding to various observables such as B($E2$) values, B($M1$) values etc; see Appendix A.

The reduced Wigner coefficients in tables 1–5 also determine the structure of the

Table 3. $O(5) \supset O(3)$ reduced Wigner coefficients $\langle [v]\, L [1] 2 \parallel [v,1] \alpha\, L' \rangle$.

L	L'_α	$\langle [v]\, L [1] 2 \parallel [v,1] \alpha\, L' \rangle$
$2v$	$2v+1$	1
$2v$	$2v$	$\left[\frac{(v-1)(4v+3)}{(v+1)(4v-1)}\right]^{1/2}$
$2v-2$	$2v$	$-\left[\frac{2(2v+1)}{(v+1)(4v-1)}\right]^{1/2}$
$2v$	$(2v-1)_1$	$\left[\frac{3(2v-1)(2v+1)}{(4v-1)(2v^2+1)}\right]^{1/2}$
$2v$	$(2v-1)_2$	$-\left[\frac{2v(v-1)(v-2)(2v+1)(4v+1)}{(v+1)(2v-1)(4v-1)(2v^2+1)}\right]^{1/2}$
$2v-2$	$(2v-1)_1$	$\left[\frac{2(v-1)^2(4v+1)}{(4v-1)(2v^2+1)}\right]^{1/2}$
$2v-2$	$(2v-1)_2$	$\left[\frac{3(v-2)v(2v+1)^2}{(4v-1)(v^2-1)(2v^2+1)}\right]^{1/2}$
$2v-3$	$(2v-1)_1$	0
$2v-3$	$(2v-1)_2$	$-\left[\frac{(2v^2+1)}{(2v-1)(v^2-1)}\right]^{1/2}$

Note: Results in this table together with $\langle [2] 2\, [1] 2 \parallel [2,1] 2 \rangle = \sqrt{9/14}$ and $\langle [2] 4\, [1] 2 \parallel [2,1] 2 \rangle = -\sqrt{5/14}$ determine all the reduced Wigner coefficients for $v \leqslant 2$.

obtained by simply deleting one or more of the reduced Wigner coefficients in the expansion (12) and, consequently, matrix elements corresponding to various observables can be calculated easily.

3.2 $Spin^{\mathrm{BF}}(5) \otimes U_k^{\mathrm{F}}(5)$ *limit*

The group chain (see figure 3d, group chain 3) and basis states in this limit are

$$\begin{array}{|l} U^{\mathrm{B}}(6) \otimes U^{\mathrm{F}}(20) \supset U^{\mathrm{B}}(5) \otimes U_s^{\mathrm{F}}(4) \otimes U_k^{\mathrm{F}}(5) \supset \\ \{N\} \quad M_{\mathrm{F}} = 1 \quad \{n_d\} \qquad \{1\} \qquad \{1\} \\ \quad O^{\mathrm{B}}(5) \otimes [Sp_s^{\mathrm{F}}(4) \sim \mathrm{Spin}_s^{\mathrm{F}}(5)] \otimes O_k^{\mathrm{F}}(5) \supset \\ \quad [v_d] \qquad\qquad [1/2,\, 1/2] \qquad\quad [1] \\ \quad \mathrm{Spin}^{\mathrm{BF}}(5) \otimes O_k^{\mathrm{F}}(5) \supset \mathrm{Spin}^{\mathrm{BFF}}(5) \supset \mathrm{Spin}(3) \supset \mathrm{Spin}(2) \end{array} \Bigg\rangle. \tag{13}$$

$2v$	$2v+1/2$	$\ldots$	1
$2v$	$2v-1/2$	$\left[\frac{(2v+1)(4v+1)}{(2v+3)(4v-1)}\right]^{1/2}$	$-\left[\frac{4(v-1)}{(2v+3)(4v-1)}\right]^{1/2}$
$2v-2$	$2v-1/2$	$\left[\frac{4(v-1)}{(2v+3)(4v-1)}\right]^{1/2}$	$\left[\frac{(2v+1)(4v+1)}{(2v+3)(4v-1)}\right]^{1/2}$

The coupled groups in (13) are same as in (2) with the exception of $\mathrm{Spin}^{\mathrm{BF}}(5)$ which is generated by [20]

$$\begin{aligned}
&\mathrm{Spin}^{\mathrm{BF}}(5)\colon \{E^{\kappa}_{\mu}(\mathrm{BF}), \kappa = 1, 3\}\\
&E^{\kappa=1}_{\mu}(\mathrm{BF}) = D^{1}_{\mu}(\mathrm{B}) - \frac{1}{\sqrt{2}} S^{1}_{\mu}(\mathrm{F})\\
&E^{\kappa=3}_{\mu}(\mathrm{BF}) = D^{3}_{\mu}(\mathrm{B}) + \frac{1}{\sqrt{2}} S^{3}_{\mu}(\mathrm{F}).
\end{aligned} \tag{14}$$

The operators $D^{\kappa}_{\mu}(\mathrm{B})$ and $S^{\kappa}_{\mu}(\mathrm{F})$ are defined in (3). Note that $O^{\mathrm{B}}(5)$ is generated by $D^{1,3}_{\mu}(\mathrm{B})$ operators. Ignoring the labels that are obvious ($M_{\mathrm{F}} = 1$ etc.) in (13), the basis states in the $\mathrm{Spin}^{\mathrm{BF}}(5) \otimes U^{\mathrm{F}}_{k}(5)$ limit are labelled by

$$|N\, n_d\, v_d\, [\tau_1\, \tau_2]\, [\bar{\tau}_1\, \bar{\tau}_2]\, \alpha J\rangle. \tag{15}$$

Just as in (7, 8), the reduction rules for the irrep labels in (15) are

$$\begin{aligned}
O^{\mathrm{B}}(5)\colon n_d \to v_d &= n_d, n_d - 2, \ldots, 1 \text{ or } 0\\
\mathrm{Spin}^{\mathrm{BF}}(5)\colon [\tau_1, \tau_2] &= [v_d] \otimes [1/2, 1/2]\\
&= [v_d + 1/2, 1/2] \oplus [v_d - 1/2, 1/2],\\
\mathrm{Spin}^{\mathrm{BFF}}(5)\colon [\bar{\tau}_1, \bar{\tau}_2] &= [v + 1/2, 1/2] \otimes [1]\\
&= [v + 1/2, 1/2] \oplus [v - 1/2, 1/2] \oplus [v + 1/2, 3/2]\\
&\quad \oplus [v + 3/2, 1/2].
\end{aligned} \tag{16}$$

The $U^{\mathrm{B}}(6) \to U^{\mathrm{B}}(5)$ and $\mathrm{Spin}^{\mathrm{BFF}}(5) \to \mathrm{Spin}(3)$ reduction rules are already given in (7, 8). The hamiltonian in the $\mathrm{Spin}^{\mathrm{BF}}(5) \otimes U^{\mathrm{F}}_{k}(5)$ limit is

$$\begin{aligned}
H_{\{\mathrm{Spin}^{\mathrm{BF}}(5) \otimes U^{\mathrm{F}}_{k}(5)\}} &= b_0 + b_1\, C_1(U^{\mathrm{B}}(5)) + b_2\, C_2(U^{\mathrm{B}}(5)) + b_3\, C_2(O^{\mathrm{B}}(5))\\
&\quad + b_4\, C_2(\mathrm{Spin}^{\mathrm{BF}}(5)) + b_5\, C_2(\mathrm{Spin}^{\mathrm{BFF}}(5)) + b_6\, C_2(\mathrm{Spin}(3)).
\end{aligned} \tag{17}$$

In (19), $(b_0, b_1, b_2, b_3, b_4, b_5, b_6)$ are free parameters. Expressions for the Casimir operators appearing in (17) are given in (10) and in addition we have

$$C_2(O^{\mathrm{B}}(5)) = 2 \sum_{\kappa=1,3} D^{\kappa}(\mathrm{B}) \cdot D^{\kappa}(\mathrm{B})$$

$$C_2(\mathrm{Spin}^{\mathrm{BF}}(5)) = 2 \sum_{\kappa=1,3} E^{\kappa}(\mathrm{BF}) \cdot E^{\kappa}(\mathrm{BF}). \tag{18}$$

Table 5. $O(5) \supset O(3)$ reduced Wigner coefficients $\langle [v_1\, v_2] L [1/2, 1/2]\, 3/2 \,\|\, [\tau_1, \tau_2] \alpha J \rangle$.

$[v_1, v_2]$	$[\tau_1, \tau_2]$	J	$L=2$	$L=4$
[2]	[3/2 1/2]	1/2	1	...
		5/2	$\frac{5}{7}$	$-\sqrt{\frac{24}{49}}$
		7/2	$\frac{2}{7}$	$\sqrt{\frac{45}{49}}$
	[5/2 1/2]	3/2	1	...
		5/2	$\sqrt{\frac{24}{49}}$	$\frac{5}{7}$
		7/2	$\sqrt{\frac{45}{49}}$	$-\frac{2}{7}$
		9/2	...	1
		11/2	...	1
			$L=1$	$L=3$
[11]	[1/2 1/2]	3/2	$-\sqrt{\frac{3}{10}}$	$\sqrt{\frac{7}{10}}$
	[3/2 1/2]	1/2	1	...
		5/2	$\sqrt{\frac{7}{15}}$	$\sqrt{\frac{8}{15}}$
		7/2	...	1
	[3/2 3/2]	3/2	$\sqrt{\frac{7}{10}}$	$\sqrt{\frac{3}{10}}$
		5/2	$\sqrt{\frac{8}{15}}$	$-\sqrt{\frac{7}{15}}$
		9/2		1

[3]	[5/2 1/2]	3/2	$\sqrt{\frac{1}{3}}$	$\sqrt{\frac{2}{3}}$	...	...
		5/2	...	$\sqrt{\frac{7}{18}}$	$\sqrt{\frac{11}{18}}$	...
		7/2	...	$-\sqrt{\frac{7}{18}}$	$\sqrt{\frac{11}{18}}$	...
		9/2	...	$-\sqrt{\frac{11}{90}}$	$-\sqrt{\frac{49}{198}}$	$\sqrt{\frac{104}{165}}$
		11/2	...	...	$\sqrt{\frac{8}{99}}$	$\sqrt{\frac{91}{99}}$
	[7/2 1/2]	3/2	$\sqrt{\frac{2}{3}}$	$-\sqrt{\frac{1}{3}}$	...	...
		5/2	...	$\sqrt{\frac{11}{18}}$	$-\sqrt{\frac{7}{18}}$	...
		7/2	...	$\sqrt{\frac{11}{18}}$	$\sqrt{\frac{7}{18}}$	...
		$(9/2)_1$	...	$\sqrt{\frac{624}{745}}$	0*	$\sqrt{\frac{121}{745}}$
		$(9/2)_2$	...	$-\sqrt{\frac{539}{13410}}$	$\sqrt{\frac{149}{198}}$	$\sqrt{\frac{5096}{24585}}$
		11/2	...	...	$\sqrt{\frac{91}{99}}$	$-\sqrt{\frac{8}{99}}$
		13/2	...	...	...	1
		15/2	...	...	...	1

The eigenvalues of the hamiltonian (17) in terms of the labels in (15) are given by

$$\begin{aligned} E_{\{\mathrm{Spin}^{\mathrm{BF}}(5)\otimes U_k^{\mathrm{F}}(5)\}}&(N\, n_d\, v_d\, [\tau_1\, \tau_2]\, [\bar{\tau}_1\, \bar{\tau}_2]\, \alpha J) \\ &= b_0 + b_1 n_d + b_2 n_d(n_d+4) + b_3 [v_d(v_d+3)] \\ &\quad + b_4[\tau_1(\tau_1+3) + \tau_2(\tau_2+1)] + b_5[\bar{\tau}_1(\bar{\tau}_1+3) \\ &\quad + \bar{\tau}_2(\bar{\tau}_2+1)] + b_6 J(J+1). \end{aligned} \tag{19}$$

[2, 1]	[3/2 1/2]	1/2	$-\sqrt{\frac{2}{5}}$	$\sqrt{\frac{3}{5}}$	…	…	…
		5/2	$-\sqrt{\frac{2}{21}}$	$\sqrt{\frac{5}{147}}$	$-\sqrt{\frac{8}{21}}$	$\sqrt{\frac{24}{49}}$	…
		7/2	…	$-\sqrt{\frac{27}{245}}$	$-\sqrt{\frac{4}{35}}$	$-\sqrt{\frac{36}{245}}$	$\sqrt{\frac{22}{35}}$
	[3/2 3/2]	3/2	$\sqrt{\frac{8}{35}}$	$\sqrt{\frac{3}{7}}$	$\sqrt{\frac{12}{35}}$	…	…
		5/2	$-\sqrt{\frac{2}{15}}$	$-\sqrt{\frac{4}{21}}$	$\sqrt{\frac{49}{120}}$	$\sqrt{\frac{15}{56}}$	…
		9/2	…	…	$\sqrt{\frac{1}{56}}$	$\sqrt{\frac{99}{280}}$	$\sqrt{\frac{22}{35}}$
	[5/2 1/2]	3/2	$-\sqrt{\frac{3}{5}}$	$\sqrt{\frac{2}{5}}$	…	…	…
		5/2	$-\sqrt{\frac{6}{35}}$	$\sqrt{\frac{100}{147}}$	$\sqrt{\frac{121}{840}}$	$-\sqrt{\frac{5}{1176}}$	…
		7/2	…	$-\sqrt{\frac{10}{49}}$	$\sqrt{\frac{5}{42}}$	$\sqrt{\frac{841}{1470}}$	$\sqrt{\frac{11}{105}}$
		9/2	…	…	$\sqrt{\frac{11}{24}}$	$-\sqrt{\frac{49}{120}}$	$\sqrt{\frac{2}{15}}$
		11/2	…	…	…	$\sqrt{\frac{2}{15}}$	$-\sqrt{\frac{13}{15}}$
	[5/2 3/2]	1/2	$\sqrt{\frac{3}{5}}$	$\sqrt{\frac{2}{5}}$	…	…	…
		3/2	$\sqrt{\frac{6}{35}}$	$-\sqrt{\frac{4}{7}}$	$\sqrt{\frac{9}{35}}$	…	…
		5/2	$\sqrt{\frac{3}{5}}$	$\sqrt{\frac{2}{21}}$	$\sqrt{\frac{1}{15}}$	$\sqrt{\frac{5}{21}}$	…
		$(7/2)_1$	…	$\sqrt{\frac{2}{35}}$	$-\sqrt{\frac{27}{40}}$	$\sqrt{\frac{15}{56}}$	0*
		$(7/2)_2$	…	$\sqrt{\frac{22}{35}}$	$\sqrt{\frac{11}{120}}$	$\sqrt{\frac{11}{840}}$	$\sqrt{\frac{4}{15}}$
		9/2	…	…	$-\sqrt{\frac{11}{21}}$	$-\sqrt{\frac{5}{21}}$	$\sqrt{\frac{5}{21}}$
		11/2	…	…	…	$\sqrt{\frac{13}{15}}$	$\sqrt{\frac{2}{15}}$
		13/2	…	…	…	…	1

Using (15–17, 19) and (7, 8), typical spectrum in the $\mathrm{Spin}^{\mathrm{BF}}(5) \otimes U_k^{\mathrm{F}}(5)$ limit is constructed as shown in figure 5. To calculate the matrix elements corresponding to various observables in the symmetry limit, the basis states (15) are expanded in terms of particle-vibrator coupled states as

$$
\begin{aligned}
&|N\, n_d\, v_d [\tau_1\, \tau_2]\, [\bar{\tau}_1\, \bar{\tau}_2]\, \alpha J\rangle \\
&= \sum_{L_d, J', j} (-1)^{2+3/2-j}\, U(L_d\, 3/2\, J\, 2; J'\, j) \\
&\quad \langle [v_d]\, L_d [1/2, 1/2] 3/2 \| [\tau_1\, \tau_2]\, J' \rangle_{O(5)\supset O(3)} \langle [\tau_1\, \tau_2]\, J' [1] 2 \| [\bar{\tau}_1\, \bar{\tau}_2] \alpha J \rangle_{O(5)\supset O(3)} \\
&\quad . \; |N\, n_d\, v_d\, L_d; j; J\rangle .
\end{aligned}
\tag{20}
$$

The phase factor in (20) is needed as $j = 2 \otimes 3/2$ is used in (3) while in the basis states (20) $j = 3/2 \otimes 2$ is employed. The expressions for $[v_d] \otimes [1/2, 1/2] \rightarrow [\tau_1, \tau_2]$ $O(5) \supset O(3)$ reduced Wigner coefficients are given in tables 4 and 5. The Wigner coefficients for the coupling $[\tau_1\, \tau_2] \otimes [1] \rightarrow [\bar{\tau}_1\, \bar{\tau}_2]$ are derived by diagonalizing $a\, C_2$ $(\mathrm{Spin}^{\mathrm{BF}}(5)) + b\, C_2$ $(\mathrm{Spin}^{\mathrm{BFF}}(5))$ in the basis $|N\, n_d\, v_d\, L_d; j; J\rangle$ for fixed values of n_d, v_d and J and using the coefficients of tables 4 and 5. The resulting Wigner coefficients, which are needed for the construction of the states (15), with $n_d \leqslant 2$ are given in tables 6 and 7. Having derived the necessary reduced Wigner coefficients, it is easy to calculate matrix elements of any operator in the $\mathrm{Spin}^{\mathrm{BF}}(5) \otimes U_k^{\mathrm{F}}(5)$ limit using the expansion (20).

3.3 $U^{\mathrm{BF}}(5) \otimes U_s^{\mathrm{F}}(2)$ *limit*

The group chain (see figure 2a, group chain 3) and basis states in this limit are

$$
\left|
\begin{array}{l}
U^{\mathrm{B}}(6) \otimes U^{\mathrm{F}}(20) \supset U^{\mathrm{B}}(5) \otimes U_k^{\mathrm{F}}(10) \otimes U_s^{\mathrm{F}}(2) \supset \\
\quad \{N\} \qquad M_{\mathrm{F}} = 1 \quad \{n_d\} \qquad\quad \{1\} \\
U^{\mathrm{B}}(5) \otimes U_k^{\mathrm{F}}(5) \otimes SU_s^{\mathrm{F}}(2) \supset U^{\mathrm{BF}}(5) \otimes SU_s^{\mathrm{F}}(2) \supset \\
\quad \{n_d\} \qquad [11] \quad s = 1/2 \qquad \{n_1\, n_2\, n_3\} \\
O^{\mathrm{BF}}(5) \otimes SU_s^{\mathrm{F}}(2) \supset O^{\mathrm{BF}}(3) \otimes SU_s^{\mathrm{F}}(2) \supset \mathrm{Spin}(3) \supset \mathrm{Spin}(2) \\
\quad [v_1\, v_2] \qquad\qquad\qquad \alpha L \qquad\qquad\qquad J = L \pm 1/2 \quad \mathrm{M}
\end{array}
\right\rangle .
\tag{21}
$$

Note that in this limit the single particle angular momenta $j = 1/2, 3/2, 5/2$ and $7/2$ are decomposed into pseudo-orbital angular momenta $l = 1, 3$ and pseudo-spin $s = 1/2$, giving rise to the $U_k^{\mathrm{F}}(10) \otimes U_s^{\mathrm{F}}(2)$ subgroup. The generators of $U_k^{\mathrm{F}}(10)$ are

$$
V_\mu^\kappa(l, l'; \mathrm{F}) = - \sum_{j, j'} [(2j' + 1)/(2l' + 1)]^{1/2}\, U(j'\, \kappa\, 1/2\, l; j l')\, (a_j^\dagger\, \tilde{a}_{j'})_\mu^\kappa . \tag{22}
$$

and the pseudo-spin generators of $SU_s^{\mathrm{F}}(2)$ are

$$
\mathscr{S}_\mu^1(\mathrm{F}) = \sum_{l=1,3} \sum_{j, j'} [(2j + 1)/2]^{1/2}\, U(j\, 1\, l\, 1/2; j'\, 1/2)\, (a_j^\dagger\, \tilde{a}_{j'})_\mu^1 . \tag{23}
$$

In the reminder of this section pseudo-orbital part will be discussed; the pseudospin is added at the end to obtain total angular momentum J. The generators of $U_k^{\mathrm{F}}(5)$ are obtained using: (i) the generators of $U(5)$ group transform as $\{1\} \otimes \overline{\{1\}} \rightarrow \{0\} \oplus \{2111\}$;

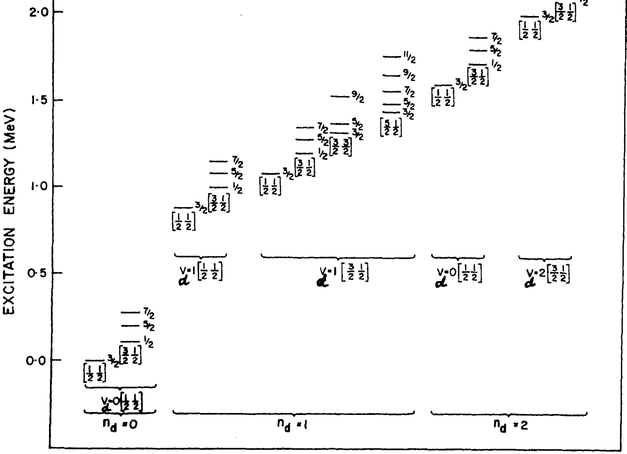

Figure 5. Typical spectrum in the $\text{Spin}^{\text{BF}}(5) \otimes U_k^{\text{F}}(5)$ limit. States are characterized with the labels defined in (13, 15). The parameters in the energy formula (19) are (in keV): $b_1 = 800, b_2 = 0, b_3 = 20, b_4 = 40, b_5 = 30$ and $b_6 = 10$.

$\{2111\} \to [2] \oplus [11]$; (iii) with respect to $O(5) \supset O(3)$, $[2] \to L = 2, 4$ and $[11] \to L = 1, 3$; (iv) the $a_l^\dagger$ and similarly $\tilde{a}_l$ behave as $[11]$ irrep of $O_k^{\text{F}}(5)$. The generators are $T_\mu^{[\omega_1\,\omega_2]\kappa}$ with $[\omega_1\,\omega_2]\kappa = [0]0;\ [2]2, 4;\ [11]1, 3$ and in terms of $V_\mu^\kappa(l, l'; F)$ of (22),

$$T_\mu^{[\omega_1\,\omega_2]\kappa} = \sum_{l,l'} \langle [11]l\ [11]l' \,\|\, [\omega_1\,\omega_2]\,\kappa \rangle_{O(5) \supset O(3)}\ V_\mu^\kappa(l, l'; \text{F}). \tag{24}$$

The $O(5) \supset O(3)$ reduced Wigner coefficients in (24) are given in [28] and using them give [10]

$$T_0^{[0]0} = \sqrt{\frac{3}{8}}\, G^0(\text{F}) = \sqrt{\frac{3}{10}}\, V^0(1, 1; \text{F}) + \sqrt{\frac{7}{10}}\, V^0(3, 3; \text{F})$$

$$T_\mu^{[11]1} = G_\mu^1(\text{F}) = \sqrt{\frac{1}{15}}\, V_\mu^1(1, 1; \text{F}) + \sqrt{\frac{14}{15}}\, V_\mu^1(3, 3; \text{F})\ .$$

$$T_\mu^{[11]3} = G_\mu^3(\text{F}) = \sqrt{\frac{2}{5}}\, \{V_\mu^3(1, 3; \text{F}) + V_\mu^3(3, 1; \text{F})\} - \sqrt{\frac{1}{5}}\, V_\mu^3(3, 3; \text{F})$$

$$T^{[2]2}_{\mu} = G^2_{\mu}(\mathrm{F}) = -\sqrt{\frac{7}{25}}\, V^2_{\mu}(1,1;\mathrm{F}) + \sqrt{\frac{2}{25}}\, V^2_{\mu}(3,3;\mathrm{F})$$
$$+ \sqrt{\frac{8}{25}}\,\{V^2_{\mu}(1,3;\mathrm{F}) + V^2_{\mu}(3,1;\mathrm{F})\}$$
$$T^{[2]4}_{\mu} = G^4_{\mu}(\mathrm{F}) = -\sqrt{\frac{11}{15}}\, V^4_{\mu}(3,3;\mathrm{F}) - \sqrt{\frac{2}{15}}\,\{V^4_{\mu}(1,3;\mathrm{F}) + V^4_{\mu}(3,1;\mathrm{F})\}. \tag{25}$$

Table 6. $O(5) \supset O(3)$ reduced Wigner coefficients $\langle [3/2, 1/2] J'\ [1] 2 \,\|\, [\bar{\tau}_1, \bar{\tau}_2] \alpha J \rangle$.

$[\bar{\tau}_1, \bar{\tau}_2]$	J	$J' = 1/2$	$J' = 5/2$	$J' = 7/2$
[1/2,1/2]	3/2	$-\sqrt{\frac{1}{8}}$	$-\sqrt{\frac{3}{8}}$	$-\sqrt{\frac{1}{2}}$
[3/2,1/2]	1/2	…	1	…
	5/2	$\sqrt{\frac{1}{3}}$	$-\sqrt{\frac{2}{147}}$	$\sqrt{\frac{32}{49}}$
	7/2	…	$-\sqrt{\frac{24}{49}}$	$\frac{5}{7}$
[3/2,3/2]	3/2	$\sqrt{\frac{21}{40}}$	$\sqrt{\frac{5}{56}}$	$-\sqrt{\frac{27}{70}}$
	5/2	$\sqrt{\frac{1}{15}}$	$-\sqrt{\frac{5}{6}}$	$-\sqrt{\frac{1}{10}}$
	9/2	…	$\sqrt{\frac{3}{14}}$	$\sqrt{\frac{11}{14}}$
[5/2,1/2]	3/2	$-\sqrt{\frac{7}{20}}$	$\sqrt{\frac{15}{28}}$	$\sqrt{\frac{8}{70}}$
	5/2	$\sqrt{\frac{3}{5}}$	$\sqrt{\frac{15}{98}}$	$-\sqrt{\frac{121}{490}}$
	7/2	…	$-\frac{5}{7}$	$-\sqrt{\frac{24}{49}}$
	9/2	…	$\sqrt{\frac{11}{14}}$	$-\sqrt{\frac{3}{14}}$
	11/2	…	…	1

$$U_k^{\mathrm{F}}(5):\{G_\mu^\kappa(\mathrm{F}),\ \kappa=0,1,2,3,4\} \tag{26}$$

and the generators of various coupled groups in (21) are

$$\begin{aligned} &U^{\mathrm{BF}}(5):\{I_\mu^\kappa(\mathrm{BF}),\ \kappa=0,1,2,3,4\}\\ &O^{\mathrm{BF}}(5):\{I_\mu^\kappa(\mathrm{BF}),\ \kappa=1,3\}\\ &O^{\mathrm{BF}}(3):\{I_\mu^1(\mathrm{BF})\}, \end{aligned} \tag{27}$$

Table 7. $O(5) \supset O(3)$ reduced Wigner coefficients $\langle [5/2, 1/2] J' \, [1] 2 \,\|\, [\bar{\tau}_1, \bar{\tau}_2] \alpha J \rangle$.

$[\bar{\tau}_1, \bar{\tau}_2]$	J	$J'=3/2$	$J'=5/2$	$J'=7/2$	$J'=9/2$	$J'=11/2$
$[3/2, 1/2]$	$1/2$	$-\sqrt{\frac{7}{25}}$	$\sqrt{\frac{18}{25}}$	$\dots$	$\dots$	$\dots$
	$5/2$	$\sqrt{\frac{1}{7}}$	$\sqrt{\frac{3}{49}}$	$-\sqrt{\frac{40}{147}}$	$\sqrt{\frac{11}{21}}$	$\dots$
	$7/2$	$-\sqrt{\frac{4}{175}}$	$-\sqrt{\frac{363}{4900}}$	$-\sqrt{\frac{48}{245}}$	$-\sqrt{\frac{3}{28}}$	$-\sqrt{\frac{3}{5}}$
$[5/2, 1/2]$	$3/2$	$-\sqrt{\frac{7}{15}}$	$\sqrt{\frac{16}{105}}$	$\sqrt{\frac{8}{21}}$	$\dots$	$\dots$
	$5/2$	$-\sqrt{\frac{32}{315}}$	$\sqrt{\frac{121}{13230}}$	$\sqrt{\frac{5776}{11907}}$	$\sqrt{\frac{1375}{3402}}$	$\dots$
	$7/2$	$\sqrt{\frac{4}{21}}$	$-\frac{38}{63}$	$\sqrt{\frac{7921}{19845}}$	$-\sqrt{\frac{4}{567}}$	$-\sqrt{\frac{16}{405}}$
	$9/2$	$\dots$	$-\sqrt{\frac{275}{1134}}$	$-\sqrt{\frac{16}{2835}}$	$\sqrt{\frac{175}{1782}}$	$-\sqrt{\frac{2912}{4455}}$
	$11/2$	$\dots$	$\dots$	$-\sqrt{\frac{32}{1215}}$	$-\sqrt{\frac{1456}{2673}}$	$\sqrt{\frac{637}{1485}}$
$[5/2, 3/2]$	$1/2$	$-\sqrt{\frac{18}{25}}$	$-\sqrt{\frac{7}{25}}$	$\dots$	$\dots$	$\dots$
	$3/2$	$\dots$	$-\sqrt{\frac{5}{7}}$	$\sqrt{\frac{2}{7}}$	$\dots$	$\dots$
	$5/2$	$\sqrt{\frac{10}{21}}$	$\sqrt{\frac{5}{18}}$	$\frac{4}{9}$	$-\sqrt{\frac{55}{1134}}$	$\dots$

$[\bar{\tau}_1, \bar{\tau}_2]$	J_α	$J' = 3/2$	$J' = 5/2$	$J' = 7/2$	$J' = 9/2$	$J' = 11/2$
	$(7/2)_1$	$\sqrt{\frac{594}{2625}}$	$\sqrt{\frac{539}{3000}}$	0*	$\sqrt{\frac{1083}{3080}}$	$-\sqrt{\frac{8}{33}}$
	$(7/2)_2$	$-\sqrt{\frac{32}{875}}$	$\sqrt{\frac{3227287}{9261000}}$	$\sqrt{\frac{8}{27}}$	$-\sqrt{\frac{1849}{7560}}$	$-\sqrt{\frac{2}{27}}$
	$9/2$	$\cdots$	$\sqrt{\frac{11}{378}}$	$-\sqrt{\frac{256}{945}}$	$-\sqrt{\frac{343}{594}}$	$-\sqrt{\frac{182}{1485}}$
	$11/2$	$\cdots$	$\cdots$	$-\sqrt{\frac{182}{405}}$	$\sqrt{\frac{289}{891}}$	$\sqrt{\frac{112}{495}}$
	$13/2$	$\cdots$	$\cdots$	$\cdots$	$\sqrt{\frac{1}{11}}$	$\sqrt{\frac{10}{11}}$
$[7/2, 1/2]$	$3/2$	$-\sqrt{\frac{8}{15}}$	$-\sqrt{\frac{2}{15}}$	$-\sqrt{\frac{5}{15}}$	$\cdots$	$\cdots$
	$5/2$	$-\sqrt{\frac{88}{315}}$	$\sqrt{\frac{88}{135}}$	$-\sqrt{\frac{11}{243}}$	$-\sqrt{\frac{40}{1701}}$	$\cdots$
	$7/2$	$\sqrt{\frac{11}{21}}$	$\sqrt{\frac{11}{324}}$	$-\sqrt{\frac{44}{405}}$	$-\sqrt{\frac{7225}{24948}}$	$\sqrt{\frac{196}{4455}}$
	$(9/2)_1$	$\cdots$	$\sqrt{\frac{216}{997}}$	$-\sqrt{\frac{1375}{2991}}$	$\sqrt{\frac{968}{2991}}$	0*
	$(9/2)_2$	$\cdots$	$-\sqrt{\frac{41327}{80757}}$	$-\sqrt{\frac{106496}{403785}}$	$-\sqrt{\frac{637}{888327}}$	$-\sqrt{\frac{997}{4455}}$
	$11/2$	$\cdots$	$\cdots$	$\sqrt{\frac{637}{1215}}$	$\sqrt{\frac{350}{2673}}$	$\sqrt{\frac{512}{1485}}$
	$13/2$	$\cdots$	$\cdots$	$\cdots$	$\sqrt{\frac{10}{11}}$	$-\sqrt{\frac{1}{11}}$
	$15/2$	$\cdots$	$\cdots$	$\cdots$	$\cdots$	1

*By choice.

$U^{\mathrm{BF}}(5)\otimes U_s^{\mathrm{F}}(2)$ limit are labelled by

$$|N\, n_d\, \{n_1\, n_2\, n_3\}\, [v_1\, v_2]\, \alpha\, L\, J = L \pm 1/2\rangle. \tag{28}$$

The reduction rules for the irrep labels in (28) are:

$$\begin{aligned}
&U^{\mathrm{BF}}(5){:}\,\{n_1\, n_2\, n_3\} = \{n_d\} \otimes \{11\} = \{n_d+1, 1\} \oplus \{n_d, 1, 1\}\\
&O^{\mathrm{BF}}(5){:}\,\{n_d+1, 1\} \to [v_1\, v_2] = [n_d, 0] \oplus [n_d-2, 0] \oplus \cdots \oplus [2,0] \text{ or } [1,0]\\
&\qquad\qquad\qquad \oplus [n_d+1, 1] \oplus [n_d-1, 1] \oplus \cdots \oplus [2,1] \text{ or } [1,1]\\
&\qquad\quad \{n_d, 1, 1\} \to [v_1\, v_2] = [n_d, 1] \oplus [n_d-1, 1] \oplus \cdots \oplus [2,1] \oplus [1,1]\\
&O^{\mathrm{BF}}(3){:}\,[v,0] \to L = (\lambda) \oplus (\lambda+1) \oplus \cdots \oplus (2\lambda-2) \oplus (2\lambda);\ \lambda = v, v-3, v-6, \ldots\\
&\qquad [v,1] \to L = (2v+1) \oplus (2v) \oplus \cdots \oplus (3)\\
&\qquad\qquad \oplus (v) \oplus (v-1) \oplus \cdots \oplus (1) \quad (v>0)\\
&\qquad\qquad \oplus (v+2) \oplus (v+1) \oplus \cdots \oplus (5) \quad (v>2)\\
&\qquad\qquad \oplus (v+3) \oplus (v+2) \oplus \cdots \oplus (7) \quad (v>3)\\
&\qquad\qquad \ldots\ \ldots
\end{aligned} \tag{29}$$

The angular momentum content of the $[v,0]$ and $[v,1]$ irreps of $O(5)$ are already given in [19] and [16] respectively and they are repeated here for completeness. The hamiltonian in the $U^{\mathrm{BF}}(5)\otimes U_s^{\mathrm{F}}(2)$ limit is

$$\begin{aligned}
H_{\{U^{\mathrm{BF}}(5)\otimes U_s^{\mathrm{F}}(2)\}} &= c_0 + c_1\, C_1(U^{\mathrm{B}}(5)) + c_2\, C_2(U^{\mathrm{B}}(5)) + c_3\, C_2(U^{\mathrm{BF}}(5))\\
&\quad + c_4\, C_2(O^{\mathrm{BF}}(5)) + c_5\, C_2(O^{\mathrm{BF}}(3)) + c_6\, C_2(\mathrm{Spin}(3)).
\end{aligned} \tag{30}$$

In (30), $(c_0, c_1, c_2, c_3, c_4, c_5, c_6)$ are free parameters. The $C_1(U^{\mathrm{B}}(5))$, $C_2(U^{\mathrm{B}}(5))$ and $C_2(\mathrm{Spin}(3))$ are defined in (10) and

$$\begin{aligned}
&C_2(U^{\mathrm{BF}}(5)) = \sum_{\kappa=0}^{4} I^{\kappa}(\mathrm{BF})\cdot I^{\kappa}(\mathrm{BF})\\
&C_2(O^{\mathrm{BF}}(5)) = 2 \sum_{\kappa=1,3} I^{\kappa}(\mathrm{BF})\cdot I^{\kappa}(\mathrm{BF})\\
&C_2(O^{\mathrm{BF}}(3)) = 10\ I^{1}(\mathrm{BF})\cdot I^{1}(\mathrm{BF}).
\end{aligned} \tag{31}$$

The eigenvalues of the hamiltonian (30) in terms of the labels in (28) are given by

$$\begin{aligned}
&E_{\{U^{\mathrm{BF}}(5)\otimes U_s^{\mathrm{F}}(2)\}}(N\, n_d\, \{n_1\, n_2\, n_3\}\, [v_1\, v_2]\, \alpha L J)\\
&\qquad = c_0 + c_1\, n_d + c_2\, n_d(n_d+4) + c_3 \sum_{i=1,2,3} n_i(n_i + 6 - 2i)\\
&\qquad\quad + c_4\, [v_1(v_1+3) + v_2(v_2+1)] + c_5\, L(L+1) + c_6\, J(J+1).
\end{aligned} \tag{32}$$

Using (28, 29, 32) typical spectrum in the $U^{\mathrm{BF}}(5) \otimes U_s^{\mathrm{F}}(2)$ limit is constructed as shown in figure 6. In the symmetry limit the basis states (28) are expanded, for calculating matrix elements of operators, in terms of particle-vibrator coupled states as

$$
\begin{aligned}
&|N\, n_d \{n_1\, n_2\, n_3\}\, [v_1\, v_2]\, \alpha L J\rangle \\
&= \sum_{v_d, L_d, l} \langle \{n_d\}\, [v_d]\, \{11\}\, [11] \| \{n_1\, n_2 n_3\}\, [v_1\, v_2]\rangle_{U(5) \supset O(5)} \\
&\quad \langle [v_d]\, L_d\, [11] l \| [v_1\, v_2]\, \alpha L\rangle_{O(5) \supset O(3)} |N\, n_d\, v_d\, L_d; l\, L J\rangle
\end{aligned}
\tag{33}
$$

and

$$
|N\, n_d\, v_d\, L_d; l L J\rangle = \sum_j U(L_d\, l\, J\, 1/2; Lj)\, |N\, n_d\, v_d\, L_d; j; J\rangle.
$$

The $U(5) \supset O(5)$ reduced Wigner coefficient in (33) is obtained by diagonalizing $T_1 = a\, C_2(U^{\mathrm{BF}}(5)) + b\, C_2(O^{\mathrm{BF}}(5))$ and $T_2 = a'\, C_2(O^{\mathrm{BF}}(5)) + b'\, C_2(O^{\mathrm{BF}}(3))$ in the basis $|N n_d v_d L_d; l\, L\rangle$. Similarly the $O(5) \supset O(3)$ Wigner coefficients in (33) are obtained by just diagonalizing T_2. The results given in tables 8–11 will enable one to construct the states (28) with $n_d \leqslant 2$. In table 11, the $O(5) \supset O(3)$ Wigner coefficients for $[3] \otimes [11] \to [21]$ are also given since they are needed in constructing basis states in the $O^{\mathrm{BF}}(6) \otimes U_s^{\mathrm{F}}(2)$ limit discussed in § 4.4. The reduced Wigner coefficients of tables 8–11 also determine the structure of the basis states of the other group chains (1 and 2) shown in figure 2a. Wave functions in those limits are obtained by deleting the $U(5) \supset O(5)$ or both $U(5) \supset O(5)$ and $O(5) \supset O(3)$ Wigner coefficients in the expansion (33).

4. Symmetry limits related to $O^{\mathrm{B}}(6)$

In this section, the $\mathrm{Spin}^{\mathrm{BF}}(6)$, $O^{\mathrm{BF}}(5) \otimes U_s^{\mathrm{F}}(4)$, $\mathrm{Spin}^{\mathrm{BF}}(6) \otimes U_k^{\mathrm{F}}(5)$ and $O^{\mathrm{BF}}(6) \otimes U_s^{\mathrm{F}}(2)$ limits of $U^{\mathrm{B}}(6) \otimes U^{\mathrm{F}}(20)$, which are all related to $O^{\mathrm{B}}(6)$ limit of IBM, are analysed (note that all three BF-1, BF-2 and BF-12 classes appear in this case). In each case given are the generators of the various groups involved and the spectrum generating hamiltonian as well as the quantum numbers labelling the states in the case $M_{\mathrm{F}} = 1$ (one fermion) relevant for odd-mass nuclei. The eigenfunctions in the symmetry limits are expanded in terms of particle-$O(6)$ coupled basis. The expansions essentially involve some $O(6) \supset O(5)$ and $O(5) \supset O(3)$ reduced Wigner coefficients, the latter are already given in § 3.

4.1 *Spin*$^{\mathrm{BF}}(6)$ *limit*

In this symmetry limit, discussed first by Ling *et al* [8], the single particle angular momenta $j = 1/2, 3/2, 5/2$ and $7/2$ are associated with the 20 dimensional irrep $[3/2, 1/2, 1/2]$ of the $\mathrm{Spin}^{\mathrm{F}}(6) \sim SU^{\mathrm{F}}(4)$ subgroup of $U^{\mathrm{F}}(20)$. The group chain (see figure 1, chain 3) and basis states in this limit are

$$
\left|
\begin{array}{ccccccccc}
U^{\mathrm{B}}(6) & \otimes & U^{\mathrm{F}}(20) & \supset & O^{\mathrm{B}}(6) & \otimes & [SU^{\mathrm{F}}(4) \sim \mathrm{Spin}^{\mathrm{F}}(6)] & \supset & \mathrm{Spin}^{\mathrm{BF}}(6) \quad \supset \\
\{N\} & & M_{\mathrm{F}} = 1 & & [\sigma] & & [1/2, 1/2, 1/2]. & & [\sigma_1\, \sigma_2\, \sigma_3]
\end{array}
\right.
$$

$$
\left.
\begin{array}{ccccc}
\mathrm{Spin}^{\mathrm{BF}}(5) & \supset & \mathrm{Spin}(3) & \supset & \mathrm{Spin}(2) \\
[\bar{\tau}_1\, \bar{\tau}_2] & & \alpha J & & M
\end{array}
\right\rangle.
\tag{34}
$$

The $O^{\mathrm{B}}(6)$ group generators are

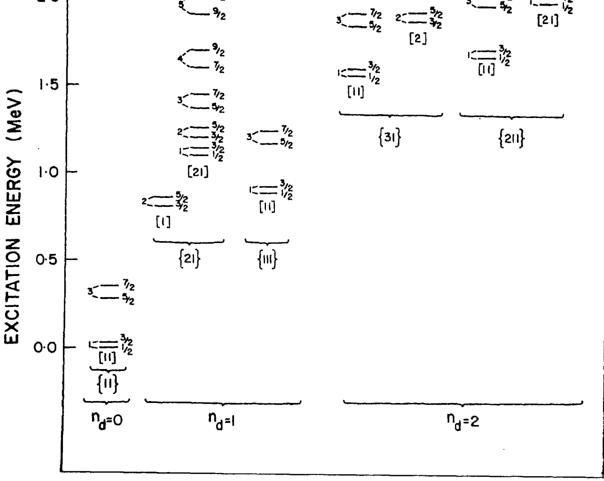

Figure 6. Typical spectrum in the $U^{\mathrm{BF}}(5)\otimes U_s^{\mathrm{F}}(2)$ limit. States are characterized with the labels defined in (21, 28). The parameters in the energy formula (32) are (in keV): $c_1=900, c_2=0, c_3=-15, c_4=50, c_5=20$ and $c_6=10$.

Table 8. $U(5)\supset O(5)$ reduced Wigner coefficients $\langle\{2\}\,[v]\,\{11\}\,[11]\,\|\,\{n_1\,n_2\,n_3\}\,[11]\rangle$.

$[v]$	$\{n_1\,n_2\,n_3\}=\{2\,1\,1\}$	$\{n_1\,n_2\,n_3\}=\{3\,1\,0\}$
[0]	$\sqrt{\frac{3}{10}}$	$\sqrt{\frac{7}{10}}$
[2]	$-\sqrt{\frac{7}{10}}$	$\sqrt{\frac{3}{10}}$

where $D_\mu^1(\mathrm{B})$ and $D_\mu^3(\mathrm{B})$ are already defined in (3) and

$$\bar{D}_\mu^2(\mathrm{B})=\frac{1}{\sqrt{2}}(s^\dagger\tilde{d}+d^\dagger\tilde{s})_\mu^2. \tag{36}$$

The Spin$^{\mathrm{F}}$(6) generators are

$$SU^{\mathrm{F}}(4):\{M_\mu^1(\mathrm{F}),\overline{M}{}_\mu^2(\mathrm{F}),M_\mu^3(\mathrm{F})\}. \tag{37}$$

$\langle [1]2\,[11]l \,\|\, [v_1, v_2]L \rangle$.

$[v_1, v_2]$	L	$l=1$	$l=3$
$[1]$	2	$\sqrt{\frac{3}{10}}$	$\sqrt{\frac{7}{10}}$
$[1,1]$	1	$\sqrt{\frac{8}{15}}$	$\sqrt{\frac{7}{15}}$
	3	$\sqrt{\frac{1}{5}}$	$-\sqrt{\frac{4}{5}}$
$[2,1]$	1	$\sqrt{\frac{7}{15}}$	$-\sqrt{\frac{8}{15}}$
	2	$-\sqrt{\frac{7}{10}}$	$\sqrt{\frac{3}{10}}$
	3	$\sqrt{\frac{4}{5}}$	$\sqrt{\frac{1}{5}}$
	4	…	1
	5	…	1

The $M^1_\mu(\mathrm{F})$ and $M^3_\mu(\mathrm{F})$ generators can be expressed in terms of $K^\kappa_\mu(\mathrm{F})$ and $S^\kappa_\mu(\mathrm{F})$ defined in (3) while the structure of $\overline{M}{}^2_\mu(\mathrm{F})$ is more complex [13],

$$
\begin{aligned}
M^1_\mu(\mathrm{F}) &= K^1_\mu(\mathrm{F}) - \frac{1}{\sqrt{2}}\, S^1_\mu(\mathrm{F}),\\
M^3_\mu(\mathrm{F}) &= K^3_\mu(\mathrm{F}) + \frac{1}{\sqrt{2}}\, S^3_\mu(\mathrm{F}),\\
\overline{M}{}^2_\mu(\mathrm{F}) &= -\sqrt{\frac{6}{25}}\,(a^\dagger_{1/2}\,\tilde{a}_{3/2} - a^\dagger_{3/2}\,\tilde{a}_{1/2})^2_\mu\\
&\quad + \sqrt{\frac{21}{100}}\,(a^\dagger_{1/2}\,\tilde{a}_{5/2} + a^\dagger_{5/2}\,\tilde{a}_{1/2})^2_\mu + \sqrt{\frac{49}{50}}\,(a^\dagger_{3/2}\,\tilde{a}_{3/2})^2_\mu\\
&\quad + \sqrt{\frac{18}{25}}\,(a^\dagger_{3/2}\,\tilde{a}_{5/2} - a^\dagger_{5/2}\,\tilde{a}_{3/2})^2_\mu\\
&\quad + \sqrt{\frac{24}{25}}\,(a^\dagger_{3/2}\,\tilde{a}_{7/2} + a^\dagger_{7/2}\,\tilde{a}_{3/2})^2_\mu - \sqrt{\frac{3}{350}}\,(a^\dagger_{5/2}\,\tilde{a}_{5/2})^2_\mu\\
&\quad + \sqrt{\frac{72}{175}}\,(a^\dagger_{5/2}\,\tilde{a}_{7/2} - a^\dagger_{7/2}\,\tilde{a}_{5/2})^2_\mu + \sqrt{\frac{3}{7}}\,(a^\dagger_{7/2}\,\tilde{a}_{7/2})^2_\mu.
\end{aligned}
\qquad (38)
$$

$[v_1, v_2]$	L'_α	$(L,l)=(2,1)$	$(L,l)=(2,3)$	$(L,l)=(4,1)$	$(L,l)=(4,3)$
$[2]$	2	$\sqrt{\frac{3}{25}}$	$-\sqrt{\frac{64}{175}}$	…	$-\sqrt{\frac{18}{35}}$
	4	…	$\sqrt{\frac{2}{7}}$	$\sqrt{\frac{2}{5}}$	$\sqrt{\frac{11}{35}}$
$[1,1]$	1	$-\sqrt{\frac{1}{3}}$	$\sqrt{\frac{8}{21}}$	…	$-\sqrt{\frac{2}{7}}$
	3	$\sqrt{\frac{8}{49}}$	$\sqrt{\frac{2}{49}}$	$-\sqrt{\frac{6}{49}}$	$-\sqrt{\frac{33}{49}}$
$[2,1]$	1	$\sqrt{\frac{1}{15}}$	$\sqrt{\frac{121}{210}}$	…	$\sqrt{\frac{5}{14}}$
	2	$-\sqrt{\frac{2}{5}}$	$\sqrt{\frac{6}{35}}$	…	$\sqrt{\frac{3}{7}}$
	3	$\sqrt{\frac{4}{35}}$	$\sqrt{\frac{7}{20}}$	$\sqrt{\frac{15}{28}}$	0
	4	…	$-\sqrt{\frac{9}{28}}$	$-\sqrt{\frac{1}{20}}$	$\sqrt{\frac{22}{35}}$
	5	…	$\sqrt{\frac{1}{7}}$	$-\sqrt{\frac{3}{10}}$	$\sqrt{\frac{39}{70}}$
$[3,1]$	1	$\sqrt{\frac{3}{5}}$	$\sqrt{\frac{3}{70}}$	…	$-\sqrt{\frac{5}{14}}$
	2	$\sqrt{\frac{12}{25}}$	$\sqrt{\frac{81}{175}}$	…	$\sqrt{\frac{2}{35}}$
	3_1	$\sqrt{\frac{27}{70}}$	$-\sqrt{\frac{21}{40}}$	$\sqrt{\frac{5}{56}}$	0*
	3_2	$\sqrt{\frac{33}{98}}$	$\sqrt{\frac{33}{392}}$	$-\sqrt{\frac{99}{392}}$	$\frac{4}{7}$
	4	…	$-\sqrt{\frac{11}{28}}$	$\sqrt{\frac{11}{20}}$	$-\sqrt{\frac{2}{35}}$
	5_1	…	$\sqrt{\frac{39}{49}}$	0	$-\sqrt{\frac{10}{49}}$
	5_2	…	$\sqrt{\frac{3}{49}}$	$\sqrt{\frac{7}{10}}$	$\sqrt{\frac{117}{490}}$
	6	…	…	…	1
	7	…	…	…	1

---

*By choice.

Table 11. $O(5) \supset O(3)$ reduced Wigner coefficients $\langle [3]L[11]l \,\|\, [21]L' \rangle$.

L	l	$L'=1$	$L'=2$	$L'=3$	$L'=4$	$L'=5$
0	1	$-\sqrt{\frac{7}{30}}$	…	…	…	…
0	3	…	…	$-\sqrt{\frac{1}{15}}$	…	…
3	1	…	$\sqrt{\frac{14}{45}}$	$\sqrt{\frac{7}{72}}$	$-\sqrt{\frac{7}{40}}$	…
3	3	$\sqrt{\frac{7}{12}}$	$\sqrt{\frac{7}{90}}$	$-\sqrt{\frac{7}{36}}$	$-\sqrt{\frac{77}{1620}}$	$-\sqrt{\frac{7}{180}}$
4	1	…	…	$\sqrt{\frac{11}{40}}$	$\sqrt{\frac{77}{1080}}$	$-\sqrt{\frac{7}{55}}$
4	3	$\sqrt{\frac{11}{60}}$	$\sqrt{\frac{11}{18}}$	$-\sqrt{\frac{1}{180}}$	$\sqrt{\frac{169}{540}}$	$\sqrt{\frac{13}{1980}}$
6	1	…	…	…	…	$\sqrt{\frac{91}{495}}$
6	3	…	…	$\sqrt{\frac{13}{36}}$	$-\sqrt{\frac{637}{1620}}$	$\sqrt{\frac{637}{990}}$

The generators of the coupled groups in (34) are now easy to write down,

$$\begin{aligned}
&\mathrm{Spin}^{\mathrm{BF}}(6)\colon \{C^1_\mu(\mathrm{BF}), \bar{C}^2_\mu(\mathrm{BF}), C^3_\mu(\mathrm{BF})\}\\
&\mathrm{Spin}^{\mathrm{BF}}(5)\colon \{C^1_\mu(\mathrm{BF}), C^3_\mu(\mathrm{BF})\},
\end{aligned}$$

where

$$\begin{aligned}
C^1_\mu(\mathrm{BF}) &= D^1_\mu(\mathrm{B}) + M^1_\mu(\mathrm{F}),\\
\bar{C}^2_\mu(\mathrm{BF}) &= \bar{D}^2_\mu(\mathrm{B}) + \bar{M}^2_\mu(\mathrm{F}),\\
C^3_\mu(\mathrm{BF}) &= D^3_\mu(\mathrm{B}) + M^3_\mu(\mathrm{F}). \qquad (39)
\end{aligned}$$

Note that the $\mathrm{Spin}^{\mathrm{BF}}(5)$ group of (34, 39) is identical to the $\mathrm{Spin}^{\mathrm{BFF}}(5)$ group defined in (5); Spin(3) is the usual angular momentum group (see (5)). Ignoring the labels that are obvious ($M_{\mathrm{F}} = 1$ etc.) in (34), the basis states in the $\mathrm{Spin}^{\mathrm{BF}}(6)$ limit are labelled by

$$|N \sigma [\sigma_1 \sigma_2 \sigma_3] [\bar{\tau}_1 \bar{\tau}_2] \alpha J\rangle. \qquad (40)$$

The $O^{\mathrm{B}}(6)$ label σ takes values [29]

$\sigma = N$ are the most important states. The reduction rules for the Spin$^{\mathrm{BF}}$(6) and Spin$^{\mathrm{BF}}$(5) irreps in (40) follow from the $U(4)$ multiplication rules and the Weyl's rules [23, 18],

$$\begin{aligned}
\mathrm{Spin}^{\mathrm{BF}}(6):[\sigma_1,\sigma_2,\sigma_3] &= [\sigma]\otimes[3/2,1/2,1/2] \\
&= [\sigma\pm 3/2,1/2,1/2]\oplus[\sigma\pm 1/2,3/2,1/2] \\
&\quad \oplus[\sigma\pm 1/2,1/2,1/2] \\
\mathrm{Spin}^{\mathrm{BF}}(5):[\sigma+1/2,1/2,1/2] &\rightarrow[\bar{\tau}_1,\bar{\tau}_2]=[\sigma+1/2,1/2] \\
&\qquad \oplus[\sigma-1/2,1/2]\oplus\cdots\oplus[1/2,1/2] \\
[\sigma+1/2,3/2,1/2] &\rightarrow[\bar{\tau}_1,\bar{\tau}_2]=[\sigma+1/2,1/2]\oplus[\sigma-1/2,1/2] \\
&\quad \oplus\cdots\oplus[3/2,1/2]\oplus[\sigma+1/2,3/2] \\
&\quad \oplus[\sigma-1/2,3/2]\oplus\cdots\oplus[3/2,3/2].
\end{aligned} \tag{42}$$

The angular momentum content of all relevant Spin$^{\mathrm{BF}}$(5) irreps is given in (8) (see also the discussion below (8)). The hamiltonian in the Spin$^{\mathrm{BF}}$(6) limit is

$$\begin{aligned}
H_{\{\mathrm{Spin}^{\mathrm{BF}}(6)\}} &= d_0 + d_1\, C_2(O^{\mathrm{B}}(6)) + d_2\, C_2(\mathrm{Spin}^{\mathrm{BF}}(6)) \\
&\quad + d_3\, C_2(\mathrm{Spin}^{\mathrm{BF}}(5)) + d_4\, C_2(\mathrm{Spin}(3)).
\end{aligned} \tag{43}$$

In (43), $(d_0, d_1, d_2, d_3, d_4)$ are free parameters. Expressions for the Casimir operators appearing in (43), in terms of the generators defined in (35, 39) are

$$\begin{aligned}
C_2(O^{\mathrm{B}}(6)) &= 2\sum_{\kappa=1,3} D^{\kappa}(\mathrm{B})\cdot D^{\kappa}(\mathrm{B}) + 2\bar{D}^2(\mathrm{B})\cdot\bar{D}^2(\mathrm{B}) \\
C_2(\mathrm{Spin}^{\mathrm{BF}}(6)) &= 2\sum_{\kappa=1,3} C^{\kappa}(\mathrm{BF})\cdot C^{\kappa}(\mathrm{BF}) + 2\bar{C}^2(\mathrm{BF})\cdot\bar{C}^2(\mathrm{BF}) \\
C_2(\mathrm{Spin}^{\mathrm{BF}}(5)) &= 2\sum_{\kappa=1,3} C^{\kappa}(\mathrm{BF})\cdot C^{\kappa}(\mathrm{BF}).
\end{aligned} \tag{44}$$

Note that $C_2(\mathrm{Spin}(3))$ is defined in (10). The eigenvalues of the hamiltonian (43) in terms of the labels in (40) are given by

$$\begin{aligned}
&E_{\{\mathrm{Spin}^{\mathrm{BF}}(6)\}}(N\,\sigma\,[\sigma_1\,\sigma_2\,\sigma_3]\,[\bar{\tau}_1\,\bar{\tau}_2]\,\alpha\,J) \\
&\quad = d_0 + d_1[\sigma(\sigma+4)] + d_2[\sigma_1(\sigma_1+4)+\sigma_2(\sigma_2+2)+\sigma_3^2] \\
&\qquad + d_3[\bar{\tau}_1(\bar{\tau}_1+3)+\bar{\tau}_2(\bar{\tau}_2+1)] + d_4\, J(J+1).
\end{aligned} \tag{45}$$

Using (40–42, 45), typical spectrum in the Spin$^{\mathrm{BF}}$(6) limit is constructed as shown in figure 7. To calculate matrix elements corresponding to various observables in this limit, we expand the basis states (40) in a particle-$O(6)$ coupled basis $|N\,\sigma\,v_d\,L_d;j;J\rangle$ as

$$\begin{aligned}
&|N\,\sigma[\sigma_1\,\sigma_2\,\sigma_3]\,[\bar{\tau}_1\,\bar{\tau}_2]\,\alpha\,J\rangle \\
&\quad = \sum_{\tau,v_d,L_d,j}\langle[\sigma][v_d][3/2,1/2,1/2][\tau,1/2]\,\|\,[\sigma_1\,\sigma_2\,\sigma_3][\bar{\tau}_1\,\bar{\tau}_2]\rangle_{O(6)\supset O(5)} \\
&\qquad \langle[v_d]\,L_d[\tau,1/2]\,j\,\|\,[\bar{\tau}_1\,\bar{\tau}_2]\alpha J\rangle_{O(5)\supset O(3)}|N\,\sigma\,v_d L_d;j;J\rangle.
\end{aligned} \tag{46}$$

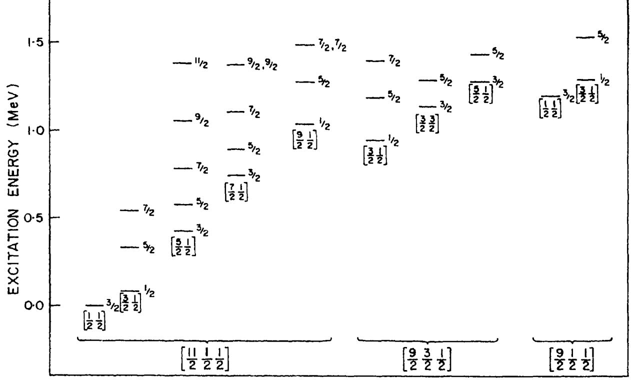

Figure 7. Typical spectrum in the Spin$^{\mathrm{BF}}(6)$ limit. States are characterized with the labels defined in (34, 40). The parameters in the energy formula (45) are (in keV): $d_2 = -85, d_3 = 35$, and $d_4 = 30$. Note that the parameter d_1 is not relevant since only states with $\sigma = N = 4$ are shown.

The summation over j in (46) has the restriction $j = 3/2$ for $\tau = 1/2$ and $j = 1/2, 5/2, 7/2$ for $\tau = 3/2$ and no other τ value is allowed. The $O(6) \supset O(5)$ reduced Wigner coefficients in (46) are determined in [8, 30] and some of the relevant $O(5) \supset O(3)$ reduced Wigner coefficients are already given in tables 4 and 5. The $O(6) \supset O(5)$ Wigner coefficients with $v_d = 0$, which determine single particle transfer strengths in the Spin$^{\mathrm{BF}}(6)$ limit for even to odd transfer reactions are colleted in table 12. Other properties of the Spin$^{\mathrm{BF}}(6)$ limit, most importantly the expressions for the B(E2) values between low-lying states, follow from the work on the Spin(6) limit with $j = 3/2$ [15]. For instance, provided we use $\bar{C}^2_\mu(\mathrm{BF})$ as the E2 transition operator and provided we consider transitions between states belonging to the irrep $[N + 3/2, 1/2, 1/2]$, the B(E2) values in the Spin$^{\mathrm{BF}}(6)$ limit follow directly from the formulas given in [15] after a simple replacement of N by $N + 1$.

4.2 $O^{\mathrm{BF}}(5) \otimes U^{\mathrm{F}}_s(4)$ *limit*

The group chain (see figure 3b, chain 3) and basis states in this limit are

$$\left| \begin{array}{ccccccc} U^{\mathrm{B}}(6) \otimes & U^{\mathrm{F}}(20) & \supset O^{\mathrm{B}}(6) \otimes & U^{\mathrm{F}}_k(5) \otimes & U^{\mathrm{F}}_s(4) \supset & O^{\mathrm{B}}(5) \otimes O^{\mathrm{F}}_k(5) \otimes & SU^{\mathrm{F}}_s(4) \supset \\ \{N\} & M_{\mathrm{F}} = 1 & [\sigma] & \{1\} & \{1\} & [v_d] & [1] \end{array} \right.$$

$$\left. \begin{array}{ccccc} O^{\mathrm{BF}}(5) \otimes & \mathrm{Spin}^{\mathrm{F}}_s(5) & \supset \mathrm{Spin}^{\mathrm{BFF}}(5) & \supset \mathrm{Spin}(3) & \supset \mathrm{Spin}(2) \\ [v_1\, v_2] & [1/2, 1/2] & [\bar{\tau}_1\, \bar{\tau}_2] & \alpha\, J & M \end{array} \right\rangle. \tag{47}$$

Note that this classification is very similar to the chain 3 in figure 3a except for the boson group $U^{\mathrm{B}}(5)$ which is replaced by $O^{\mathrm{B}}(6)$. Hence many of the properties of the

$[\sigma', 1/2, 1/2]$	$\langle[\sigma][0]\,[3/2,1/2,1/2]\,[1/2,1/2] \parallel [\sigma',1/2,1/2]\,[1/2,1/2]\rangle$
$[\sigma+3/2, 1/2, 1/2]$	$\left[\dfrac{3(\sigma+4)(\sigma+5)}{10(\sigma+2)(\sigma+3)}\right]^{1/2}$
$[\sigma+1/2, 1/2, 1/2]$	$\left[\dfrac{\sigma(\sigma+4)}{5(\sigma+2)(\sigma+3)}\right]^{1/2}$
$[\sigma-1/2, 1/2, 1/2]$	$\left[\dfrac{\sigma(\sigma+4)}{5(\sigma+1)(\sigma+2)}\right]^{1/2}$
$[\sigma-3/2, 1/2, 1/2]$	$-\left[\dfrac{3\sigma(\sigma-1)}{10(\sigma+1)(\sigma+2)}\right]^{1/2}$

$O^{BF}(5)\otimes U_s^F(4)$ limit follow from the results given in the § 3.1. The generators of $O^B(6$ are given in (35, 36), the generators of $O^B(5)$ are given below (14) and the generators o the coupled groups $O^{BF}(5)$, $\mathrm{Spin}^{BFF}(5)$ and Spin(3) are given in (5). The basis states in $O^{BF}(5)\otimes U_s^F(4)$ limit are labelled by

$$|N\,\sigma\,v_d\,[v_1\,v_2]\,[\bar{\tau}_1\,\bar{\tau}_2]\,\alpha\,J\rangle. \qquad (48$$

The $U^B(6)\supset O^B(6)$ reduction is given in (41) and the $O^B(6)\supset O^B(5)$ reduction is simple [29],

$$O^B(5){:}\,\sigma\rightarrow v_d=\sigma,\sigma-1,\ldots,0. \qquad (49$$

The $O^{BF}(5)$ irreps $[v_1\,v_2]$ follow from the rule

$$O^{BF}(5){:}\,[v_1\,v_2]=[v_d]\otimes[1]=[v_d+1]\oplus[v_d-1]\oplus[v_d,1]. \qquad (50$$

The reductions to $\mathrm{Spin}^{BFF}(5)$ and Spin(3) irreps is given in (7, 8). The hamiltonian in this limit is

$$\begin{aligned}H_{\{O^{BF}(5)\otimes U_s^F(4)\}} &= e_0+e_1\,C_2(O^B(6))+e_2\,C_2(O^B(5))\\ &\quad +e_3\,C_2(O^{BF}(5))+e_4\,C_2(\mathrm{Spin}^{BFF}(5))+e_5\,C_2(\mathrm{Spin}(3)),\end{aligned} \qquad (51$$

where the Casimir operators appearing in (51) are given in (10, 18, 44). In (51) $(e_0,e_1,e_2,e_3,e_4,e_5)$ are free parameters. The eigenvalues of the hamiltonian (51) are

$$\begin{aligned}&E_{\{O^{BF}(5)\otimes U_s^F(4)\}}(N\,\sigma\,v_d\,[v_1\,v_2]\,[\bar{\tau}_1\,\bar{\tau}_2]\,\alpha\,J)\\ &\quad=e_0+e_1\,\sigma(\sigma+4)+e_2[v_d(v_d+3)]+e_3[v_1(v_1+3)+v_2(v_2+1)]\\ &\qquad+e_4[\bar{\tau}_1(\bar{\tau}_1+3)+\bar{\tau}_2(\bar{\tau}_2+1)]+e_5\,J(J+1).\end{aligned} \qquad (52$$

Using (48, 52) typical spectrum in the $O^{BF}(5)\otimes U_s^F(4)$ limit is constructed as shown in figure 8. To calculate the matrix elements corresponding to various observables in the

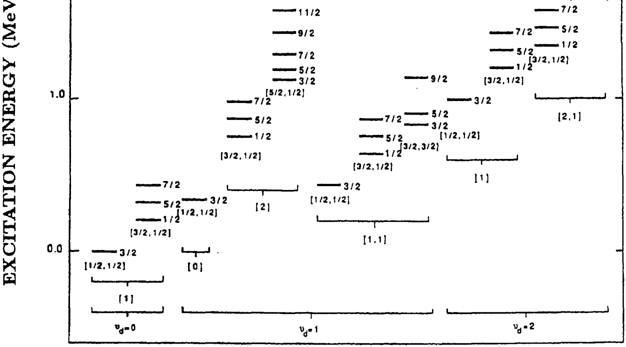

Figure 8. Typical spectrum in the $O^{\mathrm{BF}}(5)\otimes U_s^{\mathrm{F}}(4)$ limit. States are characterized with the labels defined in (47, 48). The parameters in the energy formula (52) are (in keV): $e_2=100, e_3=20, e_4=50$ and $e_5=15$. Note that the parameter e_1 is not relevant since only states with $\sigma=N=4$ are shown.

symmetry limit, the basis states (48) are expanded in terms of particle-$O(6)$ coupled states as

$$\begin{aligned}&|N\,\sigma\,v_d\,[v_1\,v_2]\,[\bar{\tau}_1\,\bar{\tau}_2]\,\alpha\,J\rangle\\ &\quad=\sum_{L_d,L,j} U(L_d\,2\;J\,3/2;Lj)\langle[v_d]\,L_d\,[1]2\,\|\,[v_1\,v_2]\,L\rangle_{O(5)\supset O(3)}\\ &\qquad\times\langle[v_1v_2]L[1/2,1/2]3/2\,\|\,[\bar{\tau}_1\bar{\tau}_2]\,\alpha\,J\rangle_{O(5)\supset O(3)}|N\,\sigma\,v_d\,L_d\,;j\,;J\rangle. \qquad (53)\end{aligned}$$

All the reduced Wigner coefficients appearing in the expansion (53) also occur in (12). Consequently, the expressions given in § 3.1 for the $O(5)\supset O(3)$ Wigner coefficients completely specify the lowest states of $O^{\mathrm{BF}}(5)\otimes U_s^{\mathrm{F}}(4)$ limit and also determine the electromagnetic and particle-transfer properties in this limit.

4.3 $\mathrm{Spin}^{\mathrm{BF}}(6)\otimes U_k^{\mathrm{F}}(5)$ *limit*

The group chain (see figure 3c, chain 5) and basis states in this limit [9, 10, 11] are

$$\left|\begin{array}{l} U^{\mathrm{B}}(6)\otimes U^{\mathrm{F}}(20)\supset O^{\mathrm{B}}(6)\otimes[SU_s^{\mathrm{F}}(4)\sim \mathrm{Spin}_s^{\mathrm{F}}(6)]\otimes U_k^{\mathrm{F}}(5)\supset\\ \{N\}\qquad M_{\mathrm{F}}=1\qquad [\sigma]\qquad\qquad [1/2,1/2,1/2]\qquad\qquad \{1\}\\ \mathrm{Spin}^{\mathrm{BF}}(6)\otimes U_k^{\mathrm{F}}(5)\supset \mathrm{Spin}^{\mathrm{BF}}(5)\otimes O^{\mathrm{F}}(5)\supset\\ [\sigma_1\,\sigma_2\,\sigma_3]\qquad\qquad\qquad [\tau_1\,\tau_2]\qquad [1]\\ \mathrm{Spin}^{\mathrm{BFF}}(5)\supset \mathrm{Spin}(3)\supset \mathrm{Spin}(2)\\ \quad[\bar{\tau}_1\,\bar{\tau}_2]\qquad\quad \alpha J\qquad\quad M \end{array}\right\rangle. \qquad (54)$$

are [15]

$$\mathrm{Spin}^{\mathrm{BF}}(6):\{E^1_\mu(\mathrm{BF}), \bar{E}^2_\mu(\mathrm{BF}), E^3_\mu(\mathrm{BF})\},$$

where

$$\bar{E}^2_\mu(\mathrm{BF}) = \bar{D}^2_\mu(\mathrm{B}) - \frac{1}{\sqrt{2}} S^2_\mu(\mathrm{F}) \tag{55}$$

and the generators $E^1_\mu(\mathrm{BF})$ and $E^3_\mu(\mathrm{BF})$ are given in (14). Generators for the other groups in (54) are defined in (3, 5, 14). The basis states in $\mathrm{Spin}^{\mathrm{BF}}(5) \otimes U^{\mathrm{F}}_k(5)$ limit are labelled by

$$|N\,\sigma\,[\sigma_1\,\sigma_2\,\sigma_3]\,[\tau_1\,\tau_2]\,[\bar{\tau}_1\,\bar{\tau}_2]\,\alpha\,J\rangle. \tag{56}$$

The $O^{\mathrm{B}}(6)$ label σ is specified in (41). For a given σ, the $\mathrm{Spin}^{\mathrm{BF}}(6)$ labels are [15]

$$\begin{aligned}\mathrm{Spin}^{\mathrm{BF}}(6):[\sigma_1, \sigma_2, \sigma_3] &= [\sigma] \otimes [1/2, 1/2, 1/2] \\ &= [\sigma + 1/2, 1/2, 1/2] \oplus [\sigma - 1/2, 1/2, 1/2].\end{aligned} \tag{57}$$

The other reductions for specifying (56) are given in (8, 16, 42). The hamiltonian in this limit is

$$\begin{aligned}H_{\{\mathrm{Spin}^{\mathrm{BF}}(6)\otimes U^{\mathrm{F}}_k(5)\}} = {} & f_0 + f_1\, C_2\big(O^{\mathrm{B}}(6)\big) + f_2\, C_2\big(\mathrm{Spin}^{\mathrm{BF}}(6)\big) \\ & + f_3\, C_2\big(\mathrm{Spin}^{\mathrm{BF}}(5)\big) + f_4\, C_2\big(\mathrm{Spin}^{\mathrm{BFF}}(5)\big) + f_5\, C_2\big(\mathrm{Spin}(3)\big).\end{aligned} \tag{58}$$

In (58), $(f_0, f_1, f_2, f_3, f_4, f_5)$ are free parameters. The Casimir operators appearing in (58), except $C_2(\mathrm{Spin}^{\mathrm{BF}}(6))$, are given in (10, 18, 44). The $C_2\ (\mathrm{Spin}^{\mathrm{BF}}(6))$ is given by

$$C_2\big(\mathrm{Spin}^{\mathrm{BF}}(6)\big) = 2 \sum_{\kappa=1,3} E^\kappa(\mathrm{BF}) \cdot E^\kappa(\mathrm{BF}) + 2\bar{E}^2(\mathrm{BF}) \cdot \bar{E}^2(\mathrm{BF}). \tag{59}$$

The eigenvalues of the hamiltonian (58) are

$$\begin{aligned}& E_{\{\mathrm{Spin}^{\mathrm{BF}}(6)\otimes U^{\mathrm{F}}_k(5)\}}\,(N\,\sigma\,[\sigma_1\,\sigma_2\,\sigma_3]\,[\tau_1\,\tau_2]\,[\bar{\tau}_1\,\bar{\tau}_2]\,\alpha\,J) \\ & = f_0 + f_1\,\sigma(\sigma+4) + f_2\,[\sigma_1(\sigma_1+4) + \sigma_2(\sigma_2+2) + \sigma_3^2] \\ & \quad + f_3\,[\tau_1(\tau_1+3) + \tau_2(\tau_2+1)] + f_4\,[\bar{\tau}_1(\bar{\tau}_1+3) + \bar{\tau}_2(\bar{\tau}_2+1)] + f_5\, J(J+1).\end{aligned} \tag{60}$$

Using (60) typical spectrum in the $\mathrm{Spin}^{\mathrm{BF}}(6) \otimes U^{\mathrm{F}}_k(5)$ limit is constructed as shown in figure 9. To calculate the matrix corresponding to various observables in the symmetry limit, the basis states (56) are expanded in terms of particle-$O(6)$ coupled states as

$$\begin{aligned}& |N\,\sigma\,[\sigma_1\,\sigma_2\,\sigma_3]\,[\tau_1\,\tau_2]\,[\bar{\tau}_1\,\bar{\tau}_2]\,\alpha\,J\rangle \\ & = \sum_{v_d,\, L_d,\, J',\, j} (-1)^{2+3/2-j}\, U(L_d\, 3/2\, J\, 2; J' j) \\ & \quad \langle [\sigma]\, v_d\, [1/2, 1/2, 1/2]\, [1/2, 1/2] \,\|\, [\sigma_1\,\sigma_2\,\sigma_3]\,[\tau_1\,\tau_2] \rangle_{O(6)\supset O(5)} \\ & \quad \langle [v_d]\, L_d\, [1/2, 1/2]\, 3/2 \,\|\, [\tau_1\,\tau_2]\, J' \rangle_{O(5)\supset O(3)} \\ & \quad \langle [\tau_1\,\tau_2]\, J'\, [1]\, 2 \,\|\, [\bar{\tau}_1\,\bar{\tau}_2]\, \alpha\, J \rangle \,|N\,\sigma\, v_d\, L_d;\, j;\, J\rangle\end{aligned} \tag{61}$$

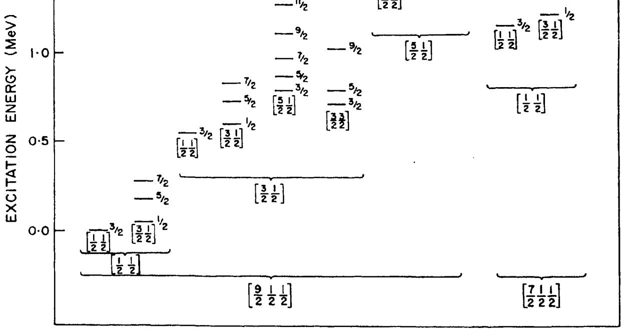

Figure 9. Typical spectrum in the $\mathrm{Spin}^{\mathrm{BF}}(6)\otimes U^{\mathrm{F}}_{k}(5)$ limit. States are characterized with the labels defined in (54, 56). The parameters in the energy formula (60) are (in keV): $f_2=-96, f_3=110, f_4=20$ and $f_5=15$. Note that the parameter f_1 is not relevant since only states with $\sigma=N=4$ are shown.

The phase factor in the expression (61) arises because of the specific coupling order (see remark after (20)). Note that all the $O(5)\supset O(3)$ reduced Wigner coefficients in (61) also occur in (20) and hence they follow from § 3.2. Expressions for the $O(6)\supset O(5)$ reduced Wigner coefficients in (61) are derived in [26] and the ones relevant for the lowest states in the $\mathrm{Spin}^{\mathrm{BF}}(6)\otimes U^{\mathrm{F}}_{k}(5)$ limit are summarized in table 13.

4.4 $O^{\mathrm{BF}}(6)\otimes U^{\mathrm{F}}_{s}(2)$ *limit*

The group chain (see figure 2b, group chain 3) and basis states in this limit are [9, 10]

$$\left|\begin{array}{ccccccccc} U^{\mathrm{B}}(6) & \otimes & U^{\mathrm{F}}(20) & \supset & O^{\mathrm{B}}(6) & \otimes & U^{\mathrm{F}}_{k}(10) & \otimes & U^{\mathrm{F}}_{s}(2) \supset \\ \{N\} & & M_{\mathrm{F}}=1 & & [\sigma] & & \{1\} & & \end{array}\right.$$
$$\begin{array}{ccccccccc} O^{\mathrm{B}}(6) & \otimes & O^{\mathrm{F}}_{k}(6) & \otimes & SU^{\mathrm{F}}_{s}(2) & \supset & O^{\mathrm{BF}}(6) & \otimes & SU^{\mathrm{F}}_{s}(2) \supset \\ [\sigma] & & [111] & & s=1/2 & & [\sigma_1\sigma_2\sigma_3] & & \end{array}$$
$$\left.\begin{array}{ccccccccc} O^{\mathrm{BF}}(5) & \otimes & SU^{\mathrm{F}}_{s}(2) & \supset & O^{\mathrm{BF}}(3) & \otimes & SU^{\mathrm{F}}_{s}(2) \supset & \mathrm{Spin}(3) & \supset \mathrm{Spin}(2) \\ [v_1 v_2] & & & & \alpha L & & & J=L\pm 1/2 & M \end{array}\right\rangle. \tag{62}$$

The subgroup $U^{\mathrm{F}}_{k}(10)\otimes U^{\mathrm{F}}_{s}(2)$ of $U^{\mathrm{F}}(20)$ is identical to the one in (21) and its generators are given in (22, 23). The generators of $O^{\mathrm{F}}_{k}(6)$ are obtained using the fact that they transform

$[v]$	$[\sigma', 1/2, 1/2] = [\sigma - 1/2, 1/2, 1/2]$	$[\sigma', 1/2, 1/2] = [\sigma + 1/2, 1/2, 1/2]$
$[\tau - 1/2]$	$\left[\dfrac{2\sigma - 2\tau + 1}{4(\sigma + 2)}\right]^{1/2}$	$-\left[\dfrac{2\sigma + 2\tau + 7}{4(\sigma + 2)}\right]^{1/2}$
$[\tau + 1/2]$	$\left[\dfrac{2\sigma + 2\tau + 7}{4(\sigma + 2)}\right]^{1/2}$	$\left[\dfrac{2\sigma - 2\tau + 1}{4(\sigma + 2)}\right]^{1/2}$

as [11] irrep of $O(6)$ and upon reduction to $O(5)$, one has $[11]_{O(6)} \rightarrow \{[1] \oplus [11]\}_{O(5)}$. Therefore, using (24) with $[\omega_1, \omega_2] = [1]$ and [11] give the $O_k^{\mathrm{F}}(6)$ generators

$$O_k^{\mathrm{F}}(6): \{G_\mu^1(\mathrm{F}), \bar{G}_\mu^2(\mathrm{F}), G_\mu^3(\mathrm{F})\}, \tag{63}$$

where $G_\mu^1(\mathrm{F})$ and $G_\mu^3(\mathrm{F})$ are defined in (25, 26) and $\bar{G}_\mu^2(\mathrm{F})$ is

$$\begin{aligned} T_\mu^{[11]2} = \bar{G}_\mu^2(\mathrm{F}) = \frac{2}{5} V_\mu^2(1,1;\mathrm{F}) - \sqrt{\frac{14}{25}}\, V_\mu^2(3,3;\mathrm{F}) \\ + \sqrt{\frac{7}{50}} \{V_\mu^2(1,3;\mathrm{F}) + V_\mu^2(3,1;\mathrm{F})\}. \end{aligned} \tag{64}$$

The V's in (64) are defined in (22). The generators of $O^{\mathrm{BF}}(6)$ in (62) are

$$O^{\mathrm{BF}}(6): \{I_\mu^1(\mathrm{BF}), \bar{I}_\mu^2(\mathrm{BF}), I_\mu^3(\mathrm{BF})\}, \tag{65}$$

where $I_\mu^1(\mathrm{BF})$ and $I_\mu^3(\mathrm{BF})$ are defined in (27) and $\bar{I}_\mu^2(\mathrm{BF})$ is

$$\bar{I}_\mu^2(\mathrm{BF}) = \bar{D}_\mu^2(\mathrm{B}) + \sqrt{3}\, \bar{G}_\mu^2(\mathrm{F}). \tag{66}$$

Other coupled groups in (62) are defined in § 3.3. The basis states in the $O^{\mathrm{BF}}(6) \otimes U_s^{\mathrm{F}}(2)$ limit are labelled by

$$|N \sigma [\sigma_1\, \sigma_2\, \sigma_3] [v_1\, v_2] \alpha L J = L \pm 1/2\rangle. \tag{67}$$

The reduction rules for the $O^{\mathrm{BF}}(6)$ and $O^{\mathrm{BF}}(5)$ irrep labels in (67) are

$$\begin{aligned} O^{\mathrm{BF}}(6): [\sigma_1, \sigma_2, \sigma_3] &= [\sigma] \otimes [1,1,1] \\ &= [\sigma+1,1,1] \oplus [\sigma-1,1,1] \oplus [\sigma,1,0] \\ O^{\mathrm{BF}}(5): [\sigma+1,1,1] &\rightarrow [v_1, v_2] = [\sigma+1,1] \oplus [\sigma,1] \oplus \cdots \oplus [1,1] \\ [\sigma-1,1,1] &\rightarrow [v_1, v_2] = [\sigma-1,1] \oplus [\sigma-2,1] \oplus \cdots \oplus [1,1] \\ [\sigma,1,0] &\rightarrow [v_1, v_2] = [\sigma,0] \oplus [\sigma-1,0] \oplus \cdots \oplus [1,0] \\ &\qquad \oplus [\sigma,1] \oplus [\sigma-1,1] \oplus \cdots \oplus [1,1]. \end{aligned} \tag{68}$$

The angular momentum content of the $[v,0]$ and $[v,1]$ irreps of $O(5)$ is already (29). The hamiltonian in the $O^{\mathrm{BF}}(6)\otimes U_s^{\mathrm{F}}(2)$ limit is

$$H_{\{O^{\mathrm{BF}}(6)\otimes U_s^{\mathrm{F}}(2)\}}=g_0+g_1\,C_2(O^{\mathrm{B}}(6))+g_2\,C_2(O^{\mathrm{BF}}(6))$$
$$+\,g_3\,C_2(O^{\mathrm{BF}}(5))+g_4\,C_2(O^{\mathrm{BF}}(3))+g_5\,C_2(\mathrm{Spin}(3)).$$

In (69), $(g_0,g_1,g_2,g_3,g_4,g_5)$ are free parameters. Note that the $C_2(O^{\mathrm{B}}(6))$ is in (44), $C_2(O^{\mathrm{BF}}(5))$ and $C_2(O^{\mathrm{BF}}(3))$ are defined in (31) and $C_2(\mathrm{Spin}(3))$ is define The expression for $C_2(O^{\mathrm{BF}}(6))$ is

$$C_2(O^{\mathrm{BF}}(6))=2\sum_{\kappa=1,3}I^{\kappa}(\mathrm{BF})\cdot I^{\kappa}(\mathrm{BF})+2\tilde{I}^2_{\mu}(\mathrm{BF})\cdot\tilde{I}^2_{\mu}(\mathrm{BF}).$$

The eigenvalues of the hamiltonian (69) in terms of the labels in (67) are give

$$E_{\{O^{\mathrm{BF}}(6)\otimes U_s^{\mathrm{F}}(2)\}}(N\sigma[\sigma_1\,\sigma_2\,\sigma_3]\,[v_1\,v_2]\,\alpha L J)$$
$$=g_0+g_1\sigma(\sigma+4)+g_2[\sigma_1(\sigma_1+4)+\sigma_2(\sigma_2+2)+\sigma_3^2]$$
$$+g_3[v_1(v_1+3)+v_2(v_2+1)]+g_4L(L+1)+g_5J(J+1).$$

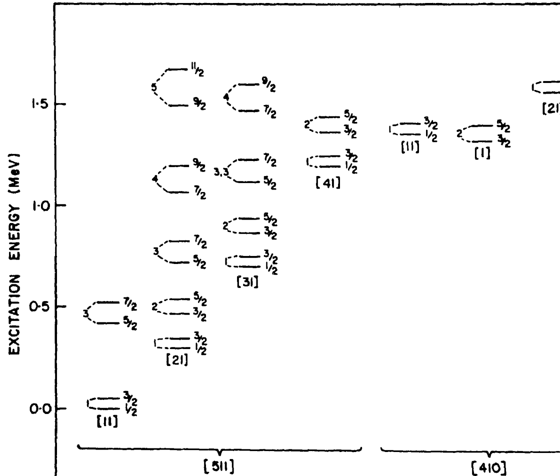

Using (67–69, 71) typical spectrum in the $O^{\mathrm{BF}}(6)\otimes U_s^{\mathrm{F}}(2)$ limit is constructed as shown in figure 10. The basis states in (67) can be expanded in terms of particle-$O(6)$ coupled states as

$$
\begin{aligned}
&|N\,\sigma\,[\sigma_1\,\sigma_2\sigma_3]\,[v_1\,v_2]\,\alpha\,L\,J=L\pm 1/2\rangle \\
&= \sum_{v_d,\,L_d,\,l,\,j} U(L_d\,l\,J\,1/2;Lj)\langle[\sigma]\,[v_d]\,[111]\,[1\,1]\,\|\,[\sigma_1\,\sigma_2\,\sigma_3]\,[v_1\,v_2]\rangle_{O(6)\supset O(5)} \\
&\quad\times\langle[v_d]\,L_d\,[11]\,l\,\|\,[v_1\,v_2]\,\alpha L\rangle_{O(5)\supset O(3)}\;|N\,\sigma\,v_d\,L_d;j;\,J\rangle. \qquad (72)
\end{aligned}
$$

The $O(5)\supset O(3)$ reduced Wigner coefficients appearing in (72) are already calculated in § 3.3 and the results of tables 9 – 11 will allow one to construct states with $[v_1\,v_2]=[11]$, $[21]$ or $[31]$. The $O(6)\supset O(5)$ reduced Wigner coefficients in (72) are obtained by diagonalizing the operator $C_2(O^{\mathrm{BF}}(6))$ in the basis $|N\sigma\,v_d[v_1v_2]L\rangle$. The Wigner coefficients with $[v_1\,v_2]=[11]$ and $[21]$ are given in table 14.

5. Applications and conclusions

The applicability of $U^{\mathrm{B}}(6)\otimes U^{\mathrm{F}}(20)$ symmetry schemes to actual nuclei requires three conditions to be satisfied: (i) for the symmetries defined by (2,13, 21) and (34, 47, 54, 62), the even–even core parameters must be close to $U^{\mathrm{B}}(5)$ and $O^{\mathrm{B}}(6)$ limits of IBM respectively; (ii) the dominant single particle orbits of the odd nucleon should have angular momenta $j=1/2, 3/2, 5/2$ and $7/2$ (with the single particle energies fixed by core parameters); (iii) the boson – fermion (core–particle) interaction should have the specific form required by the coupling scheme (its strength is related to the core hamiltonian). The second condition restricts the scope of $U^{\mathrm{B}}(6)\otimes U^{\mathrm{F}}(20)$ symmetry schemes to nuclei of the periodic table with active neutrons or protons in the $3s_{1/2}$, $2d_{3/2}$, $2d_{5/2}$ and $1g_{7/2}$ orbits of the 50–82 shell. The consideration of $U(6/20)$ supersymmetry (SUSY) scheme which combines even–even and odd-A nuclei with the same SUSY quantum number [4], is often useful in the data analysis that aims to find examples for $U^{\mathrm{B}}(6)\otimes U^{\mathrm{F}}(20)$, which is a subgroup of $U(6/20)$. Examples of even–even $O(6)$ nuclei in this mass region are the Pt isotopes [29, 31] and the Xe–Ba isotopes [32, 2] and consequently examples for the schemes discussed in § 4 have to come from the neighbouring odd-A nuclei (i.e. from the odd Au isotopes and from the odd-neutron Xe or Ba isotopes). It was shown by Ling *et al* [8] that the energies, B(E2)'s and one-proton transfer data of ^{197}Au is well described by the Spin$^{\mathrm{BF}}$(6) limit (§ 4.1). Similarly Jolie *et al* [11] showed that the energies, B(E2)'s and one-neutron transfer data of ^{129}Xe are well described by the Spin$^{\mathrm{BF}}(6)\otimes U_k^{\mathrm{F}}(5)$ limit (§ 4.3); they also studied $^{123,\,125,\,127}$Te and $^{127,\,131}$Xe isotopes. So far no examples are found for $O^{\mathrm{BF}}(5)\otimes U_s^{\mathrm{F}}(4)$ and $O^{\mathrm{BF}}(6)\otimes U_s^{\mathrm{F}}(2)$ limits. As there is good evidence for the goodness of pseudo-spin symmetry [33], it is plausible that experimental examples for $O^{\mathrm{BF}}(6)\otimes U_s^{\mathrm{F}}(2)$ limit must be present and search for this should continue. For the symmetries associated with the

consider a hamiltonian interpolating the $U^{\mathrm{BF}}(5)\otimes U^{\mathrm{F}}_{s}(4)$ and $\mathrm{Spin}^{\mathrm{BF}}(5)\otimes U^{\mathrm{F}}_{k}(5)$ lim
spectra (see figures 4, 5) in these two limits are quite similar. Examples for $U^{\mathrm{BF}}(5)$
and $\mathrm{Spin}^{\mathrm{BF}}\otimes U^{\mathrm{F}}_{k}(5)$ limits also may come from neutron deficient Te isotopes (Te
are known [36] to be close to $U^{\mathrm{B}}(5)$ limit) as both protons and neutrons in these n
particle-like unlike in the heavier Te isotopes where the neutrons are hole-like.

In this article, the dynamical symmetries of IBFM when the odd nucleon c
orbits with $j = 1/2$, $3/2$, $5/2$ and $7/2$ are described in detail for the cases wit
and $O^{\mathrm{B}}(6)$ even–even core. In each of the dynamical symmetry limit gi
the Lie algebra and generators of the various groups, classification of sta
hamiltonian and its eigenvalues, and explicit form of the wavefunctions of low
levels through the computation of the relevant reduced Wigner coefficient
results can serve as a basis for the derivation of other properties such as electron
transition rates and one and two particle transfer strengths etc., as descr
Appendix A. Though examples are available for some of the symmetry limits (f
described in §§ 3.1, 4.1 and 4.3), often only a qualitative description of
properties are obtained. Nevertheless the dynamical symmetries can be used as a
point in the analysis of a given odd-mass nucleus and thus provide different
coupling scheme in which a boson–fermion hamiltonian can be considered which
more complicated symmetry breaking terms (see [11] for some examples).

The reduced Wigner coefficients given in the tables are useful for man
applications, for instance in BF symmetry studies of odd–odd nuclei [26, 37] a
study of heavy $N \sim Z$ nuclei using the isospin invariant IBM-3 model [38]. S
the principles that led to the realization of some of the symmetry l
$U^{\mathrm{B}}(6)\otimes U^{\mathrm{F}}(20)$ are useful in many other situations, for example in construc

Table 14. $O(6)\supset O(5)$ reduced Wigner coefficients $\langle[\sigma][v][1,1,1][1,1]\,\|\,[\sigma_1,\sigma_2,\sigma_3]\,[v_1,v_2]\rangle$.

$[v_1,v_2]$	$[v]$	$[\sigma+1,1,1]$	$[\sigma,1,0]$	$[\sigma-1,1,$
$[1,1]$	$[0]$	$\left[\frac{3(\sigma+4)(\sigma+5)}{10(\sigma+2)(\sigma+3)}\right]^{1/2}$	$\left[\frac{2\sigma(\sigma+4)}{5(\sigma+1)(\sigma+3)}\right]^{1/2}$	$\left[\frac{3\sigma(\sigma-}{10(\sigma+1)(\sigma}\right.$
	$[1]$	$\left[\frac{\sigma(\sigma+5)}{2(\sigma+2)(\sigma+3)}\right]^{1/2}$	$-\left[\frac{6}{(\sigma+1)(\sigma+3)}\right]^{1/2}$	$-\left[\frac{(\sigma-1)(\sigma-}{2(\sigma+1)(\sigma}\right.$
	$[2]$	$-\left[\frac{\sigma(\sigma-1)}{5(\sigma+2)(\sigma+3)}\right]^{1/2}$	$\left[\frac{3(\sigma-1)(\sigma+5)}{5(\sigma+1)(\sigma+3)}\right]^{1/2}$	$-\left[\frac{(\sigma+4)(\sigma-}{5(\sigma+1)(\sigma}\right.$
$[2,1]$	$[1]$	$\left[\frac{2(\sigma+5)(\sigma+6)}{7(\sigma+2)(\sigma+3)}\right]^{1/2}$	$\left[\frac{3(\sigma-1)(\sigma+5)}{7(\sigma+1)(\sigma+3)}\right]^{1/2}$	$\left[\frac{2(\sigma-2)(\sigma}{7(\sigma+1)(\sigma}\right.$

schemes are realizable in purely fermionic models [40] and therefore they may be useful in the search for understanding the origin of SUSY in nuclei [41]. The large array of $U(5) \supset O(5)$, $O(5) \supset O(3)$ and $O(6) \supset O(5)$ reduced Wigner coefficients that are given in tables 1–14 clearly show that developing a general algorithm and the corresponding computer codes for generating these coefficients, just as it was done in the case of $SU(3) \supset O(3)$ [42], is an extremely important problem; see [43] for some effort in this direction. Finally the work presented in this article may also be viewed as an example-case to illustrate how symmetry arguments can be used even in fairly complex systems of bosons and fermions.

Acknowledgements

The author thanks P Van Isacker for collaboration and valuable correspondence.

Appendix A

Let us consider a transition operator $T^k_\mu(\mathrm{BF})$ of angular momentum tensor rank k in BF space and assume that it is of the form $\Sigma_r (U^{k_1}_r(\mathrm{B})\, V^{k_2}_r(\mathrm{F}))^k_\mu$. For example, to lowest order, $T^{\mathrm{E}_2}(\mathrm{BF})$ is a linear combination of E2 operators in boson and fermion spaces and then in the above form we have $r = 1,2$ with $U = 1$ for $r = 1$ and $V = 1$ for $r = 2$. Similarly the single particle transfer operator for $(N, M_\mathrm{F} = 0) \rightarrow (N-1, M_\mathrm{F} = 1)$ transfer is a linear combination of operators of the form $(\tilde{s}a^\dagger_j)^j$ and $(\tilde{d}a^\dagger_j)^{j'}$ (see eq. (2.18) of [11]). For the symmetries related to $U^\mathrm{B}(5)$ of IBM, let us denote the symmetry adopted basis states (6, 15, 28) by $|S{:}J\rangle$. In (12, 20, 33) they are expanded in terms of particle–$U^\mathrm{B}(5)$ (vibrator) coupled states $|N n_d v_d L_d; j; J\rangle$ as

$$|S{:}\,J\rangle = \sum_{\{n_d, v_d, L_d, j\}} C^{S,J}_{\{n_d, v_d, L_d, j\}}\, |N n_d v_d L_d; j; J\rangle\,. \tag{A1}$$

The C factors in (A1) follow directly from (12, 20, 33) and they involve the Wigner coefficients given in the tables and angular momentum U-coefficients. The symbol $\{n_d, v_d, L_d, j\}$ denotes that the summation is over all or some of the variables in the brackets; for example in (20) the summation is over only L_d and j and in all the three (12, 20, 33) cases there is no summation over n_d. The reduced matrix elements of $T^k_\mu(\mathrm{BF})$ in terms of reduced matrix elements in boson (B) and fermion (F) spaces is then given by

$$\begin{aligned}
&\langle S_f{:}\, J_f \,\|\, T^k(\mathrm{BF}) \,\|\, S_i{:}\, J_i\rangle \\
&= \sum_r \langle S_f{:}\, J_f \| (U^{k_1}_r(\mathrm{B})\, V^{k_2}_r(\mathrm{F}))^k_\mu \| S_i{:}\, J_i\rangle \\
&= \sum_r \sum_{\{n^i_d, v^i_d, L^i_d, j^i\}} \sum_{\{n^f_d, v^f_d, L^f_d, j^f\}} \sqrt{(2J_i+1)(2J_f+1)(2k+1)} \begin{Bmatrix} L^f_d & L^i_d & k_1 \\ j^f & j^i & k_2 \\ J_f & J_i & k \end{Bmatrix} \\
&\times C^{S_i, J_i}_{\{n^i_d, v^i_d, L^i_d, j^i\}}\; C^{S_f, J_f}_{\{n^f_d, v^f_d, L^f_d, j^f\}} \\
&\times \langle n^f_d, v^f_d, L^f_d \,\|\, U^{k_1}_r(\mathrm{B}) \,\|\, n^i_d, v^i_d, L^i_d\rangle \\
&\times \langle j_f \,\|\, V^{k_2}(\mathrm{F}) \,\|\, j_i\rangle
\end{aligned} \tag{A2}$$

the reduced matrix elements $\langle n_d^f, v_d^f, L_d^f \| U_r^{k_1}(\mathrm{B}) \| n_d^i, v_d^i, L_d^i \rangle$ in the $U^{\mathrm{B}}(5)$ limit basis of IBM are given for many cases in [19]. Using (12, 20, 33), (A2), the reduced Wigner coefficients given in tables 1–11 and the results in [19], it is straight forward to calculate matrix elements of operators in the three symmetry limits related to $U^{\mathrm{B}}(5)$ limit of IBM. Instead of the $U^{\mathrm{B}}(5)$ basis states, taking $O^{\mathrm{B}}(6)$ limit basis states $| N\, \sigma\, v_d\, L_d; j; J \rangle$ in (A1, A2) and using the $O^{\mathrm{B}}(6)$ limit results given in [29] and the reduced Wigner coefficients given in tables 1–14, it is straight forward to calculate matrix elements of operators in the four symmetry limits (i.e. for $|S:J\rangle$ given by (46, 53, 61, 72)) related to $O^{\mathrm{B}}(6)$ limit of IBM.

References

[1] F Iachello and A Arima, *The interacting boson model* (Cambridge University Press, Cambridge, 1987)

[2] *Perspectives for the interacting boson model* edited by R F Casten *et al* (World Scientific, Singapore, 1994)

[3] K H Kim, A Gelberg, T Mizusaki, T Otsuka and P Von Brentano, *Nucl. Phys.* **A604**, 163 (1996)

[4] F Iachello and P Van Isacker, *The interacting boson–fermion model* (Cambridge University Press, Cambridge, 1991)

[5] A Gizon *et al*, *Nucl. Phys.* **A605**, 301 (1996)
D Bucurescu, G Cata-Danil, N V Zamfir, A Gizon and J Gizon, *Phys. Rev.* **C43**, 2160 (1991)
G Cata-Danil, D Bucurescu, A Gizon and J Gizon, *J. Phys.* **G20**, 1051 (1994)

[6] J Vervier, *Rev. Nuovo Cimento* **10**, No. 9, 1 (1987)

[7] V K B Kota and Y D Devi, *Nuclear shell model and the interacting boson model: Lecture notes for practitioners* (IUC-DAEF, Calcutta, India, 1996)

[8] Y S Ling, M Zhang, J M Xu, M Vallieres, R Gilmore and D H Feng, *Phys. Lett.* **B148**, 13 (1984)

[9] V K B Kota, in *Nuclear structure, reactions and symmetries* edited by R A Meyer and V Paar (World Scientific, Singapore, 1986), vol. 1, p. 259

[10] V K B Kota, in *Recent trends in theoretical nuclear physics* edited by K Srinivasa Rao (Macmillan India Ltd., Madras, India, 1987) p. 70

[11] J Jolie, K Heyde, P Van Isacker and A Frank, *Nucl. Phys.* **A466**, 1 (1987)

[12] R Bijker and V K B Kota, *Ann. Phys. (N.Y.)* **187**, 148 (1988)

[13] V K B Kota and P Van Isacker, University of Rochester Report UR-1080, (1988) unpublished

[14] F Iachello, *Phys. Rev. Lett.* **44**, 772 (1980)

[15] F Iachello and S Kuyucak, *Ann, Phys. (N.Y.)* **136**, 19 (1981)

[16] A B Balantekin, I Bars, R Bijker and F Iachello, *Phys. Rev.* **C 27**, 1761 (1983)

[17] B H Flowers, *Proc. R. Soc. London* **A212**, 248 (1952)

[18] B G Wybourne, *Classical groups for physicists* (John Wiley & Sons, New York, 1974)

[19] A Arima and F Iachello, *Ann. Phys. (N.Y.)* **99**, 253 (1976)

[20] R Bijker and V K B Kota, *Ann. Phys. (N.Y.)* **156**, 110 (1984)

[21] V K B Kota, in *Group theoretical methods in physics* edited by W W Zachary (World Scientific, Singapore, 1984) p. 404

[22] J Varvier, P Van Isacker, J Jolie, V K B Kota and R Bijker, *Phys. Rev.* **C32**, 1406 (1985)

[23] B G Wybourne, *Symmetry principles in atomic spectroscopy* (John Wiley and Sons, New York, 1970)

[24] T Kishimoto and T Tamura, *Nucl. Phys.* **A163**, 100 (1971)
V K B Kota, unpublished

[25] P Van Isacker, A Frank and H Z Sun, *Ann. Phys. (N.Y.)* **157**, 183 (1984)

[26] P Van Isacker, *J. Math. Phys.* **28**, 957 (1987)

[27] A R Edmonds, *Angular momentum in quantum mechanics* (Princeton University Press,

[28] K T Hecht, *Part. Nucl.* **2**, 117 (1971)
[29] A Arima and F Iachello, *Ann. Phys. (N. Y.)* **123**, 468 (1979)
[30] M Zhang, M Vallieres, Y S Ling and R Gilmore, in *Interacting boson–boson and boson–fermion systems* edited by O Scholten (World Scientific, Singapore, 1984) p. 160
[31] R F Casten and J A Cizewski, *Nucl. Phys.* **A309**, 477 (1978)
[32] R F Casten and P Von Brentano, *Phys. Lett.* **B152**, 22 (1985)
[33] C Bahari, J P Draayer and S A Moszkowski, *Phys. Rev. Lett.* **68**, 2133 (1992)
A L Blokhin, C Bahri and J P Draayer, *Phys. Rev. Lett.* **74**, 4149 (1995)
[34] R F Casten and D D Warner, *Rev. Mod. Phys.* **60**, 389 (1988)
H Lehmann and J Jolie, *Nucl. Phys.* **A588**, 623 (1996)
[35] A K Singh, G Gangopadhay and D Banerjee, *Phys. Rev.* **C53**, 2524 (1996)
[36] T Lonnroth, A Virtanen and J Hattula, *Phys. Scr.* **34**, 682 (1986)
[37] P Van Isacker and J Jolie, *Nucl. Phys.* **A503**, 429 (1989)
P Van Isacker, J Jolie, K Heyde and A Frank, *Phys. Rev. Lett.* **54**, 653 (1985)
A Algora, T Fenyes, Z Dombradi and J Jolie, *Z. Phys.* **A352**, 25 (1995)
J Jolie and P E Garrett, *Nucl. Phys.* **A596**, 234 (1996)
[38] V K B Kota, to appear in the Proceedings of the Int'l Workshop on *Special Functions and Differential Equations* held during January 13–24, 1997 at I.M.Sc, Chennai
[39] P Navratil, H B Geyer, J Dobes and J Dobaczewski, *Ann. Phys. (N.Y.)* **243**, 218 (1995)
[40] V K B Kota (1988), unpublished
[41] P Navratil, H B Geyer and J Dobaczewski, *Nucl. Phys.* **A607**, 23 (1996)
[42] Y Akiyama and J P Draayer, *Comp. Phys. Comm.* **5**, 405 (1973)
[43] K T Hecht, *Nucl. Phys.* **63**, 177 (1965)
J C Parikh, *Nucl. Phys.* **63**, 214 (1965)
J Vanthournout, H De Meyer and G Vanden Berghe, *J. Math. Phys.* **29**, 1958 (1988); **30**, 943 (1989)
D J Rowe and K T Hecht, *J. Math. Phys.* **36**, 4711 (1996)

PRAMANA
— journal of
physics

© Printed in India

Vol. 48, No. 5,
May 1997
pp. 1077–1090

Photon interaction cross-sections and anomalous scattering factors of Cu and Ag

SANDIAGO, T K UMESH and RAMAKRISHNA GOWDA
Department of Studies in Physics, University of Mysore, Manasagangothri, Mysore 570006, India

MS received 23 July 1996; revised 24 February 1997

Abstract. Total attenuation cross sections of copper and silver have been measured in the energy range 5 to 85 keV in a narrow beam good geometry set up using X- and γ-rays emitted from radio isotopes, by employing a high resolution hyper pure germanium detector. From the measured values, the photoeffect cross-sections have been derived by subtracting a small contribution of the sum of the theoretical coherent and incoherent scattering cross sections. The photoeffect cross-sections so obtained are found to be in better agreement with the unrenormalized values of Scofield [10]. These photoeffect cross-sections have been used to evaluate the dispersion corrections (also called anomalous scattering factors) f^+ and f'' for the forward Rayleigh scattering amplitude by a numerical evaluation of the dispersion integral that relates them at the energies at which the cross-sections have been measured. To the f^+ values so obtained, the relativistic corrections proposed by different investigators are included separately and the values f' so obtained are compared with the available data and discussed. Possible conclusions are drawn from the present study.

Keywords. Photoeffect cross-section; anomalous scattering factor; copper; silver.

PACS No. 32·80

1. Introduction

The study of interaction of photons particularly the X-rays and gamma rays has drawn wide ranging attention by virtue of the diverse applications of these photons in multifarious fields of science and technology. A knowledge of the photon interaction cross-sections is essential in a variety of applications in medicine, biology, agriculture, industry, X-ray surveillance, radiation shielding calculations, industrial radiography, radiometric gauging etc., [1]. In particular, the study of photon interaction in the energy range below 150 keV is very useful for medical studies as well as determination of structure of complex media [2].

A literature survey on the photon interaction cross-section data reveals the fact that mixtures at energies from 1 keV to 100 GeV. The program called XCOM, base conclusions developed from comparison with measurements in Saloman *et al* [8] the unrenormalized photo effect cross-sections of Scofield [10] and Hubbell *et al* data for the incoherent and coherent scattering cross sections. It may be noted that tabulation of Hubbell [6] is based on the calculated photo effect cross-section Scofield [10], modified for $Z = 1$ to 54 using the relativistic Hartree–Fock renorma ation factors supplied by Scofield himself.

Theoretical photoeffect cross-sections claiming high accuracy have been provide Scofield [10]. These values have been calculated by using a model where the electr are treated to be moving relativistically in a Hartree–Slater central potential. elements with atomic number $Z = 2$ to 54, Scofield has provided correction factor the individual atomic subshells. Using these factors, the photoeffect cross-sections be renormalized so that they correspond to a relativistic Hartree–Fock model ra than the Hartree–Slater model used in the original calculation. The renormaliza results in a reduction of the predicted photoeffect cross-sections particularly for outer atomic shells.

So, reasonably accurate experimental data on the photoeffect cross-section elements in the low energy region below 100 keV, measured with high resolu detectors, are required for a critical comparison with the renormalized as well as unrenormalized theoretical data of Scofield [10]. This critical comparison is nec tated particularly because the Scofield's theoretical photoeffect values with without the Hartree–Slater to Hartree–Fock renormalization could be used as up and lower limits to the experimental photoeffect cross-sections [11].

The experimental photoeffect cross-sections can be used to determine the real imaginary parts $f'(E)$ and $f''(E)$ of the dispersion corrections to the forward Rayl scattering amplitude (also called anomalous scattering factors), where E is the energ interest. This can be done by a suitable numerical evaluation of the dispersion inte involving the photoeffect cross-section [7]. However it can be commonly observed the $f'(E)$ values evaluated in this manner are systematically higher than those obta using direct methods [12–14], thus requiring the inclusion of a relativistic correc term. Also, at incident energies larger than the absorption edges of a particular elem the value of the dispersion term is expected to approach this relativistic correction t It is also expected that the inclusion of the relativistic corrections calculated u either S-matrix approach or higher order multipole approximation together with retardation effects [15, 16], can yield good agreement between the experiment theory. In view of all these, it is worthwhile to evaluate the dispersion corrections f and $f''(E)$ using the experimental photoeffect cross-sections. In this paper, we re the dispersion corrections for Cu and Ag calculated using its photoeffect cross-sect derived from their measured total attenuation cross-sections by subtracting a s contribution of the sum of the coherent and incoherent scattering cross-sect interpolated from the XCOM data [9] for the energies of present interest. The t attenuation cross-sections were measured in the energy range 5–85 keV in a nar beam good geometry set up, by employing a high resolution hyper-pure german detector. To the values of f^+ so obtained at each energy, the relativistic corrections Δ_i have been separately added and the resulting $f_i'(E)$ values for copper and silver are compared with the available theoretical and experimental data.

2. Theoretical background

A comprehensive theoretical account of the anomalous scattering factors and their evaluation based on the photoeffect cross-sections is given in [7, 17]. In the energy region of current interest, the primary interaction of photons with atoms are photoeffect, coherent and incoherent scattering. Below 100 keV, the interaction of photons can be such that the photons are highly scattered elastically by the bound atomic electrons or completely absorbed. In this energy range the S-matrix channels of nuclear photoeffect, pair production in the field of nucleus and electron and Delbrück scattering can be neglected [7, 17]. So, the amplitude of Rayleigh scattering in the forward direction can be expressed as [18]

$$\mathrm{A}(E) = r_0 f(E) = r_0\{-N + f'(E) + if''(E)\}, \tag{1}$$

where N is the total number of bound electrons in the atom, r_0 is the classical electron radius, E is the energy of the photon and $f'(E)$ and $f''(E)$ are the dispersion corrections. If we neglect the spin flip processes, $f'(E)$ and $f''(E)$ are related by the modified Kramers–Kronig transform given by

$$f'(E) = f'(\infty) - ({}^2/_\pi)\, P \int_0^\infty \frac{E' f''(E')}{(E^2 - E'^2)} \mathrm{d}E', \tag{2}$$

where $f'(\infty)$ is the high energy limit. Following Wang [19], Wang and Pratt [20] and Henke *et al* [7], we can write

$$f''(E) = \frac{1}{2hcr_0} E\tau \tag{3}$$

according to the optical theorem where τ is the photoeffect cross-section. This is written after neglecting the contribution of the photoexcitation (bound–bound transition) cross-section and the bound pair production cross-section to the total cross-section [7, 19 and 20].

Using (3) in (2), we have

$$f'(E) = f'(\infty) - \frac{1}{\pi hcr_0} P \int_0^\infty \frac{E'^2 \tau(E')}{(E^2 - E'^2)} \mathrm{d}E'$$

or

$$f_i'(E) = \Delta_i - \frac{1}{\pi hcr_0} P \int_0^\infty \frac{E'^2 \tau(E')}{(E^2 - E'^2)} \mathrm{d}E' = \Delta_i - f^+(E), \tag{4}$$

where Δ_i are the various relativistic corrections [15, 16] and $f^+(E)$ are the non-relativistic values of $f_i'(E)$. The relativistic corrections Δ_i based on the S-matrix approach [15] for copper and silver are $-0{\cdot}0878$ and $-0{\cdot}285$ while the values based on

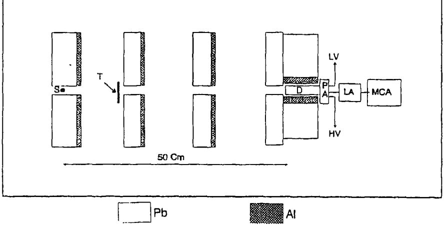

Figure 1. Schematic diagram of the experimental set up. S-Radioactive source, T-target, D-detector, PA-preamplifier, LA-linear amplifier, LV-low voltage supply, HV-high voltage supply, MCA-multichannel analyser.

Table 1. Radioactive sources, their half life and energies.

Isotopes	Mode of decay	Half life	Energy (keV)	
^{55}Fe	EC	2·7 years	5·895	(Mn–K_α)
^{57}CO	EC	270 days	6·4	(Fe–K_α)
			14·4	(γ-ray)
^{65}Zn	EC	245 days	8·041	(Cu–K_α)
^{75}Se	EC	120 days	10·53	(As–K_α)
^{113}Sn	EC	118 days	24·14	(In–K_α)
^{133}Ba	EC	7·5 years	30·8	(Cs–K_α)
			35·0	(Cs–K_β)
			81·0	(γ–ray)
^{170}Tm	β^-	127 days	52·01	(Yb–K_α)
			84·3	(γ–ray)
^{191}Os	β^-	15 days	64·3	(Ir–K_α)
^{203}Hg	β^-	47 days	70·833	(Tl–$K_{\alpha 2}$)
			72·87	(Tl–$K_{\alpha 1}$)

3. Experimental details

For an accurate calculation of the dispersion corrections, it is essential to measure the total attenuation cross sections of the element of interest with a good degree of accuracy over a wide range of energies. For this purpose, we have measured the total attenuation cross-sections of copper in the energy range 5 to 85 keV in a narrow beam good geometry set up. A schematic diagram of the experimental set up is as shown in figure 1. A list of radioactive isotopes used in the present investigation is given in table 1. The detector used was a high resolution hyper-pure germanium detector operated at liquid nitrogen temperature. It was of ORTEC make and model 23210. It had a specified resolution of 2·1 keV at 1330 keV. The detector signal was suitably amplified by a linear analyser. There was an in-built provision for dead time correction in the multichannel analyser. The entire experiment was carried out in an air-conditioned room where the mains voltage was stabilized. Due to this, there was practically no drift in the amplifier gain as a result of which there was no channel shift in the energy spectra. The elemental foils of Cu and Ag used were 99·9% pure and were made from thin uniform sheets. The thickness of the foils were chosen such that $0{\cdot}1 < \mu t < 0{\cdot}5$, where μ is the mass attenuation coefficient and t is the thickness of the foil in g/cm^2.

In the transmission experiment, spectra were recorded with and without the sample, by placing the target foils alternately in the path of the beam. The counting time was chosen such that at least 10^5 to 10^6 counts were recorded under the respective photopeaks. Thus the statistical uncertainty due to counting was kept below 0·3%. Due to the limitations imposed by the resolution of the detector, it was not possible to resolve the K_α photopeaks reasonably well. Hence the photon energies in these cases were taken to be the average of the two K_α lines. However, it was possible to separate out the $K_{\alpha 1}$ and $K_{\alpha 2}$ photopeaks of ^{203}Hg as well as K_α and K_β photopeaks of ^{133}Ba by a suitable peak fitting routine. So in these cases, the two energies were separately considered. All the photon energies used in the present study have been listed in table 1.

From the respective photopeaks, the unattenuated intensity I_0 and the attenuated intensity I were calculated. Using these values, the total attenuation cross section σ was calculated using the relation

$$\sigma = \frac{A}{N_0 t} \ln\left(\frac{I_0}{I}\right), \tag{5}$$

where A is the molecular weight of the element, N_0 is the Avogadro number and t is the thickness in g/cm^2.

4. Results and discussion

In the present study the total attenuation cross-sections have been measured for elements Cu and Ag at energies 5·895, 6·4, 10·53, 14·4, 24·14, 30·8, 35·0, 52·01, 64·3, 70·833, 72·87, 81·0 and 84·3 keV. The possible sources of error in the present method are:

a) counting statistics,
b) multiple scattering,
c) small angle scattering contribution,
d) non-uniformity of the sample,
e) sample impurity,
f) photon dose build up effects,
g) dead time of the counting instrument and
h) pulse pile up effects.

The error due to counting statistics was kept below 0·3% by accumulating 10^5–10^6 counts within the photopeak. The effects of multiple scattering have been corrected for in the present study by employing an extrapolation technique [21]. A detailed discussion of the errors is given in an earlier paper [22]. The overall error in the present

The experimental total attenuation cross-sections of the elements Cu and Ag listed in table 2. The cross-section values listed in table 2 have been plotted in figur and 3 as a function of energy alongwith the compiled data of Berger and Hubbell the Chantler data [17] interpolated to the energies of present interest, as well as som the availale experimental data cited in Saloman *et al* [8]. The data of Wang *et al* [for copper is shown in figure 2 for comparison. In the inset of each of these figur given the percentage deviation of the present values from the interpolated theore values and other available experimental values. From these figures, we can concl that there is a reasonably good agreement among the present values and the avail values [9, 17, 8] within 3–4% which is the range of experimental errors.

4.1 *Derivation of the photoeffect cross sections*

From the measured values of the total attenuation cross-section listed in table 2, total photoeffect cross-sections were derived for the elements Cu and Ag by subtrac the sum of the corresponding coherent scattering and incoherent scattering cr sections. The scattering cross-sections were interpolated from the XCOM data base to the energies of interest. Since the sum of the subtracted scattering contributio a small fraction of the total attenuation cross-section, the subtraction techniq justified in the energy region of present study.

The photoeffect cross-sections of the elements Cu and Ag so obtained are liste table 3 along with photoeffect cross-sections interpolated from XCOM [9] Hubbell values [6]. It is expected that the error on the total attenuation cross-secti carried over to the corresponding photoeffect cross-section. It is interesting to n from table 3 that the present values are generally in better agreement with the XC values [9] which are the Scofield's unrenormalized data than with the Hubbell va [6]. The Hubbell values are the photoeffect cross-section values which include re malization such that they correspond to a relativistic Hatree–Fock model rather t the Hartree–Slater model used in the original calculation of Scofield [10].

Table 2. Total attenuation cross sections (b/atom) (Experimental errors are to the extent of 3%–4%)

Energy (keV)	Copper	Silver
5·895	12618	89101
6·4	10074	71222
8·041	5388	38286
10·53	20610	18351
14·4	8583	7959
24·14	2200	1967
30·8	1060	6100
35	773	4399
52·01	248	1467
64·3	137	831
70·833	110	643
72·87	102	597
81	78	453
84·3	71	408

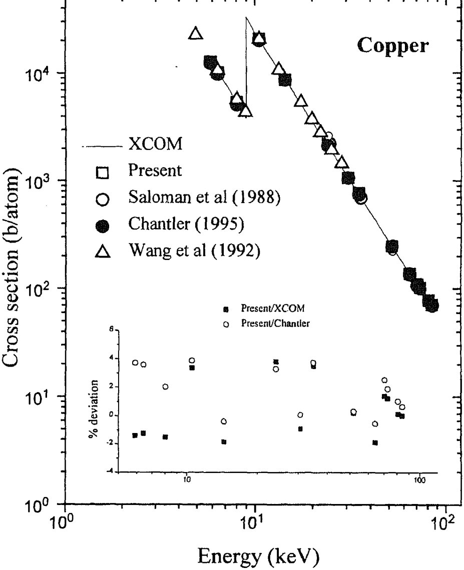

Figure 2. Plot of total attenuation cross-section for copper as a function of photon energy and in the inset percentage deviations are given (see text for details).

4.2 *Calculation of imaginary part of the anomalous scattering factor $f''(E)$*

The present values of the photoeffect cross-sections were used to calculate $f''(E)$ from equation (3) for the elements Cu, Ag at each energy of interest. The $f''(E)$ values have been plotted as a function of energy in figures 4 and 5. It can be noticed from the figures that the present values are systematically higher than Hönl's values [24] whereas these agree very well with the other available data [16, 17] at all the energies of current interest.

4.3 *Calculation of real part of the anomalous scattering factor $f'(E)$*

The dispersion correction $f'(E)$ was determined by the numerical evaluation of the dispersion integral in (4). For this purpose, it is essential to have the photoeffect cross-section data over a wide range of energies. Since our measurements were made at

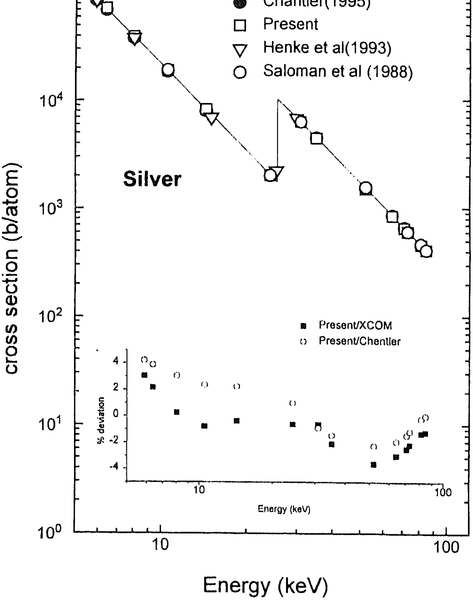

Figure 3. Plot of total attenuation cross-section for silver as a function of photon energy and in the inset percentage deviations are given (see text for details).

obtain best fit values of the photoeffect cross-sections. For this purpose, a polynomial fitting procedure was adopted to arrive at a relation between In τ vs In E. The correlation coefficient obtained in the case of both the elements was about 0·9999 but differed only in the fifth decimal place for the first, second and the third order fitting. In view of this and also since it was more convenient for further calculation, a logarithmic linear regression analysis was done on either side of the K-edge and a relation between In τ vs In E was established. The values of the cross-section at the K-edge were calculated from the lower branch as also the upper branch of In τ vs In E plot using the corresponding best fit coefficients. It is clear that the difference between the two values at the K-edge should yield the K-shell photoeffect cross-section τ_k of the elements. Using this value of τ_k and the slope of the upper

Table 3. Photoeffect cross sections (b/atom) (The errors are to the extent of 3%–4%).

Energy (keV)	Copper	Silver
5·895	12345	88368
	12500	85700
	12103	83288
6·4	9820	70534
	9960	69000
	9638	67088
8·041	5185	37716
	5260	37700
	5357	36660
10·53	20449	18002
	19900	18100
	19552	17682
14·4	8475	7630
	8630	7660
	8521	7484
24·14	2138	1850
	2060	1800
	2271	1854
30·8	1013	5968
	1020	6010
	1014	5958
35·0	732	4186
	705	4280
	700	4237
52·01	219	1395
	219	1450
	218	1440
64·3	114	774
	116	799
	116	795
70·833	88·18	592
	86·6	608
	84	605
72·87	80·28	547
	79·5	560
	77	558
81·0	57·59	408
	57·7	414
	57	412
84·3	51·05	365
	51·1	369
	51	368

First line: present values; Second line: XCOM values;

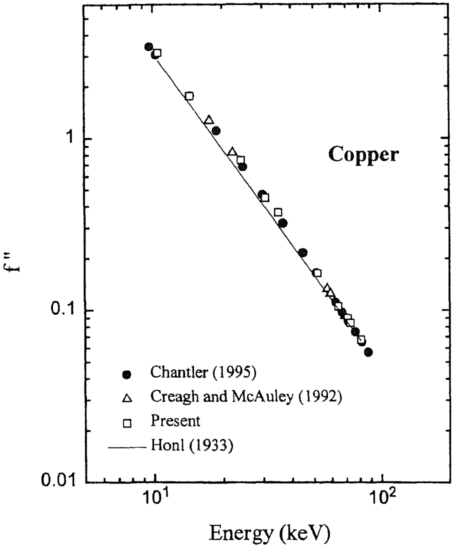

Figure 4. Plot of dispersion correction $f''(E)$ for copper versus the ener
present interest.

branch n, the value of the oscillator strength "g_k" for the K-shell of the elements Cu a
were evaluated using the relation

$$g_k = \frac{E_k \tau_k}{(n-1)} \frac{\alpha}{2\pi^2 mc^2 r_0^2},$$

where E_k is the edge energy, α is the fine structure constant, r_0 is the classical electron
n is the slope of the upper branch (portion above the K-edge) of the In τ vs In E plot a
is the rest energy of the electron. Equation (6) is a modified form of the relation

$$g_k = \frac{mcE_k \tau_k}{2\pi^2 \hbar e^2 (n-1)}$$

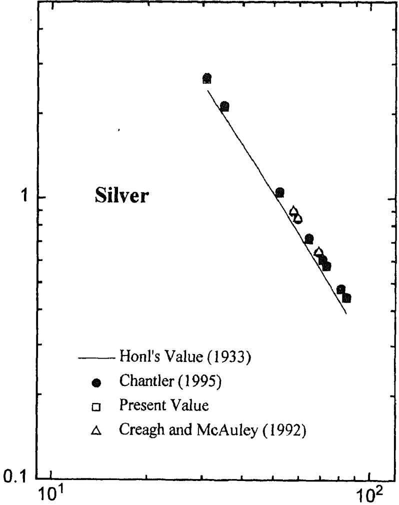

Figure 5. Plot of dispersion correction $f''(E)$ for silver versus the energies of present interest.

0·01 keV. The upper limit of integration was chosen to be 600 keV up to which the data measured earlier by Umesh *et al* [22] were used. The contribution to the integral for energies higher than this can be shown to be negligible.

Thus, the dispersion correction $f^+(E)$ as related to the photoeffect cross-section of the elements Cu and Ag was evaluated from equation (4) for the energies 5·895, 6·4, 8·041, 10·53, 14·4, 24·14, 30·8, 35·0, 52·01, 64·3, 70·833, 72·87, 81·0 and 84·3 keV. The overall error on $f^+(E)$ values was below 5%. To the values of $f^+(E)$, the various relativistic corrections Δ_i were separately added and the resulting values of $f_i'(E)$ were obtained.

The values of $f_i'(E)$ at the above energies are plotted along with the available theoretical and experimental data for the elements as a function of energy in figures 6 and 7. The curve is drawn through the Chantler's theoretical data points to indicate the trend of variation of $f_i'(E)$ with respect to energy. It is clear from these figures that the present values of $f_i'(E)$ in which the relativistic correction Δ_1 suggested by Creagh and McAuley [16] and Δ_2 of S-matrix prediction [15] are included, show good agreement

5. Conclusions

Following conclusions can be drawn based on the present study. The experimental photoeffect cross-sections of elements Cu and Ag in the low energy region 5–100 keV are in better agreement with the unrenormalized Scofield's values than with the renormalized values, within the range of experimental errors. It is possible to obtain reasonable values of the dispersion corrections $f'(E)$ and $f''(E)$ by measuring fairly accurate total attenuation cross-sections in a narrow beam good geometry set up by employing a high resolution detector to detect photons emitted from radioisotopes. The present study points to the fact that within the range of experimental errors, the real part of the dispersion correction to which the relativistic corrections calculated either by Creagh and McAuley based on the multipole approximation with retardation effects or Kissel and Pratt's *S*-matrix approach have been included are in better agreement with the theoretical values of Chantler.

Acknowledgements

One of the authors (Sandiago) would like to thank the University Grants Commission, India for awarding the F.I.P. teacher fellowship during the course of the present

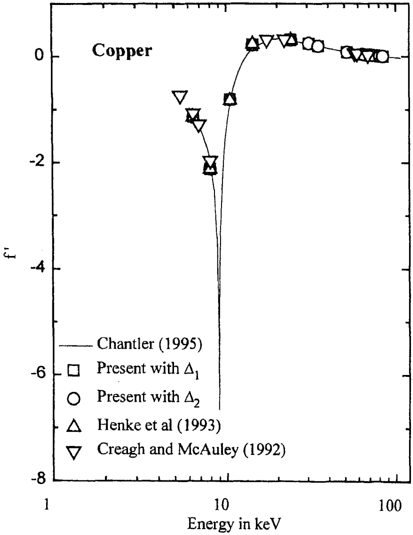

Figure 6. Plot of dispersion correction $f'(E)$ for copper as a function of photon energies of present interest.

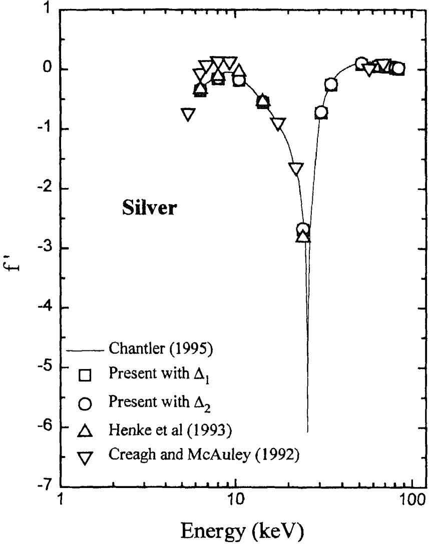

Figure 7. Plot of dispersion correction $f'(E)$ for silver as a function of photon energies of present interest.

investigation. The useful discussion with Prof. S Ramasheshan and his encouragement is also gratefully acknowledged.

References

[1] J H Hubbell, *J. Res. Natl. Inst. Stand. Technol.* **95**, 689 (1990)
[2] D F Jackson and D J Hawkes, *Phys. Rep.* **70**, 169 (1981)
[3] E Storm and H I Israel, *At. Data Nucl. Data Tables* **A7**, 565 (1970)
[4] W J Veigele, *At. Data Nucl. Data Tables* **5**, 51 (1973)
[5] J H Hubbell, W J Veigele, E A Briggs, R T Brown, D T Cromer, and R J Howerton, *J. Phys. Chem. Ref. Data* **4**, 471 (1975)
[6] J H Hubbell, *Int. J. Appl. Radiat. Iso.* **33**, 1269 (1982)
[7] B L Henke, P Lee, T J Tanaka, R L Simabukuro and B K Fujikawa, *At Data Nucl. Data Tables* **27**, 1 (1982)
B L Henke, E M Gullikson and J C Davis, *At. Data Nucl. Data Tables* **54**, 181 (1993)
[8] E B Saloman, J H Hubbell and J H Scofield, *At Data Nucl. Data Tables* **38**, 1 (1988)
[9] M J Berger and J H Hubbell, *XCOM: Natl. Bureau. Stand. Report NBSIR* **87**, (1987)

[11] L Gerward, *Indian J. Phys.* **B67**, 527 (1993)

[12] G Martens and P Rabe, *Phys. Status Solidi* **A58**, 415 (1980)

[13] T Fukamachi, S Hosoya, T Kawamura and J Hastings, *J. Appl. Crystal.* **10**, 321 (1977)

[14] U Bonse, I Hartman-Lotsch and H Lotsch, *Nucl. Instrum. Methods* **208**, 603 (1983)

[15] L Kissel and R H Pratt, *Acta. Cryst.* **A46**, 170 (1990)

[16] D C Creagh and W J McAuley, *Int. Tables X-ray Cryst.* **C**, 206 (1992)

[17] C T Chantler, *J. Phys. Chem. Ref. Data* **24**, 71 (1995)

[18] B Zhou, Lynn Kissel and R H Pratt, *Phys. Rev.* **A45**, 2983 (1992)

[19] M S Wang, *Phys. Rev.* **A34**, 636 (1986)

[20] M S Wang and R H Pratt, *Phys. Rev.* **A28**, 3115 (1983)

[21] K S Puttaswamy, Ramakrishna Gowda and B Sanjeevaiah, *Can. J. Phys.* **57**, 92 (1979)

[22] T K Umesh, C Ranganathaiah, K S Puttaswamy, Ramakrishna Gowda and B Sanjeevaiah *Phys. Rev.* **A23**, 2365 (1981)

[23] Wang Dachun, Ding Xunliang, Wang Xinfu, Yang Hua, Zhou Hongyu, Shen Xinyin and Zhu Guanghua, *Nucl. Instrum. Methods Phys. Res.* **B71**, 241 (1992)

[24] H Hönl, *Ann. Phys.* **18**, 625 (1933)

[25] R W James, *The Optical Principles of the Diffraction of X-rays* (BEL, London, 1962).

Probability distribution of normalized structure factor magnitudes for a centrosymmetric crystal with planar molecules in the unit cell

SABITA DAS and G B MITRA*
Victoria College, 78B, Acharya Prafulla Chandra Road, Calcutta 700 009, India
* CSS Department, Indian Association for the Cultivation of Science, Calcutta 700 032, India

MS received 18 October 1996; revised 17 April 1997

Abstract. The reasons and conditions for applicability of the Cauchy distribution law for crystal structure factor components are discussed. It is shown that the standardized structure factors of centrosymmetric crystals are quite prone to be Cauchy distributed for crystals having planar molecules in their unit cells.

Keywords. Cauchy distribution; planar molecules.

PACS No. 61·10

1. Introduction

Recently Mitra and Das [1] considered the use of Cauchy distribution law for the structure factor components and derived an expression for the probability of the Sayre relation being valid.

It is to be pointed out that Mitra and Das (*loc. cit.*) have established that for noncentrosymmetric crystals, there is a high probability of the distribution function being Gaussian. Hence in this paper only centrosymmetric crystals have been discussed.

2. Theoretical considerations for the Cauchy distribution

Since we are discussing the case of centrosymmetric crystals only because of the reasons mentioned above, we may write down the expression for the structure factor $F\,(hkl)$ for a general reflection (hkl) as

$$F\,(hkl) = \sum_j f_j \cos 2\pi(hx_j + ky_j + lz_j), \tag{1}$$

where f_j is the atomic scattering factor for the jth atom in the asymmetric unit of the unit cell in the (hkl) direction while $(x_j\,y_j\,z_j)$ are its fractional components in the a, b and c directions which are the repetition vectors along the principal crystallographic axes. The multiplicity factor 2 for space group $p\bar{1}$ has been omitted from equation (1) since it acts only as a constant scale factor. For space group $p\bar{1}$, only the equivalent pair of positions $(x_j\,y_j\,z_j)$ and $(\bar{x}_j\,\bar{y}_j\,\bar{z}_j)$ is relevant. For other space groups containing centres of

$$t = \frac{\zeta}{\sqrt{[l/n\,\Sigma_j^n(\zeta_n - a)^2]}}, \tag{2}$$

(where ξ is a Gaussian statistical variate, a and n are the average and number of variates in the population considered) is known to be distributed according to the student's distribution law

$$P(t) = \frac{\Gamma((m+1)/2)}{\sqrt{m\pi}\,\Gamma(m/2)}\left(1 + \frac{t^2}{m}\right)^{-((m+1)/2)} \tag{3}$$

In equation (3), $\Gamma(n)$ is a gamma function and $(m+1)$ is the appropriate degree of freedom.

Now let $F_{\underset{\sim}{h}}$ - the structure factor of the reflection $\underset{\sim}{h} = (h, k, l)$ take the place of ξ in (2). Evidently $a = \langle F_{\underset{\sim}{h}} \rangle = 0$ and

$$\begin{aligned} t &= \frac{F_{\underset{\sim}{h}}}{\sqrt{(1/n)\,\Sigma\, F^2_{\underset{\sim}{h}n}}} \\ &= \frac{F_{\underset{\sim}{h}}}{\sqrt{\langle F^2 \rangle}} \\ &= \frac{F_{\underset{\sim}{h}}}{\sqrt{\Sigma_j f_j^2}} \\ &= E_{\underset{\sim}{h}} \quad \text{(by definition).} \end{aligned}$$

3. Discussion

Let us consider the case of centrosymmetric crystals consisting of planar molecules. Let us examine the simplest case of the molecule lying along the face $x \circ z$ with $(x \circ z)$ and $(\bar{x} \circ \bar{z})$ being the corresponding positions of atom in the characteristic space group $P\bar{1}$. In other space groups of the centrosymmetric system, there will be additional equivalent positions $(x_1 \circ z_1)$ and $(\bar{x}_1 \circ \bar{z}_1)$, $(x_2 \circ z_2)$ and $(\bar{x}_2 \circ \bar{z}_2)$ etc., Each such pair gives rise to the standardized structure factor

$$E_{hkl} = \sum_j e_j \cos 2\pi(hx_j + lz_j) \tag{4}$$

$$= \sum_j e_j \cos 2\pi\, hx_j \cos 2\pi\, lz_j - \sum_j e_j \sin 2\pi\, hx_j \sin 2\pi\, lz_j. \tag{5}$$

Here,

$$e_j = \frac{f_j}{\sqrt{\Sigma_j f_j^2}}$$

and

$$e_j^2 = \frac{f_j^2}{\Sigma_j f_j^2}.$$

Therefore,

$$\sqrt{\langle e_j^2 \rangle} = \sqrt{\left\langle \left[\frac{\Sigma_j f_j^2}{\Sigma_j f_j^2} \right] \right\rangle} = 1$$

When the molecule lies partially along the plane xoz, but at a fixed height Y above it along the Y-direction, we have

$$\begin{aligned} E_{hkl} &= \sum_j e_j \cos 2\pi (hx_j + K\,Y + lz_j) \\ &= \sum_j \{ e_j \cos 2\pi\, K\,Y (\cos 2\pi\, hx_j \cos 2\pi lz_j - \sin 2\pi hx_j \sin 2\pi lz_j) \\ &\quad - e_j \sin 2\pi\, KY (\cos 2\pi\, hx_j \sin 2\pi lz_j + \sin 2\pi hx_j \cos 2\pi lz_j) \}. \end{aligned} \tag{6}$$

Characteristic terms in equations (5) and (6) are

$$\begin{pmatrix} \cos 2\pi hx \\ \sin 2\pi hx \end{pmatrix} \quad (\cos 2\pi lz \quad -\sin 2\pi lz)$$

and

$$\begin{pmatrix} \cos 2\pi hx \\ \sin 2\pi hx \end{pmatrix} \quad (\cos 2\pi lz \quad -\sin 2\pi lz)$$

$$-\begin{pmatrix} \cos 2\pi hx \\ \sin 2\pi hx \end{pmatrix} \quad (\sin 2\pi lz \qquad \cos 2\pi lz)$$

respectively. In either case, the smallest number of independent variables on which the form may be brought by a nonsingular linear transformation (Cramer, *ibid.*) is two. Thus the t for E_{hkl} is E_{hkl} and $m + 1$ of equation (3) is 2. Hence $m = 1$. Substituting these in (3) we have

$$P(E) = \frac{1}{\pi}(1 + E^2)^{-1} \tag{7}$$

which is the standard Cauchy's distribution.

If due to other space group symmetries, there are pairs of equivalent points $(x_1 o z_1)$ $(\bar{x}_1 o \bar{z}_1)$; $(x_2 o z_2)$ $(\bar{x}_2 o \bar{z}_2)$ etc., and the net standardized structure factor E will be sum of them i.e.

$$E = E_1 + E_2 + \cdots + E_n + \cdots,$$

where E_n is the standardized structure factor due to the atom pair at $(x_n o z_n)$ and $(\bar{x}_n o \bar{z}_n)$, then as per discussions above, each of E_1, E_2 etc., will have distributions of etc. Since the convolution of a number of Cauchy distributions will be a Cauchy distribution itself, E will again have a distribution of the Cauchy type. Thus we have established that centrosymmetric crystals containing planar molecules lying on a face of the unit cell or parallel to it will have structure factor components distributed according to Cauchy's law.

When the molecules lie parallel to a general plane $(x\,y\,z)$, it can be considered to have been originally lying parallel to the $(x\,o\,z)$ plane and then through one or more rotations (not necessarily crystallographic) attained its final orientation. Gnedenko [3] has shown that such rotation leaves the law of distribution unaltered. So the Cauchy distribution derived for the $(x\,o\,z)$ plane remains Cauchy distributed even when the planar molecule lies parallel to a general (xyz) plane. Thus, it is evident that centrosymmetric crystals having planar molecules in their unit cells will have great likelihood of having its standardized structure factors being Cauchy distributed. This rationalizes the conclusions of Mitra and Das [*loc. cit.*] arrived at empirically through experimental observations only.

It has already been mentioned in Mitra and Das [1] that the distribution discussed by them is a truncated Cauchy distribution. While for the pure Cauchy distribution the moments do not exist, for the truncated Cauchy distribution all the moments exist. A real intensity distribution has necessarily a minimum readable value for intensity which constitutes the limit of truncation.

Acknowledgement

One of the authors (GBM) is indebted to the Council of Scientific and Industrial Research, Government of India, for financial support.

References

[1] G B Mitra and S Das, *Acta Cryst.* **A45**, 314 (1989)
[2] H Cramer, *Mathematical methods of Statistics* (Princeton University Press, 1957) p. 237
[3] B V Gnedenco, *The theory of probability* (Mir Publishers, 1978) p. 155

Activation energy of hydrogen in Lu

N SINGH'and B KUMAR
Department of Physics, M. D. University, Rohtak 124001, India

MS received 14 February 1996; revised 6 January 1997

Abstract. The impurity induced charge density is calculated in jellium by solving the Schrödinger equation self-consistently following the procedure of Manninen and Nieminen and using Kohn–Sham density functional formalism. The host-ion contribution is included through the spherical solid model potential (SSMP). The calculated activation energy 0·27 eV is found in good agreement with experimental value $0{\cdot}28 \pm 0{\cdot}02$ eV. The estimated residual resistivity 1·02 $\mu\Omega$ cm/at% for Lu–H system using the resulting phase shifts agrees reasonably well with the observed value $1{\cdot}75 \pm 0{\cdot}10$ $\mu\Omega$ cm/at%. The calculated configurational energy shows that hydrogen prefers tetrahedral(T)-sites over octahedral(O)-sites in Lu matrix. This has been confirmed by Bonnet experimentally. A very shallow value of *s*-type bound state of energy $-0{\cdot}00316$ Ryd predicts that there is no formation of lutetium hydride solution and H^+ exists as a free ion in Lu matrix.

Keywords. Induced charge density; impurity potential; spherical solid model potential; self energy; residual resistivity; activation energy.

PACS No. 66·30

1. Introduction

The neutron scattering analysis [1] for LuH predicts that hydrogen occupies the tetrahedral interstices of the Lu lattice in α-phase. The lutetium–hydrogen solid solution shows unusual stability [2]. The stability of the α-phase is because of an unusual short-range pairing order of the hydrogen as shown by diffuse-elastic-neutron scattering (DENS) studies [3]. Although, atomic hydrogen is the simplest solute in a metal that can be thought of, a first principle theory of Lu–H interaction has yet to be developed. The standard method for calculating pairwise interaction in simple metals is based on pseudopotential theory [4–6]. The first self-consistent calculations of the non-linear screening of a proton have been made by Popovic *et al* [7] and Almbladh *et al* [8]. Since then a number of groups have published similar results [9–11]. The electronic structure of hydrogen in lutetium using Hohenberg–Kohn–Sham [12, 13] density formalism have been calculated [14] earlier, where the contribution of host-ions was neglected altogether. In this paper, we have made an attempt to calculate the electronic structure of hydrogen following the approach of Manninen and Nieminen [15]. The electron–ion interactions have been included through spherical solid model potential (SSMP) [15]. The induced charge density so obtained is further used to calculate the activation energy of hydrogen in lutetium matrix. The resulting phase shifts obtained while solving the Schrödinger equation have been used to estimate the residual resistivity of lutetium-hydrogen system.

The plan of the paper is as follows. The necessary formalism is presented in § 2. The calculations and results are presented in § 3 and are summarized in § 4.

2. Theory for nonlinear screening and screening impurity potential

Single electron eigenvalues ε_k and corresponding radial wave function $R_{lk}(r)$ are obtained by solving the following one particle Schrödinger equation

$$\left[-\frac{1}{2}\nabla^2 + V_{\text{eff}}(r) + \frac{l(l+1)}{2r^2} - \varepsilon_k\right] r R_{lk}(r) = 0. \tag{1}$$

For the continuum states $\varepsilon_k = k^2/2$, zero of energy is taken to be the potential far from the impurity where its effect almost vanishes. The effective potential field in which the electron moves, is written as

$$V_{\text{eff}}(r) = -\frac{Z}{r} + V(r) + V_{\text{ss}}(r) + V_{\text{xc}}(n(r)) - V_{\text{xc}}(n_0(r)), \tag{2}$$

for a spherically symmetric potential field. $V_{\text{xc}}(n(r))$ is the functional derivative of a universal exchange and correlation energy functional of the electron mean density. $n_0(r)$ is the charge density of jellium corresponding to host-matrix. $n(r)$ is the sum of jellium charge density and the charge density arises due to host ions and impurity. The impurity potential

$$V(r) = \int \frac{\delta n(r')\,\mathrm{d}r'}{|r - r'|} \tag{3}$$

can be obtained by solving Poisson equation

$$\nabla^2 V(r) = -4\pi\delta n(r). \tag{4}$$

Ideally, the potential $V(r)$ and the induced charge density $\delta n(r)$ should be determined self-consistently so that the eigenstates $R_{lk}(r)$ produce a charge density which is identical to that obtained from (4). In the crystal, the conduction band states are represented by the bloch function. As a result the impurity site will no longer follow the spherical symmetry of jellium model and the direct solution of second-order partial differential equation for a single electron eigenstates is no longer possible. The success has been achieved in the self-consistent solution for a proton in jellium by taking a part of ionic potential that is $V_{\text{ss}}(r)$ which is spherically symmetric around impurity [15–17]. Very recently, the Green's function matrix method has been extended to include the band structure description of the host metal [18].

In order to find self-consistent potential $V(r)$, Popovic *et al* [7] considered the case of electron gas. The induced electron charge density due to impurity in jellium is written as

$$\begin{aligned}\delta n(r) &= n(r) - n_0(r)\\ &= \frac{1}{\ } \int^{k_{\mathrm{F}}} \mathrm{d}k k^2 \sum (2l+1)[R_{lk}^2(r) - j_l^2(kr)] + 2R_b^2(r),\end{aligned} \tag{5}$$

where k is the electron wave vector and k_F is the Fermi momentum. s-type bound state sometimes occur; therefore the bound state charge density is also added in (5). Equations (1) and (2) are solved self-consistently. For starting the iteration, the following host-impurity screened Coulomb potential was considered by Popovic *et al* [7]:

$$V_{sc}(r) = -\frac{Z}{r}\exp(-\alpha r^{\beta}). \tag{6}$$

With parameter β fixed, the parameter α was determined so that the Friedel sum rule

$$Z = \frac{2}{\pi}\sum_{l}(2l+1)\delta_l(k_F) \tag{7}$$

is satisfied with high accuracy. $\delta_l(k_F)$ is the phase shift at Fermi sphere corresponding to angular momentum quantum number l. By varying β, this iterative procedure was repeated until both the initial potential $V_{sc}(r)$ and self-consistent potential $V_{eff}(r)$ satisfy the Friedel sum rule simultaneously.

After including $V_{ss}(r)$, it is always not possible to find out the proper values of α and β which may satisfy the Friedel sum rule for both $V_{sc}(r)$ and $V_{eff}(r)$ simultaneously. Therefore, Manninen *et al* [11] suggested that the impurity potential $V(r)$ may be obtained by rewriting the Poisson equation as

$$\nabla^2 V - k_{TF}^2 V = -4\pi\delta n(r) - k_{TF}^2 V. \tag{8}$$

By solving (8), we get

$$V(r) = \frac{1}{4\pi}\int \mathrm{d}r \frac{\exp(-k_{TF}|r-r'|)}{|r-r'|}\{4\pi\delta n(r') + k_{TF}^2 V(r')\}, \tag{9}$$

k_{TF} is Thomas–Fermi (TF) screening parameter $(4K_F/\pi)^{1/2}$. The TF potential may be chosen as the initial potential $V_{eff}^{(0)}(r)$ for solving (1) and (2) self-consistently. By solving (1) and (2) numerically, we get a new potential $V_{eff}^{(1)}$, which can be inserted again into (1). This procedure has to be continued until the potential $V_{eff}^{(1)}$ does not change in successive iterations. In this procedure, the Coulombic tail, if persists, gets truncated due to exponential term. The self-consistency is achieved within 0·01% in the charge density. Equation (9) leads to a convergence after 10 iterations when starting from TF potential. In the present calculation, the initial potential is taken in the form [19]

$$V_{sc}(r) = -\frac{Z}{r}\left(1 + \frac{\beta r}{2}\right)\exp(-\beta r) \tag{10}$$

instead of TF potential, because, it provides an accurate description of a proton impurity in both electron gas and transition metal [19]. The parameter β is determined self-consistently.

3. Calculations and results

3.1 *Spherical solid model potential (SSMP)* $V_{ss}(r)$

Spherical solid model potential $V_{ss}(r)$ is calculated following the procedure of

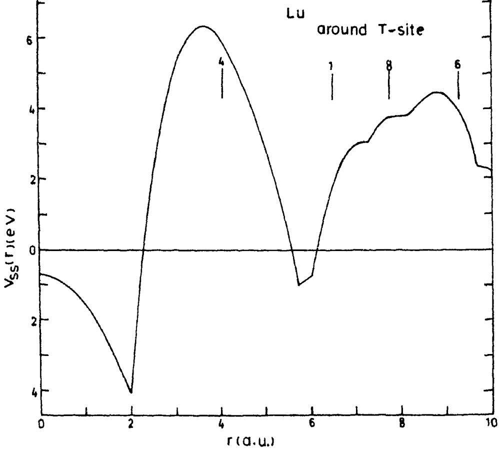

Figure 1. The spherical solid model potential (SSMP) $V_{ss}(r)$ for α-Lu around tetrahedral (T) site. The position and number of nearest neighbours to tetrahedral site are also indicated.

Table 1. The scattering phase shifts $\delta_l(E_F)$ for proton in α-Lu. $l = 0, 1, 2, \ldots$ are $s, p, d, \ldots$ phase shifts

δ_l	Putting $V_{ss}(r) = 0$	Including $V_{ss}(r)$
0	1·231149	1·256097
1	0·087173	0·100300
2	0·011145	0·007663
3	0·001653	0·000479
4	0·000302	−0·001200
5	0·000411	−0·001032
6	0·000276	−0·000428

$r_c = 2{\cdot}004$ a.u. is chosen to represent the host-ion potential for simplicity of the calculation. The atomic radius r_0 and c/a ratio for Lu are taken to be 3·629 and 1·586 a.u., respectively. The effective charge of the proton and bare host-ion are taken to be 1e and 3e, respectively. The calculated $V_{ss}(r)$ around tetrahedral site (T) is given in figure 1. The number of nearest neighbour and their positions with respect to T-site are indicated. It is found that Lu is more densely packed around T-site than O-site. $V_{ss}(r)$ has the maxima around the nearest neighbour sites and minima between the two sites.

It does not exhibit periodicity of the lattice, therefore, it can be regarded just as a correction term of $V_{\mathrm{eff}}(r)$ for discrete nature of the lattice. The relative magnitude of $V_{\mathrm{ss}}(r)$ also depends upon Z_{H} and r_{c}, because it is shifted upward by a constant amount $3r_0^2/2r_s^3$, which is obtained by taking $q \to 0$ limit of first part of $V_{\mathrm{ss}}(r)$ given by (6) in the paper of Manninen and Nieminen [15].

3.2 *Phase shifts and impurity potential*

The calculation of induced charge density and impurity potential is done using the method of Popovic *et al* [7] without including $V_{\mathrm{ss}}(r)$. The parametrized form of $V_{\mathrm{xc}}(n(r))$ proposed by Gunnarson and Lundquist [21] has been taken for the detailed calculation. The values of potential parameters (6) α and β are found to be 1·0739 and 1·2321 a.u., respectively. The resulting phase shifts are given in table 1. The above mentioned procedure (Popovic *et al* [7]) does not converge sometimes, therefore, the calculation of induced charge density by including $V_{\mathrm{ss}}(r)$ is done following the procedure of Manninen and Nieminen [15]. In the first step, the calculation is done for the perfect crystal by putting $n(r) = n_{\mathrm{H}}(r)$, $Z = 0$ and $\delta n(r) = n_{\mathrm{H}}(r) - n_0$. The self-consistently calculated $V_{\mathrm{H}}(r)$ and $\delta n_{\mathrm{H}}(r)$ are obtained. In the second step, the calculation is repeated with impurity at tetrahedral site by putting $\delta n(r) = n_{\mathrm{p}}(r)$, $Z = Z_{\mathrm{p}}$,

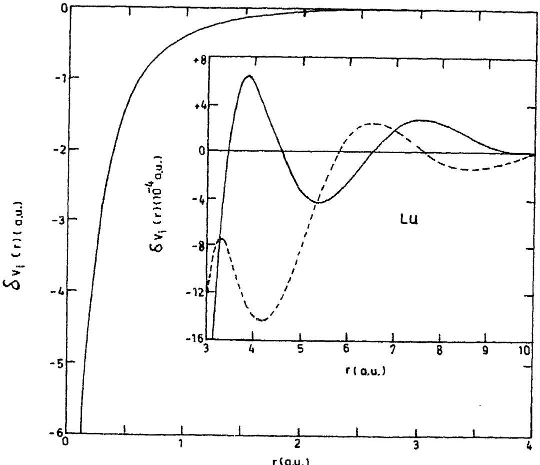

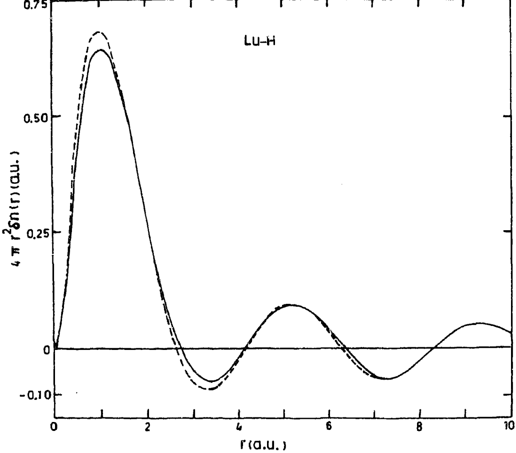

Figure 3. The proton induced charge density $4\pi r^2 \delta n_i(r)$ around tetrahedral site of α-Lu. The rest of the description is same as that of figure 2.

$\delta n(r) = n_p(r) - n_0$ and self-consistently calculated $V_p(r)$ and $\delta n_p(r)$ are obtained. In both the cases, the Friedel sum rule (7) is satisfied. The difference

$$\delta v_i(r) = V_p(r) - V_H(r), \tag{11}$$

and

$$\delta n_i(r) = \delta n_p(r) - \delta n_H(r) \tag{12}$$

gives the impurity interaction potential and the impurity induced charge density, respectively.

The phase shifts obtained by using $\delta v_i(r)$ are given in table 1. The s and p phase shifts are found dominating. The magnitude of s phase shift increases by 5% by including $V_{ss}(r)$. This shows that $V_{ss}(r)$ contributes considerably to the impurity scattering at Fermi surface in lutetium matrix. The SSMP is included in the self-consistent calculation only up to $r = 9$ a.u. because of convergency reasons [15]. The impurity potentials obtained by including $V_{ss}(r)$ and by putting off $V_{ss}(r)$ are shown in figure 2 by solid and dashed lines, respectively. The two potentials overlap each other. They can be separated from each other by plotting them on magnified scale. The impurity potential is strongly attractive in the vicinity of the impurity. It exhibits Friedel [22] oscillations at large distance. The lattice contribution enhances the magnitude of impurity interaction near the center of the proton. This is very much clear from figure 3, where we have

The value of $\delta v_i(r)$ obtained from (11) is fitted by least square method into the analytical form given by (10). The value of β so obtained is 1·7189 a.u. By solving Poisson equation using the analytical form given by (10) for δv_i, one can obtain the charge density

$$\delta n_i(r) = \frac{Z\beta^3}{8\pi} \exp(-\beta r). \tag{13}$$

This $\delta n_i(r)$ leads to the following impurity self-energy

$$\begin{aligned} E_{\mathrm{sc}} &= \frac{1}{2}\int \delta v_i(r)\,\delta n(r)\,\mathrm{d}r \\ &= -\tfrac{3}{32} Z^2 \beta \text{ a.u.} \end{aligned} \tag{14}$$

The self-energy of proton in lutetium matrix is found to be $-0·322$ Ryd.

3.4 *Activation energy*

The configurational energy is calculated by using $\delta n(r)$ and the analytical expression obtained in second order perturbation theory [4]. The configurational energy so calculated along O–O (octahedral), O–T (tetrahedral) and T–T directions in the $(11\bar{2}0)$ plane is shown in figure 4. The configurational energy is found maximum exactly at mid-point of both T–T and O–O paths. Along T–O path it is found maximum at about 40% distance of T–O path. The tetrahedral position is the most favourable position for hydrogen impurity to stay. The same conclusion has been drawn by neutron scattering analysis for $\mathrm{LuH}_{0·19}$ in α phase [1]. Because T–T barrier height is about 95% of T–O barrier and O–O barrier height is less than 50% of T–T barrier height, therefore, probable path for proton diffusion in α-Lu matrix may be off-symmetry paths and not the O–O–T and O–T–T paths. The minimum barrier height by which an impurity can cross is called the activation energy. It is found to be 0·27 eV. The experimental [23] value of activation diffusion energy (E_{ac}) is $0·28 \pm 0·02$ eV. Here it is to be noted that good agreement of calculated activation energy with experimental value is obtained by taking ionicity of hydrogen as 1. This suggests that the proton exists in ionic state in α-Lu. The diffusion coefficient is proportional to Boltzmann factor $\exp(-E_{\mathrm{ac}}/k_{\mathrm{B}}T)$, where k_{B} is Boltzmann constant.

3.5 *Residual resistivity*

To test the reliability of our calculated phase shifts, the residual resistivity $\Delta\rho$ is estimated using the following expression for liquid phase of solid [24]:

$$\Delta\rho = \frac{2·732}{k_{\mathrm{F}} Z_{\mathrm{H}}} = \sum_{l=0}^{\infty} (l+1)\sin^2(\delta_l - \delta_{l+1}), \tag{15}$$

where k_{F} is in atomic units and $Z_{\mathrm{H}} = 3$ for lutetium matrix. $\Delta\rho$ for dilute Lu –H system is calculated using the first seven phase shifts as the values of δ_l become too small for $l > 6$. The calculated value of $\Delta\rho$ obtained from jellium value of phase shifts is 1·00 μΩ

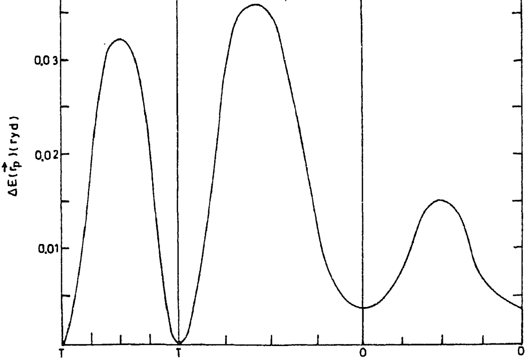

Figure 4. The configurational energy $\Delta E(r_p)$ of proton in α-Lu obtained by including $V_{ss}(r)$. r_p represents the position of proton with respect to O(T) site. Inset: O → octahedral positions; X → tetrahedral positions; O → host ions.

cm/at%. The corresponding result for $\Delta\rho$ by including $V_{ss}(r)$, i.e., 1·02 μΩ cm/at% is 2% higher. This value of $\Delta\rho$ agrees reasonably well with experimental values (1·25 ± 0·05) μΩ cm/at% and (1·70 ± 0·10) μΩ cm/at% reported by Daou and Bonnet [25] at 500 °C and 25 °C, respectively.

4. Conclusion

The induced charge density and impurity potential are calculated by including the effect of discrete lattice. Only the spherically symmetric part of the lattice potential is included. The Fermi surface is assumed essentially spherical and conduction electron wave functions are taken free particle-like. It is found that the SSMP changes the impurity scattering at Fermi surface significantly. The calculated configuration energy confirms the experimental [1] fact that hydrogen prefers T-sites over O-sites in Lu matrix. A very shallow s-type bound state of energy −0·00316 Ryd suggets that there is weak binding between proton and electron and that hydrogen does not form lutetium hydride solution and exists as a free ion in Lu matrix. The present calculations can be further improved by including crystal effects like relaxation effects, size effects in general and by taking proper account of d and f electrons in particular. In this respect, the present study is a step ahead in the process of understanding the Lu–H interactions. A careful calculations of KKR–Green function method [26] may provide better results. However, this will involve heavy computational effects.

Acknowledgements

One of the authors is grateful to Dr D K Avasthi for fruitful discussions while preparing the manuscript. Numerical calculations were done at PC/AT 386 purchased out of DST grant. Technical assistance provided by N K Abbi is greatly appreciated. Financial assistance received from Department of Science and Technology is also acknowledged.

References

[1] J E Bonnet, *J. Less-Common Met.* **49**, 123 (1976)
[2] J N Daou and J Bonnet, *C. R. Acad. Sci. Paris* **261**, 1675 (1965)
[3] O Blaschko, G Krexner, J N Daou and P Vajda, *Phys. Rev. Lett.* **55**, 2876 (1985)
[4] W A Harrison, *Pseudopotentials in the theory of metals* (Benjamin, New York, 1966)
[5] M Rasolt and R Taylor, *Phys. Rev.* **B11**, 2717 (1975)
[6] M Rasolt and R Taylor, *Phys. Rev.* **B11**, 2726 (1975)
[7] Z D Popovic, M J Stott, J P Carbotte and G R Piercy, *Phys. Rev.* **B13**, 590 (1976)
[8] C O Almbladh, U von Barth, Z D Popovic and M J Stott, *Phys. Rev.* **B14**, 2250 (1976)
[9] E Zaremba, L M Sander, H B Shore and J H Rose, *J. Phys.* **F7**, 1763 (1977)
[10] P Jena and K S Singwi, *Phys. Rev.* **B17**, 3518 (1978)
[11] M Manninen, P Hautojarvi and R Nieminen, *Soild State Commun.* **23**, 795 (1977)
[12] H Hohenberg and W Kohn, *Phys. Rev.* **136**, B864 (1977)
[13] W Kohn and L J Sham, *Phys. Rev.* **140**, A1133 (1965)
[14] N Singh, *J. Less-Common Metals* **113**, 225 (1985)
[15] M Manninen and R Nieminen, *J. Phys.* **F9**, 1333 (1979)
[16] F Perrot and M Rasolt, *Phys. Rev.* **B23**, 6534 (1981)
[17] F Perrot and M Rasolt, *Phys. Rev.* **B25**, 7331 (1982)
[18] B I Criag, *Phys. Status Solidi* **B115**, 53 (1983)
[19] C A Sholl and P V Smith, *J. Phys.* **F8**, 775 (1978)
[20] N W Ashcroft, *Phys. Lett.* **23**, 48 (1966)
[21] O Gunnarson and B I Lundquist, *Phys. Rev.* **B13**, 4274 (1976)
[22] J Friedel, *Philos. Mag.* **43**, 153 (1952)
[23] J N Daou and R Viallard, *Congres International L'Hydrogene dans les Metaux T1*, 123 edition, Sciences et Industrie, Paris (1972)
[24] F J Blatt, *Phys. Rev.* **108**, 285, 1204 (1957)
[25] J N Daou and J E Bonnet, *Phys. Chem. Solids* **35**, 59 (1974)
[26] J Deutz, P H Dederichs and R Zeller, *J. Phys.* **F11**, 1787 (1981)

Electron momentum density distribution in iridium by Compton scattering technique

K B JOSHI, R K PANDYA*, B L AHUJA† and B K SHARMA
Department of Physics, University of Rajasthan, Jaipur 302 004, India
* Department of Physics, L.B.S. (P.G.) College, Jaipur 302 004, India
† Department of Physics, M.R. Engineering College, Jaipur 302 017, India

MS received 15 October 1996

Abstract. The isotropic Compton profile of iridium, measured using 59·54 keV γ-rays, is reported in this paper. The results are compared with the theoretical Compton profiles from APW method with and without incorporating electron correlation effects. It is seen that correlation effects improve the agreement between the experiment and theory. Comparison with the renormalized-free-atom (RFA) model calculations has also been made. Behaviour of *d*-band electrons in Ir and some other 5*d* transition metals is discussed in terms of broadening in their Compton profiles.

Keywords. APW band structure calculation; Compton profiles; electron momentum density; electron–electron correlation effects; iridium.

PACS Nos 71·15; 71·25; 78·70

1. Introduction

Iridium (Ir), a transition metal of 5*d* group, has an fcc structure with lattice constant $a = 7{\cdot}225$ a.u. Since it is a heavy element, relativistic effects are expected to play an important role in describing the properties of this elemental solid. Considerable amount of work has been done to study this metal during the seventies. These include measurements of density of states, magnetoresistance, thermoelectric power, etc [1]. Traum and Smith [2] had performed relativistic band structure calculations to obtain density of states which were compared with the photoemission results [3]. Körling and Haglund [4] had reported electronic and cohesive properties of several transition metals using different approaches based on local density approximation. Using scalar relativistic augmented plane wave (SRAPW) method, Sigalas *et al* [5] had observed maximum occupancy in the valence bands of Co, Rh and Ir isogroup metals among all the transition metals. Mechanical properties of this metal had been studied by Adamesku *et al* [6]. Choy *et al* [7] had studied L_{III} edge of this metal in iridium oxide to investigate electronic configuration and covalency through XANES. As all platinum group metals are extensively used for catalytic purposes in chemistry, Kolaczkiewicz and Bauer [8] have studied the surface effects of these metals on W(110) surface at several temperatures using Auger electron spectroscopy. Recently, Chai *et al* [9] had done molecular activation analysis of Ir.

to probe the electronic structure of materials. Measurements of line shape on a polycrystalline sample yield the Compton profile, $J(p_z)$, which is the projection of electron momentum density along the direction of scattering vector. Within impulse approximation,

$$J(p_z) = 2\pi \int_{p_z}^{\infty} \langle \rho(\mathbf{p}) \rangle p \, \mathrm{d}\rho,$$

where $\langle \rho(\mathbf{p}) \rangle$ is the spherical average of electron momentum density $\rho(\mathbf{p})$. In our endeavour to make a systematic study of 5*d* transition metals, we have previously studied electron momentum density in Ta [10], W [11], Re [12], and Pt [13]. These studies on 5*d* transition metals have revealed interesting discrepancies between band structure theories and experiments. Papanicolaou *et al* [14] published theoretical Compton profiles along the three principal directions for several cubic transition metals including Ir. They have also reported isotropic Lam–Platzman correction term due to electron–electron correlation effects.

In this work we report on the first Compton profile study on polycrystalline Ir. To examine the systematics in the momentum distributions in 5*d* transition metals, a comparison of Compton profiles of 5*d* transition metals in terms of their fwhm and hence broadening due to varying 5*d* electrons has also been made. The paper is organized in the following way. First, we describe the experiment and various stages of data processing to extract the Compton profile. This is followed by a brief description of the method of theoretical calculations. In § 4 we discuss and compare our data with the available APW Compton profiles and our calculations based on RFA model. A comparison of Compton profiles of 5*d* transition metals studied so far by our group has also been made in terms of their full width at half maximum (fwhm).

2. Experiment and data analysis

Polycrystalline Ir sample used in this work was procured from M/s. Goodfellow Metals Ltd., UK. It was having 99·99% purity and 0·0125 cm thickness. The Compton spectrometer used in the measurement is the same as that reported earlier by Sharma *et al* [15]. γ-rays of 59·54 keV energy from a 5 Ci annular ^{241}Am source were Compton scattered at an angle of 165° ($\pm$2·5°). Due to the strong absorption in Am, the annular shape of the high activity ^{241}Am sources helps to spread the high activity onto a larger area while allowing the scattering angle constant. The Compton scattered γ-rays from the sample kept in vacuum of 10^{-2} torr were detected by a planar HPGe detector. The momentum resolution of the spectrometer which depends upon primary photon energy, angular divergence and the resolution of the detector, was about 0·57 a.u.. About 5×10^4 counts per channel (channel width $\sim$0·1 a.u.) were collected at the Compton peak in 43 h. The count rate at the Compton peak was $\sim$0·3 cps. The stability of the system was checked by using a weak ^{241}Am source, four times in a day during measurement.

The raw spectrum for Ir is shown in figure 1. The peak at channel number 742 is the main Compton peak. The sharp peak next to this is the elastic peak coming mainly

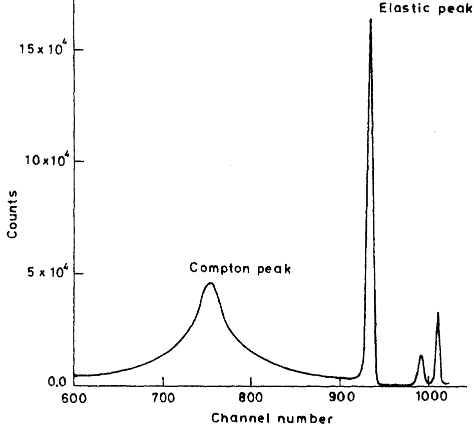

Figure 1. Energy distribution of photons from a ^{241}Am source scattered at 165° (±2·5°) from a polycrystalline iridium. Each channel corresponds to 60 eV (see text).

from the electrons which are not contributing to the Compton profile. The contribution of the elastic peak in the high energy side of Compton profile was avoided by using a weak ^{241}Am source and the 'subtract' mode of our MCA. The third peak, from left, is the Ir $K_{\alpha 1}$, while the fourth peak corresponds to Ir $K_{\alpha 2}$. In our set-up the K-shell electrons are excited by the high energy gamma-radiation of ^{241}Am source. The measured background was subtracted from the raw Compton spectrum channel-wise after scaling it to the measuring time of the raw data. Thus the resulting spectrum was deconvoluted to take into account the insufficient charge collection by the detector at low energy side and the statistical noise in the experiment. Energy dependent corrections due to sample absorption and Compton cross-section etc. were made using the computer code of Perkkiö and Paakkari [16] and then the profile was converted into momentum scale. To find the effect of multiple scattering on Compton profile, a procedure based on Monte-Carlo method of Halonen *et al* [17] has been used. It was found that effect of double scattering is manifested in increase of the profile at $J(0)$ by 3·3% and decrease in high momentum region by about 2·6%. In the present experiment, the K-shell and L-shell electrons do not contribute to the Compton profile in momentum range of 0 to 7 a.u. as their binding energies [18] are more than the recoil energy ($\leqslant 11$ keV). The experimental profile for Ir was, therefore, normalized to have an area of 26·67 electrons which excludes K and L shell

As mentioned earlier, theoretical APW Compton profiles along the three principal directions along with Lam–Platzman correction due to electron–electron correlation effects have been published by Papanicolaou *et al* [14]. In the APW formalism, within the independent particle approximation, the electron momentum distribution $\rho(\mathbf{p})$ is given by

$$\rho(\mathbf{p}) = \text{constant} \sum_{n,K,G}^{\text{occ}} \left| \int_{\text{Unit cell}} e^{-i\mathbf{p}\cdot\mathbf{r}} \psi_{n,\mathbf{k}}(\mathbf{r}) \mathrm{d}^3\mathbf{r} \right|^2 \delta_{\mathbf{p},\mathbf{k}+\mathbf{G}}$$

where $\mathbf{G}$ is the set of reciprocal lattice vectors, $\mathbf{k}$ is a vector in the first Brillouin zone, n is the band index and $\psi_{n,\mathbf{k}}(\mathbf{r})$ is the wavefunction with band index n and wavevector $\mathbf{k}$. To compute the valence electron Compton profile for polycrystalline sample, we have taken spherical average of the directional Compton profiles using the standard relation [14].

The spherical averaged valence electron Compton profile, after proper normalization, is added to the free atom profiles of the core electrons. The contribution of core electrons is taken directly from the tables of Biggs *et al* [19] taking into consideration the binding energies of all the shells and the recoil energy of the present experiment. The final profile is normalized to have an area of 26·67 electrons in the 0 to 7 a.u. range.

3.2 *RFA model*

The Compton profiles of 6*s* electrons of Ir were calculated within the RFA framework of Berggren [20]. The free atom Hartree–Fock wavefunctions for 6*s* electrons needed for computation were taken from tables of Fischer [21] and Herman and Skillman (HS) [22] which are numerical in nature. To preserve the charge neutrality, both the 6*s* electron wavefunctions were truncated separately at Wigner–Seitz (WS) radius 2·84 a.u. Only 33·7 and 42·8 per cent of the wavefunctions were contained within the Wigner-Seitz (WS) radius for Fischer and HS wavefunctions respectively. As in our earlier studies [10–13], the corresponding figures were higher ($\sim 90\%$) for 5*d* wavefunction. Therefore, the 5*d* electrons were not treated in the RFA framework. To include the crystalline effects through auxiliary function, 20 reciprocal lattice vectors were considered. The Compton profiles for 6*s* electrons with varying occupancies ($6s^x$, x ranging from 0·2 to 2·0) were computed using both the Fischer and HS wavefunctions. To obtain the total profile, contribution due to core and 5*d* electrons were suitably added and the final profiles were normalized to 26·67 electrons.

4. Results and discussion

The experimental Compton profile together with the unconvoluted theoretical results obtained using APW method with and without incorporating correlation effects are listed in table 1. The difficulties encountered in removing the systematic errors from $J(p_z)$ in the low energy side of ^{241}Am experiment, and the breakdown of impulse

Table 1. Theoretical (unconvoluted) and experimental Compton profiles of polycrystalline iridium. All quantities are in atomic units. The profiles are normalized to 26·67 electrons in the range of 0–7 a.u.. Experimental error ($\pm\sigma$) is also shown at few points. The experimental values have been derived after a complete data reduction including double scattering.

	APW		RFA $5d^{7\cdot 8}\,6s^{1\cdot 2}$			
p_z	Without LP	With LP	HS	Fischer	Experiment	RIF*
0·0	9·370	9·333	9·440	9·428	9·205 ± 0·040	1·521
0·1	9·358	9·320	9·392	9·374	9·198	1·455
0·2	9·282	9·244	9·283	9·268	9·153	1·270
0·3	9·194	9·157	9·038	9·028	9·061	0·998
0·4	8·999	8·962	8·783	8·779	8·919	0·685
0·5	8·715	8·679	8·323	8·330	8·727	0·378
0·6	8·476	8·444	8·019	8·021	8·490	0·119
0·7	8·192	8·163	7·857	7·870	8·211	− 0·067
0·8	7·925	7·900	7·660	7·672	7·906	− 0·172
0·9	7·687	7·669	7·444	7·456	7·576	− 0·205
1·0	7·371	7·368	7·172	7·184	7·231 ± 0·030	− 0·183
1·2	6·686	6·719	6·559	6·609	6·541	− 0·130
1·4	5·971	5·600	5·980	5·987	5·915	− 0·067
1·6	5·346	5·368	5·402	5·404	5·391	− 0·011
1·8	4·672	4·685	4·892	4·891	4·954	0·029
2·0	4·304	4·313	4·461	4·457	4·566 ± 0·023	0·049
3·0	3·235	3·239	3·283	3·282	3·242	0·052
4·0	2·661	2·661	2·679	2·679	2·603	0·043
5·0	2·128	2·129	2·144	2·144	2·106 ± 0·017	0·028
6·0	1·645	1·645	1·663	1·663	1·657	0·001
7·0	1·267	1·270	1·284	1·284	1·261 ± 0·01	0·000

*RIF is given from 0 to 2·0 a.u. at the mesh of 0·1.

approximation for the *K* and *L*-shell electrons lead to the conclusions that symmetric profiles will not be forthcoming from this data. For this reason the high energy data was used for discussion. It is important to note that for proper comparison of experimental data with the theoretical results, the latter has to be folded with the residual instrumental function (RIF), as given in column 7, to include the residual resolution effects. Columns 4 and 5 of the table contain RFA model profiles for $5d^{7\cdot 8}\,6s^{1\cdot 2}$ occupancy using HS and Fischer wavefunctions respectively. It can be seen from these values that in spite of different free atom wavefunctions, these profiles are almost same. For further discussion we have taken RFA values for Fischer wavefunction into consideration. The basis of reporting RFA values for only $5d^{7\cdot 8}\,6s^{1\cdot 2}$ configuration is the χ^2 fitting among RFA values and the experiment. For further discussion we have called RFA for $5d^{7\cdot 8}$ $6s^{1\cdot 2}$ configuration using Fischer's wavefunction as RFA only. The difference between APW and RFA numbers at $J(0)$ is 0·7% and becomes 1% when LP correction is incorporated indicating a difference in the solid state wavefunctions generated in APW method and modelled within the simple RFA framework. In the high momentum

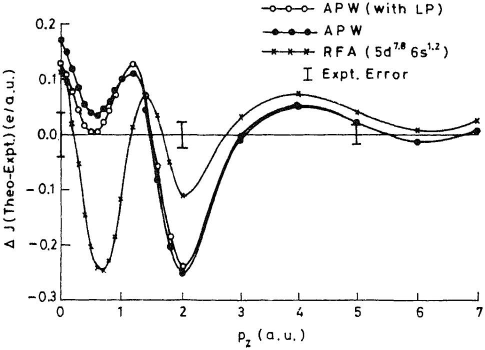

Figure 2. Difference (ΔJ) profiles for polycrystalline iridium. The theoretical result has been convoluted with the residual instrumental function (RIF).

dominated by the momentum distribution of core electrons which was same in all the calculations.

The difference profiles ΔJ calculated for experiment and convoluted theory are plotted in figure 2. This figure shows that near the Compton peak, RFA values are in better agreement with the experiment than APW method. Between 0·2–1·0 a.u., the APW calculation with LP correction shows better agreement compared to the APW without LP and RFA model. In the range 1·2 to 2·0 a.u., the RFA model is closer to experiment. In this region the incorporation of LP correction does not improve the agreement significantly. Since the LP correlation correction shifts the electrons across the Fermi momentum, consequently, the APW values with LP correction are higher for $p_z > p_F$ than those without LP correction. The differences between APW theory and experiment around 2 a.u. are larger than the RFA. The possible reason may be that Papanicolaou *et al* [14] have not included the effects of spin-orbit coupling which is important in heavy transition elements as described by Bacalis *et al* [23]. Also, Rozing *et al* [24] have observed through RAPW calculation for the two photon momentum distribution in tungsten that the inclusion of spin-orbit coupling lifts the degeneracy in bands near the Fermi surface and thus can affect the electron momentum density. It would, therefore, be important to carry out such calculation for the Ir metal also. The underestimation of the APW profile around 2·0 a.u. could also be partly due to the

Table 2. The linewidths (FWHM) of the Compton profiles for 5*d* transition metals.

Metal	FWHM in Compton profiles			RFA configuration (best agreed)
	Experiment*	RFA	APW	
Ta [10]	3·48	3·42	3·26	$5d^3 6s^2$
W [11]	3·54	3·50	3·33	$5d^{5\cdot4} 6s^{0\cdot6}$
Re [12]	3·78	3·68	—	$5d^6 6s^1$
Ir	4·02	3·92	3·67	$5d^{7\cdot8} 6s^{1\cdot2}$
Pt [13]	4·08	3·90	3·76	$5d^{9\cdot2} 6s^{0\cdot8}$

*Error = ± 0·015

to normalization of the profile. But beyond 2·0 a.u., the trend of all difference curves is almost the same.

To see the overall agreement between experiment and theoretical values based on APW model and $5d^{7\cdot8}\,6s^{1\cdot2}$ RFA calculation, we have computed χ^2 and it was found to be the least for the APW with LP correction.

On the basis of RAPW calculation, Papaconstantopoulos [25] has assigned 7.65 electrons to the 5*d* band and 0·77 electrons to the 6*s* band, the remaining 0·58 electrons have been shown to occupy 6*p* band. Davenport *et al* [26] have reported occupancies for the 5*d* transition metals using linear Slater-type orbital method with 7·51–7·19 electrons in 5*d* band, 0·67–0·92 electrons in 6*p* band and 0·82–0·89 electrons in the 6*s* band. Thus, the occupancy of 5*d* band (7·8 e) calculated by us within the RFA scheme is nearly equal to the values those predicted by Papaconstantopoulos. The difference in the 6*s* occupancy may be because of the 6*p* band also which is not considered in the RFA analysis.

Now we compare the widths of Compton profiles for 5*d* metals. In table 2 we have given full width at half maximum (fwhm) of the convoluted theoretical Compton profiles and measured Compton profiles for some 5*d* transition metals namely Ta [10], W [11], Re [12], Ir and Pt [13]. It can be noted from the table that the fwhm of the experimental Compton profiles in all these 5*d* transition metals are closer to those predicted by RFA model than the APW method. From Ta to Pt the increase in fwhm of these metals indicates that the filling in the 5*d* band gives rise to broadening of the Compton profiles. It is also supported by *d* band occupancies in the RFA model configurations (best agreed with experiment) for different 5*d* metals as given in table 2. It suggests more localization of the electron states from Ta to Pt in real space. For the neighbouring elements Ir and Pt, the fwhm of Pt experimental profile is slightly higher than Ir, while the reverse is true for RFA profiles. On the basis of photoemission studies and band structure calculation, Traum and Smith [2] have predicted that the width of the *d* bands increases (real space) when we move from Pt to Ir. The trend of experimental fwhm for Ir and Pt supports such conclusion.

5. Conclusion

Experimental Compton profile of polycrystalline iridium is presented in this paper.

LP correction and RFA method using Fischer and Herman–Skillman wavefunctions. The measurement is relatively in good agreement with the APW calculation with correlation correction. RFA model favours $5d^{7\cdot 8}$ $6s^{1\cdot 2}$ occupancy. It is also seen that the choice of free atom wavefunction does not have any noticeable effect on the Compton profile. Results based on fwhm in Compton profiles indicate that the RFA model predicts occupancy in 5*d* transition metals well in agreement with our measurements. The present work clearly points towards the need for Comtpon profile calculation using fully relativistic band structure methods and measurement of directional Compton profiles which will enable more realistic comparison as all the isotropic corrections will automatically be eliminated when differences are taken.

Acknowledgements

This work is partially supported by a grant from the Department of Atomic Energy, Bombay and Department of Science and Technology, New Delhi. One of the authors (KBJ) is grateful to CSIR, New Delhi for Senior Research Fellowship.

References

[1] A P Cracknell, *The Fermi surface of metals* (Taylor and Francis, London, 1971) and references therein
[2] M M Traum and N V Smith, *Phys. Rev.* **B9**, 1353 (1974)
[3] N V Smith, *Phys. Rev.* **B9**, 1365 (1974)
[4] M Körling and J Haglund, *Phys. Rev.* **B45**, 13293 (1992)
[5] M Sigalas, D A Papaconstantopoulos and N C Bacalis, *Phys. Rev.* **B45**, 5777 (1992)
[6] R Adamesku, S Grebenkin, A Yermakov and P Panifilov, *J. Mater. Sci. Lett.* **13**, 865 (1994)
[7] J H Choy, D K Kim, G Demazeau and D Y Jung, *J. Phys. Chem.* **98**, 6258 (1994)
[8] J Kolaczkiewicz and E Bauer, *Surf. Sci.* **314**, 221 (1994)
[9] C F Chai, P Kong, X Y Mao and S L Ma, *J. Radio Nucl. Chem. Articles* **192**, 101 (1995)
[10] B K Sharma, B L Ahuja, U Mittal, S Perkkiö, T Paakkari and S Manninen, *Pramana–J. Phys.* **46**, 289 (1996)
[11] U Mittal, B K Sharma, F M Mohammad and B L Ahuja, *Phys. Rev.* **B38**, 12208 (1988)
[12] B K Sharma, M D Sharma, K B Joshi, B L Ahuja and R K Pandya, *Phys. Status Solidi* **B196**, 347 (1996) (in press)
[13] R K Pandya, K B Joshi, Rajesh Jain, B L Ahuja and B K Sharma *Phys. Status Solidi* (B) 1997 (in press)
[14] N I Papanicolaou, N C Bacalis and D A Papaconstantopoulos, *Handbook of calculated electron momentum distributions, Compton profiles and X-ray form factors of elemental solids* (CRC Press, London, 1991)
[15] B K Sharma, A Gupta, H Singh, S Perkkiö, A Kshirsagar and D G Kanhere, *Phys. Rev.* **B37**, 6821 (1988)
[16] S Perkkiö and T Paakkari, *Rep. Ser. Phys.* HU-P-246 (University of Helsinki, 1987)
[17] V Halonen, B G Williams and T Paakkari, *Physica Fennica* **10**, 107 (1975)
[18] J A Bearden and A F Burr, *Rev. Mod. Phys.* **39**, 125 (1967)
[19] F Biggs, L B Mandelsohn and J B Mann, *At. Data Nucl. Data Tables* **16**, 201 (1975)
[20] K-F Berggren, *Phys. Rev.* **B6**, 2156 (1972)
[21] C F Fischer, *Atomic Data* **4**, 301 (1972)
[22] F Herman and S Skillman, *Atomic structure calculations* (Prentice-Hall Inc., Englewood Cliffs, New Jersey, 1963)
[23] N C Bacalis, K Blathras, P Thomaids and D A Papaconstantopoulos, *Phys. Rev.* **B32**, 4849

[24] G J Rozing, P E Mijnarends and R Benedek, *Phys. Rev.* **B43**, 6996 (1991)
[25] D A Papaconstantopoulos, *Handbook of the band structure of elemental solids* (Plenum Press, New York, 1986)
[26] J W Davenport, R E Watson and M Weinert, *Phys. Rev.* **B32**, 4883 (1985)

Magnetic behaviour of TbMnFe

KEKA CHAKRABORTY, S K PARANJPE, V SIRUGURI*
O D JAYAKUMAR† and S K KULSHRESHTHA†
Solid State Physics Division; *Inter University Consortium for DAE Facilities;
†Chemistry Division, Bhabha Atomic Research Centre, Mumbai 400085, India

MS received 17 September 1996; revised 30 December 1996

Abstract. Neutron diffraction and Mössbauer measurements have been carried out on the cubic Laves phase intermetallic TbMnFe. The magnetic moment on the transition metal atom is found to be low, $0{\cdot}2\,\mu_B$, at room temperature. This moment is temperature independent down to 10 K. Magnetic moment on the rare earth atom varies from $2{\cdot}5\,\mu_B$ at 296 K to $7{\cdot}27\,\mu_B$ at 10 K. Mössbauer spectra recorded at 298 K and 78 K have magnetic character but there is a large distribution of hyperfine field values. Both these features arise due to magnetic frustration created in the sample due to the competing ferro and antiferromagnetic interactions between the transition metal atoms.

Keywords. Rare earth intermetallics; neutron diffraction; Mössbauer; magnetic structure.

PACS Nos 75·25; 76·80; 61·12

1. Introduction

Numerous investigations of magnetic properties of heavy rare earth (R) transition metal (T) intermetallics have been carried out using different probes [1]. Amongst these intermetallics, those having the formula RT_2 crystallize in the Laves phase structure. The presence of three different competing exchange interactions namely $4f$–$4f$, $4f$–$3d$ and $3d$–$3d$ [1–3], makes the study of their magnetic properties interesting in spite of their simple crystal structure.

$\mathrm{RMn_2}$ compounds crystallize in the C15 cubic Laves phase structure for $R = \mathrm{Y}$, Gd, Tb, and Dy while a C14 hexagonal Laves phase structure exists for $R = \mathrm{Er}$, Tm and Lu. $\mathrm{HoMn_2}$ and $\mathrm{SmMn_2}$ can have either of the two structures depending on the heat treatment. $\mathrm{RFe_2}$ compounds, on the other hand, crystallize in the C15 cubic Laves phase structure for all these heavy lanthanides.

Some of the $\mathrm{RMn_2}$ intermetallics show large magnetovolume anomalies at their magnetic ordering temperatures [4]. Large changes in the cell constant are found in $\mathrm{YMn_2}$ and $\mathrm{TbMn_2}$ [5]. The cause of these large magnetovolume anomalies has been attributed to the Mn–Mn inter-atomic distance, $d_{\mathrm{Mn-Mn}}$ [6, 7]. There is a critical distance, $d_c = 2{\cdot}66$ Å, between Mn atoms to sustain the magnetic moment at Mn sites for both cubic and hexagonal structure. For $d_{\mathrm{Mn-Mn}} > 2{\cdot}66$ Å, the Mn atom has a localized magnetic moment and for $d_{\mathrm{Mn-Mn}} < 2{\cdot}66$ Å, there is no local magnetic moment. However, when $d_{\mathrm{Mn-Mn}}$ is close to 2·66 Å, the Mn moment is unstable and the magnetic properties become sensitive to external parameters like pressure, temperature, alloying, etc. [8–10]. Unlike RMn_2 intermetallics, a ferromagnetic ordering exists between Fe atoms in all RFe_2 alloys, with the moment on R aligned antiparallel to Fe moment, resulting in a ferrimagnetic structure [11]. The ordered moment on Fe site is close to $1{\cdot}6\,\mu_B$ at low temperatures.

The magnetization and Mössbauer measurements on the compound $Ho(Fe_{2-x}Mn_x)$ [12] have revealed that the magnetic moment on Fe decreases from $1{\cdot}43\,\mu_B$ to $0{\cdot}96\,\mu_B$ with increase in Mn concentration from $x = 0{\cdot}0$ to $x = 0{\cdot}6$. This concentration dependence of the magnetic moment is not linear. The moment on Mn, assuming an antiferromagnetic alignment of Fe and Mn moments, has been shown to be very low [12]. Similar observations are reported in $Y(Fe_{2-x}Mn_x)$ [13] where the two end members with $x = 0$ and $x = 2$ have ferromagnetic and helical antiferromagnetic ordering, respectively. The mixed system has two types of Mn atoms, one of high spin with moment of $2{\cdot}7\,\mu_B$ and the other of low spin with moment decreasing from $0{\cdot}6\,\mu_B$ to $0{\cdot}08\,\mu_B$ as the Mn concentration is increased.

The intermetallics $TbMn_2$ and $TbFe_2$ form a solid solution over the entire concentration range [14]. $TbFe_2$ has a ferrimagnetic ordering with $T_C = 697\,K$ with Fe moment of $1{\cdot}6\,\mu_B$ at low temperatures aligned along $\langle 111 \rangle$ direction [11, 15]. $TbMn_2$ exhibits a complex magnetic behaviour [16–20]. For $40\,K < T < 45\,K$, there is a ferrimagnetic ordering of rare earth and transition metal atoms. Below 40 K, the structure is antiferromagnetic, characterized by the propagation vector (2/3, 2/3, 0). At 2 K, magnetic ordering with propagation vector (1/2, 1/2, 1/2) is observed with magnetic peaks at (1/2, 1/2, 1/2), etc. The structure scheme is modified by application of external magnetic field [16, 17]. The replacement of 4% Mn by Fe changes the magnetic structure drastically [17, 18] where rhombohedral distortion below 70 K is reported.

To understand the magnetic behaviour of the mixed system, where an interplay of ferro and antiferromagnetic interactions could lead to frustration, we have undertaken a neutron diffraction study of TbMnFe. The results of neutron diffraction on TbMnFe and Mössbauer measurements on TbMnFe and $TbFe_2$ are reported here. In TbMnFe the T–T distance, $d_{T-T} = 2{\cdot}646$ Å, which is close to d_c. Hence, it would be interesting to study the behaviour of magnetic moments on T atom site.

2. Experimental

The sample was prepared by repeated arc melting of the constituents of 99·9% purity in an ultra pure argon atmosphere and then annealed for 200 h at temperature of 1150 K. Single phase formation for the annealed samples was tested by X-ray diffraction. The total weight loss due to evaporation of the constituents and the intermetallic formed during melting was less than 2·5%. For neutron measurements, well powdered sample was packed in a cylindrical vanadium container. For the low temperature experiments, the sample was packed in an aluminium container. Powder diffraction profiles were recorded using the least squares fitted using a computer program which solves the complete nuclear hyperfine Hamiltonian matrix. The isomeric shift values are reported with respect to Fe metal at room temperature.

3. Experimental results

3.1 *Neutron diffraction*

The diffraction pattern recorded at room temperature could be indexed using C15 cubic Laves phase structure. The X-ray as well as neutron diffraction patterns showed the presence of weak Fe lines. The sample being magnetically ordered at 300 K, refinement of the neutron diffraction pattern was carried out using higher angle data [22]. The structure of TbMnFe conforms to the space group Fd3m. The parameters varied were scale factor, zero angle of the detector, half width parameters, cell constant, temperature factor and the occupancies of the different atoms in the unit cell. The occupancies obtained were found to be consistent with the stoichiometry TbMnFe. Variation of Mn occupancy parameter yielded no change in its value. The analysis gave the cell constant as 7·485 Å, and a temperature factor (B) of 0·90 $Å^2$. The refinement converged to an agreement factor of 3·4%.

A particularity of the C15 Laves phase structure factors is that the magnetic part of the intensity of (220) reflection depends only on the magnetic moment of R-site while that of (222) reflection depends only on the magnetic moment of the T-metal site. The (222) reflection was found to be weak and hence was not used in our calculation of magnetic moment. The reflections (220), (111) and (311) were used to obtain the R- and T-site magnetic moments and were found to be $2{\cdot}50(3)\mu_B$ and $0{\cdot}20(4)\mu_B$ at RT, respectively. The form factors used were from Lander *et al* [23] and Watson *et al* [24]. The intensities of the remaining reflections were calculated using these moments and were found to be in good agreement with the observed intensities. Table 1 gives the comparison between observed and calculated intensities.

Figure 1 shows the neutron diffraction patterns of TbMnFe as a function of temperature from 10 K to 300 K. The patterns have been corrected for background and

Table 1. Observed and calculated intensities of different reflections of TbMnFe at 300 K with error bars in bracket using $M_A = 2{\cdot}5\,\mu_B$ and $M_B = 0{\cdot}2\,\mu_B$ for calculations.

hkl	I_{obs}	I_{calc}
(111)	3274 (57)	3275
(220)	6504 (81)	6206
(311)	8739 (94)	8766
(222)	1323 (36)	1208
(400)	378 (19)	430
(422)	2922 (54)	3358
(511)*		
(333)	3924 (62)	4166
(440)	3195 (56)	3195

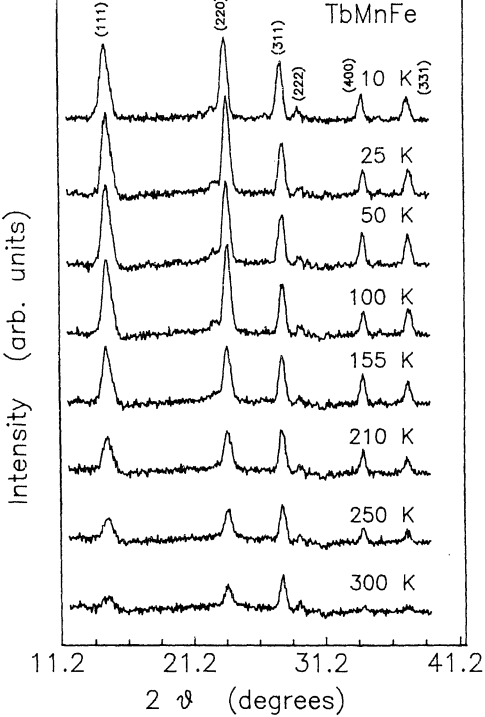

Figure 1. Temperature dependence of neutron diffraction patterns for TbMnFe.

contribution from Al peaks of the sample holder. As seen from the figure, the intensities of the (111), (220), (311), (400) and (331) reflections increase as the temperature is lowered to 10 K, but there is no observable change in the intensity of (222) reflection. No additional line suggestive of antiferromagnetic ordering was observed down to 10 K. The structure remains cubic down to 10 K. The moment obtained on *R*-site was found to be 7·27(3)μ_B at 10 K. The moment on *T*-site remains unchanged as indicated by the constant value of the intensity of the (222) reflection. Temperature dependence of the peak intensities of some of the reflections is shown in figure 2. It is of interest to note

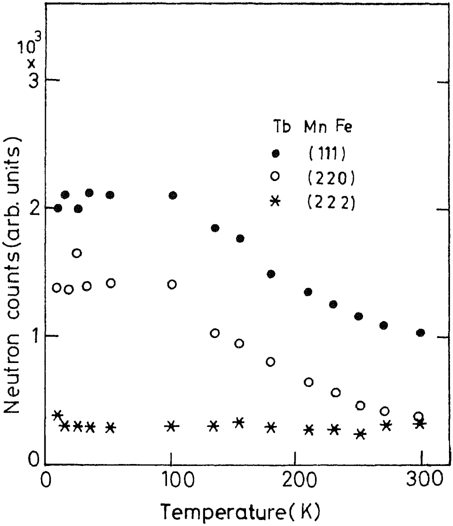

Figure 2. Temperature dependence of peak intensities of (111), (220) and (222) reflections in TbMnFe.

that the ordered Tb site moments for $TbFe_2$ and $TbMn_2$ below the Curie and Néel temperatures are 9·0 μ_B and 8·7 μ_B, respectively [11].

3.2 *Mössbauer measurements*

Mössbauer spectra of $TbFe_2$ and TbMnFe recorded at room temperature and 78 K are shown in figure 3. The observed spectrum consists of two magnetic sextets having an intensity ratio 1:3 which implied that the magnetization is along the (111) direction [25,26]. These two sextets originate from Fe atoms which are crystallographically equivalent sites of trigonal symmetry ($\bar{3}m$) but magnetically inequivalent as the two values of the angle θ between the two principal efg axis $\langle 111 \rangle$ and the magnetization direction [111] are 0° and 70° 32′, respectively. This observation is in conformity with the observations of earlier investigators [25]. From the analysis of the RT spectrum, the values of isomeric shift, δ, and quadrupole splitting ΔE_q observed were found to be $-0{\cdot}07\,\mathrm{mms}^{-1}$ and $-0{\cdot}49\,\mathrm{mms}^{-1}$, respectively, and the internal hyperfine field values for the two [25–27] Fe sites characterized by $\theta = 70° 32'$ and $\theta = 0°$ were $h_1 = 215$ kOe and $h_2 = 197$ kOe, respectively. The analysis of the 78 K data gave $\delta = 0{\cdot}03\,\mathrm{mms}^{-1}$,

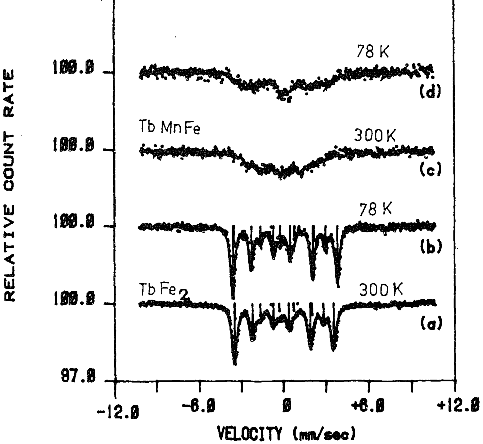

Figure 3. Mössbauer spectra of $TbFe_2$ (**a**, **b**) and TbMnFe (**c**, **d**) at 300 K.

RT and 78 K data was found to be very good. These values of internal hyperfine field correspond to $\mu_{Fe} \cong 1{\cdot}7\,\mu_B$ at 78 K assuming a value of $\cong 120$ kOe per Bohr magneton.

The TbMnFe spectra, though magnetic in nature at both the temperatures, do not exhibit well resolved patterns and show a broad distribution of internal hyperfine field values, making the analysis complicated. Hence the Fe spin orientation cannot be uniquely defined for this system. However, the average internal hyperfine field value observed at 78 K suggests that the average moment on Fe site must be more than 1 μ_B. TbMnFe spectra recorded with an external magnetic field of 1 kOe did not show any appreciable change in the line shape, hence ruling out the possibility of superparamagnetism. The spectra in paramagnetic state for both the samples showed well-defined quadrupole doublets. These observations suggest that there is a distribution of internal hyperfine fields in TbMnFe due to different types of magnetic interactions resulting in the frustration of magnetic system.

4. Discussion

Antiferromagnetic coupling has been observed between Mn and any other 3d-transition metal atom when the separation between them is less than 2·8 Å [28]. In the present system this distance was found to be 2·64 Å, which is very close to the critical value of 2·66 Å. The interaction between Mn–Mn and Fe–Mn is negative while the transition metal atoms leading to low moment. Hence no change in the intensity of scattered neutrons from the (222) planes is observed (within the instrument resolution) with lowering of temperature. In a similar system, namely $\mathrm{Tb(Mn_{0\cdot 96}Fe_{0\cdot 04})_2}$ [17, 18], the moment on Mn, i.e., T-site, is found to be low. In this system, however, there is a progressive rhombohedral distortion below the magnetic ordering temperature, conforming to the space group ($R\bar{3}m$) which decouples the Mn moments into two sites, 1b and 3d. The neutron observations have been interpreted on the basis of magnetic moment on one Mn site (1b) and nonmagnetic Mn atoms on the other site (3d). In TbMnFe, the present neutron measurements do not show any crystallographic distortion and all T sites (16d) are randomly occupied by Fe and Mn atoms. The neutron observations at 300 K are in accordance with the Mössbauer results which do not show well-split spectra indicating distribution of hyperfine fields and thus no unique value of moment on T-site. Also, as the temperature is lowered to 78 K, the Mössbauer pattern does not improve much and thus it can be concluded that frustration persists at low temperatures. This is also inferred from neutron diffraction results at low temperatures. Only the Tb site moment is ordered at 296 K and its magnetic moment increases as the temperature is lowered.

5. Conclusion

Neutron diffraction measurements on TbMnFe show that the transition site moment is low and temperature independent. The rare earth moment increases from $2\cdot 5\,\mu_{\mathrm{B}}$ at 296 K to $7\cdot 27\,\mu_{\mathrm{B}}$ at 10 K. Mössbauer spectra suggest a distribution of hyperfine fields and their direction at the T-metal atom site. The observation that the magnetic moment on T-site remains unchanged with respect to temperature is in conformity with earlier observations in similar systems [29, 30].

References

[1] K H J Buschow, *Rep. Prog. Phys.* **40**, 1179 (1977)

[2] W E Wallace, in *Rare earth intermetallics in materials science and technology* edited by A M Allen, L J Margave and A S Nowick (Academic Press, New York, 1973) ch. 11

[3] K H J Buschow, in *Ferromagnetic materials* edited by E P Wohlfarth (North-Holland, Amsterdam, 1980) vol. 1, ch. 4

[4] Y Nakamura, *Hyperfine interactions* **83**, 55 (1994)

[5] H Wada, H Nakamura, K Yoshimura, M Shiga and Y Nakamura, *J. Magn. Magn. Mater.* **70**, 134 (1987)

[6] K Yoshimura, M Tagigawa, Y Yasuko, M Shiga and Y Nakamura, *J. Magn. Magn. Mater.* **54–57**, 1075 (1986)

[7] K Yoshimura, M Shiga and Y Nakamura, *J. Phys. Soc. Jpn.* **55**, 3585 (1986)

[8] R Ballou, I Yu Gaydukova, A S Markosyan and B Ouladdiaf, *J. Magn. Magn. Mater.* **104–107**, 1465 (1992)

[9] R Ballou, J Deportes, R Lemaire, P Rowault and J L Soubeyroux, *J. Magn. Magn. Mater.* **90–91**, 559 (1990)

[10] J Voiron, R Ballou, J Deportes, R M Galera and L Lelievre, *J. Appl. Phys.* **69**, 5678 (1991)

[11] Y J Tang, X P Zhong and H L Luo, *J. Magn. Magn. Mater.* **127**, 378 (1993)

[12] C Ritter, R Cywinski, S H Kilcoyne and S Mondal, *J. Phys. Condens. Matter* **4**, 1559 (1992)

[13] H Nagai, *Hyperfine interactions* **51**, 1003 (1989)

[14] A S Ilyushin and W E Wallace, *J. Solid State Chem.* **17**, 373 (1976)
[15] K H J Buschow and R P van Stapele, *J. Appl. Phys.* **4**, 4066 (1970)
[16] M Shiga, *J. Magn. Magn. Mater.* **129**, 17 (1994)
[17] P J Brown, B Ouladdiaf, R Ballou, O J Deportes and A S Markosyan, *J. Phys. Condens. Matter* **4**, 1103 (1992)
[18] B Ouladdiaf, J Deportes, R M Galera, A S Markosyan and J L Soubeyroux, *Physica* **B180–181**, 85 (1992)
[19] R Ballou, P J Brown, J Deportes, A S Markosyan and B Ouladdiaf, *J. Magn. Magn. Mater.* **104–107**, 935 (1992)
[20] S Mondal, R Cywinski, S H Kilcoyne, B D Rainford and C Ritter, *Physica* **B180 & 181**, 606 (1992)
[21] S K Paranjpe and Y D Dande, *Pramana–J. Phys.* **32**, 793 (1989)
[22] D B Wiles and R A Young, *J. Appl. Cryst.* **14**, 149 (1981)
R A Young, E Prince and R A Sparks, *J. Appl. Cryst.* **15**, 357 (1982)
[23] G H Lander, T O Brun, J P Desclaux and A J Freeman, *Phys. Rev.* **B8**, 3237 (1973)
[24] R E Watson and A J Freeman, *Acta Crystallogr.* **14**, 27 (1961)
[25] S K Kulshresta, O D Jayakumar and R Sasikala, *J. Magn. Magn. Mater.* **117**, 131 (1992)
[26] P Raj and S K Kulshreshta, *J. Phys.* **41**, 1487 (1980)
[27] U Atzmony and M P Dariel, *Phys. Rev.* **B10**, 2060 (1974)
[28] A S Ilyushin and W E Wallace, *J. Solid State Chem.* **17**, 131 (1976)
[29] J M Moreau, C Michel, M Simmons, T J O'Keefe and W J James, *J. de Phys. Colloque* **32**, C1–**670** (1970)
[30] G E Fish, J J Rhyne, S G Sankar and W E Wallace, *J. Appl. Phys.* **50**, 2003 (1977)

Spin state and exchange in the quasi-one-dimensional antiferromagnet $KFeS_2$

SATISH KUMAR TIWARY and SUKUMARAN VASUDEVAN
Department of Inorganic and Physical Chemistry, Indian Institute of Science, Bangalore 560012, India

MS received 10 January 1997; revised 24 March 1997

Abstract. We report the optical spectra and single crystal magnetic susceptibility of the one-dimensional antiferromagnet $KFeS_2$. Measurements have been carried out to ascertain the spin state of Fe^{3+} and the nature of the magnetic interactions in this compound. The optical spectra and magnetic susceptibility could be consistently interpreted using a $S = \frac{1}{2}$ spin ground state for the Fe^{3+} ion. The features in the optical spectra have been assigned to transitions within the d-electron manifold of the Fe^{3+} ion, and analysed in the strong field limit of the ligand field theory. The high temperature isotropic magnetic susceptibility is typical of a low-dimensional system and exhibits a broad maximum at ~ 565 K. The susceptibility shows a well defined transition to a three dimensionally ordered antiferromagnetic state at $T_N = 250$ K. The intra and interchain exchange constants, J and J', have been evaluated from the experimental susceptibilities using the relationship between these quantities, and $\chi_{\max}$, $T_{\max}$, and T_N for a spin $\frac{1}{2}$ one-dimensional chain. The values are $J = -440{\cdot}71$ K, and $J' = 53{\cdot}94$ K. Using these values of J and J', the susceptibility of a spin $\frac{1}{2}$ Heisenberg chain was calculated. A non-interacting spin wave model was used below T_N. The susceptibility in the paramagnetic region was calculated from the theoretical curves for an infinite $S = \frac{1}{2}$ chain. The calculated susceptibility compares well with the experimental data of $KFeS_2$. Further support for a one-dimensional spin $\frac{1}{2}$ model comes from the fact that the calculated perpendicular susceptibility at 0 K ($2{\cdot}75 \times 10^{-4}$ emu/mol) evaluated considering the zero point reduction in magnetization from spin wave theory is close to the projected value ($2{\cdot}7 \times 10^{-4}$ emu/mol) obtained from the experimental data.

Keywords. Low-dimensional materials; magnetic ordering and exchange; spin-waves.

PACS Nos 75·10; 75·30; 78·40

1. Introduction

$KFeS_2$, a linear chain insulating antiferromagnet and one of the earliest reported ternary alkali metal thioferrates [1] has been widely studied both as a model one-dimensional magnetic system and as a spin analogue of the iron-sulfur ferrodoxin proteins. These proteins and $KFeS_2$ share a common structural motif – chains of edge sharing $[FeS_4]$ tetrahedra. $KFeS_2$ crystallizes in C2/c monoclinic space group and the chains are separated by potassium atoms (figure 1). The interchain Fe–Fe distance (6·6 Å) is much larger than the intrachain Fe–Fe distance (2·7 Å) and so, magnetically, the compound has a pronounced one-dimensional character [2].

Extensive ^{57}Fe Mössbauer [3–10], neutron diffraction [11–13], magnetic susceptibility [2, 12–15] and optical spectroscopic measurements [16–18] on $KFeS_2$ have been

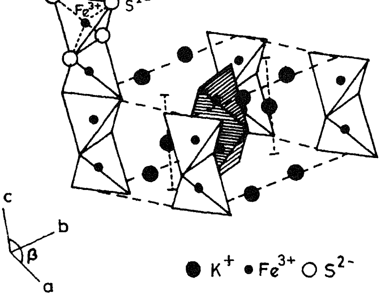

Figure 1. C 2/c crystallographic structure of $KFeS_2$. The lattice parameters arc ($a = 7{\cdot}082$, $b = 11{\cdot}329$, $c = 5{\cdot}403$, $\beta = 113{\cdot}2$).

reported. The results and their interpretation, however, differ greatly from author to author. Neutron diffraction studies have shown that below $T_N = 250$ K, the Fe^{3+} spins are antiferromagnetically coupled along the chain and form ferromagnetic sheets in the *ab* plane. Powder magnetic susceptibility studies, however, with the exception of one [14], have failed to reveal any anomaly at $T = 250$ K. One study reported $T_N = 12{\cdot}5$ K [15]. The reports on the powder magnetic susceptibility by different investigators are conflicting, that it is temperature-independent [2, 13] or that it increases with decrease in temperature below 250 K [12, 15] in contrast to the behaviour expected of an antiferromagnet. There are similar discrepancies in the reported values of the effective magnetic moment, μ_{eff}, which ranges from $0{\cdot}8\,\mu_B$ [14] to $4{\cdot}6\,\mu_B$ [3]. A recent single crystal magnetic susceptibility report [19], however, showed a clear antiferromagnetic transition at 250 K, and a value of the magnetic moment expected for an $S = 1/2$ ground state for the Fe^{3+} ion.

Although the optical spectra reported by various groups are broadly similar, their interpretations have varied widely in their attempt at accounting for the magnetic moment obtained from magnetic susceptibility studies. An early report had assigned the features in the optical spectra to *d–d* transitions of a high spin d^5 Fe^{3+} ion [16]. Later the same bands were reinterpreted as ligand to metal charge transfer (LMCT) on the basis of a spin-polarized multiple scattering $\chi\alpha$ calculation on an FeS_4^- unit [20]. A similar LMCT interpretation, but on the basis of a semi-emperical extended Huckel calculation has been recently proposed [18]. The cystal field model [17], however, supports an assignment based on *d–d* transtions of a low-spin d^5 ion. The variable energy photo-electron spectra have been interpreted assuming a high spin d^5 ion with an inverted bonding scheme due to strong covalency [21].

In general, most authors have favoured the high spin ground state ($S = \frac{5}{2}$) for the Fe^{3+} ion in $KFeS_2$ and have invoked either covalency [15] or quantum spin reduction [8, 14] to account for the intermediate to low spin values as found in susceptibility tion value, viz. ~ 20 T, of the magnetic hyperfine field in the Mössbauer spectra of $KFeS_2$. This value may be compared with 60 T expected of a high spin Fe^{3+} ion as observed, e.g., in the one-dimensional high spin K_2FeF_5 [8]. Quantum spin reduction, although expected to be enhanced in low-dimensional systems, is unlikely to account for a reduction in the room temperature magnetic moment from $\sim 5{\cdot}9\,\mu_B$ to $\sim 0{\cdot}8\,\mu_B$ for the nearly classical $S = \frac{5}{2}$ ion. Thus in spite of numerous studies, the true nature of the spin state and magnetic behaviour of $KFeS_2$ still remains unclear. With this in mind, we have carried out a detailed study of the optical spectra and an analysis of the single crystal magnetic susceptibility of $KFeS_2$.

A major source of error and the possible origin of the discrepancies in the powder susceptibility measurements reported so far is the formation of ferromagnetic oxide impurities. This has been pointed out earlier [14]. A recent report on the crystal susceptibilities of a closely related compound, $TlFeS_2$ [22] corroborates this view. It is known that on exposure to air $KFeS_2$ is slowly oxidized to $KFeO_2$, a high spin Fe^{3+} ferromagnet ($T_c = 960$ K) [23]. Another source of surface oxidation is in the preparation; $KFeS_2$ is usually grown from a carbonate flux and the crystals extracted with hot water. Even trace amounts of these oxide impurities can mask the true magnetic behaviour, especially since, as found in the present work, the susceptibility of $KFeS_2$ is extremely small ($1{\cdot}2 \times 10^{-6}$ emu/g at 300 K). In the present investigation scrupulous care has been taken to prevent formation of oxide impurities which could lead to erroneous results.

Our study shows that the anisotropic magnetic susceptibility of $KFeS_2$ is typical of a one-dimensional antiferromagnet with $T_N = 250$ K. Both optical and magnetic measurements could be consistently interpreted using a $S = \frac{1}{2}$ spin ground state. The intra- and inter-chain exchange values, J and J', have been evaluated from the experimental susceptibilities using the relationship between the exchange constants, and χ_{max}, T_{max}, and T_N for a one-dimensional Heisenberg antiferromagnet. Using these values of J and J', the susceptibility of a spin $\frac{1}{2}$ one-dimensional antiferromagnetic chain was calculated – below T_N from a non-interacting spin wave model [24], and at higher temperatures using a parametrized form of the Bonner–Fisher susceptibility curves [25]. The calculated susceptibilities compare extremely well with the experimental data for $KFeS_2$. Further support for a spin $\frac{1}{2}$ one dimensional model comes from the calculated susceptibility at 0 K from spin wave theory, which is quite close to the projected experimental value of perpendicular susceptibility at 0 K.

2. Experimental

$KFeS_2$ was prepared by heating a 4:1 molar mixture of K_2CO_3 and oxide-free iron powder in a stream of dry H_2S at 1000 K for 24 h. The product was cooled to ambient temperature over a period of 24 h, and then extracted with cold water. This procedure gave fine permanganate-colored, needle-shaped crystals typically 5–10 mm in length and 0·5–1 mm width. The needle axis is the c-axis. The crystals were again heated in flowing H_2S at 773 K for 12 h. Under these conditions, $KFeO_2$ is known to convert to $KFeS_2$ [14, 23]. Care was taken not to expose the crystals to air or moisture after dispersed in a high molecular weight paraffin and applied onto an optically polished quartz plate. The plate was mounted inside the sample holder of a closed cycle cryostat (air products).

Magnetic susceptibility measurements were made on a Faraday magnetic balance. Temperatures in the range 45–300 K were obtained using a closed cycle cryostat. Measurements in the temperature range 300 K–800 K were performed using a high temperature furnace assembly. The susceptometer was calibrated using $Hg[Co(NCS)_4]$ as a standard. A large number of needle-like crystals were aligned parallel onto a thin quartz plate using silicone grease. The plate was then suspended from the balance by an arrangement similar to that reported in [26]. For the high temperature measurements, the crystals were tightly packed and sealed under vacuum in small thin walled quartz ampoules of 0·5 mm wall thickness, 4 mm diameter and 10 mm length. Heating rates were 1–2°/min in order to ensure thermal equilibrium of the sample with the He exchange gas. Calibration with $HgCo(NCS)_4$ was repeated under identical conditions. The susceptibilities reported are for two directions. In the temperature range 250 K to 800 K, the applied field is parallel and perpendicular to the c-axis, which is also the needle axis of the crystal. For temperatures below 250 K, the field is parallel and perpendicular to the magnetization axis. The magnetization axis is known from neutron diffraction studies to be at an angle of approximately 13° to the chain axis [11]. The absence of ferromagnetic impurities in the samples was confirmed by measuring the field dependence of the magnetization at the lowest temperatures. The susceptibility measurements were repeated to ensure that the data was reproducible.

3. Results

3.1 *Optical spectra*

The optical absorption spectra of $KFeS_2$ recorded at 15 K is shown in figure 2. With the exception of the features below 400 nm ($25000\,cm^{-1}$) the spectrum is essentially temperature independent although better resolved at lower temperatures. In figure 2, the 300 K spectrum is shown only below 350 nm range. It may be seen that there is a sharpening of the intense absorptions at 227, 265 and 281 nm (44055, 37455 and $35585\,cm^{-1}$). The peaks at 815 nm ($12270\,cm^{-1}$), 770 nm ($12990\,cm^{-1}$) and 730 nm ($13700\,cm^{-1}$) are much better resolved in the low temperature spectra. Optical spectra of $KFeS_2$ in the 900–200 nm range has been previously reported. The present spectra are, however, of much better quality, and cover a wider spectral range. The positions of the various optical features are given in table 1.

3.2 *Magnetic susceptibility*

The temperature variation of the magnetic susceptibility of $KFeS_2$ crystals is shown in figure 3. The diamagnetic contributions have been subtracted from the data. The van Vleck paramagnetic contribution was evaluated from the EPR g value of 2·025 [27]

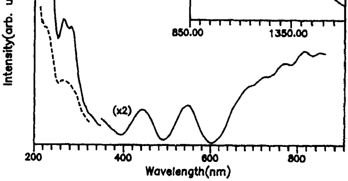

Figure 2. The optical absorption spectra of $KFeS_2$ at 15 K. The inset shows the spectra in the near infrared region (850–1600 nm). The dashed line is the spectra at 300 K.

Table 1. Calculated and observed energies for the optical transitions in $KFeS_2$ and their assignments.

Energy (cm^{-1})		
Experimental	Calculated	Assignment
7150	7535	$^2T_2 \rightarrow {}^4T_2$
8770	8780	$\rightarrow {}^6A_1$
11765	11750	$\rightarrow {}^4T_1$
12270	12485	$\rightarrow {}^2A_2$
12990	13004	$\rightarrow {}^2T_1$
13700	13341	$\rightarrow {}^2T_2$
14495		
18180	17685	$\rightarrow {}^2E$
	20285	$\rightarrow {}^2T_1$
	20818	$\rightarrow {}^2T_2$
22470	22885	$\rightarrow {}^2A_1$
35587		Charge transfer
37735		Charge transfer
44053		Charge transfer

and the energies of the optical transitions; its value is 9×10^{-7} emu/mol. The susceptibility of $KFeS_2$ is typical of a low-dimensional antiferromagnet undergoing a three-dimensional transition. The Neel temperature is 250 K. In figure 3, the data above 250 K is the susceptibility parallel and perpendicular to the c-axis and is isotropic within the experimental limits. The high temperature isotropic susceptibility shows a broad maximum at 565 K ($T_{max} = 565$ K, $\chi_{max} = 2{\cdot}7 \times 10^{-4}$ emu/mol), and even at the highest temperature, does not show Curie–Weiss behaviour. The low temperature ($T < 250$ K) behaviour is typical of antiferromagnetic ordering where the susceptibility

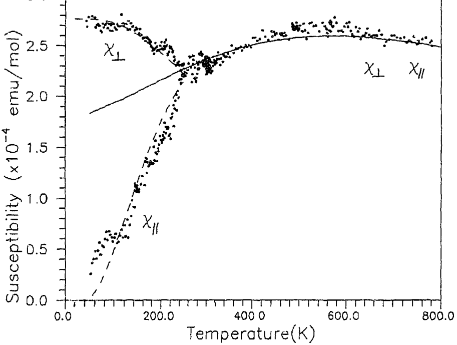

Figure 3. The experimental magnetic susceptibility of $KFeS_2$. Above 250 K, the external field is applied parallel and perpendicular to the c-axis. Below 250 K, the field is parallel and perpendicular to the magnetization axis. The solid line is the calculated susceptibility using eq. (5). The dashed lines are the susceptibility calculated in the spin wave aproximation – the parallel susceptibility using eq. (9) and the perpendicular susceptibility using eq. (13). The calculated susceptibilities over the whole temperature range are for $J = -440{\cdot}71$ K, $J' = 53{\cdot}94$ K, $g = 2{\cdot}025$, and $S = \frac{1}{2}$.

parallel to the magnetization axis shows a sharp decrease below T_N whereas the perpendicular susceptibility shows only a weak temperature dependence. The extrapolated value of the perpendicular susceptibility ($\chi_\perp$) of $KFeS_2$ at 0 K is $2{\cdot}7 \times 10^{-4}$ emu/mol. The present single crystal susceptibility value of $2{\cdot}3 \times 10^{-4}$ emu/mol at 300 K is much lower than the previously reported powder susceptibility values, with the exception of ref. [14], confirming substantial impurity contribution in their powder susceptibility data.

4. Discussion

4.1 *Optical spectra*

The optical spectra in the 400–1500 nm (25000–6667 cm^{-1}) region have been interpreted in terms of transitions within the *d*-electron manifold of a low spin Fe^{3+} ion in a tetrahedral crystal field. The absence of temperature shifts constitutes strong evidence for these features being internal crystal field transitions. The temperature dependent features in the ultraviolet part of the spectrum probably have their origin in charge transfer. An *a priori* justification for assuming a low-spin ground state comes from the low value of the magnetic susceptibility (figure 3). The *d–d* transitions were analysed in the strong field limit of crystal field theory [28]. In this limit, the crystal field is studies is 2·025 [27]. The energies were obtained by diagonalization of the appropriate strong field matrices after allowing for full interconfigurational mixing [28]. The energies of the metal ion states are a function of three variables–Dq, the crystal field splitting energy, and B and C, the Raccah inter-electron repulsion parameters. B and C are related to the Slater–Condon parameters F_2 and F_4 by the linear relation [28], $C = 5F_4$ and $B = F_2 - 5F_4$. The best fit between the experimental and calculated values were obtained for $Dq = 1410\,\mathrm{cm}^{-1}$, $B = 520\,\mathrm{cm}^{-1}$ and $C = 1285\,\mathrm{cm}^{-1}$. The experimental and calculated values alongwith their assignments are given in table 1. Attempts to fit the spectra using the high spin $^6A_1$ as the ground state were unsuccessful for reasonable values of the crystal field parameters.

The features in the near infrared region at $7150\,\mathrm{cm}^{-1}$ and $8770\,\mathrm{cm}^{-1}$ have been assigned to the spin forbidden $^2T_2 \rightarrow {}^4T_1$ and $^2T_2 \rightarrow {}^6A_1$ transitions. A possible reason for the intensity of these spin forbidden bands is that exchange interactions can relax the spin selection rules without energetically perturbing the states involved. A similar explanation had been proposed for the anomalously high intensities of the spin forbidden bands in the optical spectra of one-dimensional compounds $\mathrm{RbFe}X_3$ ($X = \mathrm{Cl}$ or Br) [29]. It was found that in these compounds the intensity of such exchange allowed bands does not show any temperature dependence. Nor is the intensity enhancement related to the three-dimensional ordering temperature. A similar behaviour is observed in the case of $\mathrm{KFeS_2}$.

4.2 *Magnetism*

4.2.1 *Exchange interactions*: The magnetic susceptibility data of $\mathrm{KFeS_2}$ is typical of a low-dimensional system. The broad maximum at 565 K and the non-Curie–Weiss behaviour are due to the short range spin correlations which manifest at temperatures much above T_N in low-dimensional systems. The T_N is, of course, subject to the interchain interactions which lead to three-dimensional ordering below 250 K. The low value of magnetic susceptibility and its isotropic behaviour above T_N suggest that $\mathrm{KFeS_2}$ may be modelled as a spin-$\frac{1}{2}$ one-dimensional Heisenberg chain. Further support comes from the experimental value of the quantity $\chi_\mathrm{max}\,T_\mathrm{max}/g^2$ which is a handy criterion for determining the spin state appropriate for the one dimensional chain compound under investigation. For a one-dimensional Heisenberg chain the values of this quantity for various spin states are 0·0353 for $S = 1/2$; 0·089 for $S = 1$; 0·16 for $S = 3/2$; 0·25 for $S = 2$; and 0·38 for $S = 5/2$ [30]. From the experimentally measured susceptibility of $\mathrm{KFeS_2}$ (figure 3) we have $T_\mathrm{max} = 565$ K and $\chi_\mathrm{max} = 2{\cdot}7 \times 10^{-4}$ emu/mol. Using the EPR determined value of $g = 2{\cdot}025$ [27] one obtains

$$\frac{\chi_\mathrm{max}\,T_\mathrm{max}}{g^2} = 0{\cdot}0375$$

which is closest to the value for $S = 1/2$ chain.

The moment values reported from the neutron scattering studies are, however, much higher ($\mu = 2{\cdot}4$ [11], 2·3 [12], and 1·9 [13]). It is, however, difficult to reconcile the present magnetic studies with higher spin states for Fe^{3+} since the experimental value of $\chi_{\max} T_{\max}/g^2$ clearly indicates a $S = 1/2$ state. Accordingly, we have evaluated the exchange constants: J, the intra-chain nearest-neighbour exchange, and J', the inter-chain exchange using the properties of spin $\frac{1}{2}$ AFM Heisenberg chains.

According to Bonner and Fisher [30, 31], for a spin $\frac{1}{2}$ chain of infinite length,

$$\frac{k_B T_{\max}}{|J|} = 1{\cdot}282 \tag{1}$$

and

$$\frac{|J| \chi_{\max}}{N g^2 \mu_B^2} = 0{\cdot}07346. \tag{2}$$

Substituting the experimental value of $T_{\max}$, 565 K, in eq. (1), we arrive at a $|J|$ value of 440·71 K. Putting this value of $|J|$ in eq. (2) and using the EPR-determined value of $g = 2{\cdot}025$ [27], we get a value of $\chi_{\max} = 2{\cdot}5 \times 10^{-4}$ emu/mol. This value is a little less than the experimental value of $2{\cdot}7 \times 10^{-4}$ emu/mol.

This discrepancy in the calculated and experimental values is probably due to the interchain coupling, which is known to be ferromagnetic. The interchain exchange, J', was calculated from T_N using a relationship originally due to Oguchi, who had calculated the ratio of the exchange parameters, J/J', from T_N by a Green's function technique [32]

$$\frac{k_B T_N}{|J|} = \frac{4S(S+1)}{3 I_{(J/J')}}. \tag{3}$$

The integral $I_{J/J'}$ has been numerically evaluated. Substituting the values of T_N, $|J|$, and S in eq. (3), the value of the integral $I_{(J/J')}$ is 1·8, and $|J'| = 53{\cdot}94$ K.

In order to evaluate how good a spin-$\frac{1}{2}$ one-dimensional antiferromagnetic system is in modelling the magnetic properties of $KFeS_2$, we have calculated the susceptibility of such a model chain for $|J| = 440{\cdot}71$ K, $J' = 53{\cdot}94$ K, $g = 2{\cdot}025$ and $S = \frac{1}{2}$ and compared it with the experimental magnetic susceptibility of $KFeS_2$, both above and below T_N.

4.2.2 *Paramagnetic susceptibility*: The high temperature paramagnetic susceptibility was calculated from the susceptibility curves of Bonner and Fisher [31] using a parametrization due to Torrence *et al* [25]

$$\chi_{\text{chain}} = \tfrac{1{\cdot}4892}{|J|}.[0{\cdot}05031 + 0{\cdot}013014x + 0{\cdot}046846x^2 - 0{\cdot}062319x^3 + 0{\cdot}030834x^4 - 0{\cdot}0076763x^5 + 0{\cdot}00096332x^6 - 0{\cdot}000048529x^7], \tag{4}$$

where $x = T/|J|$.

Interchain interactions were treated in the mean field approximation [33]

$$\chi = \frac{\chi_{\text{chain}}}{[1 - (2zj'/N g^2 \mu_B^2)\chi_{\text{chain}}]}. \tag{5}$$

Equation (5) was evaluated at various temperatures for $|J| = 440{\cdot}71$ K, a simple one-dimensional non-interacting spin wave model [24]. It might at first seem surprising that such a model would be appropriate for the low-temperature three-dimensional AFM state of $KFeS_2$. The justification comes from neutron scattering results [34] which showed that magnon dispersion along the a^* and b^* axes was very much weaker than that along the chain direction.

The effective Hamiltonian for such a system is given by

$$\mathscr{H} = \sum_{i,j} J_{i,j} S_i S_j + \mathscr{D} \sum_i S_i^2 - g\mu_B H_0 \sum_i S_i. \tag{6}$$

The interchain interactions have been included as an anisotropy term, $\mathscr{D}$,

$$\mathscr{D} = J' = g\mu_B H_A,$$

where H_A, is the anisotropic field felt by each ion. The magnetization of the antiferromagnetically ordered state was modelled using a two sublattice model. Magnon energies were calculated using the Holstein–Primakoff approximation and considering only nearest neighbour interactions along the chain axis [24]. The effective Hamiltonian (eq. (6)) thus gives rise to the following grand partition function

$$\begin{aligned}\Xi = {} & \exp(-E_0/k_B T) \exp\left(\sum_k [\beta_k - A k_B T] \right) \\ & \times \prod_k [1 - \exp(-\beta_k + \beta_H)][1 - \exp(-\beta_k - \beta_H)],\end{aligned} \tag{7}$$

where k is restricted to a one-dimensional Brillouin zone since magnon dispersion in the other directions is weak [34]. In the above equation

$$E_0 = -2N_0(\mathscr{D} + J),$$

where N_0 is the number of magnetic atoms in each sublattice,

$$\beta_k = (A^2 - |B_k|^2)^{1/2}/k_B T,$$

$$\beta_H = g\mu_B H_0 f/k_B T,$$

$$A = \mathscr{D} + 2|J|,$$

$$B_k = 2|J| \cos(\mathbf{k}.\mathbf{a}),$$

where $\mathbf{a}$ is the interatomic distance between the Fe^{3+} ions in the chain, and

$$f = (1 - \chi_\parallel / 2\chi_\perp)$$

is a correction factor coming from higher order effects [24].

4.2.4 *Parallel susceptibility*: The parallel susceptibility is given by

$$\chi_\parallel = N k_B T \cdot \frac{d^2 \ln \Xi}{dH_0^2} \tag{8}$$

$$\chi_{\parallel} = \frac{N(g\mu_{\mathrm{B}})}{k_{\mathrm{B}}T} \sum_{-\pi/a} \frac{\exp(\beta_k)}{[1-\exp(\beta_k)]^2}. \tag{9}$$

Equation (9) was evaluated at various temperatures for $|J| = 440{\cdot}71$ K and $\mathscr{D} = 53{\cdot}94$ K. The correction factor was calculated from the experimental value of $\chi_{\parallel}$ and the extrapolated value of $\chi_{\perp}$ at 0 K. The calculated susceptibility is shown as the dashed curve in figure 3. It may be seen that the agreement with the experimental susceptibility of $KFeS_2$ is reasonably good between T_{N} and ≈ 100 K. At lower temperatures, the agreement is slightly poorer.

4.2.5 *Perpendicular susceptibility*: In spin wave theory, the perpendicular susceptibility is derived [24] as

$$\chi_{\perp} = \frac{\chi_{\perp}^{0}}{(1+\alpha/2)}\left[1 - \frac{\Delta M_{s\beta}}{M_{s0}} - \frac{\Delta M_{sT}}{M_{s0}}\right], \tag{10}$$

where $\chi_{\perp}^{0}$ is the perpendicular susceptibility as given by the mean field approximation; α, the anisotropy factor, is $g\mu_{\mathrm{B}}H_{\mathrm{A}}/2Sz|J|$, which for the present one-dimensional system is $\mathscr{D}/2|J| = 0{\cdot}0612$. M_{s0} is the fully aligned sublattice magnetization; $\Delta M_{s\beta}$ is the zero point deviation from the completely aligned state and is independent of temperature, and ΔM_{sT} is the deviation at finite temperatures.

At absolute zero,

$$\chi_{\perp}(0) = \frac{\chi_{\perp}^{0}}{(1+\alpha/2)}\cdot\left[1 - \frac{\Delta M_{s\beta}}{M_{s0}}\right]. \tag{11}$$

$\chi_{\perp}^{0}$, the mean field perpendicular susceptibility is, for $J = 440{\cdot}71$ K and $J' = 53{\cdot}94$ K, $4{\cdot}11 \times 10^{-4}$ emu/mol.

According to the spin wave theory, the zero point deviation in magnetization, $\Delta M_{s\beta}/M_{s0}$, for a spin $\frac{1}{2}$ linear Heisenberg system is

$$\frac{\Delta M_{s\beta}}{M_{s0}} = -\frac{1}{2S}\left(1 + \frac{\ln 2\alpha}{\pi}\right) \tag{12}$$

which, for $\alpha = 0{\cdot}061$ and $S = \frac{1}{2}$ is 0·3304. Substituting the values of $\chi_{\perp}^{0}$, α, and $\Delta M_{s\beta}/M_{s0}$ in eq. (11) we get $\chi_{\perp}(0) = 2{\cdot}75 \times 10^{-4}$ emu/mol. This value may be compared with the extrapolated experimental value of $2{\cdot}7 \times 10^{-4}$ emu/mol.

The temperature dependence of the perpendicular susceptibility in the spin wave approximation is given by the relation

$$\chi_{\perp}(T) = \chi_{\perp}(0) - \frac{\chi_{\perp}^{0}}{(1+\alpha/2)}\left[\frac{\Delta M_{sT}}{M_{s0}}\right]. \tag{13}$$

For small value of the applied field, the H_0 term may be dropped and $\Delta M_{sT}/M_{s0}$ approximated as

$$\frac{\Delta M_{sT}}{M_{s0}} = \frac{A\mathbf{a}}{\pi k_{\mathrm{B}}T}\int [\beta_k(\exp(\beta_k - 1))]^{-1}\,\mathrm{d}k. \tag{14}$$

calculated and experimental values compare reasonably well.

5. Concluding remarks

The present optical spectroscopy and single crystal magnetic susceptibility measurements on the linear chain antiferromagnet $KFeS_2$ confirm an $S=\frac{1}{2}(^2T_2)$ ground state for the Fe^{3+} ion and that the magnetic interactions are essentially one-dimensional in nature. Three-dimensional antiferromagnetic ordering sets in at $T_N = 250$ K. The features in the optical spectra have been assigned to d–d transitions within the $3d$ electron manifold of the Fe^{3+} ions, and there is reasonable agreement with the transition energies as calculated from the strong field limit of the ligand field theory for the crystal field parameter $Dq = 1410\,\mathrm{cm}^{-1}$, and the Raccah interelectronic repulsion parameters $B = 520\,\mathrm{cm}^{-1}$ and $C = 1285\,\mathrm{cm}^{-1}$. The magnetic susceptibility data of $KFeS_2$ is typical of a low-dimensional system. The susceptibility shows a broad maximum at 565 K and non-Curie–Weiss behaviour even at very high temperatures. There is a well-defined transition at 250 K, below which the susceptibility is typical of a three-dimensional antiferromagnet. We believe that the present results – the first report of the crystal susceptibility of $KFeS_2$ – are superior to most of the previous powder results even in the high temperature isotropic region since extreme care has been taken to eliminate ferromagnetic oxide impurities which appear to have plagued previous results [2, 12, 13].

The intra- and inter-chain exchange constants, J and J' were evaluated from the relationship between these quantities and $\chi_{\max}$, $T_{\max}$ and T_N for a spin-$\frac{1}{2}$ one-dimensional Heisenberg system. The values of J and J' are $-440{\cdot}71$ K and $53{\cdot}94$ K. Using these values the susceptibility of a spin-$\frac{1}{2}$ Heisenberg chain was calculated at low temperature using a non-interacting spin wave model, and at high temperatures using a parametrized form of the Bonner–Fisher curves. The calculated and experimental susceptibilities compare extremely well. Further support for a $S=\frac{1}{2}$ model comes from the fact that the calculated perpendicular susceptibility at 0 K ($2{\cdot}75 \times 10^{-4}$ emu/mol) evaluated considering the zero point reduction from the spin wave theory is extremely close to the projected value obtained from the experimental data ($2{\cdot}7 \times 10^{-4}$ emu/mol). The low value of susceptibility in $KFeS_2$ is adequately explained by quantum spin reduction for an $S=\frac{1}{2}$ chain and there is no need to invoke covalency as has been done recently for $TlFeS_2$ [22].

The ratio $J'/2J = 0{\cdot}0612$ is rather high for a one-dimensional system. This value, however, is dictated by the fact that the experimental values, $T_{\max}$ and T_N, are themselves high. The low temperature susceptibility could, however, still be modelled by a $S=\frac{1}{2}$ one-dimensional antiferromagnetic chain since magnon dispersion in non-chain directions is comparatively weak. Interchain interactions may hence be adequately represented by an anisotropy field, and the one-dimensional spin wave model retained.

Acknowledgement

One of the authors (SKT) thanks CSIR, New Delhi, India for a research fellowship.

References

[1] W Bronger, *Angew. Chem. Int. Ed.* **20**, 52 (1981)

[2] W Bronger, *Z. Anorg. Allg. Chem.* **359**, 225 (1968)

[3] D Raj and S P Puri *J. Chem. Phys.* **50**, 3184 (1969)

[4] C A Taft, D Raj and J Danon, *J. Phys.* **35**, C6-241 (1974)

[5] C A Taft, *J. Phys.* **38**, 1161 (1977)

[6] R B Scorzelli, C A Taft, J Danon and V K Garg, *J. Phys.* **C11**, 1397 (1978)

[7] T P Arsenio, P H Domigues, N C Furtado and C A Taft, *Solid State Commun.* **38**, 205 (1981)

[8] D M Cooper, D P E Dickson, P H Domingues, C P Gupta, C E Johnson, M F Thomas, C A Taft and P J Walker, *J. Magn. Magn. Mater.* **36**, 171 (1983)

[9] J Zink and K Nagorny, *J. Phys. Chem. Solids* **49** 1429 (1988)

[10] L Cianchi, F Del Giallo and F Pieralli, *J. Phys.* **C21**, 2931 (1988)

[11] M Nishi and Y Ito, *Solid State Commun.* **30**, 571 (1979)

[12] Z Tomkowicz, A Szytula and H Bak-Ptasiewicz, *Phys. Status Solidi* **57**, K25 (1980)

[13] W Bronger, A Kyas and P Muller, *J. Solid State Chem.* **70**, 262 (1987)

[14] D C Johnston, S C Mraw and A J Jacobson, *Solid State Commun.* **44**, 255 (1982)

[15] A Mauger, M Escorne, C A Taft, N C Furtado, Z P Arguello and T P Arsenio, *Phys. Rev.* **B30**, 5300 (1984)

[16] C A Taft and M A de Paoli, *Chem. Phys. Lett.* **68**, 94 (1979)

[17] H H Schmidtke, R Packroff, W Bronger and P Muller, *Chem. Phys. Lett.* **150**, 129 (1988)

[18] R Packroff and H H Schmidtke, *Inorg. Chem.* **32**, 654 (1993)

[19] S K Tiwary and S Vasudevan, *Solid State Commun.* **101**, 449 (1997)

[20] C A Taft and M Braga, *Phys. Rev.* **B21**, 5802 (1980)

[21] K D Butcher, G S Matthew and E I Solomon, *Inorg. Chem.* **29**, 2067 (1990)

[22] D Welz and M Nishi, *Phys. Rev.* **B45**, 9806 (1992)

[23] A J Jacobson, M S Whittingham and S M Rich, *J. Electrochem. Soc.* **126**, 887 (1979)

[24] F Keffer, in *Handbuch der Physik* edited by S Flügge (Springer-Verlag, Berlin, 1966) vol. XVIII/2, pp. 1–273, and references therein

[25] J B Torrance, Y Tomkiewicz and B D Silverman, *Phys. Rev.* **B15**, 4738 (1987)

[26] D A Cruse and M Gerloch, *J. Chem. Soc. Dalton Trans.* (1977) 152

[27] W V Sweeney and R E Coffman, *Biochim. Biophys. Acta* **286**, 26 (1972)

[28] J S Griffith, *Theory of transition metal ions* (Cambridge University Press, Cambridge, England, 1961)

[29] C F Putnik, G M Cole Jr., B B Garrett and S L Holt, *Inorg. Chem.* **15**, 826 (1976)

[30] L D de Jongh and A R Miedema, *Adv. Phys.* **23**, 1 (1974)

[31] J C Bonner and M E Fisher, *Phys. Rev.* **135**, A640 (1964)

[32] T Oguchi, *Phys. Rev.* **133**, A1098 (1964)
T Oguchi and A Honma, *J. Appl. Phys.* **34**, 1153 (1963)

[33] J S Smart, *Effective field theories of magnetism* (Saunders, Philadelphia, 1986)

[34] M Nishi, Y Ito and S Funahashi, *J. Phys. Soc. Jpn.* **52**, 2210 (1983)

Field emission theory of dislocation-sensitized photo-stimulated exo-electron emission from coloured alkali halide crystals

B P CHANDRA, R S CHANDOK and P K KHARE
Department of Postgraduate Studies and Research in Physics, Rani Durgavati Vishwavidyalaya, Jabalpur 482 001, India

MS received 26 August 1996

Abstract. A new field emission theory of dislocation-sensitized photo-stimulated exo-electron emission (DSPEE) is proposed, which shows that the increase in the intensity of photo emission from F-centres during plastic deformation is caused by the appearance of an electric field which draws excited electrons out of the deeper layer and, therefore, increases the number of electrons which reach the surface. The theory of DSPEE shows that the variation of DSPEE flux intensity should obey the following relation

$$\frac{\Delta J_e(\varepsilon)}{J_e(o)} = \left[\frac{Y_S}{d_F}\exp\left(\frac{\chi}{kT}\right) - 1\right].$$

The theory of DSPEE is able to explain several experimental observations like linear increase of DSPEE intensity J_e with the strain at low deformation, occurrence of the saturation in J_e at higher deformation, temperature dependence of J_e, linear dependence of J_e on the electric field strength, the order of the critical strain at which saturation occurs in J_e, and the ratio of the PEE intensity of deformed and undeformed crystals. At lower values of the strain, some of the excited electrons are captured by surface traps, where the deformation generated electric field is not able to cause the exo-emission. At larger deformation (in between 2% and 3%) of the crystal, the deformation-generated electric field becomes sufficient to cause an additional exo-electron emission of the electrons trapped in surface traps, and therefore, there appears a hump in the J_e versus ε curves of the crystals.

Keywords. Photo-stimulated exo-electron emission; alkalihalide crystals; plastic deformation; colour centres.

PACS No. 79·75

1. Introduction

The optical excitation of electron coloured centres leads to electron emission. This phenomenon is known as photo-induced electron emission (PEE). The PEE is observed for absorption in the region of F-, K-, and L-bands of the F-centres. In any case, an extra thermal activation is required for the escape of electrons into the vacuum. The phenomenon of PEE in alkali halide crystals has been reviewed by Bichevin [1].

An additional stimulation increasing the flux of excited electrons towards the surface enhances the PEE intensity. It has been known for a long time that the role of such a stimulator can be played by plastic deformation of crystals. In 1984, Tsal *et al* [2] detected a sharp increase in the intensity of the PEE from γ-irradiated crystal of NaCl was subsequently studied by Poletaev and Shmurak [3] who referred to it as dislocation sensitized photostimulated exo-electron emission (DSPEE). Poletaev [4] and Poletaev and Shmurak [3] have investigated the spectral and kinetic features of DSPEE in additively coloured KCl crystals. Apart from the F-band, [5], they also studied the effect during the excitation of the K-, L_1- and L_2-bands. It was found that the plastic deformation barely changes the positions of the excitation bands while the integral intensity can increase by 15–30 times. Under the combined action of light in the region of the F-absorption band and deformation, the intensity of the DSPEE was 6–10 times greater than the intensity of DEE. At constant illumination the intensity of the DSPEE was non-monotonically dependent on the strain ε of the crystal. At small ε, a fall off in the emission intensity is observed, which can be understood in terms of the capture of excited electrons on the new traps which have arisen during deformation [6]. The emission intensity increases linearly with ε and when $\varepsilon \approx 2\%$, it attains a maximum, after which it falls off by 10–15% and when $\varepsilon \geq 3\%$, it remains constant up to the deformations which cause the sample to fracture. Similar behaviour in the intensity of the DSPEE was previously observed by Tsal and co-workers [2].

A field mechanism of DSPEE has been proposed by Molotskii and Shmurak [6]. Since the intensity of the DSPEE is 6–10 times greater than the intensity of DEE, the Auger process leading to DE were not taken into account in it. According to Molotskii and Shmurak [6], the increase in the intensity of the photoemission from F-centres during the plastic deformation is caused by the appearance of an electric field which draws excited electrons out of the deeper layers and thereby increases the number of electrons which reach the surface. Although the field emission theory of DSPEE proposed by Molotskii and Shmurak [6], is successful in explaining the linear increase of DSPEE intensity at low deformation, and the occurrence of saturation at higher values of the deformation, it has the following drawbacks:

(i) For $Y_S = 0{\cdot}5$, $l_d \approx 10^{-4}$ cm, [6], the value of $[\Delta J_e(\varepsilon)/J_e(o)]$, varies from 5000 to 50, when the value of α_F varies from 1 to 100. This is nearly 20 to 30 times higher as compared to that of the experimentally observed values of $[\Delta J_e(\varepsilon)/J_e(o)]$ [2, 3, 6].

(ii) As g_0, α_F and l_d are independent of the electron affinity of the crystals, the equation derived by Molotskii and Shmurak (1990), shows that the intensity of PEE in non-deformed crystals, should be independent of the electron affinity. However, the intensity of DSPEE has been found to be correlated with the electron affinity of the crystals [3].

(iii) As $\alpha_F l_d \ll 1$, the equation derived by Molotskii and Shmurak [6] suggests that the temperature dependence of the PEE intensity of non-deformed crystals should be similar to that of l_d. This is not able to explain the temperature dependence of PEE intensity of the non-deformed crystals which follows the Arrhenius plot with an activation energy equal to the electron affinity i.e. $J_e(o) \propto \exp(-\chi/kT)$ [3].

The above drawbacks in the Molotskii's field emission theory of DSPEE indicate the need of a new theory. In the present paper we report a new field emission theory of DSPEE.

2. Theory

When a crystal surface is exposed to light of intensity I_d, then light absorption takes place within a certain depth of the crystal and the light intensely falls off exponentially with the distance x from the surface. Therefore, the rate of excitation of F-centres will be equal to $g_0 \exp(-\alpha_F x)$, where α_F is the absorption coefficient of the F-centre and x is the distance from the surface of the crystal. Thus, the rate of excitation of electrons from the F-centres may be given by

$$g_e = \frac{\mathrm{d}n_e}{\mathrm{d}t} = g_0 \exp(-\alpha_F x). \tag{1}$$

If p_{e1} is the rate constant for the jumping of excited electrons to the conduction band and p_{e2} is the rate constant for the dropping back of the excited electrons to the normal F-level, then we may write the following rate equation [7]

$$\frac{\mathrm{d}n_e}{\mathrm{d}t} = g_e - p_{e1} n_e - p_{e2} n_e.$$

Integrating the above equation and taking $n_e = 0$, at $t = 0$, we get

$$n = \frac{g_e}{(p_{e1} + p_{e2})} \{[1 - \exp -(p_{e1} + p_{e2})t]\}. \tag{2}$$

For $(p_{e1} + p_{e2})t \gg 1$, i.e. in equilibrium, we get

$$n_e = \frac{g_e}{(p_{e1} + \mathrm{p}_{e2})} \tag{3}$$

Thus, the rate of generation of electrons in the conduction band may be written as

$$g_c = p_{e1} n_e = \frac{p_{e1} g_e}{(p_{e1} + p_{e2})}$$

or

$$g_c = \beta_1 g_0 \exp(-\alpha_F x), \tag{4}$$

where $\beta_1 = \frac{p_{e1}}{(p_{e1} + p_{e2})}$.

If τ_0 is the lifetime of the electrons in the conduction band of the crystal, then in equilibrium the number of electrons in the conduction band may be expressed as

$$(n_c)_{\mathrm{st}} = \beta_1 \tau_0 g_0 [\exp(-\alpha_F x). \tag{5}$$

In the steady state, the number of conduction electrons lying in between x and $x + \mathrm{d}x$, is given by

$$(\mathrm{d}N_c)_{\mathrm{st}} = n_c \mathrm{d}x.$$

Therefore, the number of conduction electrons lying in between 0 and x is given by

$$(N_c)_{\mathrm{st}} = \int^{x} \beta_1 \tau_0 g_0 [\exp(-\alpha_F x)] \mathrm{d}x \tag{6}$$

$$(N_c)_{\rm st} = \frac{\beta_1}{\alpha_F}\tau_0 g_0[-\exp(-\alpha_F x)]_\theta^x$$

or

$$(N_c)_{\rm st} = \frac{\beta_1}{\alpha_F}\tau_0 g_0[1-\exp(-\alpha_F x)]. \tag{7}$$

From the above equation, the rate at which the conduction electrons are reaching within the distance θ to x, may be given by

$$R_c = \frac{(N_c)_{\rm st}}{\tau_0}$$

or

$$R_c = \frac{\beta_1}{\alpha_F} g_0[1-\exp(-\alpha_F x)]. \tag{8}$$

When the crystal is deformed, an electrostatic field is produced on the surface of the crystal because of the movement of charged dislocations towards the surface and the strength of the field is given by [8, 6]

$$E_d = \frac{4\pi\varepsilon q}{K_0 b},$$

where q is the linear charge density of a dislocation, b is the Brugers vector, and K_0 is the dielectric constant of the crystal.

The drift length l_e is equal to $\mu_e E_d \tau_0$. Thus, we have

$$l_e = \frac{4\pi\varepsilon q}{K_0 b}\mu_e \tau_0. \tag{9}$$

Considering that the deformation induced electric field on the surface of the crystal is able to attract the conduction electrons lying within the distance θ to l_e, the intensity of DSPEE from equations (8) and (9) may be given by

$$J_e = \frac{Y_S \beta_1}{\alpha_F} g_0\left[1-\exp\left(-\frac{\alpha_F 4\pi\varepsilon q}{K_0 b}\mu_e \tau_0\right)\right], \tag{10}$$

where Y_S is the fraction of the surface on which a positive charge arises during the deformation. For smaller value of the strain ε or for the smaller value of the field E_d, equation (10) may be written as

$$J_e(\varepsilon) = Y_S \beta_1 g_0 \frac{4\pi\varepsilon q}{K_0 b}\mu_e \tau_0. \tag{11}$$

The above equation shows that at low value of ε, the intensity of DSPEE will be proportional to the strain ε of the crystal. Such results have been obtained by Molotskii and Shmurak [6].

As the electric field intensity increases with the deformation, the depth of electron escape and thereby the flux of the emitted particles increases. However, when the escape depth l_e reaches a value such that $\alpha_F l_e \approx 1$, then saturation occurs since all the excited may be obtained by writing $l_e = 1/\alpha_F$, in eq. (9) and we get

$$\varepsilon_c = \frac{K_0 b}{4\pi q \mu_e \tau_0 \alpha_F}. \tag{12}$$

From equation (10), the saturation value of $J_e(\varepsilon)$ is given by

$$J_{es}(\varepsilon) = Y_S \frac{\beta_1 g_0}{\alpha_F}. \tag{13}$$

When the crystal will not be deformed, some of the electrons from the conduction band will reach the surface due to the diffusion process. As the rate of generation of excited electrons is equal to $g_0 \exp(-\alpha_F x)$, the rate of generation of electrons in the conduction band will be $\beta_1 g_0[\exp(-\alpha_F x)]$. If χ is the electron affinity, then the probability of exo-emission of the electrons in the conduction band is, $P = \exp[-(\chi/kT)]$ [6]. Thus, the intensity of DSPEE in undeformed crystal is given by

$$J_e(0) = P\beta_1 g_0[\exp(-\alpha_F x)]$$

or

$$J_e(0) = \beta_1 g_0\left[\exp\left(\frac{\chi}{kT}\right)\right][\exp(-\alpha_F x)]. \tag{14}$$

In non-deformed crystal $\varepsilon = 0$, and thereby the electric field is absent. In this case, the depth of the layer from which excited electrons are capable to reach the surface will be equal to the diffusion length l_d. Thus, by taking $x = l_d$ in eq. (12), we get

$$J_e(0) = \beta_1 g_0\left[\exp\left(-\frac{\chi}{kT}\right)\right][\exp(-\alpha_F l_d)]. \tag{15}$$

Since $\alpha_F l_d \ll 1$, the above equation may be written as

$$J_e(0) = \beta_1 g_0\left[\exp\left(-\frac{\chi}{kT}\right)\right]. \tag{16}$$

From equations (13) and (16), we have

$$\frac{J_{es}(\varepsilon)}{J_e(0)} = \frac{Y_S}{\alpha_F}\exp(\chi/kT). \tag{17}$$

The above equation shows that the ratio of the saturation value of DSPEE intensity in deformed crystal to the DSPEE intensity in non-deformed crystal for the same intensity of light, will depend on α_F, χ and T.

The relative variation in the density of DSPEE is given by

$$\frac{\Delta J(\varepsilon)}{J(0)} = \frac{J(\varepsilon) - J(0)}{J(0)}$$

or

$$\frac{\Delta J(\varepsilon)}{\Delta J(0)} = \left[\frac{Y_S}{\alpha_F}\exp\left(\frac{\chi}{kT}\right) - 1\right]. \tag{18}$$

Correlation between the theoretical and experimental results

Molotskii and Shmurak [6] have investigated the spectral dependence of PEE for additively coloured KCl crystal by exciting the crystal to the *K*, L_1 and L_2 bands. It has been found that the plastic deformation has practically no influence on the position of the exciting ion bands, while the integral intensity of the emission increases 15–30 times (figure 1). The relationship between the band intensiy is also changed. In deformed crystal, the main contribution to emission was made by the *L* bands, and the contribution of the *F* and *K* bands is smaller. The deformation of the crystal increases the contribution of the *F*-band which grows nearly 5 times faster than the *L* bands. The intensity of all the bands increases, but non-uniformly. For example, at strain $\varepsilon = 4 \times 10^{-5}\ \mathrm{s}^{-1}$, the contribution of the *F*-band increases 28 times and that of the *K* and $L\,(L_1, L_2)$ band increases 20·9 times and 8·5 times, respectively.

It is seen from figure 2 that the DSPEE intensity depends non-monotonously on the degree of deformation ε at a constant illumination. At low strain ε, the emission intensity J_e falls which can be explained by capturing of electrons into the new traps formed during the deformation. With increasing ε, the emission intensity grows rapidly and at $\varepsilon \approx 2\%$, reaches its maximum, then J_e decreases by 10 to 15% and at $\varepsilon \simeq 3\%$ remain constant up to the deformation producing failure. This dependence is observed for all excitation bands. For comparison the dependence of the DEE intensity on ε is also shown in figure 1 (Curve 4). It is seen that with the simultaneous action of the

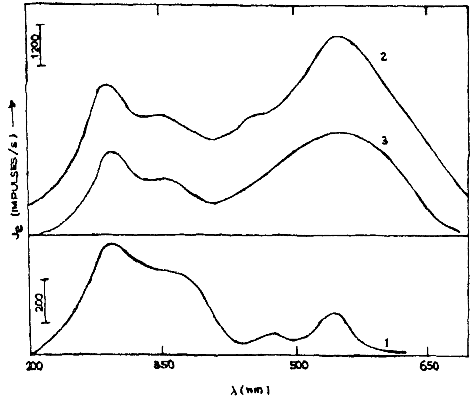

Figure 1. Spectral dependence of photo-exo-emission (PEE) for additively coloured KCl crystal. Curve 1–Initial spectrum, Curve 2 – PEE spectrum during plastic deformation, Curve 3 – PEE spectrum on applying an external electric field of $E = 10^4$ V/cm [6].

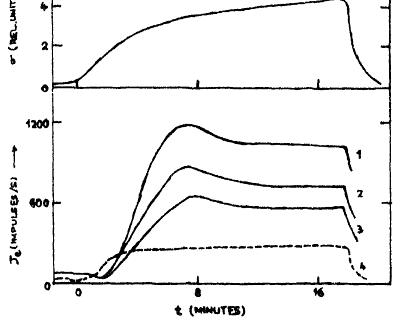

Figure 2. Photo-exo-emission with plastic deformation of an additively KCl crystal. The upper curve is the deformation diagram. Curves 1, 2 and 3 have been obtained on illuminating the crystal with $\lambda_{\max} = 560$ nm and 375 nm, respectively. Curve 4 is the dislocation exoemission of the strain rate $\varepsilon = 4 \times 10^{-5} S^{-1}$ [6].

deformation and illumination in the F-band, the DSPEE intensity is 6 to 10 times higher than that of DEE.

Equation (10) shows that for low value of ε, J_e should increase linearly with the strain ε. Such strain dependence of J_e can clearly be seen from figure 2. Equation (10) indicates that for large value of the strain ε, J_e should attain a saturation value. This fact is supported by the experimental results illustrated in figure 2.

Equation (15) shows that the PEE intensity in non-deformed crystal should follow the Arrhenius plot wih the activation energy χ. Poletaev and Shmurak [5] have measured the temperature dependence of PEE and they have found experimentally the temperature dependence similar to that suggested by equation (15). Using the temperature dependence of PEE intensity, they have succeeded in determining the value of electron affinity χ which is $0{\cdot}16 \pm 0{\cdot}2$ eV for KCl crystals.

Molotskii and Shmurak [6] have measured the dependence of PEE intensity on the externally applied electric field. They have found that PEE intensity increases linearly with the applied electric field (figure 3). This fact is in accord with the discussion made in our field emission theory of DSPEE (may be inferred from eq. (10)).

The theory proposed by us suggests that J_{es} and J_{e0} are correlated in the following way

$$\frac{J_{es}}{J_{e0}} = \frac{Y_S}{\alpha_F l_d}.$$

For KCl crystal in which most of DSPEE measurements have been made, $\chi = 0{\cdot}16$ eV and at $T = 300$ K, $\exp(\chi/kT)$ is equal to 470. The value of α_F in X- or

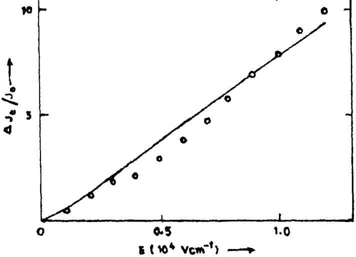

Figure 3. PEE intensity as a function of the electric field strength for additively coloured KCl crystal, 6 experimental data. Continuous curve is the calculated dependence of the PEE on the electric field strength $\Delta(J_e/J_\rho) = f(e)$ for $\mu_0\tau_0 = 2{\cdot}2 \times 10^{-7}\,\mathrm{cm}^2/\mathrm{V}$ [6].

γ-radiated KCl crystal depends on the radiation doses given to the crystal and it varies from a lower value up to nearly 100. Thus, for $\alpha_F = 1$, J_{es}/J_{e0} will be 470, however, for $\alpha_F = 100$, J_{es}/J_{e0} may be 4·7. These results are in accord with the experimental observations [4–6].

For KCl crystals, $q = 5 \times 10^{-5}$ CGS/cm, $\mu_e = 6{\cdot}4\,\mathrm{cm}^2/\mathrm{vs}$, $K_0 = 6$, $b = 4{\cdot}44\,\mathrm{\AA}$, $\alpha_F = 25\,\mathrm{cm}^{-1}$, and $\tau_0 \approx 2 \times 10^{-7}$ s. Thus, the critical value of strain ε at which saturation value in DSPEE will occur, comes out to be $\varepsilon_c \approx 2\%$ (equation 9). Experimentally DSPEE intensity is found to attain a saturation value nearly at $\varepsilon \approx 2\%$. This finding also supports the correlation between the theoretical and experimental results.

It is seen from figure 2 that there is a hump at a strain in between 2% and 3%. It seems that at lower values of the strain, some of the excited electrons are captured by surface traps, where the deformation generated electric field is not able to cause the emission of these surface trapped electrons. At larger deformation the deformation generated electric field becomes sufficient to cause the additional exo-emission of the electrons trapped in surface traps. As a matter of fact, a hump appears in the J_e versus ε curves of the crystals.

4. Conclusions

A new field emission theory of DSPEE is explored which is able to explain several experimental observations like linear increase of DSPEE intensity J_e with the strain at low deformation, occurrence of the saturation in J_e at higher deformation, temperature dependence of J_e, linear dependence of J_e on the electric field strength, the order of the critical strain at which saturation occurs in J_e, and the ratio of the PEE intensity of deformed and non-deformed crystals. The change over by which the excited electrons emerge onto the surface from a diffusion mechanism to a drift mechanism photo-stimulated emission of F-centre electrons during the plastic deformation of alkali halide crystals.

At lower values of the strain, some of the excited electrons are captured by surface traps, where the deformation generated electric field is not able to cause the exo-emission. At larger deformation (in between 2% and 3%) of the crystal, the deformation generated electric field becomes sufficient to cause the additional exo-electron emission of the electrons trapped in surface traps. Therefore, there appears a hump in the J_e versus ε curves of the crystals.

A good correlation between the theoretical and experimental results indicates that the DSPEE is primarily due to the electric field developed on the surface of the crystal during the process of their mechanical deformation.

References

[1] U V Bichevin, *Trudy Inst. Fiz. Eston SSR* **43**, 90 (1975)

[2] N A Tsal, I M Spitkouskii and Ya A Struck, *Sov. Phys. Solid State* **26**, 902 (1984)

[3] A V Poletaev and S Z Shmurak, in Synopsis of paper presented at the Xth All Union Symposium on Mechanicoemission and Mechanicochemistry of Solids, *Restov/Don*, p. 39 (1986)

[4] A V Poletaev, Thesis, Inst. Solid State Phys. Akad Nauk, SSSR, Chernagoporka (1985)

[5] A V Poletaev and S Z Shmurak, *Sov. Phys. Solid State* **A26**, 12 (1984)

[6] M I Molotskii and S Z Shmurak, *Phys. Stat. Solids* **A120**, 83 (1990)

[7] N F Mott and W R Gurney, Electronic processes in ionic crystal (Dover Publications Inc, New York, IInd edition, 1950) p. 172

[8] M I Molotskii, *Sov. Sci. Rev.* **B13**, 1 (1989)

Thermal quenching of luminescence in erbium doped semiconductors

B CHANDA and D N BOSE

Semiconductor Division, Materials Science Centre, Indian Institute of Technology, Kharagpur 721 302, India

MS received 18 March 1997

Abstract. The nature of the temperature dependence of luminescence intensity from Er^+ ions in GaInAsP, Si, InP, GaAs, AlGaAs, ZnTe, as observed by Favennec *et al* [1] has been examined in terms of a double exponential model. The smaller activation energy is found to be 58–100 meV, characteristic of a localized energy barrier at the Er^+ centre while the higher activation energy is approximately $0{\cdot}8\,E_g$ attributed to an Auger non-radiative process of carrier excitation into bands. This model has been found to describe the observed temperature dependences with reasonably good agreement.

Keywords. Luminescence; rare earths; semiconductors.

PACS Nos 71·30; 72·10

1. Introduction

There has been growing interest in rare earth (RE) doped III–V and II–VI semiconductors due to the uniqueness of optical and electrical properties of rare earth impurities in semiconductor hosts [1–11]. It is well-known that the wavelength (energy) of rare earth luminescence emission is insensitive to device processing and ambient temperature. Rare earth elements have partially filled 4*f*-shells which are deeply buried and screened by outer closed $4s^2$ and $5p^6$ orbitals that the energy levels of $4f^n$ configuration are only slightly perturbed compared to free ion energy levels. If the RE ions replace the element from column III in III–V compounds that are isovalent with respect to outer electrons of RE^{3+} ions, they create isoelectronic traps in III–V semiconductors. The luminescence emission arises from intraconfigurational $f-f$ transition in the core of the isoelectronic impurities. The presence of low-lying empty core orbitals in rare earth impurities introduces new excitation and recombination phenomena.

Yb in InP replaces In on a substitutional site [7] and acts as an isoelectronic trap. It has been confirmed that the Yb ion creates an electron trap 30 meV below the conduction band [8]. Er implantation in InP has been observed to introduce electron traps 60 meV below the conduction band [9, 10] while in GaAs two hole traps occur 84 and 340 meV above the valence band. Rochalx *et al* [5] observed that the Er^{3+} emission wavelength remains unchanged with a wavelength of 1·54 μm in binary, ternary and quaternary III–V semiconductors with band gaps ranging from 0·807 eV to 1·75 eV. This emission wavelength is also constant with temperature. Favennec *et al* [1] extended this work by incorporating the results of II–VI semiconductors.

In this paper we have attempted to describe the variation of Er^{3+} emission intensity against temperature as observed by Favennec *et al* [1]. They used single crystal substrates of Si, GaAs, InP, ZnTe as host bulk material, while for the alloys epitaxial layers of AlGaAs, GaInAsP were used. Implantation of Er ions was carried out at room temperature using a beam making an angle 7° with the normal to the sample surface. The beam energy was 330 keV and doses varied from 10^{13} to 10^{14} Er^+ cm^{-2}. After implantation, samples were annealed using rapid thermal annealing technique. The photoluminescence emission intensity at 1·53 μm was measured vs. temperature between 77–400 K. To the best of our knowledge, these results have not been explained before quantitatively.

2. Model

Variation of Er^{3+} emission intensity against temperature in Si, GaAs, InP, ZnTe, AlGaAs, GaInAsP shows that the intensity of emission for all the semiconductors is high at low temperatures. However, at higher temperature the intensity depends strongly on the nature of the host semiconductor. It has been observed that narrower the band gap the faster the decrease of luminescence intensity with temperature and the weaker the intensity at higher temperatures.

The most probable non-radiative mechanism quenching the rare earth luminescence in III–V semiconductors is the Auger energy back-transfer mechanism [12]. The rare earth excited isoelectronic trap occupied by an electron or exciton can transfer energy to the trapped electron and exciton rather than to the radiative field. The electron is consequently ejected deep into the conduction band. If the RE isoelectronic trap is E_n eV below the conduction band of the host material the intensity of emission (η) can be expressed as function of temperature (T) following the relation

$$\eta = \frac{1}{1 + \Sigma_n C_n \exp(-E_n/kT)} \;. \tag{1}$$

Lozykowski [12] has recently carried out a detailed analysis of the kinetics of luminescence in rare earth doped III–V compounds considering a variety of models. He has also involved an Auger mechanism of non-radiative energy transfer. The final expression used to explain thermal quenching however is of the form given by (1). This has been used to explain luminescence of Yb in InP [13].

3. Results

Figures 1–6 represent experimental data along with the theoretical data (solid line) as predicted by the relation (1). These figures indicate that (1) explains reasonably well the nature of temperature dependence of Er^{3+} emission intensity for various host semiconductors. The deviation of the theoretical data with respect to the experimental data is slightly more in the high temperature range. The fitted parameters corresponding to various semiconductors are listed in table 1.

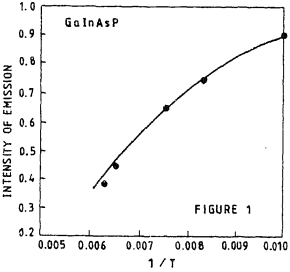
FIGURE 1

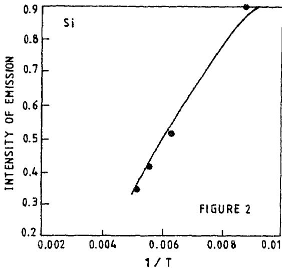
FIGURE 2

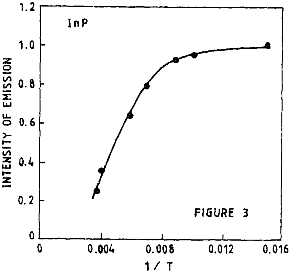
FIGURE 3

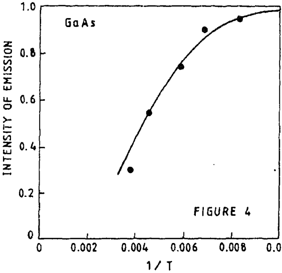
FIGURE 4

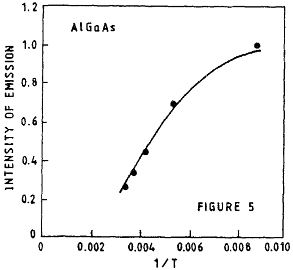
FIGURE 5

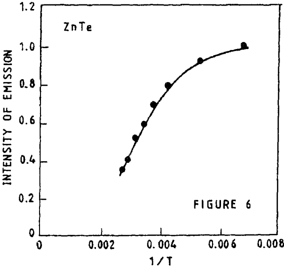
FIGURE 6

Si	1·120	40	0·0580	—	—
InP	1·270	40	0·0650	5	1·00
GaAs	1·430	30	0·0675	10	1·30
AlGaAs	1·670	40	0·0720	200	1·40
ZnTe	2·260	40	0·1000	—	—

The fitted parameter E_1 (0·065 eV) for InP and E_2 (1·3 eV) for GaAs are consistent with the reported data [9, 10] of electron and hole trap levels in InP and GaAs respectively. It is found that the E_1 values increase very slowly with band gap, with the slight exception of Si. These values varying from 58–100 meV represent energy barriers to ejection of electrons from the excited state of Er^+ as in a configuration coordinate model. Multiphonon emission has been shown to have low probability as a non-radiative energy transfer mechanism.

At relatively high temperatures, a different mechanism viz. Auger energy back transfer as postulated by Lozykowski [12] comes into play with E_2 for GaInAsP, InP, GaAs, AlGaAs being of the order of $0{\cdot}8\,E_g$. These energies represent those required for non-radiative energy transfer from Er^+ to carriers in bands in the semiconductors. It is observed that a single exponential model is adequate to explain the data for Si and ZnTe in this temperature range but not much significance can be attributed to this, although of these materials, Si has the only indirect gap and ZnTe is the only *p*-type material.

It is observed that there is not much variation in the pre-factor C_1 between the different semiconductors but the pre-factor C_2 varies strongly between the binary and the alloy semiconductors. This indicates that the nature of the localized centre is very similar in all these materials but the nature of the non-radiative mechanism at high temperatures is different, possibly due to additional defects in the alloys.

In conclusion, the nature of temperature variation of Er^{3+} emission for various semiconductors and alloys has been described quantitatively using a double exponential model with reasonably good agreement. The thermal quenching mechanisms involve localized centres at low temperatures and Auger mechanism at high temperatures.

Acknowledgement

One of the authors (BC) is grateful to the National Laser Programme project on *Semiconductor Lasers* for the grant of a Senior Research Fellowship.

References

[1] P N Favennec, H D'Haridon, A Le Corre and M Salvi, *Electron. Lett.* **23**, 684 (1987)
[2] H Ennen, J Schneider, G Pomrenke and A Axmann, *Appl. Phys. Lett.* **43**, 943 (1983)
[3] W T Tsang and R A Logan, *Appl. Phys. Lett.* **49**, 1686 (1986)

[4] G Pomrenke, H Ennen and W H Haydl, *J. Appl. Phys.* **59**, 610 (1986)

[5] C Rochalx, A Rolland, P N Favennec, B Lambert, A Le Corre, H D'Haridon and M Salvi, *Jap. J. Appl. Phys.* **27**, L2348 (1988)

[6] P S Whitney, K Uwai, H Nakagome and K Takahei, *Appl. Phys. Lett.* **17**, 351 (1988)

[7] P S Whitney, K Uwai, H Nakagome and K Takahei, *Appl. Phys. Lett.* **53**, 2074 (1988)

[8] D Seghier, T Benyattou, G Bremond, F Dueroqnet, J Gregoire, G Guillot, C Lhomer, B Lambert, Y Toudic and A Le Corre, *Appl. Phys. Lett.* **60**, 983 (1992)

[9] B Lambert, A Le Corre, Y Toudic, C Lhomer, G Grandpierre and M Gauneau, *J. Phys. Condens. Matter.* **2**, 479 (1992)

[10] J E Colon, D W Elsaesser, Y K Yeo, R L Hengehold and G S Pomrenke, *Math. Sci. Forum*, **83**–**87**, 671 (1992)

[11] Y Le Guillou, *Electron. Lett.* **25**, 718 (1989)

[12] H J Lozykowski, *Phys. Rev.* **B48**, 17 758 (1993)

[13] H J Lozykowski, A K Alshawa, G S Pomrenke and I Brown in *Rare earth doped semiconductors* edited by G S Pomrenke, P B Klein, and D W Langer, MRS Symposia Proceedings (Materials Research Society, Pittsburg, 1993) vol. 301, 263

Spectroscopic properties of Er^{3+} ions in cadmium and alkali cadmium borosulphate glasses

C K JAYASANKAR and V V RAVI KANTH KUMAR
Department of Physics, S.V. University, Tirupati 517 502, India

MS received 30 October 1996; revised 7 April 1997

Abstract. Spectroscopic properties of Er^{3+} : CBS ($CdSO_4 + B_2O_3$ and $R_2SO_4 + CdSO_4 + B_2O_3$, $R_2SO_4 = Li_2SO_4 \cdot H_2O$, Na_2SO_4, K_2SO_4 and $Gd_2(SO_4)_3 \cdot 8H_2O$) glasses are reported. The assigned energy level data of $Er^{3+}(4f^{11})$ in these glasses are analysed in terms of a parametrized model Hamiltonian. The standard deviations of the data fits are between 39 and 47 cm^{-1} so that the energy level schemes of the $Er^{3+}(4f^{11})$ ions in borosulphate (CBS) glasses are reasonably well reproduced. Radiative properties for the fluorescent levels of Er^{3+} : CBS glasses are determined by using the Judd–Ofelt theory. The potential laser transitions are identified with the help of predicted radiative properties which are compared and discussed with similar results.

Keywords. Erbium doped glasses; optical absorption; oscillator strengths; radiative properties.

PACS Nos 81·40; 81·60; 78·20; 71·55

1. Introduction

The optical properties of Er^{3+} ions have been studied in numerous crystalline hosts [1–4], glass media [5–9] and solutions [10, 11].

Laser action of trivalent erbium in silicate glasses was first obtained by Snitzer and Woodcock [12]. The lasing wavelength of 1540 nm raised strong interest for reasons of eye safety and easy detection. The lamp pump efficiency of 1.7% with a threshold of 5J was reported by Gapontsev *et al* [13] in phosphate glass. The C.W. laser action of Er^{3+} in silica fibers via argon laser pumping was achieved by Mears *et al* [14].

Among rare-earth ions, Er^{3+} is one of the most popular ions since its laser oscillation is utilized as a fiber amplifier of Er doped silica at 1·55 μm [15]. Moreover, it exhibits three fluorescent lines, blue, green and red in the visible region. Also the green-upconversion emission at 0·55 μm has been observed in Er:oxide glasses [16]. The emission properties of these transitions depend on the ligand field of the rare-earth ions.

The Judd–Ofelt theory [17, 18] is helpful in estimating the probability of the forced electric dipole transitions of rare-earth ions in various environments. In the Judd–Ofelt theory, three parameters (Ω_λ, $\lambda = 2, 4, 6$) appear and they can be determined experimentally from the measurements of absorption spectra and refractive index of host material. From these parameters several important optical properties can be evaluated [5–9]. In order to estimate the laser or upconversion efficiency of a particular transition, it is important to know the relation between the glass composition and the Ω_λ.

In this paper we present the investigations carried out on the spectroscopic properties of Er^{3+} : CBS glasses to understand the behaviour of rare-earth ions in these hosts, and to augment the earlier results on Er^{3+} : glasses [5–9].

2. Theory

2.1 *Energy level analyses*

The behaviour of rare earth ions in glasses is similar to that of rare earth ions in inorganic crystals of low symmetry except for inhomogeneous broadening of the spectra because of the multiplicity of rare earth sites in glasses [19]. Optical absorption spectra of triply ionized rare earth ions originate from the transitions between levels of the $4f^n$. The model Hamiltonian which describes the position of these levels for Ln^{3+} ions is written as [4, 20]

$$\begin{aligned} H_{\mathrm{FI}} = {} & E_{\mathrm{avg}} + \sum_k F^k \hat{f}_k + \xi_{s0} \hat{A}_{s0} + \alpha \hat{L}(\hat{L}+1) + \beta \hat{G}(\hat{G}_2) + \gamma \hat{G}(R_7) \\ & + \sum_i T^i \hat{t}_i + \sum_k P^k \hat{p}_k + \sum_j M^j \hat{m}_j, \end{aligned} \tag{1}$$

where $k = 2, 4, 6$; $i = 2, 3, 4, 6, 7, 8$; $j = 0, 2, 4$; and the operators $(\hat{f}_k, \hat{A}_{s0}, \hat{L}, \hat{G}, \hat{t}_i \hat{p}_k, \hat{m}_j)$ and their associated parameters $(E_{\mathrm{avg}}, F^k, \xi_{s0}, \alpha, \beta, \gamma, T^i, P^k$ and $M^j)$ are written according to conventional notation and meaning (with respect to the interactions they represent [4, 20]). The parametric fits are carried out using precisely the same methodologies and strategies employed in our earlier work on Er^{3+} doped crystal free-ion energy level analyses [2–5]. The $4f^{11}$ energy-level structure of Er^{3+} ion was analysed by diagonalizing the complete SLJ basis set. The quality of the fit is estimated by the root mean square deviation, σ, which is defined as

$$\sigma = \left\{ \left[\sum_i^N (E_i^{\mathrm{obs}} - E_i^{\mathrm{calc}})^2 \right] \Big/ N \right\}^{1/2}, \tag{2}$$

where E_i^{obs} and E_i^{calc} are the observed and calculated energies, respectively, for level i and N denotes the total number of levels included in the energy-level fit.

2.2 *Judd–Ofelt analyses and radiative properties*

By employing least-squares fitting of the measured spectral absorbance according to the Judd–Ofelt theory, the characteristic intensity parameters, Ω_λ, were estimated as detailed for Er:glasses [5–9]. From Ω_λ, the radiative properties for fluorescent levels of Er : CBS glasses are determined as detailed in ref. [5–9].

3. Experimental

One mol % of Er^{3+} : CBS (CdBS, *R*CdBS, R = Li, Na, K and Gd) glasses were prepared for 10–15 min:

CdBS : $49CdSO_4+50B_2O_3 + 1Er_2(SO_4)_3 \cdot 8H_2O$,
LiCdBS : $10Li_2SO_4 \cdot H_2O + 39CdSO_4 + 50B_2O_3 + 1Er_2(SO_4)_3 \cdot 8H_2O$,
NaCdBS : $10Na_2SO_4 + 39CdSO_4 + 50B_2O_3 + 1Er_2(SO_4)_3 \cdot 8H_2O$,
KCdBS : $10K_2SO_4 + 39CdSO_4 + 50B_2O_3 + 1Er_2(SO_4)_3 \cdot 8H_2O$,
GdCdBS : $1Gd_2(SO_4)_3 \cdot 8H_2O + 48CdSO_4 + 50B_2O_3 + 1Er_2(SO_4)_3 \cdot 8H_2O$.

The glasses were annealed at 300°C for 20–30 min. Good optical quality glasses of $0{\cdot}8 - 1{\cdot}5$ mm thickness and $1{\cdot}5 - 2{\cdot}5\,\mathrm{cm}^2$ area have been chosen for the measurements.

Optical measurements were made using Hitachi U-3400 spectrophotometer in the UV–VIS–NIR region (300 nm to 2500 nm) at room temperature. The refractive indices (n) for these glasses were measured using an Abbe refractometer at sodium wavelength.

4. Results and discussion

4.1 *Absorption spectra and energy level analysis*

The absorption spectra only for Er : CdBS glass is shown in figure 1 as the spectra for other glasses (Er : *R*CdBS) are very similar. The band positions and intensities closely resemble the absorption spectra of Er^{3+} ions in glass media [5–9], though there is a slight variation in relative positions and intensities of the bands. In all the five glasses, the transitions $^4I_{15/2} \rightarrow {}^4I_{13/2,\,11/2,\,9/2}$, $^4F_{9/2}$, $^4S_{3/2}$, $^2H_{11/2}$, $^4F_{7/2,\,5/2,\,3/2}$, $^2H_{9/2}$, $^4G_{11/2}$ and $^4G_{9/2}$ are located and assigned. In Er^{3+} : CdBS and GdCdBS glasses, $^4I_{15/2}$ to $^4G_{11/2}$ and $^4G_{9/2}$ are missing due to strong absorption near UV region.

The wavenumbers of the observed bands are presented in table 1 alongwith the assignments for all the five borosulphate glasses. The parameters obtained by varying the free-ion parameters, eq. (1), to minimize the r.m.s. deviation (σ) between the observed and calculated energy values (eq. (2)) for Er^{3+} : CBS glasses are given in table 2. The calculated energy values are the eigenvalues obtained by diagonalizing the $Er^{3+}(4f^{11})$ energy matrix using the corresponding parameters given in table 2. The σ values of ±40,

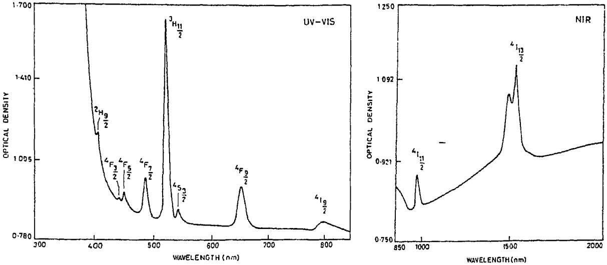

Table 1. Observed energies (E, in cm^{-1}) and oscillator strengths (f, $\times 10^{-6}$) for Er^{3+} : CBS glasses*.

	CdBS		LiCdBS		NaCdBS		KCdBS		GdCdBS	
Level	E	f	E	f	E	f	E	f	E	f
$^4I_{15/2}$	0	—	0	—	0	—	0	—	0	—
$^4I_{13/2}$	6539	11·56	6524	10·69	6536	3·15	6536	11·01	6536	4·68
$^4I_{11/2}$	10275	3·86	10263	2·86	10291	0·53	10263	1·80	10263	1·79
$^4I_{9/2}$	12552	1·05	12553	0·28	12544	0·08	12553	0·43	12549	0·76
$^4F_{9/2}$	15354	13·33	15361	3·56	15361	5·57	15354	7·27	15361	5·27
$^4S_{3/2}$	18413	1·40	18457	0·30	18433	0·21	18369	1·35	18433	0·66
$^2H_{11/2}$	19205	59·50	19216	2·41	19216	4·07	19216	63·63	19216	27·44
$^4F_{7/2}$	20500	12·75	20530	1·10	20530	1·32	20530	8·81	20517	5·45
$^4F_{5/2}$	22207	1·59	22237	0·11	22222	0·19	22222	1·00	22207	0·35
$^4F_{3/2}$	22640	0·71	22457	0·07	22543	0·10	22594	0·68	22543	0·24
$^2H_{9/2}$	24691	—	24600	0·12	24600	0·29	24618	2·40	24528	—
$^4G_{11/2}$	—	—	26434	1·07	26399	4·51	26455	77·01	—	—
$^4G_{9/2}$	—	—	27457	—	27510	0·44	27480	5·38	—	—
N	11	9	13	11	13	12	13	12	11	9
σ	±40	±0·65	±46	±0·93	±43	±0·39	±39	±1·47	±47	±0·27

* For glass title abbrevations see § 3.
The value of σ represent the r.m.s. deviation between observed and calculated values given by eq. (2).

Table 2. Best fit free-ion parameters and hydrogenic ratios for Er^{3+} : CBS glasses*.

Parameter	CdBS	LiCdBS	NaCdBS	KCdBS	GdCdBS
E_{avg}	35724	35774	35691	35725	35692
F^2	100081	100959	100484	100425	100763
F^4	71594	71308	70640	71155	70643
F^6	50762	51441	51044	50486	52078
α	13·50	13·10	8·00	11·60	10·00
β	−585	−480	−355	−430	−470
γ	1675	1360	1280	1400	1325
ξ	2394	2378	2387	2390	2377
F^4/F^2	0·72	0·71	0·70	0·71	0·70
F^6/F^2	0·51	0·51	0·51	0·50	0·52

* For glass title abbreviations see § 3. The parameter values, $T^2 = 647$, $T^3 = 46$, $T^4 = 80$, $T^6 = -321$, $T^7 = 462$, $T^8 = 451$, $M^0 = 3{\cdot}95$, $M^2 = 0{\cdot}56M^0$, $M^4 = 0{\cdot}38M^0$, $P^2 = 506$, $P^4 = 0{\cdot}75P^2$ and $P^6 = 0.50P^2$ are fixed.

±46, ±43, ±39 and ±47 cm^{-1} for Er^{3+} : CdBS, LiCdBS, NaCdBS, KCdBS and GdCdBS glasses, respectively, are quite reasonable.

The interaction of Er^{3+} ions with different glass compositions is estimated by the atomic parameters. Instead of individual F^2, F^4 and F^6 variations, it is convenient to found that the $\sum_k F^k$ experienced by the Er^{3+} ion in alkali cadmium borosulphates decreases as radius and atomic weight of alkali ions decreases. The order of $\sum_k F^k$ is found to be

$$\begin{aligned}&\mathrm{LiCdBS}(2,23,708\,\mathrm{cm}^{-1}) > \mathrm{NaCdBS}(2,22,168\,\mathrm{cm}^{-1})\\ &\quad > \mathrm{KCdBS}(2,22,066\,\mathrm{cm}^{-1}).\end{aligned}$$

It is also found that the $4f$ orbitals of Er^{3+} ions interact with the surroundings in decreasing order when CdBS glass is modified by alkali (Li, Na, K) ions as noticed from the trends of the hydrogenic ratio (F^6/F^2), but the ratio F^4/F^2 did not show any uniform trend.

4.2 *Spectral intensities and Judd–Ofelt analysis*

The oscillator strengths of the observed absorption bands are determined experimentally [5] which are tabulated in table 1. The squared reduced matrix elements, $\|U^\lambda\|^2$, required for the Judd–Ofelt analyses have been calculated from intermediate coupling approximation for all the five glasses [10, 17, 18], though the values are only slightly sensitive to the environment. Using experimental oscillator strengths, transition energies, refractive index and reduced matrix elements, the three phenomenological parameters, Ω_λ, have been evaluated by the least square fit method as carried out for energy level fits. The Ω_λ parameters for Er^{3+} : CBS glasses are presented in table 3 alongwith Ω_λ for some Er^{3+} doped systems [8, 22–24].

The oscillator strengths of the observed bands of Er^{3+} : CdBS glasses are found to be relatively higher than those found in the other four borosulphate glasses. This implies that the non-symmetric component of the electric field acting on the Er^{3+} ions in CdBS is relatively stronger than in RCdBS glasses. It is also found that the observed oscillator strengths for some transitions, ${}^4F_{9/2}$, ${}^2H_{11/2}$, ${}^4F_{7/2,\,5/2,\,3/2}$, ${}^2H_{9/2}$ and ${}^4G_{11/2}$, are found to increase from LiCdBS to NaCdBS to KCdBS glasses. This trend may not yield any significant information as other observed transitions such as ${}^4I_{13/2,\,11/2,\,9/2}$ and ${}^4S_{3/2}$ do not follow uniform trend. The r.m.s. deviations of $\pm 0{\cdot}65$, $\pm 0{\cdot}93$, $\pm 0{\cdot}39$, $\pm 1{\cdot}47$ and $\pm 0{\cdot}27$ (table 1) for Er^{3+} : CdBS, LiCdBS, NaCdBS, KCdBS and GdCdBS, respectively, suggest the validity of the Judd–Ofelt theory.

The Judd–Ofelt parameters, Ω_λ, are compared for 24 Er^{3+} : oxide glass systems [8, 22] alongwith Er^{3+} : aquo-ion [23] and Er(dpm)$_3$ vapour [24] systems in table 3. As seen from table 3, it is found that within oxide glasses, Ω_2 varies from 0·23 (Er^{3+} : NaCdBS) to 39·62 (Er^{3+} : KCdBS), Ω_4 varies from 0·37 (Er^{3+} : LiCdBS) to 7·58 (Er^{3+} : CdBS) and Ω_6 varies from 0·24 (Er^{3+} : S–K) to 11·37 (Er^{3+} : CdBS). Maximum variation in Ω_2 value indicates that Ω_2 is more sensitive to the environment than Ω_4 and Ω_6 parameters. Out of 26 systems compared in table 3, Ω_2 takes maximum value for vapour system. In general the magnitude of Ω_λ parameters are found to be relatively higher for sulphate glasses.

Table 3. Ω_λ ($\times 10^{-20}$ cm^2) parameters for Er^{3+} doped systems*.

	Ω_2	Ω_4	Ω_6
CdBS	38·963	7·575	11·3
LiCdBS	1·011	0·374	6·2
NaCdBS	0·226	3·425	2·8
KCdBS	39·622	1·641	10·5
GdCdBS	18·804	3·121	4·6
$MgSO_4 + K_2SO_4 + ZnSO_4$ [22]	18·68	2·35	7·1
$CaSO_4 + K_2SO_4 + ZnSO_4$ [22]	15·18	1·65	6·6
$BaSO_4 + K_2SO_4 + ZnSO_4$ [22]	18·37	1·36	9·3
$40Li_2O + 60SiO_2$ (S–Li) [8]	4·69	1·29	0·5
$40Na_2O + 60SiO_2$ (S–Na) [8]	4·37	0·83	0·2
$40K_2O + 60SiO_2$ (S–K) [8]	5·02	0·71	0·2
$40CaO + 60SiO_2$ (S–Ca) [8]	5·91	1·53	0·7
$40SrO + 60SiO_2$ (S–Sr) [8]	5·22	1·25	0·6
$40BaO + 60SiO_2$ (S–Ba) [8]	3·42	0·83	0·2
$20K_2O + 20MgO + 60SiO_2$ (S–K–Mg) [8]	6·52	1·07	0·3
$20K_2O + 20CaO + 60SiO_2$ (S–K–Ca) [8]	5·63	0·99	0·3
$20K_2O + 20SrO + 60SiO_2$ (S–K–Sr) [8]	5·64	1·05	0·3
$20K_2O + 20BaO + 60SiO_2$ (S–K–Ba) [8]	4·80	0·84	0·2
$30Li_2O + 70B_2O_3$ (B–Li) [8]	5·81	1·84	1·1
$30Na_2O + 70B_2O_3$ (B–Na) [8]	6·04	1·59	0·9
$30K_2O + 70B_2O_3$ (B–K) [8]	5·38	1·02	0·4
$30Li_2O + 60P_2O_5 + 10Al_2O_3$ (P–Li) [8]	6·42	1·64	0·7
$30Na_2O + 60P_2O_5 + 10Al_2O_3$ (P–Na) [8]	6·85	1·67	1·0
$30K_2O + 60P_2O_5 + 10Al_2O_3$ (P–K) [8]	6·94	1·84	1·1
Aquo ion [23]	1·59	1·95	1·9
Er (dpm)$_3$ vapour [24]	46·00	2·70	3·7

* References for the source of the data are given in square brackets and for deta the glass title see the text as well as corresponding references.

$^4S_{3/2}$, $^4F_{9/2}$, $^4I_{9/2}$, $^4I_{11/2}$, and $^4I_{13/2}$ of Er^{3+} : CBS glasses [5]. The calculated indivi parameter values are given in table 4 for Er^{3+} : CdBS glass. The predicted τ_R for al fluorescent levels are given in table 5.

The transition probabilities (A) were determined from electric (S_{ed}) and magnetic (dipole line strengths. For many transitions, the magnitude of S_{md} is either zer relatively much lower than S_{ed} and hence the magnitude of A is dependent onl $\sum_\lambda \Omega_\lambda \langle \| U^\lambda \| \rangle^2$. The values of $\| U^\lambda \|^2$ are independent of host while Ω_λ are dependent. For some laser transitions like $^4I_{13/2} \rightarrow {}^4I_{15/2}$ and $^4S_{3/2} \rightarrow {}^4I_J$, the valu $\| U^2 \|^2$ and $\| U^4 \|^2$ were either zero or much smaller than that of $\| U^6 \|^2$. For t transitions, the radiative properties varies according to Ω_6 variation. The dependenc

Table 4. Predicted electric (S'_{ed}) and magnetic (S'_{md}) dipole line strengths, radiative (A) and total radiative (A_{T}) transition probabilities, branching ratios (β_{R}), lifetimes (τ_{R}) and cross-sections (σ_a) for Er^{3+} : CdBS glasses.

SLJ	$S'L'J'$	ν cm^{-1}	$S'_{\mathrm{ed}} \times 10^{22}$ cm^2	$S'_{\mathrm{md}} \times 10^{22}$ cm^2	A s^{-1}	β_{R}	$\sigma_\alpha \times 10^{18}$ cm^2
(1)	(2)	(3)	(4)	(5)	(6)	(7)	(8)
$^4G_{11/2}$	$^2H_{9/2}$	1755	1342·973	10·6300	13	0·0001	2·542
	$^4F_{3/2}$	3806	120·618	0·0000	12	0·0001	0·491
	$^4F_{5/2}$	4239	109·767	0·0000	15	0·0001	0·497
	$^4F_{7/2}$	5946	424·816	0·0000	162	0·0011	2·701
	$^2H_{11/2}$	7241	173·971	14·1155	130	0·0009	1·469
	$^4S_{3/2}$	8033	94·653	0·0000	89	0·0006	0·813
	$^4F_{9/2}$	11092	1624·099	2·2272	4014	0·0270	19·290
	$^4I_{9/2}$	13894	280·505	0·1123	1361	0·0092	4·169
	$^4I_{11/2}$	16171	48·764	0·0116	373	0·0025	0·843
	$^4I_{13/2}$	19907	874·124	2·6659	12513	0·0842	18·668
	$^4I_{15/2}$	26446	3882·894	0·0000	129879	0·8742	109·790
	A_{T} for $^4G_{11/2} = 148562\,\mathrm{s}^{-1}$				τ_{R} for $^4G_{11/2} = 6\,\mu\mathrm{s}$		
$^2H_{9/2}$	$^4F_{3/2}$	2051	28·757	0·0000	1	0·0000	0·076
	$^4F_{5/2}$	2484	81·413	0·0000	3	0·0001	0·259
	$^4F_{7/2}$	4191	509·706	4·6512	82	0·0036	2·769
	$^2H_{11/2}$	5486	359·872	1·6582	130	0·0057	2·546
	$^4S_{3/2}$	6278	3·259	0·0000	2	0·0001	0·026
	$^4F_{9/2}$	9337	76·575	256·6590	644	0·0284	4·365
	$^4I_{9/2}$	12139	67·841	0·1232	264	0·0117	1·059
	$^4I_{11/2}$	14416	371·748	4·2299	2448	0·1082	6·963
	$^4I_{13/2}$	18152	788·806	0·0000	10238	0·4524	18·371
	$^4I_{15/2}$	24691	270·072	0·0000	8822	0·3898	8·555
	A_{T} for $^2H_{9/2} = 22633\,\mathrm{s}^{-1}$				τ_{R} for $^2H_{9/2} = 44\,\mu\mathrm{s}$		
$^4F_{5/2}$	$^4F_{7/2}$	1707	452·077	37·7000	9	0·0005	1·804
	$^2H_{11/2}$	3002	264·426	0·0000	26	0·0013	1·697
	$^4S_{3/2}$	3794	32·728	2·2190	7	0·0004	0·286
	$^4F_{9/2}$	6853	585·147	0·0000	681	0·0354	8·575
	$^4I_{9/2}$	9655	208·295	0·0000	678	0·0352	4·300
	$^4I_{11/2}$	11932	76·359	0·0000	469	0·0244	1·948
	$^4I_{13/2}$	15668	525·552	0·0000	7311	0·3800	17·608
	$^4I_{15/2}$	22207	253·970	0·0000	10060	0·5228	12·060
	A_{T} for $^4F_{5/2} = 19241\,\mathrm{s}^{-1}$				τ_{R} for $^4F_{5/2} = 51\,\mu\mathrm{s}$		
$^4F_{7/2}$	$^2H_{11/2}$	1295	984·610	0·0000	6	0·0002	2·045
	$^4S_{3/2}$	2087	4·556	0·0000	0	0·0000	0·015
	$^4F_{9/2}$	5146	87·528	17·2868	40	0·0017	0·882
	$^4I_{9/2}$	7948	624·575	6·7807	861	0·0371	8·058
	$^4I_{11/2}$	10225	391·165	0·0000	1134	0·0488	6·414
	$^4I_{13/2}$	13961	257·626	0·0000	1902	0·0818	5·768
	$^4I_{15/2}$	20500	825·685	0·0000	19296	0·8303	27·146
	A_{T} for $^4F_{7/2} = 23239\,\mathrm{s}^{-1}$				τ_{R} for $^4F_{7/2} = 57\,\mu\mathrm{s}$		
$^4S_{3/2}$	$^4F_{9/2}$	3059	29·457	0·0000	5	0·0004	0·289
	$^4I_{9/2}$	5861	345·661	0·0000	378	0·0294	6·498
	$^4I_{11/2}$	8138	92·577	0·0000	271	0·0211	2·416

(*Continued*)

Table 4. (*Continued*).

SLJ	$S'L'J'$	ν cm^{-1}	$S'_{\text{ed}} \times 10^{22}$ cm^2	$S'_{\text{md}} \times 10^{22}$ cm^2	A s^{-1}	β_R	$\sigma_\alpha \times 10^{18}$ cm^2
(1)	(2)	(3)	(4)	(5)	(6)	(7)	(8)
	$^4I_{13/2}$	11874	390·793	0·0000	3549	0·2763	14·884
	$^4I_{15/2}$	18413	255·221	0·0000	8644	0·6729	15·073
	A_T for $^4S_{3/2} = 12846\,\text{s}^{-1}$				τ_R for $^4S_{3/2} = 77\,\mu\text{s}$		
$^4F_{9/2}$	$^4I_{9/2}$	2802	525·521	0·1263	25	0·0030	1·890
	$^4I_{11/2}$	5079	1740·954	15·2004	500	0·0602	11·456
	$^4I_{13/2}$	8815	248·200	0·0000	369	0·0445	2·807
	$^4I_{15/2}$	15354	942·575	0·0000	7404	0·8923	18·568
	A_T for $^4F_{9/2} = 8298\,\text{s}^{-1}$				τ_R for $^4F_{9/2} = 120\,\mu\text{s}$		
$^4I_{9/2}$	$^4I_{11/2}$	2277	218·616	39·7462	7	0·0068	0·769
	$^4I_{13/2}$	6013	830·452	0·0000	392	0·3934	6·407
	$^4I_{15/2}$	12552	139·201	0·0000	597	0·5998	2·242
	A_T for $^4I_{9/2} = 996\,\text{s}^{-1}$				τ_R for $^4I_{9/2} = 1004\,\mu\text{s}$		
$^4I_{11/2}$	$^4I_{13/2}$	3736	1500·623	77·3845	150	0·1189	6·341
	$^4I_{15/2}$	10275	565·437	0·0000	1109	0·8811	6·212
	A_T for $^4I_{11/2} = 1259\,\text{s}^{-1}$				τ_R for $^4I_{11/2} = 794\,\mu\text{s}$		
$^4I_{13/2}$	$^4I_{15/2}$	6539	1791·167	68·7794	810	1·0000	11·196
	A_T for $^4I_{13/2} = 810\,\text{s}^{-1}$				τ_R for $^4I_{13/2} = 1234\,\mu\text{s}$		

Table 5. Radiative lifetimes (τ_R µs) for fluorescent levels of Er^{3+} : CBS glasses.

Glass	$^4G_{11/2}$	$^2H_{9/2}$	$^4F_{5/2}$	$^4F_{7/2}$	$^4S_{3/2}$	$^4F_{9/2}$	$^4I_{9/2}$	$^4I_{11/2}$	$^4I_{13/2}$
CdBS	6	44	51	57	77	120	1004	794	1234
LiCdBS	108	113	107	97	138	358	3748	1758	2355
NaCdBS	98	197	192	150	317	376	2857	3854	4536
KCdBS	6	51	63	57	86	194	1951	870	1403
GdCdBS	14	109	128	106	192	296	2526	1911	2881

these changes are minimum in the case of S–K-alkaline earths and phosphate–alkali glasses [8]. Similar observations are noticed for $^4S_{3/2} \rightarrow {}^4F_{9/2}$ and ^4I_J transitions. Out of 20 glass systems compared in table 6, it is found that Ω_6, A, A_T and β_R are found to be maximum for CdBS glasses and minimum for S–K glasses. It is also found that Ω_6 values increase in the order of K to Na to Li modifier ions for silicate and borate glasses, whereas decreasing trend is noticed for phosphate glasses. However, non-uniform trend is noticed when potassium based silicate glasses are modified with alkaline earths. Systematic variation of Ω_6 is not found for CdBS glasses when these glasses are modified by alkali elements. Therefore, it is inconclusive to establish general trend in Ω_6 when the glass network is modified by either alkali or alkaline earths. It is also noticed that among $^4S_{3/2} \rightarrow {}^4I_J$ emission channels, $^4S_{3/2} \rightarrow {}^4I_{15/2}$ exhibits maximum and $^4S_{3/2} \rightarrow {}^4I_{11/2}$ exhibits minimum values of A and/or β_R

Table 6. Judd–Ofelt parameter (Ω_6), radiative (A) and total radiative (A_T) transition probabilities and branching ratios (β_R) for Er^{3+} : glasses [8].

		$^4I_{13/2} \rightarrow$	$^4S_{3/2} \rightarrow$					
Glass	Ω_6	$^4I_{15/2}$ A/A_T	$^4F_{9/2}$ A (β_R)	$^4I_{9/2}$ A (β_R)	$^4I_{11/2}$ A (β_R)	$^4I_{13/2}$ A (β_R)	$^4I_{15/2}$ A (β_R)	A_T
(1)	(2)	(3)	(4)	(5)	(6)	(7)	(8)	(9)
CdBS	11·37	810	5 (0·000)	378 (0·029)	271 (0·021)	3549 (0·276)	8644 (0·672)	12846
LiCdBS	6·27	425	2 (0·000)	182 (0·025)	151 (0·021)	1997 (0·278)	4866 (0·676)	7199
NaCdBS	2·82	220	1 (0·000)	106 (0·034)	69 (0·022)	865 (0·275)	2106 (0·670)	3146
KCdBS	10·51	712	4 (0·000)	292 (0·025)	236 (0·021)	3178 (0·276)	7790 (0·677)	11501
S–Li	0·56	88	—	30 (0·041)	16 (0·022)	195 (0·268)	488 (0·669)	729
S–Na	0·27	60	—	15 (0·045)	8 (0·022)	89 (0·266)	223 (0·667)	334
S–K	0·24	59	—	13 (0·045)	7 (0·023)	79 (0·266)	198 (0·666)	297
S–Ca	0·77	117	—	43 (0·038)	24 (0·022)	298 (0·269)	744 (0·671)	1109
S–Sr	0·61	103	—	35 (0·038)	20 (0·022)	242 (0·267)	609 (0·673)	905
S–Ba	0·27	77	—	20 (0·045)	10 (0·022)	114 (0·264)	289 (0·669)	432
S–K–Mg	0·33	67	—	19 (0·047)	9 (0·023)	107 (0·265)	268 (0·665)	403
S–K–Ca	0·34	72	—	20 (0·044)	10 (0·022)	120 (0·267)	300 (0·667)	450
S–K–Sr	0·30	70	—	19 (0·048)	9 (0·023)	105 (0·265)	263 (0·664)	396
S–K–Ba	0·26	69	—	17 (0·046)	8 (0·022)	97 (0·266)	244 (0·666)	366
B–Li	1·18	139	—	56 (0·036)	34 (0·022)	420 (0·269)	1050 (0·673)	1559
B–Na	0·91	109	—	41 (0·037)	24 (0·021)	299 (0·269)	749 (0·673)	1113
B–K	0·44	72	—	21 (0·041)	12 (0·022)	139 (0·268)	348 (0·669)	520
P–Li	0·78	101	—	38 (0·039)	21 (0·022)	256 (0·268)	641 (0·671)	955
P–Na	1·08	117	—	45 (0·036)	27 (0·021)	342 (0·268)	860 (0·675)	1274
P–K	1·10	118	—	46 (0·036)	28 (0·022)	343 (0·270)	854 (0·672)	1271

by choosing appropriate glass composition, the intensity parameters (Ω_6) and in turn radiative properties (A, A_T and β_R) can be varied over a range. For example, A_T value

The absorption band positions, integrated absorption cross-sections, Judd–Ofelt intensity parameters and in turn radiative properties for fluorescent levels of Er^{3+} : cadmium and alkali cadmium borate glasses are investigated. The trends in predicted radiative properties are similar to ternary sulphate glasses and differ from oxide glasses. Systematic decreasing or increasing trend in the magnitudes of Judd–Ofelt parameters are not clear when the glass compositions are modified by alkali or alkaline earths which suggests that further investigations are essential in this direction. The magnitudes of the A, A_T and β_R parameter values for ${}^4I_{13/2} \rightarrow {}^4I_{15/2}$ and ${}^4S_{3/2} \rightarrow {}^4I_J$ levels are mainly attributed to the magnitude of Ω_6 parameter.

Acknowledgment

This work was supported by a research grant of the Department of Science and Technology, New Delhi under Young Scientists Programme.

References

[1] J B Gruber, J R Quagliano, M F Reid, F S Richardson, M E Hills, M D Seltzer, S B Stevens, C A Morrison and T H Allik, *Phys. Rev.* **B48**, 15561 (1993)

[2] A Renuka Devi, E Rukmini and C K Jayasankar, *Phys. Status Solidi* **A131**, 191 (1992)

[3] C K Jayasankar, A Renuka Devi, E Rukmini and M F Reid, *J. Alloys Compounds* **193**, 203 (1993)

[4] E Rukmini, A Renuka Devi and C K Jayasankar, *Physica* **B193**, 166 (1994)

[5] A Renuka Devi and C K Jayasankar, *J. Non-Cryst. Solids* **197**, 111 (1996)

[6] T Catunda, L A O Nunes, A Florez, Y Messaddeq and M A Aegerter, *Phys. Rev.* **B53**, 6065 (1996)

[7] X Zou and T Izumitani, *J. Non-Cryst. Solids* **162**, 68 (1993)

[8] H Takebe, Y Nageno and K Morinaga, *J. Am. Ceram. Soc.* **77**, 2132 (1994)

[9] P Nachimuthu and R Jagannathan, *Phys. Chem. Glasses* **36**, 194 (1995)

[10] W T Carnall, in *Handbook on the physics and chemistry of rare earths* edited by K A Gschneidner Jr. and L Eyring (Elsevier Publ. Co., Amsterdam, 1987) vol. 3, ch. 24

[11] S V J Lakshman and C K Jayasankar, *Pramana – J. Phys.* **23**, 129 (1984)

[12] E Snitzer and R Woodcock, *Appl. Phys. Lett.* **6**, 45 (1965)

[13] V P Gapontsev, A K Gromov, A A Izyneev, I Sadovskii, A A Stavrov, Yu S Tipenko and A P Shkadarevich, *Kvant. Electron* **16**, 684 (1989)

[14] R J Mears, L Reeckie, S B Poole and D N Payne, *Electron Lett.* **22**, 159 (1986)

[15] M Nakazawa, Y Kimura and K Suzuki, *Appl. Phys. Lett.* **54**, 295 (1989)

[16] S Tanabe, K Hirao and N Soga, *J. Non-Cryst. Solids* **122**, 79 (1990)

[17] B R Judd, *Phys. Rev.* **127**, 750 (1962)

[18] G S Ofelt, *J. Chem. Phys.* **27**, 511 (1962)

[19] R Reisfeld and C K Jorgensen, *Lasers and excited states of rare earths* (Springer-Verlag, New York, 1977)

[20] B G Wybourne, *Spectroscopic properties of rare earths* (Interscience, New York, 1965)

[21] J R Quagliano, F S Richardson and M F Reid, *J. Alloys Compounds* **180**, 131 (1992)

[22] Y Subramanyam, L R Moorthy and S V J Lakshman, *Mater. Lett.* **9**, 146 (1988)

[23] W T Carnall, J P Hessler, H R Hoekstra and C W Williams, *J. Chem. Phys.* **68**, 4303 (1978)

[24] D M Gruen, C W DeKock and R L Mcbeth, *Adv. Chem. Ser.* **71**, 102 (1967)

Collisional excitation among the seven lowest states of TiXII

M MOHAN[1,3] and A HIBBERT[2]

[1] International Centre for Theoretical Physics, Trieste, Italy
[2] Department of Applied Mathematics and Theoretical Physics, The Queen's University of Belfast BT7 1NN, Northern Ireland
[3] Permanent address: Department of Physics, University of Delhi, Delhi 110 007, India

MS recieved 18 November 1996; revised 7 May 1997

Abstract. Collision strengths have been calculated for electron impact excitation of sodium-like TiXII for all 21 transitions amongst its lowest seven states. Configuration interaction wave functions have been used to represent the target states. The standard and no-exchange *R*-matrix codes have been used to calculate the contribution of partial waves with $L \leqslant 8$ and $L > 8$ respectively. Collision strengths are tabulated at selected energies in the range 26 to 50 Ryd. Effective collision strengths are tabulated for electron temperatures in the range $\log T_e = 4{\cdot}0$ to $\log T_e = 6{\cdot}0$, with T_e in K. This is the first detailed calculation on this ion in which the effects of exchange, channel couplings and short-range correlation are taken into account.

Keywords. Collision strength; *R*-matrix method.

PACS No. 34·80

1. Introduction

The spectra and term systems of Na-like ions have been extensively studied over the years [1]. Recently there has been renewed interest in Na-like ions because they have proved to be a useful tool in diagnosing fusion plasmas, since their spectral lines are rather strong and easy to identify. TiXII is one of the most important constituents on the Tokamak plasma since Ti is present as a metallic impurity in the fusion reactor and is responsible for the radiative power loss from the plasma [2].

In the area of X-ray laser research, Na-like ions play an important role in understanding the lasing action in Na-like ions in an electron collision excitation scheme which has been utilized successfully in the recent work of many groups (Matthews *et al* [3], Fields *et al* [4]).

The spectrum of TiXII was first observed by Edlen [5]. Ekberg and Svensson [6] and Cohen and Behring [7] extended the analysis of the series of transitions $3s-np$, $3p-ns$, $3p-nd$ and $3d-nf$ up to $11p$, $7s$, $10d$ and $8f$. Recently, Westerlind [8] has recorded a new spectra of highly ionized Ti in the wavelength regions 335–1165Å and 1300 –1400 Å using the beam-foil technique. The term system has been extended to include all configurations up to $8f$, with the exception of $8s$. In addition, Zhang *et al* [9] have reported collision strengths for several Na-like ions using the distorted wave method.

In the present work, we have used the *R*-matrix method (Burke and Robb [10]) target states included in the calculation. We have performed a seven-state close-coupling LS calculation in which the target states are represented by configuration interaction wave functions determined using the CIV 3 code [13].

The collision strengths, Ω, have been computed at a large number of electron incident energies and tabulated at selected values in the range 26 to 50 Ryd. Further, the Ω's are integrated over a Maxwellian distribution of electron velocities to obtain the effective collision strengths γ which are tabulated in the electron temperature range of log $T_e = 4{\cdot}0$ to $6{\cdot}0$ K.These are the first detailed calculations of Ω and γ for this ion in which the important physical effects of exchange, channel coupling and short range correlation have properly been taken into account.

2. Calculations

Using the CIV3 code, Hibbert *et al* [14] have recently calculated configuration–interaction (CI) wave functions for Na-like ions, including TiXII. The CI wave function in *LS* coupling is represented by an expansion of the form

$$\psi(LS) = \sum_{i=1}^{k} a_i \Phi_i(\alpha_i LS), \tag{1}$$

where $\{\Phi_i\}$ are configuration state functions constructed from one-electron orbitals whose angular momenta are coupled as specified by $\{\alpha_i\}$ to form a total L and S common to all configurations. The radial part of each orbital is written as a linear combination of normalized Slater-type orbitals

$$P_{nl}(r) = \sum_{j=1}^{k} c_{jnl} \left[\frac{(2\zeta)^{2I_{njl}+1}}{(2I_{jnl})!} \right]^{1/2} r I_{jnl} \exp(-\zeta_{jnl} r) \tag{2}$$

with

$$\int_0^\infty P_{nl}(r) P_{n'l}(r)\,\mathrm{d}r = \delta_{nn'}.$$

The parameters $\{a_i\}$ in (1) and the parameters in (2) were determined variationally by Hibbert *et al* [14]. The 1*s*, 2*s*, 2*p* and 3*s* functions were chosen as the Hartree–Fock orbitals of the ^2S ground state of TiXII (Clementi and Roetti [15]). The remaining orbitals P_{nl} were optimized on the energies of the respective excited states $1s^2 2s^2 2p^6 nl\,^2L$.

In table 1, we list the optimized radial function parameters used in (2) for the 4*s*, 3*p*, 4*p*, 3*d*, 4*f* orbitals. Table 2 lists the configurations used to generate the seven target states which are indexed in table 3 in order of increasing energy. The choice of configurations includes some allowance for core polarization, through using the valence orbitals rather than correlation orbitals optimized specifically for this purpose so as to retain a fairly simple target wave functions. Nevertheless, there is satisfactory agreement between our calculated energies and the experimental values given by Corliss and Sugar [16].

The total wave function for TiXII plus an electron is expressed as an *R*-matrix expansion, as discussed by Burke and Robb [10] and by Mohan [12]. The *R*-matrix

Table 1. Radial function parameters.

Orbital	I_{jnl}	C_{jnl}	ξ_{jnl}
$4s$	1	0·11185	17·22634
	2	−0·59853	6·61167
	3	2·04148	3·89881
	4	−2·17776	3·33069
$3p$	2	0·49399	8·85806
	3	−1·10311	4·23216
$4p$	2	0·33946	8·62129
	3	−2·69541	3·17489
	4	3·01155	3·20437
$3d$	3	1·00000	4·38539
$4d$	3	0·79541	4·41103
	4	−1·27383	2·84074
$4f$	4	1·00000	3·01680

Table 2. Target state configurations.

Target state	State number	Configurations
^2S	1·4	$[1s^22s^2]$ $2p^63s$, $2p^64s$, $2p^53p3s$, $2p^53p4s$ $2p^53d3p$, $2p^53d4p$
$^2P^0$	2·5	$[1s^22s^2]$ $2p^63p$, $2p^64p$, $2p^53p^2$, $2p^53p4p$, $2p^53s3d$
^2D	3·6	$[1s^22s^2]$ $2p^63d$, $2p^64d$, $2p^53p3d$, $2p^54p3d$, $2p^53p4d$
$^2F^0$	7	$[1s^22s^2]$ $2p^64f$, $2p^53p^2$, $2p^53p4p$, $2p^53d^2$

Table 3. Energy threshold relative to the ground state.

		Energies (Ryd)	
Key	State	Theoretical[a]	Experimental[b]
1	$1s^22s^22p^63s\ ^2S$	0·00000	0·00000
2	$1s^22s^22p^63p\ ^2P^0$	1·90683	1·95153
3	$1s^22s^22p^63d\ ^2D$	4·52602	4·57873
4	$1s^22s^22p^64s\ ^2S$	10·24579	10·32988
5	$1s^22s^22p^64p\ ^2P^0$	10·98815	11·08645
6	$1s^22s^22p^64d\ ^2D$	11·93488	12·04416
7	$1s^22s^22p^64f\ ^2F^0$	12·26882	12·39689

[a] This work, CI wave functions.

packages of Berrington *et al* [17] were used in the present work. We have included 20 continuum orbitals for each angular momentum of the continuum electron having maximum energy up to 60 Ryd which ensure convergence in the energy range considered here. We imposed a zero logarithmic derivative at the R-matrix boundary radius of 6·0 a.u.

For the inner region ($r < 6{\cdot}0$ a.u.) we included all the short range $(N+1)$-electron correlation terms which could be constructed from the bound orbitals to take account of the channels which would otherwise be omitted.

In the outer region ($r > 6{\cdot}0$ a.u.), the coupled differential equations are solved using the asymptotic code based on the method of Seaton [17]. This treats multipole coupling by first-order perturbation theory. The LS coupled K-matrices, obtained by matching the inner and outer region solutions at the R-matrix boundary, were used to calculate the collision strengths. We have considered all partial waves up to the $(N+1)$-electron angular momentum $L=8$ for both parities and spin multiplicities (singlet and triplet). This was sufficient to obtain converged results for forbidden transitions. However, for allowed transitions it was necessary to include the contribution of higher partial waves for convergence to be achieved. Since exchange effects were found to be negligible for $L \geq 10$, a non-exchange R-matrix approximation, which amounts to neglecting the antisymmetrization and the bound type part of R-matrix expansion [10], is sufficient for higher partial waves [18]. A fast no-exchange R-matrix code (NERM) recently developed by Burke *et al* [19], has therefore been used to calculate the contribution from $L = 10$ to 40 and, finally, a 'top up' procedure, based on the sum rule of Burgess *et al* [20], which accounts approximately for $L > 40$.

3. Collision strengths and rate coefficients

In order to determine the resonances in Ω, we have undertaken calculations at a large number of incident electron energies, particularly in the threshold energy region. An energy mesh of 0·001 Ryd has been used at energies close to threshold but has gradually been increased with increasing incident energy. To give an idea of the energy density of the calculations, we show in figure 1 the variation of Ω with incident electron energy. It is clear that the collision strengths are dominated by closed-channel (Feshbach) resonances throughout the threshold energy region. These resonances converge to higher thresholds and contribute significantly to our calculations of effective collision strengths.

In table 4 we list our collision strengths (Ω) for 21 transitions involving the seven lowest states, at selected energy points. These are the first close-coupling results for collision strengths among these excited states. Zhang *et al* [8] have performed distorted wave (DW) calculations, but for inner-shell transitions ($2s^2 2p^6 3l \rightarrow 2s^2 2p^5 3l 3l'$, $2s^2 2p^6 3l \rightarrow 2s 2p^6 3l 3l'$), so comparison with our calculations is not possible.

Since the excitation collision strengths vary rapidly with energy in the threshold region, it is not practicable to tabulate them. However, for many plasma applications, excitation rate coefficients rather than the collision strengths are needed. They are

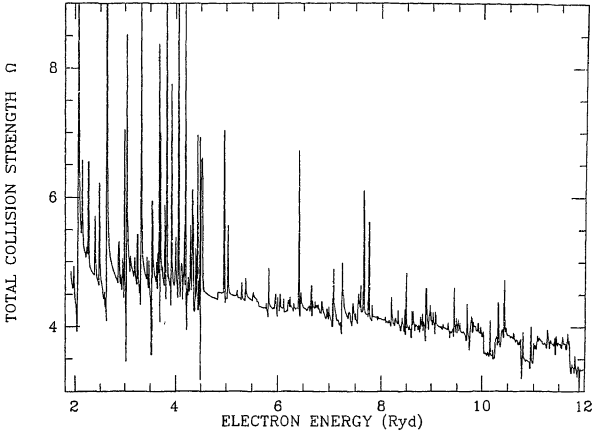

Figure 1. Energy variation of the total collision strengths for $1s^22s^22p^63s\ ^2S^e \rightarrow 1s^22s^22p^6\ ^2P^0$ allowed transition in TiXII.

Ω tabulated in table 4. The excitation rate coefficient (Eissner and Seaton [21]) for transition i to f at an electron temperature T_e is given by

$$C_{i,f} = \frac{8{\cdot}63 \times 10^{-6}}{g_i\, T^{1/2}}\, \gamma_{i,f} \exp\left[\frac{-\Delta E_{if}}{kT_e}\right] \mathrm{cm}^3\mathrm{s}^{-1}, \tag{3}$$

where $g_i = (2L_i + 1)(2S_i + 1)$ is the statistical weight of the lower state i, $\Delta E_{if} = E_f - E_i$ is the excitation energy and $\gamma_{i,f}$ defined as

$$\gamma_{i,f} = \int_0^{-\infty} \Omega(i \rightarrow f) \exp(-E_f/kT_e)\, \mathrm{d}(E_f/kT_e) \tag{4}$$

is the effective (dimensionless) collision strength for the transition i to f, E_f is the energy of the incident electron with reference to upper level f and k is the Boltzmann constant. In table 5, we have given $\gamma_{i,f}$ for all transitions over the electron temperature range from $\log(T_e) = 4{\cdot}0$ to $\log(T_e) = 6{\cdot}0$ where T_e is in K.

In general the collision strengths Ω or the effective collision strengths γ were found to be larger for the dipole allowed transitions than for the forbidden transitions. For the transitions from the ground state, the strongest corresponds to the resonance transition

Table 4. Collision strengths for transitions in TiXII in the energy range 26–50 Ryd ($a \pm b \equiv a \times 10^{\pm b}$).

on	Energy (Ryd)									
J	26·00	28·00	30·00	32·00	34·00	36·00	38·00	40·00	45·00	50·00
2	7·738 − 00	7·870 − 00	7·995 − 00	8·112 − 00	8·258 − 00	8·364 − 00	8·463 − 00	8·559 − 00	8·778 − 00	8·971 − 00
3	5·852 − 01	5·889 − 01	5·923 − 01	5·953 − 01	5·979 − 01	5·999 − 01	6·017 − 01	6·035 − 01	6·083 − 01	6·119 − 01
4	1·652 − 01	1·663 − 01	1·673 − 01	1·685 − 01	1·695 − 01	1·703 − 01	1·708 − 01	1·713 − 01	1·727 − 01	1·741 − 01
5	5·235 − 02	5·582 − 02	5·938 − 02	6·298 − 02	6·653 − 02	7·001 − 02	7·342 − 02	7·679 − 02	8·513 − 02	9·291 − 02
6	6·442 − 02	6·662 − 02	6·873 − 02	7·072 − 02	7·262 − 02	7·440 − 02	7·608 − 02	7·763 − 02	8·104 − 02	8·399 − 02
7	1·334 − 01	1·343 − 01	1·351 − 01	1·360 − 01	1·367 − 01	1·373 − 01	1·379 − 01	1·384 − 01	1·395 − 01	1·404 − 01
3	1·178 + 01	1·201 + 01	1·223 + 01	1·244 + 01	1·264 + 01	1·282 + 01	1·300 + 01	1·317 + 01	1·361 + 01	1·400 + 01
4	1·273 − 01	1·344 − 01	1·417 − 01	1·491 − 01	1·565 − 01	1·637 − 01	1·709 − 01	1·781 − 01	1·963 − 01	2·134 − 01
5	6·664 − 01	6·713 − 01	6·760 − 01	6·811 − 01	6·862 − 01	6·908 − 01	6·948 − 01	6·982 − 01	7·063 − 01	7·141 − 01
6	3·438 − 01	3·635 − 01	3·832 − 01	4·029 − 01	4·224 − 01	4·415 − 01	4·599 − 01	4·779 − 01	5·216 − 01	5·629 − 01
7	7·923 − 01	8·126 − 01	8·321 − 01	8·503 − 01	8·671 − 01	8·825 − 01	8·969 − 01	9·107 − 01	9·426 − 01	9·678 − 01
4	7·425 − 02	7·621 − 02	7·826 − 02	8·034 − 02	8·243 − 02	8·446 − 02	8·642 − 02	8·827 − 02	9·244 − 02	9·583 − 02
5	2·919 − 01	3·017 − 01	3·120 − 01	3·230 − 01	3·344 − 01	3·456 − 01	3·569 − 01	3·681 − 01	3·969 − 01	4·249 − 01
6	1·326 − 00	1·324 − 00	1·322 − 00	1·322 − 00	1·324 − 00	1·325 − 00	1·326 − 00	1·327 − 00	1·331 − 00	1·335 − 00
7	6·107 − 00	6·348 − 00	6·578 − 00	6·798 − 00	7·008 − 00	7·211 − 00	7·407 − 00	7·596 − 00	8·037 − 00	8·439 − 00
5	3·005 + 01	3·084 + 01	3·156 + 01	3·222 + 01	3·282 + 01	3·338 + 01	3·390 + 01	3·438 + 01	3·550 + 01	3·648 + 01
6	2·720 − 00	2·725 − 00	2·726 − 00	2·723 − 00	2·717 − 00	2·710 − 00	2·701 − 00	2·691 − 00	2·664 − 00	2·635 − 00
7	4·363 − 01	4·354 − 01	4·349 − 01	4·345 − 01	4·345 − 01	4·345 − 01	4·344 − 01	4·345 − 01	4·350 − 01	4·354 − 01
6	5·377 + 01	5·540 + 01	5·685 + 01	5·819 + 01	5·940 + 01	6·052 + 01	6·155 + 01	6·253 + 01	6·473 + 01	6·671 + 01
7	3·619 − 00	3·613 − 00	3·607 − 00	3·599 − 00	3·591 − 00	3·582 − 00	3·573 − 00	3·563 − 00	3·539 − 00	3·515 − 00
7	7·728 + 01	7·922 + 01	8·100 + 01	8·267 + 01	8·422 + 01	8·569 + 01	8·707 + 01	8·838 + 01	9·138 + 01	9·408 + 01

ive collision strengths for transitions in TiXII ($a \pm b \equiv a \times 10^{\pm b}$).

Temperature (log K)										
4·0	4·20	4·40	4·60	4·80	5·00	5·20	5·40	5·60	5·80	6·00
350 − 00	4·968 − 00	5·079 − 00	5·144 − 00	5·166 − 00	5·158 − 00	5·110 − 00	5·011 − 00	4·890 − 00	4·863 − 00	5·060 − 00
134 − 01	6·789 − 01	6·535 − 01	6·374 − 01	6·268 − 01	6·224 − 01	6·258 − 01	6·320 − 01	6·325 − 01	6·246 − 01	6·130 − 01
346 − 01	2·365 − 01	2·335 − 01	2·259 − 01	2·155 − 01	2·031 − 01	1·898 − 01	1·781 − 01	1·698 − 01	1·650 − 01	1·630 − 01
395 − 01	1·333 − 01	1·249 − 01	1·165 − 01	1·069 − 01	9·451 − 02	8·077 − 02	6·835 − 02	5·886 − 02	5·288 − 02	5·066 − 02
420 − 01	2·789 − 01	1·762 − 01	1·134 − 01	7·856 − 02	6·215 − 02	5·573 − 02	5·374 − 02	5·364 − 02	5·464 − 02	5·670 − 02
416 − 01	4·683 − 01	2·995 − 01	2·036 − 01	1·571 − 01	1·382 − 01	1·317 − 01	1·298 − 01	1·295 − 01	1·298 − 01	1·305 − 01
452 − 00	9·195 − 00	8·927 − 00	8·670 − 00	8·453 − 00	8·300 − 00	8·208 − 00	8·153 − 00	8·155 − 00	8·316 − 00	8·718 − 00
593 − 01	5·456 − 01	5·869 − 01	5·798 − 01	5·306 − 01	4·526 − 01	3·653 − 01	2·863 − 01	2·248 − 01	1·825 − 01	1·577 − 01
527 − 01	9·593 − 01	9·510 − 01	9·402 − 01	9·146 − 01	8·622 − 01	7·995 − 01	7·459 − 01	7·079 − 01	6·843 − 01	6·725 − 01
087 − 00	1·317 − 00	8·322 − 01	5·355 − 01	3·711 − 01	2·939 − 01	2·640 − 01	2·556 − 01	2·570 − 01	2·656 − 01	2·836 − 01
652 − 00	2·306 − 00	1·475 − 00	1·003 − 00	7·746 − 01	6·834 − 01	6·546 − 01	6·512 − 01	6·594 − 01	6·762 − 01	7·021 − 01
120 − 00	1·376 − 00	1·432 − 00	1·335 − 00	1·163 − 00	9·702 − 01	7·793 − 01	6·029 − 01	4·525 − 01	3·343 − 01	2·481 − 01
134 − 00	2·160 − 00	2·069 − 00	2·034 − 00	2·052 − 00	1·976 − 00	1·746 − 00	1·430 − 00	1·116 − 00	8·571 − 01	6·680 − 01
205 + 01	7·606 − 00	4·806 − 00	3·093 − 00	2·142 − 00	1·693 − 00	1·512 − 00	1·444 − 00	1·413 − 00	1·394 − 00	1·377 − 00
516 + 01	1·589 + 01	1·016 + 01	6·908 − 00	5·331 − 00	4·703 − 00	4·517 − 00	4·521 − 00	4·626 − 00	4·817 − 00	5·113 − 00
478 + 01	1·483 + 01	1·476 + 01	1·463 + 01	1·433 + 01	1·416 + 01	1·473 + 01	1·616 + 01	1·812 + 01	2·033 + 01	2·266 + 01
072 + 01	1·307 + 01	8·260 − 00	5·316 − 00	3·683 − 00	2·918 − 00	2·624 − 00	2·538 − 00	2·534 − 00	2·559 − 00	2·592 − 00
895 − 00	1·828 − 00	1·169 − 00	7·940 − 01	6·108 − 01	5·341 − 01	5·041 − 01	4·902 − 01	4·806 − 01	4·717 − 01	4·633 − 01
056 + 02	1·928 + 02	1·219 + 02	7·841 + 01	5·432 + 01	4·311 + 01	3·906 + 01	3·845 + 01	3·948 + 01	4·146 + 01	4·425 + 01
036 + 01	1·285 + 01	8·221 − 00	5·588 − 00	4·309 − 00	3·789 − 00	3·610 − 00	3·560 − 00	3·554 − 00	3·562 − 00	3·575 − 00
096 + 02	1·955 + 02	1·250 + 02	8·502 + 01	6·569 + 01	5·817 + 01	5·626 + 01	5·688 + 01	5·881 + 01	6·165 + 01	6·531 + 01

For the forbidden transitions, those involving promotion of orbitals within $\Delta n = 0$ have the largest Ω or γ: $4s\ ^2S - 4d\ ^2D$ and $4p\ ^2P^0 - 4f\ ^2F^0$. These strongest transitions will be very useful for intensity diagnostic purposes in Tokamak plasmas.

To conclude, we except our results to be quite reliable, as we have included all the important physical effects like exchange, channel coupling and short range correlations into our calculations. We have, however, not taken relativistic effects in our calculations which become important for members of higher Z.

Acknowledgements

One of the authors (MM) would like to thank Prof. G Denardo of the International Centre for Theoretical Physics, Trieste, for helpful discussions. He is also thankful to D.S.T. (India) and U.G.C. (India) for financial support. Computational support from an EPSRC Rolling Grant is also gratefully acknowledged.

References

[1] B Edlen, *Phys. Scr.* **17**, 565 (1978)
Y K Kim and K T Cheng, *J. Opt. Soc. Am.* **68**, 836 (1978)
J R Fuhr, W C Martin and W L Weise, *J. Phys. Chem. Ref. Data* **17**, Suppl. 4, 447 (1988)
C Jupen, L Engstrom, R Hutton, N Reistad and M Westerfind, *Phys. Scr.* **42**, 44 (1990)
[2] R K Janev, *Phys. Scr.* **T37**, 5–7 (1991)
M Bitter, H Hsuan, K W Hilf and M Zarnstorff, *Phys. Scr.* **147**, 87–95 (1993)
[3] D L Matthews, P L Hagelstein and M D Rosen *et al*, *Phys. Rev. Lett.* **54**, 110–3 (1985)
[4] D J Fields, R S Walling and G M Shimkaveg *et al*, *Phys. Rev.* **A46**, 1606–9 (1992)
[5] B Edlen, *Z. Phys.* **100**, 621 (1936)
[6] J D Ekberg and L A Svensson, *Phys. Scr.* **12**, 116 (1975)
[7] L Cohen and W E Behring, *J. Opt. Soc. Am.* **66**, 899–904 (1976)
[8] M Westerlind, *Phys. Rev.* **A42**, 3996–4000 (1990)
[9] M L Zhang, D H Sampson, R E H Clark and J B Mann, *Atom. Data Nucl. Data Tables* **41**, 1–58 (1989)
[10] P G Burke and W D Robb, *Adv. Atom. Mol. Phys.* **11**, 143–214 (1975)
[11] P L Dufton and A E Kinston, *J. Phys.* **B20**, 3899–3904 (1987)
[12] M Mohan, M Le Dourneuf and A Hibbert, *J. Phys.* **B24**, 299–306 (1991)
M Mohan, *R-matrix method and its applications in collisions of electrons with atoms (or ions) in atomic and molecular physics* edited by A P Pathak (Narosa Publishing House, Springer-Verlag, New Delhi, 1992)
M Mohan, *Pramana – J. Phys.* **40**, 485 (1993)
M Mohan, A Hibbert and A E Kingston, *Astrophys. J.* **434**, 389–94 (1994)
M Mohan, R Sharma and A Hibbert (1997) *Astrophys. J.* **108**, 389 (1997)
[13] A Hibbert, *Comput. Phys. Commun.* **9**, 141–72 (1975)
[14] A Hibbert, M Le Dourneuf and M Mohan (to be published)
[15] E Clementi and C Roetti, *Atom. Data Nucl. Data Tables,* **14**, 177–478 (1974)
[16] C Corliss and J Sugar, *J. Phys. Chem. Ref. Data* **8**, 1–62 (1979)
[17] K A Berrington, P G Burke, M Le Dourneuf, W D Robb, K T Taylor and Vo Ky Lan, *Comput. Phys. Commun.* **14**, 367–412 (1978)
K A Berrington, private communication (1991)
[18] M Mohan, M Le Dourneuf, A Hibbert and V M Burke, *Pramana – J. Phys.* **41**, 371 (1993)
M T Seaton, *J. Phys.* **B18**, 2111–31 (1985)
[19] V M Burke, P G Burke and N S Scott, *Comput. Phys. Commun.* **69**, 76–98 (1992)
[20] A Burgess, D G Hummer and J A Tully, *Philos. Trans. R. Soc.* **A 226**, 225 (1990)
[21] W Eissner and M J Seaton, *J. Phys.* **B7**, 2533–2549 (1974)

Compton profiles of electron momentum distribution in β-Ga

B K ACHARYA and N C MOHAPATRA*

Physics Department, Khallikote (Autonomous) College, Berhampur 760 001, India
*Physics Department, Berhampur University, Berhampur 760 007, India

MS received 24 January 1997; revised 13 March 1997

Abstract. We report for the first time the Compton profiles of electron momentum distribution in β-gallium calculated along the crystallographic directions (100), (110) and (111). The conduction electron states for this purpose are determined in the energy band calculations using model potential. The core states, on the other hand, are represented each by a single tight-binding function. The results show that the Compton profiles are nearly isotropic with very little directional dependence, which is suggestive of a free-electron-like distribution of the conduction electrons in this system. The latter conclusion is in close confirmity with similar conclusions drawn in augmented plane wave (APW) calculation of energy bands and the derived Knight-shift results in β-Ga.

Keywords. Compton profiles; β-gallium; electron momentum distribution.

PACS Nos 72·60; 78·70; 71·25.

1. Introduction

The scattering of photons by electrons in a solid provides useful information as to the electron momentum distribution in these systems. Measurements of Compton profiles in scattering experiments are carried out using either x-ray [1, 2] or γ-rays [3]. In free-electron-like metals [4], the Compton profiles are nearly isotropic whereas in transition metals [5, 6] there are significant deviations from the isotropy of the profiles.

There are various models using which Compton profiles are calculated. Two such early models are the free-atom-model and the renormalized-free-atom (RFA) model [3]. In the latter model atomic valence electron wave functions, truncated at the boundary of the Wigner–Seitz cell and renormalized over the cell volume, are used to describe the conduction electron states in the solid. While this model [3] is better than the free-atom-model, it is less realistic to describe the band states in metals. On the other hand, the model in which the conduction electron states are determined in band calculations is expected to yield more accurate profiles than the free-atom and RFA models. Calculations of Compton profiles using the band models [5, 6] are now available for a number of metals.

In the present work we have calculated Compton profiles in β-Ga using band model. There are two crystallographic phases of gallium metal. These are α-Ga and β-Ga. The former has orthorhombic structure while the latter crystallizes in monoclinic structure. In α-Ga, results of Compton profiles are available both from experiment [7] and theory [7]. The calculations [7] are, however, made using the less realistic RFA model [3].

neither from experiment nor from theory. This lack of result motivated us to take up β-Ga in the present work. There are also other motivations. In α-Ga, the results of Compton profile are found to be very nearly isotropic. We wanted to see how strong is the anisotropy of the Compton profiles in β-Ga. Further, it is well-known that electron correlation effects introduce a finite discontinuity with a high momentum tail at the free-electron Fermi momentum P_F in the electron momentum distribution. In taking up β-Ga, we wanted to study how strong is the eletron correlation effect in this system by calculating n_F, the number of conduction electrons with momentum larger than P_F. Lastly, the ready availability of band wave functions in β-Ga from our recent calculation [8] of electric field gradient in this system prompted us to take up β-Ga instead of α-Ga in the present investigation.

As to the various approximations used in the present calculation, we wish to state that apart from using a non-local model potential, we have made use of two other approximations namely, the impulse approximation [9] for the scattering of photons by electrons and the single tight-binding approximation for representing the core states in the solid.

In the impulse approximation [9, 10], it is assumed that the interaction of the photon with the electron until the latter is ejected is a constant potential. This approximation holds if the photon is of very short wavelength and the binding energy of the electron is much smaller than the photon-energy. In using X-ray photons, both these conditions are well satisfied for the conduction electrons. But for the core electrons, especially the innermost 1s electrons, it does not hold good. In spite of this, the impulse approximation has been used in the past to predict Compton profiles in reasonably good agreement with experiment.

In the single tight-binding approximation, each core state in solid is described by a single tight-binding function constructed from the corresponding atomic Hartree–Fock core wave function. This is a standard practice followed in many band calculations and the approximation is reasonably good as the core states in solid retain their atomic character to a large extent.

The paper is organized as follows. In § 2, we briefly describe the theory for the calculation of the Compton profiles. Section 3 summarizes the results of the present calculation and makes a comparative analysis with the available results in α-Ga. Conclusions are summarized in § 4.

2. Theory

We start with the standard expression [5]

$$J(q) = \frac{\Omega}{(2\pi)^3} \int d^3p\, \rho(p)\, \delta(q - \mathbf{p}.\hat{k}) \tag{1}$$

for the scattering cross-section of a photon by the electrons in a metal, which holds good in impluse approximation [9, 10]. In eq. (1), Ω denotes the volume of the unit cell in the solid, $\mathbf{p}$ is the initial momentum of the electron, ρ is the momentum distribution function and $\hat{k}$ is the momentum transfer to the electron by the photon.

are obtained in the standard band calculation [8] using non-local model potential.

These wave functions are used in arriving at expressions for the Compton profiles of electron momentum distribution from core and conduction electrons. The details of derivation of these expressions are given in the work of Panigrahi and Mohapatra [6]. We simply quote those results here. The fact that the core states are completely filled and each one is represented by a single tight-binding function makes core contribution to $J_{\hat{k}}(q)$ isotropic, that is independent of $\hat{k}$ direction. It has been shown [6, 11] that the contribution to $J(q)$ per atom from the core electron is

$$J(q) = \frac{2}{\pi} \sum_{nl} (2l+1) \int_q^\infty I_{nl}^2(p) p \, \mathrm{d}p, \tag{2}$$

where n, l are the principal and orbital quantum numbers of the atomic core state and I_{nl} stands for the integral

$$I_{nl}(p) = \int_0^\infty j_l(pr) \, p_{nl}(r) \, r \mathrm{d}r. \tag{3}$$

In eq. (3), j_l is the spherical Bessel function of order l and p_{nl} is the radial part of the atomic core wave function which is normalized according to

$$\int_0^\infty p_{nl}^2(r) \mathrm{d}r = 1. \tag{4}$$

The conduction electron contribution to $J_{\hat{k}}(q)$, on the other hand, is expressed [6] as

$$J_{\hat{k}}(q) = \frac{\mathrm{d} F_{\hat{k}}(q)}{\mathrm{d}q}, \tag{5}$$

where

$$\begin{aligned} F_{\hat{k}}(q) = \sum_{\mathbf{g}(\text{irred})} w_g \sum_{\mathbf{K}} & \left(\sum_\alpha \theta[q - (\mathbf{g} + \mathbf{K}) \cdot \alpha \hat{k}] \right) \Bigg(\sum_t |C_t(\mathbf{g} + \mathbf{K})|^2 \\ & - \frac{16\pi}{\Omega} S(\mathbf{K}) \sum_t C_t^*(\mathbf{g} + \mathbf{K}) \sum_{\mathbf{K}} C_t(\mathbf{g} + \mathbf{K}') \sum_{nl} (2l+1) \\ & \times I_{nl}(|\mathbf{g} + \mathbf{K}|) \, I_{nl}(|\mathbf{g} + \mathbf{K}'|) \, P_l(\cos\gamma_{\mathbf{KK}'}) \Bigg) \\ & + \left(\frac{8\pi}{\Omega} \right)^2 \sum_{\mathbf{g}(\text{irred})} \sum_{\mathbf{K}_s} S^2(\mathbf{K}_s) \sum_\alpha \theta[q - (\mathbf{g} + \mathbf{K}_s) \cdot \alpha \hat{k}] \\ & \times \sum_t \Bigg(\sum_{\mathbf{K}} C_t^*(\mathbf{g} + \mathbf{K}_s) \, S(\mathbf{K}) \\ & \times \sum_{nl} (2l+1) \, I_{nl}(|\mathbf{g} + \mathbf{K}|) \, I_{nl}(|\mathbf{g} + \mathbf{K}_s|) \, P_l(\cos\gamma_{\mathbf{KK}_s})^2 \Bigg). \end{aligned} \tag{6}$$

Here w_g is the weighting factor assigned to the sample g point in the irreducible part of the BZ, θ is the standard step function, P_l is the Legendre polynomial of order l, $\gamma_{\mathbf{KK}'}$ is the angle between the vectors $\mathbf{g}+\mathbf{K}$ and $\mathbf{g}+\mathbf{K}'$, α is the point-symmetry operators and $S(K)$ is the structure factor of the lattice.

The quantities $J_{\hat{k}}(q)$ for any $\hat{k}$ satisfies [6] the relation

$$\int_0^\infty J_k(q)\,\mathrm{d}q = n, \tag{7}$$

where n is equal to half the number of electrons per atom. Equation (7) may be used as a check for the accuracy of the band as well as core contribution $J_{\hat{k}}(q)$.

3. Results and discussion

β-Ga crystallizes in monoclinic structure with two atoms per primitive cell. The lattice parameters available [12] at 248 K are $a = 2{\cdot}766$ Å, $b = 8{\cdot}053$ Å, $c = 3{\cdot}332$ Å and $\beta = 92°\,03'$. The band calculation [8] has been carried out using the non-local model potential of Appapillai and Williams [13]. These model potentials include correction from exchange and correlation effects. Besides, these have quite successfully explained a number of electronic properties of metals, including Knight shift, electric field gradients, density of states etc. In view of the success of these model potentials we have used them in the present calculation of electron momentum distribution in β-Ga. In constructing the band wave function, the atomic core functions used are those of Clementi [14]. In order to carry out the g sum in eq. (6), 176 sample g points are suitably chosen in 1/4th irreducible part of the BZ as described in previous work [8]. The energies of the occupied bands have converged within 0·001 Ryd with the choice of 23 plane waves of the shortest wave vector $|\mathbf{g}+\mathbf{K}|$ in the expansion of pseudo wave function. The results of the present band calculation [8] compare very well with those from APW calculation [15] in regard to shapes of bands, Fermi energy and density of state at Fermi energy.

We now discuss the result of $J_{\hat{k}}(q)$ as obtained in the present work. We begin with the contribution from the core electrons. The atomic core functions of Clementi [14] are used in evaluating the integral in eq. (3). The radial integrals are evaluated using the standard 5-point numerical integration procedure after generating the integrand at 201 mesh points, chosen in a logarithmic r scale, $r_n = r_1 \exp[-(n-1)h]$ with $r_1 = 0{\cdot}00097$ atomic units (a.u) and $h = 0{\cdot}05$ a.u. The farthest distance up to which the integration is carried out has the value $r_{201} \approx 21{\cdot}45618$ a.u.

As the core states are localized, the corresponding momentum distribution is delocalized. Hence, in order to satisfy eq. (7) for the core electrons, one needs to integrate $J(q)$ in eq. (7) over a large distance in the q scale. This is particularly true for 1s electrons whose contribution to $J(q)$ varies very slowly with q. Since impulse approximation [9] is not good for the 1s electrons, one may ignore them for the purpose of checking the result in eq. (7.) By ignoring the 1s electrons, the integrated result from eq. (7) turns out to be approximately 12·63 which is close to 13, the number of 2s–3d core electrons in half an atom of Ga. The remaining discrepancy is attributed to 2s and 2p electrons whose contributions to $J(q)$ vary so slowly that unless the integration in eq.

Now coming to the band contribution $J_{\hat{k}}(q)$, we note that the band states being lelocalized, their momentum distributions are expected to be fairly localized. Using eq. 6) we have evaluated the function $F_{\hat{k}}(q)$ for the three crystallographic directions of $\hat{k}$, amely, (100), (110) and (111). In carrying out the sum in eq. (6) over **g** in the irreducible art of the BZ, we have used 176 sample **g** vectors. In order to study the dependence of he result on the number of sample points, the calculation was repeated at a smaller set of **g** vectors than 176. The result shows that the change due to this effect is less than 1%. The derivative of $F_{\hat{k}}(q)$ with respect to q, which has been evaluated numerically rovides the corresponding $J_{\hat{k}}(q)$. In order to study the convergence of $F_{\hat{k}}(q)$ with espect to the number of reciprocal lattice vectors **K** and $\mathbf{K}_s$ occurring in eq. (6), we split he contribution F_k into two parts; one arising from the plane wave and hybrid (i.e. lane wave-tight binding combination) part of band wave function and the other from he tight-binding part. The first three lines in eq. (6) give the plane wave and hybrid ontribution while the remaining terms give the tight-binding contribution. The former

Table 1. Present results of Compton profiles $J_{\hat{k}}(q)$ of β-Ga along the directions (100), (110) and (111). The results are expressed in atomic units.

	Core contribution	Band contribution		
q	$J(q)$	$J_{100}(q)$	$J_{110}(q)$	$J_{111}(q)$
0·0	3·620	2·599	2·617	2·609
0·1	3·618	2·342	2·328	2·350
0·2	3·614	2·801	2·813	2·808
0·3	3·606	2·198	2·202	2·200
0·4	3·592	2·011	2·012	2·011
0·5	3·573	1·483	1·483	1·478
0·6	3·548	1·122	1·124	1·117
0·7	3·517	1·013	1·015	1·011
0·8	3·479	0·536	0·544	0·538
0·9	3·433	0·132	0·142	0·138
1·0	3·381	0·010	0·017	0·018
1·2	3·253	0·023	0·026	0·029
1·4	3·097	0·019	0·017	0·019
1·6	2·921	0·021	0·012	0·013
1·8	2·726	0·019	0·009	0·009
2·0	2·527	0·007	0·008	0·007
2·2	2·325	0·002	0·007	0·006
2·4	2·131	0·003	0·005	0·005
2·6	1·943	0·004	0·004	0·004
2·8	1·769	0·006	0·003	0·003
3·0	1·610	0·006	0·001	0·002
3·5	1·271	0·000	0·000	0·000
4·0	1·019	0·001	0·000	0·000
4·5	0·829	0·000	0·000	0·000
5·0	0·687	0·000	0·000	0·000
6·0	0·496	0·000	0·000	0·000
7·0	0·373	0·000	0·000	0·000
7·2	0·353	0·000	0·000	0·000

[illegible]
eciprocal lattice vectors **K**. But the tightbinding contribution which involves more ocalized wave functions than plane waves required 315 reciprocal lattice vectors $\mathbf{K}_s$ for he result to converge. In order to test the accuracy of the band contribution to $J_{\hat{k}}(q)$, we ave used eq. (7). For all the three directions of $\hat{k}$, the integral in eq. (7) gives $n \approx 1{\cdot}499$, which s very close to exact result of 1·5 conduction electrons in half an atom of Ga.

We present our results of $J_k(q)$ in table 1 for the three directions, (100), (110) and (111). ince the core contribution in the present work is isotropic, it has the same value for all he three directions. It is evident from table 1 that the Compton profiles are very nearly sotropic. Therefore, in order to economise figure space, we have preferred to plot the esults of $J_{\hat{k}}(q)$ for only one direction, namely, (100) and this is shown in figure 1. But to how the direction dependence, we have plotted the difference functions, $J_{110}(q)$– $_{100}(q)$ and $J_{110}(q)$–$J_{111}(q)$ in figures 2 and 3 respectively. These figures also display ear isotropy property of $J_{\hat{k}}(q)$. The maximum value of the difference is about 0·68% of (0) due to conduction electrons. This result is not surprising because the band tructure results, such as, Fermi energy and density of state at Fermi energy in β-Ga uggest that the conduction electrons in this metal are mostly free-electron-like. The esults from APW [15] calculation as well as the Knight-shift data [15] also lead one to his conclusion. The structures seen in the profiles of conduction electron contributions figure 1) are similar to those noted in the work of Rath *et al* [5].

In a free-electron gas, n_{F}, the number of electrons with momentum larger than Fermi nomentum P_{F} is exactly zero at absolute zero temperature. But for an interacting

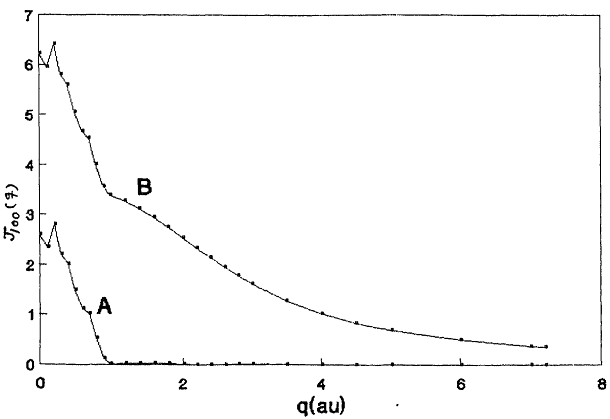

Figure 1. $J_k(q)$ for β-Ga with $\hat{k}$ along (100) direction: curve A, band contribution; curve B, total contribution (core + band).

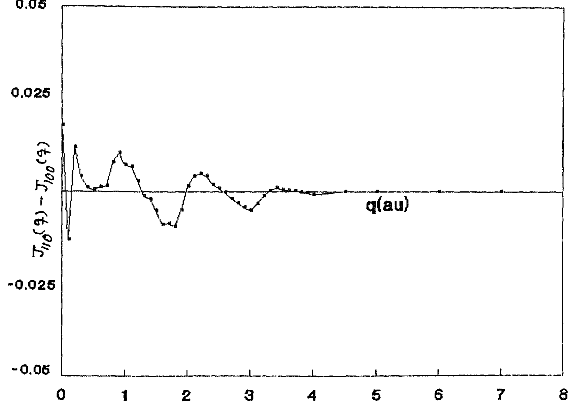

Figure 2. Difference profile $J_{110}(q)$–$J_{100}(q)$ in β-Ga.

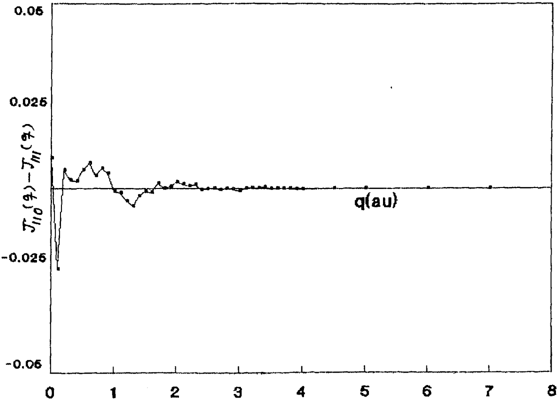

Figure 3. Difference profile $J_{110}(q)$–$J_{111}(q)$ in β-Ga.

on system, it has been shown by Luttinger [16] that there are non-zero number of ons with momentum larger than P_F. In the present work, P_F is found equal to

Table 2. Comparison of the present results in β-Ga of the conduction electron contribution to Compton profiles with those in α-Ga. All the results are expressed in atomic units. The data in α-Ga taken from ref. [7] are isotropic.

q	$J(q)$ in α-Ga	$J_{100}(q)$ in β-Ga
0·0	2·4 ± 1·5%	2·599
0·1	2·31	2·342
0·2	2·17	2·801
0·3	2·05	2·198
0·4	1·84	2·011
0·5	1·60	1·483
0·6	1·27	1·222
0·7	0·94	1·013
0·8	0·56	0·536
0·9	0·21	0·132
1·0	0·15 ± 10%	0·010
1·1	0·15	0·030
1·2	0·07	0·023
1·3	0·07	0·021
1·4	0·08	0·019
1·5	0·08 ± 20%	0·019
1·6	0·06	0·021
1·7	0·05	0·020
1·8	0·06	0·019
2·0	0·04	0·007
2·2	0·02	0·002
2·4	0·00	0·003

The result shows that there are about 2·2% such electrons. We remark that n_F so obtained includes both the band structure and electron correlation effects, the latter through the non-local model potential whose parameters are determined by fitting with the experiment.

Results of Compton profile from experiment or from other works are not available to compare with the present results. The present results in β-Ga are however compared with those available [7] in α-Ga. The calculated results [7] in α-Ga obtained in RFA model [3] agree well with experiment [7]. The latter [7] obtained for (100), (010) and (001) directions show near isotropy. The comparisons of the present result with those in α-Ga are made for two reasons. Firstly, to see if the present results are of the same order of magnitude as those in α-Ga. Secondly, to find if the present results are also very nearly isotropic as those in α-Ga. For this purpose we list the present results as well as those for α-Ga in table 2. The data in this table show that the present results are of the same order of magnitude as those in α-Ga and that they are nearly isotropic. Further we have also compared n_F in both the systems. While in α-Ga, about 6·7% of conduction electrons have momentum larger than P_F, it is about 2·2% in β-Ga. We note that any quantitative comparison of numbers in columns 2 and 3 of table 2 will not be meaningful as these are obtained in two different methods.

The higher value of n_F in α-Ga may be attributed to the renormalized conduction electron wave functions in RFA model [7]. Since the valence electron wave functions, 4*s* and 4*p* in α-Ga are truncated and renormalized within the Wigner Seitz cell in RFA model, it forces localization of the valence electron distribution. As a consequence, its momentum distribution becomes more delocalized than in the band model where no truncation of wave functions is made. A delocalized momentum distribution $J_k(q)$ is more stretched out in q-space than a localized distribution and is therefore expected to give a larger n_F as is obtained in α-Ga.

4. Conclusion

The results of Compton profiles in β-Ga are calculated for the first time in band model along the crystallographic direction (100), (110) and (111). The results show near isotropy suggesting the conduction electrons in this metal to be very nearly free electron-like, a conclusion in perfect agreement with band structure results from APW calculations and the Knight Shift data in β-Ga. About 2·2% of conduction electrons are found to have momentum larger than P_F.

References

[1] S Manninen, *J. Phys.* **F1**, L60 (1971)
[2] R J Weiss, *Philos. Mag.* **26**, 761 (1972)
[3] T Pakari, K-F Berggren, R Ribberfors and V Halonen, *Phys. Rev.*. **B14**, 2301 (1976)
[4] S Wachtel, J Felsteiner, S Kahane and R Opher, *Phys. Rev.* **B12**, 1285 (1975)
[5] J Rath, C S Wang, R A Tawil and J Callaway, *Phys. Rev.* **B8**, 5139 (1973)
[6] B B Panigrahi and N C Mohapatra, *J. Phys: Condens. Matter.* **5**, 8557 (1993)
[7] B Lengeler, R Lasser and G Mair, *Phys. Rev.* **B22**, 5748 (1980)
[8] B K Acharya and N C Mohapatra, *Pramana – J. Phys.* **43**, 391 (1994)
[9] W C Phillips and R J Weiss, *Phys. Rev.* **171**, 790 (1968)
[10] P M Platzman and N Tzoar, *Phys. Rev.* **139**, A410 (1965)
[11] K-F Berggren, *Phys. Rev.* **B6**, 2156 (1972)
[12] K W Lodge, *J. Phys.* **F8**, 443 (1978)
[13] M Appapillai and A R Williams, *J. Phys.* **F3**, 359 (1973)
[14] E Clementi, *Tables of atomic functions* (IBM, New York, 1965)
[15] J D Stroud and M J Strott, *J. Phys.* **F5**, 166 (1975)
[16] J M Luttinger, *Phys. Rev.* **119**, 1153 (1960); **121**, 942 (1961)

SUBJECT INDEX

Mathematical Aspects of Dynamical Systems

Random matrices and matrix models: The JNU lectures *Madan Lal Mehta* 7–48

Hölder exponents of irregular signals and local fractional derivatives *Kiran M Kolwankar and Anil D Gangal* 49–68

Signature of chaos in power spectrum *M C Valsakumar, S V M Satyanarayana and V Sridhar* 69–85

Dynamics of simple one-dimensional maps under perturbation *Somdatta Sinha and Parichay K Das* 87–98

Chaos in modulated logistic systems *V M Nandakumaran* 99–108

Effect of boundary conditions on the invariant density of noisy maps at fully-developed chaos *V Balakrishnan, G Nicolis and C Nicolis* 109–128

Symplectic integration of nonlinear Hamiltonian systems *Govindan Rangarajan* 129–142

Integrable Systems and Solitons

Painlevé analysis and integrability aspects of some nonlinear partial differential equations *K Porsezian* 143–161

Localized coherent structures of (2 + 1) dimensional generalizations of soliton systems *M Lakshmanan and R Radha* 163–188

Geometry and nonlinear evolution equations *Radha Balakrishnan* 189–204

Nonlinear chiral models: Soliton solutions and spatio-temporal chaos *M S Sriram and J Segar* 205–229

Spatio-temporal Chaos, Synchronization and Control

Control methods for problems of mixing and coherence in chaotic maps and flows *Ashutosh Sharma and Neelima Gupte* 231–248

Characterization and control of chaotic dynamics in a nerve conduction model equation *S Rajasekar* 249–258

Control of chaos *Sangeeta D Gadre and V S Varma* 259–270

Effect of noise on coupled chaotic systems *Manojit Roy and R E Amritkar* 271–285

Lattice dynamical models of adaptive spatio-temporal phenomena
Sudeshna Sinha 287–302

Control of spatio-temporal chaos: A study with an autocatalytic reaction-diffusion system *Nita Parekh, V Ravi Kumar and B D Kulkarni* 303–323

Turbulence

Some recent advances in the theory of homogeneous isotropic turbulence
Sujan K Dhar, Anirban Sain, Ashwin Pande and Rahul Pandit 325–364

The randomly stirred fluid–Turbulence as a problem in statistical mechanics *J K Bhattacharjee* 365–378

Quantum Aspects of Chaos

Chaos in the hydrogen atom interacting with external fields
K Ganesan and R Gębarowski 379–410

Resonances and chaos in the collinear collision system (He, H_2^+) and its isotopic variants *Susanta Mahapatra, N Sathyamurthy and Ramakrishna Ramaswamy* 411–424

Chaos in intrinsic motion of nuclei and its role in dissipative collective dynamics *Santanu Pal* 425–437

Chaos and localization in coupled quartic oscillators
M S Santhanam, V B Sheorey and A Lakshminarayan 439–457

Experiments on quantum chaos using microwave cavities: Results for the pseudo-integrable L-billiard *A Kudrolli and S Sridhar* 459–467

Quantum chaology: The photoeffect and beyond *Bala Sundaram* 469–486

Periodic orbits in polygonal billiards *Debabrata Biswas* 487–501

Semiclassical theory for many-body fermionic systems
Pierre Gaspard and Sudhir R Jain 503–516

Accuracy of trace formulas *Arul Lakshminarayan* 517–535

The phase of the Riemann zeta function *Avinash Khare* 537–553

Exotic spectra, wavefunctions and transport in incommensurate lattices
A Lahiri, T K Roy and A Bhowal 555–588

Fractal characteristics of critical and localized states in incommensurate quantum systems *Indubala I Satija and Jukka A Ketoja* 589–601

Applications

Dynamical signatures of 'phase transitions': Chaos in finite clusters
Vishal Mehra, Saroj K Nayak and Ramakrishna Ramaswamy 603–615

Classical gauge theories as dynamical systems — Regularity and chaos *S Lakshmibala, Bindu A Bambah, M S Sriram and C Mukku* 617–635

Chaos in Josephson junctions *G Ambika* 637–654

Collective thermalization in quark gluon plasma *S Sengupta, J R Bhatt, P K Kaw and J C Parikh* 655–674

Nonlinear propagation of relativistically intense electromagnetic waves in a collisionless plasma *P K Kaw and A Sen* 675–692

The onset of chaos in the wake of an oscillating cylinder: Experiment and the dynamics of the circle map *D J Olinger, A B Chhabra and K R Sreenivasan* 693–703

Chaos in jerky flow — Experimental verification of a theoretical prediction *S J Noronha, G Ananthakrishna, L Quaouire and C Fressengeas* 705–718

Chaos and predictability of the Indian summer monsoon *B N Goswami* 719–736

Some recent applications of cell dynamical modelling to phase ordering dynamics *Sanjay Puri* 737–748

Noisy nonlinear coupled equations — Some new insights *J K Bhattacharjee, Anita Mehta and J M Luck* 749–758

Nonlinear fluctuating hydrodynamics and sequence of time scales of relaxation in supercooled liquids *Shankar P Das* 759–773

General and Mathematical Physics

The Larmor nutation *K N Srinivasa Rao and A V Gopala Rao* 775–786

Coherent and squeezed states on physical basis *R R Puri* 787–798

Classical limit of scattering in quantum mechanics – A general approach *D Sen, A N Basu and S Sengupta* 799–810

Surface harmonics for pentagonal point groups *K Rama Mohana Rao, P Hemagiri Rao and V Satyavathi* 859–870

Characterization of chaos in a serrated plastic flow model *S V M Satyanarayana, V Sridhar and S Koka* 871–882

Structural phase transition in substituted La_2CuO_4 and Pr_2CuO_{4-y} *Meena Chaudhri, Kunal B Modi, K M Jadhav and G K Bichile* 883–890

The geometric phase and ray space isometries *Joseph Samuel* 959–967

Thomas rotation and polarized light: A non-abelian geometric phase in optics *Joseph Samuel and Supurna Sinha* 969–975

Relativity and Gravitation

Creation or destruction of sourceless abelian gauge strings in a Robertson–Walker universe *D Bhattacharyya and S Banerji* 811–818

Higher dimensional Vaidya metric in Einstein and de Sitter background *L K Patel and Lakshmi S Desai* 819–824

Particle Physics

Non-leptonic weak charmed baryon decays in the $SU(4)$ semi-dynamical scheme *S M Sheikholeslami* 837–848

Weak decay constants of light and heavy pseudoscalar mesons *N Barik, S Kar and P C Dash* 985–995

Meson spectroscopy with confined one gluon exchange potential *K B Vijaya Kumar, A K Rath and S B Khadkikar* 997–1004

Two body non-leptonic decays $B \rightarrow D\pi$ with heavy quark and chiral symmetry *A K Giri, L Maharana and R Mohanta* 1005–1013

Solution of approximate gluon evolution equation for small-x at fixed 'ρ' *A Saikia* 1015–1019

Nuclear Physics

Algebraic expressions for effective potential characteristic parameters in heavy ion scattering *I Jamir, E F P Lyngdoh and C S Shastry* 825–836

Heavy-ion scattering at low energies: First-order correction to the eikonal phase shift *S K Charagi* 1021–1026

Semi-empirical formulae for Λ-binding energy in hypernuclei using mass distribution *M Z Rahman Khan, Nasra Neelofer and M A Suhail* 1027–1034

Group theoretical aspects of $U^{B}(6) \otimes U^{F}(20)$ symmetry limits of IBFM related to the $U^{B}(5)$ and $O^{B}(6)$ limits of IBM *V K B Kota* 1035–1075

Atomic and Molecular Physics

Photon interaction cross-sections and anomalous scattering factors of Cu and Ag *Sandiago, T K Umesh and Ramakrishna Gowda* 1077–1090

Collisional excitation among the seven lowest states of TiXII *M Mohan and A Hibbert* 1161–1168 melts *Shobha Dass, Gautam Johri and Lakshman Pandey* 891–922

Superconducting state parameters of metallic glass $Mg_{70}Zn_{30}$ using linearized screened pseudopotential *Manish Gupta, K S Sharma and L Dass* 923–928

Electron paramagnetic resonance studies of photorefractive crystals II: Fe^{3+} doped $Bi_{12}SiO_{20}$ with copper vapour laser illumination in 10–100 K range *N K Porwal, R M Kadam, Y Babu, M D Sastry, M D Aggarwal and Putcha Venkateswarlu* 929–936

Probability distribution of normalized structure factor magnitudes for a centrosymmetric crystal with planar molecules in the unit cell *Sabita Das and G B Mitra* 1091–1094

Activation energy of hydrogen in Lu *N Singh and B Kumar* 1095–1103

A study of electron momentum density distribution in iridium by Compton scattering technique *K B Joshi, R K Pandya, B L Ahuja and B K Sharma* 1105–1113

Magnetic behaviour of TbMnFe *Keka Chakraborty, S K Paranjpe, V Siruguri, O D Jayakumar and S K Kulshreshtha* 1115–1122

Spin state and exchange in the quasi-one-dimensional anti-ferromagnet $KFeS_2$ *Satish Kumar Tiwary and Sukumaran Vasudevan* 1123–1134

Field emission theory of dislocation-sensitized photo-stimulated exo-electron emission from coloured alkali halide crystals *B P Chandra, R S Chandok and P K Khare* 1135–1143

Thermal quenching of luminescence in erbium doped semiconductors *B Chanda and D N Bose* 1145–1149

Spectroscopic properties of Er^{3+} ions in cadmium and alkali cadmium borosulphate glasses *C K Jayasankar and V V Ravi Kanth Kumar* 1151–1160

Brief Report

Kramers-Kronig analysis of the reflectance spectra of Pb-doped Bi-4334 type glass and the corresponding glass-ceramic superconductor *Souri Banerjee, S Chatterjee and B K Chaudhuri* 951–958

Compton profiles of electron momentum distribution in β-Ga *B K Acharya and N C Mohapatra* 1169–1177

Rapid Communication

Helium atom in intense and superintense laser fields: A new theoretical approach *Bijoy Kr Dey and B M Deb* L849–L858

AUTHOR INDEX

Acharya B K
Compton profiles of electron momentum distribution in β-Ga 1169
Aggarwal M D
see Porwal N K 929
Ahuja B L
see Joshi K B 1105
Ambika G
Chaos in Josephson junctions 637
Amritkar R E
see Roy Manojit 271
Ananthakrishna G
see Noronha S J 705

Babu Y
see Porwal N K 929
Balakrishnan Radha
Geometry and nonlinear evolution equations 189
Balakrishnan V
Effect of boundary conditions on the invariant density of noisy maps at fully-developed chaos 109
Bambah Bindu A
see Lakshmibala S 617
Banerjee Souri
Kramers–Kronig analysis of the reflectance spectra of Pb-doped Bi-4334 type glass and the corresponding glass-ceramic super-conductor 951
Banerji S
see Bhattacharyya D 811
Barik N
Weak decay constants of light and heavy pseudoscalar mesons 985
Basu A N
see Sen D 799
Bhatt J R
see Sengupta S 655
Bhattacharjee J K
The randomly stirred fluid–Turbulence as a problem in statistical mechanics 365
Noisy nonlinear coupled equation—Some new insights 749
Bhattacharyya D
Creation or destruction of sourceless abelian gauge strings in a Robertson–Walker universe

Bichile G K
see Chaudhri Meena 883
Biswas Debabrata
Periodic orbits in polygonal billiards 487
Biswas Nandita
Resonance de-enhancement in the $2^1 A_u$ state of *trans*-azobenzene 937
Bose D N
see Chanda B 1145

Chakraborty Keka
Magnetic behaviour of TbMnFe 1115
Chanda B
Thermal quenching of luminescence in erbium doped semiconductors 1145
Chandok R S
see Chandra B P 1135
Chandra B P
Field emission theory of dislocation-sensitized photo-stimulated exo-electron emission from coloured alkali halide crystals 1135
Charagi S K
Heavy-ion scattering at low energies: First-order correction to the eikonal phase shift 1021
Chatterjee S
see Banerjee Souri 951
Chaudhri Meena
Structural phase transition in substituted La_2CuO_4 and Pr_2CuO_{4-y} 883
Chaudhuri B K
see Banerjee Souri 951
Chhabara A B
see Olinger D J 693

Das Parichay K
see Sinha Somdatta 87
Das Sabita
Probability distribution of normalized structure factor magnitudes for a centrosymmetric crystal with planar molecules in the unit cell 1091
Das Shankar P
Nonlinear fluctuating hydrodynamics and sequence of time scales of relaxation in supercooled liquids 759
Dash P C
see Barik N 985
Dass L
see Gupta Manish 923

Helium atom in intense and superintense laser fields: A new theoretical approach 849
Dhar Sujan K
Some recent advances in the theory of homogeneous isotropic turbulence 325

Fressengeas C
see Noronha S J 705

Gadre Sangeeta D
Control of chaos 259
Ganesan K
Chaos in the hydrogen atom interacting with external fields 379
Gangal Anil D
see Kolwankar Kiran M 49
Gaspard Pierre
Semiclassical theory for many-body fermionic systems 503
Gębarowski
see Ganesan K 379
Giri A K
Two body non-leptonic decays $B \to D\pi$ with heavy quark and chiral symmetry 1005
Goswami B N
Chaos and predictability of the Indian summer monsoon 719
Gowda Ramakrishna
see Sandiago 1077
Gupta Manish
Superconducting state parameters of metallic glass $Mg_{70}Zn_{30}$ using linearized screened pseudopotential 923
Gupte Neelima
see Sharma Ashutosh 231

Hibbert A
see Mohan M 1161

Jadhav K M
see Chaudhri Meena 883
Jain Sudhir R
see Gaspard Pierre 503
Jamir I
Algebraic expressions for effective potential characteristic parameters in heavy ion scattering 825
Jayakumar O D
see Chakraborty Keka 1115
Jayasankar C K
A study of electron momentum density distribution in iridium by Compton scattering technique 1105

Kadam R M
see Porwal N K 929
Kar S
see Barik N 985
Kaw P K
see Sengupta S 655
Nonlinear propagation of relativistically intense electromagnetic waves in a collisionless plasma 675
Ketoja Jukka A
see Satija Indubala I 589
Khadkikar S B
see Vijaya Kumar K B 997
Khan Rahman M Z
Semi-empirical formulae for Λ-binding energy in hypernuclei using mass distribution 1027
Khare Avinash
The phase of the Riemann zeta function 537
Khare P K
see Chandra B P 1135
Koka S
see Satyanarayana S V M 871
Kolwankar Kiran M
Hölder exponents of irregular signals and local fractional derivatives 49
Kota V K B
Group theoretical aspects of $U^B(6)\otimes U^F(20)$ symmetry limits of IBFM related to the $U^B(5)$ and $O^B(6)$ limits of IBM 1035
Kudrolli A
Experiments on quantum chaos using microwave cavities: Results for the pseudo-integrable L-billiard 459
Kulkarni B D
see Parekh Nita 303
Kulshreshtha S K
see Chakraborty Keka 1115
Kumar B
see Singh N 1095
Kumar V Ravi
see Parekh Nita 303
Kumar V V Ravi Kanth
see Jayasankar C K 1151

Lahiri A
Exotic spectra, wavefunctions and transport in incommensurate lattices 555

sional generalizations of soliton systems 163
Lakshmibala S
Classical gauge theories as dynamical systems—Regularity and chaos 617
Lakshminarayan A
see Santhanam M S 439
Accuracy of trace formulas 517
Luck J M
see Bhattacharjee J K 749
Lyngdoh E F P
see Jamir I 825

Mahapatra Susanta
Resonances and chaos in the collinear collision system (He, H_2^+) and its isotopic variants 411
Maharana L
see Giri A K 1005
Mehra Vishal
Dynamical signatures of 'phase transitions': Chaos in finite clusters 603
Mehta Anita
see Bhattacharjee J K 749
Mehta Madan Lal
Random matrices and matrix models: The JNU lectures 7
Mitra G B
see Das Sabita 1091
Modi Kunal B
see Chaudhri Meena 883
Mohan M
Collisional excitation among the seven lowest states of TiXII 1161
Mohanta R
see Giri A K 1005
Mohapatra N C
see Acharya B K 1169
Mukku C
see Lakshmibala S 617

Nandakumaran V M
Chaos in modulated logistic systems 99
Nayak Saroj K
see Mehra Vishal 603
Neelofer Nasra
see Khan Rahman M Z 1027
Nicolis C
see Balakrishnan V 109
Nicolis G
see Balakrishnan V 109
Noronha S J
Chaos in jerky flow—Experimental verification of a theoretical prediction 705

cylinder: Experiment and the dynamics of the circle map 693
Pal Santanu
Chaos in intrinsic motion of nuclei and its role in dissipative collective dynamics 425
Pande Ashwin
see Dhar Sujan K 325
Pandey Lakshman
see Dass Shobha 891
Pandit Rahul
see Dhar Sujan K 325
Pandya R K
see Joshi K B 1105
Paranjpe S K
see Chakraborty Keka 1115
Parekh Nita
Control of spatio-temporal chaos: A study with an autocatalytic reaction-diffusion system 303
Parikh J C
see Sengupta S 655
Patel L K
Higher dimensional Vaidya metric in Einstein and de Sitter background 819
Porsezian K
Painlevé analysis and integrability aspects of some non-linear partial differential equations 143
Porwal N K
Electron paramagetic resonance studies of photorefractive crystals II: Fe^{3+} doped $Bi_{12}SiO_{20}$ with copper vapour laser illumination in 10–100 K range 929
Puri R R
Coherent and squeezed states on physical basis 787
Puri Sanjay
Some recent applications of cell dynamical modelling to phase ordering dynamics 737

Quaouire L
see Noronha S J 705

Radha R
see Lakshmanan M 163
Rajasekar S
Characterization and control of chaotic dynamics in a nerve conduction model equation 249
Ramaswamy Ramakrishna
see Mahapatra Susanta 411
see Mehra Vishal 603
Rangarajan Govindan
Symplectic integration of nonlinear Hamiltonian systems 129

  - *see* Rao Srinivasa K N 775
- Rao P Hemagiri
  - *see* Rao K Rama Mohana 859
- Rao K Rama Mohana
  - Surface harmonics for pentagonal point groups 859
- Rao Srinivasa K N
  - The Larmor nutation 775
- Rath A K
  - *see* Vijaya Kumar K B 997
- Roy Manojit
  - Effect of noise on coupled chaotic systems 271
- Roy T K
  - *see* Lahiri A 555

- Saikia A
  - Solution of approximate gluon evolution equation for small-x at fixed 'ρ' 1015
- Sain Anirban
  - *see* Dhar Sujan K 325
- Samuel Joseph
  - The geometric phase and ray space isometries 959
  - Thomas rotation and polarized light: A non-abelian geometric phase in optics 969
- Sandiago
  - Photon interaction cross-sections and anomalous scattering factors of Cu and Ag 1077
- Santhanam M S
  - Chaos and localization in coupled quartic oscillators 439
- Sastry M D
  - *see* Porwal N K 929
- Sathyamurthy N
  - *see* Mahapatra Susanta 411
- Satija Indubala I
  - Fractal characteristics of critical and localized states in incommensurate quantum systems 589
- Satyanarayana S V M
  - *see* Valsakumar M C 69
  - Characterization of chaos in a serrated plastic flow model 871
- Satyavathi V
  - *see* Rao K Rama Mohana 859
- Segar J
  - *see* Sriram M S 205
- Sen A
  - *see* Kaw P K 675
- Sen D
  - Classical limit of scattering in quantum mechanics–A general approach 799
- Sen Gupta N D
  - On periodically kicked quantum systems 977
- Sengupta S
  - 655
- Sengupta S
  - *see* Sen D 799
- Sharma Ashutosh
  - Control methods for problems of mixing and coherence in chaotic maps and flows 231
- Sharma B K
  - *see* Joshi K B 1105
- Sharma K S
  - *see* Gupta Manish 923
- Shastry C S
  - *see* Jamir I 825
- Sheikholeslami S M
  - Non-leptonic weak charmed baryon decays in the $SU(4)$ semi-dynamical scheme 837
- Sheorey V B
  - *see* Santhanam M S 439
- Singh N
  - Activation energy of hydrogen in Lu 1095
- Sinha Somdatta
  - Dynamics of simple one-dimensional maps under perturbation 87
- Sinha Sudeshna
  - Lattice dynamical models of adaptive spatio-temporal phenomena 287
- Sinha Supurna
  - *see* Samuel Joseph 969
- Siruguri V
  - *see* Chakraborty Keka 1115
- Sreenivasan K R
  - *see* Olinger D J 693
- Sridhar S
  - *see* Kudrolli A 459
- Sridhar V
  - *see* Valsakumar M C 69
  - *see* Satyanarayana S V M 871
- Sriram M S
  - Nonlinear chiral models: Solition solutions and spatio-temporal chaos 205
  - *see* Lakshmibala S 617
- Suhail M A
  - *see* Khan Rahman M Z 1027
- Sundaram Bala
  - Quantum chaology: The photoeffect and beyond 469

- Tiwary Satish Kumar
  - Spin state and exchange in the quasi-one-dimensional anti-ferromagnet $KFeS_2$ 1123

- Umapathy Siva
  - *see* Biswas Nandita 937
- Umesh T K
  - *see* Sandiago 1077

Valsakumar M C
  Signature of chaos in power spectrum 69
Varma V S
  see Gadre Sangeeta D 259
Vasudevan Sukumaran
  see Tiwary Satish Kumar 1123
  see Porwal N K
Vijaya Kumar K B
  Meson spectroscopy with confined one gluon exchange potential 997